Global Positioning System (GPS) Measurements in Turkey (1988-1992): Kinematics of the Africa-Arabia-Eurasia Plate Collision Zone

by

M. Burc Oral

B.S. Geophysical Engineering, Istanbul Technical University (1985)
M.S. Geophysical Engineering, Istanbul Technical University (1987)

Submitted to the Department of
Earth, Atmospheric, and Planetary Sciences
in partial fulfillment of the requirements
for the degree of
Doctor of Philosophy in Geophysics

at the

Massachusetts Institute of Technology

March, 1994

Signature of Author .....
Department of Earth, Atmospheric, and Planetary Sciences
March, 1994

Certified by .....
Professor M. Nafi Toksöz
Thesis Supervisor

Certified by .....
Principal Research Scientist Robert W. King
Thesis Co-Supervisor

Certified by .....
Principal Research Scientist Robert E. Reilinger
Thesis Co-Supervisor

Accepted by .....
Professor Thomas H. Jordan
Department Head

Dedicated to the late
M. Ali Gençoğlu,
Nezihi Canıtez
and in memory of
the victims of the
1992 Erzincan earthquake

Global Positioning System (GPS) Measurements in Turkey (1988-1992): Kinematics of the Africa-Arabia-Eurasia Plate Collision Zone

by

M. Burc Oral

Submitted to the Department of Earth, Atmospheric, and Planetary Sciences
on March 14, 1994, in partial fulfillment of the requirements
for the degree of
Doctor of Philosophy

Abstract

Much of the deformation in the eastern Mediterranean is caused by the northerly motion of the African and Arabian plates against the Eurasian plate. As a result, various tectonic features are observed: collision (Bitlis-Zagros, Caucasus), subduction (the Hellenic and Cyprean arcs), strike-slip faulting (the East and North Anatolian and Dead Sea faults) and extension (the North Aegean trough, the Marmara, Gediz, and Büyük Menderes grabens). Most of the constraints for the kinematics of this actively deforming region have been provided by seismological and geological observations. Other than sparse Satellite Laser Ranging (SLR) observations, there are, as yet, no detailed geodetic measurements that would quantify the rates and style of deformation across active boundaries.

Our challenge was to geodetically observe motions across tectonic boundaries and in the interiors of plates, in order to gain insight into the kinematics of the Africa-Arabia-Eurasia collision zone, and to quantify rates of crustal deformation. To meet this challenge we initiated Global Positioning System (GPS) measurements in Turkey in 1988. Since then, we have conducted six GPS experiments simultaneous with the SLR observations. Between 1988 and 1992, 102 GPS sites were occupied over 121 days, and we acquired 2–4 epoch observations at 66 sites. This thesis investigates effective approaches to GPS data analyses and presents the results of these GPS measurements. By providing a GPS derived velocity field for Turkey, we quantify the motions within and across the plate boundaries, and discuss the tectonic implications of geodetically observed rates of crustal deformation.

We used GAMIT/GLOBK software packages to analyze our GPS measurements. In order to handle increasingly volumuous data, we devised and tested a "combi-

nation" approach to data analysis, and applied it to the 1991 and 1992 spring/fall experiments. Our results show that this combination of regional and global GPS measurements effectively provides the highest precision by better determining the orbital parameters of GPS satellites.

Our GPS derived velocity field indicates four major domains, each having distinct kinematics: the Pontus block, the Anatolian and Arabian plates, and the Caucasus domain. The most prominent feature in this velocity field is the Anatolian plate, which is separated from neighboring domains by strike-slip fault zones (East and North Anatolian faults, North Aegean trough), subduction (Hellenic and Cyprean arcs), and collision zones (Bitlis-Zagros suture, Caucasus domain). Given the consistency between GPS and SLR velocities, we have extended the Anatolian plate farther west to include the southern Aegean and Greece. In the east, the velocity field for the Van block, located east of Karlıova, is in concert with that of Anatolia, so we consider it a part of the Anatolian plate as well. The Pontus block has a small amount of motion ($8\pm7_{95\%}$ mm/yr) relative to Eurasia.

As a first approximation to a rigid plate, we parameterize the velocity field observed for the Anatolian plate by Euler vectors, and find that Pontus-Anatolia can be defined by an Euler vector ($_{PON}\mathbf{E}_{ANA}$), located at 33.4±0.5°E, 31.1±1.3°N (north of the Sinai peninsula), with a counterclockwise angular velocity of 1.25±0.15°/Myr. We show that this Euler vector clearly delineates the North Anatolian fault as the boundary and suggests $25\pm8_{95\%}$ mm/yr slip. We also tie GPS observations on the Anatolian plate to the NUVEL-1 model by $_{ARA}\mathbf{E}_{ANA}$ [ϕ=43.2±0.7°E, λ=31.2±1.2°N, ω=1.22±0.15°/Myr]. Predicted slip on the East Anatolian fault is $18\pm12_{95\%}$ mm/yr. We have inferred subduction rates and characterized the internal deformation of the Anatolian plate. Anatolia-Africa motion is $50\pm10_{95\%}$ mm/yr at the Hellenic arc, and decreases easterly to $20\pm10_{95\%}$ mm/yr, converging to the Anatolia-Arabia motion. Our GPS derived velocity field indicates site velocities in western Turkey which are higher by 10 mm/yr than those predicted by these Euler vectors. This suggests that there is a considerable amount of internal deformation. Residuals to rigid plate motion in southwestern Turkey and in the southern Aegean indicate that the roll-back of the subducted African plate beneath the Hellenic arc induces the extrusion of the Anatolian plate as a whole over the African plate. Further, we quantify the partitioning of oblique convergence between the Arabian and Eurasian plates into strike-slip and shortening, and show that Arabian plate motion is transferred to the Anatolian plate. In the Eurasia fixed frame, the strike-slip component is $26\pm14_{95\%}$ mm/yr, while shortening in the Caucasus is about $13\pm 9_{95\%}$ mm/yr.

Our GPS observations suggest that deformation in the eastern Mediterranean is controlled by the collision in the east at the Bitlis-Zagros/Caucasus zones and subduction at the Hellenic arc.

We compare our GPS derived velocity with geological observations by back-rotating the plate boundaries to the Pliocene. We show that the North and East Anatolian faults have sustained the boundaries for the Anatolian plate since the Pliocene. We find that the contemporary motions can account for the total cumulative offset (25 km) along the East Anatolian fault since the Pliocene. Along the North Anatolian fault, the calculated 75km displacement, however, appears to exceed the lower bound (35 km) for geologically observed cumulative slip since the Pliocene. This suggests that the present-day velocities may not be completely projected back into the geological time scale for periods longer than a couple of million years, due to frequent changes in boundary conditions.

We further compute the velocity gradient tensor from GPS and SLR observations and compare them with the strain rates observed from seismic moment tensors. Overall, we find a good agreement between patterns of principal strain rates across the North Anatolian fault and those of the northern Aegean.

Thesis Committee:
Prof. M. Nafi Toksöz (Thesis Supervisor/MIT),
Prof. Bradford H. Hager (MIT),
Prof. Thomas A. Herring (MIT),
Dr. Katharine Kadinsky-Cade (Philips Laboratory, Hanscom AFB).
Dr. Robert. W. King (Thesis Co-Supervisor/MIT),
Dr. Robert E. Reilinger (Thesis Co-Supervisor/MIT),

Acknowledgments

Over the years at MIT (a lot of years!), I have come to understand that a thesis requires advisors to guide and teach, research funds to buy computers and optical platters, and a project with lots of data to do science with. Above all, it takes a very enthusiastic crowd composed of the lords of institute regulations, advisors who wish to meet NSF deadlines and beloved spouse ready to invest in a house to bring the thesis to the end. I have had plenty of all!

I have greatly benefited from Nafi Toksöz, Robert Reilinger and Robert W. King as my advisors. I acknowledge the vision of Nafi Toksöz and Robert Reilinger to conceptualize the GPS experiments in Turkey. Robert Reilinger spending months in the field, executed all experiments with support from Aykut Barka. The Reilinger-Barka team drove hundreds of miles to make the site selections with, so far, only two casualties: One was buried by highway maintenance (Kahta), the other appears to be a wandering boulder (Şebinkarahisar). Aykut Barka's help (from neotectonics to cars) was immense.

Although this is a data-driven thesis, it took several years to accumulate just enough data to measure plate motions. First, there was that wait for data!

James Stowell taught me how to set up a tent so that the GPS receiver would not get wet. I am lucky that I learned how to operate GPS receivers from James Stowell; since his drills, the image of the Trimble screen has never left my dreams. I must admit that one experiment in Turkey and another in southern California were enough for me. Not that I did not like setting up the tripod and observing the GPS satellites, it just left me too little time for diving into the pool in Indio, CA (N/A in eastern Turkey!).

In the mean time, Nafi Toksöz got me interested in finite element modeling. Thus I became a frequent visitor at the Aeronautics department. Professor Theodore Pian introduced me to contact mechanics. It sure was not enough to model plate motions in 2-D. By the time I started to conceive the relation between impact mechanics and plate tectonics, the GPS data and visitors began to arrive. Then, there was the rush for results!

Barb Perin tutored me on GPS analyses with Bernese software, but, later Kurt Feigl convinced me of the beauty of GAMIT. Without Kurt's help I would have taken another year to adapt GAMIT to DECstations. He also introduced me to UNIX shell scripts. Mark Murray showed me what fiducials and SV5 are. His excellently written thesis has been my Bible to GPS. Da-nan Dong answered all my questions after Kurt and Mark left MIT. I stole quasi-observation jargon from him. His thesis is yet

another Bible for GPS.

Robert W. King "fathered" my thesis. He taught me almost everything about GPS analysis. We spent quite a bit of time an all aspects of GPS data analysis. He had patience and wisdom. He never shooed me out of his office (This sentence, with all due respect, is stolen from Kurt Feigl's thesis!).

I have greatly benefited from discussions with Thomas A. Herring. He answered all of my naive questions about GLOBK, which led to Appendix A (the combination stuff).

Brad Hager insisted that I measure velocities rather than naive finite element models which had a number of rheological assumptions. And, I have learned a lot from the lengthy discussions with Katharine Kadinsky-Cade.

In addition to our own, regional GPS observations in Turkey, General Command of Mapping of Turkey provided the GPS measurements conducted at the Bozdağ network sites in 1989 and at the Marmara network sites in 1990 and 1992, as well as the GPS measurements at the Ankara permanent station. I thank Gillian Foulger (Durham University, England) and Hans-Gert Kahle (Eidgenössiche Technische Hochschule-Zurich, Switzerland) for allowing me to use their data from the Bozdağ and Marmara networks. I also thank Peter Wilson and Hermann Seeger (Institute für Angewandte Geodäsie, Germany) for providing the GPS measurements at the SLR collocation sites.

No GPS analysis is complete without global tracking data. Indeed, the global tracking data used in this thesis comprise two thirds of the millions of observations. The bulk of the earlier global data were retrieved from NGS for which I appreciate the assistance of Ernie Marion, Miranda Chin, and Linda Nussear. Some global data for the 1991 experiment were provided by David Starr at JPL. For later experiments, 1991 and onward, the SIO GPS Orbit Facility not only provided the raw global tracking data, but also global solutions, along with cleaned, one-way GPS observables. Special thanks to Yehuda Bock, Keith Stark, and Shimon Wdowinski at the SIO GPS Orbit Facility. Without their global analyses, I would have not been able to devise and test global-regional combination.

Several colleagues from Hacettepe, Istanbul and Bosphorus Universities gave us a hand in the field by patiently sitting next to the GPS receivers. The General Command of Mapping (Turkey) staff greatly contributed to the field operations and tedious data translation. Special thanks to Maj. Ömür Demirkol, Maj. Ibrahim Kınık, Capt. Onur Lenk, Lt. Ulvi Kocailik, and Lt. Kemal Şahin at the General Command of Mapping, Turkey. Judah Levine and Myron McCallum at UNAVCO

and Werner Gurtner at the Astronomical Institute of Berne, Switzerland helped me to solve rather obscure data translation problems.

I have benefited from discussions and correspondence with several colleagues at various occasions: Boudewijn Ambrosius, Reneta Dmowska, Levent Gülen, Ken Hudnut, Hans Kahle, Kim Kastens, Shawn Larson, Christine Larson, Chiching Liu, Robert McCaffrey, Simon McClusky, Peter Morgan, Stephan Mueller, Ron Noomen, Erricos Pavlis, Jim Rice, John Robbins, Doug Roberts, Leigh Royden, Wolfgang Seemueller, Paul Sellers, David Smith, Christian Straub, Mark Torrence, and Tonie VanDam.

At the Earth Resources Laboratory, Jane Maloof and Albert Taylor tried to meet my computer demands. Linda Meinke, at the Green Building, always came up with solutions for my system problems. Thanks to fellow students at the Earth Resources Laboratory, Ted Charrette, Robert Cicerone, Joseph Matarese, Ed Reiter, Craig Schulz, and Lynn Smith, for their friendship.

Last but not least, I am grateful to my wife, N. Leah Crandall. If it were not for her companionship, I would have been lost. She has read every single line of this thesis, I have forgotten how many times. I believe that her excellence in editing all of my papers earned her a minor in geophysics.

This thesis has been typeset with LaTeX and its graphics were produced with Generic Mapping Tools (GMT) [Wessel and Smith, 1991]. Two figures had to be generated by Facility for Interactive Generation of figures under X11 (Xfig). All analyses were performed on DECstations and SUN SparcStations.

Major support for this thesis came through a fellowship from the Ministry of Education, Turkey. This project has been funded by NSF Grant EAR-8709461 and NASA Grant NAGW-1961.

Contents

Chapter 1

Introduction

Crustal deformation in Turkey (Türkiye) is a piece of the mosaic in the framework of the eastern Mediterranean (Figure 1-1). Here, deformation is controlled by the interaction of the African, Arabian and Eurasian plates. Much of the deformation in the eastern Mediterranean is caused by the northerly motion of the African and Arabian plates against the Eurasian plate. As a result, various tectonic features including subduction, strike-slip faulting and extension are recognizable in this area: e.g., the North Anatolian fault, the western Turkey grabens, the Bitlis-Zagros collision zone, the Hellenic arc, etc.

Most of the constraints for the deformation of this region are provided by global plate models, in which spreading rates, earthquake slip vectors and transform fault azimuths are used (see Westaway [1990] for discussion). There are, as yet, no extensive geodetic measurements, other than sparse Satellite Laser Ranging (SLR), observations that would quantify the rates and style of deformation across active boundaries. The immediate challenge of this thesis is to geodetically observe motions across tectonic boundaries and in the interiors of plates in order to gain insight into the kinematics of

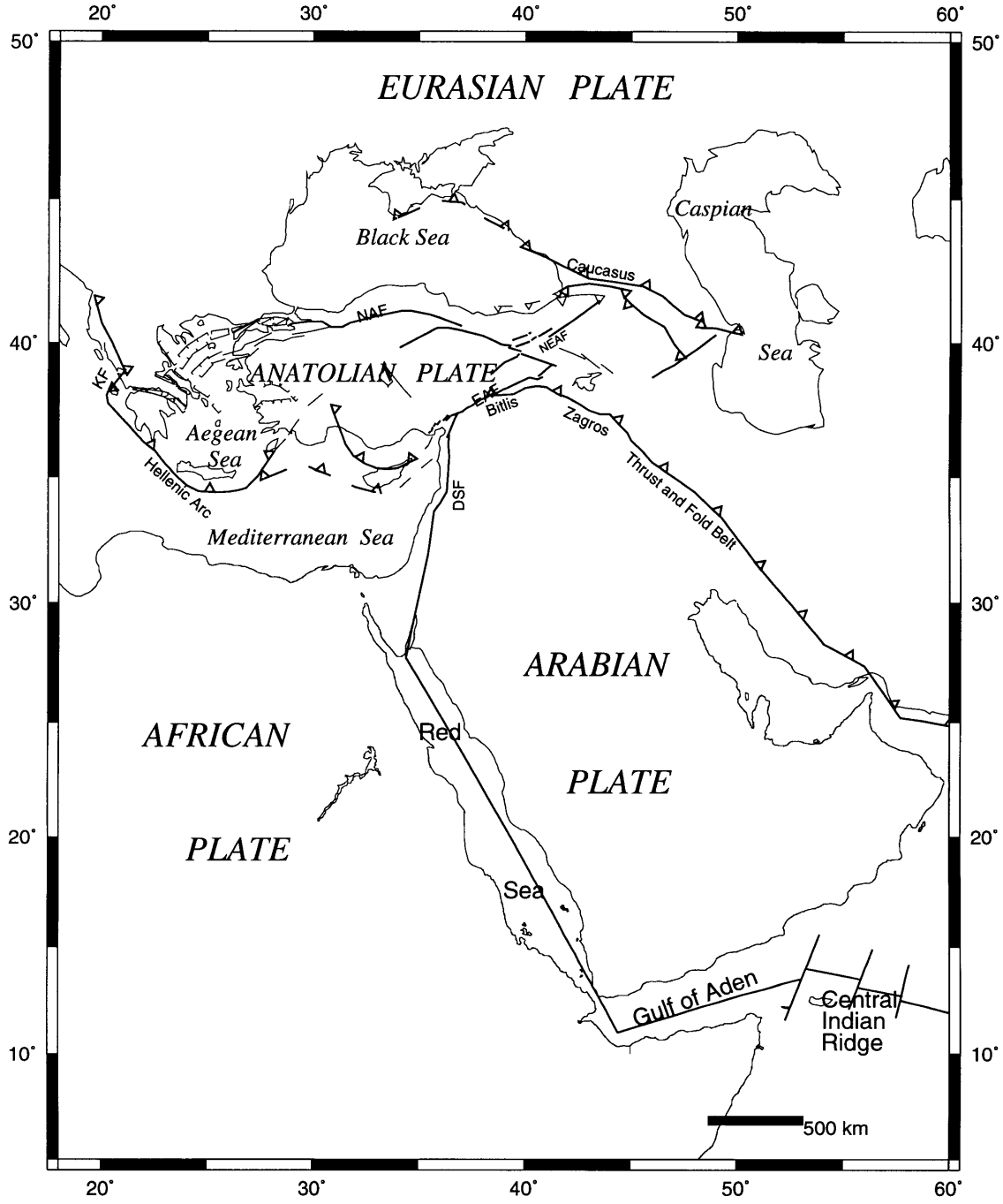

Figure 1-1: Tectonic elements of the Middle East. Thick lines: major faults and plate boundaries. Thin lines: minor faults. Ticks are shown on the downthrown side of the faults. Open triangles are on the overriding plate. NAF: North Anatolian fault, EAF: East Anatolian fault, DSF: Dead Sea fault, NEAF: Northeast Anatolian fault, KF: Keffalinia fault. Also, see Figure 1-2. Compiled from Hempton[1987], Şengör et. al [1985], Aykut Barka [pers. comm., 1991], Levent Gülen [pers. comm., 1993]., Le Pichon and Angelier, [1979], Kiratzi and Langston, [1991]

this active region, and to estimate rates of deformation in the eastern Mediterranean, particularly in Turkey.

1.1 Objectives and Contributions

To meet this challenge we initiated Global Positioning System (GPS) measurements in Turkey in 1988. Since then, six GPS experiments have been conducted in Turkey simultaneously with SLR observations in the Aegean. Between 1988 and 1992, we occupied 102 GPS sites with 2-4 epoch observations at most of them.

In an attempt to constrain the kinematics of the eastern Mediterranean, this thesis presents the results of GPS measurements obtained between 1988 and 1992. We investigate effective approaches to data processing and discuss the tectonic implications of our results.

The objectives of this thesis are two-fold:

1. To collect and analyze GPS data in order to obtain rates of deformation, constrain the kinematics of the eastern Mediterranean, and gain insight into its driving mechanisms;
2. To develop and test robust alternative approaches in GPS data reduction which are geodetically sound, and utilize them in the analyses of the Turkish data.

Objective 1 is the primary goal and is discussed in Chapters 2 and 3, as well as in Appendices B, C, and D. Objective 2 is required for Objective 1 and, for succinctness, is presented in Appendix A.

In addition, this thesis makes other contributions:

1. Estimating co- and post-seismic deformation, due to the 13 March 1992 M=6.9 Erzincan earthquake;

2. Establishing a unified GPS geodetic network in Turkey by combining data from Durham (England), IfAG (Germany)[1], ETH-Z (Switzerland)[2] and GCM (Turkey)[3] GPS networks;

3. Providing a basis for combining the Turkish network with the Caucasus network (The second epoch observations planned for 1994 should enable us to compute overall shortening across the Eurasia-Arabia collision zone);

4. Providing a basis for combining GPS and SLR data with their respective quasi-observations.

1.2 Outline

A brief review of the tectonic setting and neotectonic evolution of the eastern Mediterranean is given in the next section (1.3)

Chapter 2 focuses on overall analyses of the GPS observations between 1988 and 1992, and the derivation of site velocities. The tectonic implications of GPS derived velocities are addressed in Chapter 3. These velocities are compared to those derived from global plate motions, earthquake slip vectors and SLR. We also derive Euler vectors for the Anatolian plate, and present strain and rotation fields obtained from velocity gradient tensor analysis.

Approaches to combining global and regional/local GPS data are developed and

[1]Institute für Angewandte Geodäsie.
[2]Eidgenössiche Technische Hochschule-Zurich.
[3]General Command of Mapping.

presented in Appendix A. Results of extensive testing, carried out using the 1992 spring data, are also reported in this appendix. To provide continuity and conciseness, the description of GPS measurements, analyses, and short-term precision of each experiment are allocated to Appendix B. Appendix C focuses on the analysis of long-term errors. Co- and post-seismic deformation by the 13 March 1992 M=6.9 Erzincan Earthquake within our GPS network are reported in Appendix D.

1.3 Tectonic Setting

Present-day kinematics and active deformation in the eastern Mediterranean are governed by the interaction of three major plates (Eurasia, Arabia and Africa), as well as other small plates/blocks (Figure 1-1). The bulk of deformation in the region appears to have originated from subduction and collision related processes, i.e., the forces applied at the plate boundaries [Şengör et al., 1985]. The style of present-day deformation, however, is closely related to the stage of collision, specifically, to the rate of convergence and subduction (Royden and Burchfiel [1989]; Royden [1993a,b]).

Present-day tectonic deformation of the eastern Mediterranean region (Figures 1-1 and 1-2) is closely related to the northerly motion of the Afro-Arabian plate relative to Eurasia, and to the medial to late Eocene (23 to 50 Ma) events in the Red Sea [Hempton, 1987]. During this period, Africa and Arabia formed a single plate and the continental margin of the Arabian platform collided with the Eurasian plate, closing the back arc basin of the Tethys. Thus, suturing began as subduction of Africa beneath Eurasia continued. As this process progressed into the early Miocene (20 Ma), the extension in the Red Sea and Gulf of Aden was accommodated by the separation of Arabia from Africa, resulting in the rapid convergence of the Arabian plate against Eurasia. Contemporaneously, the Dead Sea fault initiated.

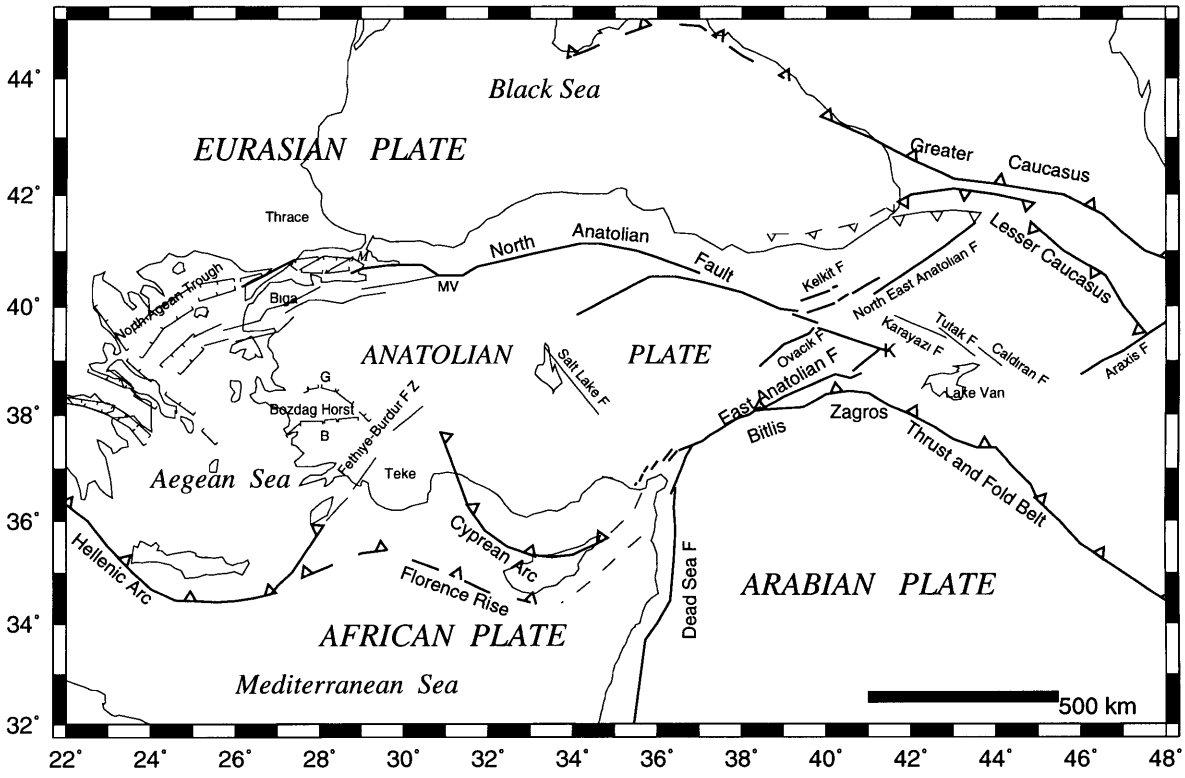

Figure 1-2: Tectonics elements of the eastern Mediterranean. M: Marmara, K: Karlıova, G: Gediz breakaway zone, B: Büyük Menderes breakaway zone. Compiled from Hempton[1987], Şengör et. al [1985], Aykut Barka [pers. comm., 1991], Levent Gülen [pers. comm., 1993], and Le Pichon and Angelier [1979].

By medial Miocene, the wide continental margin of Arabia was consumed, arresting its independent northerly motion. Subsequently, the first phase of extension in the Red Sea came to an end, as did the left-lateral motion along the Dead Sea fault. Arabia and Africa, however, continued moving northward as a single plate, causing excessive crustal thickening and shortening, and uplift in the convergent zone, until the early Pliocene (5.2 Ma). The resulting convergent stresses were alleviated by the extrusion of continental wedges along transform faults [McKenzie, 1972]. Therefore, between late Miocene (14–10 Ma) and early Pliocene (5–3 Ma), Anatolian strike slip faults (the North and East Anatolian faults) were initiated [Şengör, 1979; Le Pichon and Angelier, 1979; Barka and Hancock, 1984] and the Anatolian plate (see below

and Chapter 3) started to wedge out of the zone of maximum compression. Such escape tectonics along transforms triggered Arabia to move independently of Africa [Le Pichon and Gaulier, 1991]. Consequently, the second stage of the Red Sea's opening commenced, providing a faster convergence rate for the Arabian plate. Şengör and Yılmaz [1981], Robertson and Dixon [1984], Şengör [1987a], Gealey [1988], and Mueller and Kahle [1993] review the tectonic and geological evolution of the eastern Mediterranean within the Alpine-Himalayan orogenic belt, and its collisional development.

The westerly motion by Anatolia relative to Eurasia, continental collision by the Adriatic plate against NW Greece and Albania, and by Arabia against Eurasia, and the subduction at the Hellenic arc control the present-day kinematics of deformation in the eastern Mediterranean. West of the Caspian Sea, the active deformation is driven by oblique convergence by the Arabian plate against Eurasia, the subsequent buoyancy forces arising from differential crustal thickness, and the slab-pull (or roll-back) at the Hellenic arc and subsequent extrusion of Anatolia over Africa. However, a rather lucid picture of overall deformation can be formed by considering the Hellenic arc and the Bitlis-Zagros/Caucasus as retreating and advancing plate boundaries, respectively [Royden, 1993a, b, pers. comm., 1994].

The subduction of the African plate, which initiated 40–26 Ma [Spakman et al., 1988], and the later collision of Arabia against Eurasia around middle Miocene, which marked the onset of the neotectonic period for Turkey [Şengör, 1985], caused drastic changes in the tectonic evolution, and has lead us to observe a number of coexisting tectonic regimes in this section of the Tethian belt (Figure 1-2): a continent-continent collision zone (Bitlis-Zagros, Caucasus); an extensional province (western Turkey, the northern Aegean Sea, southern Greece); major transform faults (the North, East and Northeast Anatolian faults, the Dead Sea fault); and different stages of subduction (the Hellenic and Cyprean arcs, the Black Sea). (For further discussion see, e.g.,

Barka and Kadinsky-Cade [1988], Ben-Menahem [1991], Jackson [1992], Jackson and McKenzie [1984, 1988], Lort [1978], Lyberis [1984], McKenzie [1970, 1972], Philip et al. [1989], Şengör [1985], and Taymaz et al. [1991a, 1991b].) The surface expression of these tectonic features is reflected in the bathymetry and topography of this region. Figure 1-3 illustrates the pronounced impressions of collision at the Bitlis-Zagros and Caucasus ranges, of extensional features in the Aegea, and of the Hellenic arc, etc. Present day topography of eastern Anatolia, extending to the Caspian Sea, is much higher than that of western Turkey and Aegea. Crustal thickness in the Aegea, deduced from seismic profiles and Bouguer gravity, is 20–30 km [Makris and Stöbbe, 1984]. Inversion of Bouguer gravity shows that the Moho depth beneath eastern Turkey reaches to 45–50 km [Oral et al., in prep.]. These data suggest that although buoyancy forces arising from differential crustal thickness did not play a role in the initiation of the westerly escape of Anatolia [Şengör et al., 1985], it may maintain the present-day escape.

Based on the epicentral distribution and focal mechanism solutions of large earthquakes, McKenzie [1972] recognized several small plates in this region of active deformation: Turkey, the Aegean, the Black Sea, Iran and the Caspian . The epicentral location of earthquakes ($M > 4$) illustrates the diffuse nature of seismic activity in the eastern Mediterranean (Figure 1-4) and their general association with tectonic features. Focal mechanisms of major earthquakes which occurred in this century (Jackson [1992], Eyidoğan [1988], Jackson and McKenzie [1988]) have demonstrated the underthrusting of the African plate at the Hellenic arc, the back-arc extension in the Aegea, the strike-slip motion across the North and East Anatolian faults, and the collision at the Caucasus and Bitlis-Zagros belt (Figure 1-5).

Global models for present-day plate motions, using spreading rates, earthquake slip vectors, and transform fault azimuths, show that the Arabian plate converges against Eurasia faster than the African plate [Minster and Jordan, 1978; Chase,

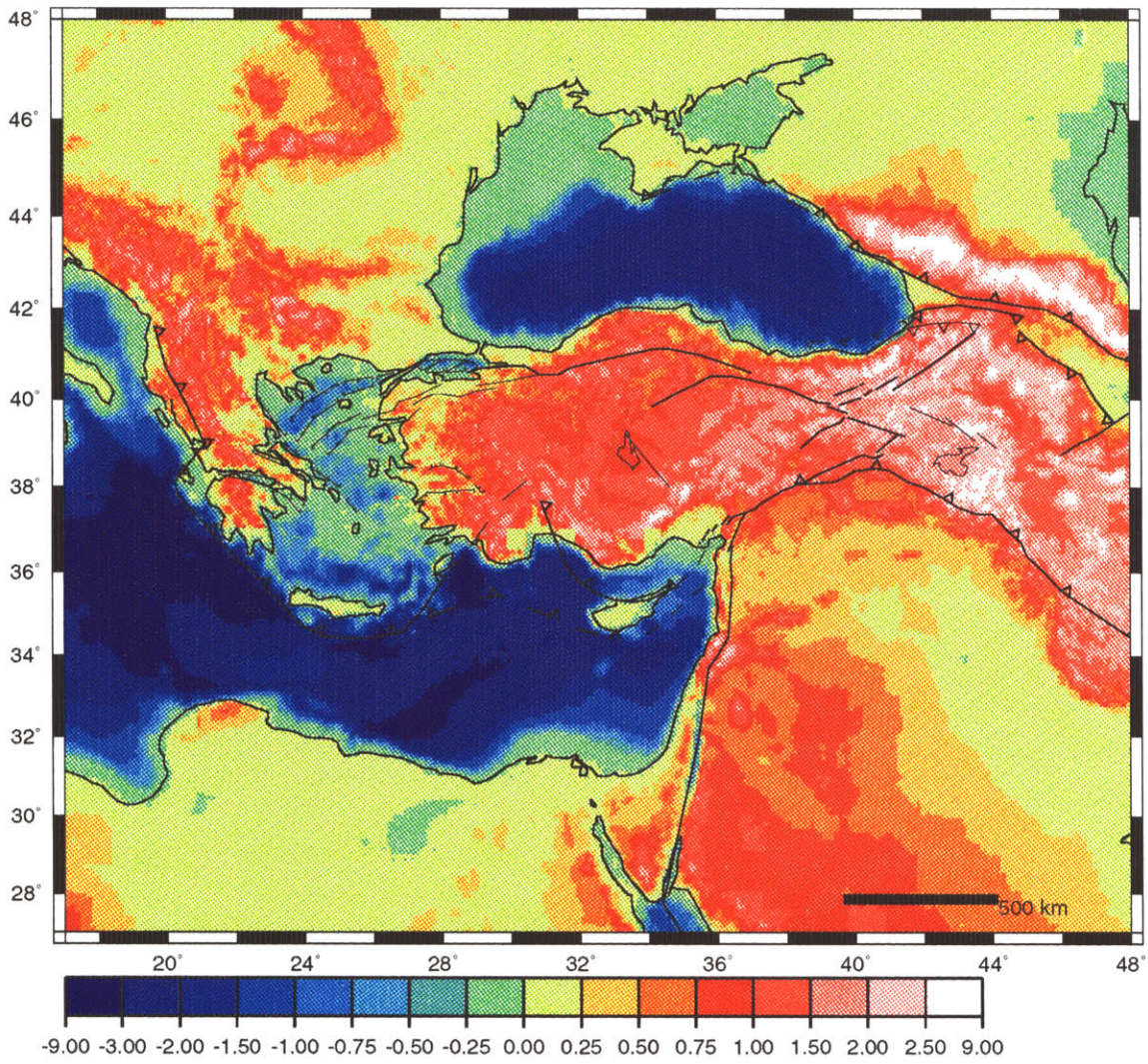

Figure 1-3: Topography and bathymetry.

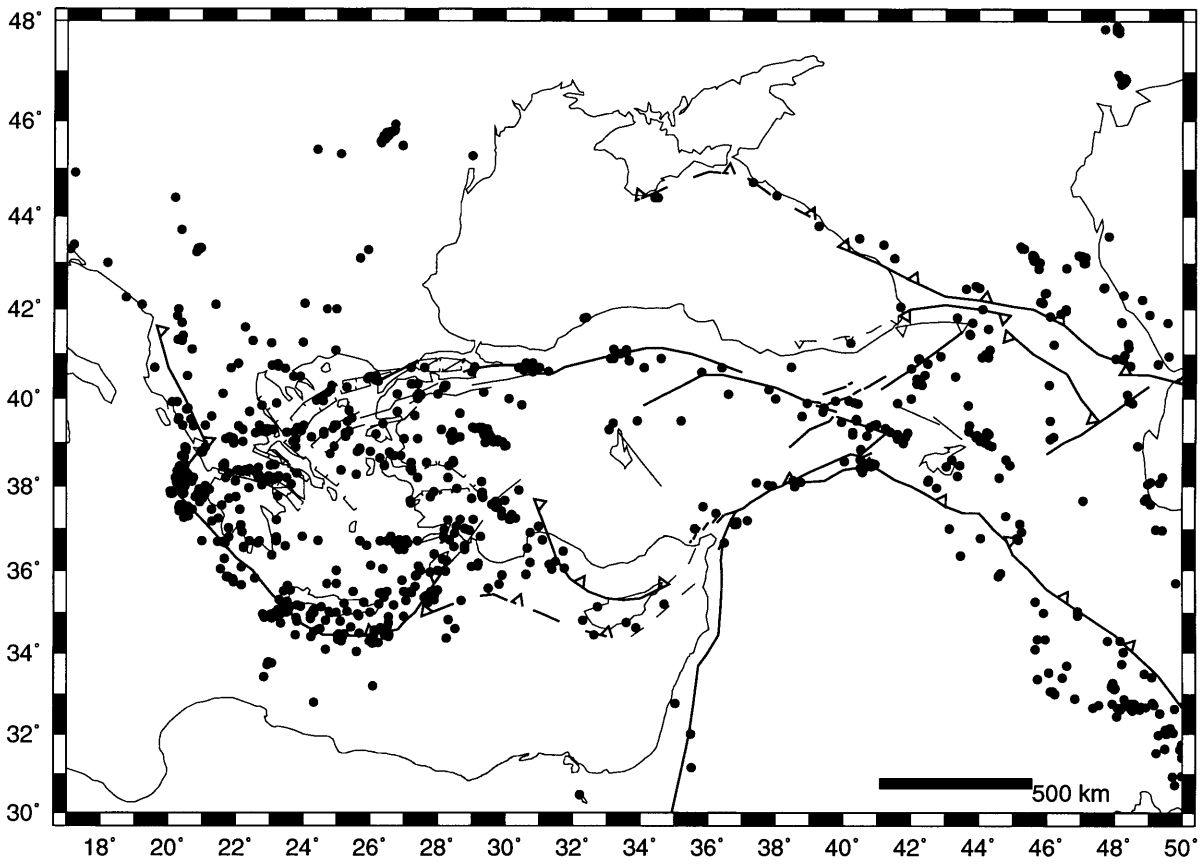

Figure 1-4: Locations of earthquakes with magnitude greater than 4. Compiled primarily from ISC data (1964-1989). We have also added locations of earthquakes for earlier/later periods reported by Jackson [1992], Eyidoğan [1988], Jackson and McKenzie [1988].

1978; Gordon and Jurdy, 1986; DeMets et al., 1990]. Figure 1-6 shows NUVEL-1 rates for Arabia and Africa relative to Eurasia. The differential motion between Arabia and Africa with respect to stable Eurasia, taken up along the Dead Sea fault, amounts to ~12 mm/yr (from De Mets et al., 1990). The African plate, which has been moving northward relative to Eurasia since 95 Ma, converges on Eurasia at ~10 mm/yr (from De Mets et al., 1990). The NUVEL-1 data for the relative motion of Eurasia and Africa is obtained from the Azore-Gibraltar ridge, and that for Arabia and Africa comes from the Sheba ridge in the Gulf of Aden. Because there are no data for the relative motion between Eurasia and Arabia, this motion is indirectly

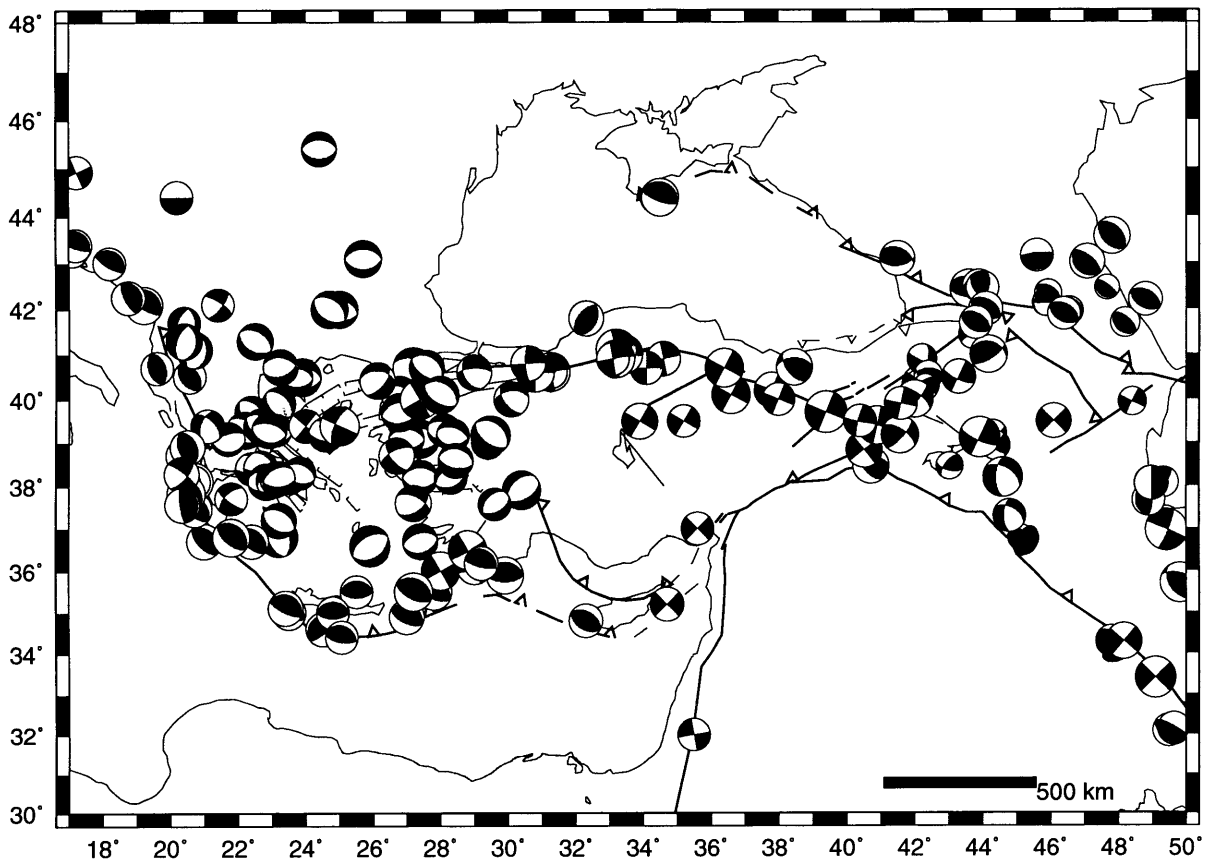

Figure 1-5: Focal mechanisms of major earthquakes in the eastern Mediterranean (projected to the lower hemisphere). Compiled from Jackson [1992], Eyidoğan [1988], Jackson and McKenzie [1988].

calculated from plate circuits. The data pertaining to Eurasia-Africa relative motion has been gathered outside the Mediterranean. Since the Nubia-Somalia motion is neglected, the spreading rates from the Red Sea do not constrain the Arabia-Africa motion. Further problems arise due to the diffuse nature of regional continental deformation which make rigid plate assumption less valid [McKenzie, 1977]. Because global models for present-day plate motions do not consider small plates/blocks in the eastern Mediterranean, evidence for relative motions in Turkey cannot be obtained from NUVEL-1. In Figure 1-6 we also show rates for eastern and western regions of the collision zone computed from Euler vectors reported by Jackson and McKenzie, [1984] (also see Table 3.2). The plate velocities at the Europe and Aegean consum-

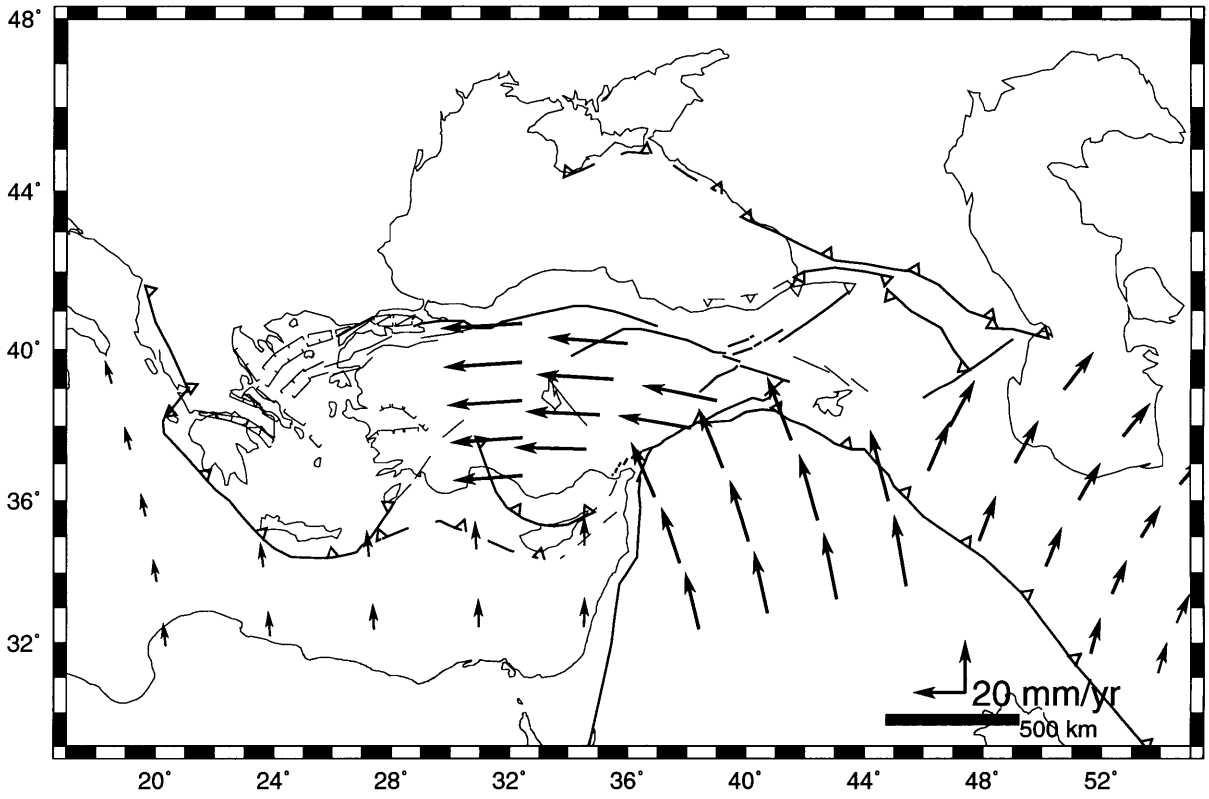

Figure 1-6: Plate velocities in the Eastern Mediterranean relative to Eurasia. NUVEL-1 motions for Eurasia-Africa [ϕ=-20.612°E, λ=21.026°N, ω=0.128°/Myr] and Eurasia-Arabia [ϕ=13.737°E, λ=24.564°N, ω=0.520°/Myr] are calculated from DeMets et. al [1990]. (No rescaling has been applied to NUVEL-1 rates as suggested by recent revisions in the time scale.) We used Table.2 of Jackson and McKenzie [1984] for Eurasia-Turkey [ϕ=34.0°E, λ=14.6°N, ω=.643°/Myr] and Eurasia-Iran [ϕ=65.8°E, λ=27.5°N, ω=-0.56°/Myr]. All motions are calculated on small circles.

ing boundary are oriented SW and decrease from 40 mm/yr (western Hellenic arc) to 15 mm/yr (eastern Hellenic arc) [Le Pichon and Angelier, 1979]. The horizontal velocity field obtained from seismic moment tensors for the Aegean [Jackson et al., 1992] suggest that Aegean region moves SW at 30 mm/yr relative to Eurasia. Jackson and McKenzie [1984] (also see McKenzie [1972]) foresaw a westerly motion for Turkey at 30 mm/yr and a northwesterly motion for Iran at 15 mm/yr . To obtain Euler vectors they used global plate motions [Chase, 1978] and slip vectors of

earthquakes which occurred on the North and East Anatolian faults, in the Gulf of Antalya and in central to western Turkey (*cf. their Fig.7*) for Turkey, and of earthquakes in the Zagros for Iran. Based on the agreement between the slip vectors and motions computed from Euler vectors, they concluded that Iran and central Turkey could be described as plates [McKenzie 1970; 1972] and that their rates of internal deformation were considerably smaller than those of the adjacent belts. Although Rotstein [1984] disagreed with such a distant pole of rotation and suggested that central Turkey could have some degree of internal deformation and thus could not be considered as a rigid plate, he supported the presence of two distinct blocks (the Anatolian and Aegean blocks) west of Karlıova (the juncture of the EAF and the NAF). Furthermore, he suggested that the rotation of Anatolia was also a natural consequence of counterclockwise rotation of the Arabian plate.

Anatolia continues to accommodate shortening by westward drift along the dextral North and sinistral East Anatolian strike-slip faults. The rate of dextral slip across the NAF estimated from earthquake and geologic studies, however, is quite uncertain, with values reported between 5 and 30 mm/yr (e.g., Şengör [1979]; Barka and Hancock [1984], Barka and Kadinsky-Cade [1988]). West of the Mudurnu valley the NAF gains an extensional component [Barka and Kadinsky-Cade, 1988] and this feature becomes dominant in the North Aegean trough [Lyberis, 1984; Taymaz et al., 1991a]. Although the central province of the Anatolian plate manifests relatively little internal deformation (termed "ova" by Şengör[1985]), the western province (western Turkey) is rich in extensional features. The Büyük Menderes and Gediz breakaway zones (see Figure 1-2), and their cross horsts and grabens [Şengör et al., 1985; Şengör, 1987b], demonstrate N-S and E-W extension, respectively. As for the NAF, there is considerable uncertainty in the sinistral slip rate for the EAF. Geological observations suggest that the slip rate along the East Anatolian fault is ~5mm/yr [Gülen et al., 1987]. Using the slip vectors obtained from earthquakes along the East Anatolian fault, and Euler vectors for the Arabia-Eurasia (NUVEL-1) and Turkey-Eurasia pairs

(revised after Jackson and McKenzie [1984], but not significantly different), Taymaz et al. [1991b] suggest a 29±5 mm/yr motion across this fault, which is comparable to the value 34 mm/yr reported by Jackson and McKenzie [1988]. From the focal mechanisms of earthquakes in eastern Turkey and the Caucasus, Jackson [1992] suggested that the oblique convergence of Arabia against Eurasia is partitioned into pure strike-slip motion in eastern Turkey and a pure shortening in the Caucasus. Seismic moment tensor analyses by Jackson [1992] suggest that seismicity accounts for 4 mm/yr shortening in the Caucasus by thrusting.

In the eastern Mediterranean, indirect methods of estimating plate motions and their probable uncertainties, and the lack of quantitative knowledge for contemporary deformation, are important reasons for using space geodetic methods (SLR and GPS) to obtain direct measurements of plate motions and deformation.

The SLR method is a two-way ranging method, operating at visible EM frequencies. In this method the time of flight of a laser pulse between observing station and satellite, which has corner reflectors, is measured and then converted to distance. With third generation laser-systems, accuracies of 1–3 cm are possible [Seeber, 1993]. After the launch of the LAGEOS I satellite in 1976 [e.g., Cohen and Smith, 1985], the WEGENER-MEDLAS[4] project [Reinhart et al., 1985; Wilson and Reinhart, 1993] provided a basis for the acquisition of space geodetic data that would quantify deformations in this very active region. The first observational campaign started in 1986. Published results for the eastern Mediterranean sites include four sites in Turkey (1987, 1989) and six sites in Greece (1986, 1987, and 1989) which were occupied with mobile laser systems ranging to LAGEOS I. SLR observations in the eastern Mediterranean provide direct measurement of plate deformation. Analyses of normal point data show a right lateral motion across the North Anatolian fault [v_H=10–30±$10_{95\%}$

[4]Working Group of European Geoscientists for the Establishment of Networks for Earthquake Research Mediterranean Laser Ranging.

mm/yr], convergence between Arabia and Eurasia by $32\pm6.0_{95\%}$ mm/yr, and south-westerly motion in the Aegea [$30\text{–}50\pm10_{95\%}$ mm/yr] relative to Eurasia [Sellers et al., 1991; Noomen et al., 1993; Cenci et al., 1993; Wilson and Reinhart, 1993; Reigber et. al, 1993; Gendt et. al, 1993]. The SLR velocities reported, however, vary from one study to another by a couple of cm/yr, since they do not share common datum and analysis parameters. In our study we will exclusively refer to the SLR estimates provided by Noomen et al. [1993], because their coordinate system is rigidly attached to the European plate, and that makes their approach very similar to ours. They also tabulate estimates and uncertainties (but not correlations) in a fashion convenient for meaningful graphic reproduction. The SLR derived velocity field in the eastern Mediterranean, relative to Eurasia, is illustrated in Figure 1-7.

1.4 Why GPS?

As discussed, global plate models do not account for small plates, such as Anatolia, in the eastern Mediterranean. Motions for small plates in this region, which are deduced from earthquake slip vectors, lack direct magnitude information. Although SLR observations provide constraints on contemporary deformation, SLR site distribution in the eastern Mediterranean is rather sparse due to the high cost of transporting and operating a mobile system. Therefore, the nature of tectonic deformation is not known for the region between between central Turkey and Greece or eastern Turkey, and across active faults in Turkey.

In the last decade, geodetic measurements of crustal deformation using NAVSTAR[5] GPS, with cost-cutting($2,000 site/year with overhead and research costs!), brief-case size instrumentation and minimal maintenance, have proven successful (see e.g., Bevis

[5]NAVigation System with Time and Ranging.

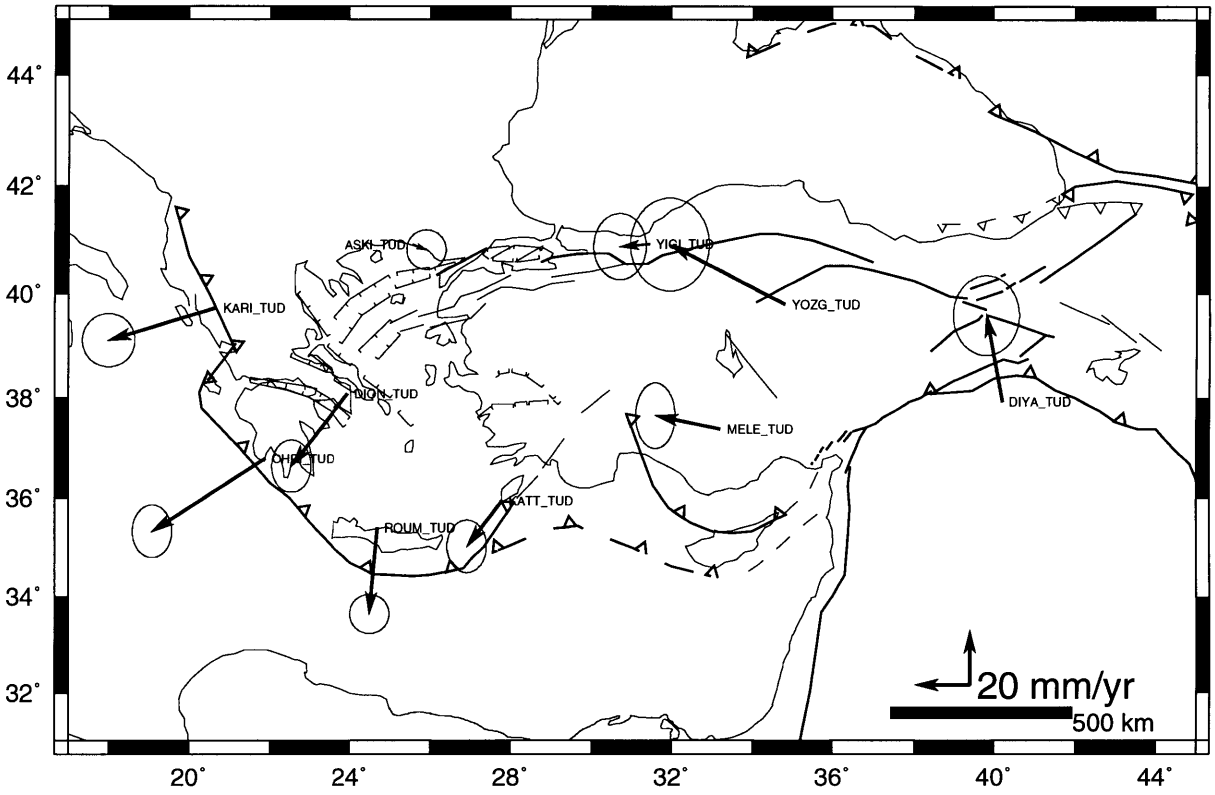

Figure 1-7: Observed velocities relative to the Eurasian plate estimated from SLR observations between 1986 and 1990 [Noomen et al., 1993]. The ellipses denote the 95% confidence region. Because no correlation information was available for the SLR estimates, the area of 95% confidence is defined by circles. SLR sites not common to our GPS experiments are Askites [ASKI], Chrisokellaria [CHRI], Dionysos [DION], Karitsa [KARI], Kattavia [KATT], and Roumeli [ROUM]. GPS measurements (Chapters 2 and 3) have been collected at Melengiçlik [MELE], Yığılca [YIGI], Yozgat [YOZG], and Diyarbakır [DIYA].

et al. [1990]; Kellog and Dixon [1990]; McCaffrey [1990]; Feigl et al. [1993]; Shimida and Bock [1992]; Billiris [1991]; Heki et al. [1993]; Oral et al. [1993]). GPS measurements have further advantages over terrestrial methods: They offer higher precision and accuracy and are less time consuming. Also, they do not require interstation visibility and can be performed for much longer baselines (~1000 km).

GPS is a passive radio navigation system which utilizes transmissions from satel-

lites deployed at an altitude of three earth radii (see, e.g., Janiczek [1980, 1984, 1986]). These satellites have nearly circular orbits and complete a revolution about the earth in 12 hours. There are six orbital planes inclined at 55°, each of which will eventually contain four satellites. All GPS satellites have atomic clocks aboard. Currently 26 GPS satellites are operational (including those Block I satellites launched earlier at orbital planes inclined at 63°).

Each GPS satellite transmits a unique spread-spectrum signal at two carrier frequencies in L band (L_1 and L_2) which are modulated with the P and/or C/A codes and the ephemeris message [Spilker, 1978]. Using the pseudo-range (code measurements), the system provides real-time, three-dimensional positioning as well as navigational and time information. Once the positions of four satellites are known, the time and position of the ground receiver can be calculated using range information with some algebra and trigonometry.

These measurements allow a 10- to 100-meter accuracy in real time. Unfortunately, this mode of operation would require us to wait another millenium or so to delineate crustal deformation. Alternatively, we can use the phase measurements of the carrier wave, possible at the level of 1–2 mm (e.g., Counselman and Shapiro [1979]; King et al. [1985]). The key to achieving this level of accuracy in relative positioning is a better determination of satellite orbital motion than that provided by the broadcast ephemerides, which have an accuracy of 1 to 0.1 ppm. Orbital improvements to the level of ~0.01 ppm can be achieved by including observations from a global network of ground trackers in the solutions.

The carrier phase, or carrier beat phase, is the difference between the wave generated by the receiver's oscillator and the incoming Doppler-shifted satellite signal. Each receiver type (code correlating, codeless, P-code) has a different way of carrier phase reconstruction. Carrier phase measurements, though not as much as pseudor-

ange measurements, are vulnerable to multipath effects (reflections from surrounding structures) and ionospheric perturbations. They are also ambiguous. The initial integer-cycle ambiguity is unknown, but can be computed from a linear combination of doubly differenced carrier phases [Dong and Bock, 1989].

With dual-frequency observations, we can construct a linear combination (LC observable) of the two L-band observations(L_1 and L_2) to reduce the dispersive effects of the ionosphere below 1 mm (most of the time). Double-differencing is an effective way to reduce the clock effects of both the receivers and the satellites (for discussion see Feigl [1991]). The troposphere also presents a complication for the propagation of radio waves, however, the resulting delay at the zenith can be modeled to an extent by assuming standard surface temperature, pressure and relative humidity (see Appendix B).

Further information on GPS and its applications to geophysical studies can be found in reviews by Dixon [1991] and Hager et al. [1991]. Also, books by Wells [1986], Leick [1990] and Seeber [1993] offer detailed descriptions of GPS theory and general applications.

In the next chapter we present our GPS observations from experiments conducted between 1988 and 1992 in Turkey, and analysis approaches to deriving a velocity field for Turkey.

Chapter 2

Analyses of GPS Measurements in Turkey: 1988-1992

2.1 Regional GPS Measurements

In 1988 we initiated a five year program to measure crustal deformation in Turkey, using the Global Positioning System (GPS). During this period we conducted 5 regional GPS experiments. Following the 13 March 1992 Ms=6.8 Erzincan Earthquake, as an emergency response, we conducted an additional GPS survey to quantify the co-seismic deformation in the earthquake area and to establish a basis for monitoring possible post-seismic deformation. Each experiment took approximately 3 weeks and was realized with support from UNAVCO[1], and in collaboration with TUJJB (Turkey)[2] and GCM (Turkey)[3]. Several universities in Turkey (Hacettepe University, Bosphorus University and Istanbul Technical University) contributed to data acqui-

[1]University NAVSTAR Consortium.
[2]Turkish Union of Geodesy and Geophysics.
[3]General Command of Mapping.

Table 2.1: GPS experiments and networks observed in Turkey between 1988 and 1992.

Experiment	Year	MIT Core Network	Additional Network
1	1988	western Turkey	
2	1989	eastern Turkey	Bozdağ
3	1990	western Turkey	Marmara
4	1991	eastern Turkey	
5	Spring 1992	Erzincan earthquake	
6	Fall 1992	western Turkey	Marmara
		Erzincan earthquake	Bozdağ

sition. Due to the logistical constraints imposed by large interstation distances, we carried out our experiments in western and eastern Turkey in alternate years: the western network in 1988, 1990 and 1992, and the eastern network in 1989 and 1991 (Table 2.1). We reobserved the Erzincan earthquake control network sites in the fall of 1992, simultaneously with the western Turkey experiment. To tie the eastern and western networks together, we utilized GPS data collected at 2-4 common sites during each regional survey, including the data from the Ankara permanent site.

In addition to our own experiments, Durham University (England), IfAG (Germany)[4] and ETH-Z (Switzerland)[5] also conducted GPS experiments in Turkey. In order to assist in the establishment of a first degree geodetic control network for Turkey, we utilized some observations performed by these groups as a supplement to our core sites. Accordingly, we included in our analyses 5 sites[6] observed by ETH-Z in the Marmara network in 1990 and 1992. Also, in an effort to obtain four repeat measurements at the western Turkey network sites, we considered the data from the

[4]Institute für Angewandte Geodäsie.
[5]Eidgenössiche Technische Hochschule-Zurich.
[6]Data has been provided by GCM, Turkey, in order to obtain unified solutions.

Table 2.2: Tally of GPS experiments in Turkey between 1988 and 1992.

Experiment	Dates	Days of Year	Observation Days	Regional Sites	Global Sites	Tracked Satellites
1	09/06 - 09/28 1988	250-272	20	18	6	6
2	08/21 - 09/10 1989	232-252	21	55	5	6
3	08/26 - 09/29 1990	240-268	20	26	4	10
4	09/06 - 09/26 1991	249-269	21	25	18	12
5	03/26 - 04/07 1992	086-098	15	16	20	17
6	08/27 - 09/20 1992	240-264	24	64	26	18

Durham University Bozdağ network[6], which has 4 sites in common with our western Turkey network. In 1992, some sites of this network were observed by both IfAG and ourselves, both data sets being integrated into our analyses. During each regional experiment we tracked GPS satellites each day at the Ankara and SLR collocation sites[7]. Most sites were occupied on at least three consecutive days during a given experiment. At the sites in the Bozdağ and earthquake control networks, however, GPS observations were carried out for only two days. The distribution of GPS sites used in our analyses is depicted by Figure 2-1.

Between 1988 and 1992, we collected GPS data in Turkey at a total of 102 sites over 121 days (Table 2.2). We discuss the details pertaining to each experiment and to daily site occupations in Appendix B. Because we observed the eastern and western networks in alternate years, the number of repeat observations ranged from two to five. Figure 2-1 and Table 2.3 show the number of epoch observations at each site in Turkey. The sites in western and eastern Turkey are shown in Figure 2-2 and Figure 2-3, respectively. We acquired measurements for at least two epochs at each of 66 sites. At 16 primary sites, however, we collected GPS observations for three or more epochs. During each regional experiment, with the exception of spring of

[7]Some observations at the SLR collocation sites were also conducted by IfAG.

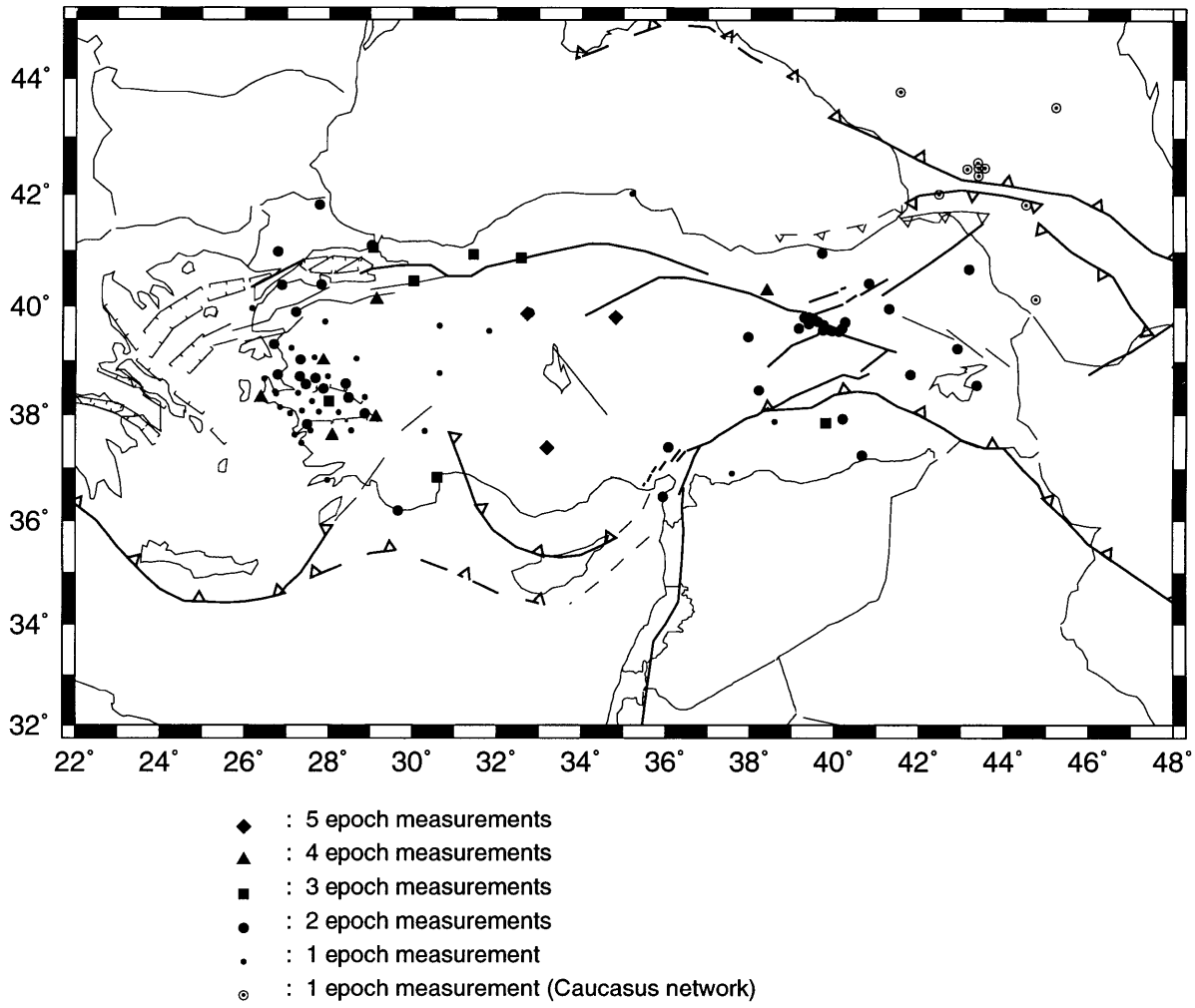

Figure 2-1: Regional GPS sites occupied in Turkey between 1988 and 1992. A detailed description is given in Appendix B. The Caucasus network is shown for reference purposes only, and its analysis is not included in this study (see Roberts et al., 1993).

1992, we occupied ANKA, MELE and YOZG, acquiring observations at five epochs. We obtained measurements for four epochs at six sites (AKGA, CEIL, CINE, PAMU, SEBI, and ULDA), and for three epochs at seven sites (ANTU, IKAN, ISME, KARA, MEKE, ODME, and YIGI). At the other fifty sites[8], two epoch observations were taken. We acquired only one epoch of observations for 36 additional sites, fourteen[9]

[8]AKCA, AKTO, ALSE, ANKM, ANKR, AYVA, BAYO, BULD, DEMI, DIYA, ER01, ER02, ER03, ER04, ER05, ER07, ER08, ER09, ER10, ER11, ER12, ERDE, ERZ2, ERZU, HAPA, HEMI, ISPI, ITAY, KADI, KALE, KARS, KASO, KEM2, KEMA, KINI, KIRE, KIZI, KORK, MALA, MER2, MERC, PATN, SEUR, SEVK, SINC, SIPD, SOKE, ULUC, USUM, and YIG2.

[9]AFYO, ANKS, BAF2, BALI, BURD, DMIR, ESKI, MARM, MENT, OZDE, SINO, SIVR ,

of them for the first time during the fall 1992 experiment. The ANKS site on the new Ankara SLR pad was established in 1992. First epoch measurements were taken at the GAZI site in 1991. The KAHT site, established in 1989, was destroyed by road construction in 1990. Sixteen sites[10] in the Bozdağ network have not yet been reoccupied. Three other sites were used as temporary tie marks (KAR2, PAT2, and YOZ1).

A variety of GPS receivers and antennas were utilized during these experiments: TI-4100, Minimac, Trimble (SLD, SST, and SSE), and WM-102 (see Appendix B). During the 1988 experiment we made all observations with TI-4100 receivers and antennas. By 1990, these were phased out and replaced by Trimble receivers and antennas. Trimble SLD and Minimac receivers and antennas were both available in 1989 and 1990. The Marmara network sites were surveyed with WM-102 receivers. In 1991 and 1992, all our regional surveys were accomplished with Trimble (SST and SSE) receivers and antennas, with the exceptions of the Ankara permanent site at which the GCM began operating a Minimac in August of 1991.

2.2 Global GPS Data

The accuracy of GPS estimates of site positions and velocities depends primarily on the ability of the global tracking network to determine the satellites' orbits [Murray, 1991; Larson et al., 1991]. Therefore we attempted to include data from a homogeneously distributed global tracking network in our analyses (Figure 2-4 and Table 2.4). Until 1991, however, our choices were limited. In 1988 and 1989, there were only 9 sites available [Chin, 1989]. Of these, three were in Europe (Wettzell,

SUBA, and TER2.

[10]AHME, BAFA, BAYI, BEDA, DOBE, GOMA, IZMR, KABU, KIRK, KOBE, KRNC, SEFE, SUGE, TERZ, TIRE, and URIS.

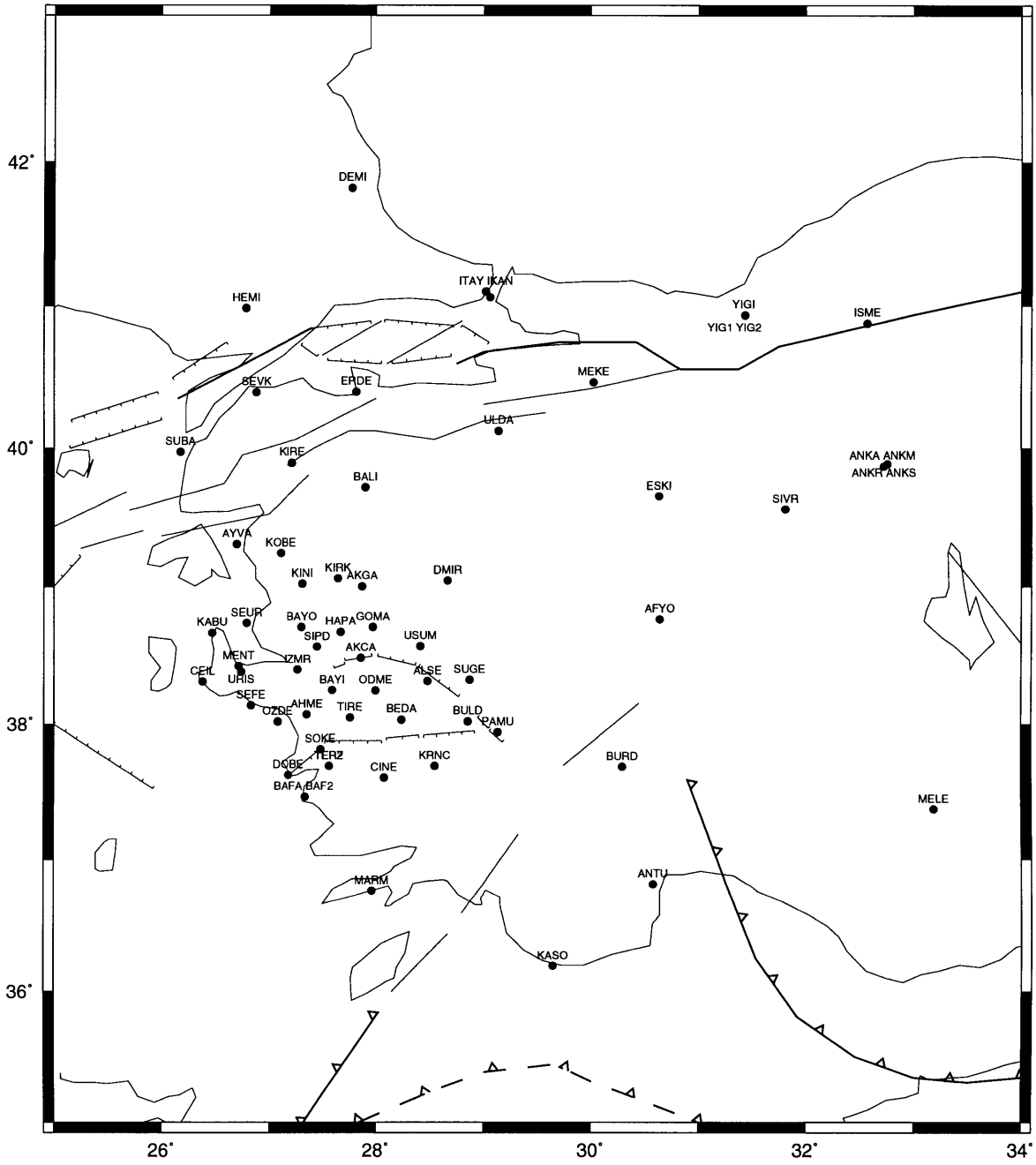

Figure 2-2: Distribution of regional sites in western Turkey between 1988 and 1992.

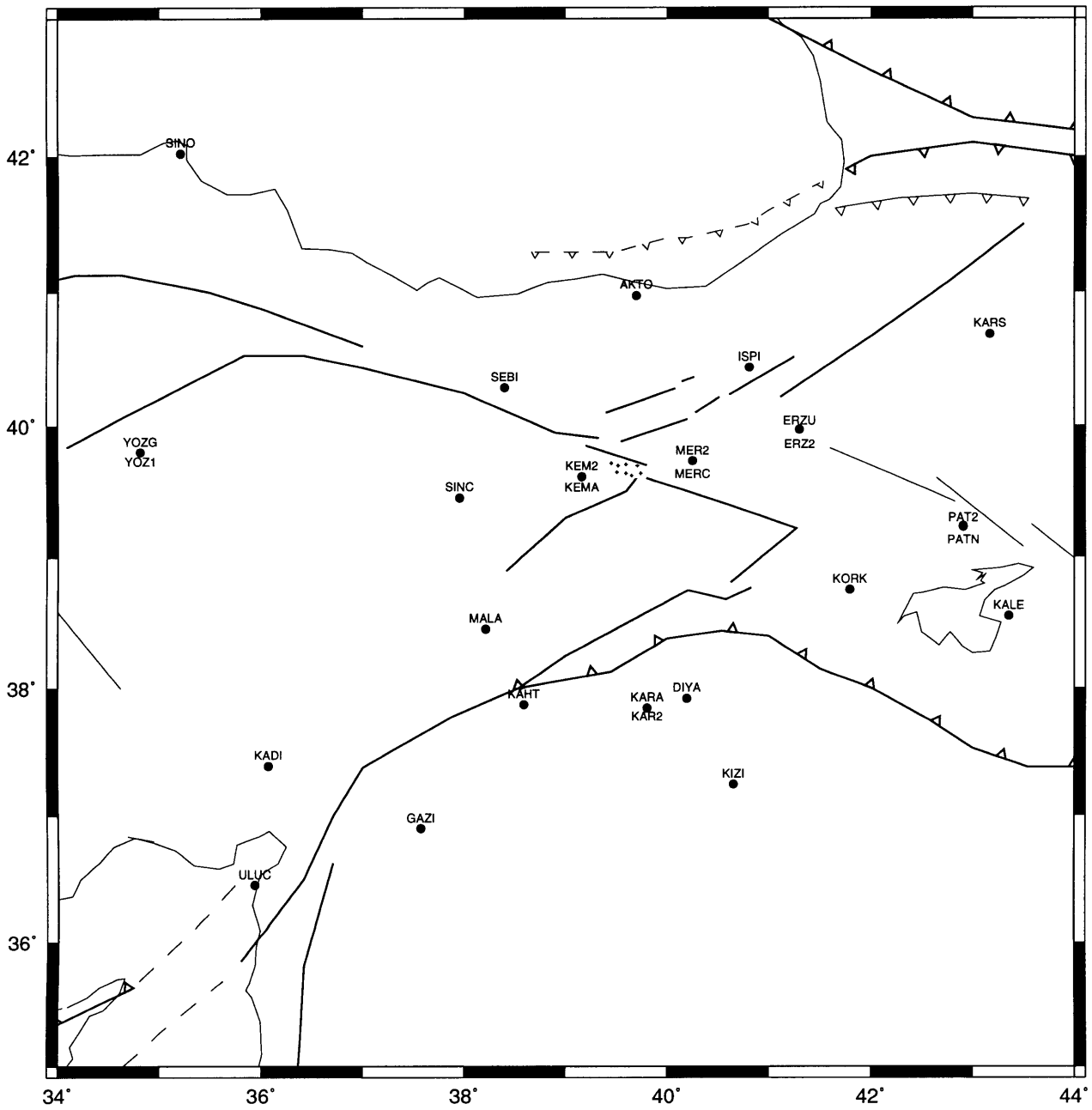

Figure 2-3: Distribution of regional sites in eastern Turkey between 1988 and 1992.

Table 2.3: Regional GPS sites in Turkey experiments: 1988-1992.

Site stamping or location	ID	1988	1989	1990	1991	Spring 1992	Fall 1992
Afyon	AFYO						•
Ahmetli	AHME		⋈				
Akçapınar	AKCA		⋈				•
Akhisar Gaziler	AKGA	⋈	⋈	•			•
Aktoprak	AKTO				•		•
Alaşehir	ALSE		⋈				•
Ankara Hacettepe 88	ANKA	⋈	⋈	•	•		•
Ankara MMAC	ANKM					◇	◇
Ankara 91	ANKR				◇		•
Ankara SLR	ANKS						•
Antalya Tünektepe	ANTU	⋈		•			•
Ayvalık	AYVA	⋈					•
Bafa Gölü 2 (92)	BAF2						•
Bafa Gölü	BAFA		⋈				•
Balıkesir	BALI						•
Bayındır	BAYI		⋈				
Bağyolu	BAYO		⋈				•
Beydağ	BEDA		⋈				
Buldan	BULD		⋈				•
Burdur	BURD						•
Çeşmeılıca	CEIL	⋈	⋈	•			•
Çine	CINE	⋈	⋈	•			•
Demirköy	DEMI	⋈					•
Diyarbakır	DIYA	⋈	⋈				
Demirci	DMIR						•
Doğanbey	DOBE		⋈				
Erzincan EQ 01	ER01					•	•
Erzincan EQ 02	ER02					•	•
Erzincan EQ 03	ER03					•	•
Erzincan EQ 04	ER04					•	•
Erzincan EQ 05	ER05					•	•
Erzincan EQ 07	ER07					•	•
Erzincan EQ 08	ER08					•	•
Erzincan EQ 09	ER09					•	•
Erzincan EQ 10	ER10					•	•
Erzincan EQ 11	ER11					•	•
Erzincan EQ 12	ER12					•	•
Erdek	ERDE			⋆			⋆

Symbols denote various antenna types: •↦ Trimble SST, ○↦ Trimble SLD, ◇↦ Minimac 2816AT, ⋈↦ TI-4100, and ⋆↦ WM-102.

Table 2.3: Regional GPS sites in Turkey experiments: 1988-1992.

Site stamping or location	ID	1988	1989	1990	1991	Spring 1992	Fall 1992
Erzurum 92	ERZ2					•	•
Erzurum	ERZU		○		•		
Eskişehir	ESKI						•
Gaziantep	GAZI				•		
Gölmarmara	GOMA		⋈				
Halitpaşa	HAPA		⋈				•
Hemit	HEMI			★			★
Kandilli	IKAN	⋈		•			•
Ismetpaşa	ISME	⋈		•			•
Ispir	ISPI		○		•		
Ist Ayazağa	ITAY			★			★
Izmir	IZMR		⋈				
Karaburun	KABU		⋈				
Kadirli	KADI		○		•		
Kahta	KAHT		○				
Kalecik	KALE		○		•		
Karacadağ 91	KAR2				•		
Karacadağ 89	KARA		○		•		•
Kars	KARS		○		•		
Kaş	KASO	⋈					•
Kemah 92	KEM2					•	•
Kemah	KEMA		○		•		
Kınık	KINI		⋈				•
Kiremit	KIRE			★			★
Kırkağaç	KIRK		⋈				
Kızıltepe	KIZI		○		•		
Kozak Bergama	KOBE		⋈				
Korkut	KORK		○		•		
Karıncalı	KRNC		⋈				
Kumköy/Soma	KUS0		⋈				
Malatya	MALA		○		•		
Marmaris	MARM						•
Mekece	MEKE	⋈		•			•
Melengiçlik	MELE	⋈	◇	◇	•		•
Menteş	MENT						•
Mercan 92	MER2					•	•
Mercan	MERC		○		•		
Ödemiş	ODME	⋈	⋈				•
Özdere	OZDE						•

Symbols denote various antenna types: •↦ Trimble SST, ○↦ Trimble SLD, ◇↦ Minimac 2816AT, ⋈↦ TI-4100, and ★↦ WM-102.

Table 2.3: Regional GPS sites in Turkey experiments: 1988-1992.

Site stamping or location	ID	1988	1989	1990	1991	Spring 1992	Fall 1992
Pamukkale	PAMU	⋈	⋈	•			•
Patnos 91	PAT2				•		
Patnos 89	PATN		○		•		
Şebinkarahisar	SEBI		○		•	•	•
Seferihisar	SEFE		⋈				
Şebinurla	SEUR		⋈				•
Şevketiye	SEVK			★			★
Sincan	SINC		○		•		
Sinop	SINO						•
Sipildağı	SIPD		⋈				•
Sivri	SIVR						•
Söke	SOKE		⋈				•
Subaşı	SUBA						•
Süzgeç	SUGE		⋈				
Terziler 92	TER2						•
Terziler	TERZ		⋈				
Tire	TIRE		⋈				
Uludağ	ULDA	⋈		•	•		•
Uluçınar	ULUC		○		•		
Urlaiskelesi	URIS		⋈				
Üşümüş	USUM		⋈				•
Yığılca	YIGI	⋈		◇	•		
Yığılca 1	YIG1		◇				
Yığılca 2	YIG2		◇				•
Yozgat 1	YOZ1		○				
Yozgat	YOZG	⋈	○	○	•		•

Symbols denote various antenna types: •↦ Trimble SST, ○↦ Trimble SLD, ◇↦ Minimac 2816AT, ⋈↦ TI-4100, and ★↦ WM-102.

Onsala and Tromso), one in Asia (Tsukuba), four in North America (Westford, Richmond, Mojave and Yellowknife), and one in the Pacific (Kokee). In recent years the availability of additional tracking sites (e.g., 26 global tracking sites were operating during the 1992 western Turkey experiment) has offered better coverage and a more homogeneous distribution. TI-4100 receivers with TI-4100 or FRPA-2 antennas were deployed at the global tracking sites in 1988. In 1989, except Onsala, Tromso, Yellowknife and Kokee, they were replaced by Minimac 2816AT receivers and antennas.

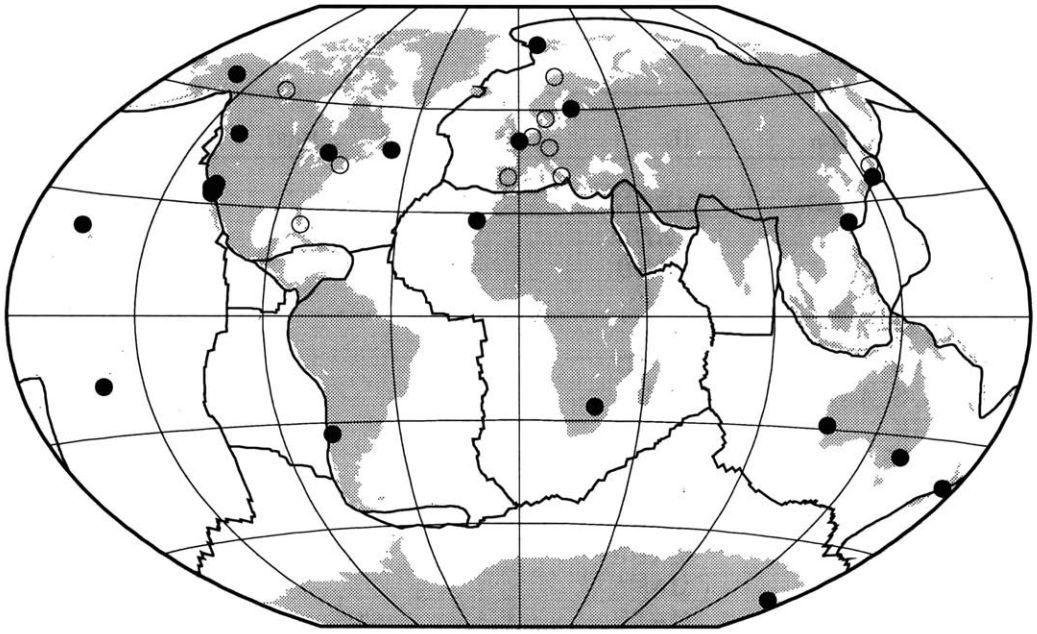

Figure 2-4: Global tracking sites used in solutions between 1988 and 1992. Open circles indicate global sites used in simultaneous and augmented regional data analyses. Filled circles are global sites used in combination type analyses. See text and also *cf.* Appendices A and B.

Minimac and TI-4100 receivers were operating at the global tracking sites used in the analysis of the 1990 experiment. All global tracking data included in our analyses of the 1991 and 1992 experiments were acquired by Rogue receivers and Dorne-Margolin antennas, except for that of Richmond, Tsukuba and Westford, at which Minimac receivers were operated.

During our 1988 and 1989 experiments, there were 6 satellites visible during observation sessions, of which the TI-4100 receivers could track only 4 simultaneously. By the 1990 experiment, we were tracking 10 satellites, 8 simultaneously, using Trimble and Minimac receivers. In the years to follow, the number of GPS satellites steadily increased. By fall of 1992, 18 satellites were available.

Table 2.4: Antenna types for the global tracking sites used in the Turkey experiments.

Site stamping or location	ID	1988	1989	1990	1991	Spring 1992	Fall 1992
Algonquin N Pier, Canada	ARON				□	□	□
Tidbinbilla, Australia	CAN1					□	
Tidbinbilla, Australia	CANB				□		
Tidbinbilla tower, Australia	DS42						□
Fairbanks, AK, USA	FAIR					□	□
Goldstone,CA, USA	GOLD				□	□	□
Hartebeesthoek, S. Africa	HART						□
Herstmonceux,UK	HERS				□		
JPL Mesa, CA, USA	JPLM				□	□	□
Kokee 3028-S, HI, USA	KOKB				□	□	□
Kootwijk, Netherlands	KOSG				□	□	□
Madrid tower,Spain	MADR				□	□	□
Mas Palomas, Canary Is.	MASP						□
Matera, Italy	MATE					□	□
McMurdo, Antarctica	MCMU					□	□
Metsahovi, Finland	METS						□
Ny Allesund, Norway	NALL					□	□
Onsala DO3-1, Sweden	ONS0	⋈	⋈	⋈	□	□	□
Pamatai, Tahiti	PAMA						□
Penticton 887006, Canada	PENT				□	□	□
Pinyon Flat 1, CA, USA	PIN1				□	□	
Richmond FRPA-2, FL, USA	RICH	∞					
Richmond Mini-Mac, FL, USA	RICM		◇	◇	◇		
Santiago, Chile	SANR					□	□
Scripps 1, CA, USA	SIO1				□		
Scripps 2, CA, USA	SIO2						□
St. Johns, Canada	STJO						□
Taipei, Taiwan	TAIW						□
Tromso, Norway	TROM	⋈	⋈		□	□	□
Tsukuba, Japan	TSUK		◇		◇		
Usuda, Japan	USUD				□	□	
Wellington, New Zealand	WELL				□		
Wettzell (Mini-Mac), Germany	WETM			◇			
Wettzell (Rogue), Germany	WETR				□	□	□
Wettzell (TI-4100), Germany	WETT	⋈					
Westford (FRPA-2), MA, USA	WSFF	∞					
Westford (Mini-Mac), MA, USA	WSFM		◇	◇	◇		
Yarragadee (RM-4), Australia	YAR1				□	□	□
Yellowknife 889201, Canada	YKN1		⋈		□	□	□
Yellowknife TI-4100, Canada	YKNF	⋈					

Symbols denote various antenna types: ◇↦ Minimac 2816AT, ⋈↦ TI-4100, ∞↦ FRPA-2, and □↦ Dorne Margolin with the JPL choke ring.

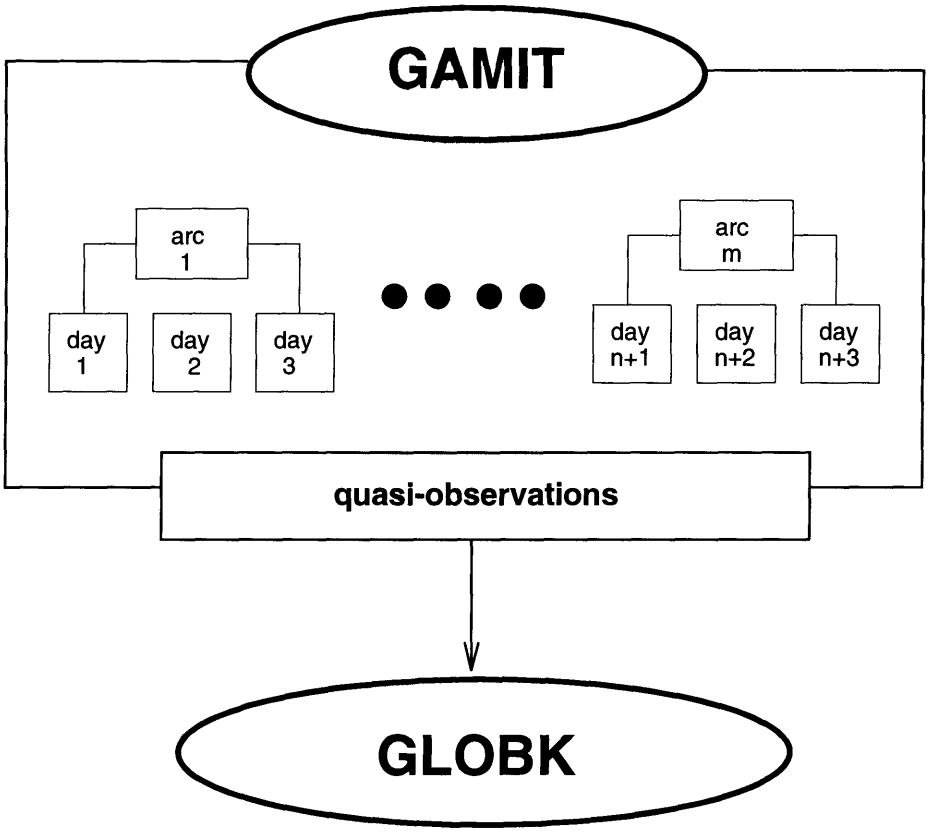

Figure 2-5: Two-step solutions with GAMIT [King and Bock, 1993] and GLOBK [Herring, 1991].

2.3 Data Analyses

We analyzed the GPS observations in two-steps (Figure 2-5). In the first step, we used GAMIT software [King and Bock, 1993] to estimate relative positions of observing sites, and orbital, atmospheric, clock and ambiguity parameters, from a weighted least squares analysis of phase delay measurements for each single-session (day). During this step, by viewing the phase residuals, we edited phase data to remove outliers and repair cycle-slips caused by the receivers' loss of lock on the satellite signal. Typi-

cally, the rms for the LC[11] phase residuals (observed minus calculated) was ~ 0.1 cycle (20 mm). In order to obtain an improved determination of satellite orbits we estimated initial conditions [IC] for arcs over 3–4 days (long-arc), rather than for 8–12 hour observation sessions (short-arc). The common orbital arc provided a tie between the observation sessions (see below and Appendix B). Its strength was determined by the level of stochastic variation allowed between the orbital parameters estimated from each session. Our long-arc, single-session GAMIT solutions were performed with loose a priori constraints on the site and satellite parameters in order to produce unbiased quasi-observations (see Appendix 3 of Dong [1993]) for the next step in our analysis. These quasi-observations (GAMIT h-files) consist of estimates of site coordinates and orbital parameters and their variance-covariance matrices.

In the second step of our analyses, we used GLOBK software [Herring, 1991] to estimate the global parameters, i.e., site positions and velocities, satellite state vectors and earth orientation parameters (polar motion and UT1-UTC). GLOBK employs a discrete time, non-adaptive Kalman filter [Herring et al., 1990], incorporating the parameter estimates and their variance-covariance information which are provided by the quasi-observations. GLOBK also allows for stochastic estimation of parameters which are modeled by a random walk. Invoking stochastic options enabled us to investigate the sensitivity of site positions and velocities, obtained from each session/experiment, to the effective length of the dynamical arc (see Appendix B).

There are several advantages in this two-step approach to data analysis. Several giga-bytes of data are condensed into megabytes, so that data handling becomes manageable and analysis time is shortened. This approach also provides a rigorous solution to the problem of inhomogeneous tracking networks by consistently imposing uniform constraints on the global tracking network [Feigl et al., 1993].

[11]LC is the linear combination of GPS phase observations at the L_1 and L_2 GPS frequencies with which ionospheric effects are eliminated.

Repeated measurements to determine site velocities should ideally be performed with identical network configurations. This, unfortunately, has not been the case for the Turkish experiments. Since our initial experiment, the GPS receivers/antennas have evolved, the constellation has expanded, and the number of global tracking sites has steadily increased. The most important factor is the distribution of global tracking sites because the data from these *fiducial* sites determine the orbital parameters of satellites. One method of keeping a homogeneous fiducial network is to incorporate the same global trackers in the analysis of regional data for all experiments. In our case, however, the set of global trackers common to all experiments provides a much weaker fiducial network than that obtained by using whatever trackers are available for each experiment. Therefore, in our analyses of the regional data, we utilized almost all of the global tracking data (Table 2.5) available from the Cooperative International GPS Network (CIGNET), the Scripps Institute of Oceanography (SIO) and the Jet Propulsion Laboratory (JPL) archives. Overall, our data set comprises 18 million doubly differenced GPS phase delay observations from 29,000 one-way records, obtained during 2800 station-days of observations (Table B.1). Of these data, global tracking contribute two thirds.

For the three earliest experiments (1988, 1989 and 1990), we simultaneously analyzed the global and regional data. This is the natural and straightforward choice, provided that the amount of data is manageable. After 1990, however, the number of observations, both regional and global, increased 2–3 fold. To overcome problems of computation and editing time, and mass storage, we devised, tested, and utilized a combination approach as described in Appendix A. This approach takes advantage of the two-step data analyses offered by our processing software, and involves combining the global and regional data via their quasi-observations, tying them through common satellites and sites (Figure 2-6). We performed *two separate, parallel* GAMIT analyses: one with regional data and the other with global data. In our analyses, we augmented the regional data with data from a subset of the fiducial network com-

Table 2.5: Global tracking sites used in the Turkey experiments: 1988-1992. Those global sites analyzed simultaneously with the regional data are denoted by ⊙.

Site stamping or location	ID	1988	1989	1990	1991	Spring 1992	Fall 1992
Algonquin N Pier,Canada	ARON				•	•	•
Tidbinbilla, Australia	CAN1					•	
Tidbinbilla, Australia	CANB				•		
Tidbinbilla tower, Australia	DS42						•
Fairbanks, AK, USA	FAIR					•	•
Goldstone,CA, USA	GOLD				•	•	•
Hartebeesthoek, S. Africa	HART						•
Herstmonceux,UK	HERS				•		
JPL Mesa, CA, USA	JPLM				•	•	•
Kokee 3028-S, HI, USA	KOKB				•	•	•
Kootwijk, Netherlands	KOSG				•	⊙	⊙
Madrid tower,Spain	MADR				•	•	⊙
Mas Palomas, Canary Is.	MASP						•
Matera, Italy	MATE					•	⊙
McMurdo, Antarctica	MCMU					•	•
Metsahovi, Finland	METS						•
Ny Allesund, Norway	NALL					•	•
Onsala DO3-1, Sweden	ONS0	⊙	⊙	⊙	⊙	⊙	⊙
Pamatai, Tahiti	PAMA						•
Penticton 887006, Canada	PENT				•	•	•
Pinyon Flat 1, CA, USA	PIN1				•	•	
Richmond FRPA-2, FL, USA	RICH	⊙					
Richmond Mini-Mac, FL, USA	RICM		⊙	⊙	•		
Santiago, Chile	SANR					•	•
Scripps 1, CA, USA	SIO1				•		
Scripps 2, CA, USA	SIO2						•
St. Johns, Canada	STJO						•
Taipei, Taiwan	TAIW						•
Tromso, Norway	TROM	⊙	⊙		⊙	⊙	⊙
Tsukuba, Japan	TSUK		⊙		•		
Usuda, Japan	USUD				•	•	
Wellington, New Zealand	WELL				•		
Wettzell (Mini-Mac), Germany	WETM			⊙			
Wettzell (Rogue), Germany	WETR				⊙	⊙	⊙
Wettzell (TI-4100), Germany	WETT	⊙					
Westford (FRPA-2), MA, USA	WSFF	⊙					
Westford (Mini-Mac), MA, USA	WSFM		⊙	⊙	•		
Yarragadee (RM-4), Australia	YAR1				•	•	•
Yellowknife 889201, Canada	YKN1		⊙		⊙	⊙	•
Yellowknife TI-4100, Canada	YKNF	⊙					

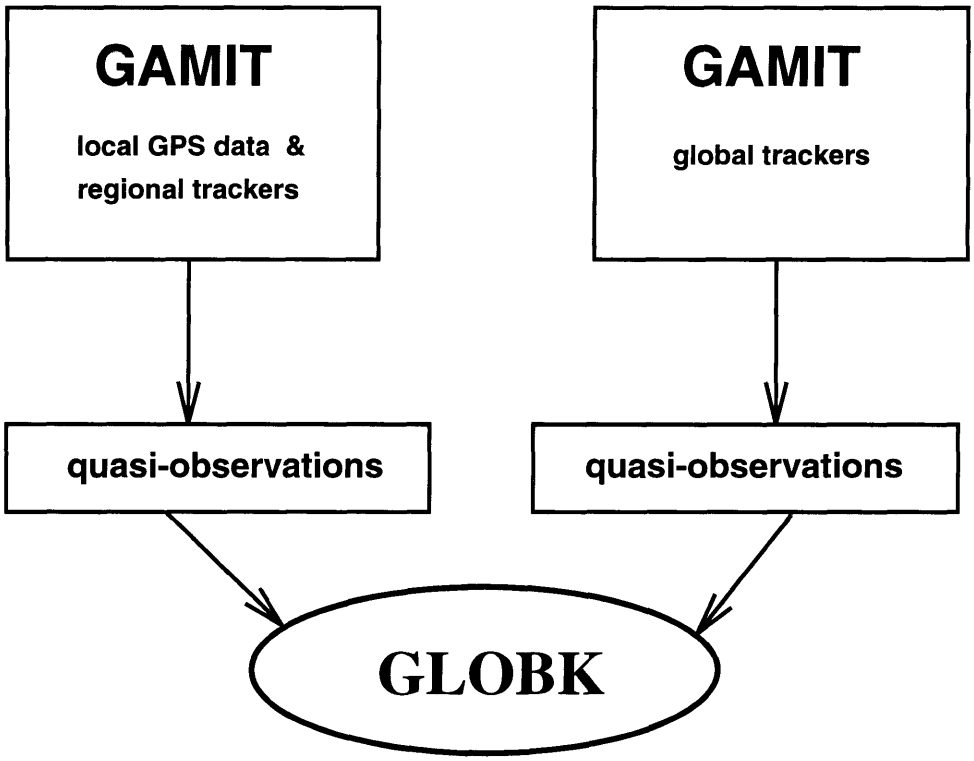

Figure 2-6: Combining regional GPS data with global tracking GPS data. Two GAMIT solutions are carried out separately but in parallel, and their quasi-observations are combined with GLOBK.

mon to all regional experiments. This network consisted of global trackers located in Europe and eastern North America. Accordingly, we analyzed and reduced the augmented regional and global data from the 1991, spring 1992, and fall 1992 experiments separately, with GAMIT, and then combined them via their quasi-observations in GLOBK. Such a scheme is nearly equivalent to a simultaneous analyses, and saves enormous amounts of time and storage space. Details of these analyses are given in Appendices A and B.

We made no attempt to resolve integer-cycle ambiguities in the GPS phase obser-

vations due to the large interstation distances in our regional networks. The majority of baselines during each observation session spanned 300 to 600 km; some were as long as 1400 km. Resolving phase ambiguities mainly decreases the uncertainties in the east-west components of regional baselines, which are otherwise about twice the north-south uncertainties.

In order to estimate site positions and velocities we performed a series of solutions, each reducing the volume of the data to be stored. First, we obtained experiment-based *compact* quasi-observations [12] from the quasi-observations of each single-session, long-arc GAMIT solution, by imposing sufficiently loose constraints on the site positions while applying appropriate process noise to the satellites (see Appendix B). This solution compresses the information from several days' observations into experimentally averaged estimates of site positions and their variance-covariance matrices. Such an approach eliminates the need to re-analyze the quasi-observations of each session from earlier experiments, and thus simplifies analyses of several years of observations when and if data from additional experiments are merged. Next, we used these *compact* quasi-observations to estimate all site positions and their velocities with (sufficiently) loose constraints to obtain *final* quasi-observations which contain the estimates of site positions and velocities and their variance-covariance matrices. Only at this last stage did we impose constraints to define the reference frame for velocity and position estimates. Use of these final quasi-observations (a version of the 2.5 Gb of GPS observations compressed into 5Mb) allowed us to quickly and efficiently test the effect of imposing a variety of constraints on our velocity estimates.

We defined a consistent reference frame by constraining the coordinates and veloc-

[12] We analyzed the first five experiments with the pole and UT1-UTC values derived from the VG (**V**LBI-**G**PS) solutions, giving uncertainties on the order of 5 milliarcseconds. Because these were not available during the analysis of the fall 1992 experiment, we used the less accurate "rapid-service" values of the IERS (International Earth Rotation Service). To prevent inconsistency, we imposed IERS Bulletin B estimated values, while obtaining the *compact* quasi-observations for all experiments.

ities of a number of global tracking sites at values determined from a global analysis of VLBI and GPS observations over a 6-year period [Feigl et al., 1993; T. A. Herring, pers. comm., 1993]. This VG (**V**LBI-**G**PS) reference frame (Eurasian datum fixed) is approximately aligned with the ITRF-92[13] frame which is consistent with the NUVEL-1 model for the relative motion of the major tectonic plates.

To estimate site positions and velocities, we performed *velocity* and *coordinate* solutions by GLOBK using the final quasi-observations [14]. In the *velocity* solution, we forced the horizontal velocities of three European sites (Wettzell, Onsala and Tromso) and three North American sites (Richmond, Westford and Yellowknife), common to our experiments, to their VG a priori values, and estimated velocities for all other sites. Constraining the velocities of six global tracking sites is sufficient to estimate site velocities so that the system's rank-deficiency (three rotation rates) is resolved. Imposing no constraints on the positions of the global tracking sites diminishes the effects of possible errors in their positions projecting into the velocity estimates. In the velocity solutions, we assumed that the velocities of the offset/relocation marks are equal to that of the main mark (velocity ties). That is, we equated the velocities of all offset/relocation marks at the Wettzell, Richmond, Yellowknife and Westford sites. The positions and velocities of unconstrained global tracking sites, along with those of regional sites, were also estimated. We did not estimate velocity for Usuda and Tsukuba due to inaccurate VG a priori values, but estimated their positions stochastically. In order to test the robustness of our velocity estimates, we performed a second solution. In this *coordinate* solution, we forced the horizontal positions of these sites, as well as their velocities, to their VG a priori values. Imposing constraints also on the coordinates of these six global tracking sites resolved the rank-deficiency in

[13]International Terresterial Reference Frame. 1992 IERS Annual report, Central Bureau of IERS, 1993.

[14]As discussed in Feigl et al. [1993], a *frame* solution is precedent. In our analysis we did not perform a frame solution because no VLBI data had been incorporated in our solutions. We implemented the VG-derived reference frame instead.

rotation. Comparisons of site velocities obtained from these two solutions (coordinate and velocity) showed no significant difference.

2.4 Discussion of Geodetic Quality

In order to assess the quality of our geodetic parameter estimates, we investigated short- and long-term repeatability. Such analyses provided insight into suspect data and aided in pinpointing sites which tend to behave as outliers. We carried out short-term precision analyses at the experiment level by examining the day-to-day scatter of estimates of relative site positions. In doing so, we assumed that there was no significant relative site motion during a given experiment. Short-term repeatabilities provide us with a measure of precision and include a component of orbital and atmospheric effects. They are not sensitive, however, to those systematic errors which may be constant over several days, such as multipath. Furthermore, we understand that operating various receivers/antennas may have affected our results. Errors related to the antenna phase center (e.g., occupying a site/baseline with different antennas, and variations of the phase center as a function of azimuth and elevation of the satellite being tracked) may be at the level of several centimeters in the vertical component of site positions. Mixing different antennas, in fact, might have induced larger systematic errors. For instance, baselines formed between sites at which Minimac antennas were deployed and those at which TI-4100 or Trimble antennas were deployed could have errors as much as 15 cm in the vertical [Simon McClusky, pers. comm., 1993]. We studied long-term repeatability by examining the year-to-year scatter of estimates of relative site positions about a best-fitting straight line. From this scatter, we derived a calibration factor by which to multiply the formal uncertainties in order to reflect realistic 1-σ errors. The evolving nature of the GPS constellation, the number of global trackers, the type of receivers and antennas, and changes in observing

monuments (reset and/or reference marks) have all potentially affected the accuracy of our results.

Short-term precision

To investigate short-term repeatability/precision, we performed smoothing Kalman filter solutions (back solutions) [Herring et al., 1991] for each experiment. In these solutions, we treated the coordinates of most of the global tracking sites as deterministic parameters, but allowed stochastic perturbations in the coordinates of the regional sites. We constrained the coordinates of most global tracking sites to their VG values within 1 cm in the horizontal and 20 cm in the vertical, and estimated them deterministically. Horizontal positions of the Santiago (SANR) and Taiwan (TAIW) sites were constrained to 5 cm. We allowed the positions of Usuda (USUD), Tsukuba (TSUK) and Wettzell (WETM) to be determined stochastically, since their VG positions and velocities were not accurate. Due to a poor global tracking configuration, we deterministically estimated the positions of ANKA, MELE and DIYA in addition to the global tracking sites for the 1989 experiment. The combination analyses used for the 1991 and Spring 1992 data had Ankara sites ANKR and ANKM in common with the global and augmented regional data sets, respectively. We had to delete the DIYA site from our 1988 experiment due to its instability. Due to an insufficient amount of quality data available and/or a rather large day-to-day scatter in their estimates, we had to discard a number of Bozdağ network sites from the 1989 experiment: AKCA, ALSE, BAFA, BAYI, BEDA, GOMA, KRNC, TERZ, TIRE, and USUM. Since there were only two repeat observations at most of the Bozdağ network sites, it was impossible to pinpoint the problem session and/or the one-way record. The short-term repeatabilities for the 1990 experiment demonstrated that the wrms scatters of baselines involving WM-102 receivers were relatively large. We

retained most of them, however, we were forced to delete outlier KIRE, a Marmara network site, from our solutions since we could not pinpoint the anomalous observation in either of the two observation sessions. Except for observations at the GAZI site, we recognized no problems with the 1991 data set repeatability. Though we returned to phase data, we could not identify any particular day's one-way observation as problematic. Since only one-epoch measurements had been taken at this site, we elected to discard it for now. We also removed ER12 (observed only twice) from the spring 1992 experiment due to its outlier behavior.

We quantified the day-to-day scatter by wrms (weighted rms) and nrms [normalized rms = $\sqrt{\chi^2/f}$, where χ^2 is the chi-square statistic and f is the number of degrees of freedom] of baseline estimates about their weighted mean. We summarized the precision of estimates for the north, east, and vertical components, and length, as a function of baseline length (L), by an error model in the form of $\sigma^2 = a^2 + b^2L^2$, where a is the constant term and b reflects proportional errors. (In Appendix B, we also present an error model in the form of $\sigma = c + m\ L$.)

In determining day-to-day scatter, we used baseline estimates from at least two observation sessions to provide statistical information for all the sites observed during each experiment. Overall, we achieved a short-term precision better than 20 parts per billion (ppb) for all baseline components (*cf.* Appendix B). In Table 2.6 we tabulate the constant [a] and proportional [b] terms of error model for short-term repeatability, as well as mean wrms and nrms. The baseline length dependent term was 5–10 ppb in the north and 3–17 ppb in the east. The north-south components yielded a mean wrms of 7 mm, and the east-west components, 13 mm. The determination of vertical components was less precise, with a mean wrms of 25 mm.

The nrms values for these six experiments (Table 2.6) vary between 0.6 and 3. We obtained the lower values for the 1988 and 1989 experiments and higher values

Table 2.6: Short- and Long-term Repeatability of Regional Sites.

Year	N¶	N-S component a (mm)	N-S component b (ppb)	N-S mean wrms	N-S mean nrms	E-W component a (mm)	E-W component b (ppb)	E-W mean wrms	E-W mean nrms	U-D component a (mm)	U-D component b (ppb)	U-D mean wrms	U-D mean nrms
1988†	28	5.96	5.55	6.40	0.55	12.76	10.80	13.53	0.58	17.67	1.68	17.69	0.58
1989†	102	3.49	5.06	4.45	0.59	10.38	9.66	11.67	0.77	17.18	0.00	17.18	0.83
1990†	63	3.71	10.16	5.21	1.02	6.81	13.21	8.36	0.86	16.60	21.02	18.36	0.91
1991†	121	6.76	0.00	6.76	2.05	8.54	2.74	8.68	1.21	22.36	0.00	22.36	1.55
1992†*	25	5.55	4.31	5.88	1.60	7.22	17.13	10.32	1.48	15.89	23.46	19.00	1.00
1992†	439	6.71	3.82	7.06	3.12	13.14	6.74	13.71	2.80	16.19	17.26	18.89	1.82
ALL‡	79	2.59	4.22	3.04	0.79	7.04	18.06	9.78	1.17	15.28	21.18	17.15	0.93

¶ N is the number of baselines used in obtaining error model parameters from $\sigma^2 = a^2 + b^2L^2$, by linearized inversion.

* 1992 Spring, Erzincan earthquake control survey (several-site-common combination).

† Short-term repeatability statistics are about the weighted means. There has been no scaling of the a priori uncertainties.

‡ Long-term repeatability statistics: All experiments. The statistics are about the best fitting straight line, except the vertical component, which is about the weighted mean.
In calculating the long-term repeatability statistics, we have multiplied the a priori errors of all experiments by a factor of 2. An additional factor of 3 has been applied to the 1990 experiment.

for the 1991 and 1992 experiments. This suggests that the uncertainties for earlier experiments might have been overestimated, and those for later experiments, underestimated. To investigate the magnitude of formal errors we deterministically estimated all the geodetic parameters of each experiment. In the 1988 experiment, for instance, we obtained formal uncertainties of 9.6 mm in the north and 17.7 mm in the east, for a 500 km baseline. We tracked a total of 6 satellites, and the reference frame was determined by 6 global trackers located in eastern North America and Europe. By fall of 1992 the number of satellites tripled, and that of global sites quadrupled. As a result, we achieved formal uncertainties of 1.8 mm in the north and 3.4 mm in the east, for a similar baseline. Because we analyzed all the experiments using the same a priori uncertainties on the observations (see Appendix B), the decrease in formal uncertainties is a consequence of stronger determination of the orbital parameters using globally well distributed fiducial sites tracking several satellites. Such an im-

pact is also observed on the precision of long baselines. In 1988, for instance, the formal uncertainties obtained for the 2500 km long Ankara to Onsala baseline was 41.4 and 52.9 mm in the north and east, respectively. The formal uncertainties were reduced by a factor of 2-3 when we analyzed the augmented regional data (regional and a subset of global sites) from the fall 1992 experiment. With the combination type analyses, using 26 global sites, we further improved these formal uncertainties to 2.6 mm in the north and 3.6 mm in the east.

Using nrms as a calibrating factor for each experiment, we could have equalized the formal uncertainties (see below and Appendix C for further discussion). However, since short-term repeatabilities do not provide a measure of systematic errors for longer periods of time, we chose to apply such a calibration using the nrms obtained from long-term repeatability analyses.

We also used the short-term precision analyses to determine the sensitivity of wrms scatter to the level of stochastic process noise applied to the satellites. We found that defining a single orbital arc (one set of state vector per satellite) common to several days, and allowing a very tight (small) stochastic perturbation between each day, provided the highest precision for all experiments, except that of 1989. For this experiment, we had to allow some degree of decoupling between days (See Appendix B).

Long-term precision

Using experiment-based compact quasi-observations, we performed a smoothing Kalman filter solution (back solution) to calculate the year-to-year scatter of the rates of change of baseline components. In this solution we constrained the global tracking sites outside our regional network to their VG values by 2 cm in the horizontal and 20 cm in the vertical, and by 1 mm in velocity for all components. We allowed

the positions of our regional sites to vary from year to year by estimating them stochastically. We characterized long-term repeatability by wrms and nrms about the best-fitting straight line.

In our error analysis for long-term repeatability, we considered only baselines simultaneously observed during 3 or more experiments ($f \geq 1$). Since the majority of sites within the eastern Turkey and Erzincan control networks had been observed only twice over the five year period, we did not include them in our long-term error analyses. During the course of the experiments some benchmarks were replaced and/or abandoned. For instance, the Ankara site was relocated twice, from ANKA to ANKR and later to ANKM. In some experiments, observations were taken at the offset marks of SLR collocation sites YIGI (YIG2 in 1989 and 1992) and YOZG (YOZ1 in 1989). A number of sites in the Bozdağ network were visited once. Consequently, the number of simultaneously observed baselines used in long-term repeatability analysis was small: 79 baselines. Given the inadequacies in temporal and spatial distribution, we were forced to extrapolate our statistics from shorter to longer time scales and interstation distances. We assumed that the noise processes were stationary such that their characteristics did not change temporally and/or spatially. This is difficult to justify because the number and type of receivers and satellites have evolved since our first experiment in Turkey. Also, due to orbital errors, the velocity estimations were more likely to be affected by interstation distances.

We derived our error analysis for the long-term repeatability from 79 simultaneously observed regional baselines. These involve 16 primary sites at which we have at least 3 epoch observations: AKGA, ANKA, ANTU, CEIL, CINE, IKAN, ISME, KARA, MEKE, MELE, ODME, PAMU, SEBI, ULDA, YIGI, and YOZG. The error statistics for eastern Turkey were obtained from baselines between KARA, MELE, ANKA and YOZG. Eighteen baselines were observed in four experiments, while only three of them (YOZG-MELE, YOZG-ANKA and MELE-ANKA) were observed in

five. Suspect sites (AKCA, ALSE, KINI, USUM, and DIYA) were discarded in long-term error analyses. We also eliminated the outlier measurements at AKGA during the 1989 experiment. Rather high rates (> 100 mm/yr) observed at the SEBI site convinced us that this site was unstable. Unfortunately, we have no long-term error statistics for most sites in the eastern Turkey and Erzincan earthquake networks since they were observed only twice.

In our analyses of long-term errors, we assumed uniform horizontal site velocities and no significant vertical motions. The time evolution of baseline estimates manifested certain anomalous behaviors in the horizontal and vertical components which are discussed in Appendix C. Some of the outliers were associated with very long baselines formed between the regional and global tracking sites (e.g., ANKA-ONS0), and were dominant in the estimates of the vertical components. Others were among the regional baselines and were predominantly evident in the estimates from the 1990 experiment. The vertical components of all very long baselines estimated from the 1989 and 1990 experiments manifested large offsets (see Appendix C). Such large vertical offsets were also observed in the regional baseline components. However, they were limited to baselines formed with Melengiçlik (MELE), Yığılca (YIGI and YIG2) or Karacadağ (KARA) at one end. The year-to-year scatter of horizontal component estimates depicted the 1990 experiment as an outlier. A large portion of the long-term errors, in particular, those associated with the very long baselines, stemmed from the poor geometry of the global tracking sites in the earlier experiments, especially in 1989 and 1990. Other error sources could as well be traced to the receivers and to modeling of the GPS observables (e.g. hardware/software related problems, antenna phase center variations, tropospheric delay).

In order to reflect the scatter in position estimates and to obtain a value of nrms close to unity, we introduced a scaling factor of 2 to the a priori uncertainties of all experiments. To reduce the effects of outliers, an additional rescaling of 3 was

applied to the a priori uncertainties of the 1990 experiment. Overall, the mean nrms of the estimates of baseline components about the best fitting straight line is about 1, with these scaling factors applied to the formal uncertainties of all experiments (Figures 2-7 and 2-8). After reweighting, we achieved long-term proportional errors comparable to those of the short-term(Table 2.6). The mean wrms of north and east component velocities is 4.2 ppb and 18.1 ppb, respectively (Figures 2-9 and 2-10). The mean wrms scatter is 3.1 mm in the north and 9.8 mm in the east. The wrms scatter of components, as a function of baseline length, is shown in Figure 2-9. The wrms scatter in the north is less than 10 mm. Because we have not resolved ambiguities, the wrms scatter in the east is greater; however, all are under 25 mm. Because we assumed no significant vertical motions and no velocity has been estimated for this component, long-term error statistics for the vertical components are about their weighted means. In doing so, however, we excluded those baselines involving anomalous sites (see Appendix C). With proper scaling applied to each experiment, the mean nrms of the vertical components is about one (Figures 2-7 and 2-10). The vertical wrms scatter about the weighted means of baselines has an upper value of 50 mm (Figure 2-9).

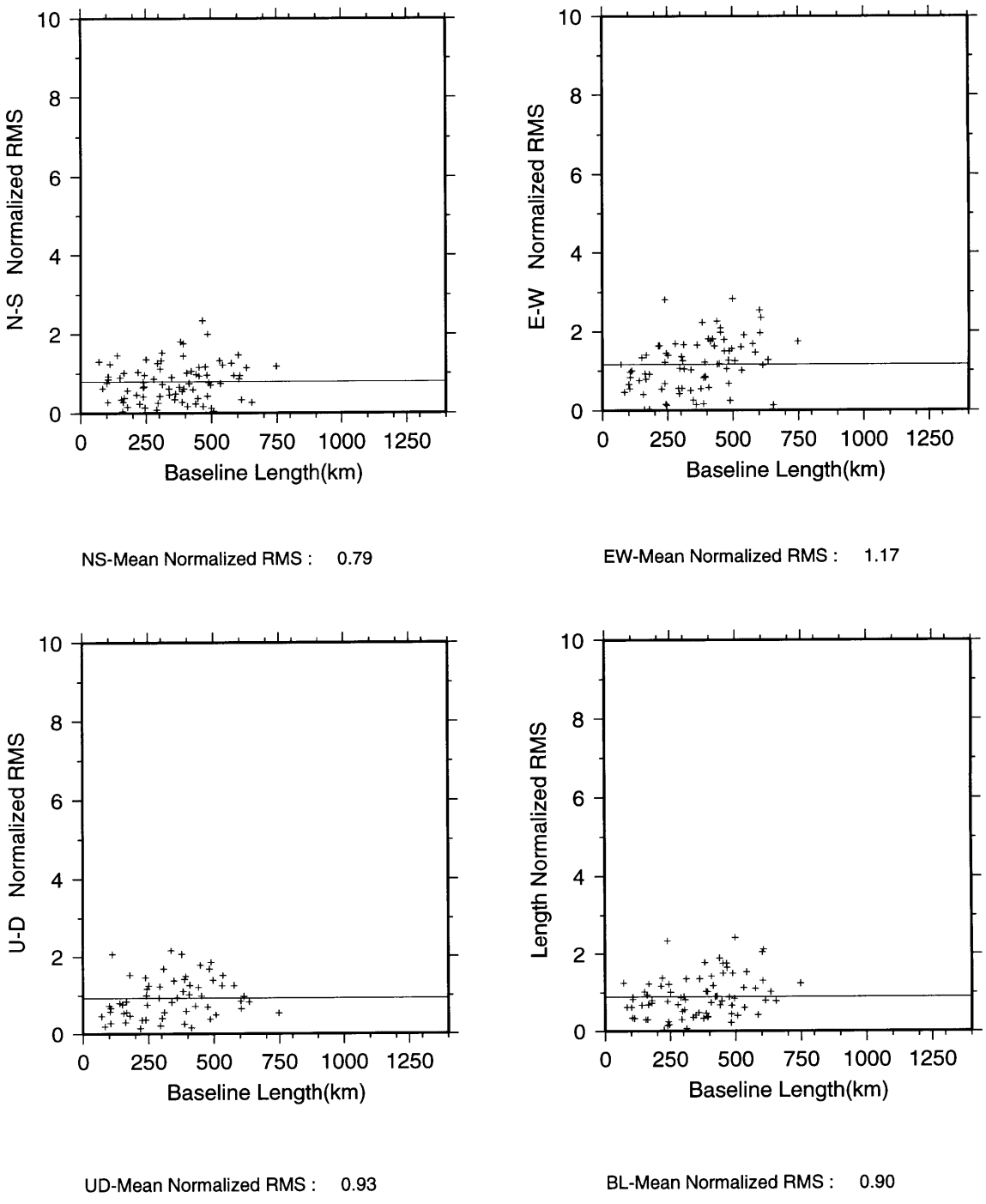

Figure 2-7: Long-term nrms scatter of NS, EW, UD components and length, as a function of baseline length. Formal uncertainties are scaled to reflect realistic 1-σ errors. The continuous line represents the mean nrms scatter.

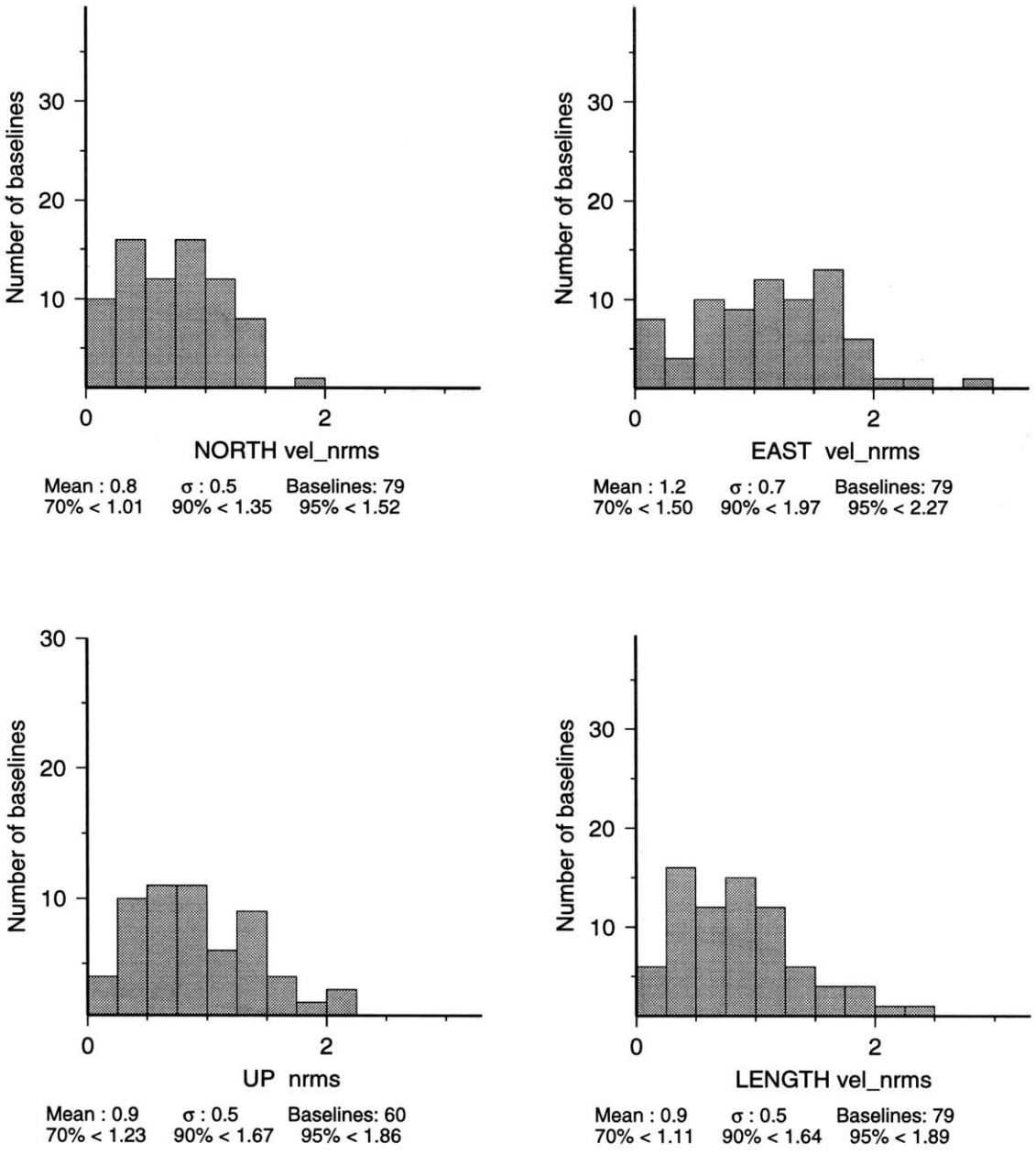

Figure 2-8: Histogram of the long-term nrms scatter of NS and EW components and length, about the best fitting straight line. The long-term nrms scatter of UD components is obtained about their weighted means. We scaled the formal uncertainties by a factor of 2 (after rescaling the 1990 experiment by 3) to reflect realistic 1-σ errors.

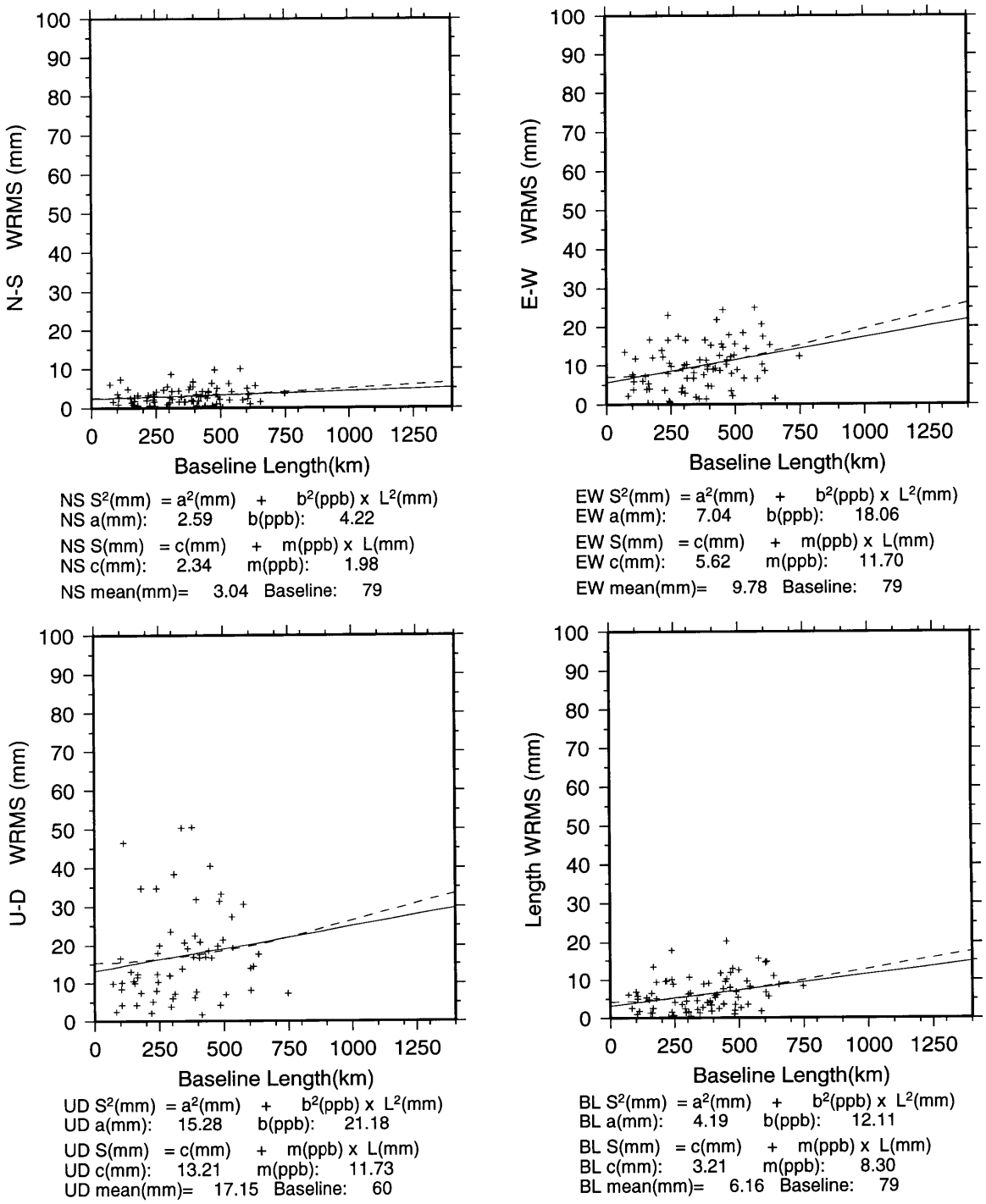

Figure 2-9: Long-term wrms scatter and model parameters of NS, EW, UD components and length, as a function of baseline length. We scaled the formal uncertainties by a factor of 2 (after rescaling the 1990 experiment by 3) to reflect realistic 1-σ errors. Dashed line is a functional in the form of $\sigma^2 = a^2 + b^2L^2$. The continuous line is a linear fit to the wrms scatter ($\sigma = c + m\ L$).

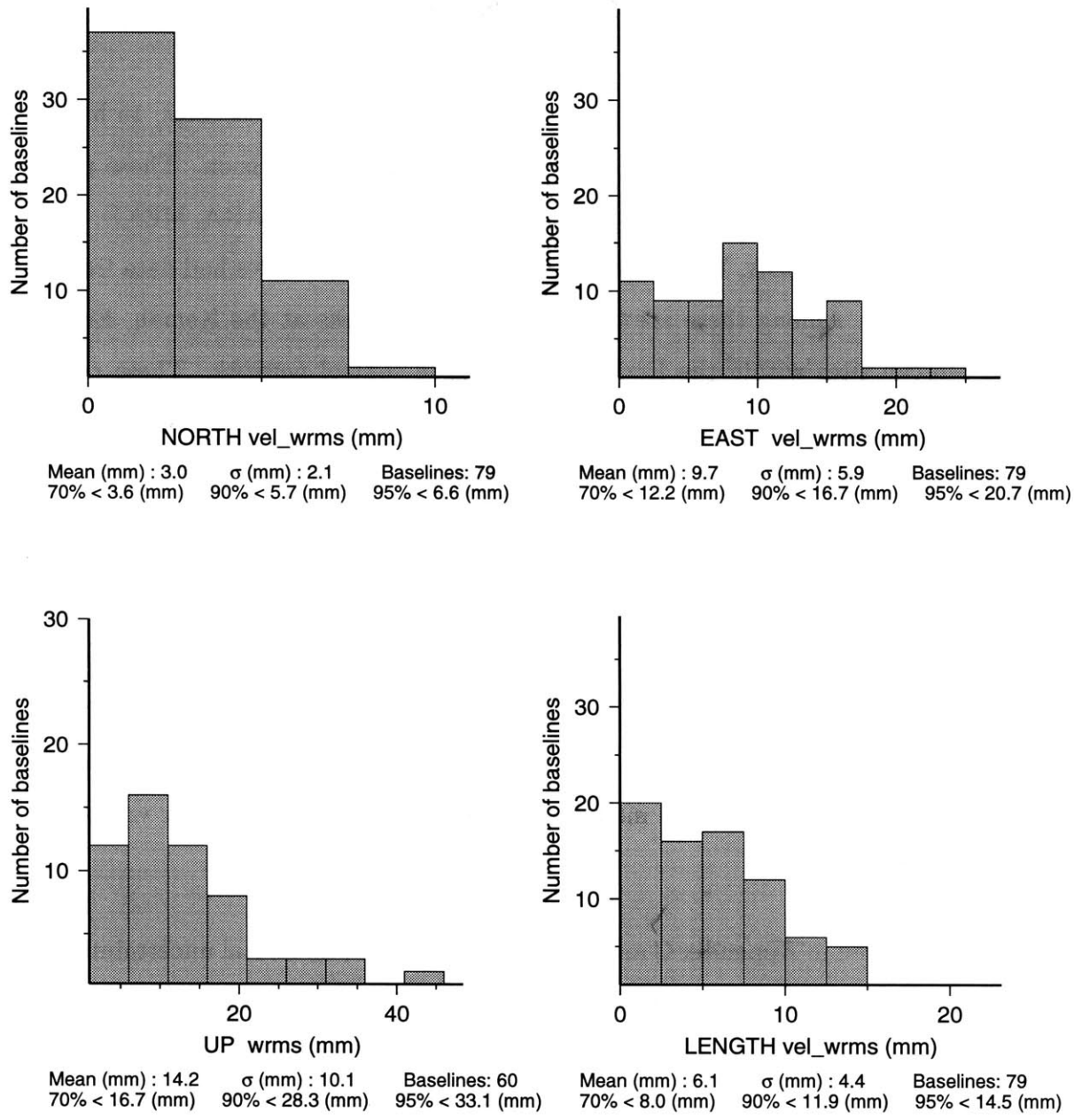

Figure 2-10: Histogram of the long-term wrms scatter of NS and EW components and length, about the best fitting straight line. The long-term wrms scatter of UD components is obtained about their weighted means. We scaled the formal uncertainties by a factor of 2 (after rescaling the 1990 experiment by 3) to reflect realistic 1-σ errors.

2.5 GPS Derived Velocity Field

We obtained relative site motions for 61 sites in Turkey. Of these sites, 15 had data from at least 3 epochs, providing a measure of long-term precision. These primary sites are AKGA, ANKA, ANTU, CEIL, CINE, IKAN, ISME, KARA, MEKE, MELE, ODME, PAMU, ULDA, YIGI, and YOZG. The remaining 46 sites had data from only two epochs[15]. Among these are the renamed benchmarks at the Kemah, Erzurum, and Mercan sites within the Erzincan earthquake control network. These renamed sites simply served to eliminate the co-seismic site position changes induced by the earthquake (see Appendix D). We excluded suspect sites (AKCA, ALSE, DIYA, KINI, SEBI, and USUM) from the estimation process.

In order to minimize the effect of large systematic errors in the vertical on our velocity results (see Appendix C), we allowed the vertical coordinates of the regional sites to vary stochastically. For four sites which had large scatters in the vertical (MELE, YIGI, YIG2, and KARA) we permitted their vertical positions to vary from year-to-year by as much as 0.5 m. For other sites we allowed 0.05 m/yr variations in the vertical positions.

As discussed in Appendix C and section 2.4, we scaled all formal uncertainties by a factor of 2, after first rescaling the 1990 uncertainties by a factor of 3. In our analysis, we assumed that velocities at nearby sites were equal, applying velocity ties for Yığılca (YIGI, YIG1, YIG2), Ankara (ANKA, ANKR, ANKM, ANKS), Karacadağ (KARA, KAR2), and Patnos (PATN, PAT2). Since observations were taken for only one epoch at the YIG1, ANKS, KAR2, and PAT2 sites, we applied velocity ties effectively at Yığılca and Ankara. We used the velocity estimates at YIGI and YIG2 as a control

[15] "Two-epoch velocity" estimated sites: AKTO, ANKM, ANKR, AYVA, BAYO, BULD, DEMI, ER01, ER02, ER03, ER04, ER05, ER07, ER08, ER09, ER10, ER11, ER12, ERDE, ERZ2, ERZU, HAPA, HEMI, ISPI, ITAY, KADI, KALE, KARS, KASO, KEM2, KEMA, KINI, KIRE, KIZI, KORK, MALA, MER2, MERC, PATN, SEUR, SEVK, SINC, SIPD, SOKE, ULUC, and YIG2.

and found no significant difference within 1-σ.

The rather long interstation distances between Turkish and European sites (> 2500 km), and the possible projection of vertical errors into estimates of the horizontal (see Appendix C) prevented us from obtaining a reliable velocity field relative to the fiducial sites on the European plate, unless a velocity constraint for at least one regional site was introduced via explicit velocities ties. Thus, in our unconstrained solutions, we expressed our GPS derived velocity field relative to regional sites.

For the unconstrained GPS derived velocity field we expressed the observed site velocities relative to a site on the Pontus block. To facilitate comparisons, we chose the SLR/GPS site Yığılca, located on this block. These velocities, relative to Yığılca (YIGI/YIG2), are shown in Figure 2-11 with 95% confidence ellipses, which adequately describe the accuracy and precision of our relative horizontal velocity estimates for primary sites. The semi-major and semi-minor axes of these ellipses are roughly oriented east-west and north-south, respectively. The magnitudes of the axes of the ellipses are a function of the number of observations and of the time lapses between epochs. The semi-major and semi-minor axes of the 95% confidence ellipses, for sites visited 5 times (ANKA, MELE, YOZG), are 7 mm/yr and 4 mm/yr, respectively. For sites where we have only 3-epochs of observation, we witness an increase in the area of the ellipse. We find a magnitude of 10 mm/yr for the semi-major axis, and 5 mm/yr for the semi-minor axis. Figure 2-12 also shows relative velocities for those sites at which we have data from only two epochs, mostly in eastern Turkey and some in western Turkey. For these sites and those in the Erzincan earthquake network (see Appendix D) we have no reliable long-term error statistics, so the error ellipses at these secondary sites must be considered less reliable.

We have assumed that the statistics inferred for primary sites (roughly western and central Turkey sites) apply also for secondary sites (eastern Turkey and Erzincan

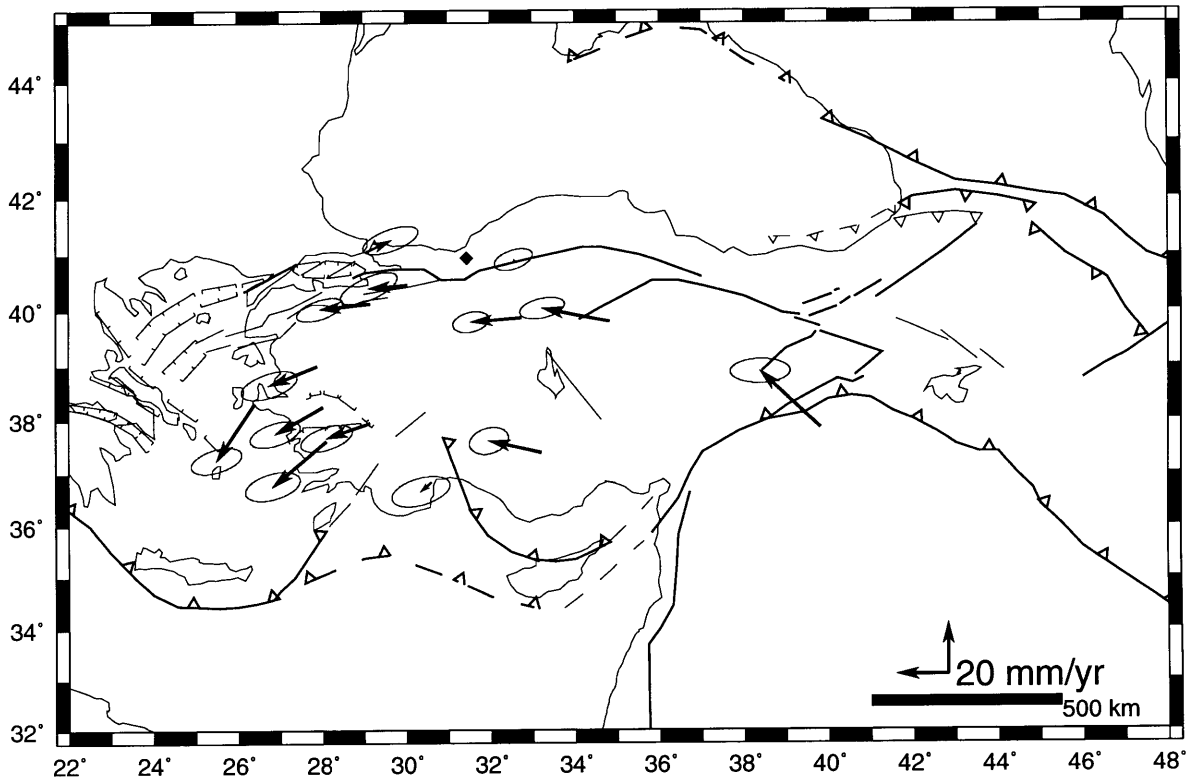

Figure 2-11: Observed velocities (unconstrained solution) of primary sites relative to Yığılca (shown with a diamond) estimated from 5-years of GPS observations in Turkey: 1988-1992. The ellipses denote the 95% confidence region, after scaling the formal uncertainties, as described in the text.

earthquake network sites), applying the same scaling factor. The actual errors, however, could be higher/lower. The area of 95% confidence ellipses, especially for sites in eastern Turkey, is at least twice as large as those for the primary sites. Due to their large uncertainties, in Figure 2-12 we omitted velocities at the HEMI, SEVK, ERDE and ITAY sites, which were occupied in 1990 and fall 1992.

The 1-σ uncertainties quoted in Table 2.7 are obtained after applying appropriate scaling to the formal uncertainties of each experiment. These standard deviations are one-dimensional quantities and should be multiplied by an additional factor of 1.96 for a confidence level of 95%. Two-dimensional uncertainties (joint probability) at the 95% confidence interval can be calculated for the east and north components of

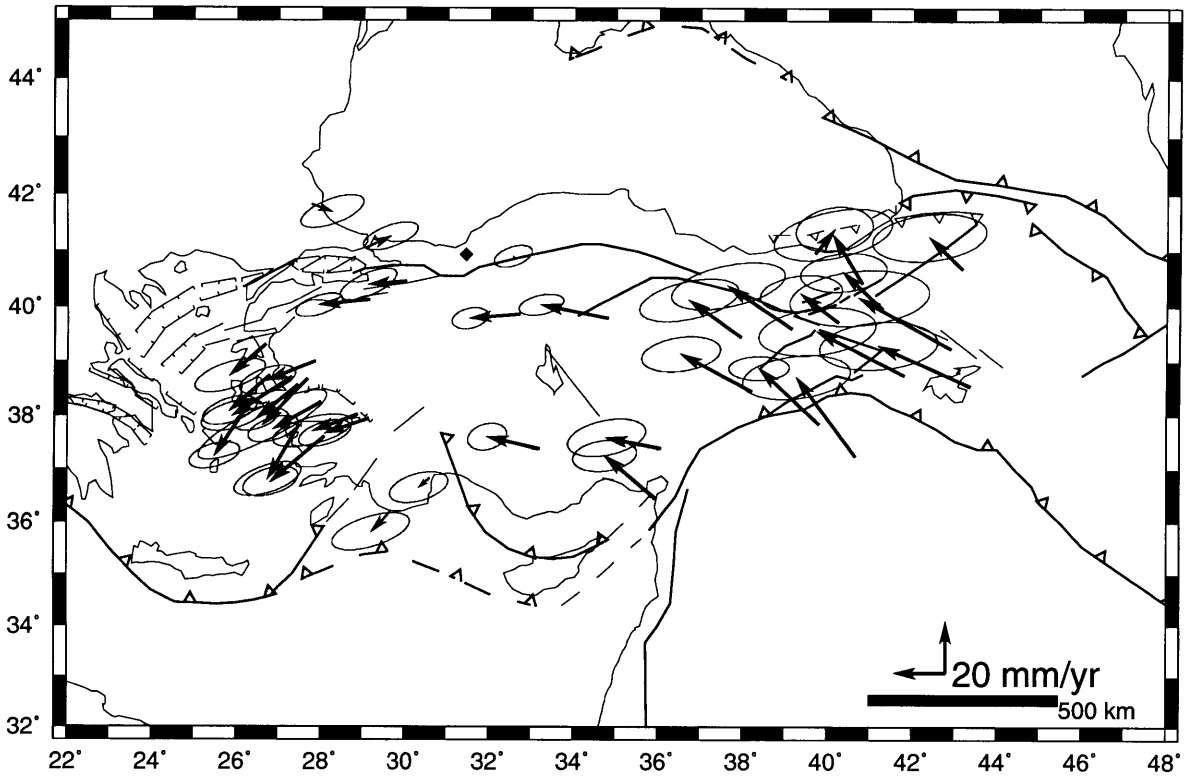

Figure 2-12: Observed velocities (unconstrained solution) of all sites relative to Yığılca (shown with a diamond) estimated from GPS observations in Turkey: 1988-1992. The ellipses denote the 95% confidence region, after scaling the formal uncertainties, as described in the text.

velocities, when the σ_E and σ_N given in Table 2.7 are multiplied by 2.447.

As discussed in Appendix C, constraining the velocity for one regional site allows us to resolve velocities relative to a distant site. Such constraints also reduce the effects of long-term systematic errors and enable us to tie rather weak eastern Turkey measurements to those of western Turkey. So we chose to force the Karacadağ site to its NUVEL-1 determined value [DeMets et al., 1990] for the "constrained" velocity field. The constrained velocity field is illustrated in Figure 2-13. The area of 95% confidence ellipses are fundamentally the same as in Figure 2-12, except at Karacadağ, since its velocity has been explicitly prescribed.

Table 2.7: Regional site velocities relative to Yığılca obtained from unconstrained solution.

	East (mm/yr)		North (mm/yr)		
SITE	v_E	σ_E	v_N	σ_N	ρ_{EN}
AKGA	-18.9	4.5	-7.5	2.3	0.532
AKTO	7.5	6.2	9.4	3.6	0.165
ANKA	-19.8	2.9	-1.7	1.7	0.282
ANTU	-4.0	4.7	-3.5	2.4	0.429
AYVA	-14.1	5.7	-12.3	2.7	0.597
BAYO	-23.2	5.0	-15.1	2.5	0.487
BULD	-17.6	6.4	-6.5	2.6	0.556
CEIL	-15.0	4.1	-22.3	2.1	0.459
CINE	-21.1	4.4	-17.7	2.3	0.426
DEMI	7.9	5.1	-2.9	2.6	0.618
ERDE	-11.5	12.2	-10.1	7.4	0.125
ERZU	-15.4	6.9	14.3	3.1	0.173
HAPA	-17.6	10.3	-18.0	5.6	0.862
HEMI	5.5	17.3	3.9	9.8	-0.007
IKAN	9.6	4.5	4.4	2.2	0.599
ISME	-0.3	3.1	0.7	1.8	0.449
ISPI	-11.4	9.5	19.0	4.1	0.408
ITAY	4.5	9.4	-2.0	5.2	0.156
KADI	-21.5	6.3	4.2	3.0	0.353
KALE	-36.0	9.5	15.9	3.9	0.160
KARA	-23.7	4.9	22.0	1.9	0.034
KARS	-12.9	9.1	12.6	3.8	0.232
KASO	-7.4	6.3	-7.7	3.0	0.558
KEMA	-25.3	9.1	16.8	3.8	0.462
KIZI	-23.1	8.7	31.1	3.5	0.251
KORK	-34.0	9.4	17.3	3.9	0.249
MALA	-27.9	6.4	14.7	2.8	0.264
MEKE	-15.1	4.6	-1.3	2.5	0.666
MELE	-20.6	3.1	4.8	2.2	0.236
MERC	-14.7	6.6	11.2	2.9	0.199
ODME	-18.8	4.0	-10.6	2.1	0.496
PAMU	-17.3	4.2	-5.9	2.2	0.509
PATN	-36.0	11.2	20.1	4.5	0.199
SEUR	-15.8	4.4	-13.8	2.3	0.511
SEVK	-7.6	17.9	-10.2	10.1	0.100
SINC	-20.6	8.0	14.6	3.4	0.450
SIPD	-16.3	3.6	-13.3	2.0	0.482
SOKE	-12.3	5.4	-21.1	2.7	0.563
ULDA	-19.8	3.8	-2.0	1.9	0.562
ULUC	-20.1	5.2	16.5	2.5	0.210
YOZG	-26.4	3.6	5.2	1.7	0.383

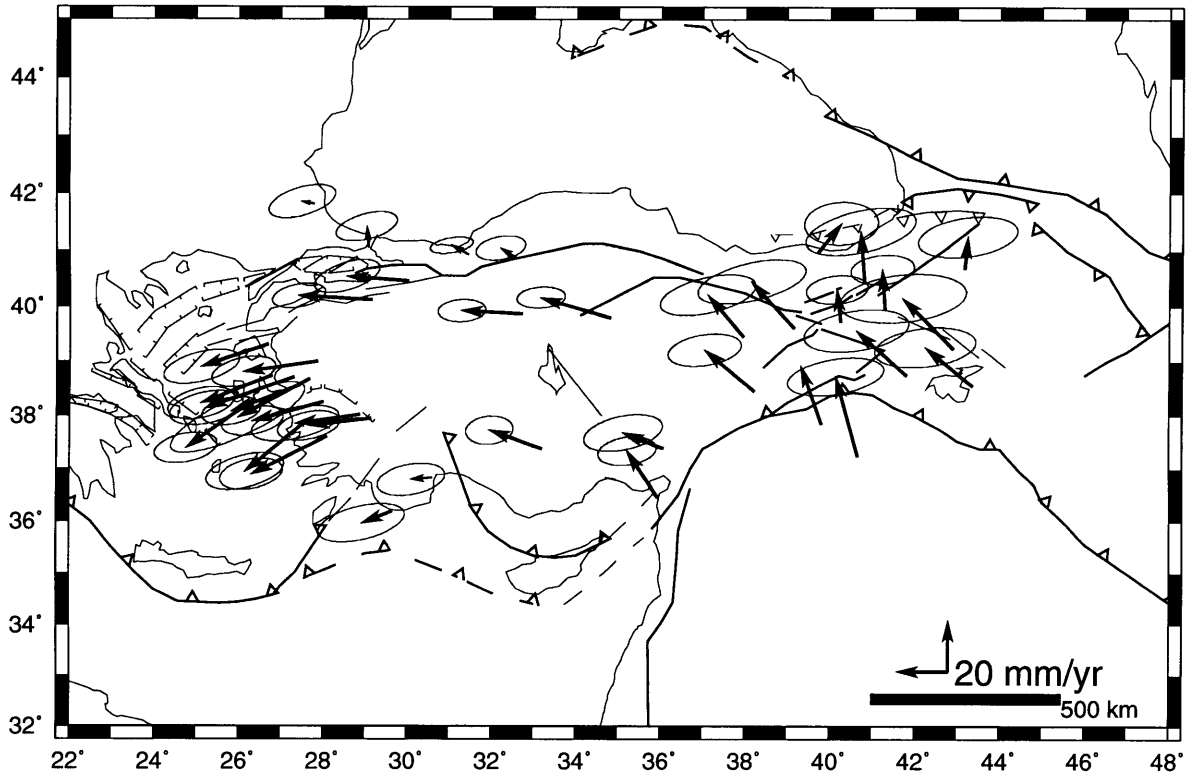

Figure 2-13: Observed velocities (constrained solution) of all sites relative to Onsala estimated from GPS observations in Turkey: 1988-1992. The velocity at the Karacadağ site is forced to its NUVEL-1 determined value [DeMets et al., 1990] using ${}_{EUR}\mathbf{E}_{ARA}$ Euler vector[ϕ=13.7°E, λ=24.6°N, ω=0.520°/Myr]. The ellipses denote the 95% confidence region, after scaling the formal uncertainties, as described in the text.

Given the NUVEL-1 ${}_{EUR}\mathbf{E}_{ARA}$ Euler vector [ϕ=13.7°E, λ=24.6°N, ω=0.520°/Myr] and uncertainties in the pole position (σ_{max}=5.2^o, σ_{min}=1.7^o, $\theta_{\sigma_{max}}$=-72^{o}N) and angular velocity (σ =0.05^o/Myr), the motion at Karacadağ relative to Eurasia is 25±6$_{95\%}$ mm/yr at -23±21$_{95\%}$ °N [v_E=-10±2 mm/yr, v_N=23±4 mm/yr]. Because of their large uncertainties, the velocities at HEMI, SEVK, ERDE and ITAY sites are not shown in Figure 2-13, but are given in Table 2.8.

We have repeated long-term error analyses with constraints imposed for velocities at the Karacadağ site, and observed insignificantly small changes for the statistical quantities quoted above for the regional baselines. However, the time evolution of

very long baselines improved remarkably (Appendix C). We summarize the regional site velocities relative to Onsala in Table 2.8 with 1-σ uncertainties quoted. In order to obtain two-dimensional uncertainties (joint probability) for the east and north components of velocities at the 95% confidence interval, the σ_E and σ_N given in Table 2.8 have to be multiplied by 2.447.

The regional velocities obtained from our constrained solution are consistent with those obtained from two epoch observations by SLR [Noomen et al., 1993] as illustrated in Figure 2-14. At two collocation sites, Melengiçlik [MELE] and Yığılca, we find good agreement between SLR and GPS derived site motions as shown in Table 2.9. At Yığılca, SLR and GPS estimates agree within 1-σ and show no significant motions relative to Eurasia at the 95% confidence interval. There is a remarkable agreement both in magnitudes and orientation of velocity vector, except with Yozgat. At Melengiçlik [MELE], SLR and GPS provide almost identical estimates, well within 1-σ [MELE$_{GPS}$:v_H=22$\pm$9$_{95\%}$ mm/yr, θ =-71$\pm$17$_{95\%}$ °N, MELE$_{SLR}$:v_H= 24$\pm$ 8$_{95\%}$ mm/yr, θ = -78$\pm$ 28$_{95\%}$ °N]. Nevertheless, there is a considerable discrepancy between our GPS estimate and that reported by SLR [Noomen et al., 1993] at the Yozgat [YOZG] collocation site. Although the orientations are consistent, the magnitude obtained by SLR [v_H=48$\pm$15$_{95\%}$ mm/yr] and GPS [v_H=29$\pm$9$_{95\%}$ mm/yr] differ by 21 mm/yr. This discrepancy probably stems from insufficient SLR observations at this site[16] leading to underestimated 1-σ errors. Cenci et al. [1993], for instance, provide rather a large 1-σ error for Yozgat [47$\pm$26$_{95\%}$ mm/yr]. The mismatch at Yozgat may also be related to the length of the LAGEOS I arc integrated for the analysis. Two different analyses by Gendt et al. [1993], one with a 5-day arc and another with a 30-day, produce rather different results. Although the Karacadağ [KARA] and Diyarbakır [DIYA] sites are not collocated, their GPS (from unconstrained solution)

[16]We note that with the addition of a third epoch SLR observation at this site such a mismatch reduces to insignificant level (John Robbins on unpublished Goddard Flight Center solutions, pers. comm., 1993)

Table 2.8: Regional site velocities relative to Onsala obtained from constrained solution.

	East (mm/yr)		North (mm/yr)		
SITE	v_E	σ_E	v_N	σ_N	ρ_{EN}
AKTO	9.3	5.9	11.5	3.4	0.062
ANKA	-23.9	3.8	1.2	1.8	0.101
ANTU	-8.2	5.5	-0.6	2.6	0.319
AYVA	-26.3	6.1	-8.8	2.7	0.485
BAYO	-34.5	5.9	-12.2	2.8	0.373
BULD	-25.4	7.1	-3.6	2.8	0.459
CEIL	-27.1	5.1	-19.4	2.4	0.332
CINE	-29.6	5.0	-14.9	2.5	0.315
DEMI	-4.8	5.4	0.8	2.6	0.498
ERDE	-22.8	12.4	-6.7	7.4	0.112
ERZU	-1.1	5.1	15.4	2.3	0.167
HAPA	-28.3	10.8	-15.2	5.7	0.806
HEMI	-7.8	17.4	7.4	9.9	-0.013
IKAN	-0.6	5.0	8.0	2.3	0.459
ISME	-6.1	4.0	3.7	2.0	0.307
ISPI	-1.5	8.8	20.1	3.8	0.456
ITAY	-6.0	9.6	1.5	5.2	0.136
KADI	-15.9	6.3	6.0	3.0	0.371
KALE	-18.6	8.1	15.3	3.2	0.259
KARA	-8.1	0.0	22.9	0.0	0.001
KARS	1.2	8.0	12.6	3.3	0.294
KASO	-12.1	7.0	-4.7	3.1	0.460
KEMA	-16.9	8.7	18.4	3.5	0.503
KIZI	-8.7	7.7	31.3	3.0	0.361
KORK	-19.6	8.4	17.5	3.4	0.323
MALA	-19.6	5.9	16.2	2.6	0.297
MEKE	-24.5	5.3	1.7	2.6	0.524
MELE	-20.7	3.8	7.3	2.3	0.114
MERC	-1.5	4.9	12.7	2.3	0.174
ODME	-27.8	5.0	-7.5	2.4	0.352
PAMU	-24.6	5.0	-2.8	2.4	0.353
PATN	-19.9	10.2	19.9	3.9	0.247
SEUR	-27.9	5.4	-11.0	2.6	0.372
SEVK	-20.0	18.0	-6.8	10.1	0.093
SINC	-14.1	7.7	16.5	3.3	0.470
SIPD	-27.1	4.7	-10.3	2.3	0.303
SOKE	-22.1	6.2	-18.2	3.0	0.440
ULDA	-28.7	4.3	1.6	2.0	0.341
ULUC	-12.1	4.7	18.3	2.3	0.226
YIGI	-6.6	3.5	3.6	1.3	0.405
YOZG	-27.5	3.9	7.9	1.7	0.138

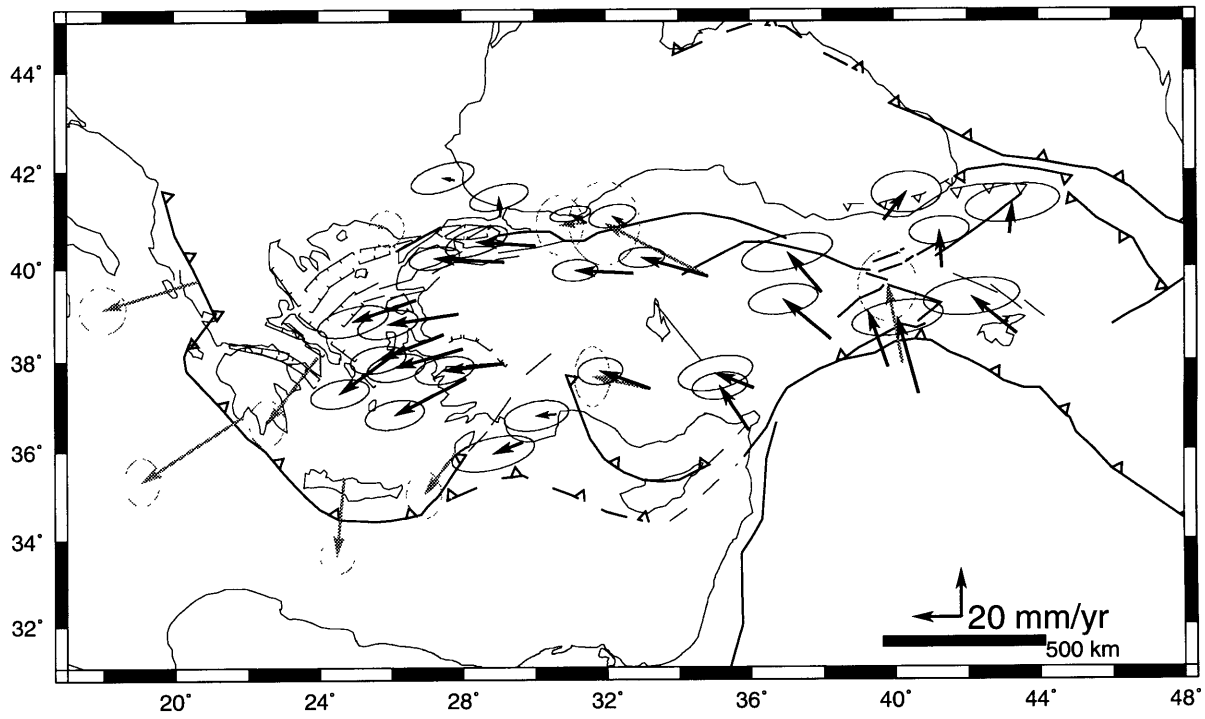

Figure 2-14: GPS and SLR velocities. Observed velocities (black arrows) at the Turkish sites relative to Onsala (Sweden) estimated from GPS observations in Turkey between 1988 and 1992. For clarity, velocities of some GPS sites are not shown (*cf.* Figure 2-13). Gray arrows indicate observed velocities estimated from SLR observations at the Greek sites between 1986-1990 and are relative to the Eurasian Plate [Noomen et al., 1993]. The ellipses denote the 95% confidence region, after scaling the formal uncertainties. Because no correlation information was available for the SLR estimates, the 95% confidence ellipse is obtained only from uncertainties in the east and north. SLR sites not common to our GPS experiments are Askites [ASKI], Chrisokellaria [CHRI], Dionysos [DION], Karitsa [KARI], Kattavia [KATT], and Roumeli [ROUM].

and SLR velocities are comparable within the 95% error ellipses.

In the next chapter we discuss and interpret the GPS derived velocity field obtained from our constrained solutions. We label this solution (Figure ?? and Table 2.8) as TR94GTN in order to associate it with the data used in the analyses, type of analyses, and software versions (GAMIT release 9: lib [9.32], arc [9.11], model [9.20], solve [9.28]; GLOBK release 3.1; EULER 1.2).

Table 2.9: SLR velocities in the eastern Mediterranean [Noomen et al., 1993] relative to Eurasia.

	East (mm/yr)		North (mm/yr)		
SITE	v_E	σ_E	v_N	σ_N	ρ_{EN}
ASKI	5.0	3.0	-2.0	3.0	0.000
CHRI	-42.0	3.0	-27.0	4.0	0.000
DION	-21.0	3.0	-27.0	4.0	0.000
DIYA	-6.0	5.0	32.0	6.0	0.000
KARI	-40.0	4.0	-12.0	4.0	0.000
KATT	-13.0	3.0	-17.0	4.0	0.000
MELE	-24.0	3.0	5.0	5.0	0.000
ROUM	-3.0	3.0	-32.0	3.0	0.000
YIGI	-11.0	4.0	-1.0	5.0	0.000
YOZG	-43.0	6.0	22.0	7.0	0.000

Chapter 3

Results of GPS Measurements and their Tectonic Implications

3.1 Present Day Kinematics of the Eastern Mediterranean

Synopsis. In Figure 2-13, relative site motions obtained from our GPS measurements between 1988 and 1992 indicate four major domains each having distinct kinematics (Figure 3-1): the Pontus block, the Anatolian and Arabian plates, and the Caucasus. There is an overall consistency between SLR [Noomen et al., 1993] and our GPS velocity fields. We observe a very small amount of deformation at the sites located on the Pontus block (the region roughly north of the North Anatolian fault) relative to one another and to Eurasia. The relative motions remarkably depict two distinct tectonic units (the Pontus block and the Anatolian plate) separated by the North Anatolian fault (NAF). Right lateral strike slip motion across the NAF [v_H=25$\pm$10$_{95\%}$ mm/yr] is clearly evident. The most prominent feature in the velocity

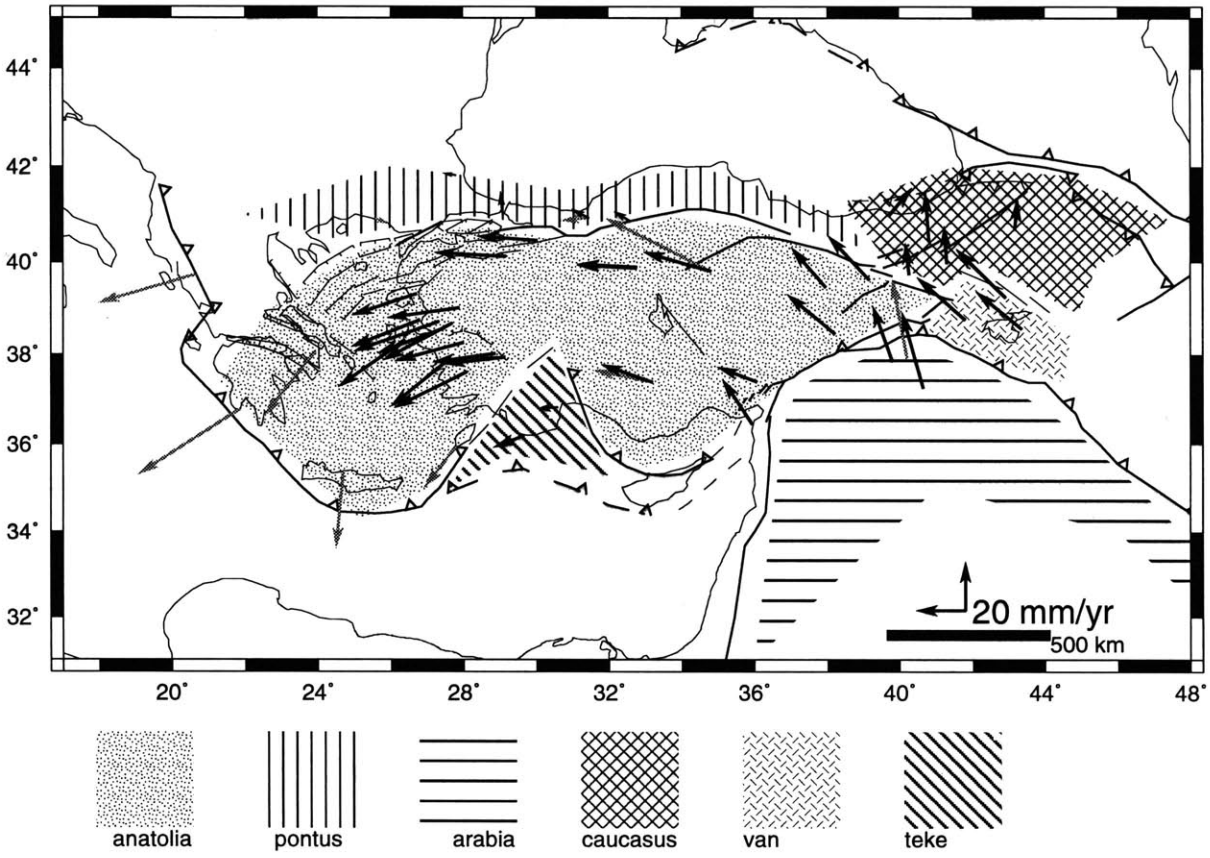

Figure 3-1: Tectonic units in Turkey with distinct kinematics derived from space geodetic observations. Velocities are relative to Eurasia (Onsala, Sweden). To avoid confusion we have not shown the error ellipses which are the same as in Figure 2-13 and Figure 2-14. Black arrows: GPS (this study); gray arrows: SLR (after Noomen et al. [1993]). Four major domains with distinct kinematics are the Pontus block, the Anatolian and Arabian plates, and Caucasus domain. Teke and Van domains are considered a part of the Anatolian plate (see discussion about the rotation of the Anatolian plate in section 3.2).

field is an apparent counterclockwise rotation of the Anatolian plate: sites in central and western Turkey move westerly and southwesterly relative to Eurasia, respectively. SLR observed velocities along the Hellenic arc and in Greece suggest that this coherent rotation includes the central and southern Aegean. Overall agreement between velocity fields from GPS measurements in Turkey and from SLR measurements in the Aegean Sea indicates not only a coherent rotation of the Anatolian plate, but also its westerly continuation towards Greece as a single tectonic unit with some degree

of internal deformation. The northern boundary of the Anatolian plate is clearly defined by the NAF. The northern splay of the NAF in the Marmara Sea and the North Aegean trough are likely to represent the boundary farther to the west[1]. In the east, the Anatolian plate is separated from the Arabian plate by the East Anatolian fault (EAF). Our GPS results indicate that the easternmost extent of Anatolia is not at the Karlıova basin, where the NAF and EAF meet. Instead, Anatolia continues farther eastward to include the Van block. In this scenario, a set of strike slip faults (the Tutak, Çaldıran and Karayazı faults) north of Lake Van are likely to determine the easternmost boundary of the Anatolian plate. The Hellenic arc clearly marks the southern boundary of the Anatolian plate, separating it from the African plate. Motions in the Teke domain, relative to Pontus, are rather small due to its proximity to the rotation pole. This domain behaves as part of the Anatolian plate. Relative velocities in eastern Turkey show that there is significant convergence between the Arabian plate and the Eurasian and Anatolian plates. Our GPS observations indicate a smaller relative motion across the EAF than that across the NAF. North of the Bitlis suture, we observe two distinct domains: the Van block and Caucasus. The behavior of each domain differs from the predominantly north to northwest motion of the Arabian plate relative to Eurasia. Rather than a northward gradual decrement in velocities, our GPS observations indicate that the oblique convergence between the Arabian and Eurasian plates in eastern Anatolia is partitioned into a NW-SE oriented slip and a N-S shortening. This is in good agreement with the orientation of slip vectors obtained from earthquake focal mechanism solutions, and the partitioning of oblique convergence into strike-slip and dip-slip motion [Molnar, 1992; Jackson, 1992].

Below we first present GPS observations on the Pontus block, and establish it as a regional reference frame. Rather than focus on distinct domains, we discuss relative

[1]Due to the absence of space geodetic observations we cannot speculate on the westernmost boundary.

motions as they apply to geographical regions: Central and east-central Turkey, the Marmara, western Turkey, Teke and eastern Turkey. In this context, the relative motions across the North and East Anatolian fault zones and the Bitlis suture are described, and the rotation of the Anatolian plate is portrayed. In the next section we parameterize this rotation and show evidence for the likely boundaries of the Anatolian plate. This is followed by the derivation of the velocity gradient tensor for subregions and discussion on rates of strain and rotation.

Pontus. Our GPS observations show that the sites north of the North Anatolian fault zone have very small or insignificant motion relative to Eurasia (Figure 3-2; for site names refer to Figures 2-2 and 2-3). We observe an average of $8\pm7_{95\%}$ mm/yr motion relative to Onsala (Sweden) at three primary sites: Yığılca [YIGI], Ismetpaşa [ISME] and Kandilli [IKAN]. This GPS detected motion is comparable to SLR [Noomen et al., 1993] observed velocity (Eurasia fixed frame) at Yığılca [$YIGI_{GPS}$:v_H= 8± $7_{95\%}$ mm/yr, θ = -62± $43_{95\%}$ °N vs. $YIGI_{SLR}$: v_H= 11± $10_{95\%}$ mm/yr, θ = -95± $59_{95\%}$ °N]. At the Thracean sites (Demirköy [DEMI] and Hemit [HEMI]) there is no significant motion relative to Eurasia [e.g., DEMI: v_H=$5\pm12_{95\%}$ mm/yr], which is in agreement with the SLR observed velocities at Askites [$ASKI_{SLR}$: v_H=$5\pm7_{95\%}$ mm/yr]. This suggests that the motions on the Pontus block, relative to Eurasia, manifest a westerly decrease. If this is the case, we may consider the Caucasus domain sites, for instance, Aktoprak [AKTO: v_H=$15\pm12_{95\%}$ mm/yr], as a part of the Pontus block. However, within our current observations, neither the eastern nor the northern boundary of the Pontus block can be clearly defined. We have, as yet, no repeat observations at Sinop [SINO], which lies between AKTO and ISME. Relative site motions do not strongly suggest the Northeast Anatolian fault (NEAF) to be a major tectonic boundary. There is significant motion at Aktoprak and Ispir [ISPI] relative to Yığılca. However, the sites in the Caucasus domain have been observed only twice and as a result, have large uncertainties. In view of these facts, we tentatively consider the Pontus block to be a unit different than the Black Sea plate

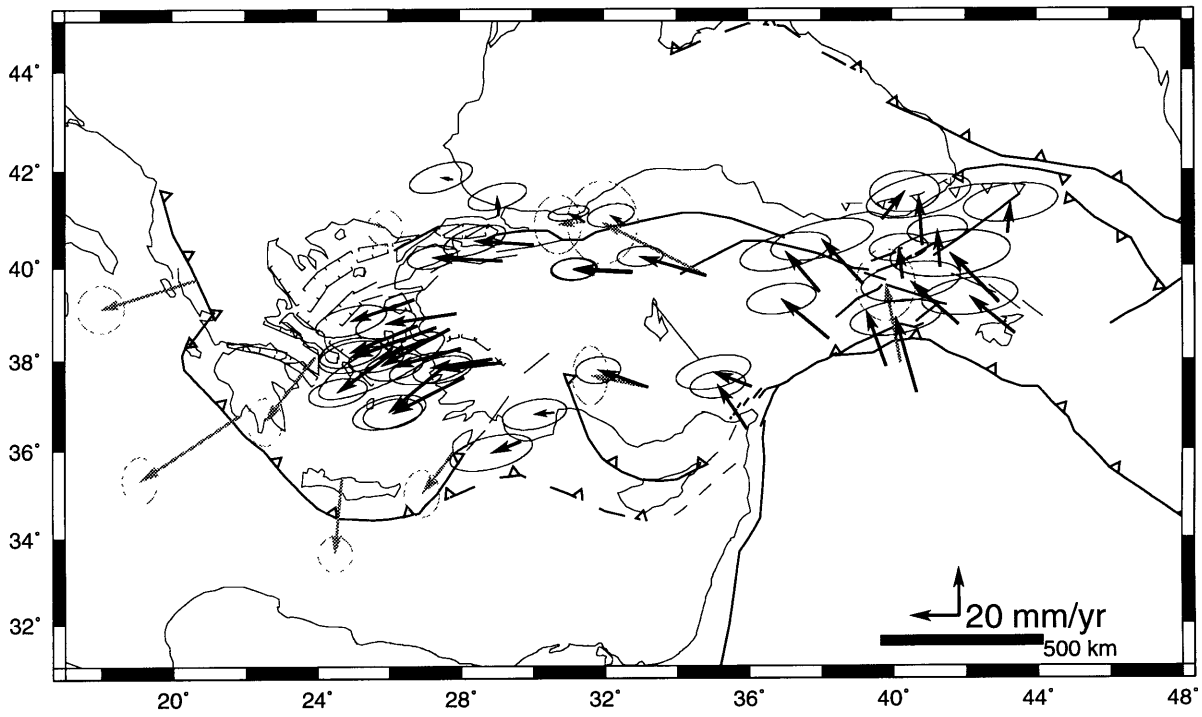

Figure 3-2: Observed velocities (black arrows) at the Turkish sites relative to Onsala [ONS0] estimated from GPS observations in Turkey between 1988 and 1992. Gray arrows indicate observed velocities estimated from SLR observations at the Greek sites between 1986 and 1990, and are relative to the Eurasian plate [Noomen et al., 1993]. The ellipses denote the 95% confidence region, after scaling the formal uncertainties. Because no correlation information was available for the SLR estimates, the area of 95% confidence is determined by their uncertainties in the east and west.

[McKenzie, 1972] and the Caucasus domain. We also speculate that the Pontus block and Caucasus domain may be a single unit experiencing gradual westerly decrease in velocity while overthrusting in the southeastern and southwestern Black Sea. Given the focal mechanisms for earthquakes in the Black Sea (Figure 1-5), it is probable that the northern boundary of the Pontus block is defined by offshore thrusting [Alptekin et al., 1986] (Figure 1-5).

We also observe no significant relative motion among six Pontus sites (Figure 3-3, HEMI and ITAY are not shown) and conclude that Yığılca presents an adequate reference frame for the relative motions in Turkey. This removes the small amount of

westerly motion, if any, relative to Eurasia. (In Appendix C we have already shown that both constrained and unconstrained solutions are identical when baselines are short. Also, see Figure C-21.) Observing no significant motion between Ismetpaşa [ISME] and Yığılca, from analysis of 1988 and 1990 GPS measurements, Oral et al. [1993] had already argued that Yığılca presented an adequate reference frame for the relative motions in western Turkey, although unaware of its small motion relative to Eurasia. Figure 3-3 shows GPS derived velocities at the Turkish network sites

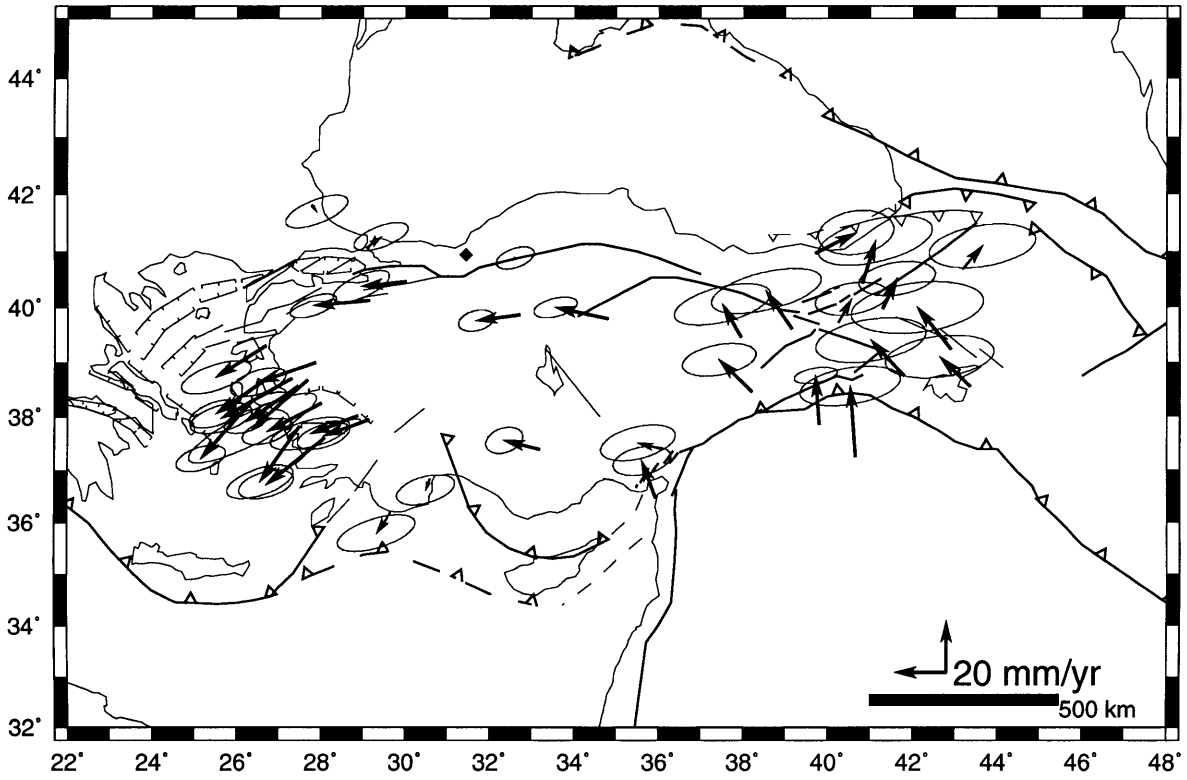

Figure 3-3: Observed velocities at all sites relative to Yığılca [YIGI and YIG2] (shown with a diamond), estimated from GPS observations in Turkey between 1988 and 1992. The ellipses denote the 95% confidence region, after scaling the formal uncertainties.

(primary and secondary) relative to Yığılca. With four additional experiments providing one additional measurement at Ismetpaşa and three more at Yığılca, we find no horizontal motion along the 95 km ISME-YIGI baseline [v_H=1±8$_{95\%}$ mm/yr]. It is rather interesting to find no motion at Ismetpaşa, lying only a couple of kilometers

north of the fault. This may indicate that the motion between Anatolia and Pontus may be taken up by creep along this section of the NAF at the narrow shear zone. Ambraseys [1970] documented local creep at about 20 mm/yr in the vicinity of Ismetpaşa. Similarly, triangulation-trilateration measurements conducted in 1972 and 1982 in the Ismetpaşa microgeodetic network (sites $\sim$ 200 meters north and south of the fault zone) suggest a 10–12 mm/yr motion [Eren, 1984]. In this sense, the $18\pm 9_{95\%}$ mm/yr motion we observe between the Ismetpaşa and Ankara sites could well be localized at a narrow zone from the fault.

Further, we observe rather insignificant motions at Kandilli [v_H=$7\pm11_{95\%}$ mm/yr] relative to Yığılca. None of the three secondary sites on Thrace (Ayazağa [ITAY], Demirköy [DEMI], and Hemit [HEMI]) show significant motion relative to Yığılca at the 95% confidence interval (Figure 3-4). Demirköy was occupied in 1988 and fall 1992. The rate of change in the horizontal for the 321 km long Demirköy to Yığılca baseline [v_H=$3\pm5_{95\%}$ mm/yr] is not significant at the 95% confidence interval (Figure 3-4). The other secondary site on Thrace, Hemit [HEMI], is 391 km west of Yığılca and also shows no motion relative to Yığılca [v_H= $4\pm 26_{95\%}$ mm/yr]. Separated by the Bosphorus strait, the Ayazağa and Kandilli sites are 5.8 km apart (no velocity ties were applied between these sites) and have no motion relative to Yığılca. The motion at Ayazağa (occupied in 1990 and fall 1992) relative to Kandilli [v_H=$8\pm19_{95\%}$ mm/yr] is also negligible.

We also performed solutions in which one common velocity was estimated for all Pontus block sites. With this constraint, the velocities at other sites located in western and central Turkey changed as much as 4 mm/yr. In no case were these statistically significant. Thus, we can argue that the motions on the Pontus block (between Ismetpaşa [GPS] and Askites [SLR]) are not significantly different from zero. Therefore, Yığılca and/or the Pontus block offer an appropriate reference frame for regional site motions in Turkey, especially for the western region, in the case of

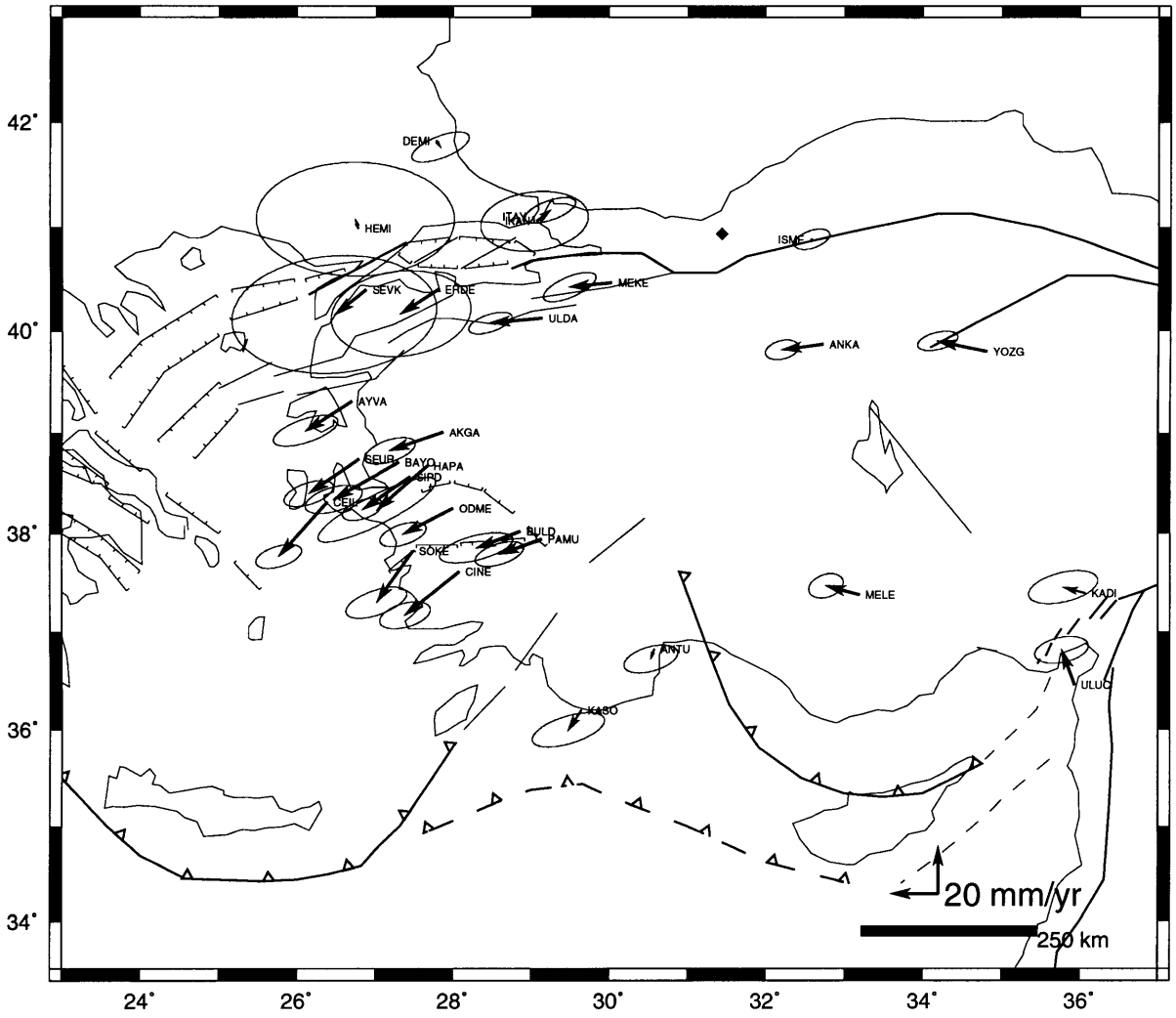

Figure 3-4: Observed velocities at the western Turkey sites relative to Yığılca [YIGI and YIG2] (shown with a diamond), estimated from GPS observations in Turkey between 1988 and 1992. The ellipses denote the 95% confidence region, after scaling the formal uncertainties.

unconstrained solutions (Appendix C).

Central and east-central Turkey. The direction of velocities for sites on the Anatolian plate relative to Pontus is subparallel to the arcuate trace of the NAF and its splays in the Marmara region, especially to the northern strand. The azimuth of the site velocities changes from northwest in the vicinity of Kemah [KEMA] to almost westerly motion in central Turkey, and gains a southwestern heading in the

Biga peninsula (Figure 3-3). Kemah [KEMA] and Sincan [SINC] are 30 km and 100 km south of the eastern portion of the NAF[2], respectively. The azimuth of their motion relative to Yığılca is -35±62$_{95\%}$ °N (Figure 3-5). Sites south of the NAF in

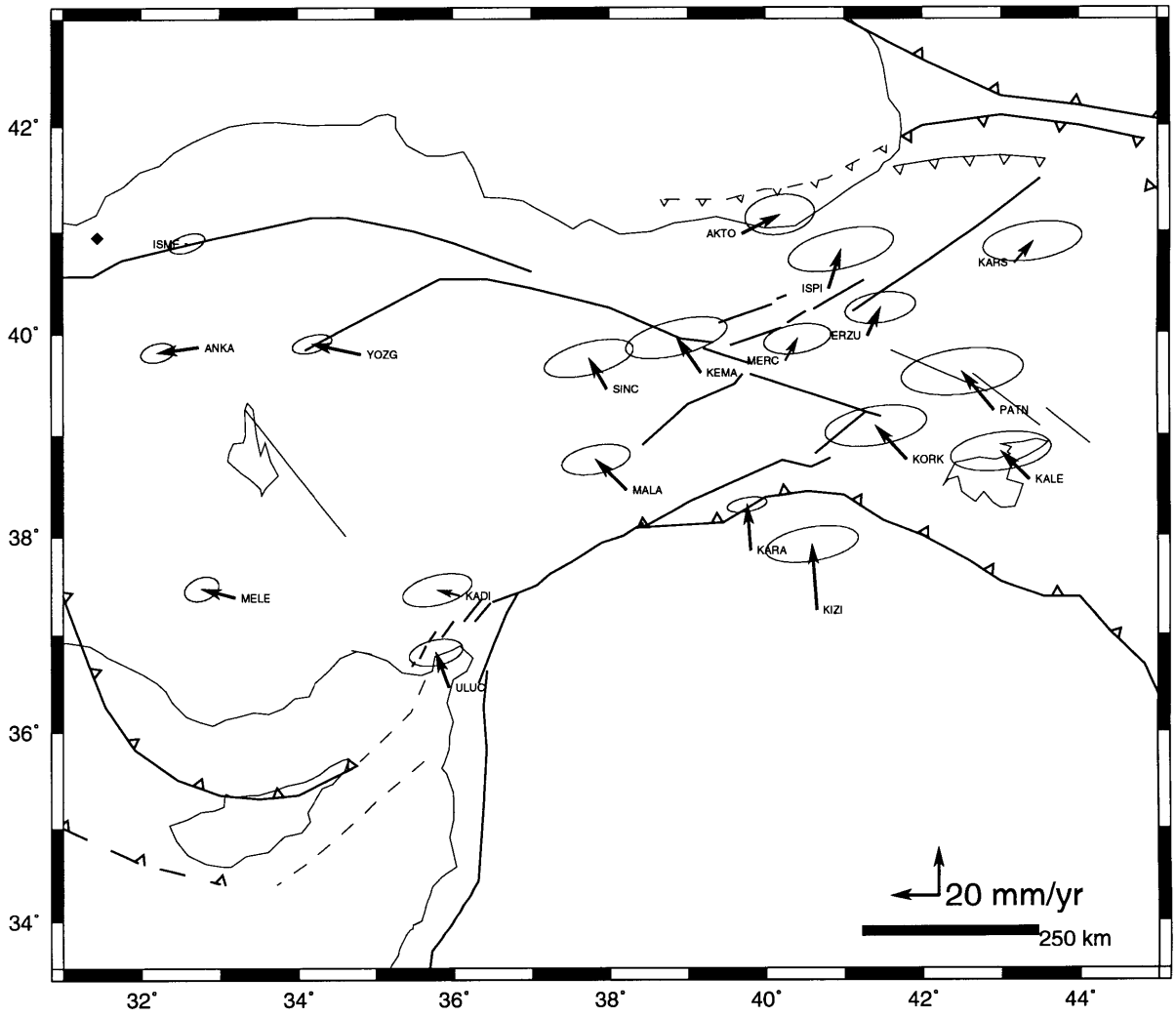

Figure 3-5: Observed velocities at the eastern Turkey sites relative to Yığılca [YIGI and YIG2] (shown with a diamond), estimated from GPS observations in Turkey between 1988 and 1992. The ellipses denote the 95% confidence region, after scaling the formal uncertainties.

central Turkey[3] (Ankara and Yozgat), however, have westerly headings with rather

[2]Fault segments 1 through 12 [Barka and Kadinsky-Cade, 1988].
[3]Fault segments 15 through 29 [Barka and Kadinsky-Cade, 1988].

small uncertainties. At the Yozgat [θ =-78$\pm$13$_{95\%}$ °N] and Ankara [θ =-98$\pm$12$_{95\%}$ °N] sites, which are about 150 km south of the central segment of the NAF, we observe a dominant westerly motion relative to Yığılca.

The magnitude of velocities relative to Yığılca at the sites in close proximity to the NAF remains fairly constant, and longitudinal variations within the 95% confidence intervals, if any, cannot be resolved. Estimates for relative site motions at the Kemah [KEMA: v_H=18$\pm$11$_{95\%}$ mm/yr] and Sincan [SINC: v_H=15$\pm$9$_{95\%}$ mm/yr] sites are comparable to those at Yozgat [YOZG: v_H=21$\pm$8$_{95\%}$ mm/yr] and Ankara [ANKA:v_H=18$\pm$7$_{95\%}$ mm/yr], and to those at Uludağ [ULDA: v_H=22$\pm$9$_{95\%}$ mm/yr] and Mekece [MEKE: v_H=18$\pm$12$_{95\%}$ mm/yr].

Overall, our GPS measurements detect a westerly 20$\pm$10$_{95\%}$ mm/yr motion relative to Pontus at sites 50–100 km south of the NAF zone. However, the magnitude of this motion does not necessarily reflect what would be experienced on and along the fault zone (see section on rotation). The dextral sense of this motion is in agreement with earthquake focal mechanisms (Figure 1-5). All focal mechanisms manifest right-lateral slip along the NAF. (In section 3.3 we discuss the rates of slip obtained from geology.)

The azimuth of velocities relative to Yığılca at other sites on the Anatolian plate, which are several hundred kilometers south of the NAF, also follow the arcuate geometry of the NAF. The azimuth, as well as the magnitude of the Malatya [MALA] velocity [v_H=18$\pm$10$_{95\%}$ mm/yr, θ =-46$\pm$39$_{95\%}$ °N], is quite comparable to that at Sincan or Kemah. There is remarkably good agreement about the MELE-YIGI motions between GPS [MELE$_{GPS}$: v_H=15$\pm$7$_{95\%}$ mm/yr, θ =-75$\pm$23$_{95\%}$ °N] and SLR [MELE$_{SLR}$: v_H=14$\pm$8$_{95\%}$ mm/yr, θ =-65$\pm$45$_{95\%}$ °N]. We also observe that motion at the Melengiçlik [MELE] site is similar to that at Yozgat/Ankara, as shown in Figure 3-6. In the Yığılca-fixed frame, the smaller magnitude observed at MELE

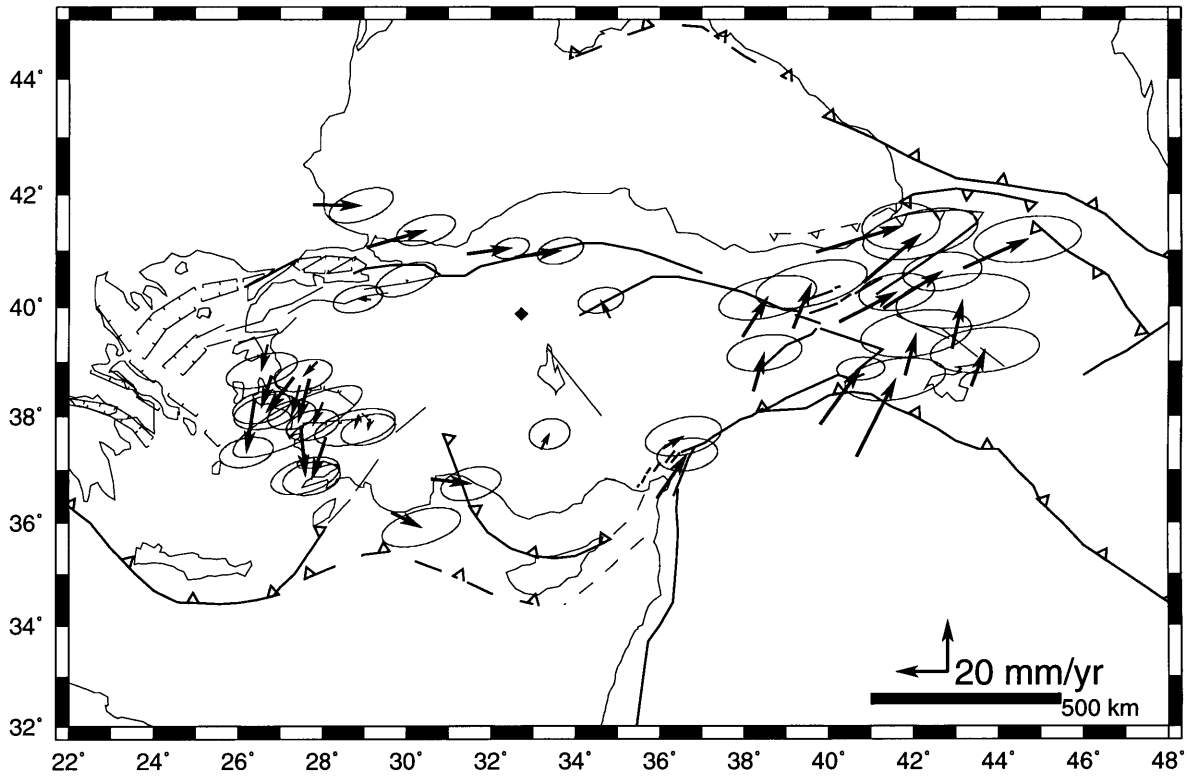

Figure 3-6: Observed velocities at all sites relative to Ankara [ANKA, ANKR, and ANKM] (shown with a diamond), estimated from GPS observations in Turkey between 1988 and 1992. The ellipses denote the 95% confidence region, after scaling the formal uncertainties.

relative to ANKA is due merely to the proximity to the rotation pole of ${}_{PON}\mathbf{E}_{ANA}$ (see next section).

Longitudinal variations in the direction of the velocity vectors (Figures 2-13, 3-2, and 3-3) depict the picturesque counterclockwise rotation of Anatolia (see section on western Turkey). The velocities expressed in the Ankara fixed frame (Figure 3-6) lend evidence for this counterclockwise rotation. (Suffice it to say that Ankara does not provide a convenient frame of reference for relative motions on the Anatolian plate.) The right lateral strike slip motion taken up by the NAF is clearly evident in Figure 3-6. The sites east of Ankara have distinct northward motion, while those in the west exhibit southward motion (see section on rotation). Although this counterclockwise

rotation of Anatolia is in agreement with Rotstein [1984], it presents a picture contrary to popular models (e.g., McKenzie [1972], Taymaz et al. [1991]) which foresee a simple westward motion of Turkey based on focal mechanisms. After discussing the relative site motions in western Turkey, we address this issue in the next section as we invert for the Euler vector.

Marmara. In the Marmara region, where the strike slip character of the NAF is enriched by extensional features as the fault splays into several branches north and south of the Marmara Sea, the westerly dominant motion of the Anatolian plate is sustained (Figure 3-7). At the two primary sites, Mekece [MEKE:v_H= 18± $12_{95\%}$

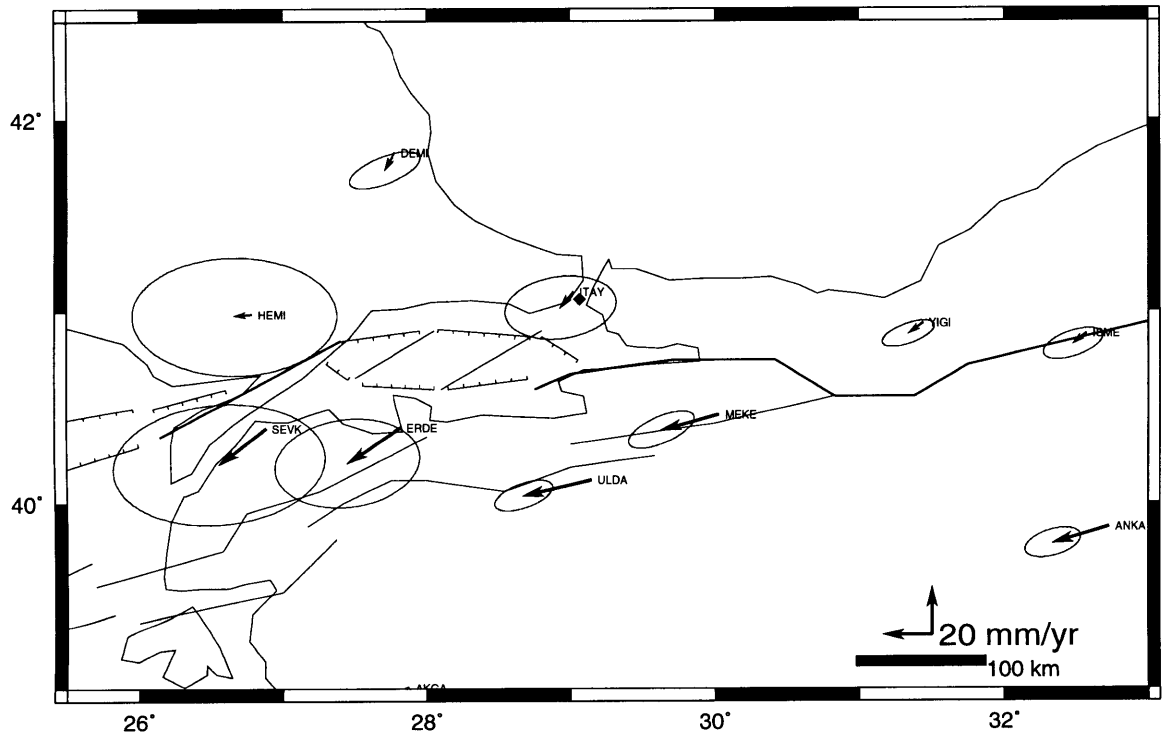

Figure 3-7: Observed velocities in Marmara region relative to Kandilli [IKAN] (shown with a diamond), estimated from GPS observations in Turkey between 1988 and 1992. The ellipses denote the 95% confidence region, after scaling the formal uncertainties. Immediately south of MEKE is the Iznık Mekece fault. Izmit-Sapanca fault is located ~50 km north of MEKE.

mm/yr, θ = -96± $17_{95\%}$ °N] and Uludağ [ULDA: v_H= 22± $9_{95\%}$ mm/yr, θ = -95±

$11_{95\%}$ °N], a westward motion relative to Pontus at -96±$12_{95\%}$ °N is evident.

Both Mekece and Uludağ are located west of the Mudurnu fault and south of the Izmit-Sapanca fault. The Mudurnu fault marks the western termination of the pure strike-slip character of the NAF. This section of the NAF ruptured in 1967 and produced a dextral strike-slip focal mechanism [McKenzie, 1972]. The Izmit-Sapanca[4] and Iznik-Mekece[5] faults are westerly splays of the NAF zone. The Iznik-Mekece fault lies between Mekece and Uludağ. We notice that the motions at both of these sites are comparable, but that we cannot resolve any significant relative motion between them.

Our GPS derived velocities suggest that the Izmit-Sapanca fault is active and defines the northern boundary of the Anatolian plate at the eastern end of the Sea of Marmara. Both sites south of this fault manifest westward motion. Microearthquake studies [Nishigami et al., 1990] conducted in the vicinity of these faults in 1988 also show high activity along the Izmit-Sapanca fault, which has predominantly normal faulting focal mechanism solutions. Earlier, Evans et al. [1985] had reported normal faulting with some strike-slip component dominant in the Izmit bay area, from fault plane solutions for microearthquakes between 1976–1981.

Further to the west, the direction of the site velocity vectors at the Erdek [ERDE] and Şevketiye [SEVK] secondary sites is subparallel [-127±37 °N] to the Yenice-Gönen[6] and Ganoşdağ[7] faults and to the North Aegean trough [Lyberis, 1984]. Although the magnitude of horizontal motion at these sites (18 mm/yr) is comparable to that near ULDA and ANKA, uncertainties at the 95% confidence interval for

[4]In the area located between fault segment 43 and fault segment 59, and also fault segments 59, 60, 61, and 62 [Barka and Kadinsky-Cade, 1988]. This fault zone has been termed Izmit-Lake Sapanca graben by Şengör [1979].

[5]Fault segments 44, 45,46, and 47 [Barka and Kadinsky-Cade, 1988].

[6]Fault segments 37, 38, and 39 [Barka and Kadinsky-Cade, 1988], which ruptured in 1953.

[7]Fault segment 68 [Barka and Kadinsky-Cade, 1988], which ruptured in 1912.

these twice-observed secondary sites are 28 to 39 mm/yr, due primarily to additional downweighting (rescaled by a factor of 3) of the 1990 experiment. They may be overestimated by a factor of two if the area of error ellipse for ITAY is allowed to be large enough so that its velocity is not statistically different than that of IKAN (Figure 3-4). We can make the same argument for DEMI and HEMI. If the uncertainties at HEMI and ITAY are overestimated by a factor of two, then so are the uncertainties at ERDE and SEVK. These assumptions lead us to obtain statistically significant velocities at the Erdek [ERDE] and Şevketiye [SEVK] sites, and suggest that most tectonic activity may indeed be concentrated on the northern strand of the NAF. Microseismicity between 1976–1981 displays pronounced activity in the Marmara Sea and the Gulf of Saros [Üçer et al., 1985].

Western Turkey. In western Turkey, our GPS sites south of Ayvalık are located around east-west striking graben structures (the Gediz and Büyük Menderes breakaway zones, separated by the Bozdağ horst) and their north-south striking cross horsts and grabens [Dewey and Şengör, 1979; Şengör, 1985, 1987b]. At the western Turkey sites, which cluster around the Bozdağ horst, we observe a southwesterly motion relative to Pontus. The heading of these sites is θ =-130$\pm$20$_{95\%}$ °N, with magnitudes varying from 24$\pm$12$_{95\%}$ mm/yr to 30$\pm$11$_{95\%}$ mm/yr at the sites farthest from Yığılca (Figure 3-4). Given the level of our 95% uncertainties, it is rather difficult to resolve significant difference in velocities at the western Turkey sites relative to Yığılca. Nevertheless, we observe a consistent difference in velocities by about 10 mm/yr between sites distal to the Gediz and Büyük Menderes breakaway zones. The magnitude of horizontal motion relative to Yığılca at sites distal to the Gediz breakaway zone (Akdağ [AKGA], Ayvalık[AYVA], Buldan [BULD] and Pamukkale [PAMU]) is v_H=24$\pm$12$_{95\%}$ mm/yr. Sites distal to the Büyük Menderes breakaway zone (Çeşmeılıca [CEIL], Çine [CINE] and Söke [SOKE]) move southwest at v_H=30$\pm$11$_{95\%}$ mm/yr. To support this observation and eliminate possible motion across other structures, we present velocities at the western Turkey sites relative to Uludağ in Figure 3-8 (also, see Figure 3-

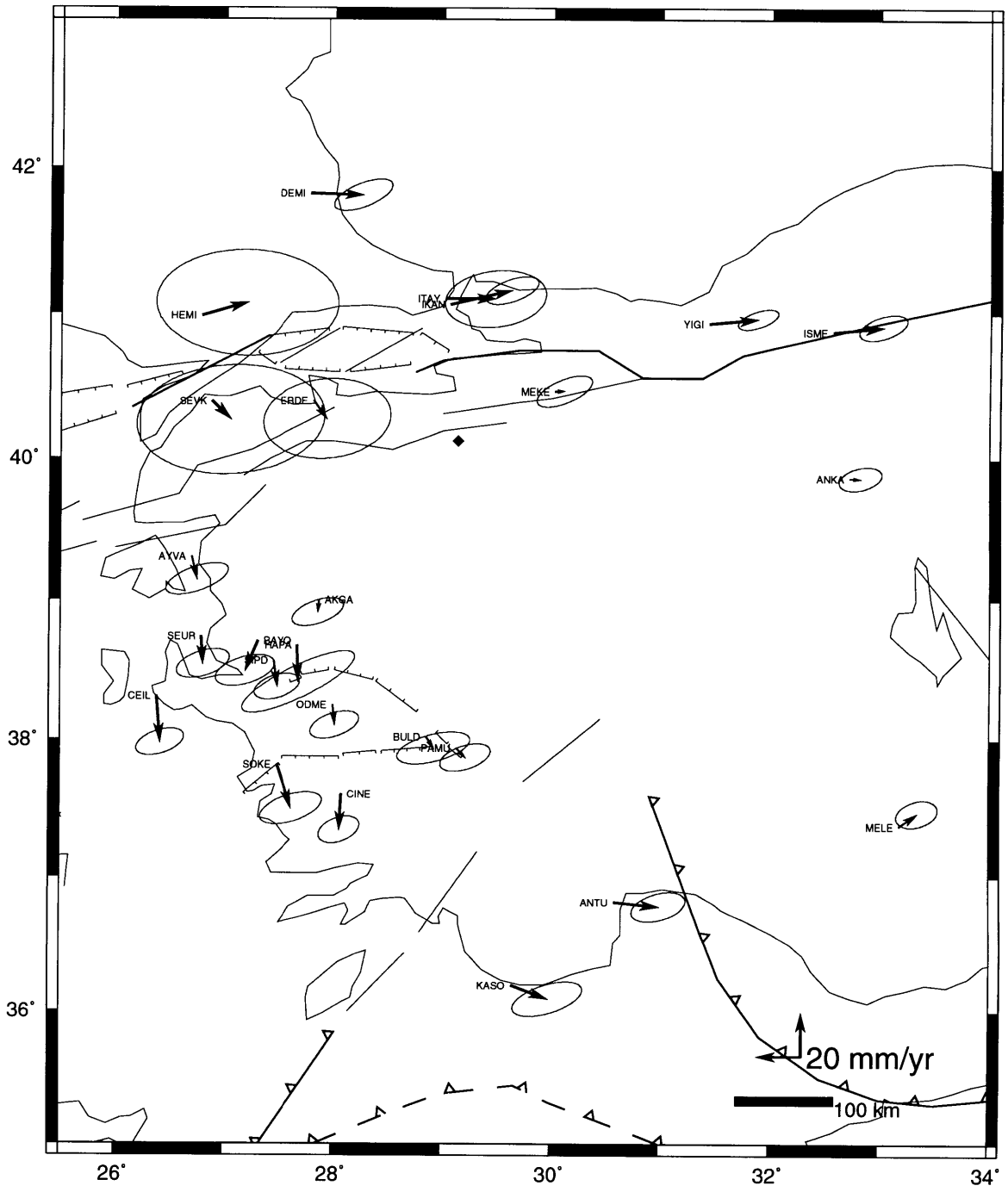

Figure 3-8: Observed velocities at the western Turkey sites relative to Uludağ [ULDA] (shown with a diamond), estimated from GPS observations in Turkey between 1988 and 1992. The ellipses denote the 95% confidence region, after scaling the formal uncertainties.

6). We cannot resolve significant motion between Uludağ and Akdağ [ULDA-AKGA: v_E=-0$\pm$12$_{95\%}$ mm/yr, v_N=-6$\pm$6$_{95\%}$ mm/yr], thus, if there is any motion taken up across the Simav fault it is about 6$\pm$7$_{95\%}$ mm/yr. Southerly, as well as westerly, increase in the velocities is evident. We observe elongation of the ODME-ULDA baseline (230 km) by 9$\pm$6$_{95\%}$ mm/yr. Çine, south of the Bozdağ horst, is apparently moving southwestward relative to Uludağ, twice as fast at 16$\pm$6$_{95\%}$ mm/yr. A clearer relative motion is, of course, shown in Figure 3-9, in which the velocities are

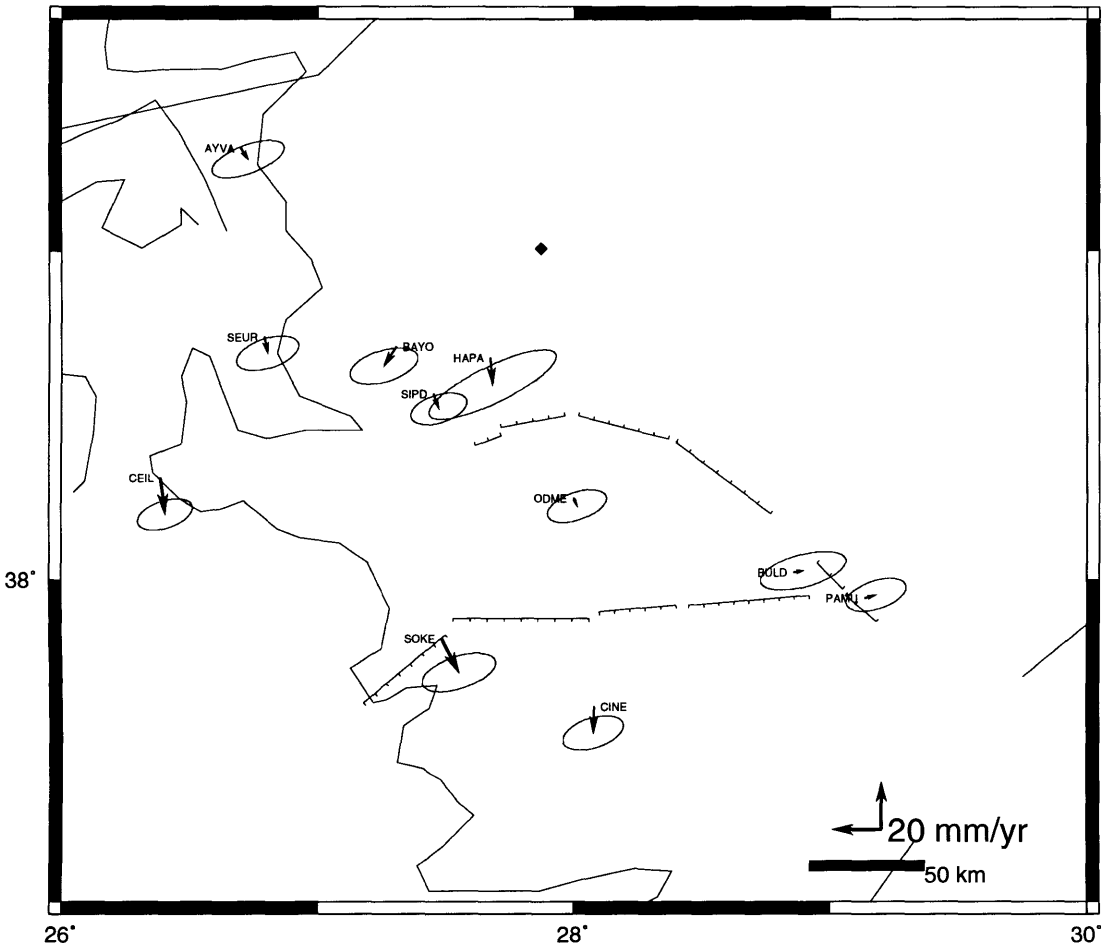

Figure 3-9: Observed velocities at the western Turkey sites relative to Akdağ [AKGA] (shown with a diamond), estimated from GPS observations in Turkey between 1988 and 1992. The ellipses denote the 95% confidence region, after scaling the formal uncertainties.

relative to Akdağ [AKGA]. We observe no significant motion at sites located north of the Gediz breakaway zone relative to Akdağ. However, sites south of the Büyük Menderes breakaway zone show southerly motion at a rate of $12 \pm 7_{95\%}$ mm/yr. Velocities relative to Ödemiş [ODME] do not allow us to resolve significant motion at sites north of the Gediz breakaway zone (Figure 3-10), but do provide upper limits to the possible motions across this zone. As shown in Figure 3-11, the total amount of

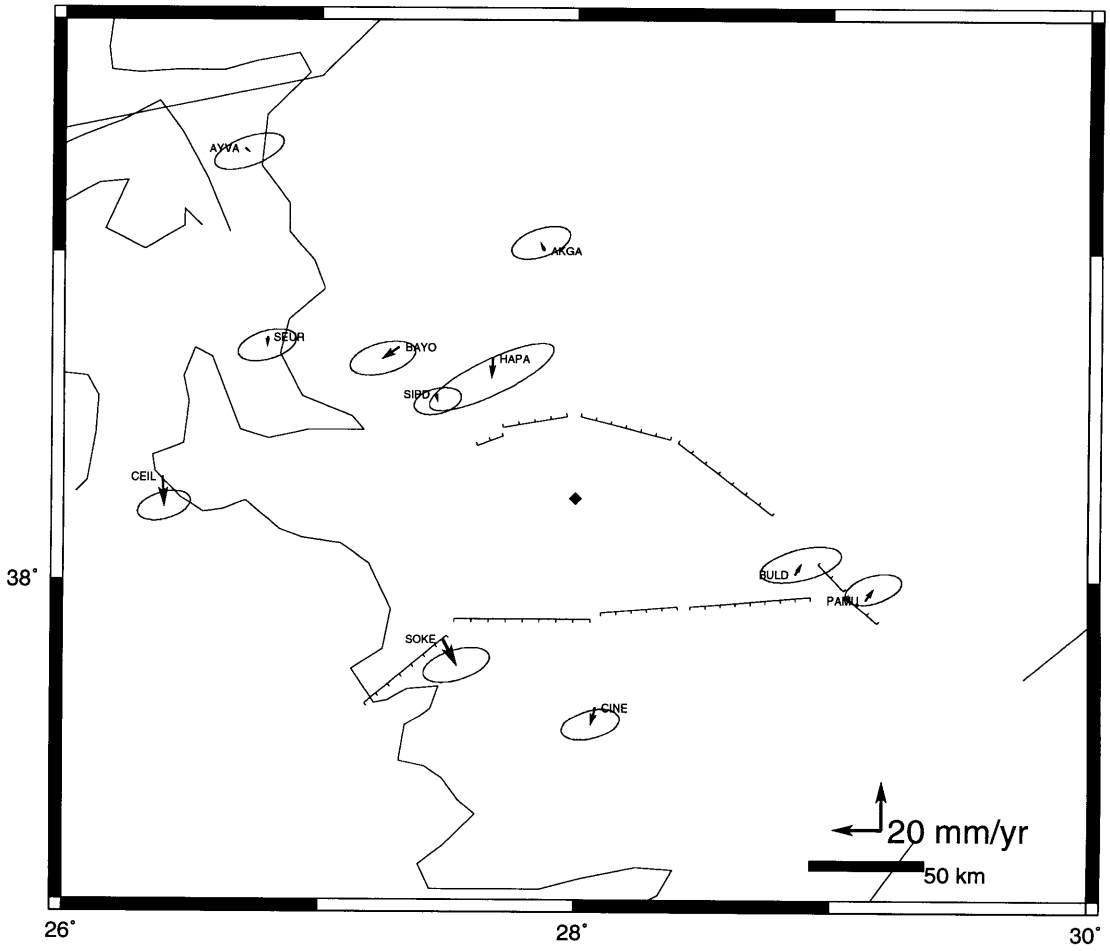

Figure 3-10: Observed velocities at the western Turkey sites relative to Ödemiş [ODME] (shown with a diamond), estimated from GPS observations in Turkey between 1988 and 1992. The ellipses denote the 95% confidence region, after scaling the formal uncertainties.

extension, if any, across the western Turkey breakaway zones is $15 \pm 7_{95\%}$ °N (AKGA

to SOKE/CEIL). This elongation observed by GPS is in agreement with geological observations [Şengör et al., 1985; Şengör, 1987b] and with the focal mechanisms of earthquakes which show dominant normal faulting [Eyidoğan, 1988] (Figure 1-5).

The GPS derived velocity field that we present in this study manifests remarkable similarities with those derived from SLR observations [Noomen, 1993] (Figures 2-13, 3-2, and 3-3). The magnitude of velocity vectors in western Turkey, eastern Greece and the southern Aegean Sea, relative to Yığılca, appear to be comparable (e.g., $AYVA_{GPS}$: [v_H=23±$14_{95\%}$ mm/yr] v. $DION_{SLR}$: [v_H=28±$10_{95\%}$ mm/yr]; $MELE_{GPS}$: [v_H=15±$7_{95\%}$ mm/yr] & $PAMU_{GPS}$: [v_H=19± $11_{95\%}$ mm/yr] v. $KATT_{SLR}$: [v_H=16± $10_{95\%}$ mm/yr]; $CINE_{GPS}$: [v_H=30±$11_{95\%}$ mm/yr] v. $ROUM_{SLR}$: [v_H=32±$7_{95\%}$ mm/yr]). We also argue that the direction of relative motions in western Turkey, eastern Greece and the southern Aegean Sea are comparable within their uncertainties (see next section on rotation). As shown in Figure 3-12, slip vectors obtained for earthquakes in the central and northern Aegean Sea (-137 – -124±7–11 °N, Taymaz et al [1991]; motion of the southern side of each fault rupture shown relative to the northern side) are not significantly different from azimuths of the relative motions in northern Aegean and Turkey [$GPS_{average}$: θ =-130±$20_{95\%}$ °N], and eastern Greece [$SLR_{@DION}$: θ =-159±$16_{95\%}$ °N]. Based on the slip vector distribution in the Aegean (Figure 3-12), Taymaz et al. [1991a] proposed a broken slat model. Later this kinematic model has been revisited by Jackson et al. [1992] after obtaining a velocity field from seismic moment tensors. The overall velocity field required by this model, and that obtained from seismic moment tensors, is not present in geodetic velocity fields. The horizontal velocity field obtained from seismic moment tensors for the Aegean [Jackson et al., 1992] indicate that Aegean region moves SW at 30 mm/yr relative to Eurasia. Both of these studies predict a westerly decrease in velocities for the Aegean. Instead, SLR results suggest higher rates at Karitsa [v_H= 42± $10_{95\%}$ mm/yr, θ =]±$a_{95\%}$ °Nnd Chrisokellaria [v_H= 50± $8_{95\%}$ mm/yr, θ =]±,$_{95\%}$ °N relative to Eurasia. Indeed, the faster rates observed at the western Hellenic arc may facilitate

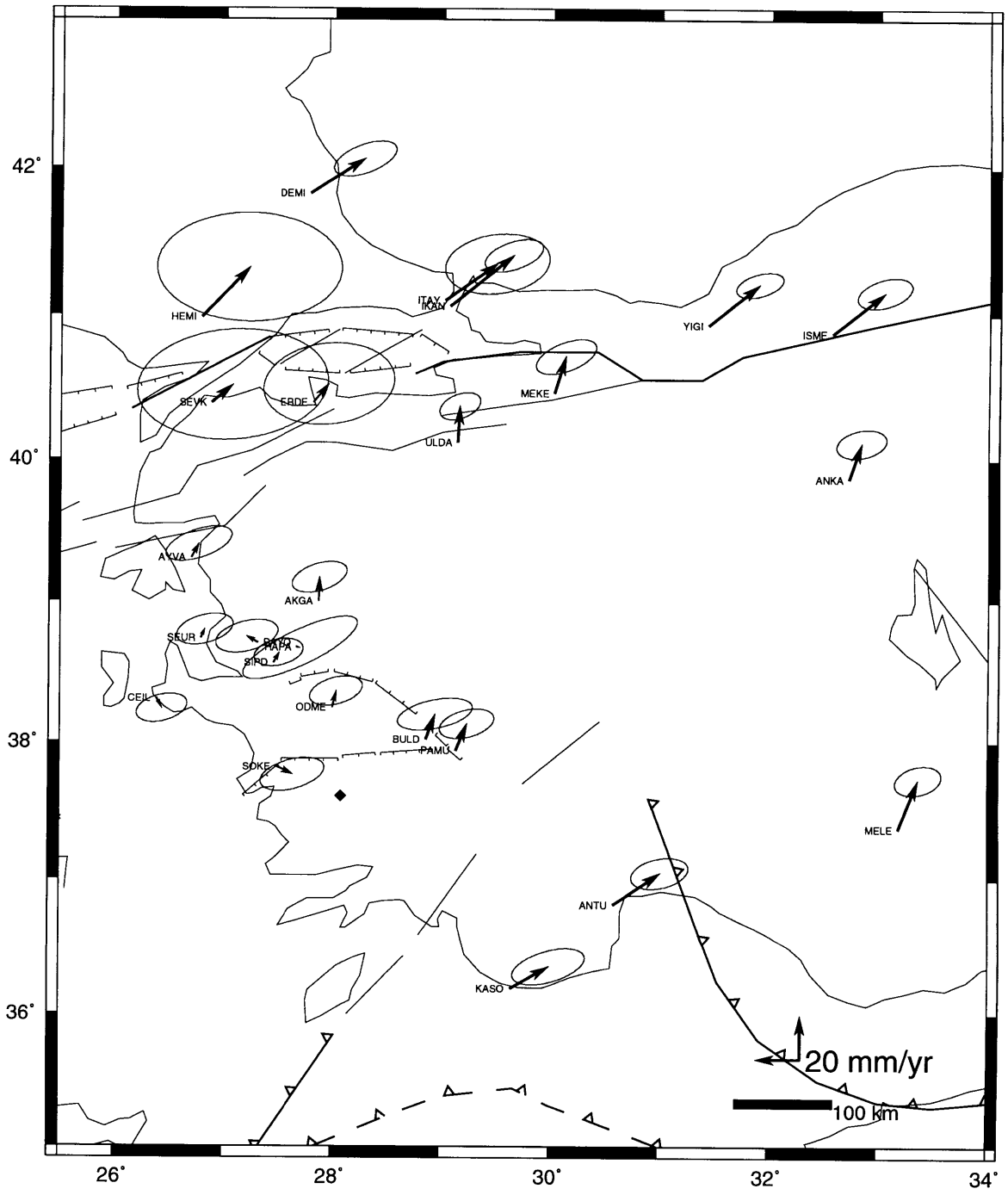

Figure 3-11: Observed velocities at the western Turkey sites relative to Çine [CINE] (shown with a diamond), estimated from GPS observations in Turkey between 1988 and 1992. The ellipses denote the 95% confidence region, after scaling the formal uncertainties.

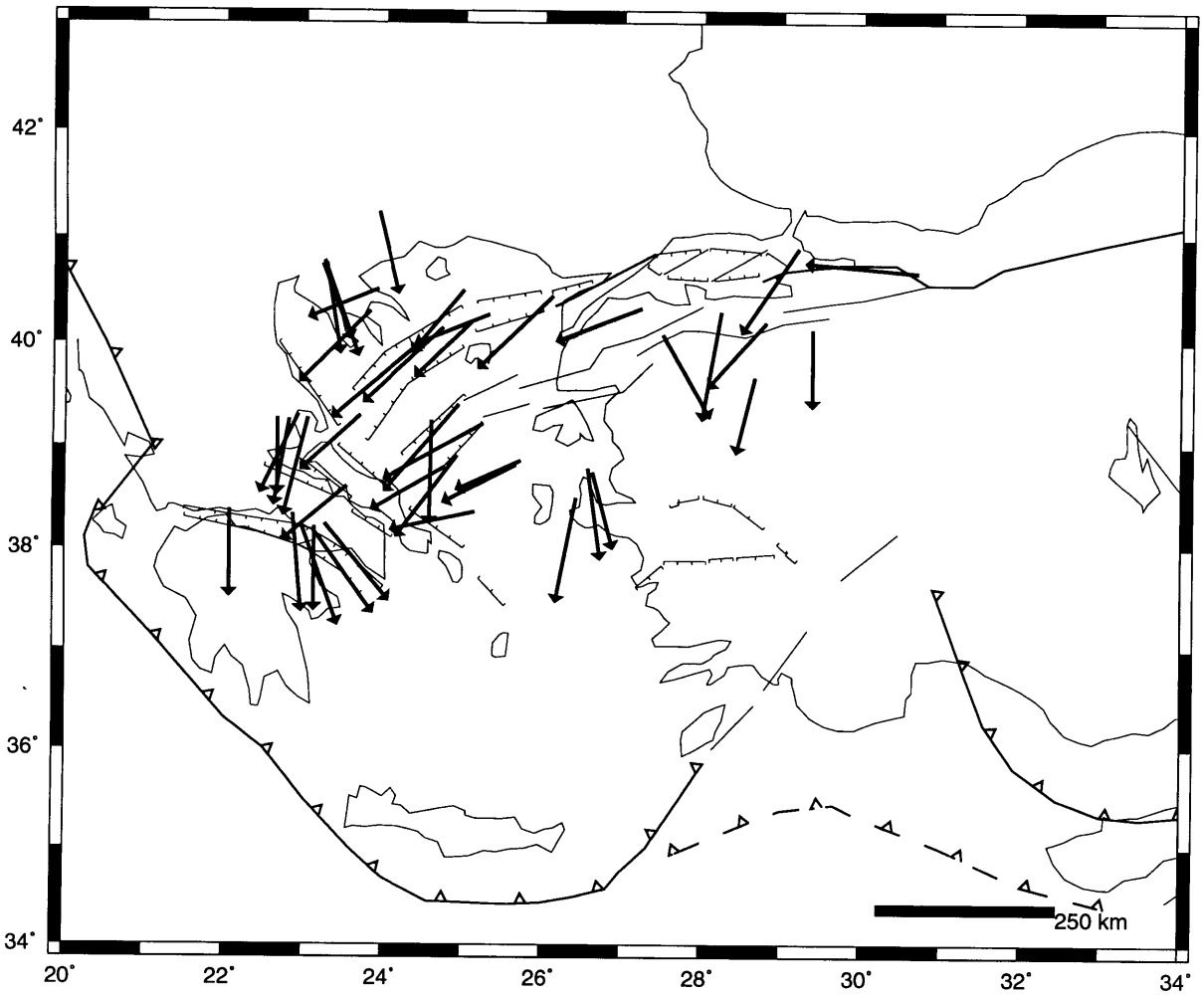

Figure 3-12: Horizontal projections of slip vectors for the focal mechanism of major earthquakes in the Aegean region (after, Taymaz et al. [1991a]). Arrows show the direction of motion of the south side relative to the north. The length of the arrows scaled arbitrarily by the magnitude (mostly Ms) of the earthquakes.

normal faulting observed north of Evvoia.

We observe that the azimuth and magnitude of site velocities relative to Yığılca in western Turkey are not drastically different than those in central and east-central Turkey. Instead, there is a smooth transition from east-central to central, and then to western Turkey. Thus, GPS velocity field does not illustrate a distinct boundary between the previously recognized Turkish [McKenzie, 1972] (a.k.a. the Anatolian

Scholle [Şengör et al., 1985] or the Anatolian block [Rotstein, 1984]) and the Aegean plates. The direction of relative motion in western Turkey strongly depicts a counterclockwise rotation. This suggests that deformation in western Turkey is integral to that in central and east-central Turkey. The magnitude of velocities, relative to Pontus, in western Turkey and the Aegean, however, is larger than that in central and east-central Turkey by about $10\pm8_{95\%}$ mm/yr ([YOZG: v_H=$21\pm8_{95\%}$ mm/yr] v. [CEIL: v_H=$31\pm9_{95\%}$ mm/yr] & [DION: v_H=$28\pm10_{95\%}$ mm/yr] & [ROUM: v_H= $32\pm 7_{95\%}$ mm/yr] in the Yığılca fixed frame). Similarity in the velocity vectors across this region strongly suggests that western Turkey, Aegea and eastern Greece have to be considered as a single tectonic unit, to a first approximation, deforming as a response to a common driving force, that is, the collision in eastern Turkey. The additional $10\pm8_{95\%}$ mm/yr in the Aegea can be maintained by the roll-back of the subducted African plate beneath the Hellenic arc [Meulenkamp et al., 1988], inducing the extrusion of the Anatolian plate as a whole over the African plate [Oral et al., 1993]. This is also supported by the extensional structures seen in southern Greece (Gulf of Corinth) and in western Turkey, and by the higher velocities observed in the southern Aegean by SLR. In favor of roll-back, based on gravity and deflection data, Royden [1993a] showed that subduction at the Hellenic arc is driven predominantly by subsurface loads. Royden [1993b] indicated the escape of boundaries into the open ocean at the retreating boundaries. The Hellenic arc provides an outstanding example.

Teke Peninsula. The magnitudes of velocity vectors in Teke, relative to Yığılca, are significantly different than those in central and southwestern Turkey. Their relative motion with respect to Yığılca is almost zero and can not be resolved at the 95% confidence level. We do not interpret these velocities in Teke as a drastically different motion. As we show in the next section, the small relative motion observed at these sites is due primarily to their proximity to the rotation pole of the Anatolian plate. In this sense, the azimuths of the velocities at the Teke sites, relative to Çine(Figure 3-11), which are parallel to the Fethiye-Burdur fault zone and perpendic-

ular to the Aksu thrust [e.g., ANTU, v_H=26±13$_{95\%}$ mm/yr, θ =56±17$_{95\%}$ °N], have to be interpreted accordingly. Suffice it to note that the motion between Antalya [ANTU] and Kaş [KASO] is not different than zero (Figures 3-11 and 3-4).

Eastern Turkey. In eastern Turkey we collected GPS measurements for three epochs only at Karacadağ [KARA], and twice at the other sites. Given the 1989 and 1991 observations at secondary sites, velocities in the east are fundamentally affected by the implicit velocity ties at the common sites (ANKA, MELE, YOZG, YIGI and KARA). Time-series plots obtained from the unconstrained solution for Karacadağ (Figures C-40 and C-41) illustrate the large uncertainties involved with the 1989 observations. The greater area circumscribed by the 95% confidence ellipses for eastern Turkey sites is thus mainly due to the large uncertainties of the 1989 measurements, and is closely related to their poor quality. Nevertheless, with two epoch GPS measurements we capture the shortening between Pontus/Eurasia and Arabia at the two sites located south of the Bitlis-Zagros collision zone (Figures 3-2 and 3-3). As discussed in Chapter 2, in our constrained solutions we forced the velocity at Karacadağ to its NUVEL-1 determined value relative to Eurasia. The velocity at Kızıltepe [KIZI: v_H=32±7$_{95\%}$ mm/yr, θ =-16±33$_{95\%}$ °N] agrees with that at Karacadağ [KARA$_{NUVEL-1}$: v_H=25±6$_{95\%}$ mm/yr, θ =-23±21$_{95\%}$ °N]. Velocities at these sites are comparable to the velocity observed at Diyarbakır by SLR [DIYA$_{SLR}$: v_H=33±15$_{95\%}$ mm/yr, θ =-11±22$_{95\%}$ °N]. Velocities relative to Eurasia (the Onsala site) demonstrate that the oblique convergence of the Arabian plate is partitioned into a northwestward motion in the immediate vicinity of the suture (Van domain) and further north, in the Caucasus domain, into a northerly shortening. This is in agreement with the focal mechanisms of earthquakes and especially with the relevant slip vectors as shown in Figure 3-13 [Jackson 1992]. The ratio of transcurrent/convergent motion at the Arabian plate sites relative to Eurasia [KARA: v_E= -8± 9$_{95\%}$ mm/yr, v_N= 23± 3$_{95\%}$ mm/yr; KIZI: v_E= -9± 19$_{95\%}$ mm/yr, v_N= 31± 7$_{95\%}$ mm/yr] is 0.35, which satisfies the conditions for the onset of the strain partitioning at oblique plate

boundaries [Braun and Beaumont, 1994; submitted]. Velocities relative to Eura-

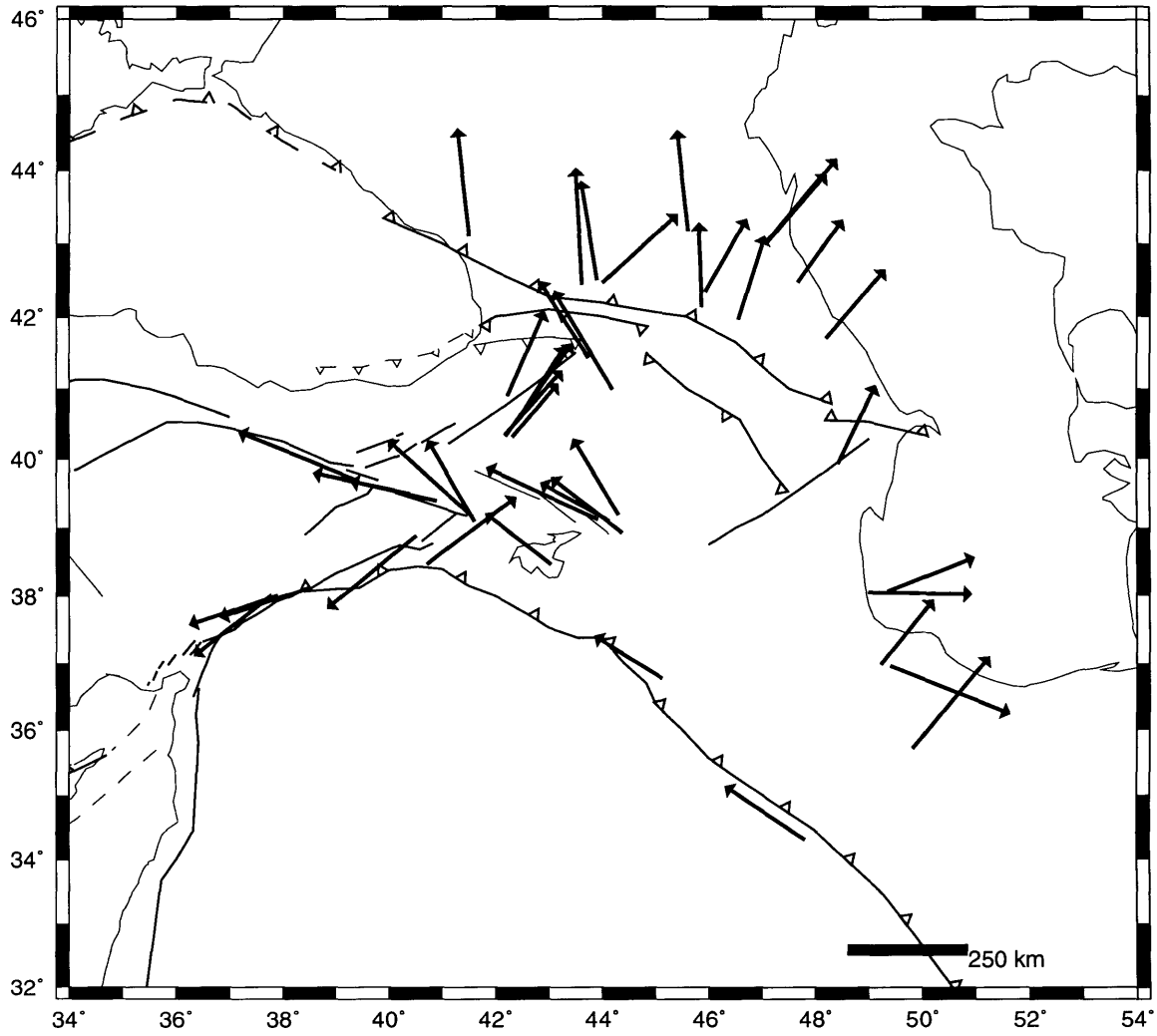

Figure 3-13: Horizontal projections of slip vectors for the focal mechanism of major earthquakes in eastern Turkey and the Caucasus (after Jackson [1992] and Taymaz et al., [1991b]). Arrows show the direction of motion of the south side relative to the north, except those on the EAF which are the other way around. The length of the arrows scaled arbitrarily by the magnitude (mostly Ms) of the earthquakes.

sia (Onsala) show that the "pure strike-slip" Van domain sites (e.g. KALE) move $24\pm15_{95\%}$ mm/yr at -$51\pm36_{95\%}$ °N, while the majority of the "pure dip-slip" Caucasus domain sites (e.g. KARS) move $13\pm 9_{95\%}$ mm/yr at $6\pm 78_{95\%}$ °N. The magnitude of motions, relative to Eurasia, at sites on the Arabian plate [KARA: v_H=$25\pm6_{95\%}$

mm/yr, θ =-23±21$_{95\%}$ °N] and on the east-central section of the Anatolian plate [e.g., MALA: v_H=25±11$_{95\%}$ mm/yr, θ =-50±26$_{95\%}$ °N] are comparable. The northwesterly motion of Arabia relative to Eurasia appears to be transferred to the Anatolian plate, at least to its central and east-central section.

The slight westerly motion of the Pontus block, relative to stable Eurasia, is removed when we examine the GPS site motions relative to the Pontus block(Figure 3-3). We observe a northerly motion at all Arabian plate sites relative to Yığılca. Karacadağ [KARA] moves northward [θ =-4±25$_{95\%}$ °N] relative to Yığılca at a rate of 19±3$_{95\%}$ mm/yr (Figure 3-5). The motion at Kızıltepe [KIZI: v_H= 28± 7$_{95\%}$ mm/yr] relative to Yığılca is parallel to Karacadağ (Figure 3-5). Motions at the sites north of the Arabian plate (the Van and Caucasus domains, and east-central Anatolia) vary from northwestward to northeastward (Figure 3-5). We observe identical velocity vectors at the sites in east-central Anatolia and in the Van domain. Neither the magnitude nor the sense of site motions relative to Yığılca are statistically different [MALA (west of Karlıova): v_H= 18± 10$_{95\%}$ mm/yr, θ = -46± 39$_{95\%}$ °N; KORK (east of Karlıova): v_H= 19± 14$_{95\%}$ mm/yr, θ = -43± 53$_{95\%}$ °N]. Sites in both domains have predominant northwesterly motion relative to Yığılca, and appear to be welded to each other. Within the uncertainties of our GPS observations, resolving a differential motion between these two domains is not possible. The motion at these sites (west and east of Karlıova) is, however, significantly different from that for sites on the Arabian plate and suggests not only the westerly motion of Anatolia and the Van domain as a whole, but also their counterclockwise rotation relative to Pontus, which is taken up along the NAF and EAF, as well as at the Bitlis-Zagros zone.

The azimuth, and especially the magnitude, of velocity vectors relative to Yığılca at the sites in the Caucasus domain are different drastically from those at sites in other domains. This leads us to consider the Çaldıran, Karayazı and Tutak faults[8] as

[8]The most recent rupture occurred on the Çaldıran fault in 1976 (Figure 1-5, fault segments 1

the southern boundary for the Caucasus domain. Velocity vectors at the Caucasus domain sites have a northeasterly direction with rather large uncertainties. The magnitudes of velocities relative to Yığılca are fundamentally lower than those in the Van domain or on the Anatolian plate. The sites east of the NEAF (Mercan [MERC], Erzurum [ERZU] and Kars [KARS]) move at v_H=10±$10_{95\%}$ mm/yr relative to Yığılca, while the sites west of the NEAF (Aktoprak [AKTO] and Ispir [ISPI]) move at v_H=18±$14_{95\%}$ mm/yr relative to Yığılca. Although the observed velocities suggest a possible differential motion across the NEAF at about 10 mm/yr, we cannot resolve it at the 95% confidence level with the current occupations at these sites [ERZU-AKTO: v_H=11±$18_{95\%}$ mm/yr].

Relative site motions at the eastern Turkey sites with respect to Yığılca require baselines at the order of 800 km, along which several tectonic structures are crossed. There may also be systematic errors involved in the secondary site velocities for long baseline apertures. Hence, it is instructive to inspect motions relative to sites on the Arabian plate. (In Appendix C we have shown that both constrained and unconstrained solutions are identical when baselines are short. Also, see Figure C-22.) Figure 3-14 depicts the westerly increase in the southward motion of the Anatolian plate, relative to Karacadağ (from ~10mm/yr in the east to 40 mm/yr in the west). The picturesque rotation of the Anatolian plate relative to Arabia illustrated in this figure is unequivocal.

In Figure 3-14, the convergence between all Pontus sites and Arabia is evident [e.g., ISME: v_H= 19± $5_{95\%}$ mm/yr, θ = 174± $29_{95\%}$ °N]. Figure 3-15 offers a detail velocity map for the eastern Turkey sites. The primary signature in Figure 3-15 is the approximately north-south shortening observed at the sites in the Caucasus domain [e.g., KARS: v_H= 14± $13_{95\%}$ mm/yr, θ = 138± $65_{95\%}$ °N]. We observe a marginally significant shortening (8±$7_{95\%}$ mm/yr) along the 100 km long KARA-KIZI baseline

and 2). Tutak fault (fault segments 1 thru 4) [Barka and Kadinsky-Cade, 1988].

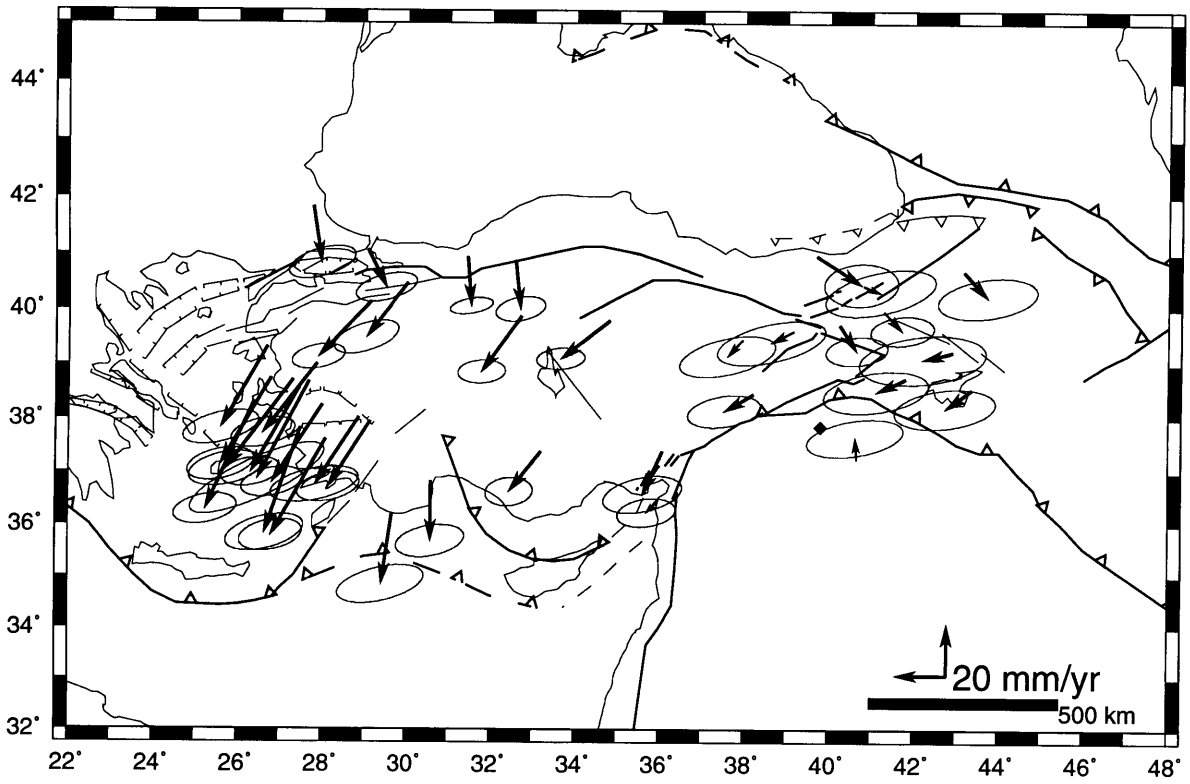

Figure 3-14: Observed velocities at the western Turkey sites relative to Karacadağ [KARA] (shown with a diamond), estimated from GPS observations in Turkey between 1988 and 1992. The ellipses denote the 95% confidence region, after scaling the formal uncertainties.

(Figure 3-16). This is probably related either to internal deformation taken up by the border folds along the leading edge of the Arabian plate or to the geodetic quality of two-epoch velocity at the secondary Kızıltepe site. (As discussed in Appendix C, the type of solution, whether it is constrained or unconstrained, becomes irrelevant for short baselines, especially for those in eastern Turkey.)

The site motions relative to Karacadağ at sites west and east of Karlıova cannot be significantly determined. Thus, whether or not Karlıova (where the NAF and EAF meet) is a triple-junction, remains unanswered. The level of uncertainties for two-epoch velocities is greater than the tectonic signature. Given the proximity of the rotation pole (e.g. $_{ARA}\mathbf{E}_{ANA}$), smaller motion at the Anatolian plate sites in eastern

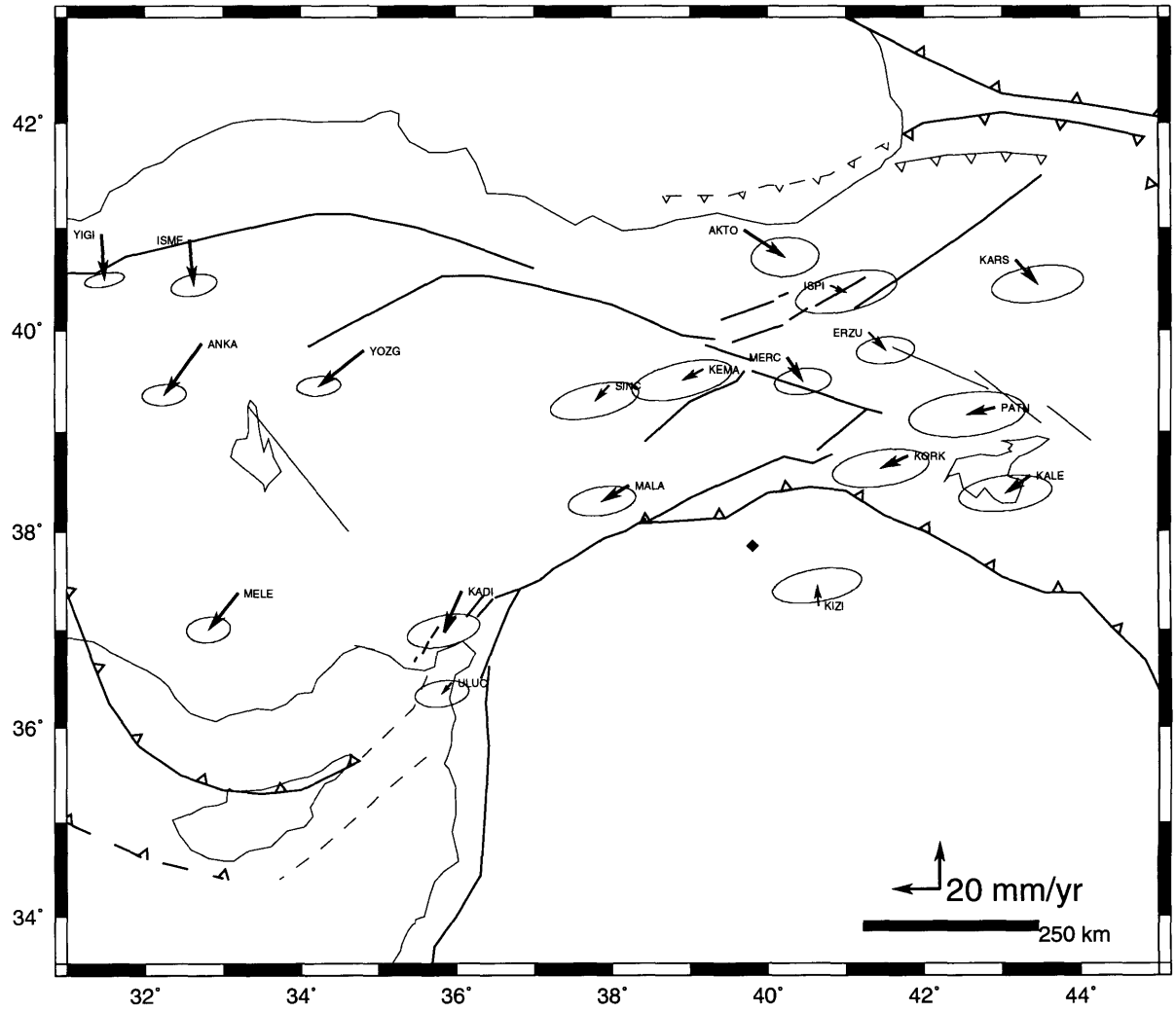

Figure 3-15: Observed velocities at eastern Turkey sites relative to Karacadağ [KARA] (shown with a diamond), estimated from GPS observations in Turkey between 1988 and 1992. The ellipses denote the 95% confidence region, after scaling the formal uncertainties.

Turkey is expected (see next section on rotation). The velocities at Malatya [MALA] and Kadirli [KADI], relative to Karacadağ, provide us with an estimate of motion along the EAF zone[9]. It is clear that with these site configurations we can neither characterize the Arabia-Africa-Anatolia triple junction near the SW end of the EAF, nor the deformation on individual structures. The MALA-KARA baseline crosses the

[9]Fault segments 1 through 14 [Barka and Kadinsky-Cade, 1988]. Main strand of the EAF zone: northeastern and central parts [Perinçek and Çemen, 1990].

EAF and the Bitlis suture. Integrated motion along the baseline formed from Kadirli or Uluçınar to Karacadağ (or Kızıltepe) includes not only the EAF zone, the Amanos and the Dead Sea fault zones, but also the Hatay graben system. (For detailed description of tectonic structures see Gülen et al. [1987], Perinçek and Çemen [1990] and Lyberis et al. [1992].) At Malatya, resolving motion relative to Karacadağ is rather difficult due to high uncertainties [v_H=13±14$_{95\%}$ mm/yr, θ =-120±33$_{95\%}$ °N], however, direction of the motion is subparallel to the trace of the EAF zone. The motion between Karacadağ and Kadirli [KADI] is 19±11$_{95\%}$ mm/yr and is oriented -155±40$_{95\%}$ °N. Uluçınar [ULUC] is located west of the Dead Sea fault. Given the complex pattern of faulting around Gulf Iskenderun, it is debatable whether the motion at Uluçınar represents that of the African plate. We cannot resolve statistically significant motion at ULUC [v_H=6± 10$_{95\%}$ mm/yr, θ =-138± 73$_{95\%}$ °N] relative to Karacadağ. However, ULUC moves 13± 11$_{95\%}$ mm/yr at 17± 64$_{95\%}$ °N] relative to KADI. Between these two sites, the major structure is the Misis-Yumurtalık fault[10] which is likely to mark the boundary between the Anatolian and African plates. Thus, we consider Uluçınar to be located on the African plate. The NUVEL-1 determined value for this site relative to Arabia is 13 mm/yr at 133 °N and agrees with the GPS derived velocity relative to Kızıltepe [ULUC: v_H=13±12$_{95\%}$ mm/yr, θ =195±75$_{95\%}$ °N] (Figure 3-16).

Although we cannot resolve statistically significant velocities at the 95% confidence level, at sites east and west of Karlıova relative to Karacadağ, we observe statistically significant velocities relative to Kızıltepe [KIZI]. Regional site velocities relative to Kızıltepe show an overall oblique convergence, between eastern Turkey and the Arabian plate, of 20±10$_{95\%}$ mm/yr. The direction of motions relative to Kızıltepe, at sites on the Van block and east-central Anatolia, are similar. We observe that the integrated motion between Malatya and Kızıltepe is 19±16$_{95\%}$ mm/yr, and that the

[10]Southwestern part of the main strand of the EAF [Perinçek and Çemen, 1990].

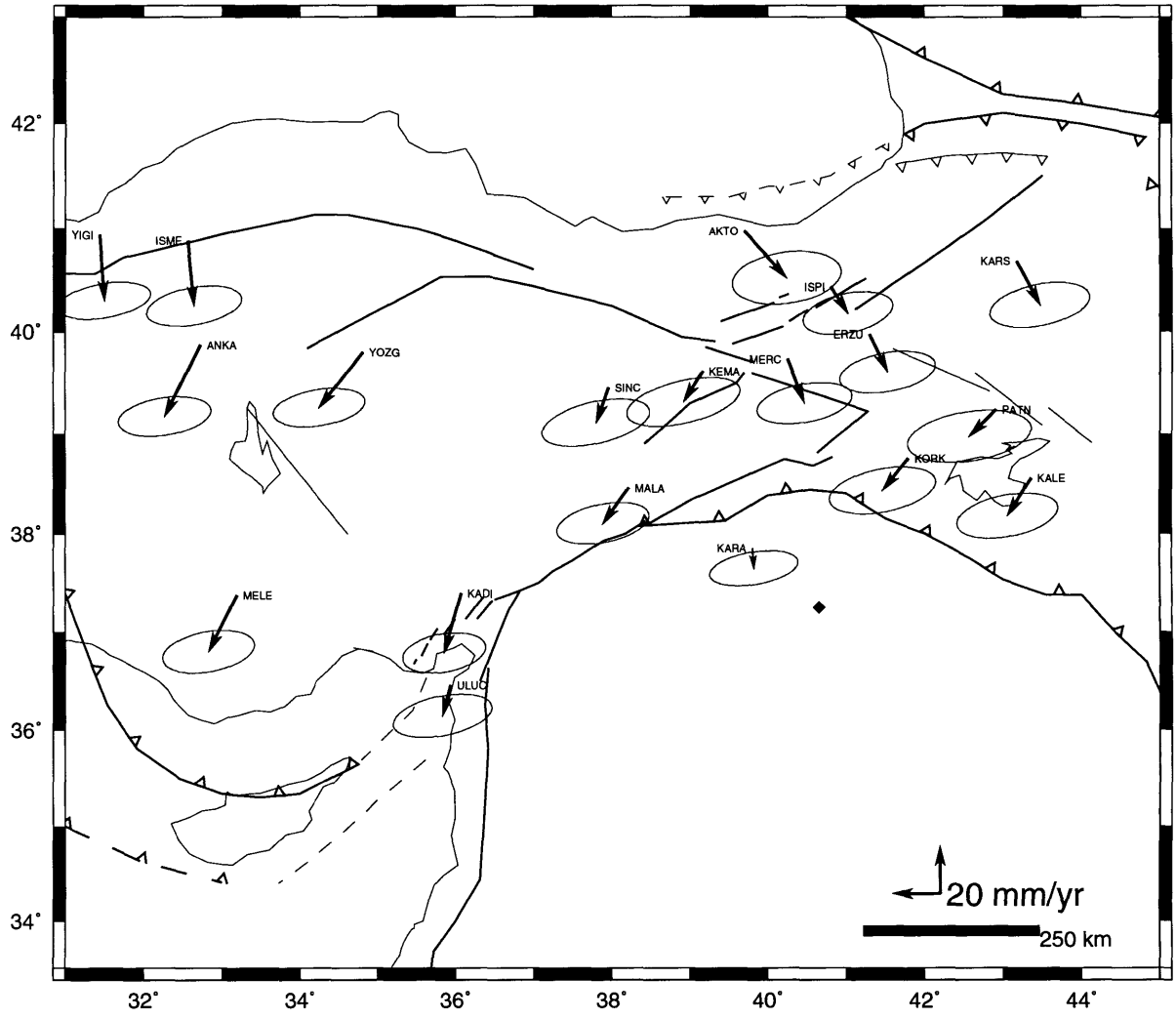

Figure 3-16: Observed velocities at eastern Turkey sites relative to Kızıltepe [KIZI] (shown with a diamond), estimated from GPS observations in Turkey between 1988 and 1992. The ellipses denote the 95% confidence region, after scaling the formal uncertainties.

direction of motion is parallel to the East Anatolian fault [-144±$44_{95\%}$ °N].

3.2 Rotation of the Anatolian Plate

The GPS derived velocity field lends us the first direct evidence for the counterclockwise rotation of Anatolia and for its probable boundaries. As described in the previous section, this picturesque rotation is unequivocal, regardless of reference frame [e.g., site velocities relative to Onsala (Figure 3-2), Yığılca (Figure 3-3), Ankara (Figure 3-6), or Karacadağ (Figure 3-14)]. Evidenced by the GPS velocity field, this coherent rotation includes not only the region bounded by the EAF and NAF in central and central-east Turkey, but neighboring regions as well. There is remarkable agreement between velocities in the central-eastern Turkey and Van region. The kinematics determined by GPS in western Turkey, and by SLR in Aegea, also support a coherent Anatolian plate extending further west than previously thought.

How well can we define a coherent Anatolian plate, or are the Turkish and Aegean plates distinct as postulated by McKenzie [1970, 1972]? Does Anatolia have a component of rotation or pure westerly motion? What are the relative motions at its boundaries? Is there a 38 mm/yr motion along the EAF as suggested by Taymaz et al. [1991b]? Does Anatolia undergo a significant amount of deformation as proposed by Rotstein [1984], or is it rigid, after all?

In order to find answers to these questions we parameterized the GPS and SLR observed velocities on the Anatolia with Euler vectors relative to Pontus and Arabia. Plate motions defined by an Euler vector would account for rigid body rotation about a pole [Le Pichon et al., 1976]. Residuals (calculated – observed) thus provide a litmus test as to whether a domain, such as Teke or Van, belongs to the Anatolian plate, and delineate the amount of internal deformation. The Euler vector (E) is defined by a pole position ($\mathbf{E}[\phi, \lambda]$; ϕ: longitude, λ: latitude) and an instantaneous angular rotation rate (ω, angular velocity). The euler pole is the point where the rotation axis pierces the surface of the earth. Motion about the Euler pole takes place on small

circles at a constant magnitude with a changing azimuth. Given the instantaneous angular rotation rate (ω) about an Euler pole ($\mathbf{E}[\phi, \lambda]$), the local velocity ($v$) at point $\mathbf{P}[\phi\prime, \lambda\prime]$ is

$$v = \omega \, R \, \mathbf{E} \times \mathbf{P} \, , \tag{3.1}$$

where $\times$ denotes curl and R is the earth's radius [Cox and Hart, 1986]. Using this forward model, we inverted the GPS derived velocities at sites on the Anatolian plate for pole position and angular velocity. In doing so, we performed a weighted least squares scheme [e.g., Menke, 1984]. By propagating the variance-covariance matrices, we obtained the uncertainties for the Euler vector, after its variance-covariance matrix was multiplied by the solution variance factor [King et al., 1985]. Hence, the uncertainties quoted for the Euler vectors obtained in our study are scaled uncertainties.

We inverted the GPS site velocities to obtain the Euler vector for the Anatolian plate relative to Pontus (Yığılca) [$_{PON}\mathbf{E}_{ANA}$] (constrained solution: Table 2.8). In order to investigate the extent of the Anatolian plate, we grouped our GPS sites in subregions whose kinematics are described in the previous section. In Table 3.1 these subregions are summarized: we systematically augmented subregions from east to west so that variations in the estimated Euler vector ($_{PON}\mathbf{E}_{ANA}$), as well as those in the computed and residual fields, could be investigated. We started with the sites located in the region defined as the Turkish plate or Anatolian scholle (central and central-eastern Turkey) and later included western Turkey and Marmara/Biga sites. Additionally, sites in the Teke and Van domains were considered in the estimation. Further, we extended our inversion for $_{PON}\mathbf{E}_{ANA}$ using velocities in the Aegean which were reported by SLR. The pole positions and instantaneous angular velocities for each solution are also presented in Table 3.1. For data sets with good azimuthal and radial distribution from the pole, the uncertainty in the estimated pole position is about 0.5° for E-W and 1.2° for N-S, and in angular velocity it is about 0.2°/Myr. Since we had only three sites in the Van domain, distributed over a small area, no

successful inversion was possible for an Euler vector specific to the Van block. Euler vectors obtained solely for western Turkey, as well as for the central to eastern Turkey regions, produced rather high uncertainties for both the angular velocity and rotation pole.

In Figure 3-17 we show the observed and calculated velocities from our preferred Euler vector, located at 33.419±0.537°E, 31.109±1.249°N, with a counterclockwise angular velocity of 1.248±0.152°/Myr relative to Pontus. In estimating this ${}_{PON}\mathbf{E}_{ANA}$ vector we used only velocities at GPS sites in Marmara, central, central-eastern, and western Turkey, the Van and Teke domains (SLR sites were not included in the inversion). The residual velocity field (observed – calculated) is shown in Figure 3-18 for GPS sites in Turkey and SLR sites in the Aegean, with 95% error ellipses (of the observed velocity field). Computed and residual velocities at the SLR sites are also shown in Figures 3-17 and 3-18, although we have not used SLR data in inversion for this particular Euler vector.

As illustrated in Table 3.1, the Euler vector used for Figure 3-17 is not significantly different than others which were estimated from data sets comprising several subregions. For instance, the Euler vector estimated for central and east-central Turkey is essentially the same as that for a region which extends from Karlıova to the Aegean, including the Van domain. Whether sites in the Van domain are included or not, we obtain fundamentally the same Euler vector. Neither does adding the SLR derived velocities significantly change the outcome of inversion for the pole position and angular velocity. The residual field from one solution to another varied by 3-5mm/yr. These differences are well within the 95% confidence area of observed GPS velocities.

Regardless of which and how many subregions are included in the inversion process, the estimates for Euler vectors and their resultant residuals are not significantly different than those shown in Figures 3-17 and 3-18 . This implies that the Anatolian

Table 3.1: Euler vectors $[_{PON}\mathbf{E}_{ANA}]$ obtained from inversion of GPS and SLR velocities relative to Yığılca (PON: Pontus, ANA: Anatolia). Anatolia rotates relative to Pontus. Counterclockwise rotation is positive.

Region/sites/data	Euler vector								
	Euler pole				Angular velocity		Correlations		
	Longitude [°]		Latitude [°]		[°/Myr]				
	ϕ	σ_ϕ	λ	σ_λ	ω	σ_ω	$\rho_{\phi\lambda}$	$\rho_{\phi\omega}$	$\rho_{\lambda\omega}$
r^1r^2	30.424	4.804	30.648	5.476	0.765	0.430	0.706	0.943	0.845
$r^1r^2r^3$	32.315	1.524	30.010	2.561	0.917	0.233	0.589	0.836	0.843
$r^1r^2r^3r^4r^5$	33.736	0.517	31.231	1.152	1.268	0.142	-0.454	-0.202	0.643
$r^1r^2r^3r^4r^5r^6$†	33.419	0.537	31.109	1.249	1.248	0.152	-0.460	-0.198	0.679
$r^1r^2r^3r^4r^5r^6r^7$	33.412	0.516	31.125	1.200	1.246	0.146	-0.462	-0.205	0.681
r^2r^3	32.881	1.009	32.488	2.300	1.277	0.396	0.480	0.703	0.873
$r^2r^3r^4$	33.345	0.535	31.632	1.179	1.408	0.176	-0.557	-0.387	0.698
$r^2r^3r^4r^5$	33.273	0.520	31.984	1.094	1.427	0.173	-0.591	-0.448	0.687
$r^2r^3r^4r^6$	33.020	0.557	31.616	1.279	1.393	0.189	-0.577	-0.399	0.731
$r^2r^3r^4r^5r^6$	32.968	0.541	31.958	1.184	1.415	0.186	-0.611	-0.458	0.720
$r^2r^3r^4r^5r^6r^7$	32.962	0.519	31.971	1.133	1.412	0.177	-0.613	-0.463	0.722
r^4	30.409	1.976	34.973	1.525	3.174	1.031	-0.963	-0.990	0.950
r^3r^4	33.054	0.690	31.865	1.413	1.521	0.263	-0.723	-0.666	0.788
r^4r^{tud}	31.791	1.807	33.359	1.811	1.956	0.631	-0.884	-0.938	0.884
$r^2r^3r^4r^5r^6r^7r^{tud}$	32.867	0.629	32.331	1.134	1.460	0.202	-0.601	-0.529	0.723
$r^1r^2r^3r^4r^5r^6r^7r^{tud}$	33.311	0.607	31.642	1.186	1.304	0.168	-0.480	-0.327	0.690
$r^1r^2r^3r^4r^5r^6r^{tud}$	33.315	0.627	31.634	1.225	1.306	0.174	-0.479	-0.323	0.688

† : Preferred Euler vector obtained from inverting only GPS site velocities (Figures 3-17 and 3-18).
r^1 : Sites on the Van block [KALE, KORK, PATN].
r^2 : Sites in central-eastern Turkey [KADI, KEMA, MALA, SINC].
r^3 : Sites in central Turkey [ANKA, MELE, YOZG].
r^4 : Sites in western Turkey [AKGA, AYVA, BAYO, BULD, CEIL, CINE, HAPA, ODME, PAMU, SEUR, SIPD, SOKE].
r^5 : Sites on the Teke peninsula [ANTU, KASO].
r^6 : Sites in southern Marmara [MEKE, ULDA].
r^7 : Sites on the Biga peninsula [ERDE, SEVK].
r^{tud} : Sites in the Aegean [CHRI, DION, KARI, KATT, MELE, ROUM]. (After, Noomen et al. [1993].)

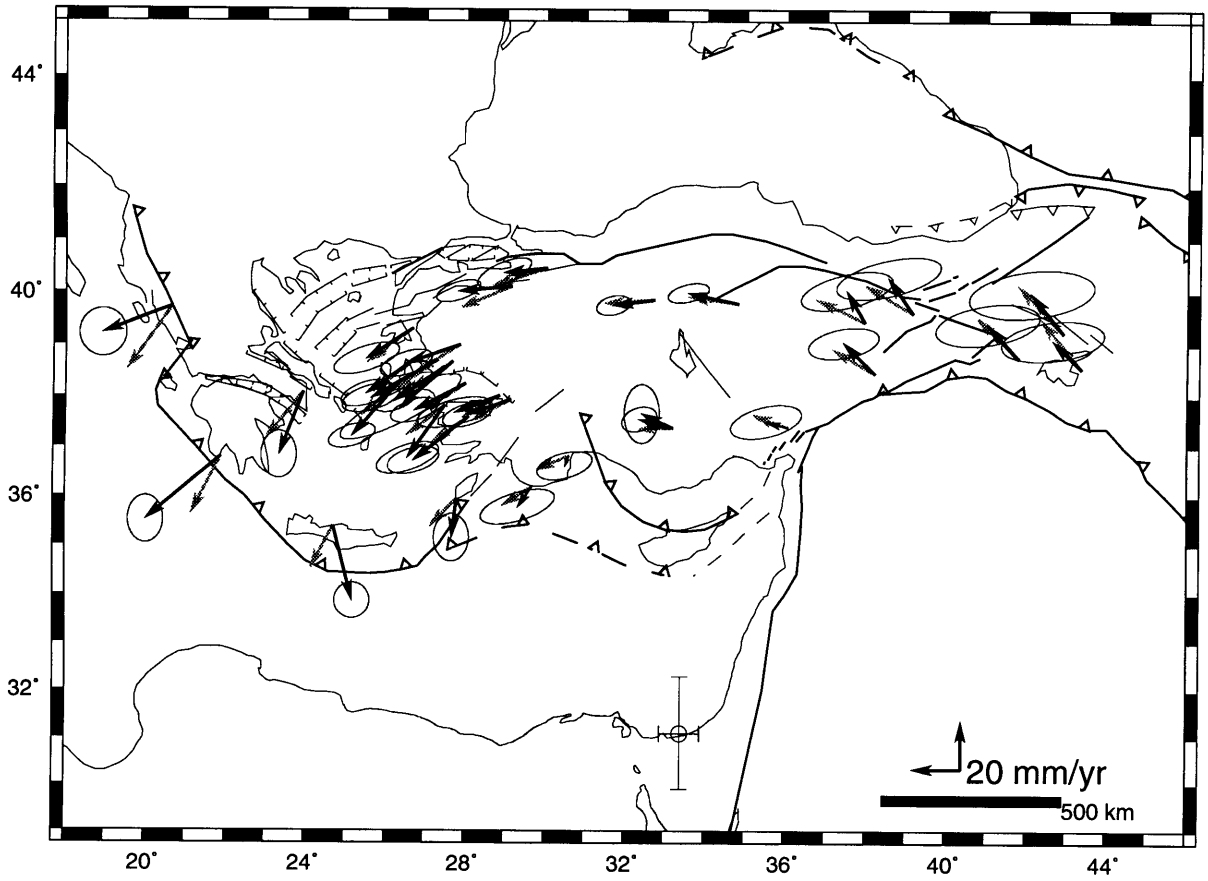

Figure 3-17: Regional sites and their velocities (black arrows) relative to Yığılca, used in inverting for the instantaneous pole position and angular velocity. Gray arrows indicate velocities calculated after inversion from a pole located at 33.419±0.537°E, 31.109±1.249°N, with a counterclockwise angular velocity of 1.248±0.152°/Myr relative to Pontus. Euler pole is shown with uncertainties in N-S and E-W.

plate includes not only the region bounded in the east by the NAF and EAF, but also the Van and Teke domains. It also extends west to include the Aegean Sea and Greece.

To a first approximation, we consider Anatolia as a rigid plate coherently rotating about an Euler pole located north of the Sinai peninsula [ϕ=33.419±0.537°E, λ=31.109±1.249°N, ω=1.248±0.152°/Myr] relative to Pontus. In eastern Turkey, the misfit is not significant within the 95% confidence area of our GPS observations

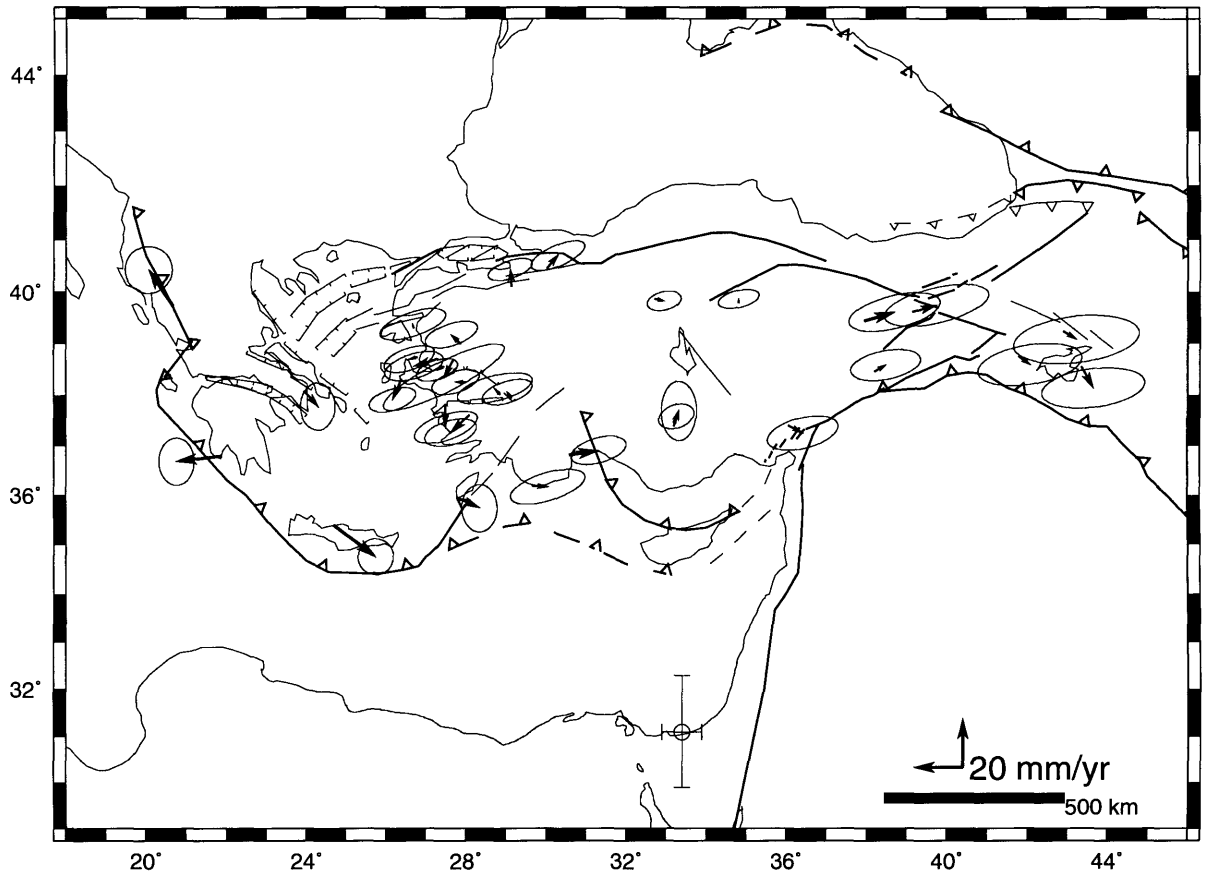

Figure 3-18: Residual velocities (observed – calculated) at the GPS and SLR sites, as calculated in Figure 3-17. Euler pole is shown with uncertainties in N-S and E-W.

(Figure 3-18). There is a remarkable agreement between the observed and predicted velocity in central Turkey. The upper bounds for internal deformation in central to eastern Turkey, if any, are determined by our uncertainties at the 95% confidence level, and are, hence, less than 10–15 mm/yr. However, as depicted in Figure 3-19, we observe significant deviations from the rigid plate assumption at some sites in western Turkey (Bozdağ horst area) and the southern Aegean. These are addressed below, and we will subsequently remark on the general characteristics of the predicted field.

It is interesting to focus on the point previously considered the eastern edge of

the Anatolian plate. Residuals for the sites west and east of the intracontinental Karlıova basin [Tutkun and Hancock, 1990; Şaroğlu and Yılmaz, 1991; Şengör et al., 1985] show that both regions are coherently rotating about the same pole. Hence, the GPS measurements conducted so far provide no clue concerning the so-called Karlıova triple junction. This question will be addressed below, when we obtain the ${}_{ARA}\mathbf{E}_{PON}$ Euler vector.

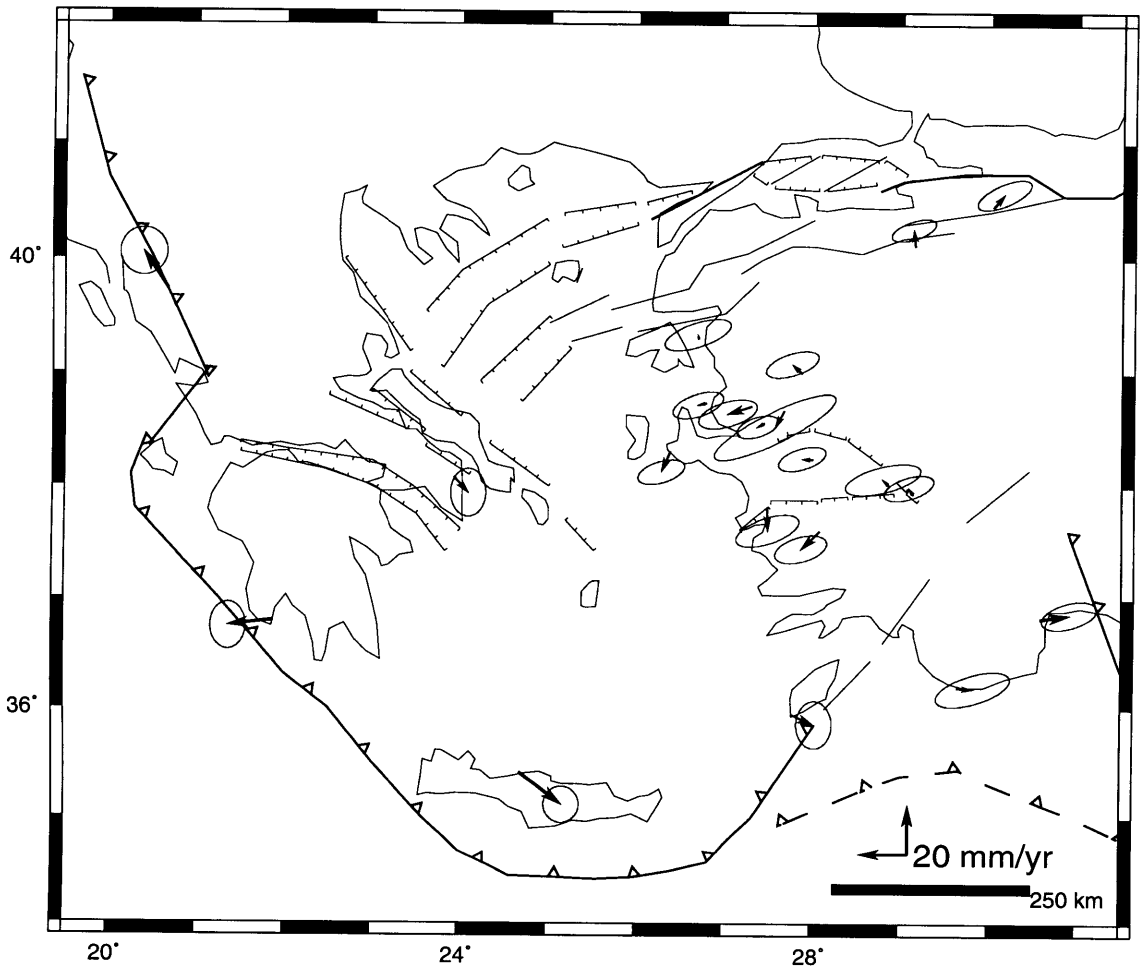

Figure 3-19: Residual velocities (observed – calculated) at the GPS and SLR sites, as calculated in Figure 3-17. Detail of Figure 3-18. See Figures 1-7 and 2-2 for site locations.

The Marmara region near Istanbul is of interest because previous studies have suggested that the NAF is broken into strands here, and that the region has been the

site of both normal and strike-slip earthquakes [e.g., Barka and Kadinsky-Cade, 1988]. In our description of the GPS velocities in the Marmara region, we mentioned that Uludağ [ULDA] and Mekece [MEKE] demonstrate pure westerly motion relative to Yığılca. The residuals to rigid plate deformation show a $7\pm4_{95\%}$ mm/yr discrepancy only at Uludağ. This misfit at Uludağ is primarily in the azimuth, by about 20°. Given the additional extension in southwestern Turkey and Aegea, we would expect a southerly residual. The northward orientation of the residual vector suggest that this region is likely to be caught within the strain accumulation region of the NAF zone. Uludağ is located very close to the southern strand of the NAF. As remarked in the previous section, this strand may take up some of the dextral slip along the NAF. It is possible that some slivers of crust, bounded by the southern and middle strands of the NAF, are decoupled slightly from the Anatolian plate. However, the signal is less than 10 mm/yr and is bracketed within our uncertainties.

In western Turkey the residuals are small and statistically insignificant at all GPS sites except Çeşmeılıca [CEIL], Söke [SOKE], and Çine [CINE]. These sites have a $10\pm7_{95\%}$ mm/yr misfit oriented south (Figure 3-19). The residual field is quite comparable to Figure 3-9, in which we depict GPS site velocities relative to Akdağ [AKGA] in order to describe the extension in western Turkey. The $10\pm7_{95\%}$ mm/yr deviation observed in western Turkey can be associated with the windshield-wiper-like opening at the Gediz and Büyük Menderes breakaway zones, and it is closely linked to the residuals at the SLR sites in the Aegean. We also observe significant deviations from a rigid plate assumption farther to the west and south, in the Aegean region (see Figures 1-7 and 2-2 for site locations). At Kattavia [KATT] the misfit amounts to $10\pm8_{95\%}$ mm/yr and is comparable to that in western Turkey. The residual motion at Dionysos [DION] is $9\pm9_{95\%}$ mm/yr and cannot be resolved at the 95% confidence level. The discrepancy between the observed and the predicted velocities increases two fold at sites in close proximity to the Hellenic arc and the Adriatic-Dinaride collision zone [e.g., ROUM: $22\pm 10_{95\%}$ mm/yr]. The amount of misfit does, of course, depend

upon the geodetic quality of the SLR velocities [Robbins, pers. comm., 1993 (Goddard Flight Center solutions)] and is likely to be smaller by 5–10 mm/yr than that shown in Figure 3-19. The observed residual field in western Turkey and the Aegean can be interpreted by considering the extensive normal faulting and graben like structures in western Turkey [Şengör et al., 1985; Şengör, 1987b; Seyitoğlu and Scott, 1991, 1992], and in the Gulf of Corinth [Doutsos and Piper, 1990]. Dewey and Şengör [1979] have argued that the north-south extensional regime in western Turkey and the Agean area is a consequence of the east-west compression (westerly escape of Anatolia triggered by the Eurasia-Arabia collision). As indicated by terrestrial and space (GPS) geodetic observations, which are separated by 90 years, there is significant stretching at the Gulfs of Corinth and Evvoia [Billiris et al., 1991].

We have previously shown that the magnitudes of velocity vectors in western Turkey are 10 mm/yr larger that those in eastern Turkey. They can be accounted for neither by the collision nor by the gravitational forces arising from differential crustal thickness. GPS site velocities indicate an almost complete transfer of Arabian motion to Anatolia, and fall short of source for the additional 10 mm/yr in western Turkey. Crustal thickness in the Aegean, deduced from seismic profiles and Bouguer gravity, is 20–30 km [Makris and Stöbbe, 1984]. Inversion of Bouguer gravity shows that the Moho depth beneath eastern Turkey reaches to 45–50 km [Oral et al., in prep.]. These data suggest that although buoyancy forces arising from differential crustal thickness did not play a role in the initiation of the westerly escape of Anatolia [Şengör et al., 1985] they may help maintain present-day escape. This 20–30 km differential crustal thickness between eastern Turkey and the southern Aegean, which could maintain the escape, is evenly distributed from east to west, and cannot explain an abrupt increase in velocities south of the Gediz breakaway zone. An alternative model for western Turkey was proposed by Seyitoğlu and Scott [1991, 1992]. It favors a high thermal profile of the crust after the Oligocene compressional events, but requires a single graben system exposed to pure shear and cannot explain the existence of

two major breakaway zones. Also, rather than a broad signature in the Bouguer gravity anomalies in western Turkey, there is a narrow zone of decrement in the anomalies above each breakaway zone which can simply be explained by the presence of sedimentary fill [Oral, 1987].

We interpret the residuals in western Turkey, as well as those in the southern Aegean, as a result of trench suction at the Hellenic arc and extrusion of the overriding plate due to the roll-back of the subducting slab. This is characteristic of retreating boundaries, for which the Hellenic arc provides a good example, where the subduction rate exceeds the convergence rate, and hence horizontal extension occurs in the overriding plate [Royden, 1993a]. We foresee that it is this suction that would be responsible for an additional 10–20 mm/yr motion, and that would provide the necessary force for the development of simple shear structures [Wernicke, 1981, 1985] in western Turkey, asymmetric rifting in the Gulf of Corinth, and fragmentation of Crete into several basins [Meulenkamp et al., 1988], etc.

Above, we remarked that the residuals at sites east and west of Karlıova are not significant. This picture becomes clearer as we estimate the Euler vector for Anatolia relative to Arabia [$_{ARA}\mathbf{E}_{ANA}$]. In doing so we used the same site configuration as for Figure 3-17 and inverted GPS velocities relative to Karacadağ. In Figure 3-20 we show the velocities for the Anatolian sites computed from an Euler pole located at 43.156±0.650°E, 31.147±1.171°N (SW Iraq) with a counterclockwise angular velocity of 1.215±0.154°/Myr. The residual field for rotation relative to Arabia (Figure 3-21) is not fundamentally different than that relative to Pontus (Figure 3-18). Predicted velocities for the east-central Turkey sites [MALA, SINC, KEMA] are parallel to the EAF zone. However, their magnitude is systematically higher than those observed. Despite the fact that their residuals are not statistically significant, they rather interestingly foretell the possible internal deformation in this transpressional zone. Comparison of observed and predicted velocities show that once the uncertain-

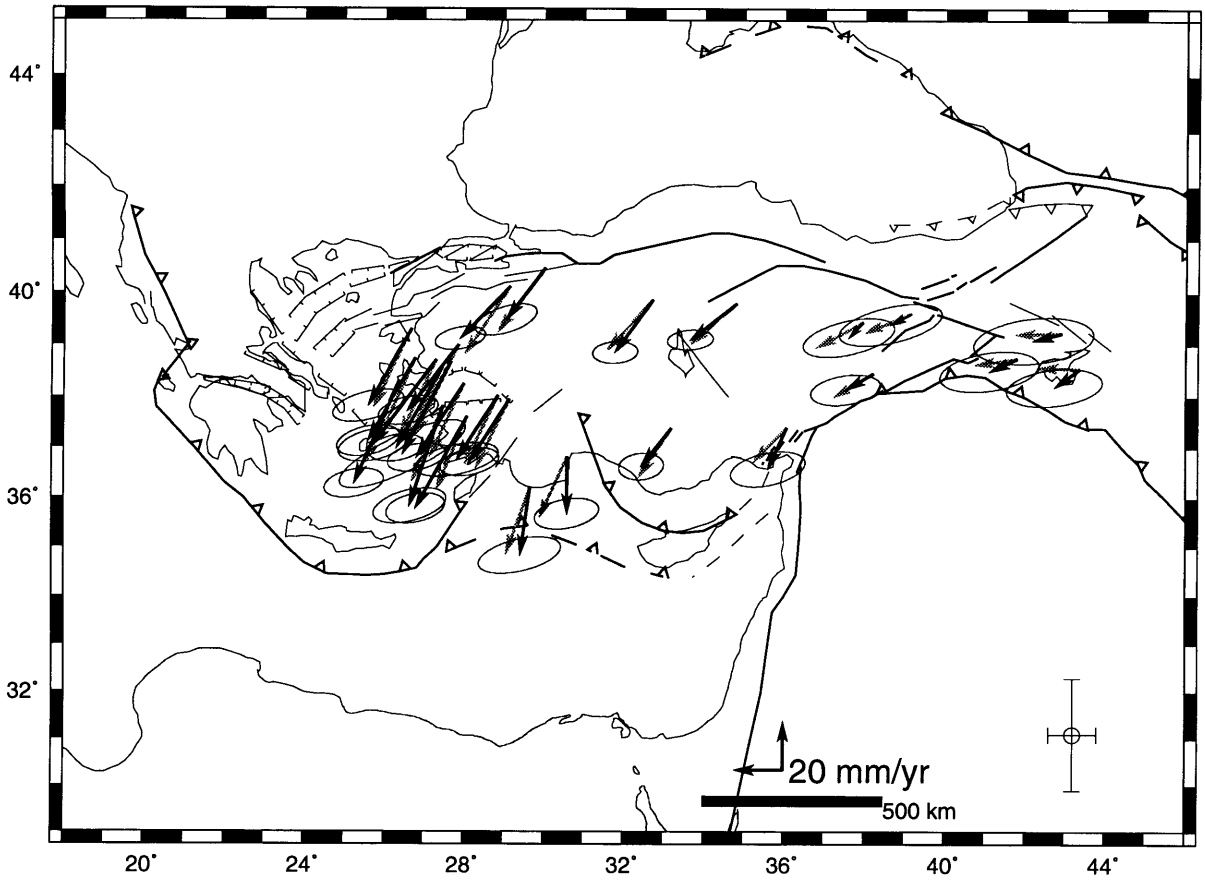

Figure 3-20: Regional sites and their velocities (black arrows) relative to Karacadağ used in inverting for the instantaneous pole position and angular velocity. Gray arrows indicate velocities calculated after inversion from a pole located at 43.156±0.650°E, 31.147±1.171°N, with a counterclockwise angular velocity of 1.215±0.154°/Myr relative to Arabia. Euler pole is shown with uncertainties in N-S and E-W.

ties are reduced by further observations, we should be able to resolve the differential motion between central-eastern Turkey and the Van block, as well as place some constraints on the possible internal deformation in eastern Turkey.

Predicted velocity fields unequivocally demonstrate the counterclockwise rotation of the Anatolian plate relative to both Pontus and Arabia. The general character of predicted velocities relative to Pontus shows that they are parallel to the arcuate trace of the North Anatolian fault zone, especially to the eastern and central segments. To

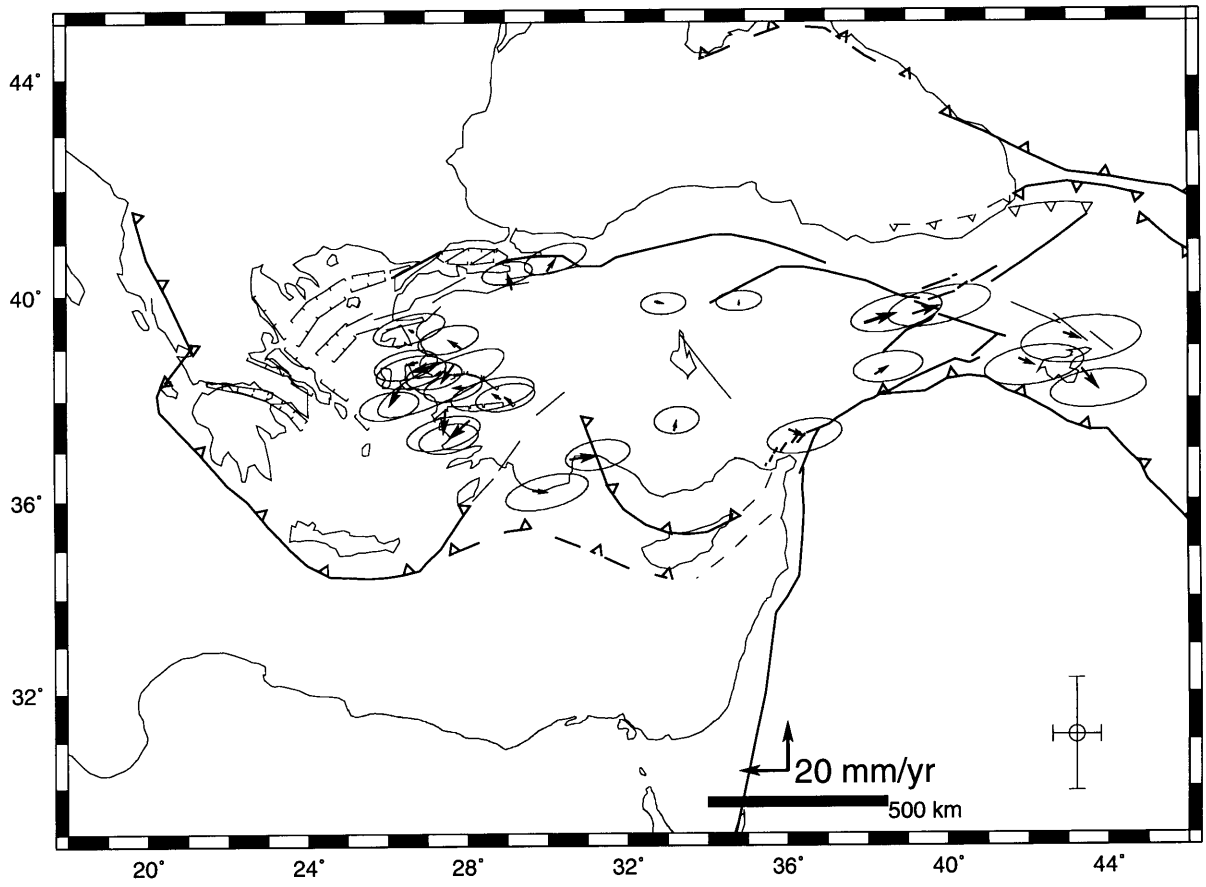

Figure 3-21: Residual velocities (observed – calculated) at the GPS and SLR sites as calculated in Figure 3-20. Euler pole is shown with uncertainties in N-S and E-W.

exemplify this, small circles at various radii, computed from ${}_{PON}\mathbf{E}_{ANA}$, are shown in Figure 3-22. There is a good agreement between the small circle at the radius of 10° and the trace of the NAF zone in central and central-eastern Turkey. In Marmara, however, there is a divergence from this small circle demonstrating the fragmented nature of the Anatolia-Pontus boundary. Indeed, the small circle that would be fitted to the NAF zone is strongly dependent upon the fault segments used for this purpose. Figure 3-23 shows small circles fitted to the trace of the NAF zone. We obtained the best fitting small circle when the eastern and central sections of the NAF were considered, and found a pole at 34.09°E, 29.72°N with a radius of 11.135°. This agrees well with that obtained from GPS observations (33.419±0.537°E, 31.109±1.249°N).

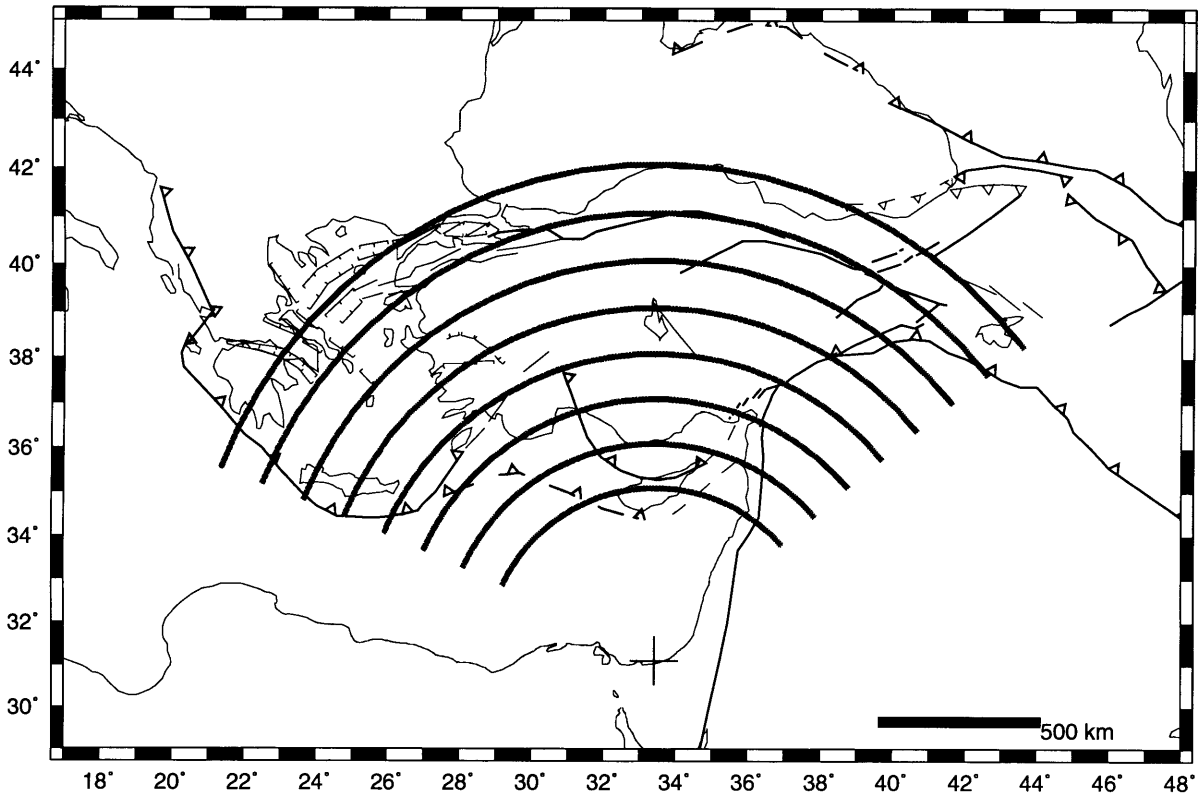

Figure 3-22: Small circles for Pontus-Anatolia motion at various radii [4° (10 mm/yr), 5° (12 mm/yr), 6° (14 mm/yr), 7° (17 mm/yr), 8° (19 mm/yr), 9° (22 mm/yr), 10° (24 mm/yr), and 11° (26 mm/yr)] using the pole shown in Figure 3-17 (Table 3.2). Pole location is shown with a cross.

However, when the northern strand of the western NAF and North Aegean trough or the southern strand of the western NAF were included, we could not find an acceptable pole (Figure 3-23). The motion is more complicated than a simple rigid plate rotation.

We conclude that the eastern and central segments of the NAF zone provide an excellent boundary for Anatolia-Pontus. We further exemplify this by rotating the boundaries of Anatolia, Arabia and Africa, relative to Pontus, back to their positions during the Pliocene. In Figure 3-24 we show plate boundaries after a finite rotation about the Euler poles, which are given in Table 3.2 [Cox and Hart, 1986]. In doing so, we assumed that the plate motions within the last ~3 Ma can be represented by their

Table 3.2: Euler vectors. Second plate rotates relative to the first one. Counterclockwise rotation is positive.

	Euler vector		
	Euler pole		Angular velocity
Plate pair	Longitude [°] ϕ	Latitude [°] λ	[°/Myr] ω
${}_{PON}\mathbf{E}_{ANA}$ †	33.419 ± 0.537	31.109 ± 1.249	1.248 ± 0.152
${}_{ARA}\mathbf{E}_{ANA}$ †	43.156 ± 0.650	31.147 ± 1.171	1.215 ± 0.154
${}_{EUR}\mathbf{E}_{ANA}$ †	31.709 ± 0.573	28.087 ± 1.533	1.185 ± 0.140
${}_{PON}\mathbf{E}_{ARA}$ ‡	137.379	-5.193	-0.182
${}_{PON}\mathbf{E}_{AFR}$ ‡	52.106	23.703	-0.386
${}_{EUR}\mathbf{E}_{PON}$ ‡	86.904	65.864	-0.094
${}_{AFR}\mathbf{E}_{ANA}$ ‡	38.028	29.606	1.618
${}_{EUR}\mathbf{E}_{AFR}$ *	-20.612	21.026	0.128
${}_{EUR}\mathbf{E}_{ARA}$ *	13.737	24.564	0.520
${}_{AFR}\mathbf{E}_{ARA}$ *	24.000	24.100	0.420
${}_{EUR}\mathbf{E}_{IRA}$ §	65.800	27.500	-0.560
${}_{EUR}\mathbf{E}_{TUR}$ §	34.000	14.600	0.643
${}_{EUR}\mathbf{E}_{TUR}$ +	34.000	14.600	0.778
${}_{TUR}\mathbf{E}_{ARA}$ +	61.900	-3.3	0.351

† This study from inversion of GPS velocities.
‡ Addition of the Euler vectors from this study and NUVEL-1.
* DeMets et al. [1990].
§ McKenzie and Jackson [1984].
+ Taymaz et al. [1991b].

PON: Pontus, ANA: Anatolia, ARA: Arabia, TUR: Turkish, AFR: Africa, IRA: Iran.

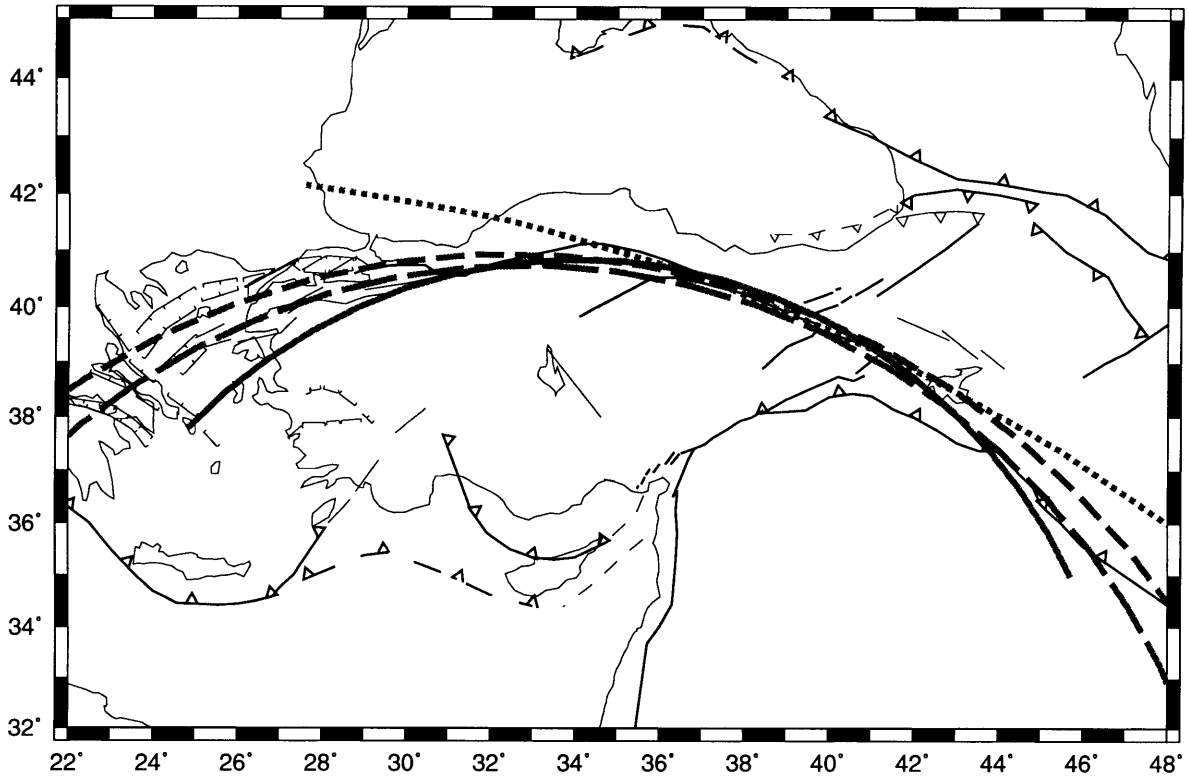

Figure 3-23: Best fitting small circles to the North Anatolian fault. Continuous line represents the small circle fitted to the eastern and central segments (pole at 34.09°E, 29.72°N and a radius of 11.135°). Line with short dashes is obtained by also including the northern splay of the western NAF (pole at 32.48°E, 23.53°N and a radius of 17.4233°). We included the southern splay instead to compute the line with longer dashes (pole at 32.817°E, 25.651°N and a radius of 15.0993°). The dotted line represents the small circle (pole at 22.9756°E, -4.1692°N and a radius of 46.5164°) for which we used only a small portion of the eastern segment.

respective instantaneous Euler poles (Table 3.2). In their kinematic reconstruction, using the instantaneous pole positions, Lyberis et al. [1992] rotate plate boundaries back to 13 Ma, the time when the collision along the Bitlis-Zagros suture took place. Our choice of the Pliocene, in contrast, is based on the lower bound for the approximate age of the EAF and NAF which, in turn, is calibrated by the total amount of observed slip along these faults. It is clear from Figure 3-24 that the only portion of the NAF that would sustain the transcurrent motion is composed of the central and

eastern segments. In the Marmara and north Aegean area, it is rather difficult to

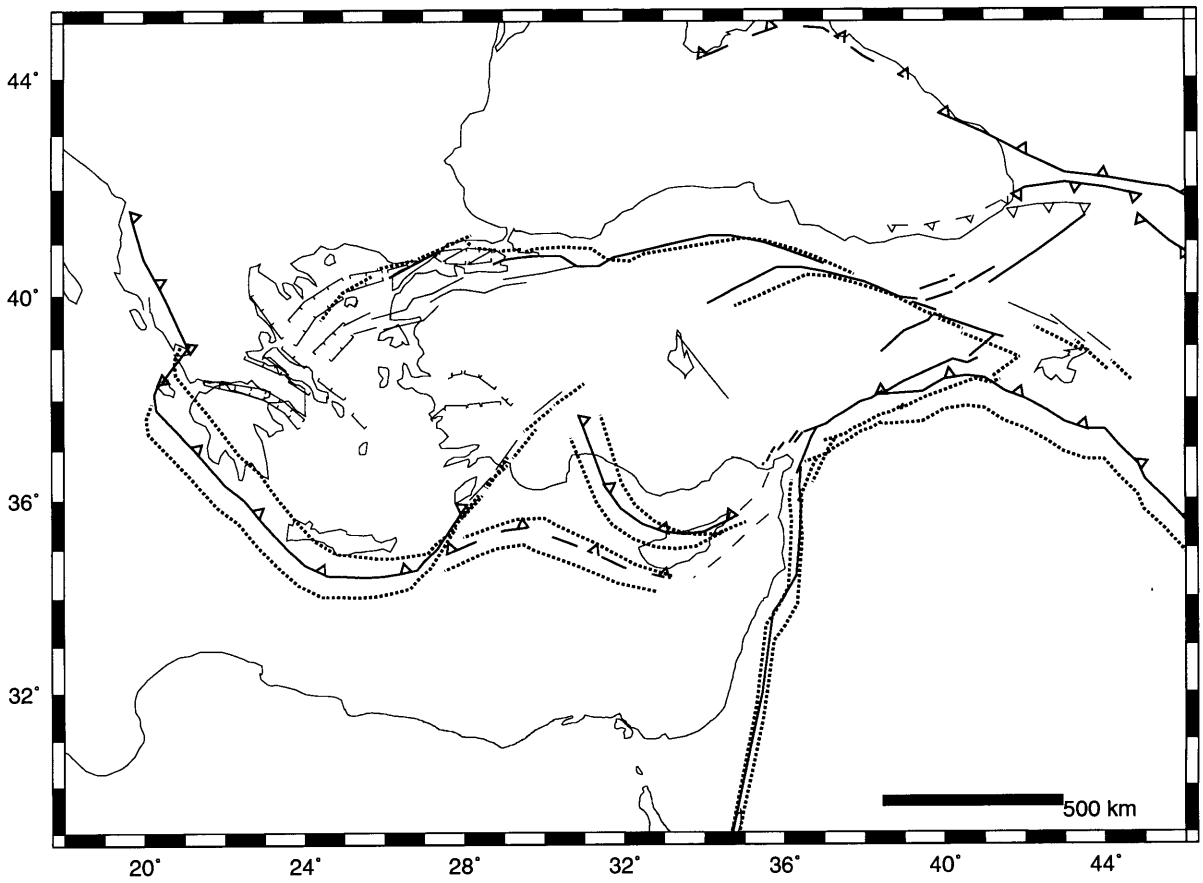

Figure 3-24: A "reconstruction" of plate boundaries at ~3-4 Ma (dotted lines). Finite rotations are applied about the Euler poles given in Table 3.2. Anatolia, Arabia and Africa are rotated relative to Pontus by -3.5°, -0.6° and -1.0°, respectively. In the Marmara and north Aegean area, for clarity, we back-rotated only the present-day northern strand of the NAF, and southern boundary for the Marmara grabens and north Aegean trough.

conserve the geometry of the plate boundaries. To avoid confusion, the dotted lines in Figure 3-24 show only the back-rotated, present-day northern strand of the NAF, and the southern boundary for the Marmara grabens and north Aegean trough. Overlap of the back-rotated southern boundary and the present-day northern boundary of the Marmara Sea grabens indicates extension due merely to boundary incompatibilities. Such a degree of overlap cannot be observed for the North Aegean trough, however,

along the Ganoşdağ fault (in southern Thrace) the transcurrent motion appears to be preserved. As Pavlides et al. [1990] emphasized, in this transtensional environment the intracontinental deformation cannot be simply accounted for by plate constructions which assume rigid plates. We consider the transtensional North Aegean trough zone as marking the boundary of Anatolia-Pontus. To the west, however, the termination for the Anatolian plate cannot be constrained by GPS nor SLR observations. Figure 3-24 shows two sets of dotted lines at the Hellenic arc. The northern one is the "retreated" Pliocene boundary. The difference between the northern and southern boundaries roughly corresponds to the amount of subduction since the Pliocene. We also note how well the strike-slip regime is preserved at the Keffalinia transform fault.

Velocities on each small circle (Figure 3-22) are constant and increase by $\sim$2 mm/yr/° northward. Therefore, we can discuss the relative motion for sites on the Anatolian plate provided that the separation between the sites is not greater than a couple of degrees. Minute motion at the Teke sites, relative to Pontus, is consequential to their proximity to the rotation pole which is located north of the Sinai peninsula. Therefore, in order to delineate motion relative to Pontus at sites located in southern Turkey and in Cyprus, our current uncertainties should be reduced by at least a factor of 3.

Subduction west of Rhodes, at the Hellenic arc, appears to be perpendicular to the trench. As delimited by small circles at radii of 6° and 7°, there is pronounced transcurrent motion at the Pliny-Strabo system. A better representation of subduction at the Hellenic and Cyprean arcs is given by Figure 3-26 The gradual westerly increase in velocities by 2.5 mm/yr/° (Figure 3-25) shows why rather slow motion and less seismic activity are observed in the Gulf of Iskenderun. The Anatolian plate motion, relative to Arabia, also conforms to a small circle at a radius of 8° coinciding with the EAF zone (Figure 3-25).

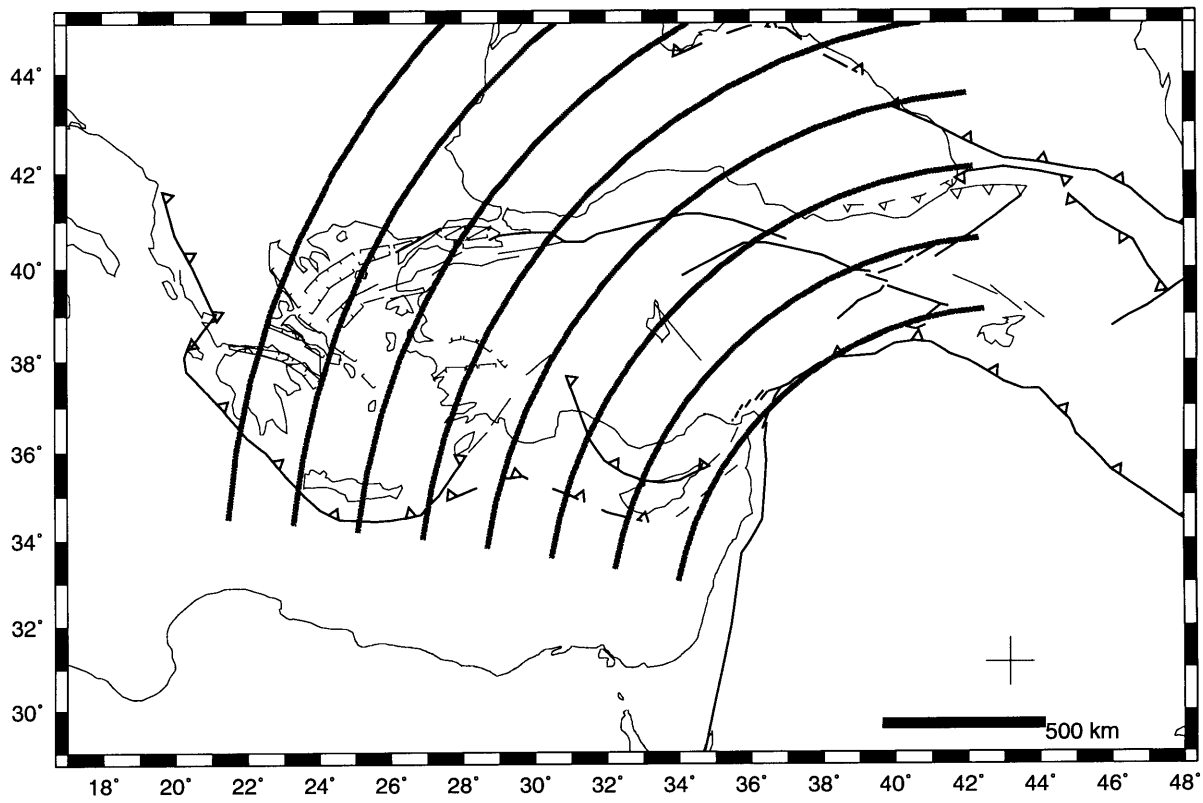

Figure 3-25: Small circles for Arabia-Anatolia motion at various radii [8° (19 mm/yr), 9.5° (22 mm/yr), 11° (26 mm/yr), 12.5° (29 mm/yr), 14° (33 mm/yr), 15.5° (36 mm/yr), 17° (40 mm/yr), and 18.5° (43 mm/yr)] using pole shown in Figure 3-20 (Table 3.2). Pole location is shown with a cross.

In summary, the GPS velocities observed in Anatolia can be parameterized, to a first approximation, by a set of Euler vectors (Table 3.2). Deviations from this model (non-rigid motion) is at the order of 10 mm/yr and the areas of largest misfit are concentrated in southwestern Turkey and in the southern Aegean. As a first approximation, using these Euler vectors, we can calculate the relative motion at plate boundaries. Figure 3-26 shows relative motions along the boundaries of the Anatolian plate. Accordingly, we obtain a $25\pm8_{95\%}$ mm/yr motion across the NAF. The motion between Anatolia and Arabia, on the EAF zone, is $19\pm11_{95\%}$ mm/yr. The motion calculated for the Gulf of Iskenderun, from both ${}_{ANA}\mathbf{E}_{ARA}$ or ${}_{ANA}\mathbf{E}_{AFR}$ is comparable at $20\pm11_{95\%}$ mm/yr and is similar to that along the EAF. The convergence across the

African and Anatolian plates reaches to $49 \pm 8_{95\%}$ mm/yr south of Pelleponnes. At the Bitlis suture zone, we express the velocities relative to Pontus and find a motion of $20 \pm 6_{95\%}$ mm/yr, oriented north.

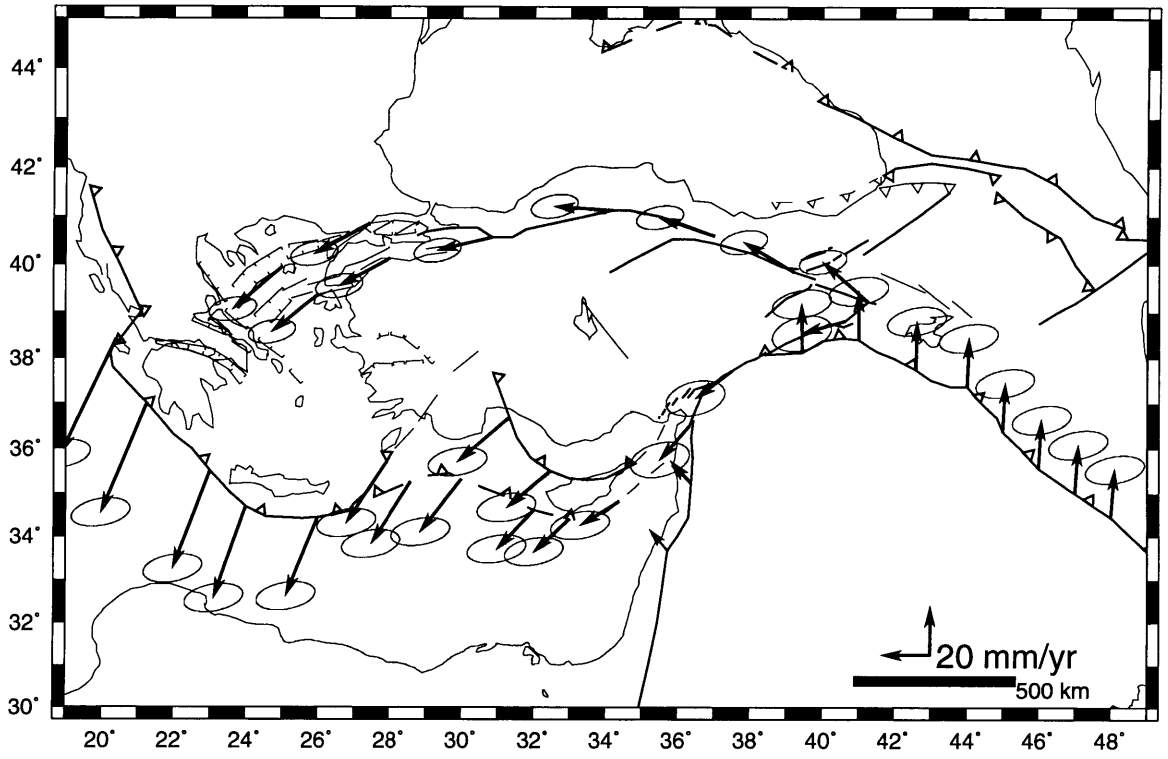

Figure 3-26: Computed velocities at the boundaries of the Anatolian plate relative to Pontus, Africa and Arabia. At the Bitlis-Zagros thrust, the velocities are relative to Pontus. Euler vectors are given in Table 3.2.

Prior to our GPS observations, information regarding the motion along the NAF and EAF zones was composed of terrestrial geodetic, geological and seismological observations. These observations have inherently different time scales and sensitivity. The controversy over the cumulative offset at these fault zones and their relevant age has not yet been settled. Dewey et al. [1986] provide a thorough summary and discussion of these observations. They state that the total slip along the NAF varies between 25–85 km. According to Seymen [1975 (after Dewey et al., 1986)],

the NAF has a total offset of 85 km and is post-Burdugalian (16 Ma). A lower bound of 25 km for the total offset since late Miocene (Tortonian: 10.4 – 6.7 Ma) has been suggested by Barka and Hancock [1984]. Further, their observations indicate an 8 km displacement since Quaternary (1.64 Ma) based on displacements observed in Quaternary deposits. They suggest the development of a broad zone of shear between the late Tortonian and early Pliocene, and conclude that by approximately 3 Ma the NAF was initiated as a narrow belt. Based on studies in the eastern section of the NAF, in the Gölova basin, Koçyiğit [1990] demonstrates a minimum of 35 km slip since the Pliocene. In the western segment, Koçyiğit [1990] illustrates a 32 km offset at the Gerede-Bolu segment of the NAF zone (east of Ismetpaşa [ISME]). The total offset along the East Anatolian fault zone varies between 22 km and 27 km and is post-Miocene (Pliocene) [Arpat and Şaroğlu, 1972]. Plate boundaries back-rotated to the Pliocene (Figure 3-24) provide an adequate visual basis for investigating the relationship between our GPS measurements and the geological observations. In doing so, of course, we assumed that the plate motions within the last 3 Ma could be represented by their respective instantaneous Euler poles given in Table 3.2, and we ignored the internal deformation. We observe a 25±10 km dextral motion along the EAF fault so our GPS observations are consistent with the cumulative slip since the Pliocene. Along the NAF the calculated 75±10 km displacement appears to exceed the lower bound (35 km, Koçyiğit [1990]) for geologically observed cumulative slip since the Pliocene, and suggests that the present-day velocities may not be completely projected back into the geological time scale for periods longer that a couple of million years, due to the frequent changes in boundary conditions such as the increased motion of the Arabian plate.

Triangulation-trilateration measurements along the NAF vary between 8 mm/yr and 28 mm/yr [Uğur, 1974 (after Dewey et al., 1986); Eren, 1984] and are not significantly different from those we have derived from 4 years of GPS observations. However, we did not have access to the error analysis of these studies. Comparison of

1946 and 1972 measurements shows a motion of 28 mm/yr and 8 mm/yr east and west of Mudurnu, respectively. Analysis of terrestrial measurements conducted in 1972 and 1982, in the Ismetpaşa microgeodetic network, suggests a 10–12 mm/yr motion [Eren, 1984]. It has long been known that least squares adjustment of terrestrial geodetic measurements in western Turkey networks, spanning 20-40 years, yields residuals to weighted least squares adjustments as great as a meter [Ö. Demirkol (GCM), pers. comm.]. Despite the less precise nature of terrestrial surveys, this amount of misfit is consistent with the residual field depicted by our GPS observations, and has a component of systematics which is due to the rigid rotation.

Slip vectors and the moment tensors of large earthquakes provide another set of constraints for crustal deformation in the eastern Mediterranean. (We will address the issue of moment tensors in the next section within the context of velocity gradient tensors.) In order to obtain relative motions, it has been common practice to combine slip vectors with the relative motions provided by global plate models (e.g., PO7 by Chase [1978], NUVEL-1 by DeMets et al. [1990]) since there are no spreading centers in the eastern Mediterranean by which to calibrate the directions [McKenzie, 1972; McKenzie and Jackson, 1984; Taymaz, 1991b; Lyberis, 1992; etc.].

Table 3.2 summarizes some of the Euler vectors from other studies. For instance, using the slip vectors (Figures 3-12 and 3-13) and Euler vector reported by McKenzie and Jackson [1984] (slightly revised) and the NUVEL-1 Arabia-Eurasia motion, Taymaz et al. [1991b] suggest 29 mm/yr and 38 mm/yr motion along the EAF and NAF zones, respectively. Because almost every estimate of plate motion in the eastern Mediterranean uses the Euler poles by McKenzie and Jackson [1984] and NUVEL-1 (or PO7 by Chase[1978]), these studies inherit similar uncertainties, especially systematics aliased in the ${}_{EUR}\mathbf{E}_{TUR}$. We have discussed the plate motions (Figure 1-6) computed from these Euler vectors in Chapter 1 and have attempted to furnish a new velocity field for the eastern Mediterranean, specifically for the Anatolian plate, from

our GPS observations (e.g., Figures 3-2, 3-3, 3-6, and 3-14). Given that the NAF zone determines the northern boundary for the Anatolian plate, it is difficult to reconcile with a rotation pole located at ϕ=34.0°E, λ=14.60°N, ω=0.643°/Myr . This tends to under/overestimate the actual motion and its direction along and across active deformation zones of the NAF and EAF. Indeed, the strong southwesterly motion in the Aegean that makes it popular to consider a distinct Aegean plate because the pure westerly motion for the Anatolian plate predicted by such a distant pole cannot account for the motions in the Aegean.

Velocities predicted via plate tectonic models, because they tend to ignore the deformation in the interior of the plates and their boundaries, tend to provide only approximations to the actual deformation. In Figure 3-26, for example, although the residuals are still within our 95% confidence area, the motion along the EAF is slightly over-estimated since the Anatolian plate is assumed to be perfectly rigid. Likewise, the same type of argument can be made for the southern Aegean and western Turkey. In this respect, we define the Anatolian plate in a first approximation, as a rigid plate whose motions can be determined by Euler vectors. The Anatolian plate also undergoes some internal and boundary deformation (~10 mm/yr).

3.3 Velocity Gradient Tensor

GPS and SLR observations in the eastern Mediterranean portray a substantial amount of strain accumulation and rotation. First order results of our GPS measurements in Turkey demonstrate the unequivocal counterclockwise rotation of the Anatolian plate, primarily along the NAF and EAF zones, as a result of collision between Arabia and Eurasia. The differences from a rigid plate motion in western Turkey and the southern Aegean point to significant internal deformation due to roll-back at the Hellenic arc. In order to investigate the amount of strain accumulation, internal deformation and rotation about the vertical axis, we computed the two-dimensional velocity gradient tensor $\mathbf{V}$ [Malvern 1969] from GPS and SLR velocities :

$$\mathbf{V}_{i,j} = \frac{\partial v_i}{\partial x_j} , \qquad i : \underline{e}ast, \quad j : \underline{n}orth, \tag{3.2}$$

for triangular subregions. These subregions are obtained by connecting Thiessen neighbors of GPS and SLR sites to form a Delaunay triangular network [Davis, 1986; Watson, 1982]. The deformation gradient relates changes in baseline component to changes in their velocity components [Malvern, 1969]:

$$\Delta v = \mathbf{V}.\Delta x , \tag{3.3}$$

and by definition,

$$\begin{bmatrix} \Delta v_e \\ \Delta v_n \end{bmatrix} = \begin{bmatrix} \mathbf{V_{ee}} & \mathbf{V_{en}} \\ \mathbf{V_{ne}} & \mathbf{V_{nn}} \end{bmatrix} \begin{bmatrix} \Delta x_e \\ \Delta x_n \end{bmatrix} . \tag{3.4}$$

If any one of the vertices of the triangular subregion is chosen as the local origin, then Δv is the velocity difference relative to that origin, and Δx is the baseline length from the origin. We obtained triangular subregions using GPS and SLR sites and estimated the velocity gradient tensor from velocities relative to Eurasia (Tables 2.8 and 2.9) for each subregion, as described by Feigl [1991]. In case of small rotations and strains, the velocity gradient tensor can be written as a sum of two matrices:

$$\mathbf{V} = \dot{\mathbf{E}} + \dot{\mathbf{W}} , \tag{3.5}$$

where $\dot{\mathbf{E}}$ is the strain rate tensor (stretching tensor) and $\dot{\mathbf{W}}$ is the rate of rotation tensor (spin/vorticity tensor). The strain rate tensor, $\dot{\mathbf{E}}$, can be defined in terms of velocity gradient tensor, $\mathbf{V}$:

$$\dot{\mathbf{E}} = \frac{1}{2}\left(\mathbf{V} + \mathbf{V}^T\right) . \tag{3.6}$$

This $\dot{\mathbf{E}}$ tensor provides a measure of internal deformation within a subregion and can be compared with seismic strain rate tensors obtained from the summation of moment tensors of large earthquakes [Scholz, 1990] reported by several studies [e.g., Jackson and McKenzie, 1988; Eyidoğan, 1988; Kiratzi, 1991; Papazachos et al., 1992]. In a direct comparison, however, ample caution should be taken in terms of the area (baseline length) considered in geodetic strain rate estimates and the deforming volume considered in seismic strain rate estimates.

From the symmetric strain rate $\dot{\mathbf{E}}$ tensor, we obtained the principal strains $\dot{\epsilon}_1$ and $\dot{\epsilon}_2$, and expressed their orientation ($\theta_{\dot{\epsilon}}$) by the azimuth $\dot{\epsilon}_2$.

The asymmetric rate of rotation tensor $\dot{\mathbf{W}}$ (also see discussion in Jackson and McKenzie [1988], Scholz [1990], Jackson et al. [1992], and Haines and Holt [1993]) is:

$$\dot{\mathbf{W}} = \frac{1}{2}\left(\mathbf{V} - \mathbf{V}^T\right) . \tag{3.7}$$

And by definition,

$$\dot{\mathbf{W}} = \begin{bmatrix} 0 & \dot{\Omega} \\ -\dot{\Omega} & 0 \end{bmatrix} , \tag{3.8}$$

where $\dot{\Omega}$ is the rigid body rotation about the local vertical. (Clockwise rotation is positive.) The rotation rate ($\dot{\Omega}$) can be compared with those reported by paleomagnetic observations [e.g. Van der Berg and Zijderveld, 1982; Kissel and Laj, 1988; Kissel et al., 1989] and with those determined from the moment tensors of eartquakes [Jackson et al., 1992] . However, great caution has to be taken due to the reference frame and time scale differences as discussed by Feigl et al. [1993]. Although we have

used velocities relative to Eurasia, because a local origin is defined for each triangular subregion by an arbitrarily chosen vertex, the reference frame for velocities becomes irrelevant. In this aspect, the rotations derived from the velocity gradient tensor imply only a local reference frame. Below we present our preliminary results obtained from velocity gradient analysis, limiting our discussion to strain and rotation rates resolved at the 95% statistical testing level.

In Table 3.3 we summarize the derived quantities $\dot{\epsilon}_1$, $\dot{\epsilon}_2$, $\theta_{\dot{\epsilon}_2}$, and $\dot{\Omega}$, and their scaled uncertainties, for each triangular subregion. The uncertainties in Table 3.3 are obtained by the propagation of errors provided in Tables 2.8 and 2.9. Figure 3-27 shows the principal strain rates at the centroid of each triangular subregion. The subregions are shown with dotted lines. The uncertainties for strain rates, however, are not shown due to the already crowded nature of the plots. Instead, we defined rejection criteria for the uncertainty in principal strains ($\dot{\epsilon}_1$ and $\dot{\epsilon}_2$) and in their orientation ($\theta_{\dot{\epsilon}_2}$). In Figure 3-27, we show only those principal strains which satisfy the following conditions at the 95% statistical testing level (one-dimensional):

$$\sigma_{\theta_{\dot{\epsilon}_2}} \leq 30^\circ \ , \quad max\left[\sigma_{\dot{\epsilon}_1} \ , \ \sigma_{\dot{\epsilon}_2}\right] \ \leq \ \| \ \dot{\epsilon}_1 \ or \ \dot{\epsilon}_2 \ \|.$$

Rotations computed from the asymmetric rate of rotation tensor, for subregions with significant strain rates (above criteria) and significant rotation ($\sigma_{\dot{\Omega}} \leq \dot{\Omega}$), are shown with wedges in Figure 3-28. Their scaled uncertainties at the 95% confidence level are shown with darker wedges.

Figures 3-27 and 3-28 show that the strain and rotation rate tensors cannot be resolved for 90% of the subregions at the 95% confidence intervals (one-dimensional). This is closely related to the level of errors associated with our GPS velocities. As shown in Table 3.3, the magnitude of the observed strain rate in Turkey, and across the Aegean, is less than $2.5 \times 10^{-7} yr^{-1}$. The one-dimensional velocity gradient for a

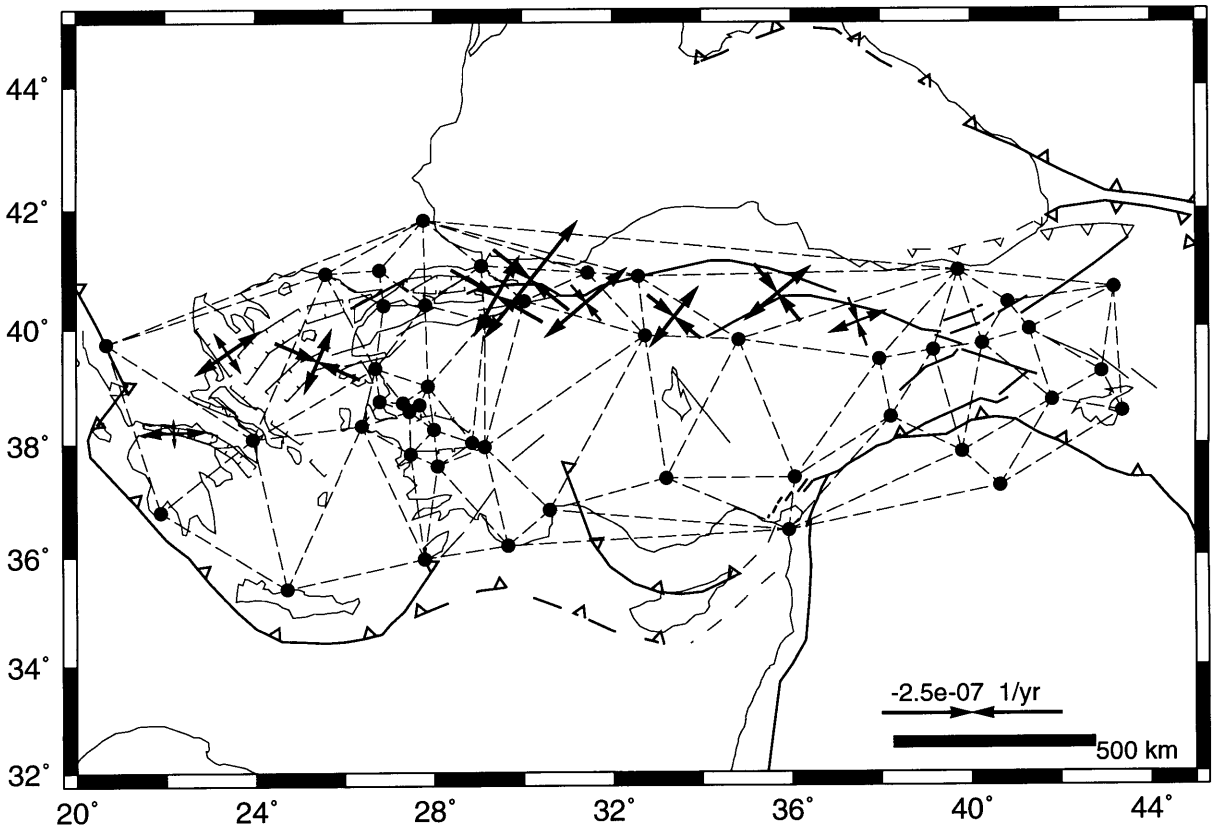

Figure 3-27: Principal strain rates derived from GPS and SLR velocities. Outward arrows represent extension.

velocity difference of 10 mm/yr between two sites separated by 100 km is $10^{-7}yr^{-1}$. In order to resolve this gradient the uncertainty in velocity has to be less than 10 mm/yr. As we have shown in the previous section, the non-rigid deformation is at the order of 10 mm/yr, while sites in the subregions used in our analysis are separated by ~300–400 km. Since the 95% scaled uncertainties at GPS sites are rarely less than 10 mm/yr, we cannot resolve significant strain and rotation rates for most of the subregions, except those which contain parts of the NAF zone. Because motion across the NAF amounts to $25\pm8_{95\%}$ mm/yr (see pages 81 and 118), we observe significant strain rates. However, no strain rates are statistically resolvable at the Arabia-Anatolian convergence zone since the motion between Karacadağ and Malatya is $13\pm14_{95\%}$ mm/yr (see page 99). Subregions within the Anatolian plate have small

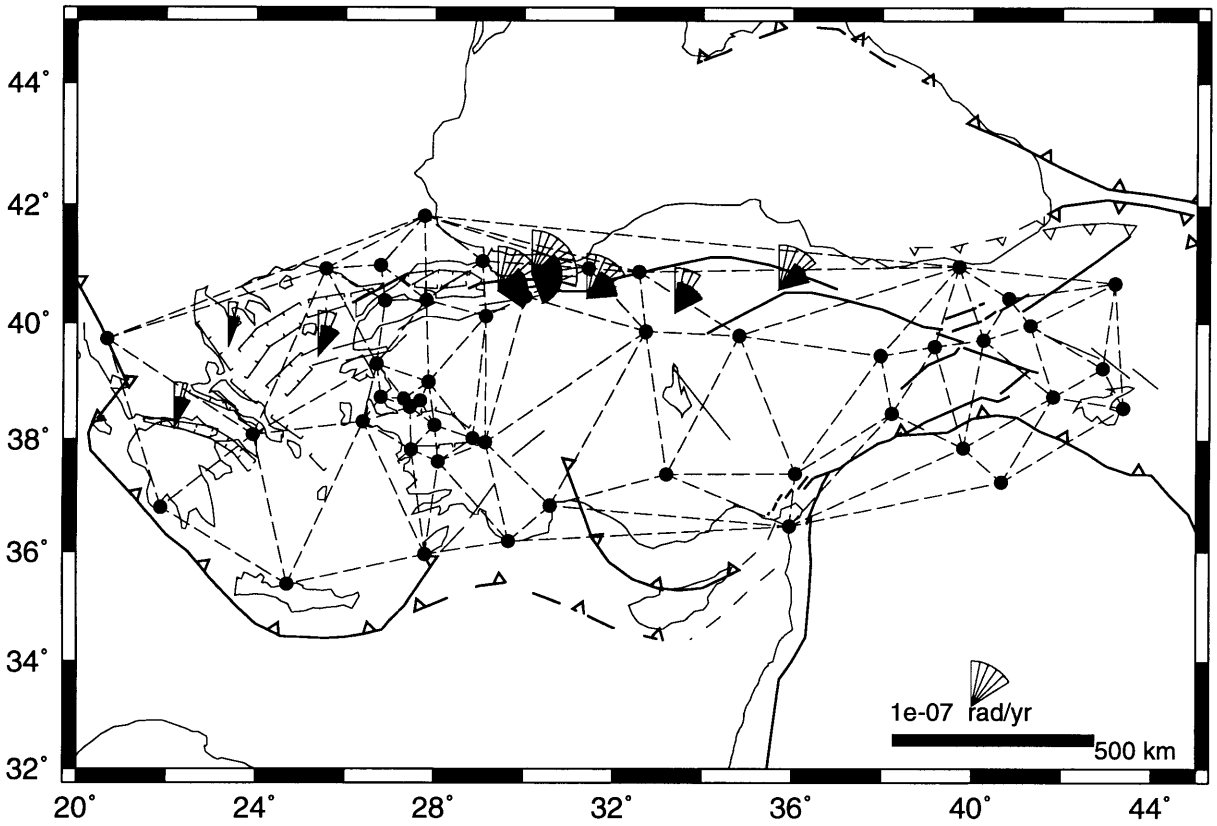

Figure 3-28: Rotations derived from GPS and SLR velocities. Clockwise rotation is positive. Scaled uncertainties at the 95% confidence level are shown with darker wedges.

to no velocity gradients, indicating little, if any, internal deformation. A non-zero rotation rate tensor ($\dot{\Omega}$) is observed from geodetic data, and is seen as an indicator of how the overall deformation is partitioned as "stretch" and "rotation." In this aspect, dextral slip along the NAF cannot be expressed simply in terms of strain rate tensor (Figure 3-27) but also in terms of rotation rate tensor(Figure 3-28). Therefore, motions obtained solely from symmetric strain rate tensor may under/over estimate the actual deformation.

Most of the subregions in Figure 3-27, which contain the Anatolia-Pontus boundary, have similar patterns and strain rates: NE-SW extension and NW-SE compression. These patterns reflect the dextral transcurrent motion along the NAF.

For instance, the extensional strain rate for the subregion defined by ISME-ANKA-YOZG is oriented ($\theta_{\dot{\epsilon}_2}$) 128±4 °N, while $\dot{\epsilon}_1$ is $1.06 \pm 0.42 \times 10^{-7}\ yr^{-1}$ and $\dot{\epsilon}_2$ is $-0.94 \pm 0.21 \times 10^{-7}\ yr^{-1}$.

For comparison we compiled the strain rate tensors reported by Jackson and McKenzie [1988], Eyidoğan [1988], Kiratzi [1991] and Papazachos et al. [1992]. These tensors were obtained from large earthquakes which occurred over the last ~70 years. Because the principal strains and their orientations were given in descending order by Jackson and McKenzie [1988], we obtained strain rate tensors from their moment rate tensors. From these strain rate tensors we computed principal strain rates ($\dot{\epsilon}_1$, $\dot{\epsilon}_2$ and $\theta_{\dot{\epsilon}_2}$) which are shown in Figures 3-29, 3-30, 3-31, and 3-32; their strain scale being identical to that in Figure 3-27. These seismic strain rates demonstrate transcurrent motion along the NAF fault and N-S extension in the Aegean.

In general, we find good agreement between the GPS and seismic strain rate patterns along the Pontus-Anatolia boundary. We note that there are no uncertainties cited by any of these studies. Estimation of scalar moment M_o of the earthquake from surface wave magnitude M_S (which itself may be in error by 0.25) largely contributes to the error budget of seismic moment tensor analysis. With this in consideration, Jackson and McKenzie [1988] provide upper and lower bounds for their assumed seismic moment tensor. Other sources of error include the volume of the deforming area and the focal mechanism parameters (strike dip, and rake) and time span (which may not represent the complete earthquake cycle).

Using the earthquakes that occurred in the Marmara region, Eyidoğan [1988] calculated strain rates (Figure 3-30) [$\dot{\epsilon}_1 = 1.18 \times 10^{-7}\ yr^{-1}$, $\dot{\epsilon}_2 = -1.06 \times 10^{-7}\ yr^{-1}$ at $\theta_{\dot{\epsilon}_2} = 127°$N] which are quite comparable to our estimates. As shown in Figure 3-31, the strain rates obtained by Kiratzi [1991] for a comparable region [$\dot{\epsilon}_1 = 0.52 \times 10^{-7}\ yr^{-1}$, $\dot{\epsilon}_2 = -0.36 \times 10^{-7}\ yr^{-1}$ at $\theta_{\dot{\epsilon}_2} = 106°$N] are smaller than those reported

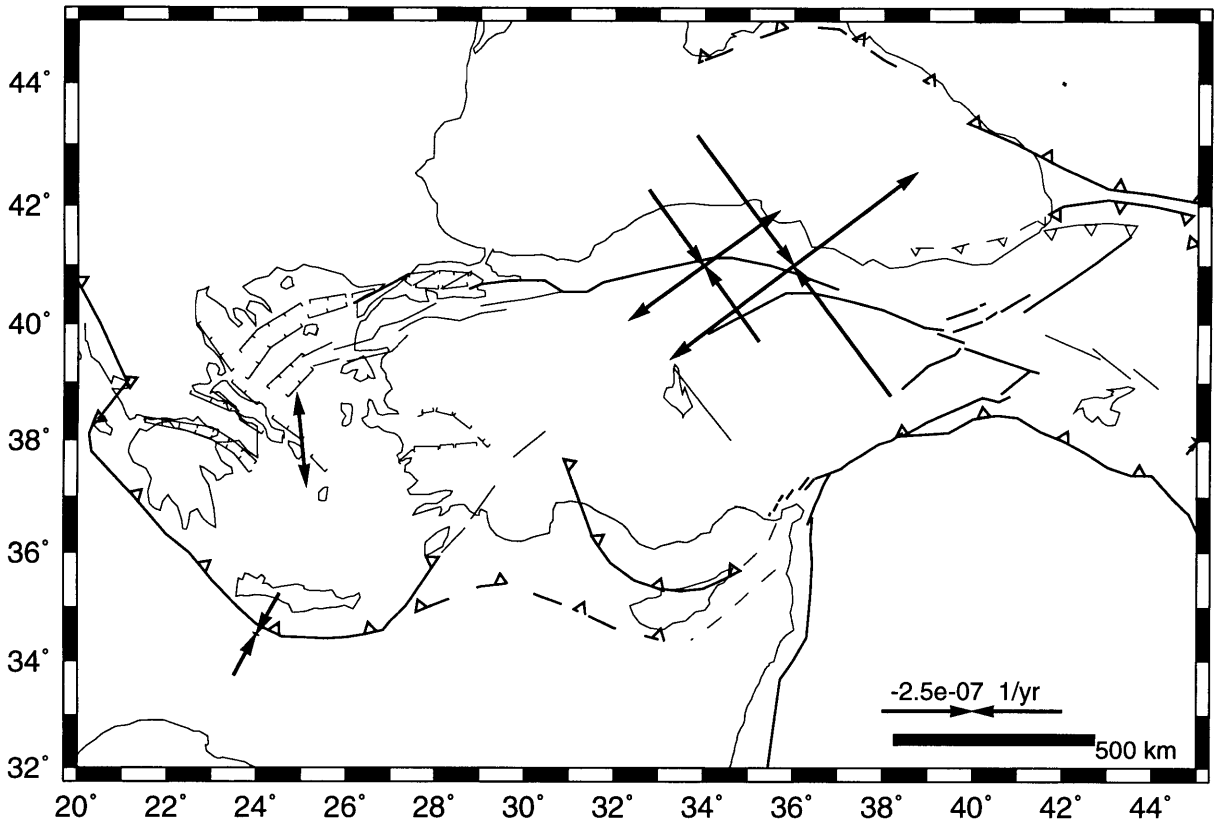

Figure 3-29: Principal strain rates after Jackson and McKenzie [1988]. The smaller and greater strain crosses plotted on the NAF are from their minimum and assumed seismic moment tensors, respectively.

by Eyidoğan [1988]. This is probably due to the different time, area and volume used in these two studies. They also used different M_o–M_s relations. Indeed, a later study by Papazachos et al. [1992] offers strain rates similar to those obtained from GPS and Eyidoğan [1988] (Figure 3-32). Papazachos et al. [1992] considered a northern Anatolian region (Marmara: belt 9, zone 15) [$\dot{\epsilon}_1 = 1.00 \times 10^{-7}\ yr^{-1}$, $\dot{\epsilon}_2 = -0.93 \times 10^{-7}\ yr^{-1}$ at $\theta_{\dot{\epsilon}_2} = 110°$N]. If the strain rates of Kiratzi [1991] are at the lower end of the spectrum, those reported by Jackson and McKenzie [1988] provide the higher end. The strain rates obtained from their (minimum) moment rate tensor [$\dot{\epsilon}_1 = 2.6 \times 10^{-7}\ yr^{-1}$, $\dot{\epsilon}_2 = -2.6 \times 10^{-7}\ yr^{-1}$ at $\theta_{\dot{\epsilon}_2} = 144°$N] are twice greater than those derived from GPS (their assumed estimates are 4 times greater than ours) and

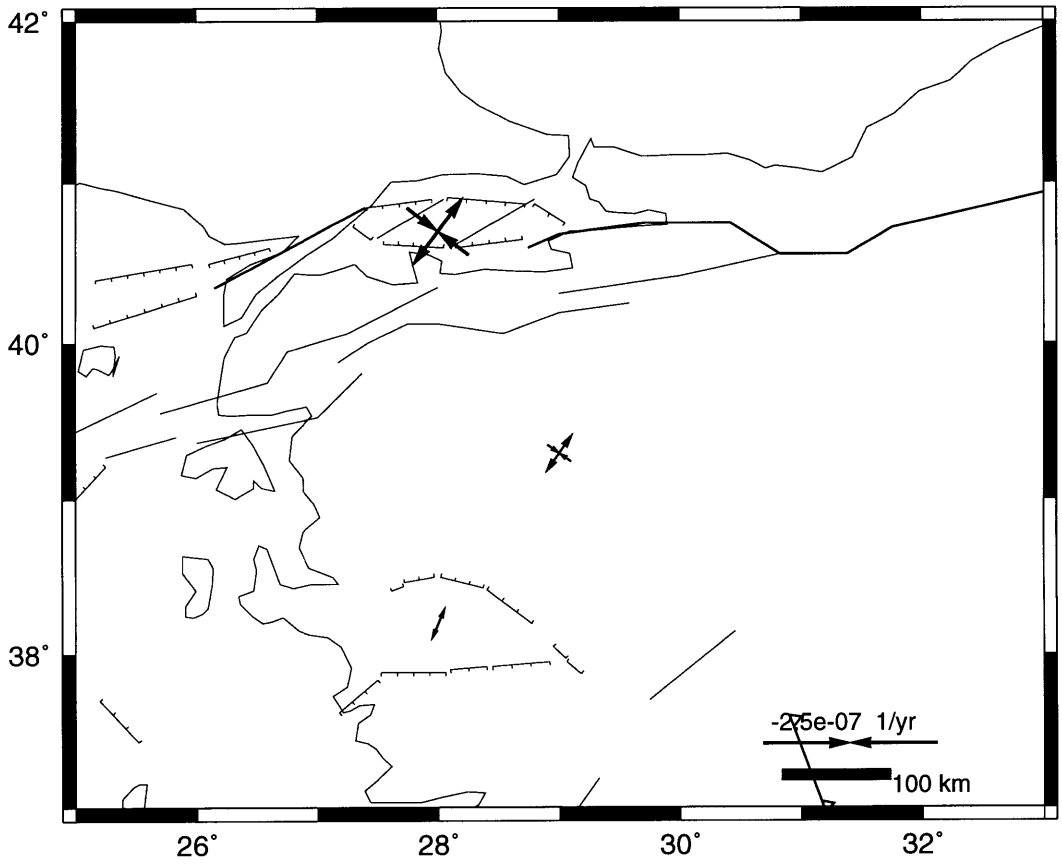

Figure 3-30: Principal strain rates after Eyidoğan [1988]. The strain cross located in the middle of the plot is for the entirety of western Turkey. The northern and southern strain crosses correspond to the Marmara region and southwestern Turkey.

may be primarily related to the estimation of seismic moments for earlier earthquakes.

This comparison between seismic and geodetic strain rates serves several purposes and has implications for the nature of tectonic deformation in this area. The agreement between seismic and geodetic strain rates shows that strain accumulation along the Marmara region of the NAF zone is taken up seismically. As historical and instrumental data indicate, the NAF zone has long been an active seismic belt, and it is well known that the deformation is being taken up seismically. Not all regions in the eastern Mediterranean, however, manifest this property. In Caucasus, for instance, seismicity can account for only a small portion of the observed deformation [Philip et al., 1989; Jackson, 1992]. This agreement between the geodetic and seismic strain

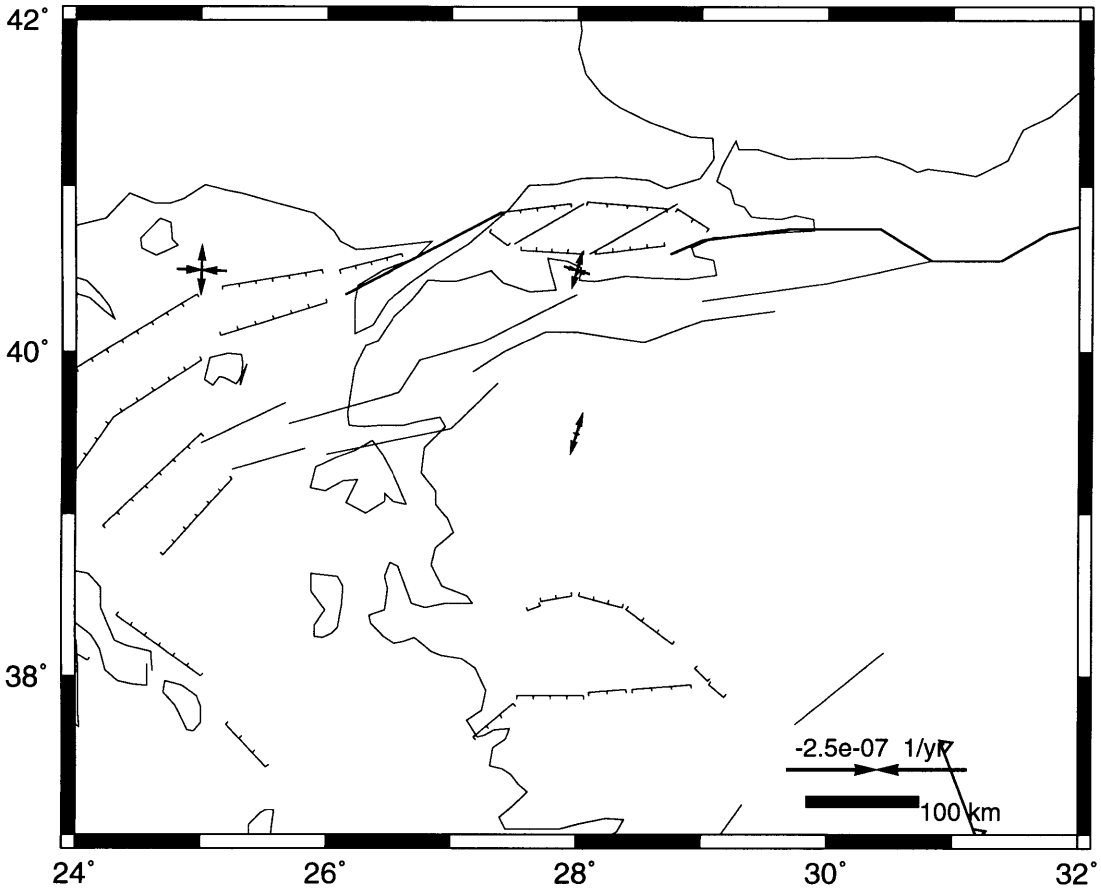

Figure 3-31: Principal strain rates after Kiratzi [1991]. Crosses represent strains in the North Aegean trough, and north and south of the NAF.

rate estimates in a seismically active belt is encouraging for the potential of velocity gradient tensor analysis of space geodetic observations to quantify the aseismic portion of the deformation. Further, a short period of observations with GPS (in this case) shows that they can provide information which otherwise would have to be acquired over decades. Indeed, if we consider that our GPS observations span only four years, the potential for geodetic observations is striking. (Currently, across the NAF zone, we have 3-5 epoch observations which have been conducted between 1988 and 1992.)

Eyidoğan [1988] suggests 24 mm/yr right-lateral displacement across the Marmara. This estimate from seismic moment tensors agrees with our GPS estimates

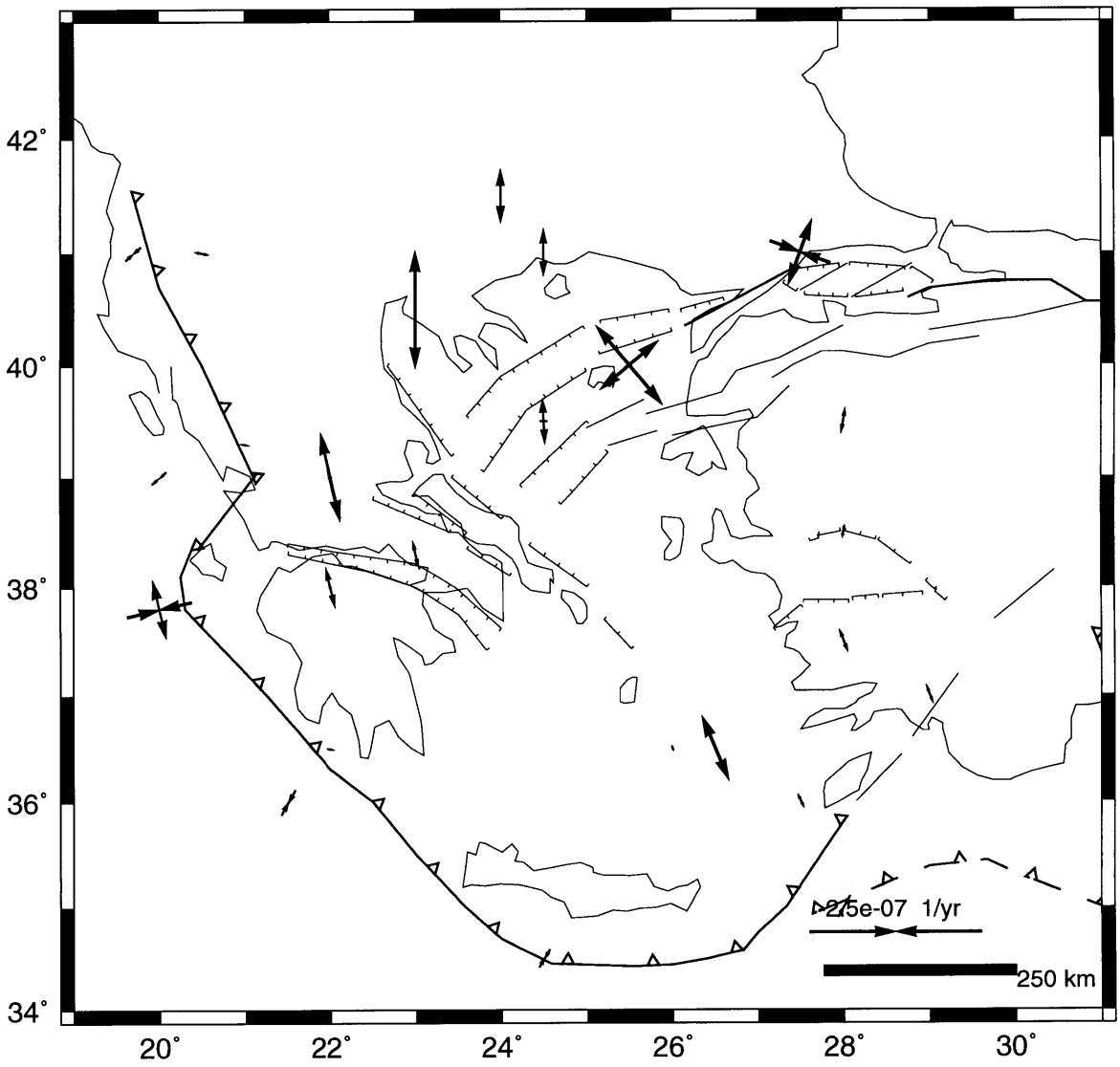

Figure 3-32: Principal strain rates after Papazachos et al. [1992]. Approximate locations for each seismic zone.

for the baseline between Kandilli and Uludağ [IKAN-ULDA: v_H=29±13$_{95\%}$ mm/yr, θ =77±10$_{95\%}$ °N]. From minimum and assumed moment tensor estimates, Jackson and McKenzie [1988] find 25 mm/yr and 39.6 mm/yr along the NAF, respectively. It is clear that the minimum estimate is much closer to our GPS estimates. The horizontal velocity field obtained from seismic moment tensors for the Aegean [Jackson et al., 1992] is not compatible with that derived from SLR observations in the Aegean, especially in western Greece. They systematically underestimate the velocities at

Karitsa, Chrisokellaria and Roumeli by several centimeters per year. Their estimated velocities in the Teke region are much greater than our GPS estimates. Therefore, it is hard to reconcile space geodetic observations with the velocity field obtained from seismic moment tensors by Jackson et al. [1992]. The source of discrepancy in the seismic and geodetic velocity fields for the Aegean region may as well be related to a larger amount of deformation being taken up aseismically. The velocity rate reported by Papazachos et al. [1992], on the other hand, provides support for the non-rigid component in GPS and SLR velocity fields in the Aegean. Their velocity rates, computed from the summation of seismic moment tensors, show 5-12 mm/yr extension in the southern Aegean.

The geodetic strain field computed for subregions in the northern Aegean and central Greece does not have a corresponding seismic strain rate due to the sparse distribution of GPS and SLR sites. Subregions defined in our analyses cross several structures in the Aegean; therefore, comparison with seismic observations is difficult. Extensive work done by Papazachos et al. [1992] considers several seismic zones in western Turkey, the Aegean Sea and central Greece. Their estimates for the strain rate suggest primarily N-S extension in this region (Figure 3-32). The dominant extension in the North Aegean trough is captured by geodetic observations. Pattern and strain rates for the subregion defined by the DION-ASKI-AYVA subregion are quite similar to those observed for subregions containing the NAF, suggesting that the dextral transcurrent motion extends into this region. Further to the west, this pattern changes drastically in the DION-KARI-ASKI subregion and implies a NE-SW and NW-SE extension, which are inherited from the SLR velocity field. Rather high velocity at Karitsa relative to Askites naturally creates this gradient. Indeed, the velocity observed by SLR at Karitsa relative to Eurasia shows that this region is overthrusting the African plate. This probably occurs aseismically since the seismic strain rates, which estimate more of a N-S extension (Figure 3-32) in central and northeastern Greece, account for only a small portion of this observed deformation.

Over the Gulf of Corinth, the SLR derived strain rates in the DION-KARI-CHRI subregion show N-S and E-W extension. However, the E-W extension is dominant [$\dot{\epsilon}_1 = 0.90 \pm 0.17 \times 10^{-7}\ yr^{-1}$]. Preliminary results of GPS observations in the southern Aegean network (north of Crete, between Pelleponnes and southwestern Turkey) by Gilbert et al. [1993] show that all subnetworks have undergone dilatation but no compression. They note that the dominant mode of deformation is E-W extension by about $\dot{\epsilon} = 0.50 \times 10^{-7}\ yr^{-1}$. This value is quite comparable to the strain rates obtained from the DION-ROUM-CEIL subregion, which includes both GPS and SLR sites (Table 3.3). (Strain rates for this subregion are not shown in Figure 3-27 because testing criteria were not completely satisfied). Gilbert et al. [1993] emphasize the E-W, and express their concern about the lack of N-S, extension. Indeed, our analysis shows that there is a comparable, significant N-S extension in the DION-ROUM-CEIL subregion [$\dot{\epsilon} = 0.299 \pm 0.174 \times 10^{-7}\ yr^{-1}$]. The E-W extension in the southern Aegean Sea does not necessarily preclude N-S extension.

Given the ~10 mm/yr residuals, representing the non-rigid component of plate motions in western Turkey and southern Aegean (see page 109), both N-S and E-W extension is clearly demonstrated in Figure 3-19. That residuals at Chrisokellaria and Roumeli/Kattavia point in opposite directions is consistent with the E-W extension reported by Gilbert et al. [1993]. Accordingly, we observe not only the trench migration and the resulting extrusion of the southern Aegean over the African plate at a higher speed, but also E-W stretching of the southern Aegean. Because the uncertainties at the 95% confidence level did not satisfy the above set criteria, we have not included other subregions in 3-27, but they are reported in Table 3.3. Nonetheless, our velocity gradient analysis places upper bounds on the internal deformation interior to the Anatolian plate. Accordingly, the strain rates in western Turkey can be as much as $\dot{\epsilon} = 1.31 \pm 0.59 \times 10^{-7}\ yr^{-1}$ (e.g., ODME-CINE-SOKE) in the N-S direction. This is comparable to the estimate made by Eyidoğan [1988] for southwestern Anatolia.

For central and central eastern Turkey, the strain rates are one order magnitude smaller [e.g., ANKA-YOZG-MELE, YOZG-MELE-KADI: $\dot{\epsilon} \approx 10^{-8}\ yr^{-1}$], indicating little, if any, internal deformation. This is in agreement with the residual velocity field shown in Figure 3-18. In eastern Turkey, insufficient site distribution produces subregions which contain several active zones, making the delineation of strain rates rather difficult. Compressional strains across the Bitlis suture zone are N-S and about $0.97 \pm 0.33 \times 10^{-7}\ yr^{-1}$ (e.g., KARA-KIZI-KORK).

In Figure 3-28, the rather high level of uncertainties makes interpretation of rotation rates ($\dot{\Omega}$) quite difficult. Clockwise rotation obtained from subregions containing the NAF zone is characteristic of right lateral motion. We observe a rate of rotation at about $80 \pm 50\ nanorad/yr$. (Also see Dong [1993] for a comparison with the San Andreas fault.) This clockwise rotation cannot be compared with rotations from paleomagnetic observations or those about the Euler pole, since it is more likely to represent a component of dextral shear along the NAF. Counterclockwise rotations are characteristic for subregions crossing sinistral strike-slip boundaries, such as the EAF. Large uncertainties, however, do not allow us to resolve statistically significant rotation rates across the EAF zone. Subregions which do not contain any boundaries provide "real" rotational rates about their vertical axis. The upper bound for rotation rates in the interior of the Anatolian plate vary from 10 $nanorad/yr$ to 50 $nanorad/yr$ (counterclockwise). This roughly translates to from $0.5°/Myr$ to $2.5°/Myr$ rotations, and may be comparable to the rotation rate estimated for the Anatolian plate as a whole in the previous section. Unfortunately, none of these rotation rates are statistically significant at the 95% confidence level, thus, they disallow conclusions based on our current observations and their uncertainties. Therefore, there are no grounds for comparison between our GPS results and paleomagnetic results, or those reported by Jackson et al. [1992], before the uncertainties involved with our velocity field is reduced by at least a factor of two.

Table 3.3: Principal strains and rotations obtained from velocity gradient tensor analysis. Extension and clockwise rotations are taken as positive. 1-σ uncertainties have to be multiplied by 1.96 for statistical testing at the 95% level.

	Strain rate 1		Strain rate 2		Orientation		Rotations [CW]	
Triangle corners	[10^{-7} yr^{-1}]		[10^{-7} yr^{-1}]		[°]		[nanorad yr^{-1}]	
	$\dot{\epsilon}_1$	$\sigma_{\dot{\epsilon}_1}$	$\dot{\epsilon}_2$	$\sigma_{\dot{\epsilon}_2}$	θ	σ_θ	$\dot{\Omega}$	$\sigma_{\dot{\Omega}}$
AKGA-AYVA-BAYO	1.880	1.180	-0.544	0.596	122.9	10.1	25.3	71.7
AKGA-AYVA-ERDE	0.262	0.775	-0.558	0.514	134.8	27.3	0.5	47.6
AKGA-BAYO-HAPA	3.660	1.700	1.440	1.680	65.4	21.5	-29.1	294.0
AKGA-BULD-ULDA	0.293	0.472	0.140	0.327	-35.7	122.3	-23.9	26.9
AKGA-HAPA-ODME	2.550	3.610	-1.750	2.170	127.4	27.2	-227.0	118.0
AKGA-ODME-BULD	0.664	1.130	0.093	0.616	124.7	49.3	-40.4	49.0
AKGA-ULDA-ERDE	0.288	0.336	-0.845	1.010	127.7	28.1	-14.1	52.5
AKTO-ISME-DEMI	0.686	0.473	-0.259	0.276	-41.2	6.0	33.6	33.0
AKTO-ISME-YOZG	1.180	0.238	-1.020	0.205	-39.1	2.1	95.2	20.4
AKTO-ISPI-KARS	0.186	0.968	-1.950	0.818	-22.7	19.6	86.5	97.6
AKTO-KEMA-MERC	1.540	1.080	-0.356	0.277	-11.3	14.1	92.4	31.3
AKTO-KEMA-SINC	0.534	0.397	-1.640	0.968	134.5	17.7	82.3	64.8
AKTO-MERC-ISPI	0.699	0.749	-1.250	0.864	117.4	12.7	-30.0	38.6
AKTO-YOZG-SINC	0.849	0.183	-0.704	0.310	-21.1	7.4	29.5	36.8
ANKA-MELE-ANTU	-0.136	0.093	-0.516	0.292	105.2	19.9	-28.5	11.9
ANKA-PAMU-ANTU	0.668	0.343	-0.168	0.131	24.0	13.5	-45.9	18.8
ANKA-PAMU-MEKE	0.157	0.151	0.023	0.236	95.1	64.3	-1.4	17.1
ANKA-YOZG-MELE	-0.070	0.161	-0.297	0.228	129.9	38.9	-25.9	11.5
ASKI-AYVA-SEVK	0.222	0.873	-1.880	2.130	95.6	25.7	52.9	88.0
ASKI-DEMI-HEMI	-0.206	0.845	-2.730	3.150	-42.4	22.5	22.4	187.0
ASKI-HEMI-SEVK	2.650	2.530	-1.740	1.130	106.9	25.0	45.9	203.0
AYVA-BAYO-SEUR	0.316	0.605	-1.460	1.890	87.3	33.4	16.0	73.9
AYVA-CEIL-SEUR	1.090	0.764	-1.020	2.250	120.3	36.5	-72.3	94.9
AYVA-ERDE-SEVK	0.295	0.661	-0.483	2.940	114.3	119.3	27.3	127.0
BAYO-HAPA-SIPD	2.670	2.740	-3.220	4.430	25.7	18.2	-111.0	232.0
BAYO-SIPD-SEUR	1.600	2.170	-5.000	4.930	47.1	22.6	-291.0	292.0
CINE-PAMU-BULD	1.550	2.150	0.161	3.100	115.3	88.4	-23.5	240.0
CINE-PAMU-KASO	0.935	0.695	0.173	0.197	-31.5	28.7	-80.4	27.5
DEMI-HEMI-ERDE	0.452	0.509	-0.881	2.200	86.5	31.5	120.0	76.6

Table 3.3: Strain rates and rotations obtained from velocity gradient tensor analysis. Extension and clockwise rotations are taken as positive. 1-σ uncertainties have to be multiplied by 1.96 for statistical testing at the 95% level.

	Strain rate 1		Strain rate 2		Orientation		Rotations [CW]	
Triangle corners	[10^{-7} yr^{-1}]		[10^{-7} yr^{-1}]		[°]		[nanorad yr^{-1}]	
	$\dot{\epsilon}_1$	$\sigma_{\dot{\epsilon}_1}$	$\dot{\epsilon}_2$	$\sigma_{\dot{\epsilon}_2}$	θ	σ_θ	$\dot{\Omega}$	$\sigma_{\dot{\Omega}}$
DION-ASKI-AYVA	0.961	0.141	-1.290	0.345	113.1	4.7	41.3	16.5
DION-AYVA-CEIL	0.927	0.385	-0.334	0.424	98.6	18.8	-4.6	42.3
DION-KARI-ASKI	1.090	0.111	0.653	0.172	-34.0	8.3	20.5	9.5
DION-KARI-CHRI	0.897	0.173	0.371	0.185	-2.1	14.4	30.4	13.4
DION-ROUM-CEIL	0.299	0.174	-0.255	0.268	71.5	14.6	-48.7	12.7
DION-ROUM-CHRI	1.400	0.164	0.111	0.199	9.0	5.3	-8.9	13.3
ERZU-ISPI-KARS	0.637	0.715	0.043	0.494	67.2	39.3	24.1	82.1
ERZU-KARS-PATN	0.213	0.503	-1.230	0.553	133.0	11.5	65.9	43.0
ERZU-KORK-PATN	0.403	0.829	-1.160	0.553	123.3	14.0	43.2	44.5
HAPA-SIPD-ODME	-0.160	1.880	-2.520	3.920	18.7	22.6	37.7	163.0
HEMI-ERDE-SEVK	2.460	2.790	-0.656	1.950	107.8	32.8	91.2	211.0
IKAN-DEMI-ERDE	2.060	0.966	-0.284	0.322	-34.7	12.2	4.4	47.5
IKAN-MEKE-ULDA	1.270	0.551	-1.460	0.560	119.7	7.4	146.0	36.7
IKAN-ULDA-ERDE	2.270	0.784	-1.370	0.733	131.5	9.2	89.1	46.3
ISME-ANKA-YOZG	1.060	0.421	-0.943	0.207	128.9	4.1	59.6	26.3
ISME-YIGI-ANKA	1.020	0.619	-0.624	0.230	134.1	9.7	79.0	27.2
ISME-YIGI-DEMI	0.183	1.580	-0.350	0.816	-25.1	109.1	20.6	110.0
KALE-KORK-PATN	0.594	0.639	0.026	0.950	79.0	88.5	-4.0	87.0
KARA-KIZI-KORK	-0.419	0.542	-0.975	0.332	7.1	40.7	-33.1	41.6
KARA-MERC-KORK	-0.386	0.134	-1.050	0.532	112.2	22.4	25.8	19.7
KARI-ASKI-DEMI	4.630	1.050	-1.810	0.847	29.0	8.2	-307.0	77.5
KARS-KALE-PATN	2.320	3.410	-0.264	0.333	7.0	15.4	131.0	70.9
KATT-CEIL-SOKE	0.348	0.738	-0.109	0.567	21.4	28.9	-25.0	27.3
KATT-CINE-KASO	0.252	0.394	-0.032	0.305	22.7	40.8	-83.2	22.1
KATT-CINE-SOKE	0.022	0.227	-1.720	1.510	89.9	12.8	-65.4	40.4
KATT-ROUM-CEIL	0.155	0.134	-0.240	0.150	79.8	17.4	-57.5	13.6
KEMA-KARA-MERC	1.670	1.050	-0.421	0.106	7.2	6.1	28.4	27.7
KEMA-MALA-KARA	0.715	0.597	-0.119	0.179	-6.2	23.8	-33.5	26.1
KEMA-SINC-MALA	0.217	0.477	-0.504	0.984	118.3	44.6	13.0	48.8
KIZI-KALE-KORK	0.210	0.886	-0.895	0.419	27.1	27.2	-19.0	53.4
MALA-ULUC-KADI	0.195	0.621	-1.540	0.493	-17.8	8.6	-87.4	53.9
MALA-ULUC-KARA	0.518	0.296	-0.434	0.237	14.6	14.7	-53.2	25.7
MELE-ULUC-ANTU	0.307	0.328	-0.669	0.467	45.9	5.9	-86.9	33.5
MELE-ULUC-KADI	0.225	0.219	-1.210	0.404	8.2	13.4	-17.7	36.1

Table 3.3: Strain rates and rotations obtained from velocity gradient tensor analysis. Extension and clockwise rotations are taken as positive. 1-σ uncertainties have to be multiplied by 1.96 for statistical testing at the 95% level.

	Strain rate 1		Strain rate 2		Orientation		Rotations [CW]	
Triangle corners	[10^{-7} yr^{-1}]		[10^{-7} yr^{-1}]		[°]		[nanorad yr^{-1}]	
	$\dot{\epsilon}_1$	$\sigma_{\dot{\epsilon}_1}$	$\dot{\epsilon}_2$	$\sigma_{\dot{\epsilon}_2}$	θ	σ_θ	$\dot{\Omega}$	$\sigma_{\dot{\Omega}}$
MERC-ERZU-ISPI	0.931	0.635	0.057	0.918	89.3	48.6	-2.1	81.0
MERC-ERZU-KORK	0.602	0.674	-0.997	0.420	129.9	11.3	47.4	41.4
ODME-CINE-BULD	1.470	0.751	0.085	0.866	119.5	21.5	-29.5	54.6
ODME-CINE-SOKE	1.310	0.595	-1.530	1.340	103.4	12.4	-52.1	60.1
PAMU-ANTU-KASO	0.856	0.694	0.173	0.272	4.2	25.5	-39.1	27.5
PAMU-BULD-ULDA	0.323	2.610	0.104	1.200	-36.2	462.4	-27.5	78.5
PAMU-MEKE-ULDA	0.684	0.908	0.152	0.147	13.6	31.7	-5.0	29.1
SINC-MALA-KADI	0.357	0.309	-0.683	0.798	118.7	26.3	-3.0	45.3
SIPD-CEIL-SEUR	1.370	0.912	0.049	0.939	97.6	40.1	-39.6	93.8
SIPD-CEIL-SOKE	0.977	0.474	0.179	0.659	93.3	36.1	-63.5	50.1
SIPD-ODME-SOKE	1.070	0.582	-0.681	1.240	102.0	18.4	-97.3	54.9
ULUC-ANTU-KASO	0.554	0.859	-0.485	0.568	132.5	5.3	11.2	63.7
ULUC-KARA-KIZI	0.160	0.146	-0.844	0.341	-19.5	10.7	-16.6	42.1
YIGI-ANKA-MEKE	1.490	0.524	-0.635	0.220	-40.0	5.3	99.8	26.0
YIGI-IKAN-DEMI	-0.045	0.254	-1.520	0.917	28.2	7.3	-29.3	56.5
YIGI-IKAN-MEKE	2.070	0.711	-1.340	0.457	128.7	4.7	182.0	50.8
YOZG-MELE-KADI	0.335	0.234	-0.094	0.142	35.7	19.8	-15.2	13.7
YOZG-SINC-KADI	0.476	0.355	0.206	0.117	-11.3	42.0	-29.1	15.1

Chapter 4

Discussions and Conclusions

Conclusions to this thesis can be summarized under two topics: geodetic and tectonic. Our geodetic results and discussion pertain to data analysis and to obtaining a reliable and accurate velocity field. Since our first experiment in 1988, space and user segments of GPS have developed immensely. We also observed a parallel advancement in techniques and analysis softwares. In this thesis, we recognized the ever increasing number of GPS observations, and attempted to reduce the amount of analyses time and to enhance the precision of velocity estimates so that small relative motions could be resolved. For this purpose, we devised and tested a "combination" approach to data analysis, and applied it to the 1991 and 1992 spring/fall experiments. Our combination scheme simplifies the regional data analyses by performing *two separate, parallel* (GAMIT) analyses of the GPS phase delay data. We show that data from large regional networks can be analyzed independent of the global tracking network. Both analyses can be later combined by the GLOBK Kalman filter, using their quasi-observations.

We show that the level of systematic error in baseline component estimates can

be several decimeters when a deficient fiducial network is used. As a corrollary to this, if two experiments are analyzed with different fiducial configurations, the rate estimate may be artificially offset by several centimeters, leading to erraneous tectonic interpretations. Thus, we devote a rather lengthy chapter to long-term error analyses. We show that for short baselines these systematic errors may be undetectable, but that for a regional network the size of ours, they reverse the entire tectonic interpretation. If we had been satisfied with the unconstrained solution, we would have deduced a different scenario for the kinematics of the eastern Mediterranean. We are bound to GPS observations collected earlier until we achieve a good amount of redundancy. In our analyses we stress the fact that all constraints on the fiducial sites are imposed consistently. The different fiducial configurations of 1988 and 1992 cannot be handled otherwise. There are no means to add new satellites or fiducials sites to the 1988 observations.

Because the experiments were carried out in western and eastern Turkey in alternate years, sites with three or more epoch observations comprised only a fraction (15%) of our GPS sites in Turkey. Statistically reliable and relatively smaller uncertainties were obtained for these sites. For only twice observed sites the minor and major axis of the 95% confidence ellipses are greater than 10 mm/yr, and are as much as 40 mm/yr. Systematic errors involved in the vertical, as well as in the horizontal components, and in orbital determination and modeling, without doubt, have been folded into our estimates of the relative site motions. The fact remains that although we delineate motions across major structures, there are several structures across which we have yet to obtain reliable estimates.

We have successfully resolved motions at most of our sites and have defined Anatolia as a coherent plate. However, 10 mm/yr uncertainty at the 95% confidence level places an upper bound for internal deformations. For the site motions in eastern Turkey, the frequency and number of observations were, of course, a factor. As a

result, uncertainties at the eastern Turkey sites are at the order of 20–30 mm/yr. This level of uncertainty does not allow us to reliably observe the differences in the velocities between the Van block and the Anatolian plate, if any.

In the early fall of 1988, as our GPS antennas were mounted on their leveled tripods, the prevailing popular model for the kinematics of the eastern Mediterranean had already been laid out [McKenzie 1970, 1972, 1978; Jackson and McKenzie, 1984]. Several microplates had been recognized, based primarily upon focal mechanisms of earthquakes: the Turkish, Aegean, Black Sea, Iran, and south Caspian plates. Accordingly, deformation in the eastern Mediterranean is a result of small plates moving away[1] from eastern Turkey and western Iran, as convergence between the Eurasian and Africa-Arabian plates occurred. Such escape tectonics occur along the strike-slip North and East Anatolian faults to relieve excessive crustal thickening in eastern Turkey and the Caucasus. An intercontinental basin, Karlıova, where these two major transcurrent systems meet, has been recognized as the location of the triple junction for the Turkish-Arabia-Eurasia plates. A westerly motion of the Turkish plate required an Aegean plate to satisfy the vast seismic activity and boundary conditions for the subduction at the Hellenic arc.

The new information provided by space-based geodetic measurements (GPS and SLR), however, does not support the existance of two distinct plates: Turkish and Aegean. Instead, we recognize the Anatolian plate as a single plate which behaves, to the first order, as a coherent unit.

Our GPS derived velocity field, obtained from observations conducted between 1988 and 1992, indicates four major domains, each having distinct kinematics: the Pontus block, the Anatolian and Arabian plates, and the Caucasus domain. The most prominent feature in the velocity field is the Anatolian plate, which is separated

[1] Jackson and McKenzie [1984], however, mention "away from the Lake Van region".

from neighboring domains by major strike-slip and subduction zones. The northern boundary of the Anatolian plate is clearly defined by the North Anatolian fault. The northern splay of the NAF in the Marmara Sea and the North Aegean trough are likely to represent the boundaries farther to the west. In the east, the Anatolian plate is separated from the Arabian plate by the East Anatolian fault (EAF). Our GPS results indicate that the easternmost extent of Anatolia is not at the Karlıova basin, where the NAF and EAF meet. Instead, Anatolia continues farther eastward to include the Van block. The relative site motions in this domain are not different from those on the Anatolian plate. In this scenario, a set of strike slip faults (the Tutak, Çaldıran and Karayazı faults) north of Lake Van are likely to determine the easternmost boundary of the Anatolian plate. Since we have no observations in western Iran, it is not clear whether we can extend the Van block farther east by associating the Çaldıran fault with the Tabriz fault or the Salmas rupture. The Hellenic arc marks the southern boundary of the Anatolian plate, separating it from the African plate. We consider the Teke peninsula, as well, a part of the Anatolian plate. Within our uncertainties, Teke domain does not behave differently from Anatolia. It is yet to be understood whether or not Teke is decoupled from Anatolia as a crustal wedge along the Teke-Burdur fault zone and the Aksu thrust. Our GPS observations indicate a smaller relative motion across the EAF than that across the NAF. The motions at sites on the Pontus block, defined as the region roughly north of the NAF and south of the Black Sea, relative to Eurasia, are quite small (8±7 mm/yr). The general character of observed velocities at the sites on the Anatolian plate, relative to Pontus, shows that they are parallel to the arcuate trace of the North Anatolian fault zone, especially to its eastern and central segments. Right lateral strike slip motion across this fault is clearly evident. Similarly, velocities relative to Arabia indicate the left-lateral slip along the East Anatolian fault.

In eastern Turkey, it appears that Arabian plate motion is transferred to the Anatolian plate; however, the velocities relative to Eurasia confirm the partitioning of the

oblique convergence in eastern Turkey and the Caucasus: the strike-slip component is about $26\pm14_{95\%}$ mm/yr for the Van domain, while the shortening in the Caucasus is about about $13\pm 9_{95\%}$ mm/yr. Our GPS observations do not show whether Karlıova is indeed a triple junction since the signal is absorbed by the uncertainties.

As a first approximation to a rigid plate, we parameterize the velocity field for the Anatolian plate by Euler vectors. The Pontus-Anatolia can be defined by an Euler vector ($_{PON}\mathbf{E}_{ANA}$), located at 33.4±0.5°E, 31.1±1.3°N (north of the Sinai peninsula), with a counterclockwise angular velocity of 1.25±0.15°/Myr. This Euler vector remarkably delineates the NAF as the boundary and suggests a $25\pm8_{95\%}$ mm/yr slip. We also tie GPS observations on the Anatolian plate to the NUVEL-1 model by $_{ARA}\mathbf{E}_{ANA}$ [ϕ=43.2±0.7°E, λ=31.2±1.2°N, ω=1.22±0.15°/Myr]. Predicted slip along the East Anatolian fault is $18\pm12_{95\%}$ mm/yr. Given these Euler vectors and that for $_{ARA}\mathbf{E}_{AFR}$ from NUVEL-1, the inferred Anatolia-Africa motion is $50\pm10_{95\%}$ mm/yr at the Hellenic arc, and decreases easterly to $20\pm10_{95\%}$ mm/yr, converging the Anatolia-Arabia motion in the Gulf of İskenderun. Our GPS derived velocity field indicates site motions in western Turkey higher by 10 mm/yr than those predicted by these Euler vectors. This suggests a considerable amount of internal deformation. We interpret the residuals in western Turkey, as well as those in the southern Aegean, as a result of trench suction at the Hellenic arc and extrusion of the overriding plate due to the roll-back of the subducting slab. This is characteristic of retreating boundaries, for which the Hellenic arc provides a good example, where the subduction rate exceeds the convergence rate, and hence horizontal extension occurs in the overriding plate [Royden, 1993a]. We foresee that it is this suction that would be responsible for an additional 10–20 mm/yr motion, and that would provide the necessary force for the development of simple shear structures [Wernicke, 1981, 1985] in western Turkey, asymmetric rifting in the Gulf of Corinth, and fragmentation of Crete into several basins [Meulenkamp et al., 1988], etc.

We compare our GPS derived velocity with geological observations by back-rotating the plate boundaries to the Pliocene. We show that the North and East Anatolian faults have sustained the boundaries for the Anatolian plate since the Pliocene. We find that contemporary motions can account for the total cumulative offset (25 km) along the EAF since the Pliocene. Along the NAF, the calculated 75 km displacement appears to exceed the lower bound (35 km) for geologically observed cumulative slip since the Pliocene and suggests that the present-day velocities may not be completely projected back into the geological time scale for periods longer that a couple of million years, due to changes in boundary conditions.

We further compute the velocity gradient tensor from GPS and SLR observations, and compare them with the strain rates observed from seismic moment tensors. Overall, we find a good agreement in patterns of principal strain rates across the North Anatolian fault and the northern Aegean. For the rest of the region, however, the level of uncertainties do not allow us to resolve strain and rotation tensor.

Suggested Future Work

Since our final number crunching in mid-1993, there have been new developments concerning the antenna phase center problem, and that of atmospheric delay. Problems encountered with the vertical require further attention. We understand that accuracy of earlier experiments (1988, 1989, and 1990) can be enhanced by incorporating unused fiducial sites. We believe that forcing the Karacadağ velocity to its NUVEL-1 determined value is only an interim solution for reducing long-term systematic errors. Instead, the $3\frac{1}{2}$ years of GPS observations at the Ankara site should be incorporated into the solutions. We suggest that bi-weekly analyses of the Ankara data would provide enough redundancy for long-term error analysis. Although analysis of Ankara data with all global tracking sites is a tedious and cumbersome task, it will provide a regional fiducial for observations in the eastern Mediterranean.

Given the success in combining VLBI, GPS and EDM measurements via their respective quasi-observations, we are enthusiastic about combining GPS and SLR measurements. This would provide a unified geodetic velocity field. It is also imperative to combine all GPS observations in Turkey with those in the Caucasus, Greece and the Adriatic region.

Ambiguity resolution is yet another issue. East-west uncertainties can be brought to the level of the north-south uncertainties by an aggressive ambiguity resolution. However, large interstation distances prevented us from successfully resolving the ambiguities. Also, based on difficulties of tying together the eastern and western Turkey networks, we conclude that more sites in Turkey have to be simultaneously occupied during a given experiment and that the baseline apertures for daily sessions have to be reduced.

We emphasized the large magnitude of the uncertainties in the velocity field and associated it with and insufficient number of observations. Therefore, new observa-

tions are imperative for better geodetic quality.

We computed the Euler vectors have been obtained exclusively from GPS and/or SLR velocities. We suggest that including earthquake slip vectors as observables in the inversion process may enable us to estimate an Euler vector for the Caucasus region.

In this study we quantified the residual velocity field in the Aegean using two-epoch SLR velocities. Further comparisons, however, have to be carried out with the SLR results which incorporate the 3rd epoch observations of 1992.

Appendix A

Combination of Regional and Global GPS Measurements

An evenly distributed, dense global tracking network is fundamental to accurately determining the orbits of GPS satellites. Orbital accuracy, in turn, determines the accuracy and precision of geodetic parameter estimates for the regional network. The rule of thumb is that the precision of regional baseline estimates is roughly proportional to the precision of the satellites' orbits [Murray, 1991; Lichten and Bertiger, 1989]. In other words, the errors involved in the orbits map directly into the estimates of geodetic parameters.

In our GPS data analyses, we determined the orbital parameters by using all global tracking data concurrently available to enhance the precision of our estimates for site positions and velocities. Initially, there were few global tracking sites available. As discussed in Chapter 2, simultaneous analyses of this global tracking data with the regional data was the straightforward and natural choice. For example, during the 1988 Turkish experiment we tracked only 6 satellites and simultaneous analyses of 6

regional sites and 7 global trackers was manageable.

In the past few years, however, the number of satellites and continuously operating global tracking sites has increased tremendously. Today, for instance, there are almost three dozen global tracking sites in operation, tracking 25 GPS satellites. This enlarged network paved the way to the better modeling of orbits, and a corresponding improvement in the precision of geodetic parameter estimates. At the same time, the large volume of observations has introduced problems with data handling and editing, mass storage and computation time[1]. By fall of 1992 we had to deal with 26 global tracking sites, 29 regional sites and 18 satellites. Because a homogeneously distributed, dense global tracking network is crucial to the accurate modeling of satellite orbits, we devised and tested alternative methods for combining regional data with global tracking data. Our goal was to make data analysis more manageable while incorporating the strength that a global tracking network provides into regional network solutions.

Historically (during the last couple of years!) the combination of VLBI and GPS [Herring et al., 1991; Feigl et al., 1993], and of GPS and EDM [Dong, 1993], using the quasi-observation, approach has been successful in determining the earth's rotational parameters, site positions and relative site velocities. Encouraged by the success of these combinations we implemented a scheme that combines global and regional GPS data via their quasi-observations. We took advantage of the two-step data analyses offered by our processing software. As discussed in Chapter 2 and Appendix B, in the first step we analyze the GPS phase observables by GAMIT and obtain quasi-observations. In the second step, we use these quasi-observations to obtain the adjusted global parameters.

[1]Excluding the intermediate steps (forward model calculations and data editing), solutions for a configuration of 30 stations, having 8-12 hours of observations sampled at 30 seconds, (e.g., fall 1992 Turkey regional data) take 110 minutes on a SUN SparcStation, with 32 MB RAM and 120 MB swap space allocated.

In our combination scheme, we perform *two separate, parallel* (GAMIT) analyses of the GPS phase delay data. One analysis includes primarily regional data and the second, global tracking data. We then combine the regional and global data sets by GLOBK Kalman filter, using their quasi-observations. The common satellites and sites offer an effective tie between these data sets. Satellites alone provide a certain degree of tie which is rather weak. To establish a stronger tie, we include observations from one site or several sites in both the regional and global GAMIT analyses.

If only one site is common to both analyses, there are no duplicate baselines; the combination is mathematically equivalent to a simultaneous analyses. The drawback of this combination is that the regional network may be too small to provide adequate control of orbits in the GAMIT analyses. There are two possible remedies for this problem. One is to perform the global analysis first to obtain a converged orbit, and then to heavily constrain this orbit in the GAMIT analyses of the regional data. This would be a zeroth-order combination and does not incorporate the global tracking sites into the regional data analyses. A second approach is to include in the regional analysis data from a sufficient number (usually four, but it depends on several factors discussed below) of global tracking sites to determine the orbits. With this approach, some doubly differenced observations (rather, their quasi-observations) are included (approximately) twice. Nevertheless, we would argue that the additional weight given the global tracking sites in the proximity of the regional network is reasonable since we want the orbital motion to be determined best in this region. When we include more than one global site in the (GAMIT) regional data(analysis), we coin the term "augmented regional data (analysis)".

A "one-site-common" analysis (first-order combination) is rigorous and there is no duplication. If the regional network is far away from global tracking sites (Turkey, Caucasus, Central Asia, etc.), then we concluded that a regional site, observed in all sessions and preferably located in the middle of the regional network, would be

an adequate choice. Otherwise, the ideal choice would be a global tracking network site which is located within the regional network and whose position and velocity are accurately known. The analyses for "one-site-common" combinations involve:

⇒ Analysis 1. All regional sites,

⇒ Analysis 2. All global sites and one regional site;

alternatively,

⇒ Analysis 1. All regional sites and one global site,

⇒ Analysis 2. All global sites.

The quasi-observations obtained from these GAMIT analyses are used in GLOBK to effectively tie the two data sets. The GAMIT solution of the regional data, however, will not be very strong since no precise orbit determination is possible. Therefore, we have to evaluate the final, adjusted solution obtained after the GLOBK combination.

The "several-sites-common" analyses (nth-order combination), on the other hand, provides a relatively stronger GAMIT solution for the regional data set. In this type of combination solution we select a subset of global tracking sites, preferably observed during all sessions, common to both data sets. The analyses for the "several-sites-common" combination involve:

⇒ Analysis 1. Augmented regional data,

⇒ Analysis 2. All global sites.

This augmented regional data is simply the regional data augmented with a subset of global tracking data. It is, indeed, a simultaneous analyses of regional data with only a very small number of global trackers. Because a nominal set of global trackers is incorporated into the analyses of the regional data, the GAMIT solutions of augmented regional data is stand-alone and stronger. Using the augmented regional data solutions, data quality examinations and cleaning/editing, short-term precision analyses may be carried out, and outliers, if any, may be identified. Augmented data analysis also provides an adequate basis for ambiguity resolution. In step two, the two sets of quasi-observations are strongly tied with the common global sites us-

ing GLOBK Kalman filter. The "several-sites-common" solution also addresses the problem of handling voluminous data. Since 1991, the SIO Global Data Processing Center has offered quasi-observations, as well as cleaned/edited data, which can be directly harnessed to the solutions. That is, we can skip the global data analyses and significantly reduce our processing efforts.

Application to the spring 1992 Turkey experiment

We tested our approach to combination by analyzing the spring 1992 GPS measurements (also, see Appendix B). Table A.1 summarizes the type of data included in the single-session, long-arc GAMIT analyses. The combinations of quasi-observations with GLOBK, obtained from these analyses, are shown in Table A.2. In all cases, our GAMIT and GLOBK analyses were identical: satellite ICs, site and satellite constraints, etc. As a reference solution, we simultaneously analyzed all global and regional data using a global tracking network solution of 20 sites (ARON, CAN1, FAIR, GOLD, JPLM, KOKB, KOSG, MADR, MATE, MCMU, NALL, ONS0, PENT, PIN1, SANR, TROM, USUD, WETR, YAR1, and YKN1). Next, we combined the global and regional data by tying them with sites in common. We chose the Ankara (ANKM) site for the one-site-common solution (first-order combination), since it has been observed throughout each experiment and has a history of prior occupations. It is also located in the center of our regional networks. In the several-site-common combination (sixth-order combination), we augmented our regional data set with a subset of global tracking sites located in Europe and North America (KOSG, ONS0, TROM, WETR, and YKN1) that had good interstation visibility with our regional network. Also, most of these sites were available throughout our experiments and were a part of our earlier core global tracking network utilized in 1988, 1989, and 1990. The Ankara site was also included in the global data set. For other experiments such choices may vary. In the California experiments, there are sites available

Table A.1: GAMIT solutions and data sets used to obtain quasi-observations.

Solution descriptor	GPS phase data	Characteristics duration & sampling
data for simultaneous analysis		
all	all global tracking sites [glb]	[24 hour @ 2 min]
	regional Turkish sites [reg]	[24 hour @ 2 min]†
global data		
glb	all global tracking sites	[24 hour @ 2 min]
	one regional site (ANKM)	[24 hour @ 2 min]†
augmented regional data		
aug	core global tracking sites	[12 hour @ 30 sec]
	regional Turkish sites [reg*]	[12 hour @ 30 sec]
regional data		
reg	regional Turkish sites	[24 hour @ 2 min]†
*reg**	regional Turkish sites	[12 hour @ 30 sec]

† Data for regional sites were not collected over a full 24 hour. To prevent data epoch misalignment, however, it has been treated as if observations were 24 hours long by manipulating the start and stop times of the GAMIT observation files (**x-files**, similar to RINEX files).

Data epoch alignment: The quasi-observations obtained from long-arc, single-session GAMIT solutions have a data epoch to which the earth orientation parameters (EOP) are referred. This epoch lies in the middle of the observation session and depends on its start and stop time. Global tracking data are stored in the SIO archive in a 24 hour format (typically, from 0:00 to 23:58). This format defines a data epoch at 11:59. The regional experiment observation scenarios rarely comply with this format. If we were to have session scenarios as described in Appendix B ($\sim$ 12 hours), then this epoch would have been offset by 2 to 3 hours, relative to that of the global data. The importance of the data epoch, and the reason combination solutions with these two data sets would produce different results, can be understood by considering the nature of Kalman filtering. Kalman filtering is a sequential estimate of parameters in which the process noise depends on the time separation of observations. The time separation is determined by the data epoch offsets. Accordingly, the stochastic process is not activated when two sets of quasi-observations of the same data epoch (no time separation) are sequentially supplied to the Kalman filter; this was the situation encountered with the *glb+reg* combination. However, when the two data sets have misaligned data epochs the random walk is triggered and the process noise, in proportion to the offset, is applied to the satellites (and to the sites, if repeatabilities are investigated). This is the situation when global (*glb*) and regional (*reg**) are combined. When the amount of process noise applied is small ('tight' stochastic constraints), the epoch mismatch has little effect in combining the global (*glb*) and regional (*reg**) solutions. When looser stochastic constraints are used, however, the global and regional solutions can become decoupled. For example, a 10 m/day variation on the cartesian position of the satellites translates into a 1 m variation for an offset of 2 to 3 hours in the data epoch. Thus, this type of combination should be avoided. Such a situation also occurs for *glb* and *aug* combinations; however, the effects are minimal since the GAMIT analysis of augmented data is strong and stand-alone. Accordingly, we define the "stability" of a solution with respect to the satellites' process noise. A combination solution would be stable: 1) if the proportional term obtained from day-to-day scatter does not worsen by several ppm as looser stochastic constraints are applied to the satellites, 2) if baseline/coordinate estimates do not significantly diverge from those values obtained by allowing tight stochastic variations as looser stochastic constraints are applied. The *glb* and *aug/reg* combinations are stable with respect to the process noise applied to the satellites.

Table A.2: A summary of solutions combined with GLOBK and considered in testing.

Solution	Quasi-observation set 1	Quasi-observation set 2
simultaneous analysis	all data	—
one-site-common combination	*glb*	*reg*
several-sites-common combination	*glb*	*aug*
augmented regional analysis	*aug*	—

that are already in the global tracking network. If the regional experiment takes place in Sumatra, it would be more appropriate to choose global tracking sites located in Australia and southern Asia. Additionally, we considered the analyses of augmented regional data as an example of a case in which the regional analyses has been carried out with a deficient global tracking network; such as occurred for our 1988, 1989 and 1990 data sets.

To investigate the short-term repeatability of our position estimates, as a function of analysis approach, we performed GLOBK back solutions using the quasi-observations obtained from single-session, long-arc GAMIT solutions (Table A.2). In these solutions we treated the coordinates of global tracking sites as deterministic parameters, but allowed stochastic perturbations in the coordinates of regional sites, except Ankara[2], in order to examine the wrms scatter of baseline components about their weighted means (see Chapter 2 and Appendix B). In order to understand the orbital dynamics, we considered **T**, **T_L**, and **L** sets of process noise, as described in Table B.4. We summarize the error model parameters for each solution in Table A.3 and tabulate the wrms in Table A.4, at 100 km and 600 km, about which the regional

[2]The coordinate of the Ankara site was deterministically estimated.

Table A.3: Short-term repeatability: spring 1992 experiment.

Solution Descriptor	N-S component a (mm)	b (ppb)	mean wrms	nrms	E-W component a (mm)	b (ppb)	mean wrms	nrms	U-D component a (mm)	b (ppb)	mean wrms	nrms
simultaneous analyses of global and regional data												
S_L†	5.19	0.58	5.19	0.78	9.73	10.37	10.79	0.85	13.91	42.79	22.91	0.65
S_T	5.41	0.58	5.42	0.84	11.35	14.87	13.14	1.07	14.53	39.49	22.32	0.64
S_T_L	5.14	0.58	5.15	0.79	11.04	17.46	13.47	1.10	13.95	44.57	23.49	0.67
one-site-common combination of regional and global data												
S_L†	4.83	0.58	4.84	0.66	8.65	19.09	11.98	0.75	14.81	51.13	26.16	0.56
S_T	4.89	0.58	4.89	0.67	8.79	21.14	12.68	0.80	15.48	49.43	26.07	0.56
S_T_L	4.91	0.58	4.91	0.67	8.89	21.59	12.88	0.81	15.50	49.03	25.96	0.56
several-sites-common combination of augmented regional and global data												
S_L	5.20	5.04	5.67	1.35	8.20	19.13	11.65	1.47	16.16	29.36	20.69	0.93
S_T†	5.55	4.31	5.88	1.60	7.22	17.13	10.32	1.48	15.89	23.46	19.00	1.00
S_T_L	5.62	4.66	6.00	1.58	7.59	16.14	10.33	1.48	15.61	28.47	19.99	1.02
analyses of augmented regional data												
S_L	5.21	6.16	5.89	1.17	8.47	20.08	12.12	1.20	15.69	35.10	21.89	0.92
S_T†	5.44	7.08	6.29	1.38	8.18	15.84	10.72	1.31	16.17	22.54	19.03	0.90
S_T_L	5.71	4.42	6.05	1.33	8.06	15.68	10.58	1.28	16.69	24.98	20.03	0.94

† Preferred solution.

baselines cluster.

The preferred solutions produced wrms values of about 5 mm in the north, 10 mm in the east, and 20 mm in the vertical components of the regional baselines. Each data set responded differently to various levels of process noise on the satellites. Simultaneous analyses and one-site-common combination yielded the smallest wrms with solutions in which we treated the satellites as loosely stochastic (**L**). For the combination analyses of the global and augmented regional data (several-sites-common combination), we found that tight stochastics (**T**) on the satellites would produce the best repeatabilities. Analysis of the augmented regional data also required tight stochastics on the satellites. Allowing additional process noise (**T_L**) on only the eclipsing satellites did not improve repeatabilities. Actual wrms scatters of baseline

Table A.4: The wrms calculated at 100 and 600 km using $\sigma^2 = a^2 + b^2L^2$. (*cf.* Table A.3.)

Solution Descriptor	wrms(mm) @ 100 km North	East	Vertical	Length	wrms(mm) @ 600 km North	East	Vertical	Length
simultaneous analyses								
S_L†	5.19	9.79	14.55	8.71	5.20	11.55	29.20	11.59
S_T	5.41	11.45	15.06	10.25	5.42	14.44	27.79	14.74
S_T_L	5.14	11.18	14.64	9.95	5.15	15.22	30.16	15.29
one-site-common combination of regional and global								
S_L †	4.83	8.86	15.67	7.80	4.84	14.35	34.07	14.46
S_T	4.89	9.04	16.25	7.98	4.90	15.43	33.45	15.75
S_T_L	4.91	9.15	16.26	8.10	4.92	15.71	33.25	15.97
several-sites-common combination of augmented regional and global								
S_L	5.22	8.42	16.42	7.66	6.02	14.11	23.91	13.90
S_T†	5.57	7.42	16.06	6.56	6.12	12.56	21.23	12.61
S_T_L	5.64	7.76	15.87	6.73	6.28	12.30	23.14	12.03
augmented regional								
S_L	5.25	8.70	16.08	7.90	6.39	14.73	26.26	14.42
S_T†	5.49	8.33	16.33	7.55	6.90	12.54	21.08	12.40
S_T_L	5.73	8.21	16.88	7.24	6.30	12.39	22.43	12.28

† Preferred solution.

estimates for the preferred solutions, using each approach, are shown in Figures A-1, A-2, A-3, and A-4. Little difference is evident between any of the solutions except, perhaps, for a degradation in vertical repeatability in the one-site-common combination. As shown in Table A.3, the wrms computed from error models for all solutions indicates that the wrms is different by 1–2 mm in the horizontal for all types of analyses and orbital stochastics. We observe small improvements in the short-term precision as global sites are included in the solutions, with respect to those repeatabilities of the 1991 and fall 1992 experiments (see Appendix B). The vertical components for the several-site-common combination and augmented regional analyses display a smaller wrms scatter due possibly to the lesser impact of mixing antennas in the GAMIT analysis.

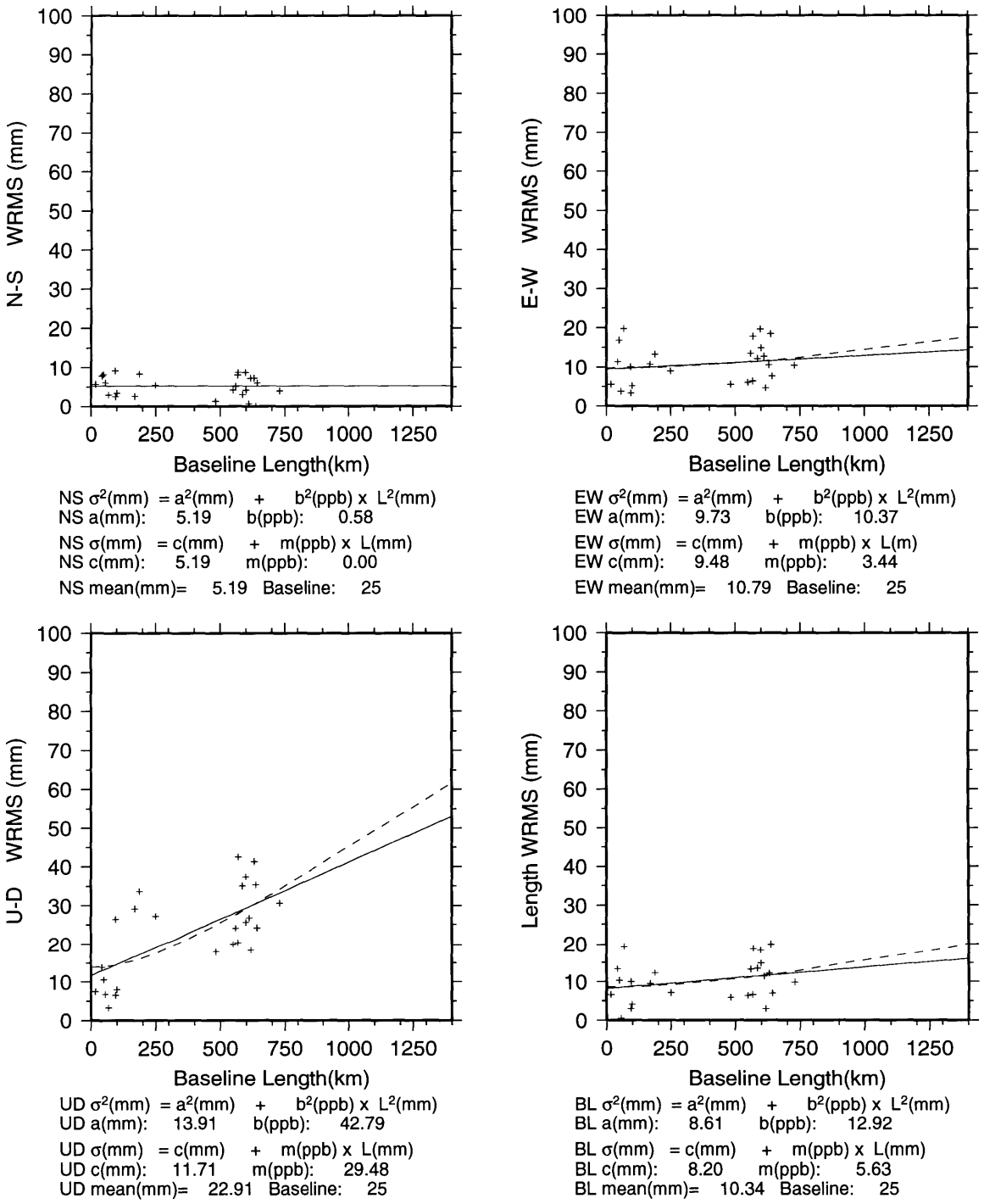

Figure A-1: The wrms scatter and model parameters of the NS, EW, UD components and length, as a function of baseline length. They are obtained from a simultaneous analyses of the global and regional data (spring 1992 experiment), with loose ($\mathbf{L}$) stochastic constraints applied to the satellites. Dashed line is a functional in the form of $\sigma^2 = \mathrm{a}^2 + \mathrm{b}^2\mathrm{L}^2$. Continuous line is a linear fit to the wrms scatter ($\sigma = \mathrm{c} + \mathrm{m}\ L$).

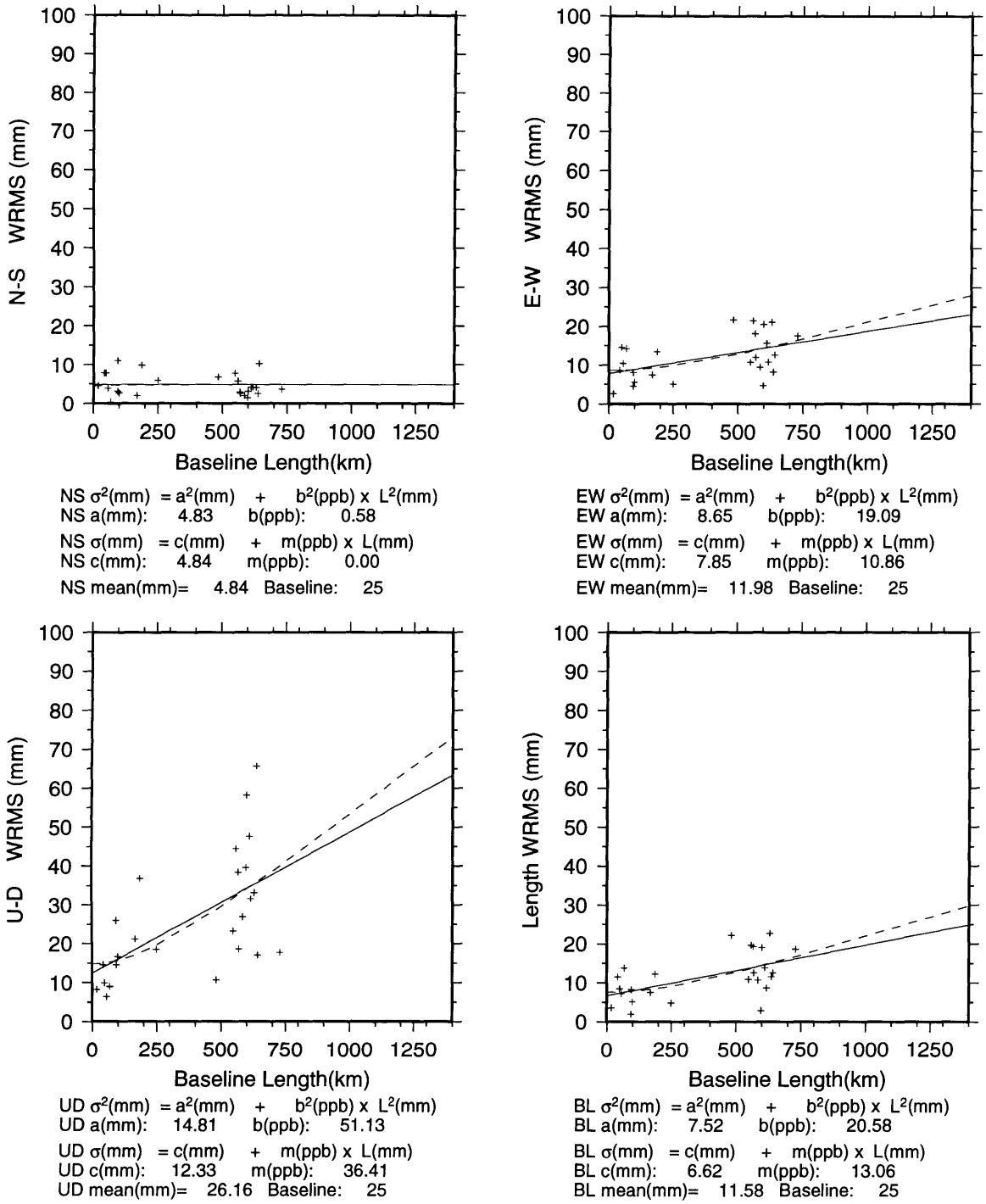

Figure A-2: The wrms scatter and model parameters of the NS, EW, UD components and length, as a function of baseline length. They are obtained from one-site-common combination of regional and global data (spring 1992 experiment), with loose ($\mathbf{L}$) stochastic constraints applied to the satellites. Dashed line is a functional in the form of $\sigma^2 = \mathrm{a}^2 + \mathrm{b}^2\mathrm{L}^2$. Continuous line is a linear fit to the wrms scatter ($\sigma = \mathrm{c} + \mathrm{m}\ L$).

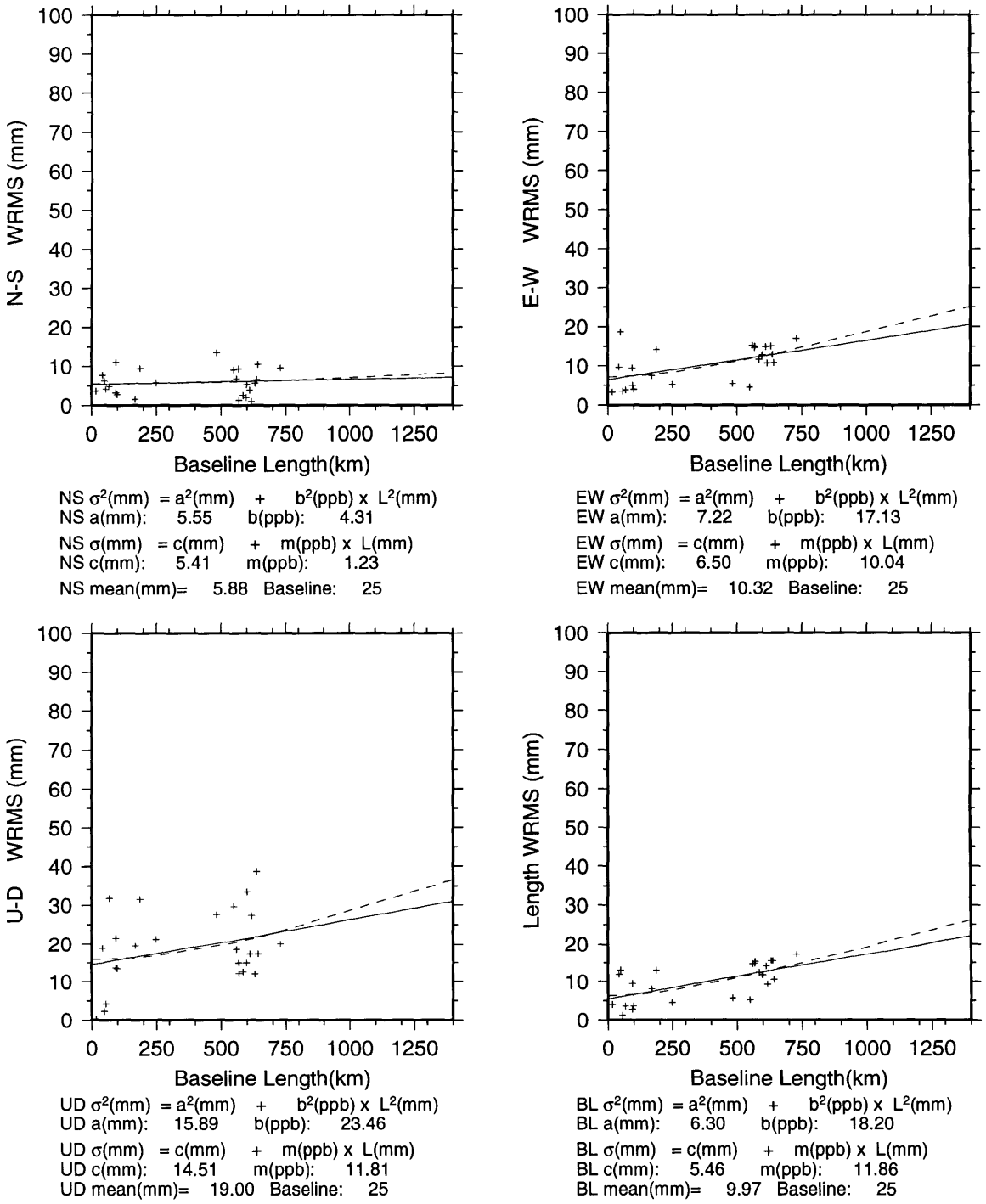

Figure A-3: The wrms scatter and model parameters of the NS, EW, UD components and length, as a function of baseline length. They are obtained from the several-sites-common combination of regional and global data (spring 1992 experiment), with tight (**T**) stochastic constraints applied to the satellites. Dashed line is a functional in the form of $\sigma^2 = a^2 + b^2L^2$. Continuous line is a linear fit to the wrms scatter ($\sigma = c + m\ L$).

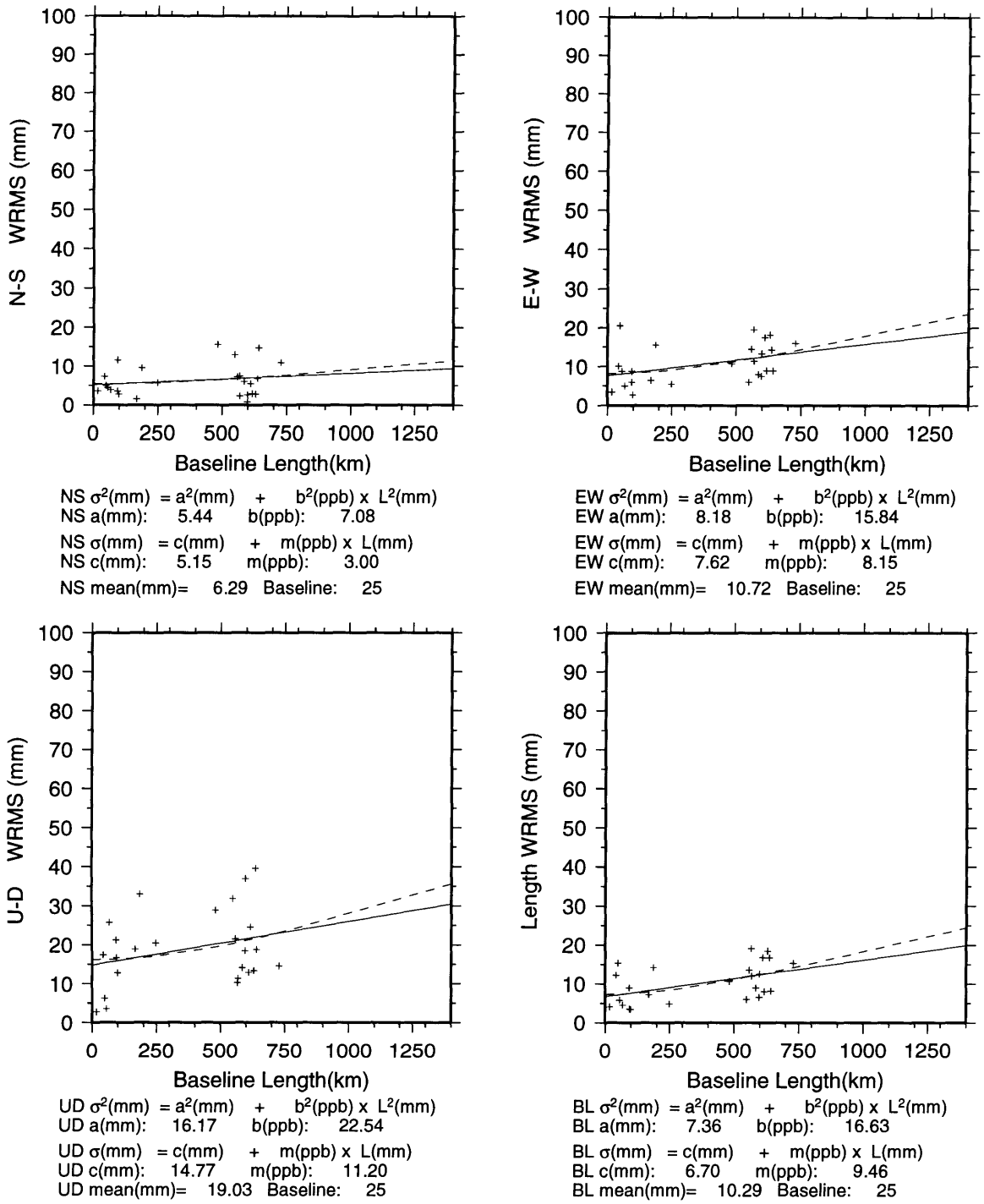

Figure A-4: The wrms scatter of the NS, EW, UD components and length, as a function of baseline length. They are obtained from the analysis of the augmented regional data (spring 1992 experiment), with tight (**T**) stochastic constraints applied to all satellites. Additional process noise, (L), is applied on the non-eclipsing satellites. Dashed line is a functional in the form of $\sigma^2 = a^2 + b^2L^2$. Continuous line is a linear fit to the wrms scatter ($\sigma = c + m\ L$).

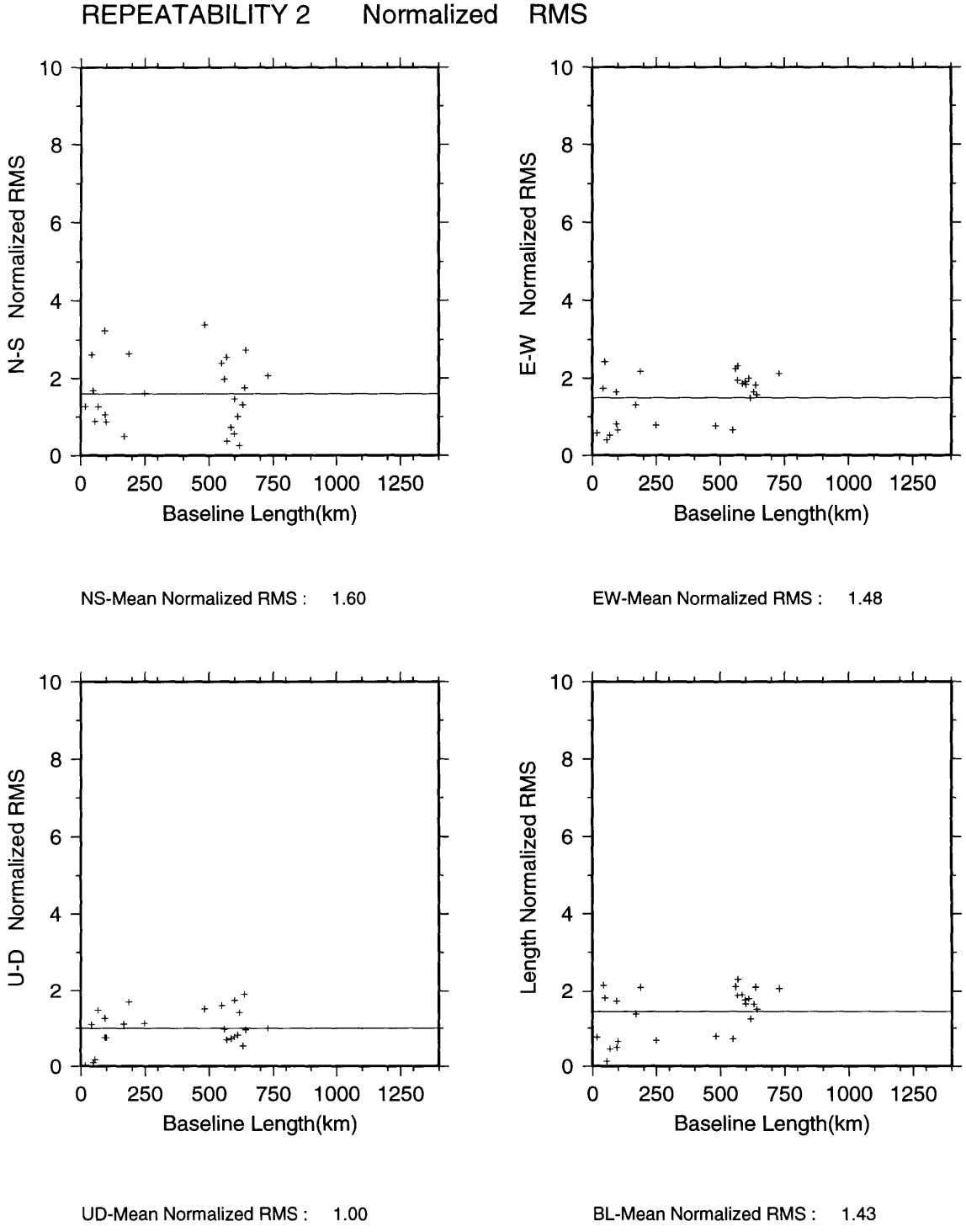

Figure A-5: The nrms scatter of NS, EW, UD components and length [for the solution described in Figure A-3], as a function of baseline length. They are obtained from the several-sites-common combination of regional and global data (spring 1992 experiment), with tight (**T**) stochastic constraints applied to the satellites. Continuous line represents the mean nrms scatter.

The nrms scatter of each component is smaller for simultaneous and one-site-common combination analyses by almost a factor of two. This is as expected since the regional data in these solutions were sampled every two minutes, whereas 30 second samples of data were used for the analyses of the augmented regional data. (Sampling the GPS observations at every nth point increases the uncertainties by $\sqrt{n}$. This is reflected in the nrms scatters as $1/\sqrt{n}$.) Figure A-5 shows the nrms for baseline components as a function of baseline length obtained from the combination of global and augmented regional data. The mean nrms is ≤ 2.

The short-term scatter of baselines from various solutions provides some indication of quality but is a flawed indicator for two reasons:

1. There may be systematic errors that are common to all days from a particular solution and that show up only in the year-to-year scatter;

2. We estimate velocities with regional sites being deterministic, not stochastic, a difference that may be relatively more important for some data combinations/analyses.

Therefore, we examined the consistency of the solutions from several types of analysis. To do so we performed GLOBK forward solutions and estimated all site coordinates deterministically (see Chapter 2 and Appendix B). In these solutions the coordinates of most global tracking sites were constrained to their VG defined values within 1-2 cm in the horizontal and 20 cm in the vertical. In these comparisons we examined the impacts of data sampling intervals, the contributions of the redundancy of observations, and the effects of process noise[3] on the orbital parameters.

In comparing baseline estimates we considered 4 representative baselines: ER05-ER10 (17 km), ER03-ER09 (55 km), KEMA-MERC (94 km), and ANKM-MERC (641 km). For baselines less than 60 km, we observed no differences between the estimates

[3]We applied **T**, **T_L**, **M**, and **L** sets of process noise to the satellites.

of baseline components obtained from each type of analysis (Figure A-6). Nor was the process noise on the satellites or data alignment contributing factors. The formal uncertainties of baselines obtained from simultaneous and one-site-common combination analyses are about a factor of two larger since the regional data incorporated in them were 120-second samples. For the 94 km (KEMA-MERC) baseline (Figure A-7), we observed no significant differences between the estimates obtained from either type of combination analysis or those obtained from the simultaneous analysis. For the augmented regional data, there are differences of up to 2-σ (formal) with respect to the combination and simultaneous analyses. After applying appropriate scaling (dense sampling and long-term scatter) to the solutions, the differences for baselines of this length are not significant (also, see next section).

For the longest baseline (641 km), there are significant differences among the estimates obtained from the four types of analysis (Figure A-8). Most noticeable is the systematic offset in the estimates obtained from the analyses of augmented regional data, especially in the north, compared to those of the simultaneous and combination analyses. This demonstrates the significance of incorporating an evenly distributed tracking network into the regional data analysis. It also suggests that the analyses of earlier experiments with a deficient and incomplete global tracking network may have included such systematic offsets. The effects of process noise on the satellites were also most pronounced for the longest baselines. For the simultaneous and one-site common combination analyses, the orbital stochastics did not play a significant role. That is, applying tight (**T**) or loose (**L**) stochastic constraints on the orbital parameters yields the same estimates. The combination of augmented regional and global data, however, demonstrated a sensitivity to the level of stochastic constraints. This, we believe, is an artifact of data epoch misalignment (see footnote in Table A.2). In any case, for this type of combination (several-sites-common), the preferred process noise set is tight (**T**). The comparison of several-site-common combination and simultaneous analyses reveals that the estimates of the horizontal

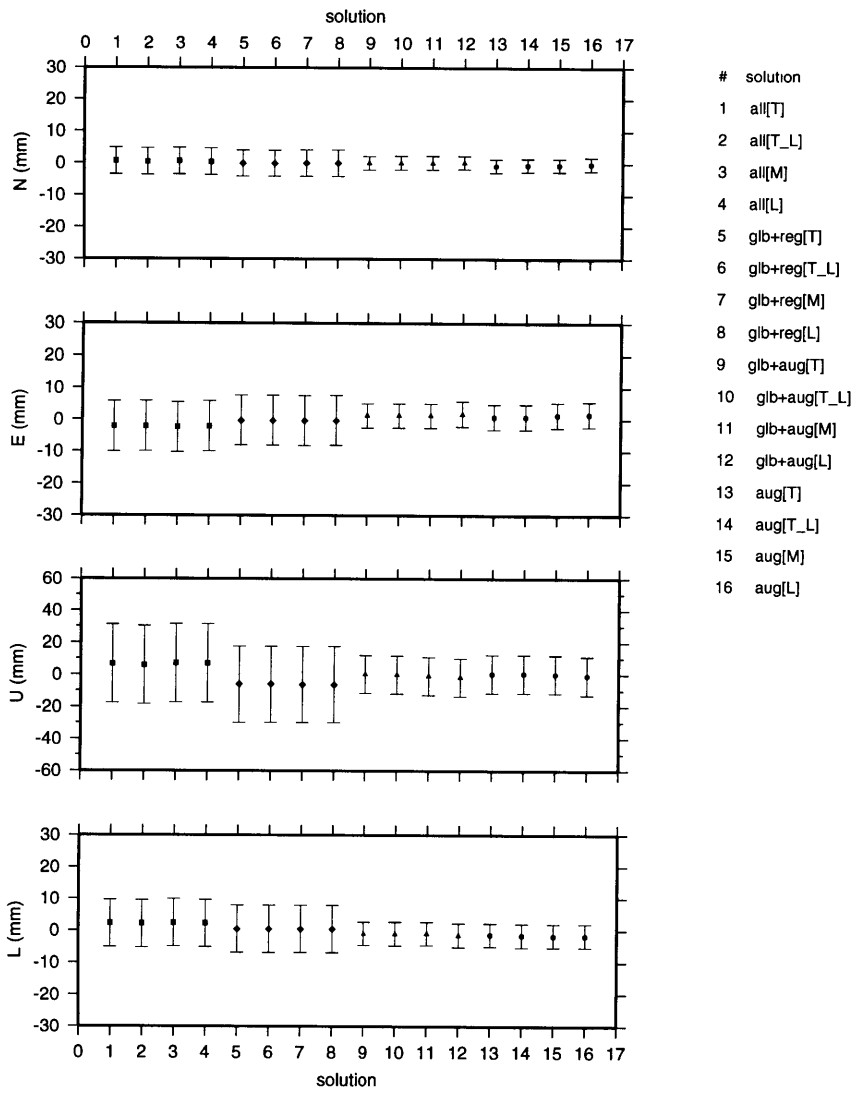

Figure A-6: Baseline ER05-ER10 (17 km). Comparison of all baseline estimates. We removed a common mean from all estimates for north(N), east(E), vertical(U) and length(L). Each successive group of four solutions in the figure represents one of the analysis approaches: square↦simultaneous analysis (1-4); diamond↦one-site-common combination (5-8); triangle↦several-sites-common combination (9-12); circle↦augmented regional (13-16). Within each group, different levels of stochastic variability are allowed in the orbital parameters:**T**, **T_L**, **M**, and **L**. The table on the right shows the type of solution and process noise applied to the satellites. Similar results are obtained for ER03-ER09 (55 km) baseline. No scaling has been applied to the formal uncertainties.

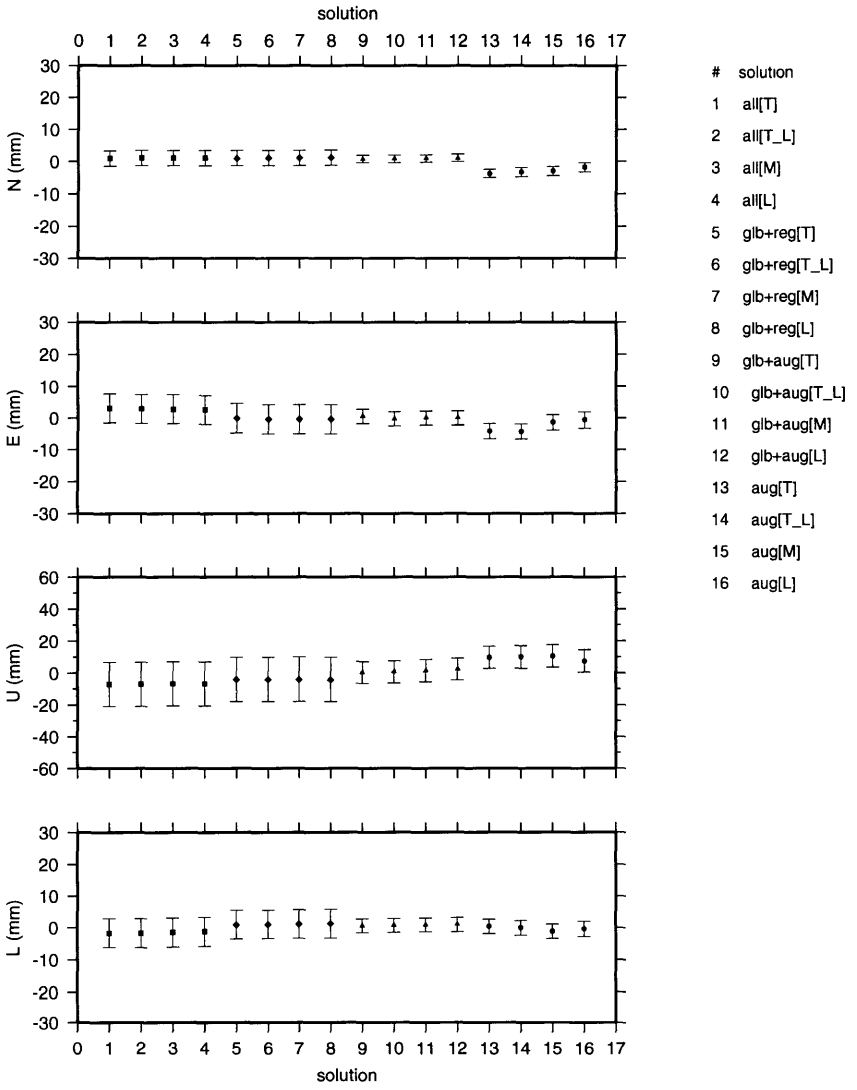

Figure A-7: Baseline KEMA-MERC (94 km). Comparison of all baseline estimates. We removed a common mean from all estimates for north(N), east(E), vertical(U) and length(L). Each successive group of four solutions in the figure represents one of the analysis approaches: square↦simultaneous analysis (1-4); diamond↦one-site-common combination (5-8); triangle↦several-sites-common combination (9-12); circle↦augmented regional (13-16). Within each group different levels of stochastic variability are allowed in the orbital parameters:(**T**, **T_L**, **M**, and **L**). The table on the right shows the type of solution and process noise applied to the satellites. No scaling has been applied to the formal uncertainties.

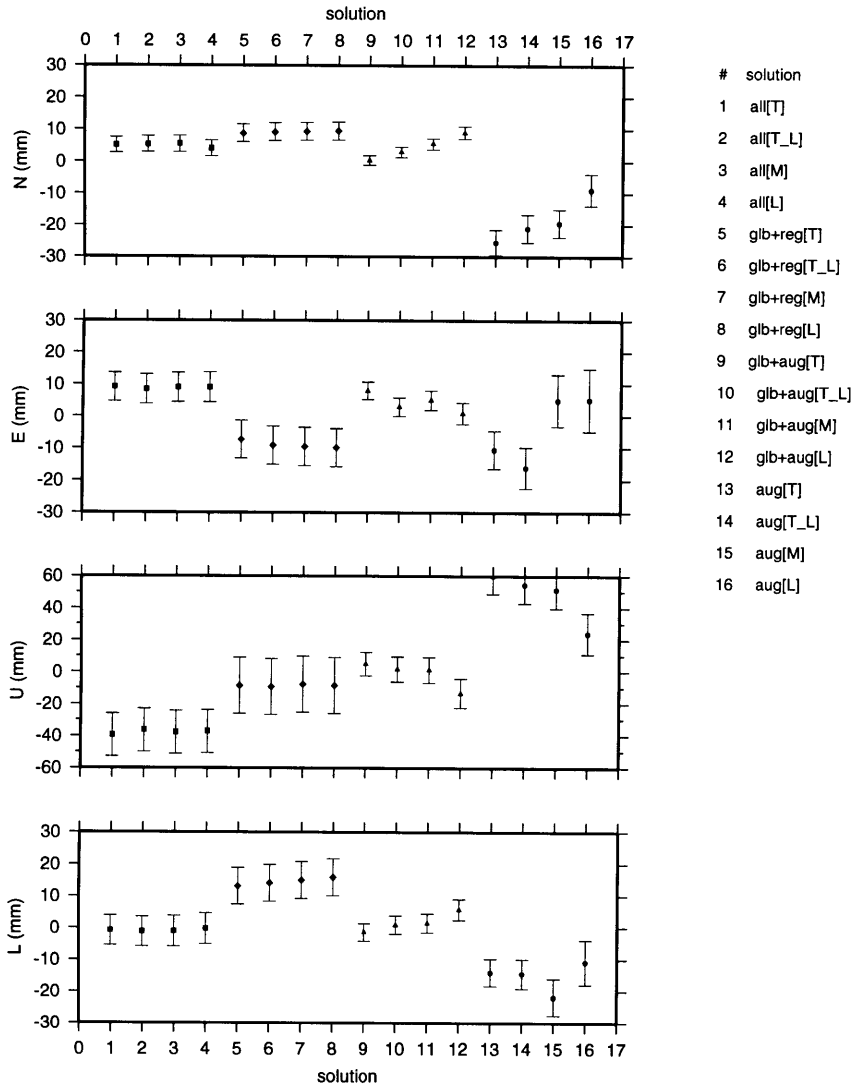

Figure A-8: Baseline ANKA-MERC (641 km). Comparison of all baseline estimates. We removed a common mean from all estimates for north(N), east(E), vertical(U) and length(L). Each successive group of four solutions in the figure represents one of the analysis approaches: square↦simultaneous analysis (1-4); diamond↦one-site-common combination (5-8); triangle↦several-sites-common combination (9-12); circle↦augmented regional (13-16). Within each group different levels of stochastic variability are allowed in the orbital parameters:(**T**, **T_L**, **M**, and **L**). The table on the right shows the type of solution and process noise applied to the satellites. No scaling has been applied to the formal uncertainties.

components and length are very similar. The one-site-common analyses, however, shows a systematic offset. The estimates of vertical components are different among analyses at the level of centimeters. It is possible that several-site-common analysis provides better estimates for the vertical than the simultaneous analysis since there are fewer baselines with mixed antennas. The baseline length estimates obtained from the simultaneous and several-site-common combinations are also in good agreement.

We also compared the estimates of regional site coordinates which were determined relative to the global tracking sites. Since the closest fiducial site was about 2000 km distant, the coordinate estimates for each site in our regional network manifested a similar pattern. Therefore, we will limit our discussion to one representative site, KEMA. We again observed a systematic offset with the position estimates obtained solely from the analysis of augmented data. The deficient global tracking network used in this analyses translated into at least a 10 cm position error (Figure A-9) for all regional sites. Figure A-10 offers a closer look at the estimates obtained from simultaneous and combination analyses with various process noise sets applied to the satellites. We observed 1-2 cm difference between the estimates of each solution. We argue that this level of variation is not significant since we have constrained (not fixed!) most of the global tracking sites' horizontal coordinates to 1–2 cm in the horizontal and 20 cm in the vertical, within their VG-defined values. Such an argument is also supported by the 20 mm mean wrms scatter of vertical components about their weighted means. Additionally, if we were to apply the scaling factor of 2 derived from long-term repeatability analysis, such differences among the position estimates would be statistically insignificant.

Comparison of relative site motions

We have not carried out extensive tests with the data from other experiments (also, see Appendix C). However, using the 1991 and spring 1992 experiments (Appendix

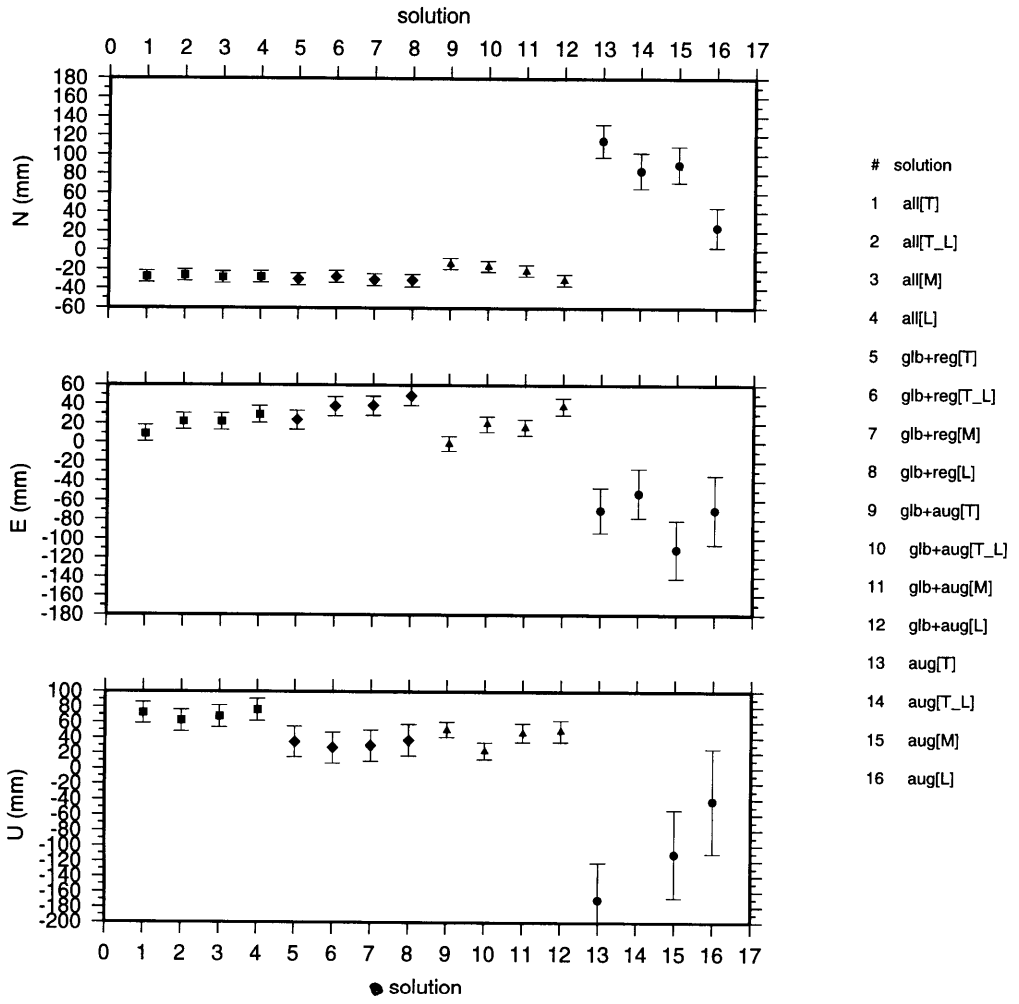

Figure A-9: Site: KEMA. Comparison of all coordinate estimates. We removed a common mean from all estimates for north(N), east(E), and vertical(U). Each successive group of four solutions in the figure represents one of the analysis approaches: square↦simultaneous analysis (1-4); diamond↦one-site-common combination (5-8); triangle↦several-sites-common combination (9-12); circle↦augmented regional (13-16). Within each group, different levels of stochastic variability are allowed in the orbital parameters: **T**, **T_L**, **M**, and **L**. The table on the right shows the type of solution and process noise applied to the satellites. No scaling has been applied to the formal uncertainties.

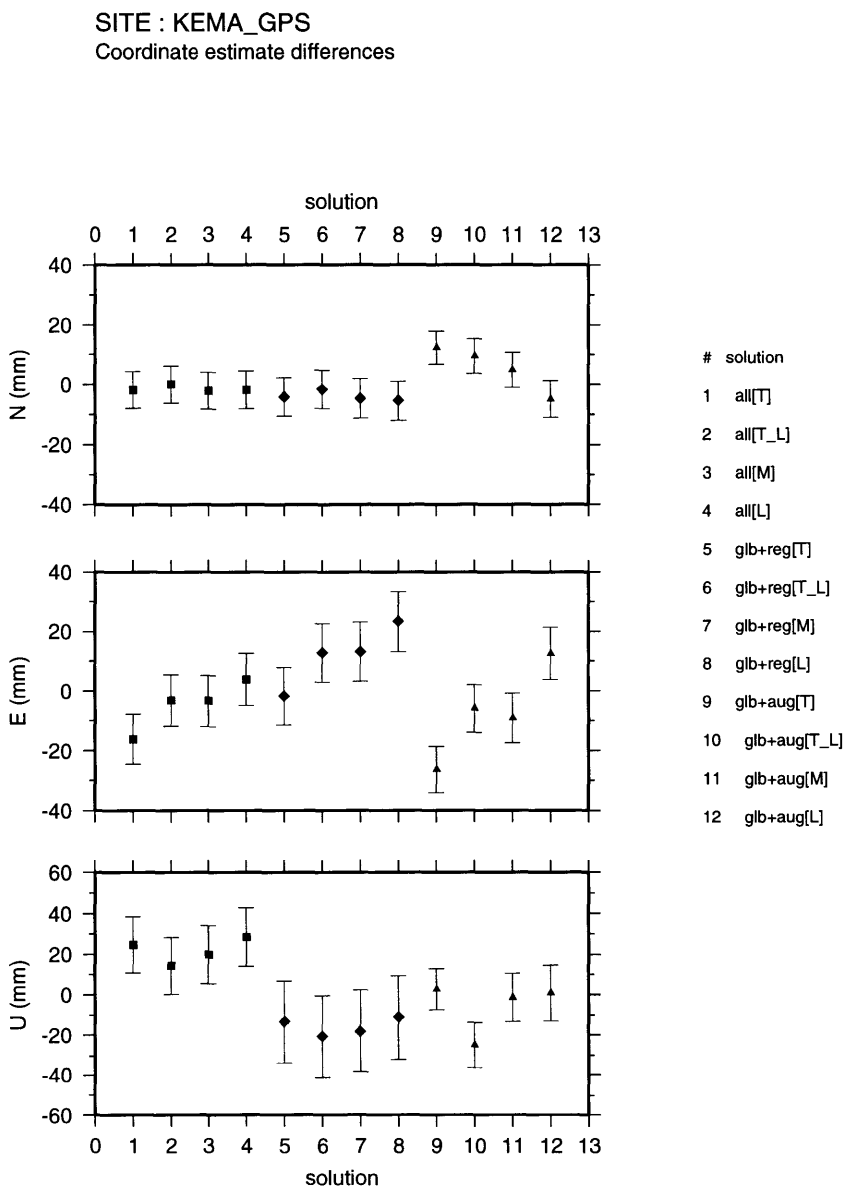

Figure A-10: Site: KEMA. Comparison of simultaneous and combination analyses' baseline estimates. We removed a common mean from all estimates for north(N), east(E), and vertical(U). Each successive group of four solutions in the figure represents one of the analysis approaches: square↦simultaneous analysis (1-4); diamond↦one-site-common combination (5-8); triangle↦several-sites-common combination (9-12). Within each group, different levels of stochastic variability are allowed in the orbital parameters:(**T**, **T_L**, **M**, and **L**). The table on the right shows the type of solution and process noise applied to the satellites. No scaling has been applied to the formal uncertainties.

B), which provide augmented regional and several-site-common combination analyses, we investigated the effects of combination on the estimates of relative site motions for 100–200 km long baselines. If our earlier findings are plausible, then the observed site velocities relative to Kemah, at Mercan (94 km) and Erzurum (187 km), should be similar for both augmented regional and several-site-common combination analyses. The computed residual displacements, with respect to those reported in Appendix D (several-site-common combination), are shown in Figure A-11 and Table A.5. The displacements differed by 2–3 mm and are not significant at the 95% confidence level.

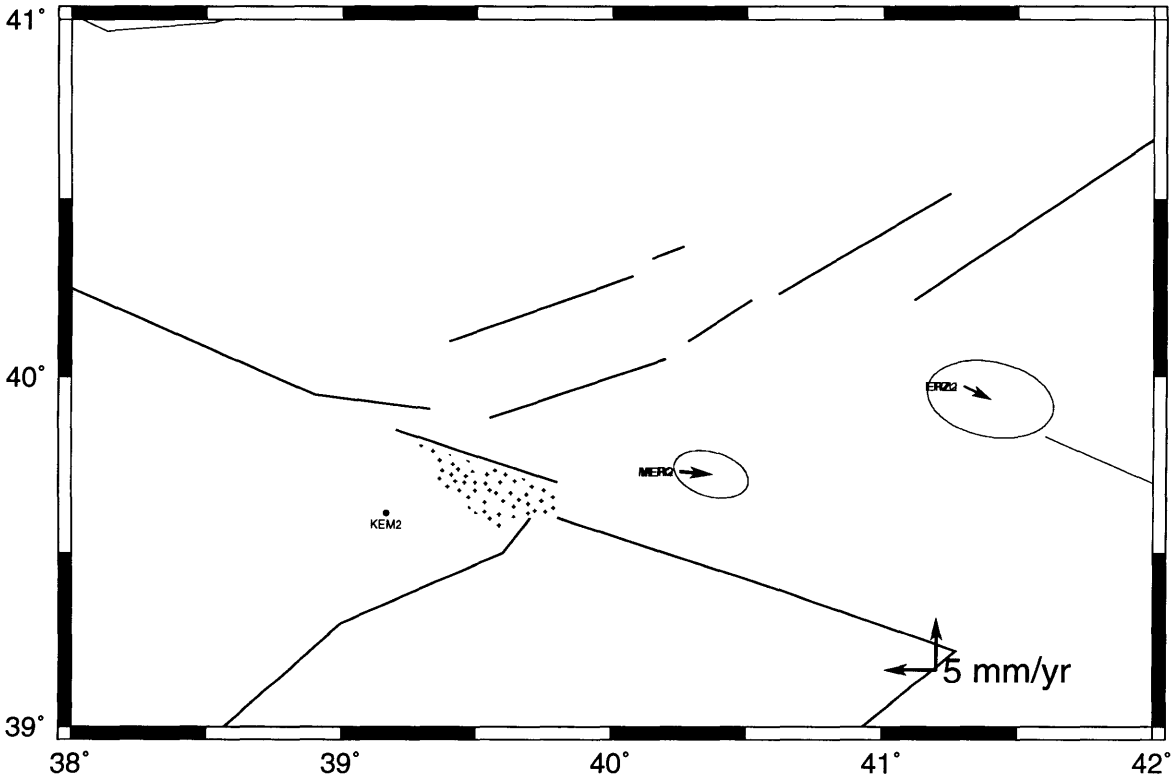

Figure A-11: Residual displacement at the Erzurum and Mercan sites, relative to Kemah, estimated from 1991 and spring 1992 GPS measurements in Turkey. We subtracted the augmented regional data analysis estimates from those of several-site-common combination analyses. The ellipses denote the 95% confidence region, after scaling.

Table A.5: Residual site velocities relative to KEMA (uncertainties are scaled as discussed in Chapter 2).

	East (mm/yr)		North (mm/yr)		
SITE	v_E	σ_E	v_N	σ_N	ρ_{EN}
ERZU	2.6	2.5	-1.2	1.6	-0.214
MERC	3.1	1.5	-0.2	1.0	-0.300

We allocated the discussion relevant to the comparison of velocity fields obtained from augmented regional and several-site-common analyses to Appendix C.

Conclusions

We investigated the feasibility of a GPS data analysis scheme which combines the GPS measurements at the regional and global sites. In GLOBK solutions we used the quasi-observations obtained from two separate, parallel GAMIT analyses. In doing so, we examined the repeatability (precision) and consistency of the estimates of baseline components, site positions and velocities, as a function of process noise on the satellites and of number/type of tie sites.

With short-term precision analysis we revealed that the repeatabilities of combination type analyses were similar to those of simultaneous analysis. The implications of our study on the consistency of these estimates appears to be closely related to the location and size of the regional network. We found that for baselines shorter than $\sim$100 km, the number of global tracking sites included in the analyses of the regional data, as well as how they were incorporated, was not important: both simultaneous and combination type analyses provided similar baseline, coordinate and velocity estimates. This suggests that single-session GAMIT analyses can be carried out with short-arcs instead of long-arcs. Also, a one-site-common combination analysis (first-order combination) may be sufficient, although it provides a weak first-step (GAMIT)

solution. For longer baselines, however, we noticed that a several-site-common type combination, with very small stochastic perturbations on the satellites, produced results most consistent with those obtained from simultaneous analyses. In this case we can use the augmented data, which is a constituent in this several-site-common type combination, in preliminary data quality examinations and cleaning/editing, short-term precision investigation, and ambiguity resolution.

Although we have developed and tested the combination approach for a single regional network, the applications of our techniques can be easily expanded to the combination of several local/regional experiments, each of which consists of a manageable volume of data. Several local (or regional) surveys can be effectively tied by an nth-order combination. For instance, we could easily combine GPS observations which were and will be collected at dozens of sites in Turkey, the Caucasus, Syria, Greece, and the Aegean and Ionian Seas, using this type of combination analysis.

Appendix B

Description of GPS Measurements, Analyses and Short-Term Precision

In this appendix we describe the GPS experiments accomplished in Turkey between 1988 and 1992. Specifically, we detail regional site occupations, observation scenarios, global tracking sites included in the solutions, receiver and antenna types, and the nature of the data (Tables 2.1, 2.2, 2.3, 2.4 and B.1). First, we present details of our approach to the analysis of each experiment. Further, we investigate the short-term precision of baseline estimates, and determine the process noise to be applied to the satellites.

Table B.1: A tally of analyzed GPS data.

		number of		
	experiment	observing sites	one-way records	double difference observations
Regional Data				
	1988	75	450	364,450
	1989	207	1,210	1,258,266
	1990	143	1,435	1,537,264
	1991	72	675	681,210
	Spring 1992	221	2,724	3,316,956
	Fall 1992	873	7,946	8,471,194
Global Data				
	1988	91	392	284,426
	1989	81	356	170,522
	1990	128	1,018	740,812
	1991	364	4,600	1,870,010
	Spring 1992	155	2,089	821,910
	Fall 1992	499	7,725	2,638,572

Sampling interval for most of the 1991 and 1992 global data was 120 seconds.

B.1 On the Data Analysis

As discussed in Chapter 2, we analyzed the GPS observations in two-steps. In the first step, we analyzed the GPS phase observables using GAMIT software [King and Bock, 1993]. In the second step, we used GLOBK software [Herring, 1991] to obtain the adjusted global parameters. (Details pertinent to the combination analysis have already been discussed in Appendix A.)

Step one : analyses with GAMIT

GAMIT is a suite of programs which accomplish the essential processing tasks of: (1) converting raw field data into internal formats; (2) generating tabulated coordinates for reference orbits and their partial derivatives with respect to satellite parameters; (3) calculating theoretical observations based on a geometrical model, and (4) computing the partial derivatives of these observables with respect to satel-

lite and site parameters; (5) detecting outliers and gaps, and editing one-way data; and (6) estimating three-dimensional relative positions of the observing sites, satellite orbits, and atmospheric, clock and ambiguity parameters from a weighted least squares analysis of phase residuals (observed - calculated). A review of GAMIT is given by Murray [1991]. Below, we present the specifics pertaining to reduction of the Turkish experiments.

We used carrier beat phase and pseudorange (indirectly) observations in data processing. The geometric models used in GAMIT processing are described by King et al. [1985], Feigl [1991], and Murray [1991]. We assigned a priori uncertainties of 10 mm to the one-way phase observations (L_1 and L_2), which is equivalent to 64 mm a priori uncertainty for the doubly differenced LC observable. We assumed a nominal set of meteorological conditions at sea level (20°, 1013.25 mb, 50% relative humidity), and then the Saastamoinen [1972] model and an elevation-dependent mapping function described by Davis et al. [1985], to determine the atmospheric zenith delay. Ionospheric delay was not modeled explicitly but rather eliminated by forming a linear combination of the L_1 and L_2 phases (the LC [or L_3] observable). Satellite clock parameters (offset, rate and acceleration) were modeled with a quadratic polynomial. The receiver clock offsets were estimated using the pseudoranges at each epoch (but also see Feigl [1991]).

Six state parameters (cartesian position and velocity at an initial epoch) and three non-gravitational parameters (direct radiation pressure, Y-axis bias and Z-axis bias [always set to zero]) were used as input to a numerical integration to obtain an ephemeris for satellite orbits for each session, at intervals of 22.5 minutes (Ash, 1972; Abbot et al., 1985). For single-session analyses, however, we only considered the direct radiation pressure, and also set the Y-axis bias to zero.

In our calculations we used updated GM values, earth rotation parameters (polar

motion and UT1) determined by VLBI [1] [T. A. Herring pers. comm., 1993], with rotation matrices for precession [Lieske et al., 1977], and for nutation [Wahr, 1981]. The earth's gravity field was determined by the GEM-L2 model [Lerch et. al, 1985] up to degree and order eight.

We used a weighted least-square scheme to estimate site coordinates, satellite state vectors (six Keplerian elements and three non-gravitational parameters), atmospheric delays, and clock and ambiguity parameters (wide-lane [L_2-L_1], and narrow-lane [L_1] biases). We carried out a series of solutions with GAMIT:

I. tightly-constrained solutions:
   - ambiguity-free,
   - ambiguity-fixed;

II. loosely-constrained solutions:
   - ambiguity-free,
   - ambiguity-fixed.

In the tightly-constrained solutions we defined a reference frame by constraining the coordinates (1–2 cm in the horizontal, 20 cm in vertical) of a number of global tracking sites at values determined from a global analysis of VLBI and GPS observations (**VG**) over a 6 year period [Feigl et al., 1993; T. A. Herring, pers. comm., 1993]. In the ambiguity-free solution we estimated all parameters and allowed phase ambiguities to have real values. For the ambiguity-fixed solution, in which the phase ambiguities were resolved, a bootstrapping procedure (as described by Dong and Bock [1989]) was sequentially used in GAMIT, and phase ambiguities were constrained to integer values. First, geodetic parameters obtained from the ambiguity-free solution were held fixed and wide-lane ambiguities were estimated using the LC observable under an ionospheric constraint of 8 ppm. As statistical confidence requirements were

[1] Although we analyzed the first five experiments with the VG derived pole and UT1-UTC tables, these were not available at the time of our analysis of the fall 1992 experiment. We had to use those produced by USNO(United States Naval Observatory). To prevent inconsistency, however, we later imposed IERS Bulletin B estimated values while obtaining the *compact* quasi-observations for all experiments.

set, wide-lane ambiguities were fixed to integers. Next, the narrow-lane ambiguities and all geodetic parameters were estimated while wide-lane ambiguity parameters were held fixed to their resolved values. Similarly, narrow-lane ambiguities were fixed to integers when statistical requirements were satisfied. Finally, as is the case for the ambiguity-fixed solution, all geodetic parameters were estimated, as the resolved ambiguity parameters were held fixed to their successfully resolved values.

For loosely-constrained solutions, we repeated both ambiguity-free and ambiguity-fixed solutions, applying loose constraints to the sites and satellites. These intermediate solutions should be loose enough so that the final solution is not biased by the constraints applied to the parameters. Such solutions typically have uncertainties of 100 m for site positions, 100 ppm for Keplerian elements, and 1000% for non-gravitational parameters. With these intermediate solutions we obtained ambiguity-free and ambiguity-fixed quasi-observations [Dong, 1993] which contain estimates of site and orbital parameters and their variance-covariance matrices. Either of these quasi-observations can later be used as input for the "global" solution, to be performed by GLOBK Kalman filtering.

Since the ambiguities were not resolved due to large inter-station distances in the Turkish network (the majority of the baselines per session spanned 300 to 600 km, some being as long as 1400 km), we used ambiguity-free quasi-observations exclusively.

In our GAMIT analyses we considered 3 sets of data:

$\Rightarrow$ regional data: regional GPS sites in Turkey,

$\Rightarrow$ global data: all global tracking sites,

$\Rightarrow$ augmented regional data: a subset of the global tracking sites and regional GPS sites in Turkey.

The subset of the global network used in our analyses comprises mainly sites in

Europe and eastern North America which we will refer to as core global tracking sites. Because these sites were available during the earlier experiments (1988, 1989 and 1990), we kept such a configuration throughout most of our data analyses. Indeed, during the earlier experiments the global tracking network was essentially composed of these sites . In the several-site-common combination analyses of 1991 and 1992 experiments (Appendix A) we augmented our regional data with a similar subset of global trackers.

Observation periods in most of the Turkish experiments were ~8 hrs. However, we chose to analyze the data in 12-13 hour sessions (GAMIT single-sessions)[2], because by extending our observations 2 hours before and after regional observations we could obtain more double-difference data from global trackers, especially in the earlier experiments. Such a scheme provided a better estimate of orbital parameters due to the longer satellite trajectories being observed. For one-site-common combination solutions (see Appendix A), however, ~8 hr sessions were sufficient. Both regional and core global tracking data were sampled at 30 second intervals, Marmara network sites at 1 minute intervals, and the rest of the global tracking data at 2 minute intervals.

Although outliers were removed and cycle-slips repaired in the phase observations using automatic procedures, we visually inspected the data (Table B.1) as it was imperative to further clean the one-way, between-satellite difference, and double difference data. After adequate cleaning we introduced long-arcs and utilized a satellite state vector, common to the 3 to 4 consecutive days' observations, for each single-session. Since most of the Turkish field work[3] involved 3-consecutive-day site

[2]Single-session is understood to be GPS data recorded for a period of 24 hours or less. A typical GPS session may last 7-8 hours. A multi-session is a collection of several single sessions. The duration for which the satellites orbits' are integrated is termed short- and long-arc. A short-arc is used for a single-session solution. A long-arc, on the other hand, spans several single-sessions. When a long-arc is used for single-session solutions, the ICs for satellites are common to each session's solutions. That is, the orbital parameters for those days are identical.

[3]MIT experiments and SLR site occupations.

occupations (the 4th day being a "move" day), a common satellite state vector, with an IC epoch centered in the middle of the long-arc, was quite convenient. We obtained quasi-observations, for use as input for GLOBK, by applying loose constraints on the sites and satellites (see above) in GAMIT long-arc, multi-session solutions. These quasi-observations, which are composed of parameter estimates and their variance-covariances, intrinsically contain the information that would be obtained from a constrained GAMIT solution.

Before moving to step two, we assessed the quality of each single-session GAMIT solution, making sure that the LC phase residuals were "flat" and that no unflagged cycle-slips existed in double-difference combinations. The residuals appeared "flat" under visual inspection, showing no evidence of cycle-slips. (Some residuals, nevertheless, presented deviations when satellite(s) were at low elevations.) When this criterion was met, the nrms (normalized rms = $\sqrt{\chi^2/f}$, where f is the degrees of freedom) was 0.2–0.3, corresponding to post-fit phase residual (LC) with rms ~0.1 cycle (20 mm). Appropriate weighting of data should result in nrms = 1. However, GPS measurements sampled at 30 second intervals are highly correlated due to multipath and atmospheric fluctuations, with a typical correlation time of 300–900 seconds[4]. Thus the data are oversampled by a factor of 10-30. With this in mind, we did not scale GAMIT formal uncertainties by the nrms.

Step two: analyses with GLOBK

After reducing GPS measurements into quasi-observations, we used a discrete time, non-adaptive GLOBK Kalman filter [Herring et al., 1990; Herring, 1991] to combine the parameter estimates and their variance-covariance matrices, and estimate global parameters (i.e., site positions and velocities, satellite state vectors and

[4]Empirically derived from California experiments [Murray, 1991; R. W. King and T. A. Herring pers. comm.]. The correlation time is not exactly known.

earth orientation parameters [polar motion and UT1-UTC]). GLOBK allows for deterministic or stochastic adjustment of these parameters with the stochastic processes modeled by random walk, which characteristics are set by the power spectral density of white noise. By setting this process noise to zero we can essentially treat selected parameters deterministically, viz., no day to day variations are allowed into the estimates, but an integrated gross adjustment is, as dictated by the a priori constraints. Adding stochastic process to the solution allows a day-to-day or year-to-year variation for the parameter(s) in question. If all parameters are treated deterministically and similar constraints are applied, Kalman filter solutions of GLOBK are equivalent to GAMIT solutions.

Using GLOBK, we performed two types of solutions to analyze our GPS data:

1. *Forward solution:* yields final estimates of nonstochastic global parameters from quasi-observations, from a forward running filter. With this type of solution we iterated regional site positions and satellite state vectors, obtained compact quasi-observations (Chapter 2), and finally, estimated site positions and velocities.

2. *Backward solution:* yields weighted mean estimates of stochastic global parameters per quasi-observation, as each is sequentially added to the solution, from a backward running smoothing filter. By perturbing a set of parameters (i.e. setting them stochastic), this smoothing filter solution provides a basis for assessing stochastic parameters' estimations and aids in the analyses of parameters estimated from each session or compact quasi-observation (short- and long-term repeatability, and variation of orbital parameters over several days, defined in a long-arc solution).

We performed a series of solutions to assess the precision of geodetic parameters' estimates, and to iterate regional site coordinates and satellite state vectors. These solutions, defined by the type of constraints imposed, are summarized in Table B.2. Accordingly, we considered deterministic and stochastic processes for both sites and

Table B.2: GLOBK solutions: site and satellite constraints.

Solution Descriptor	sites regional	non-eclipsing satellites	eclipsing satellites
D_D	deterministic	deterministic	same as non-eclipsing
D_T	deterministic	tightly stochastic	same as non-eclipsing
S_D	loosely stochastic	deterministic	same as non-eclipsing
S_T	loosely stochastic	tightly stochastic	same as non-eclipsing
S_M	loosely stochastic	moderately stochastic	same as non-eclipsing
S_L	loosely stochastic	loosely stochastic	same as non-eclipsing
S_T_M	loosely stochastic	tightly stochastic	moderately stochastic
S_T_L	loosely stochastic	tightly stochastic	loosely stochastic

First, second and third descriptors refer to regional sites, non-eclipsing satellites, and eclipsing satellites, respectively. Global sites are kept deterministic. D and S denote deterministic and stochastic regional sites, respectively. T, M, and L designate the stochastic set applied to the satellite orbital parameters and are abbreviations for tightly, moderately and loosely stochastic treatments, respectively.

satellites. We treated the eclipsing satellites with a higher process noise in order to account for the extra non-gravitational forces acting on them as they enter and exit the earth's shadow.

Tables B.3 and B.4 tabulate the a priori constraints and process noise used in various solutions. Setting the process noise to zero yields deterministic estimates (**D**). Setting higher process noise tends to decouple the estimates of parameters between consecutive days. Variations of 10 m/day in the cartesian position and 1 mm/s/day in cartesian velocity of satellites essentially yields independent orbits between days (**L**, loose). This decoupling of orbits, defined over several days, in turn, replicates short-arc, single-session GAMIT solutions. By *tightening* these stochastic constraints, that is, reducing the process noise, we can arrive at a single dynamic arc. Moderately stochastic constraints (**M**) are in between the *tight* (**T**) and the *loose* (**L**).

Table B.3: GLOBK constraints for sites.

a priori constraints on sites						
	Position (m)			Velocity (m/yr)		
Single-epoch	N	E	U	N	E	U
Regional sites	10.00	10.00	10.00	0.00	0.00	0.00
Global sites	0.02	0.02	0.20	0.00	0.00	0.00
Multi-epoch	N	E	U	N	E	U
Regional sites	10.00	10.00	10.00	1.00	1.00	1.00
Global sites	0.02	0.02	0.20	0.001	0.001	0.001

stochastic constraints on sites						
	Position (m/DAY)			Velocity (m/yr/DAY)		
Single-epoch	N	E	U	N	E	U
(**D**)Regional sites	0.00	0.00	0.00	0.00	0.00	0.00
(**S**)Regional sites	1.00	1.00	1.00	0.00	0.00	0.00
Global sites	0.00	0.00	0.00	0.00	0.00	0.00
	(m/YEAR)			(m/yr/YEAR)		
Multi-epoch	N	E	U	N	E	U
(**D**)Regional sites	0.00	0.00	†0.05	0.00	0.00	0.00
(**S**)Regional sites	10.00	10.00	10.00	0.00	0.00	0.00
Global sites	0.00	0.00	0.00	0.00	0.00	0.00

† 0.50 m/yr/YEAR for anomalous sites.
Global sites are kept deterministic. D and S denote deterministic and stochastic regional sites, respectively. N: north, E: east, and U: Up (vertical).

Table B.4: GLOBK constraints for satellites.

a priori constraints on satellites									
	Position (m)			Velocity (mm/s)			Non-gravitational %/DAY		
	X	Y	Z	$\dot{X}$	$\dot{Y}$	$\dot{Z}$	Rad-P	Y-Bias	Z-Bias
general	50.00	50.00	50.00	5.00	5.00	5.00	50%	50%	F
iteration	50.00	50.00	50.00	5.00	5.00	5.00	50%	F	F

stochastic constraints on satellites									
	Position (m/DAY)			Velocity (mm/s/DAY)			Non-gravitational %/DAY		
	X	Y	Z	$\dot{X}$	$\dot{Y}$	$\dot{Z}$	Rad-P	Y-Bias	Z-Bias
(tight) **T**	0.10	0.10	0.10	0.01	0.02	0.01	1	1	0
(moderate) **M**	1.00	1.00	1.00	0.10	0.10	0.10	10	10	0
(loose) **L**	10.00	10.00	10.00	1.00	1.00	1.00	100	100	0

Non-gravitational terms are expressed in scale factors. Rad-P denotes the direct radiation parameter. F means that the parameter was fixed to its a priori value.

For all solutions, unless otherwise stated, we applied a priori (1-σ) constraints of 2 cm in horizontal and 20 cm in the vertical coordinates of the global tracking sites defined by VG. For sites whose VG position and velocity were less accurately known, such as WETM, TSUK, TAIW, etc., we assigned higher uncertainties. We allowed regional site positions in single-epoch solutions to freely adjust (also see Chapter 2). In several-epoch solutions their velocities were also freely adjusted. Only in repeatability analyses did we stochastically estimate all regional sites. Because GAMIT has no knowledge of stochastic variations, only the direct radiation parameter was estimated, along with the cartesian position and velocity for satellites, to obtain precise ICs whilst

the process noise was set to zero. For both cases (iterations) we returned to long-arc, single-session GAMIT solutions to obtain quasi-observations, so that non-linearity effects were avoided when adjustments to sites and satellite IC cartesian positions were greater than 1 m and 10 m, respectively.

We have used χ^2/f in judging the plausibility of this series of solutions to provide a *relative sense* of consistency in sequential estimates. The χ^2/f provided by the GLOBK Kalman filter is the norm of the residuals weighted by the a priori variances divided by the number of degrees of freedom (f). If the data are properly weighted and the dynamic models are correct, χ^2/f will be close to unity.

We evaluated the short- and long-term precision of our observations by fitting two error models to the wrms scatter in the form of $\sigma^2 = a^2 + b^2L^2$and $\sigma = c + m\ L$, where a and c are constant terms and L is the baseline length. The proportional errors are represented by c and slope. We refer to the linear error model, however, only in the wrms plots. We used the wrms scatter (short-term) about the weighted means of baseline component estimates as a criteria to test for sensitivity to orbital errors. Accordingly, we performed a series of solutions for each experiment, with different process noise on the satellites (*cf.* Table B.4), to select the preferred process noise set with the highest precision, viz., the smallest proportional errors (*cf.* Table B.2). By applying the preferred process noise to the orbital parameters we further reduced the quasi-observations obtained from long-arc, single-session GAMIT analyses into one *compact* quasi-observation for each experiment. Utilizing this compact form of data as yet another input to GLOBK, we estimated all site positions and velocities with loose a priori constraints. The geometrical relationship of the tightly constrained solution intrinsically remains, provided that the a priori model is in the linear range. As discussed in Chapter 2, such an approach allows a rigorous estimate of position and velocity without being biased by inconsistent constraints on the global tracking network.

B.2 GPS Experiments in Turkey

B.2.1 1988 Western Turkey Experiment

In 1988 we initiated GPS measurements in Turkey with support from UNAVCO and in collaboration with Hacettepe University. This experiment took place between September 6 and 28, 1988 (days: 250-272). We collected GPS data for 20 days and occupied 18 sites. We established fourteen primary sites (Figure B-1) in western

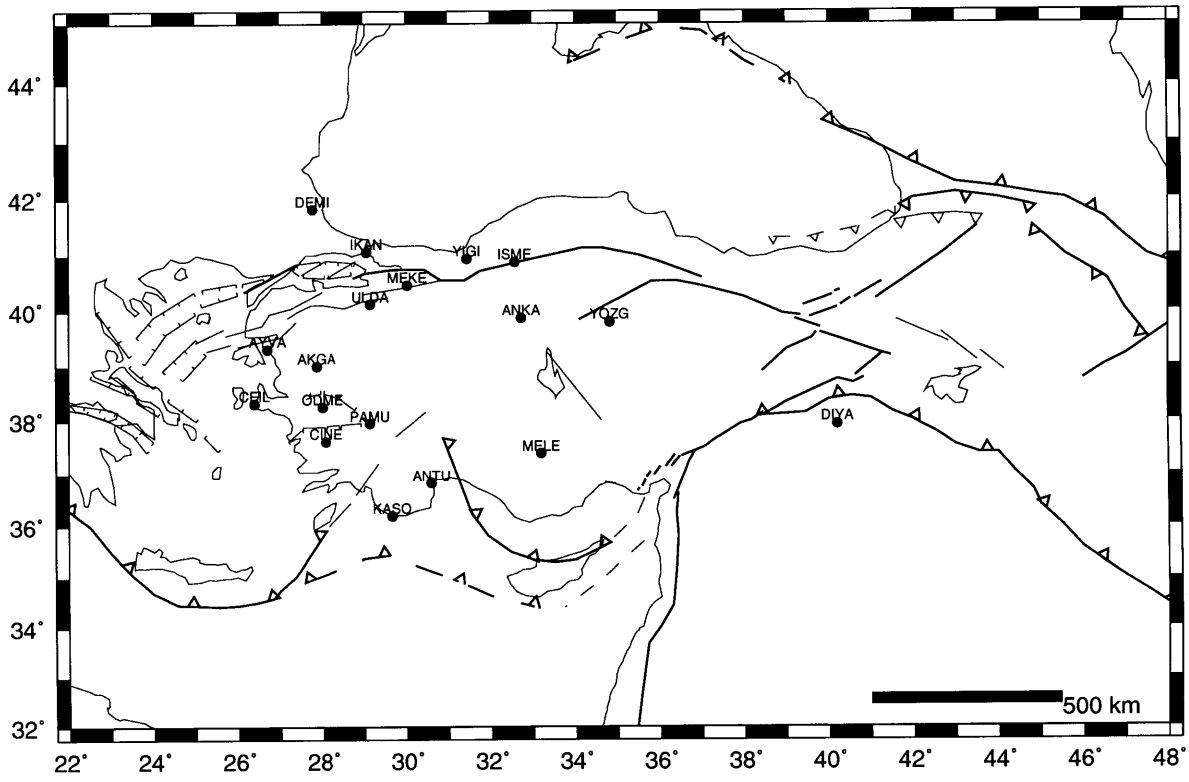

Figure B-1: Distribution of regional sites occupied during the 1988 experiment.

and central Turkey (AKGA, ANKA, ANTU, AYVA, CEIL, CINE, DEMI, IKAN, ISME, KASO, MEKE, ODME, PAMU, and ULDA). During this campaign we also made GPS measurements at the four mobile SLR stations (YIGI, YOZG, DIYA, and

Table B.5: Regional sites and long-arc groupings: 1988 western Turkey experiment.

ARC	DAY	GPS SITES			
1	250	AKGA	ANKA	ANTU	DIYA
	251	AKGA	ANKA	ANTU	DIYA
	252	AKGA	ANKA	ANTU	DIYA
	253	ANKA	DIYA		
2	254	ANKA	AYVA	DIYA	KASO
	255	ANKA	AYVA	DIYA	KASO
	256	ANKA	AYVA	KASO	
3	258	ANKA	CINE	MELE	ULDA
	259	ANKA	CINE	MELE	ULDA
	260	ANKA	CINE	MELE	ULDA
4	262	ANKA	DEMI	PAMU	YOZG
	263	ANKA	DEMI	PAMU	YOZG
	264	ANKA	DEMI	PAMU	YOZG
5	266	ANKA	IKAN	ODME	YIGI
	267	ANKA	IKAN	ODME	
	268	ANKA	MEKE	ODME	YIGI
	269	ANKA	YIGI		
6	270	ANKA	CEIL	ISME	YIGI
	271	ANKA	CEIL	ISME	YIGI
	272	ANKA	CEIL	ISME	YIGI

MELE) established in Turkey by WEGENER-MEDLAS[5] (Table B.5).

We carried out six-hour long, night-time observation sessions at 18 sites for 20 days, tracking 6 satellites. PRNs 3, 6, 9, 11, 12 and 13 were visible during the observation scenario. During this experiment, PRNs 6, 9 and 12 were in eclipsing season. A daily site occupation schedule is given in Table B.5. Each site was occupied at least three times except MEKE, which was observed only once. We observed at the Ankara site (ANKA) for 20 days throughout the experiment. We collected data at the Diyarbakır SLR site (DIYA) for six consecutive days, but had to remove this data from our analyses (see below). We occupied most other sites for three consecutive days. Because of the great interstation distances, a fourth day was designated as a

[5]Working Group of European Geoscientists for the Establishment of Networks for Earthquake Research-Mediterranean Laser Ranging project [Reinhart et al., 1985].

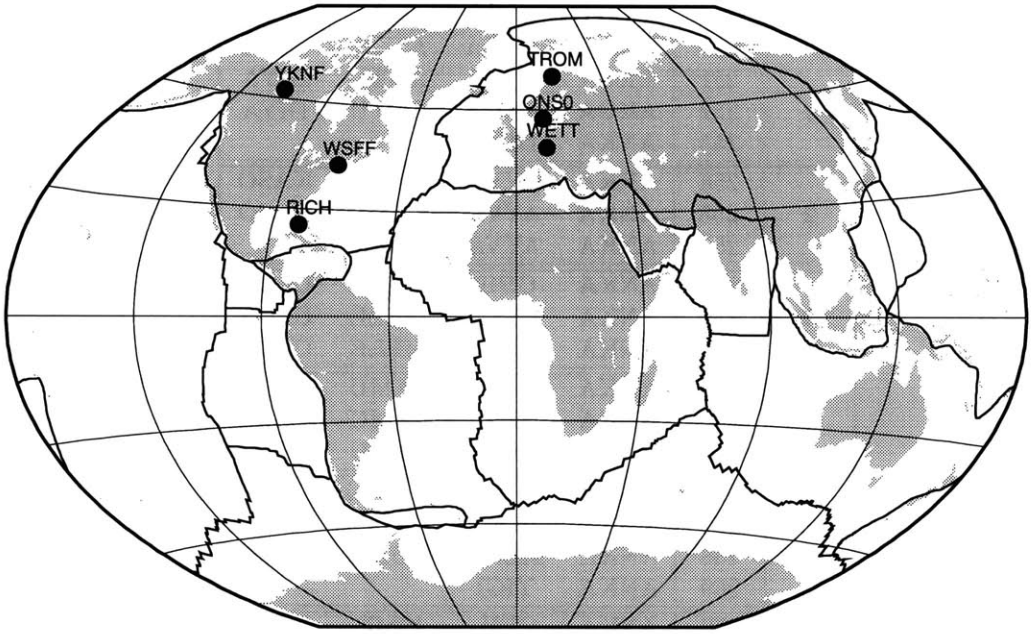

Figure B-2: Distribution of core global tracking sites included in the analyses of the 1988 western Turkey experiment.

"move day". Observations continued at some sites during the move, however, with a smaller regional network. A total of 74 observation sessions were recorded.

All receivers and antennas operating in the regional network were TI4100. All receivers had GESAR 1.6 navigation software, except ANKA, with ROM 1.11. The raw data were translated into RINEX format [Gurtner et al., 1989] at UNAVCO.

We obtained global tracking data from the National Geodetic Survey (NGS) in ARGO format and translated them into FICA. We used an intercontinental network (Figure B-2 and Table B.6) of 6 global tracking sites (ONS0, RICH, TROM, WETT, WSFF, and YKNF) in our solutions. All global sites had TI4100 receivers with TI4100 antennas, except WSFF and RICH, which had FRPA-2 antennas. Navigation

software for fiducial sites was CORE 4.1 and 4.8. Table B.6 depicts the availability of these sites. Days 251, 262 and 271 had the poorest fiducial control, with only three trackers available.

Table B.6: Regional tracking sites and long-arc groupings: 1988 western Turkey experiment.

ARC	DAY	GPS SITES					
1	250	WETT	WSFF	YKNF	ONS0	RICH	TROM
	251	WETT	ONS0	RICH			
	252	WETT	WSFF	ONS0	RICH	TROM	
	253	WETT	WSFF	YKNF	ONS0	RICH	TROM
2	254	WETT	WSFF	YKNF	ONS0	RICH	TROM
	255	WETT	WSFF	ONS0	RICH	TROM	
	256	WETT	WSFF	ONS0	TROM		
3	258	WETT	YKNF	ONS0	RICH	TROM	
	259	WETT	YKNF	ONS0	RICH	TROM	
	260	WETT	WSFF	ONS0	RICH		
4	262	WSFF	YKNF	ONS0			
	263	WETT	WSFF	YKNF	ONS0	RICH	
	264	WETT	WSFF	YKNF	ONS0	RICH	TROM
5	266	WETT	WSFF	ONS0	RICH	TROM	
	267	WETT	WSFF	ONS0	TROM		
	268	WETT	WSFF	ONS0	RICH	TROM	
	269	WETT	WSFF	RICH	TROM		
6	270	WETT	ONS0	RICH	TROM		
	271	WETT	ONS0	RICH			
	272	WETT	ONS0	RICH	TROM		

We simultaneously analyzed the regional and the global tracking data, extending the observation scenarios used in the GAMIT solution to 12 hours[6]. This provided more double difference data from global trackers and assisted in better determination of the satellite orbits. We started with broadcast ephemeris (later solutions were carried out with iterated satellite state vectors obtained from GLOBK solutions), and cleaned the data (30 second samples) iteratively.

We could not form any double-differences with Yellowknife for days 251 and 252.

[6] 11 hours and 50 minutes to be exact, so that the day boundary is not crossed.

Table B.7: Normalized RMS of long-arc, single-session GAMIT solutions: 1988 western Turkey experiment.

GPS DAY	tight solution	loose solution
250	0.274	0.225
251	0.237	0.216
252	0.278	0.246
253	0.268	0.228
254	0.242	0.228
255	0.281	0.245
256	0.284	0.257
258	0.268	0.243
259	0.256	0.234
260	0.246	0.230
262	0.230	0.209
263	0.251	0.216
264	0.243	0.218
266	0.242	0.218
267	0.260	0.238
268	0.246	0.224
269	0.268	0.239
270	0.259	0.244
271	0.239	0.223
272	0.245	0.228

Wettzell had very little data on day 262, which had been sampled at 15–minute intervals, so we deleted it. Data acquired on day 263 had several gaps and cycle-slips. Tromso, on day 266, contained quite a few cycle slips and provided limited data. On day 267, we had to delete PRN 12 from all sites. Due to poor data quality, we removed Richmond on day 267, and Tromso and Westford on day 271. Other than these, no major problems were encountered in data reduction.

Later, we divided the experiment into 6 multi-day arcs (Table B.5), each three to four days long, and performed long-arc, single-session GAMIT solutions (step-one). Table B.7 shows the normalized rms obtained from these solutions for each day. All are less than 0.3, indicating that the rms of the phase residuals is ≤ 0.1 cycle (20 mm).

In the second step, by applying loose constraints to the sites and satellites, we

obtained quasi-observations from long-arc, single-session GAMIT solutions, and estimated the global parameters with GLOBK.

As discussed in the earlier section, we performed a series of solutions, each with a different level of process noise on the eclipsing and non-eclipsing satellites. Solutions with tight stochastic constraints (**T**) applied to all satellites gave the highest short-term precision (Figure B-3). The GLOBK χ^2/f for this solution was 0.44. Allowing looser stochastic constants on eclipsing satellites resulted in a higher wrms scatter in baseline components(Table B.8), so we did not treat them differently. We suspect that for this experiment, with only 6 satellites (4 simultaneously), the inherently weak geometry of the constellation degraded the precision more than the unmodeled perturbations on the satellites. Hence the use of tight constraints was optimal.

Table B.8: Short-term repeatability: 1988 western Turkey experiment.

Solution Descriptor	N-S component a (mm)	N-S component b (ppb)	N-S component mean nrms	E-W component a (mm)	E-W component b (ppb)	E-W component mean nrms	U-D component a (mm)	U-D component b (ppb)	U-D component mean nrms	Length component a (mm)	Length component b (ppb)	Length component mean nrms
S_T†	5.96	5.55	0.55	12.76	10.80	0.58	17.67	1.68	0.58	5.44	22.23	0.57
S_L	4.15	30.10	0.63	10.20	76.41	0.78	15.84	41.55	0.55	2.43	59.97	0.74
S_M	4.98	15.07	0.59	11.29	29.62	0.61	18.72	0.60	0.56	1.76	31.44	0.56
S_T_L	3.49	24.99	0.67	15.05	27.68	0.64	14.95	32.86	0.57	6.10	31.66	0.60
S_T_M	4.91	14.93	0.60	13.55	17.39	0.61	17.34	0.60	0.54	4.99	23.08	0.53

† The preferred solution is obtained by applying tight constraints to all satellites (*cf.* Table B.2).

Repeatability statistics were obtained for sites observed more than twice. The DIYA site's daily baseline estimates showed a drift of 10 mm and 18 mm in the north and east components, respectively, so we deleted this site from our error analyses and quasi-observations. The mean nrms of baseline estimates was ~0.6 (Figure B-3). The proportional errors for the horizontal component were less then 10 ppb. We obtained 5.5 ppb baseline length dependency for the north component. We observed a mean wrms of 6.4 mm and 13.5 mm, in the north and east components, respectively.

By performing a **D_T** (*cf.* Table B.2) type solution, with which all sites were estimated deterministically, we investigated how well the baselines were determined:

σ_{NS}(mm) =	5.04(mm)	+	9.22x10^{-3} L(km)	@500km baseline:	9.65(mm)
σ_{EW}(mm) =	9.84(mm)	+	15.65x10^{-3} L(km)	@500km baseline:	17.66(mm)
σ_{UD}(mm) =	18.82(mm)	+	7.82x10^{-3} L(km)	@500km baseline:	22.73(mm)
σ_{BL}(mm) =	6.95(mm)	+	12.64x10^{-3} L(km)	@500km baseline:	13.27(mm).

Accordingly, the propagated formal uncertainties for the 1988 western Turkey experiment baselines ($\sim$ 500 km) are approximately 10 mm in the north and 18 mm in the east.

Finally, we applied the tight (**T**) process noise set to the satellites and loose constraints to all sites, and obtained compact quasi-observations for the 1988 western Turkey experiment, to be used in velocity estimation.

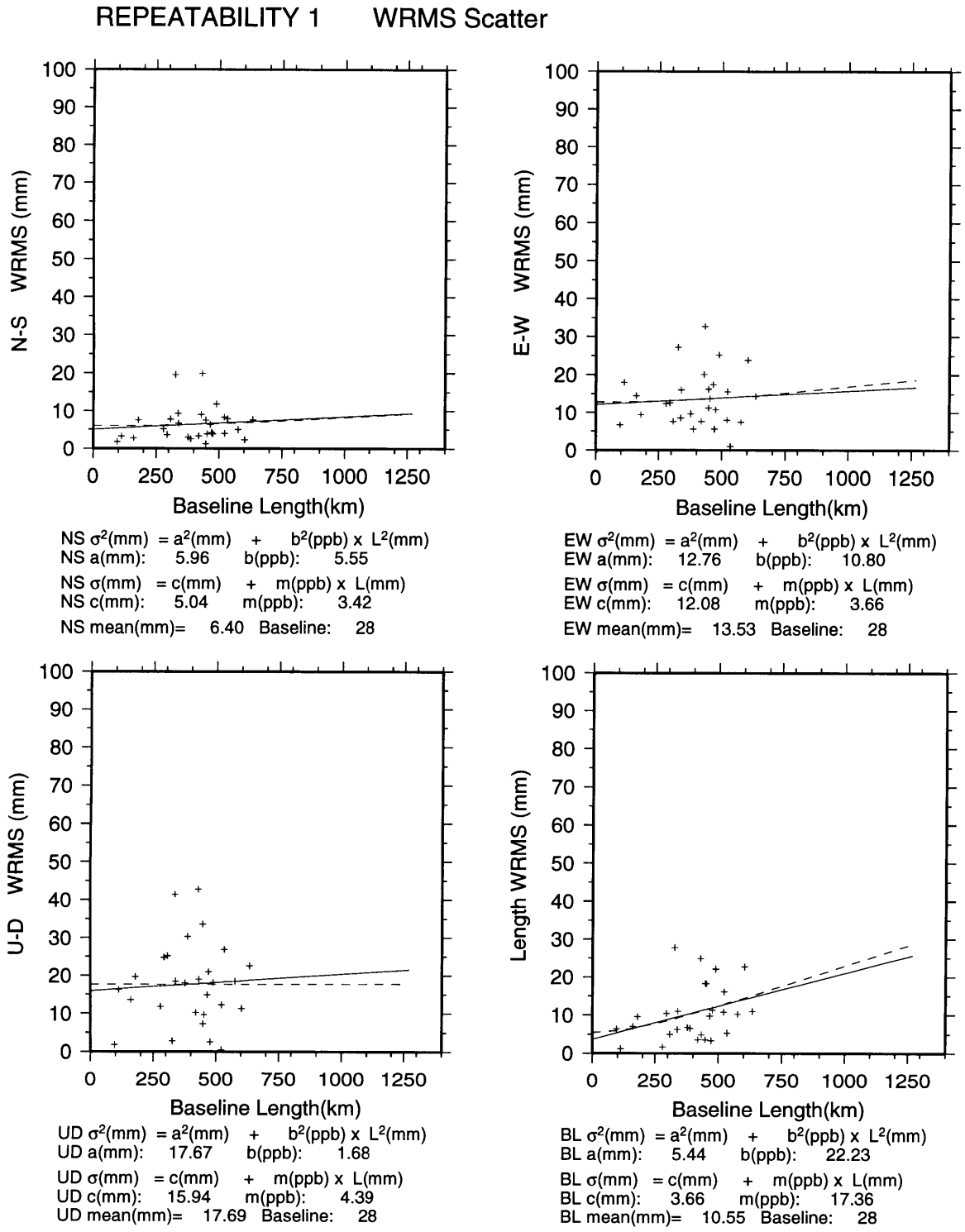

Figure B-3: The wrms scatter and model parameters of NS, EW, UD components and length, as a function of baseline length. They are obtained from the 1988 western Turkey experiment with tight (**T**) stochastic constraints applied to the satellites. DIYA is not included in the scatter plots. The wrms of baselines with 2 or more repeat observations are shown. Dashed line is a functional in the form of $\sigma^2 = a^2 + b^2L^2$. Continuous line is a linear fit to the wrms scatter ($\sigma = c + m\ L$).

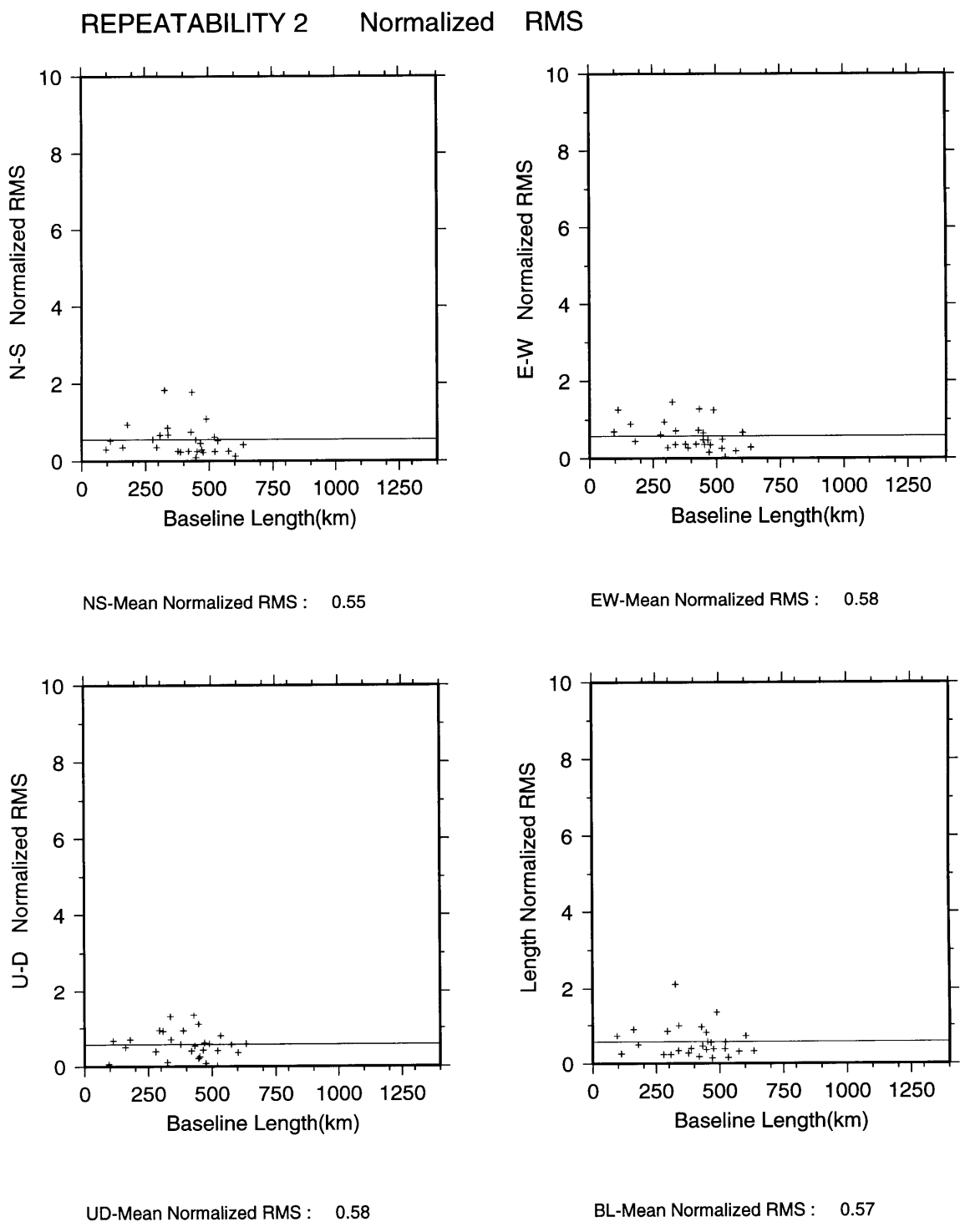

Figure B-4: The nrms scatter of NS, EW, UD components and length [for the solution described in Figure B-3], as a function of baseline length. They are obtained from the 1988 western Turkey experiment with tight (**T**) stochastic constraints applied to the satellites. Continuous line represents the mean nrms scatter.

B.2.2 1989 Eastern Turkey Experiment

We initiated the second phase of our GPS observations in Turkey in 1989, in collaboration with GCM[7]. This experiment began on August 21 and was completed by September 10 (days: 232-252). During this experiment we established another network in eastern Turkey which comprised 16 sites (Figure B-5) : ERZU, ISPI, KADI, KAHT, KALE, KARA, KARS, KEMA, KIZI, KORK, MALA, MERC, PATN, SEBI, SINC, and ULUC. We also occupied the ANKA and DIYA sites for 18 and 16 days, respectively. Due to the malfunctioning of one of the Trimble receivers we had to

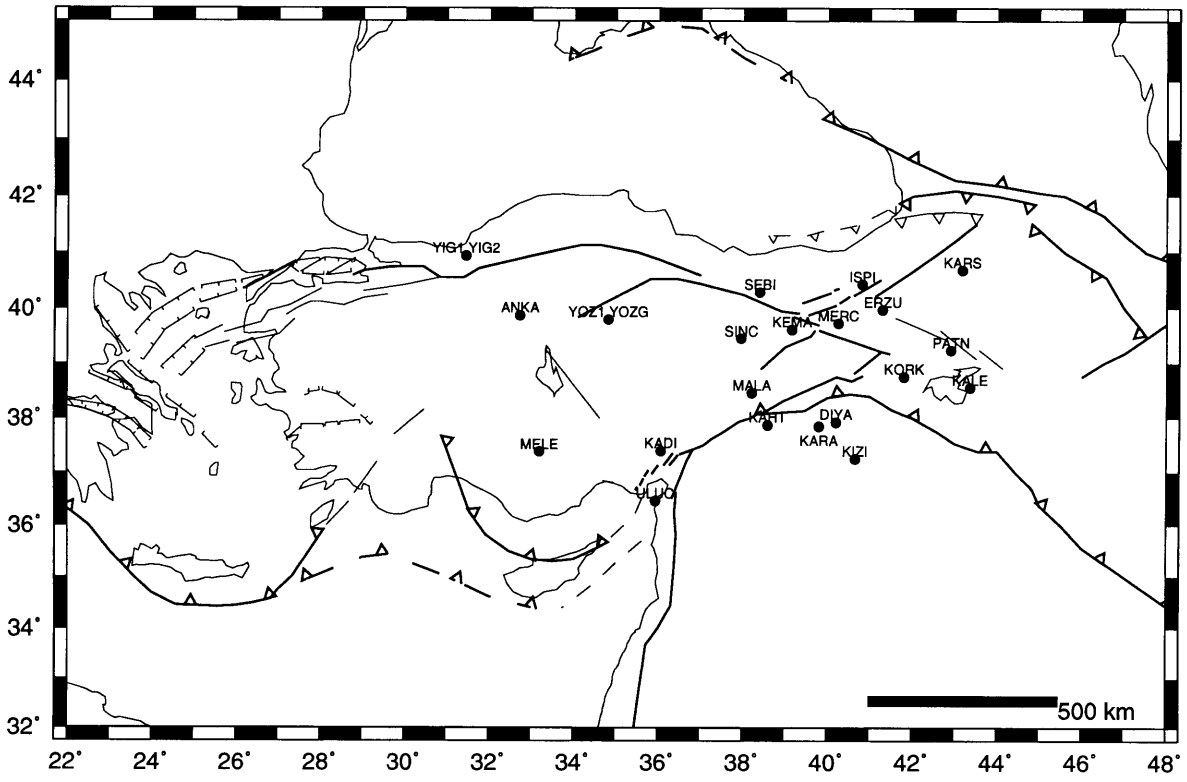

Figure B-5: Distribution of regional sites (eastern Turkey) occupied during in 1989.

change our observation schedule, resulting in only two observations at PATN.

[7]General Command of Mapping, Ankara, Turkey.

Table B.9: Regional sites and long-arc groupings (eastern Turkey): 1989 eastern Turkey experiment.

ARC	DAY	GPS SITES								
1	232	MELE	YIG1	YOZ1						
	233	MELE	YIG1	YOZ1						
2	234	DIYA	ERZU	KARA	MELE	MERC	ULUC	YIG2	YOZ1	
	235	ANKA	DIYA	ERZU	KARA	MELE	MERC	ULUC	YIG2	YOZ1
	236	ANKA	DIYA	ERZU	KARA	MELE	MERC	ULUC	YIG2	YOZ1
	237	ANKA	MELE	YIG2						
3	238	ANKA	ISPI	KADI	KEMX	KIZI	MELE	YIG2		
	239	ANKA	DIYA	ISPI	KADI	KEMX	KIZI	MELE	YIG2	
	240	ANKA	DIYA	ISPI	KADI	KEMX	KIZI	MELE	YIG2	
	241	ANKA	DIYA	YIG2	YOZ1					
4	242	ANKA	DIYA	KAHT	KORK	YIG2	YOZ1			
	243	ANKA	DIYA	KAHT	KORK	PATN	YIG2	YOZ1		
	244	ANKA	DIYA	KAHT	KORK	PATN	YIG2	YOZ1		
	245	ANKA	DIYA	MELE	YIG2	YOZ1				
5	246	ANKA	DIYA	KALE	KARS	MALA	MELE	YIG2	YOZ1	
	247	ANKA	DIYA	KALE	KARS	MALA	MELE	YIG2	YOZ1	
	248	ANKA	DIYA	KALE	KARS	MALA	MELE	YIG2	YOZG	
	249	ANKA	DIYA	MELE	YOZG					
6	250	ANKA	DIYA	KEMA	MELE	SEBI	SINC	YIG2		
	251	ANKA	DIYA	KEMA	MELE	SEBI	SINC	YIG2		
	252	ANKA	SEBI	SINC						

We operated a TI4100 receiver and antenna at ANKA and experienced difficulties with its RINEX translation. Due to the type of navigation software (NAVDAPT version 2), existing translators failed to produce the data in RINEX format. Nonetheless, we managed to use the Bernese GPS analysis software internal modules for translation. At the DIYA site we used a TI4100 antenna and receiver. Raw data from TI4100 receivers were translated at UNAVCO facilities. Trimble SLD antennas and receivers, running navigation software 3.25, were used at other sites. We observed at a given site for three consecutive days. During the move day, ANKA, DIYA and SLR collocation sites were observed (Table B.9).

Independent GPS campaigns were also carried out by IfAG and the University

of Durham, in central and western Turkey, simultaneously with our experiments. IfAG made measurements at the reference marks of the SLR collocation sites of YIGI (YIG1 and YIG2) and YOZG (YOZ1) because the original markers were occupied by SLR equipment. GPS measurements were taken at YOZG and YOZ1 on different days, so there are no short baseline GPS ties between these sites. No GPS ties to the main marker, YIGI, were established at the new Yığılca sites (YIG1 and YIG2). Observations at YIG1, YIG2 and MELE were recorded by Minimac receivers and antennas. The tracking navigation software was 1.89. We discovered that GPS observations at these sites were mistagged as 59.000. We estimated the clock offsets from phase data and postulated that the acquisition software might have been 1.49, and that the data was actually collected at 59.001, with one millisecond error in the time tags. A Trimble SLD receiver was operated at the YOZG and YOZ1 sites, and was running a navigation software, version 3.12.

The Durham group had occupied a denser network (Figure B-6) in the Bozdağ region of western Turkey, which included 5 of our 1988 established sites (AKGA, CEIL, CINE, ODME, and PAMU). As a part of the Bozdağ network, they established 27 additional sites (AHME, AKCA, ALSE, BAFA, BAYI, BAYO, BEDA, BULD, DOBE, GOMA, HAPA, IZMR, KABU, KINI, KIRK, KOBE, KRNC, KUSO, SEFE, SEUR, SIPD, SOKE, SUGE, TERZ, TIRE, URIS, and USUM) and acquired GPS data for 16 days. SIPD was observed almost every day (14 days). GPS observations were repeated twice at all sites, except at the BULD and IZMR sites, which were occupied three times (Table B.10). Some observations were not made on two consecutive days. Although simultaneous observations were carried out, the Bozdağ network site occupation schedule was not coordinated with ours. TI4100 antennas and receivers (navigation software COR 4.11) were used at the Bozdağ network sites.

During the 1989 experiment, GPS measurements were acquired at a total of 55 sites by IfAG, Durham, and ourselves. Observation sessions were ~6-7 hours long

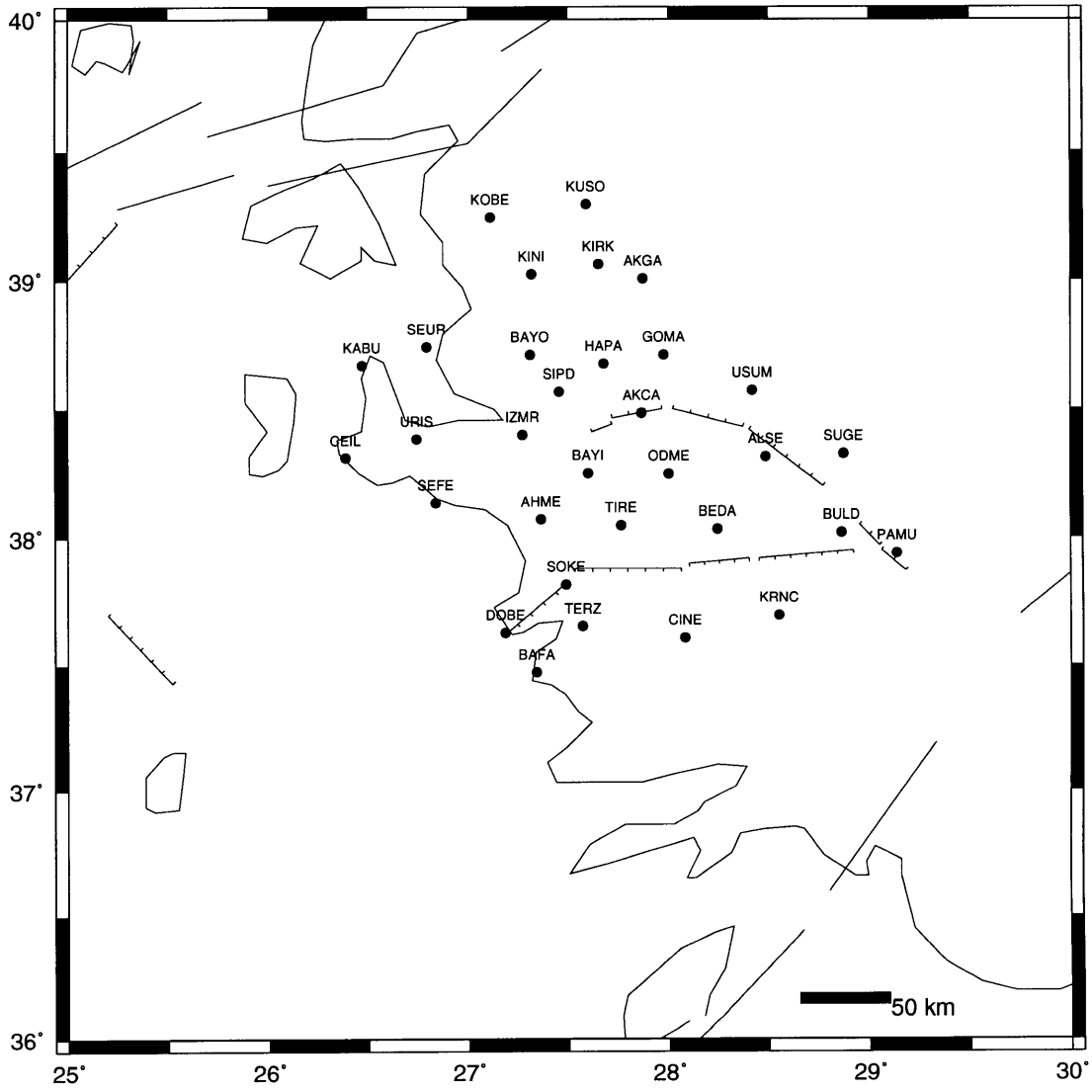

Figure B-6: Distribution of regional sites (Bozdağ network) occupied during the 1989 experiment.

and six satellites (PRNs 3, 6, 9, 11, 12, and 13) were tracked. Three satellites (PRNs 6, 9 and 12) were in eclipsing season.

All sets of data have been included in the solutions to obtain a unified 1st degree geodetic network in Turkey. Due to delays in accessing the other groups' data we reduced the observations in 3 stages; starting with our own data set, later reducing

Table B.10: Regional sites and long-arc groupings: 1989 Bozdağ Network Experiment.

ARC	DAY	GPS SITES				
1	232					
	233	AHME	BAYI	IZMR	SIPD	URIS
2	234	CEIL	KABU	IZMR	SEFE	URIS
	235	CEIL	KABU	BAYO	SEUR	SIPD
	236	KINI	KIRK	KOBE	SEUR	SIPD
	237	KINI	KIRK	KOBE	SIPD	
3	238	AKGA	BAYO	HAPA	KUSO	SIPD
	239	AKCA	AKGA	GOMA	HAPA	SIPD
	240	AKCA	GOMA	IZMR	USUM	SIPD
	241	ALSE	SUGE	ODME	USUM	SIPD
4	242	ALSE	BULD	PAMU	SIPD	
	243	BULD	KRNC	PAMU	SIPD	
	244	KRNC	CINE	BEDA	BULD	SIPD
	245	BAFA	CINE	SOKE	TIRE	SIPD
5	246	BAFA	DOBE	SOKE	TERZ	SIPD
	247	AHME	DOBE	SEFE	TERZ	SIPD
	248	BAYI	ODME	BEDA	TIRE	SIPD

IfAG and finally adding the Durham observations to the solutions. As discussed, GAMIT enables us to merge fresh data with solutions without cleaning those previously reduced. In our solutions, we used 30 second samples of regional and global observations.

The constellation was set unhealthy during the first half of the 1989 experiment for real-time navigation purposes, reducing the quality of pseudo-range measurements. This did not significantly affect our analyses, since we estimated orbital parameters and used carrier phase observations (pseudo-range measurements for timing).

Global tracking data were provided by NGS in ARGO format for five global sites: ONS0, RICM, TROM, WSFM, and YKN1 (Figure B-7). TI4100 receivers and antennas were deployed at the Onsala (COR 4.11), Tromso (COR 4.11) and Yellowknife (COR 4.8) sites. GPS data at the Richmond and Westford sites were acquired by

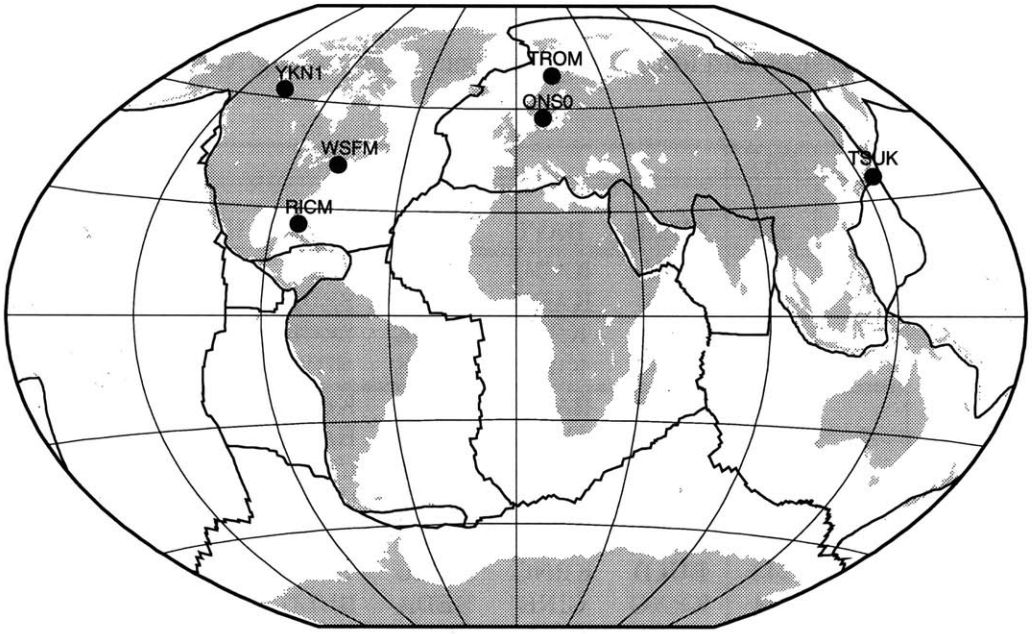

Figure B-7: Distribution of core global tracking sites included in the analyses of the 1989 experiment.

Minimac 2816AT receivers (1.61) and antennas.

We simultaneously analyzed the regional and global tracking sites. Availability and quality of the global tracking data during the 1989 experiment, however, posed serious problems (Table B.11). Wettzell data (Minimac), when included in the solutions, increased the nrms of GAMIT solutions, causing double-difference phase residuals to be other than "flat". In a nutshell, we decided to remove Wettzell from our reductions. The absence of Wettzell and the scarcity of data from the North American sites were typical of the problems we initially encountered. Further, due to inconsistent phase residuals during data reduction, we had to either partially or entirely delete data from RICM on days 240, 241, 245 and 248, and from WSFM on day 240. The weakest coverage happened on days 240 and 252: only two sites were usable.

We had no major problems in cleaning or reducing our observations, or those

Table B.11: Core Global tracking sites and long-arc groupings: 1989 experiment.

ARC	DAY	GPS SITES				
1	232	ONS0	RICM	WSFM	YKN1	
	233	ONS0	RICM	WSFM	YKN1	
2	234	ONS0	RICM	TROM	WSFM	YKN1
	235	ONS0	RICM	TROM	WSFM	YKN1
	236	ONS0	RICM	TROM	WSFM	YKN1
3	237	ONS0	RICM	TROM	WSFM	YKN1
	238	ONS0	RICM	TROM	WSFM	YKN1
	239	ONS0	RICM	TROM	WSFM	YKN1
	240	ONS0	YKN1			
4	241	TROM	WSFM	YKN1		
	242	RICM	TROM	WSFM	YKN1	
	243	RICM	TROM	WSFM	YKN1	
	244	RICM	TROM	WSFM	YKN1	
	245	RICM	TROM	WSFM	YKN1	
5	246	RICM	TROM	WSFM		
	247	ONS0	RICM	TROM	WSFM	
	248	ONS0	TROM	WSFM		
	249	ONS0	RICM	WSFM		
6	250	ONS0	RICM	WSFM		
	251	ONS0	RICM	WSFM		
	252	ONS0	WSFM			

collected by IfAG. In our final solutions, however, we decided to remove the first three occupations of the Kemah site (renamed as KEMX) because of inconsistent baseline estimates. The receiver operated at this site manifested internal oscillator malfunctions[8] and eventually failed on the 6th day of the experiment. We deleted PRNs 6 and 11 from KORK because of noisy phase residuals. Due to poor data content, we were forced to delete PRN 3 from all sites on day 252.

The Bozdağ network data were provided by GCM to promote a unified 1st degree geodetic network for Turkey. Observations taken at some of these sites were of poor quality, being full of gaps and cycle slips. We suspect that some of the operators ac-

[8]This fact was verified by Trimble quite some time later, thus acquitting the author, who operated this receiver in the field.

tually stopped recording as they supplied new PRN scenarios to the TI4100 receivers, creating gaps and cycle-slips on all channels. While we tried to repair most of these, we were compelled to discard some portions of the one-way phase data. Alas, we had to introduce several ambiguity parameters, weakening our results. Due to insufficient clean data for the solutions we "lost" some sites on certain days: ALSE (241, 242), BAYI (248), BEDA (248), CINE (245), GOMA (241), KRNC (244), TERZ (246, 247), TIRE (245), and USUM (240).

We extended the processing sessions to 13 hours to provide more double-difference observations from global tracking sites. As a result, we crossed the day boundary such that the beginning of observations taken on day 238 moved to day 237. We started with broadcast ephemerides. (Eventually, we iterated the orbital parameters and site positions with the GLOBK estimates.) Later, we divided the experiment into six long-arcs and obtained quasi-observations by applying loose constraints to the satellites. We have not attempted to fix the ambiguity parameters to integers because of the large interstation distances. We considered two sets of data for reduction: that including all observed sites, and that excluding the Bozdağ network sites. All long-arc, single-session GAMIT solutions, regardless of the sites used, produced a nrms of $\sim$0.25 (Table B.12). Solutions in which all sites were incorporated produced similar nrms. Table B.12 indicates that the double-difference data is free of cycle-slips, and that the rms of LC phase residuals is below 20 mm.

In step-two (GLOBK solution), it was extremely difficult to obtain the right process noise and a plausible repeatability, due to complications with the regional data, limited availability of global trackers. We initially considered the **T**, **M**, **L**, **M_L**, **T_L**, and **T_M** sets of process noise, settling with **M**. We attributed "bad" repeatabilities to poor determination of orbital parameters (insufficient fiducial control) and decided to incorporate some sites from the regional network (ANKA, MELE, YIG2, DIYA and SIPD), estimating them deterministically. Estimating only one of these sites

Table B.12: Normalized RMS of long-arc, single-session GAMIT solutions: 1989 experiment.

GPS DAY	tight solution	loose solution
232	0.206	0.194
233	0.240	0.234
234	0.252	0.236
235	0.234	0.223
236	0.247	0.237
237	0.236	0.222
238	0.262	0.236
239	0.265	0.249
240	0.238	0.223
241	0.253	0.240
242	0.257	0.244
243	0.234	0.222
244	0.231	0.223
245	0.245	0.237
246	0.213	0.206
247	0.227	0.217
248	0.248	0.238
249	0.197	0.184
250	0.213	0.207
251	0.225	0.218
252	0.173	0.161

deterministically reduced the wrms scatter. We noticed, however, the proportional errors remained high. We forced a second, and finally a third site in the solution to be deterministically estimated. In all cases, we compared solutions to avoid any bias that may have been inherited by removing a baseline from the repeatability analyses (Table B.13). We first performed this type of solution with the eastern Turkey sites and then with the entire 1989 data set. Such a scheme provided us with a reasonable short-term repeatability and assisted us in detecting outliers (Tables B.13 and B.14).

All one-site-deterministic solutions provided improved repeatabilities. The error model parameters obtained from the wrms scatter of these solutions were comparable. This indicated that the orbital parameters were better determined by having a network stretching from YKN1 to Turkey. We performed further solutions in which two

Table B.13: Short-term repeatability: 1989 eastern Turkey experiment

Solution Descriptor	N-S component a (mm)	N-S component b (ppb)	N-S component mean nrms	E-W component a (mm)	E-W component b (ppb)	E-W component mean nrms	U-D component a (mm)	U-D component b (ppb)	U-D component mean nrms	Length a (mm)	Length b (ppb)	Length mean nrms
L	1.89	28.80	0.55	3.73	77.20	0.91	26.96	16.26	0.69	4.58	68.87	1.09
T	4.60	25.14	1.00	12.78	33.44	0.94	20.56	42.44	1.08	12.19	33.26	1.17
M‡	3.07	13.54	0.49	8.91	39.18	0.78	24.79	25.54	0.92	7.70	31.92	0.85
T_L	3.90	15.11	0.52	8.35	56.73	0.99	23.72	20.61	0.84	4.51	49.94	1.04
T_M	4.33	25.00	0.96	12.91	35.95	0.98	20.22	43.23	1.08	11.81	36.52	1.22
M_d1	2.92	14.97	0.64	11.67	42.88	1.08	22.89	17.42	0.93	5.51	39.87	1.02
M_d1_d4	4.27	6.57	0.68	11.84	13.94	0.86	19.68	0.00	0.87	7.43	16.71	0.87
M_d1_d4_d2†	3.49	5.06	0.59	10.38	9.66	0.77	17.18	0.00	0.83	7.34	12.24	0.82
M_d1_d2	3.62	10.78	0.62	9.37	30.64	0.89	21.65	14.27	0.92	5.30	29.88	0.89
M_d1_d2_d3	3.42	10.89	0.65	9.09	27.94	0.86	20.59	8.71	0.91	5.53	27.44	0.89
M_d4	2.98	17.23	0.77	11.14	34.49	0.98	23.49	20.66	1.01	4.69	35.74	0.97
M_d2	3.06	17.38	0.70	11.19	41.17	0.93	23.89	29.57	0.98	5.32	40.58	0.94
M_d2_d4	4.01	5.41	0.58	11.81	10.95	0.79	20.98	0.58	0.91	8.16	16.62	0.86
M_d3	3.23	16.11	0.73	12.43	34.40	0.97	22.35	23.90	0.97	6.59	35.86	0.97
M_d3_d4	4.47	0.49	0.59	12.84	10.80	0.87	21.12	0.58	0.94	8.90	16.13	0.94
M_d3_d2	3.41	11.84	0.64	9.79	30.83	0.89	22.47	15.35	0.95	5.93	30.42	0.92

d1(ANKM), d2(MELE), d3(YIG2), d4(DIYA) and d5(SIPD) denote solutions in which regional sites are deterministically estimated.
† Preferred solution. Obtained from moderate constraints applied to all satellites (*cf.* Table B.2).
‡ Reference solution (*cf.* Table B.2).

sites (ANKA-MELE, ANKA-YIG2, YIG2-MELE, MELE-DIYA, and ANKA-DIYA) were deterministically estimated. In other words, we deterministically estimated one baseline in our regional network. The ANKA-MELE, ANKA-YIG2 or YIG2-MELE baselines involved solutions which provided a sharp decrease in the north component wrms scatter, but very poor results in the east. When we deterministically estimated the ANKA-DIYA or MELE-DIYA baseline, we noticed a distinct decrease in the east component wrms scatter, but relatively less improvement in the north. The improved wrms scatter for different components was closely related to the direction of the baselines chosen. The ANKA-MELE, ANKA-YIG2 and YIG2-MELE baselines are approximately north-south oriented and so provided improvements in this component. On the other hand, ANKA-DIYA and MELE-DIYA baselines are east-west oriented, and reduced the east-west component scatter. Subsequently, we considered solutions in which a triplet of sites were deterministically estimated: ANKA-MELE-DIYA, ANKA-MELE-SIPD and ANKA-MELE-YIG2. These solutions, using the eastern

Turkey observations, provided an enhanced wrms scatter and showed that no outliers existed. Figure B-8 shows the short-term precision obtained from a solution in which ANKA-MELE-DIYA was deterministically estimated as moderate process (**M**) noise set was applied to the satellites. On the average, the nrms of most of this solution's baselines are below 2. (Figure B-9)

In these GLOBK solutions it was necessary to remove some quasi-observations (days 233, 238 and 252) due to their high χ^2/f and inconsistent baselines estimates. These days, however, were not "Bumps in the Night"[9] days [Ison et al., 1992].

We applied this same scheme to the entire data set, including the Bozdağ network observations (Table B.14). Since Sipildağ (SIPD) had been observed over several days, we included it as a deterministic site. Precision analyses confirmed our judg-

Table B.14: Short-term repeatability (all sites included): 1989 experiment.

Solution Descriptor	N-S component a (mm)	N-S component b (ppb)	N-S component mean nrms	E-W component a (mm)	E-W component b (ppb)	E-W component mean nrms	U-D component a (mm)	U-D component b (ppb)	U-D component mean nrms	Length a (mm)	Length b (ppb)	Length mean nrms
M‡	5.46	9.46	0.54	14.88	35.96	0.89	30.35	22.67	1.01	11.55	32.83	0.97
M_d1	5.63	15.72	0.84	12.72	49.75	1.26	28.23	6.68	0.97	8.97	46.63	1.29
M_d4	5.21	18.82	0.97	13.09	34.15	1.02	28.28	16.72	1.06	9.06	35.46	1.10
M_d1_d4	5.12	12.44	0.94	11.34	25.05	0.95	25.25	15.70	1.03	8.91	26.14	1.06
M_d2_d4	5.04	9.07	0.77	12.43	18.27	0.83	24.83	18.61	1.04	10.16	20.64	0.95
M_d1_d4_d2	5.18	9.55	0.88	10.67	17.59	0.82	23.03	17.80	1.03	8.70	19.03	0.94
M_d1_d4_d5	7.00	9.29	1.03	11.57	15.03	0.82	25.72	3.84	1.03	10.13	16.54	0.96
M_d1_d2_d5	6.84	11.11	1.06	9.76	30.00	0.99	27.26	0.00	1.06	7.69	31.03	1.15
M_d3_d4†	5.08	9.69	0.85	11.67	25.61	0.98	24.88	16.27	1.04	9.15	26.69	1.11

d1(ANKM), d2(MELE), d3(YIG2), d4(DIYA) and d5(SIPD) denote solutions in which regional sites are deterministically estimated.
† Preferred solution. Obtained from moderate constraints applied to all satellites (*cf.* Table B.2).
‡ Reference solution (*cf.* Table B.2).

ments concerning the sites "lost" in step-one with GAMIT. We had to discard BEDA, GOMA, and TIRE. (Long-term repeatability analyses led us to also discard AKGA). Since most of the Bozdağ sites were repeated only twice it was impossible to pin-

[9]Unscheduled orbit events.

point the problematic day and/or the one-way observations for AKCA and BAFA. In our final analyses we removed AKCA, ALSE, BAFA, BAYI, BEDA, GOMA, KRNC, TERZ, TIRE, and USUM as well. Because we had to omit days 233, 238 and 252 from our solutions, no repeatability statistics are available for KINI, KIRK or KOBE. Figures B-10 and B-11 show repeatabilities obtained when Bozdağ sites were included in the solutions excluding the discarded sites ($\sim$ 10 cm wrms scatter.) The repeatabilities are significantly worse than those for eastern Turkey (Figure B-8). The nrms values are similar (Figure B-9), indicating higher formal uncertainties for the Bozdağ baselines.

To investigate the propagated formal uncertainties of baseline estimates, we estimated all regional sites deterministically (*cf.* Table B.3, **D** set of constraints). Again, we first looked at the eastern Turkey network:

σ_{NS}(mm) =	1.98(mm)	+	11.29x10^{-3} L(km)	@500km baseline:	7.62(mm)
σ_{EW}(mm) =	5.12(mm)	+	17.95x10^{-3} L(km)	@500km baseline:	14.09(mm)
σ_{UD}(mm) =	13.12(mm)	+	5.08x10^{-3} L(km)	@500km baseline:	15.66(mm)
σ_{BL}(mm) =	4.12(mm)	+	11.85x10^{-3} L(km)	@500km baseline:	10.04(mm).

The baseline formal uncertainties for this network could well be defined by a linear polynomial, provided that the first three days of observations (during which the receiver malfunctioned) at the Kemah sites (KEMX instead of KEMA) were deleted. We found that the formal uncertainties for baseline estimates were below 15 mm. The GLOBK χ^2/f for this solution was 1.02.

We expected a similar result from a solution which included all sites observed in Turkey during the 1989 experiment. To our surprise, the formal uncertainties for baseline estimates displayed several trends. Each one of these trends corresponded to baselines involving a certain Bozdağ network site. The formal uncertainties of the Bozdağ network baselines were at least twice those of the eastern Turkey network, at comparable lengths, provided that GOMA, TIRE, BEDA, AKCA, BAFA, ALSE,

TERZ, USUM, DOBE, HAPA, KOBE, and BAYI were discarded. The χ^2/f for the entire network solution rose to 1.5. When GOMA, TIRE, BEDA, AKCA, BAFA, ALSE, TERZ, USUM, DOBE, HAPA, KOBE, and BAYI were included, the formal uncertainties of baseline estimates manifested an additional 15 mm and 60 mm in the north and east components, respectively.

The weakness of fiducial control during the 1989 experiment is reflected in the parameter estimates. Though we can justify using the eastern Turkey network observations on a statistical basis, it is quite difficult to make any conclusive remarks about the Bozdağ network due to an insufficient temporal distribution. We decided to keep the Bozdağ data set even though more than half of the observations were discarded to provide an additional repeat observation at the western Turkey sites.

We generated two sets of the compact quasi-observations, one including all observed sites and one excluding the Bozdağ network sites. We applied moderately loose stochastic constraints to the satellites with which the best short-term repeatabilities had been obtained. Because regional sites were deterministically estimated they were used implicitly in determining the orbital parameters. (We later used the compact quasi-observations with all sites, since no noticeable differences were obtained from the velocity field of either solution.)

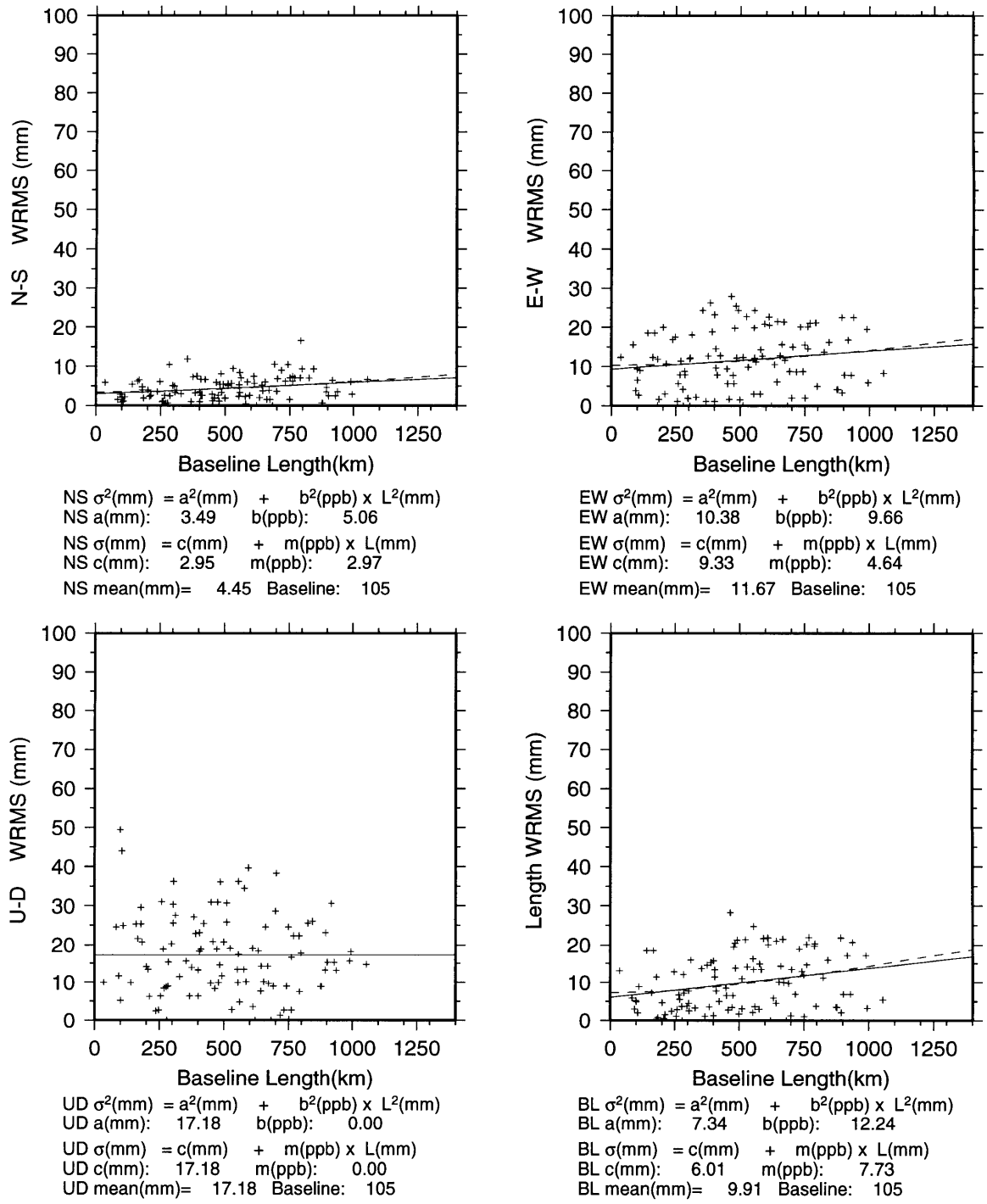

Figure B-8: The wrms scatter and model parameters of NS, EW, UD components and length, as a function of baseline length. They are obtained from the 1989 experiment with moderate (**M**) stochastic constraints applied to the satellites. ANKA, DIYA and MELE are deterministically estimated. Observations in the Bozdağ network are excluded. The wrms of baselines with 2 or more repeat observations are shown. Dashed line is a functional in the form of $\sigma^2 = a^2 + b^2L^2$. Continuous line is a linear fit to the wrms scatter ($\sigma = c + m\ L$).

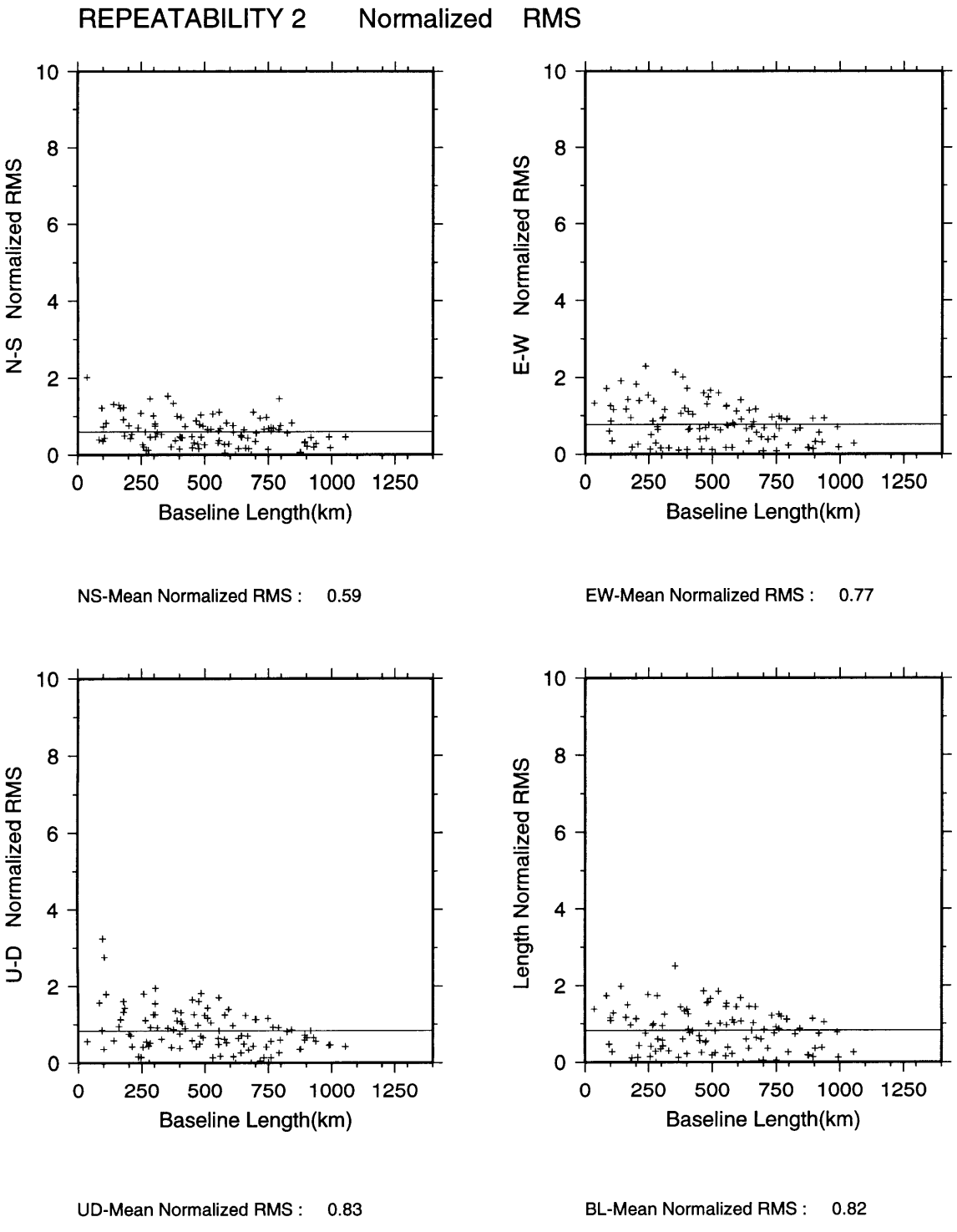

Figure B-9: The nrms scatter of NS, EW, UD components and length [for the solution described in Figure B-8], as a function of baseline length. They are obtained from the 1989 experiment with moderate (**M**) stochastic constraints applied to the satellites. ANKA, DIYA and MELE are deterministically estimated. Observations in the Bozdağ network are excluded. Continuous line represents the mean nrms scatter.

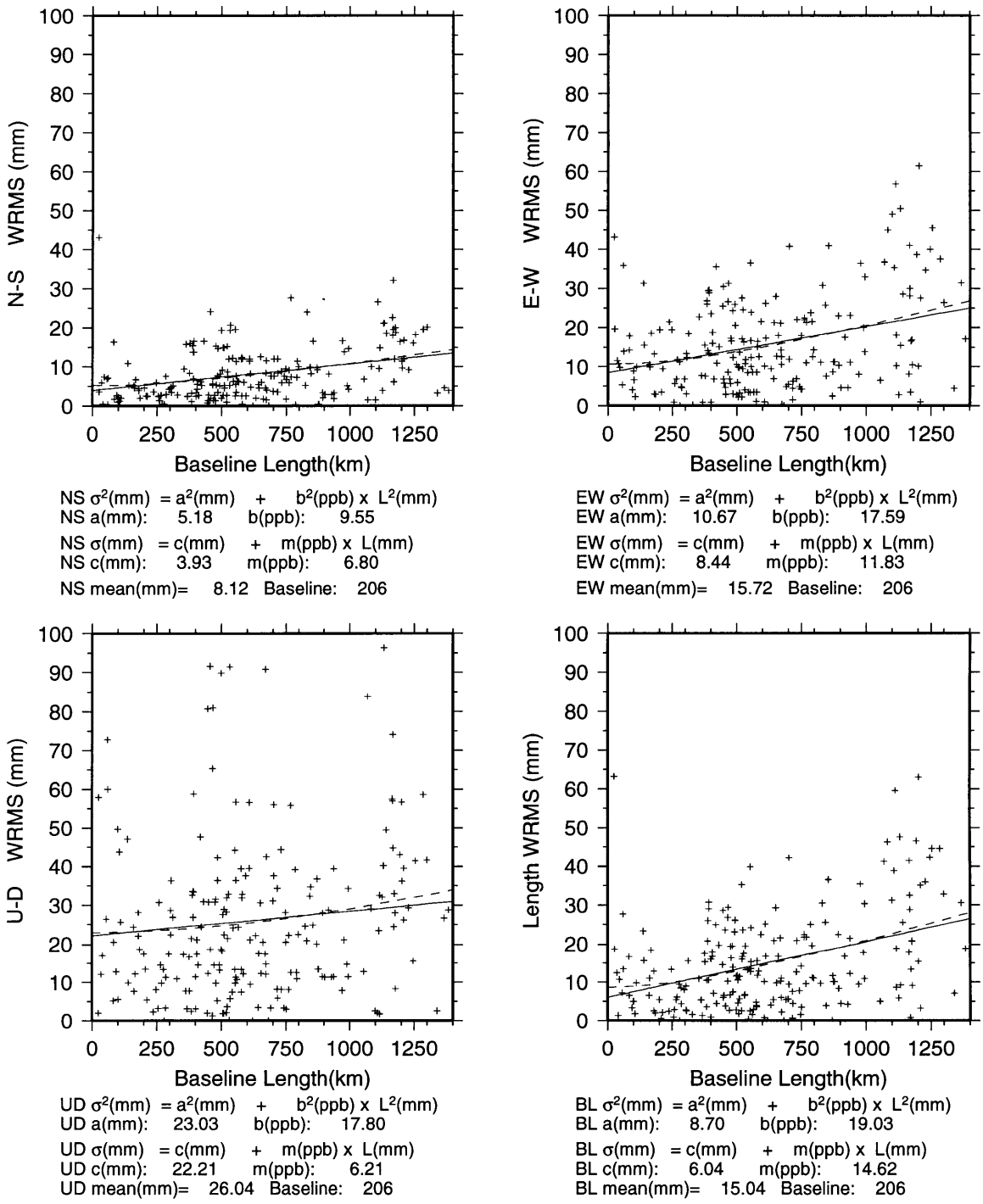

Figure B-10: The wrms scatter and model parameters of NS, EW, UD components and length, as a function of baseline length. They are obtained from the 1989 experiment with moderate (**M**) stochastic constraints applied to the satellites. ANKA, DIYA and MELE are deterministically estimated. Bozdağ sites are included. The wrms of baselines with 2 or more repeat observations are shown. Dashed line is a functional in the form of $\sigma^2 = a^2 + b^2L^2$. Continuous line is a linear fit to the wrms scatter ($\sigma = c + m\ L$).

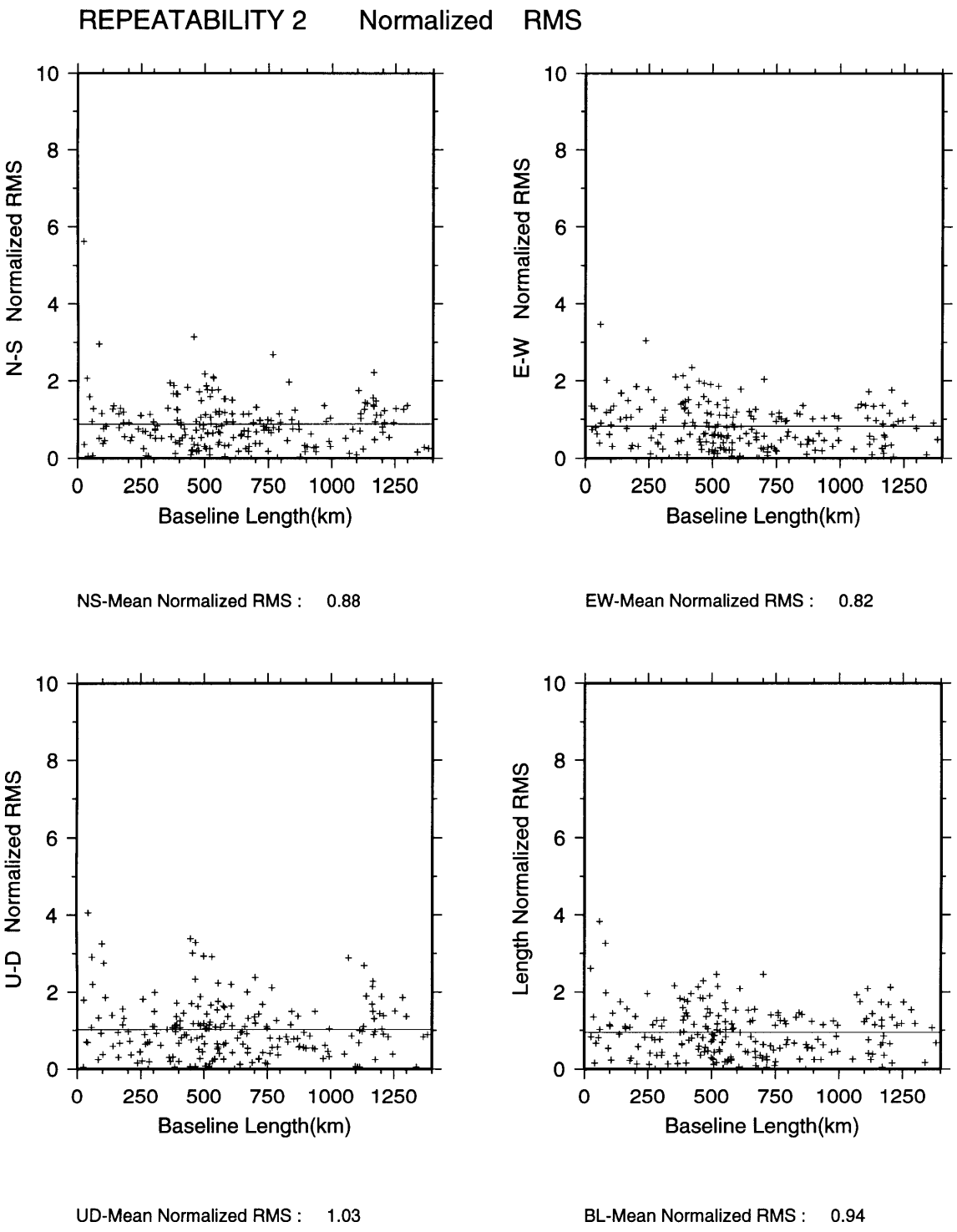

Figure B-11: The nrms scatter of NS, EW, UD components and length [for the solution described in Figure B-10], as a function of baseline length. They are obtained from the 1989 experiment with moderate (**M**) stochastic constraints applied to the satellites. ANKA, DIYA and MELE are deterministically estimated. All 1989 experiment sites are included. Continuous line represents the mean nrms scatter.

B.2.3 1990 Western Turkey Experiment

During the summer/fall of 1990, between August 26 and September 29 (days 240–268), we undertook another regional GPS survey in western Turkey, in collaboration with the GCM. During this experiment we reobserved ten GPS sites in western Turkey (AKGA, ANKA, ANTU, CEIL, CINE, IKAN, ISME, MEKE, PAMU, and ULDA) that had been established in 1988 (Figure B-12). Simultaneous observations were carried out by IfAG at three SLR sites (MELE, YIGI and YOZG) in central Turkey,

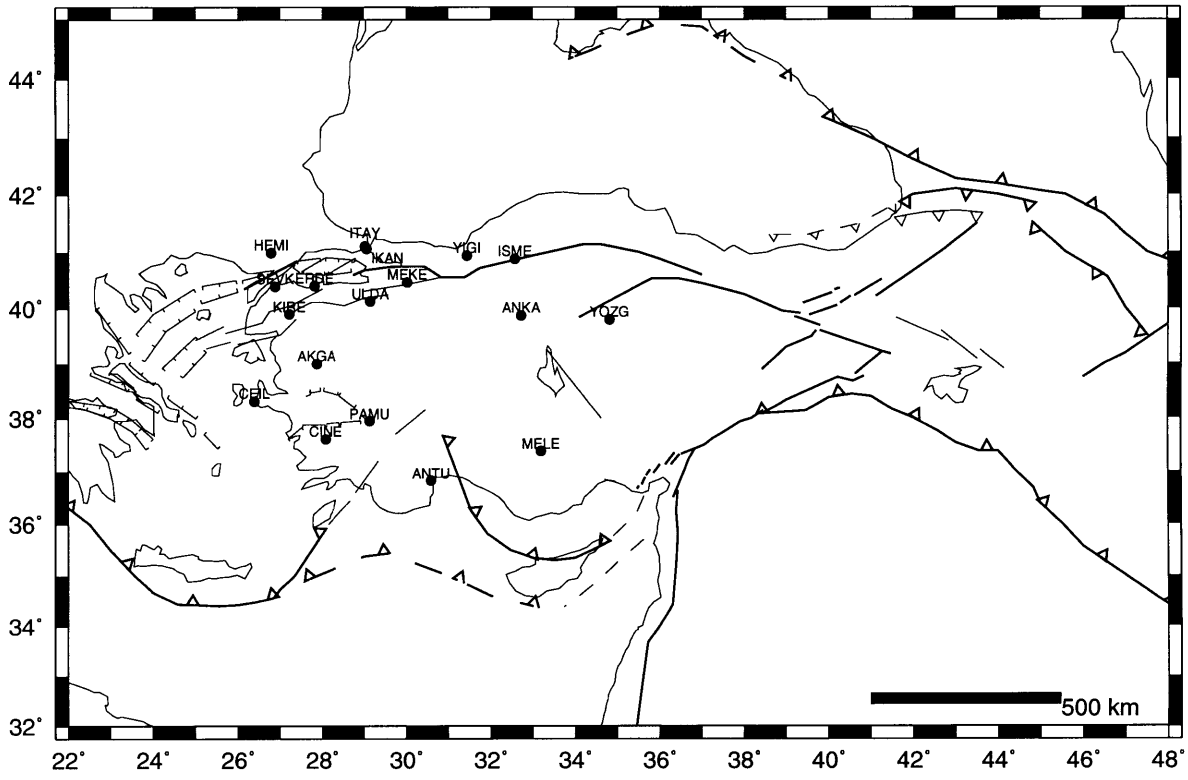

Figure B-12: Distribution of regional sites occupied during the 1990 experiment.

and by ETHZ in the Marmara region. To tie all independent regional networks together for the GCM first degree geodetic network, we replenished our core data set with 3 observations at the SLR sites and 5 sites in the Marmara network (ITAY, KIRE, SEVK, ERDE and HEMI). With the 1990 western Turkey experiment we

made GPS observations for 20 days at a total of 18 sites, by tracking 10 satellites (PRNs 2, 3, 6, 9, 11, 12, 13, 16, 18, and 20). PRNs 2 and 16 were in eclipsing season. PRN 14 started to eclipse on the fifth day of the experiment.

We used Trimble SST receivers and antennas with data acquisition software version 4.1. The IfAG receivers and antennas at MELE and YIGI were Minimac. Both receivers had data acquisition software version 1.61. A Trimble SLD receiver, navigation software 3.28, was used at Yozgat (YOZG). Marmara sites were occupied by WM-102 receivers and antennas. Their RINEX data were provided by GCM. We made GPS observations at ANKA throughout the experiment and at other sites on three to seven consecutive days, except MEKE, where we observed for only 2 days. Observations at the SLR sites were primarily made in the first half of our experiment: 16 days at MELE, 14 days at YIGI and 5 days at YOZG. ITAY was observed for 7 days. The rest of the Marmara sites were occupied twice. Table B.15 shows the sites observed during the 1990 western Turkey experiment.

Global tracking data were provided by NGS in ARGO format. We used 4 sites: ONS0, RICM, WETM, and WSFM (Figure B-13). Tromso observations were only available during the first quarter of the experiment. We did not use them in our analyses because data sampling at this site varied (4 minutes or more) and provided insufficient data for editing. Minimac receivers (navigation software 1.61) and antennas were operating at RICM, WSFM and WETM. A TI4100 receiver and antenna was operating at Onsala, running CORE version 4.11. Data acquisition times varied with this receiver: even seconds on days 248, 252 and 262, 59.08 and 0.08 seconds on other days (CORE version 4.1). All four sites were available, except on days 244, 261, and 266 (Table B.16).

We started with short-arc, single-session GAMIT solutions (30 second samples of data) and broadcast orbits (later iterating the orbital parameters). We cleaned and

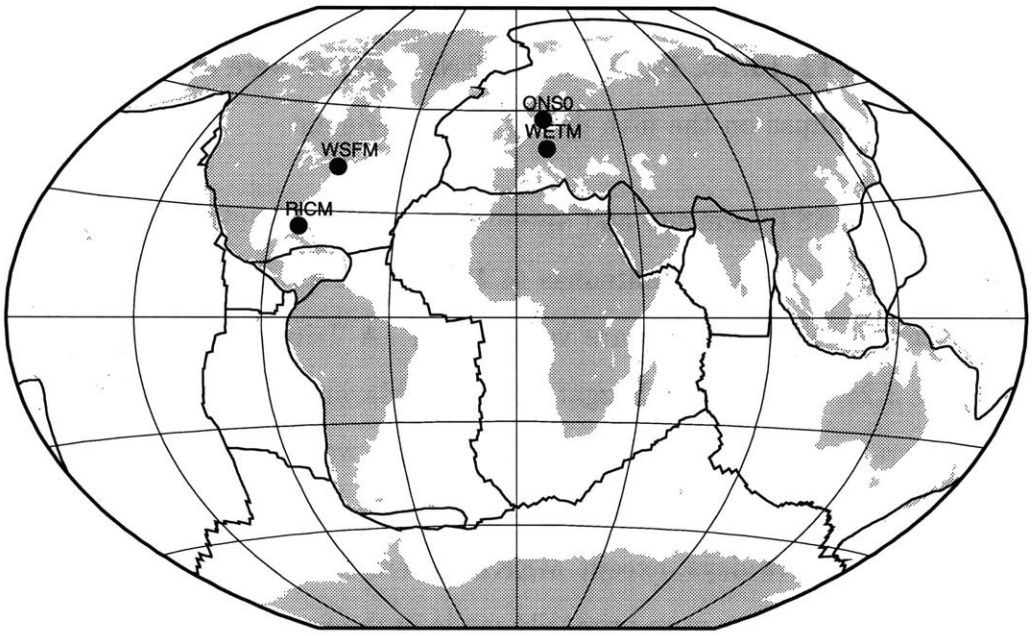

Figure B-13: Distribution of core global tracking sites included in the analyses of the 1990 western Turkey experiment.

edited the data. Though we tried hard to get a viable reduction for days 258 and 265, we failed to obtain an admissible nrms and had to discard these days. Because several repeat observations were available on other days, we did not lose any sites. We suspect that more than one satellite had unscheduled thrusts, although solutions for unscheduled small thrusts by Ison et al. [1992] do not finger these days. Because the GPS observations at the SLR and Marmara sites were provided much later, we added them to our reductions as they became available. Marmara network data were poor in quality and not continuous, requiring additional ambiguity parameters. Some one-ways had cycle-slips beyond repair and we had to leave a number of ambiguity parameters behind, weakening our results. ONS0 had to be deleted on day 261 due to inconsistent phase residuals.

After cleaning the data we applied the standard two-step approach. First, we divided the experiment into 8 long-arcs, each 3 to 4 days long. By applying tight

Table B.15: Regional sites and long-arc groupings: 1990 western Turkey experiment.

ARC	DAY	GPS SITES							
1	240	ANKA	ANTU	MELE	PAMU	YIGI			
	241	ANKA	ANTU	MELE	PAMU				
	242	ANKA	ANTU	MELE	PAMU	YIGI			
	243	ANKA	ANTU	MELE	YIGI				
2	244	ANKA	ANTU	CINE	MELE	YIGI			
	245	ANKA	ANTU	CINE	MELE	YIGI			
	246	ANKA	ANTU	CINE	MELE	YIGI			
	247	ANKA	CINE	MELE	YOZG				
3	248	ANKA	CEIL	CINE	MELE	YIGI	YOZG		
	249	ANKA	CEIL	CINE	MELE	YIGI			
	250	ANKA	CEIL	CINE	MELE	YIGI			
	251	ANKA	CEIL	MELE	YIGI	YOZG			
4	252	AKGA	ANKA	CEIL	MELE	YIGI	YOZG		
	253	AKGA	ANKA	CEIL	MELE	YIGI	YOZG		
	254	AKGA	ANKA	CEIL					
5	257	AKGA	ANKA	IKAN					
	257	AKGA	ANKA	IKAN	ITAY				
	259	AKGA	ANKA	IKAN	ITAY	YIGI			
	260	ANKA	IKAN	ITAY	KIRE	YIGI			
6	261	ANKA	ERDE	IKAN	ITAY	KIRE	ULDA		
	262	ANKA	IKAN	ULDA	YIGI				
	262	ANKA	ERDE	IKAN	ITAY	ULDA	YIGI		
	263	ANKA	ERDE	HEMI	IKAN	ITAY	SEVK	ULDA	YIGI
7	264	ANKA	ERDE	HEMI	ISME	ITAY	SEVK	ULDA	YIGI
	266	ANKA	ISME	ULDA	YIGI				
8	267	ANKA	ISME	MEKE					
	268	ANKA	ISME	MEKE					

and loose constraints to the sites and satellites we performed long-arc, single-session GAMIT solutions with two sets of data: one with Marmara sites, the other without. Table B.17 shows the nrms obtained from each long-arc, single-session GAMIT solution. A nrms of ~0.25 was obtained for each day using the western Turkey sites, indicating that the rms of LC residuals were less than 15 mm. Similar results were achieved when the Marmara sites were included in the solutions.

As a part of the second step, we applied **T**, **M**, **L**, **T_M**, and **T_L** sets of pro-

Table B.16: Core global tracking sites and long-arc groupings: the 1990 western Turkey experiment.

ARC	DAY	GPS SITES			
1	240	WETM	WSFM	ONS0	RICM
	241	WETM	WSFM	ONS0	RICM
	242	WETM	WSFM	ONS0	RICM
	243	WETM	WSFM	ONS0	RICM
2	244	WSFM	ONS0	RICM	
	245	WETM	WSFM	ONS0	RICM
	246	WETM	WSFM	ONS0	RICM
	247	WETM	WSFM	ONS0	RICM
3	248	WETM	WSFM	ONS0	RICM
	249	WETM	WSFM	ONS0	RICM
	250	WETM	WSFM	ONS0	RICM
	251	WETM	WSFM	ONS0	RICM
3	252	WETM	WSFM	ONS0	RICM
	253	WETM	WSFM	ONS0	RICM
	254	WETM	WSFM	ONS0	RICM
5	257	WETM	WSFM	ONS0	RICM
	259	WETM	WSFM	ONS0	RICM
	259	WETM	WSFM	ONS0	RICM
	260	WETM	WSFM	ONS0	RICM
6	261	WETM	WSFM	RICM	
	262	WETM	WSFM	ONS0	RICM
	263	WETM	WSFM	ONS0	RICM
7	264	WETM	WSFM	ONS0	RICM
	264	WETM	WSFM	ONS0	RICM
	266	WSFM	ONS0	RICM	
8	267	WETM	WSFM	ONS0	RICM
	268	WETM	WSFM	ONS0	RICM

cess noise to investigate the short-term repeatability, using the quasi-observations of the western Turkey network measurements. We did not observe any significant enhancement in short-term repeatability as looser stochastic constraints were applied to the eclipsing satellites. Tight (**T**) stochastics yielded smaller proportional errors (Table B.18). In the north component the wrms scatter was as much as 10 mm. The east component wrms scatter was slightly worse; between 15 and 20 mm. The anomalous wrms values in the east and vertical components are due to the poor estimates of baselines on day 262.

Table B.17: Normalized RMS of long-arc, single-session GAMIT solutions: the 1990 western Turkey experiment.

GPS DAY	tight solution	loose solution
240	0.210	0.205
241	0.214	0.207
242	0.208	0.204
243	0.215	0.210
244	0.221	0.219
245	0.212	0.207
246	0.230	0.227
247	0.181	0.173
248	0.192	0.190
249	0.202	0.197
250	0.199	0.190
251	0.171	0.168
252	0.188	0.183
253	0.223	0.215
254	0.216	0.211
257	0.137	0.133
259	0.187	0.183
260	0.192	0.189
261	0.209	0.205
262	0.116	0.105
263	0.245	0.243
264	0.225	0.221
266	0.186	0.180
267	0.188	0.185
268	0.195	0.191

Later, when the Marmara network data were added to our solutions, we witnessed an increase in nrms scatter (Table B.19). Using the **T** type process noise set also resulted in the best repeatabilities. There was, however, a significant degradation (15 to 20 mm) in the east repeatabilities, as depicted in Figure B-16. Baselines to KIRE were responsible for the outliers in the wrms scatter of the north component. Removing this site did not reduce the east component's wrms scatter. The 70-90 mm wrms in the vertical was caused by SEVK. There were only two observations taken at these Marmara sites. We decided to remove KIRE from our solutions.

We also investigated how well the baselines were determined by solutions in which

Table B.18: Short-term repeatability (excluding Marmara network sites): 1990 western Turkey experiment.

Solution Descriptor	N-S component a (mm)	N-S component b (ppb)	N-S component mean nrms	E-W component a (mm)	E-W component b (ppb)	E-W component mean nrms	U-D component a (mm)	U-D component b (ppb)	U-D component mean nrms	Length component a (mm)	Length component b (ppb)	Length component mean nrms
S_L	1.83	38.13	1.28	9.26	34.18	0.98	22.67	15.47	0.92	6.26	34.80	1.07
S_M	2.93	19.27	1.06	7.11	16.61	0.80	16.47	30.04	0.90	5.64	19.79	0.95
S_T†	3.71	10.16	1.02	6.81	13.21	0.86	16.60	21.02	0.91	6.28	12.52	0.99
S_T_L	3.92	10.62	1.03	7.52	12.00	0.88	16.94	19.75	0.91	6.66	12.28	1.00
S_T_M	3.86	10.40	1.03	7.80	11.35	0.90	16.67	20.37	0.90	6.94	11.70	1.02

† Preferred solution. Obtained from applying tight constraints to all satellites (*cf.* Table B.2).

Table B.19: Short-term repeatability (including all sites): 1990 western Turkey experiment.

Solution Descriptor	N-S component a (mm)	N-S component b (ppb)	N-S component mean nrms	E-W component a (mm)	E-W component b (ppb)	E-W component mean nrms	U-D component a (mm)	U-D component b (ppb)	U-D component mean nrms	Length component a (mm)	Length component b (ppb)	Length component mean nrms
S_L	1.48	34.24	1.00	8.61	38.59	0.96	23.38	9.84	0.88	5.48	39.73	1.02
S_M	2.73	19.79	0.93	7.72	23.57	0.87	21.13	18.39	0.91	5.69	27.99	0.98
S_T†	3.91	12.45	0.99	7.58	22.10	0.96	20.67	0.60‡	0.91	7.48	22.58	1.11
S_T_L	4.41	13.43	1.02	8.12	21.29	0.96	20.82	0.64‡	0.91	8.12	21.88	1.12
S_T_M	4.15	13.54	1.02	8.38	22.12	1.00	20.19	0.60‡	0.89	8.16	22.80	1.15

† Preferred solution. Obtained from tight constraints applied to all satellites (*cf.* Table B.2).
‡ Small proportional errors are artifacts of outliers in this component.

we kept all sites deterministic and applied tight stochastic constraints to the satellites. Both of the data sets (western Turkey and all sites excluding KIRE) gave similar results and the χ^2/f did not change (1.1). The formal uncertainties of baseline estimates are as follows:

$$\begin{aligned}
\sigma_{NS}(\text{mm}) &= 1.25(\text{mm}) + 4.77\text{x}10^{-3}\ \text{L(km)} \quad \text{@500km baseline: } 3.63(\text{mm}) \\
\sigma_{EW}(\text{mm}) &= 3.01(\text{mm}) + 5.73\text{x}10^{-3}\ \text{L(km)} \quad \text{@500km baseline: } 5.88(\text{mm}) \\
\sigma_{UD}(\text{mm}) &= 8.24(\text{mm}) + 1.94\text{x}10^{-3}\ \text{L(km)} \quad \text{@500km baseline: } 9.21(\text{mm}) \\
\sigma_{BL}(\text{mm}) &= 2.45(\text{mm}) + 3.06\text{x}10^{-3}\ \text{L(km)} \quad \text{@500km baseline: } 3.98(\text{mm}).
\end{aligned}$$

The uncertainties in the horizontal components are less than 6 mm for a 500 km baseline. This is better than those obtained in the 1988 and 1989 Turkey experiments

by a factor of 2.

To prevent any adverse effects which may have been caused by the Marmara network data, we obtained two sets of compact quasi-observations: one with all sites, the other without Marmara network data. (We later used the compact quasi-observations with all sites since no noticeable differences were obtained from the velocity field of either solution.)

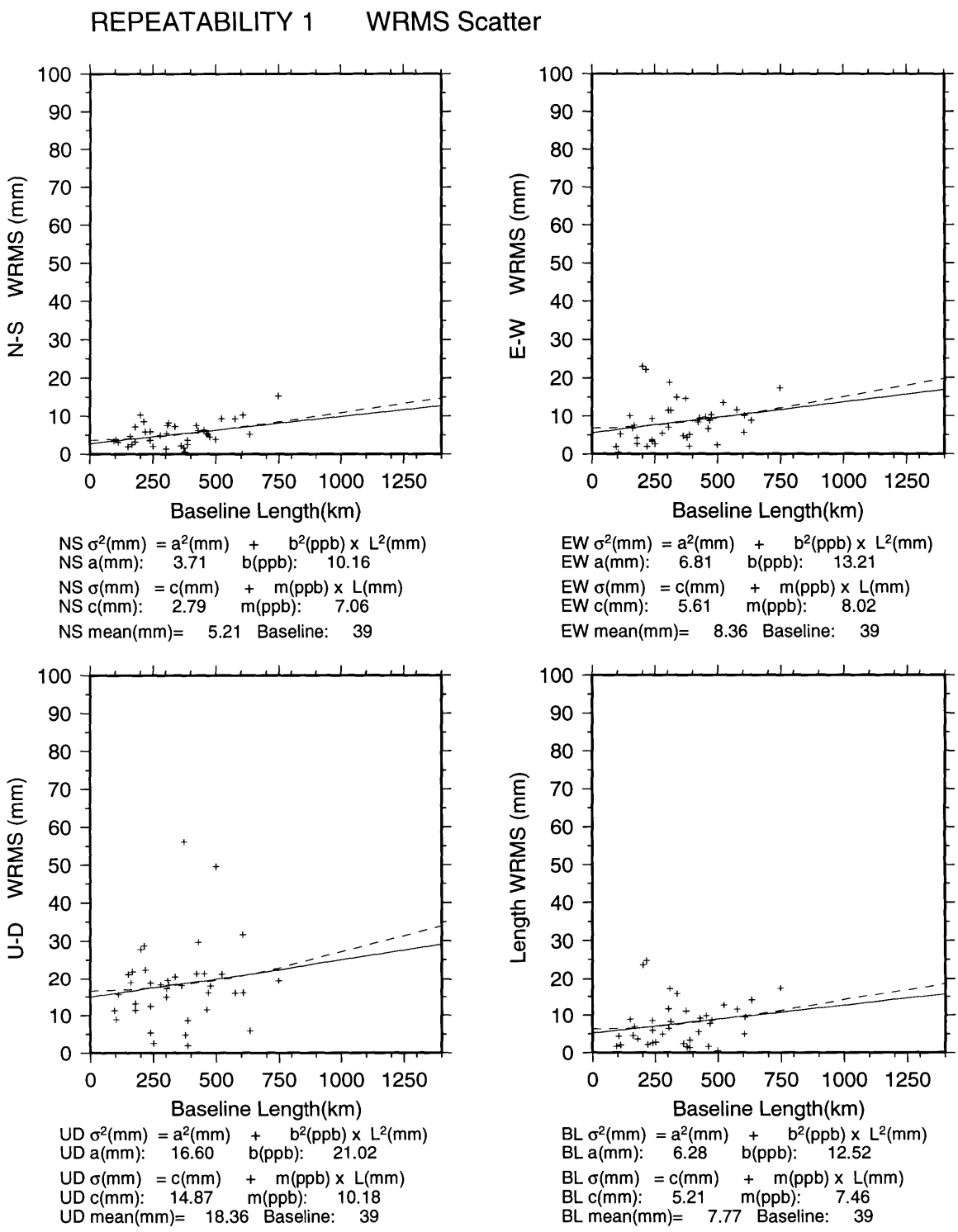

Figure B-14: The wrms scatter and model parameters of NS, EW, UD components and length, as a function of baseline length. They are obtained from the 1990 western Turkey experiment with tight (**T**) stochastic constraints applied to the satellites. Marmara sites are excluded. The wrms of baselines with 2 or more repeat observations are shown. Dashed line is a functional in the form of $\sigma^2 = a^2 + b^2L^2$. Continuous line is a linear fit to the wrms scatter ($\sigma = c + m\ L$).

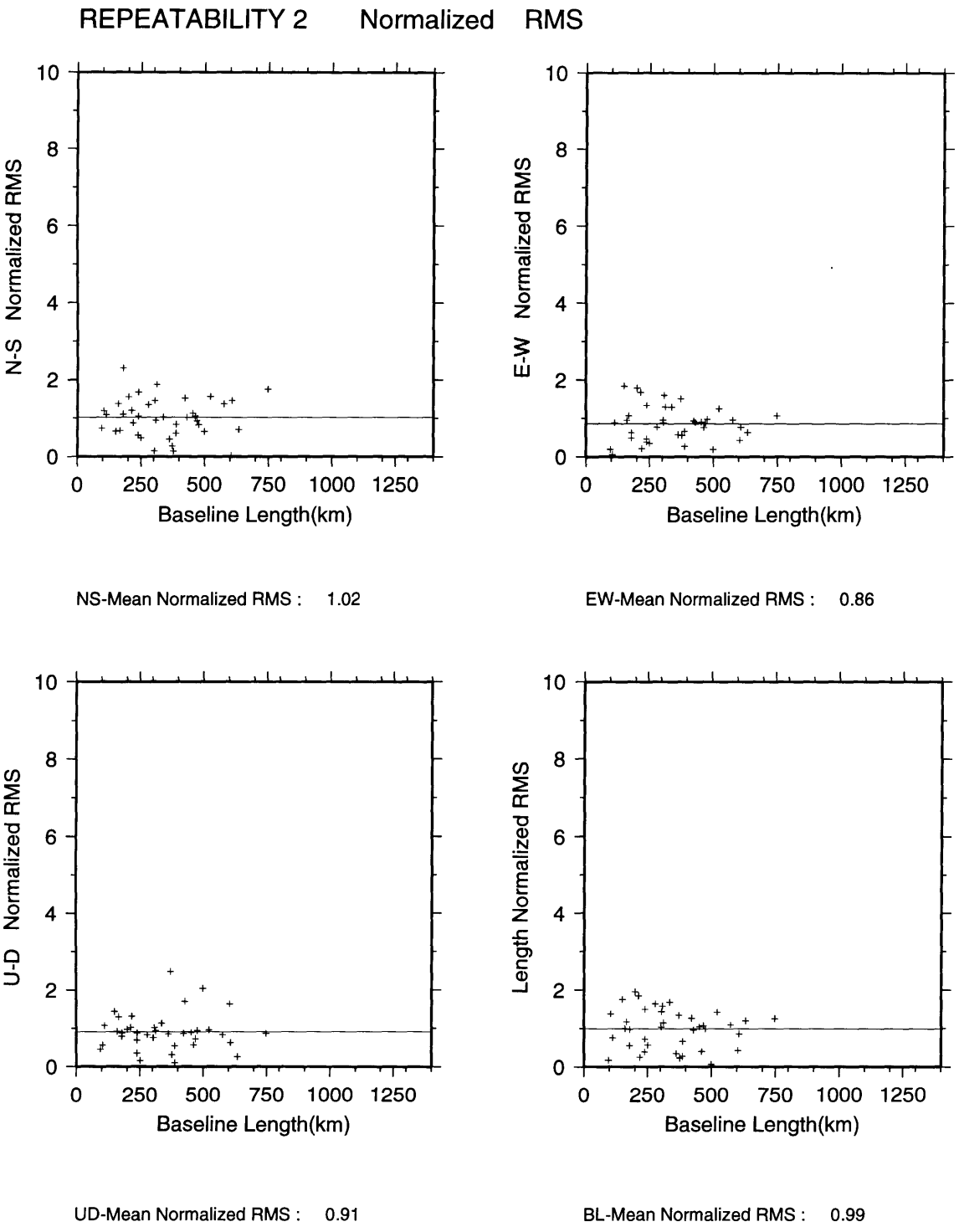

Figure B-15: The nrms scatter of NS, EW, UD components and length [for the solution described in Figure B-14], as a function of baseline length. They are obtained from the 1990 western Turkey experiment with tight (**T**) stochastic constraints applied to the satellites. Marmara sites are excluded. Continuous line represents the mean nrms scatter.

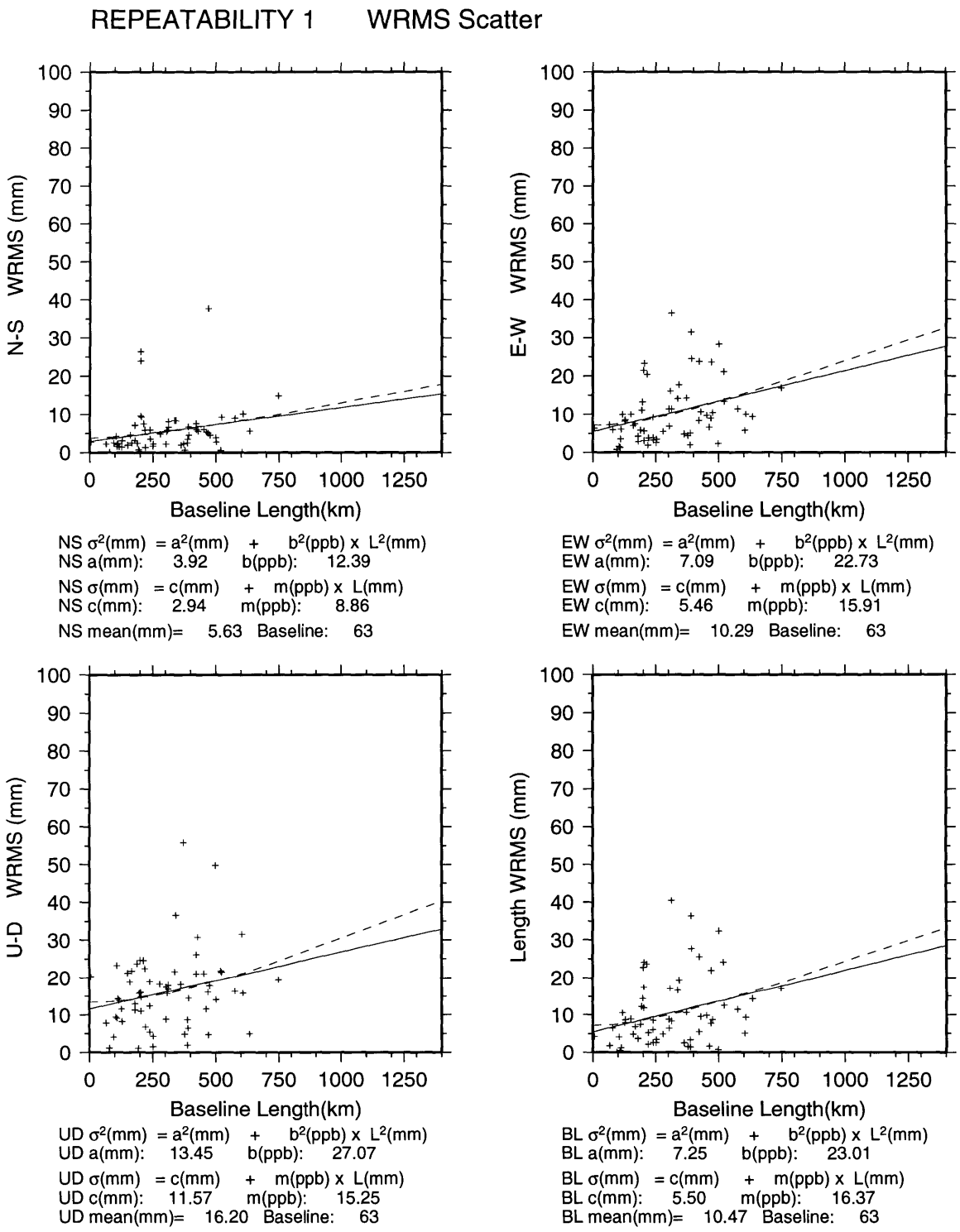

Figure B-16: The wrms scatter and model parameters of NS, EW, UD components and length, as a function of baseline length. They are obtained from the 1990 western Turkey experiment with tight (**T**) stochastic constraints applied to the satellites. All sites are included. The wrms of baselines with 2 or more repeat observations are shown. Dashed line is a functional in the form of $\sigma^2 = a^2 + b^2L^2$. Continuous line is a linear fit to the wrms scatter ($\sigma = c + m\ L$).

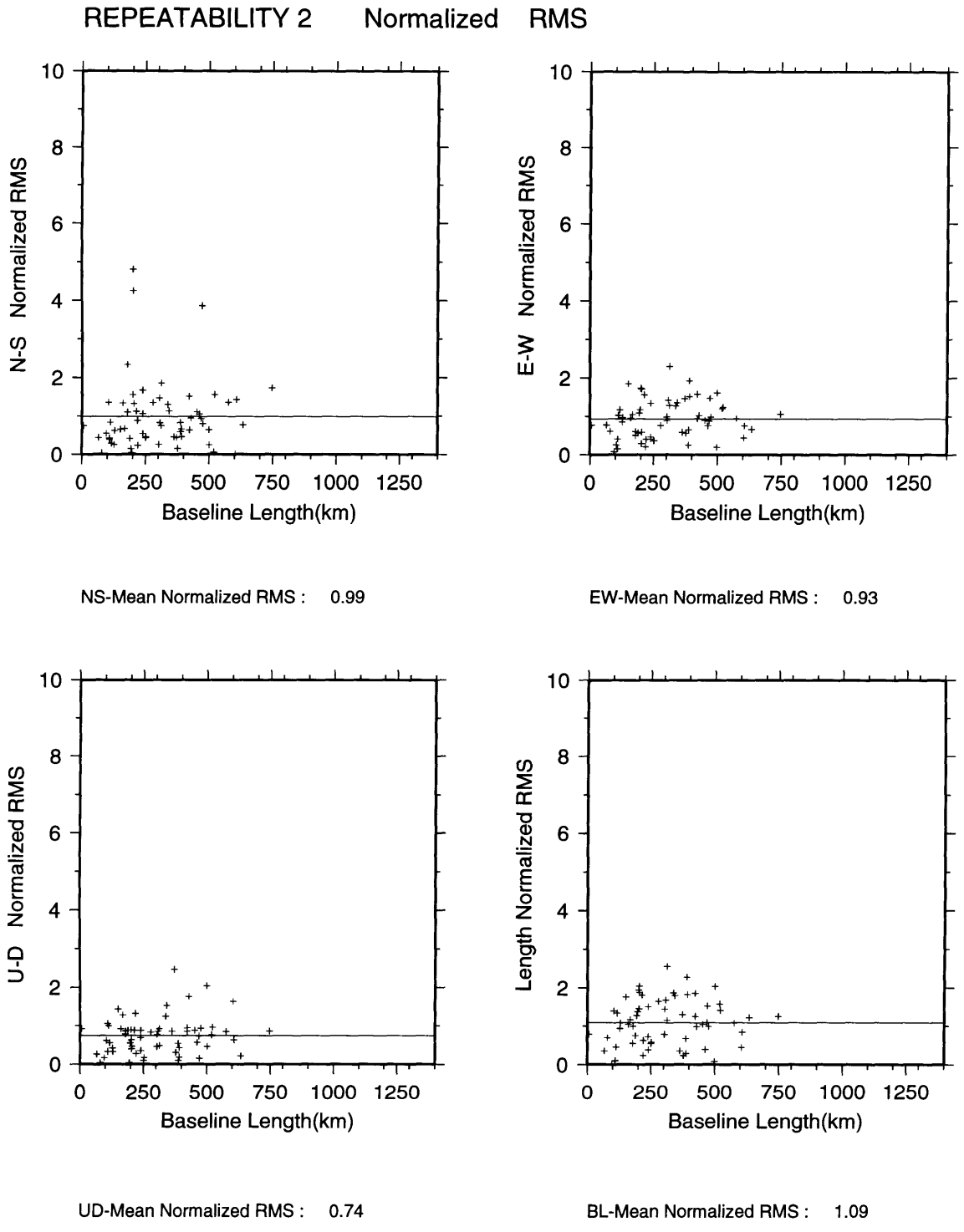

Figure B-17: The nrms scatter of NS, EW, UD components and length [for the solution described in Figure B-16], as a function of baseline length. They are obtained from the 1990 western Turkey experiment with tight (**T**) stochastic constraints applied to the satellites. All sites are included. Continuous line represents the mean nrms scatter.

B.2.4 1991 Eastern Turkey Experiment

The 1991 experiment was geared to reoccupy the 1989 established, eastern Turkey network. It was another collaborative effort undertaken with GCM and IfAG. The 1991 eastern Turkey experiment was coordinated between September 6 and 26 (days 249-269), with GPS measurements being made for 21 days. With seven Trimble SST receivers provided by UNAVCO, we collected GPS data at 22 sites (Table B.20): AKTO, ANKA, ERZU, GAZI, ISPI, KADI, KALE, KAR2, KARA, KARS, KEMA, KIZI, KORK, MALA, MELE, MERC, PAT2, PATN, SEBI, SINC, ULDA, and ULUC (Figure B-18). Initial GPS measurements were taken at the new SLR pad in Kara-

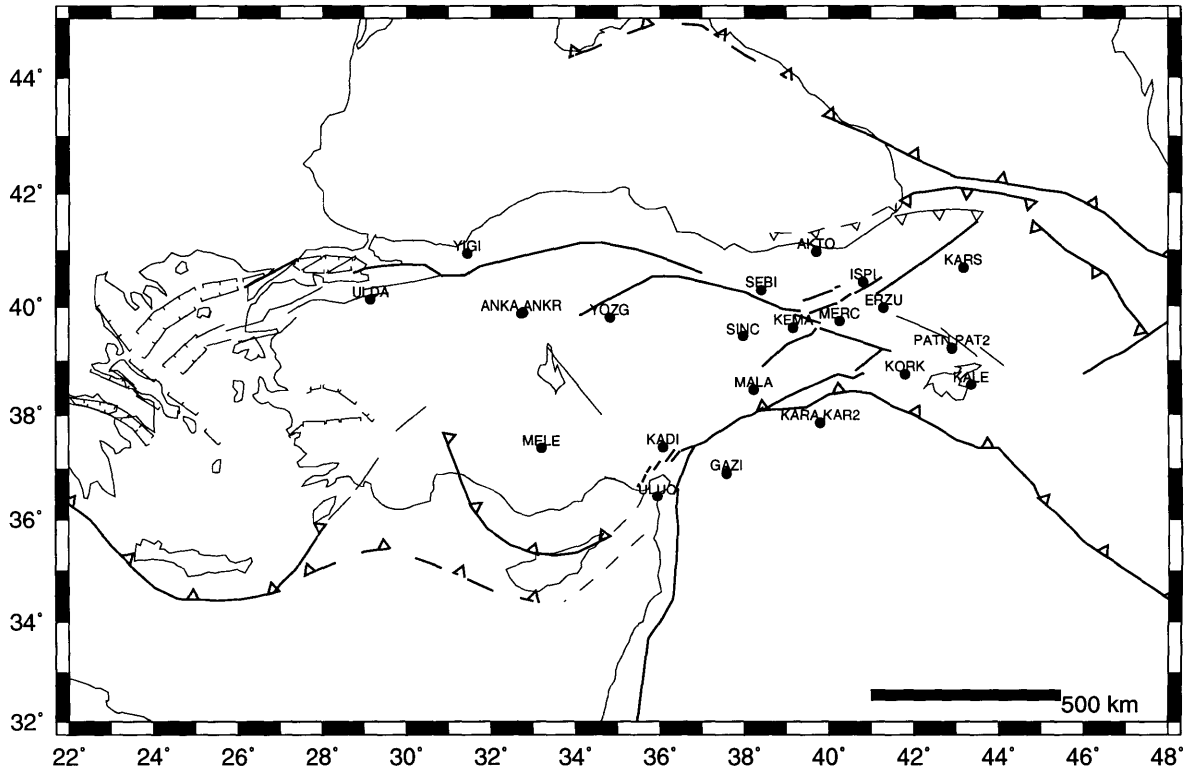

Figure B-18: Distribution of regional sites occupied during the 1991 experiment.

cadağ (KAR2), to replace the Diyarbakır site. We tied KAR2 and KARA with

simultaneous observations for only one day. The permanent[10] Ankara GPS station (ANKR), established by GCM as a CIGNET station, was tied to the previous Ankara site, ANKA, which was established in 1988 and has since been observed. The PATN site, established in 1989, was replaced by PAT2. GPS ties were made with one-session observations. Additionally, two new sites, GAZI and AKTO, were established during the eastern 1991 experiment. IfAG made GPS measurements at 3 SLR sites: MELE, YIGI and YOZG. The Melengiçlik site, MELE, was occupied both by IfAG (days 249-254) and MIT (days 255-268). Though selective availability (SA) began in 1991, it was not operational during the 1991 experiment. Five repeat observations were taken at YOZG by IfAG. All other sites were observed on three consecutive days. On the fourth day, the move day, only ANKR was operated.

Daily GPS measurements were 8 hours long and night-time observations were made at 25 sites, tracking 12 satellites at the regional sites. PRNs 3, 11, 12, 13, 14, 15, 16, 17, 20, 21, 23, and 24 were visible during the observation scenario. PRNs 2, 14, 16, 20, 21, and 23 were in eclipsing season. PRN 20 was not available between days 258 and 265. ANKR, KARA, MELE and YIGI were occupied throughout the experiment.

All antennas and receivers used in the 1991 experiment were Trimble SST, with data acquisition software version 4.53, except for version 4.40 being used at YOZG and version 4.42 for MELE, when observed by IfAG.

Data from global tracking sites were provided primarily by SIO archives in "clean" GAMIT x-file and RINEX formats, but also by JPL[11] in RINEX format and NGS in ARGO format.

In this experiment we decided to incorporate all global tracking data into our solu-

[10]Moved to another location on October 7, 1991. Receiver was provided by IfAG.
[11]Jet Propulsion Laboratory, Pasadena, California.

Table B.20: Regional sites and long-arc groupings: 1991 experiment.

ARC	DAY	GPS SITES							
	249	ANKR	MELE	ULDA	YIGI	YOZG			
	250	ANKR	KARA	MALA	MELE	PAT2	PATN	SEBI	ULDA
		ULUC	YIGI	YOZG					
1	251	ANKR	KARA	MALA	MELE	PAT2	SEBI	ULDA	ULUC
		YIGI	YOZG	YOZG					
	252	ANKR	KAR2	KARA	MALA	MELE	PAT2	SEBI	ULDA
		ULUC	YIGI	YOZG	YOZG				
	253	ANKR	KAR2	MELE	YIGI	YOZG			
	254	AKTO	ANKR	KALE	KARA	MELE	SINC	ULUC	YIGI
	255	AKTO	ANKR	KALE	KARA	MELE	SINC	ULUC	YIGI
2	256	AKTO	ANKR	KALE	KARA	MELE	SINC	ULUC	YIGI
	257	ANKR							
	258	AKTO	ANKR	KADI	KARA	KEMA	KORK	MELE	YIGI
3	259	AKTO	ANKR	KADI	KARA	KEMA	KORK	MELE	YIGI
	260	AKTO	ANKR	KADI	KARA	KEMA	KORK	MELE	YIGI
	261	ANKR							
	262	ANKR	GAZI	ISPI	KARA	KARS	KEMA	MELE	YIGI
4	263	ANKR	GAZI	ISPI	KARA	KARS	KEMA	MELE	YIGI
	264	ANKR	GAZI	ISPI	KARA	KARS	KEMA	MELE	YIGI
	265	ANKR							
	266	ANKR	ERZU	KARA	KARS	KIZI	MELE	MERC	YIGI
5	267	ANKR	ERZU	KARA	KARS	KIZI	MELE	MERC	YIGI
	268	ANKR	ERZU	KARA	KARS	KIZI	MELE	MERC	YIGI
	269	ANKA	ANKR						

tions with the *combination* approach described in Appendix A. To establish a basis for comparison (augmented data analysis), however, we also analyzed the data using the core global tracking network as we had for the 1988, 1989 and 1990 experiments. For this purpose we used 7 sites (Figure B-19): ONS0, WETR, TROM, WSFM, RICM, YKN1, and TSUK (Table B.21) to augment our regional data. Richmond, Tsukuba and Westford had Minimac receivers and antennas; Onsala, Wettzell, Tromso and Yellowknife had Rogue receivers with Dorne Margolin antennas. This data set was retrieved in RINEX format from the SIO GARNER archive and NGS, and 30 second samples of the data were used.

For the *combination* study (Appendix A) we obtained the entire set of "clean"

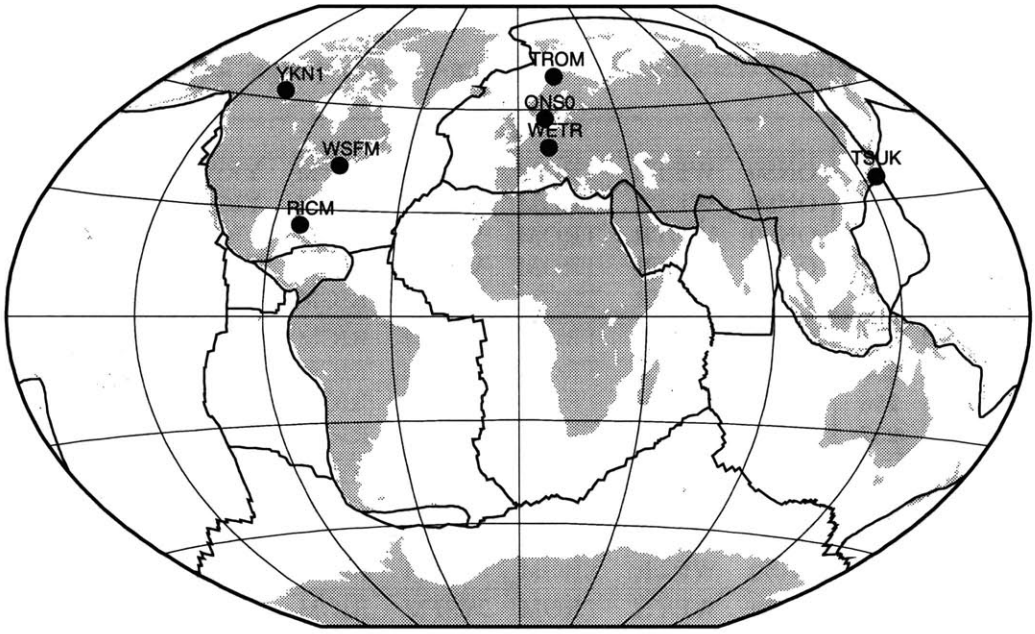

Figure B-19: Distribution of core global tracking sites included in the analyses of the 1991 experiment.

global tracking data (Figure B-20) from the SIO GARNER archive in GAMIT x-file format (2 minute samples). This global tracking network of 18 sites (ARON, CANB, GOLD, HERS, JPLM, KOKB, KOSG, MADR, ONS0, PENT, PIN1, SIO1, TROM, USUD, WELL, WETR, YAR1, and YKN1) had ROGUE receivers and Dorne Margolin antennas. Table B.22 shows the daily availability of each site.

Initially, we analyzed the augmented regional data, in which we considered the sites from the regional and core global tracking networks. This analysis provided a stand-alone solution for which data editing and cleaning was fairly manageable. A 12 hour processing scenario was chosen to include additional double-difference data from the global tracking network.

As in earlier experiments, we started with broadcast ephemeris and performed short-arc, single-session GAMIT solutions to clean and edit the data. Due to inconsistent phase residuals we had to delete PRN 21 from days 260 and 261 and PRN

Table B.21: Core global tracking sites and long-arc groupings: 1991 experiment.

ARC	DAY	GPS SITES						
1	249	ONSO	WETR	TROM	WSFM	RICM	YKN1	TSUK
	250	ONSO	WETR	TROM	WSFM	RICM	YKN1	TSUK
	251	ONSO	WETR	TROM	WSFM	RICM	YKN1	TSUK
	252	ONSO	WETR	TROM	WSFM	RICM	YKN1	TSUK
	253	ONSO	WETR	TROM	WSFM	RICM	YKN1	TSUK
2	254	ONSO	WETR	TROM	WSFM	RICM	YKN1	TSUK
	255	ONSO	WETR	TROM	WSFM	RICM	YKN1	TSUK
	256	ONSO	WETR	TROM	WSFM	RICM	YKN1	TSUK
	257	ONSO	WETR	TROM	WSFM	RICM	YKN1	TSUK
3	258	ONSO	WETR	TROM	WSFM	RICM	YKN1	TSUK
	259	ONSO	WETR	TROM	WSFM	RICM	YKN1	TSUK
	260	ONSO	WETR	TROM	WSFM	RICM	YKN1	TSUK
	261	ONSO	WETR	TROM	WSFM	RICM	YKN1	TSUK
4	262	ONSO	WETR	TROM	WSFM	RICM	YKN1	TSUK
	263	ONSO	WETR	TROM	WSFM	RICM	YKN1	TSUK
	264	ONSO	WETR	TROM	WSFM	RICM	YKN1	TSUK
	265	ONSO	WETR	TROM	WSFM	RICM	YKN1	TSUK
5	266	ONSO	WETR	TROM	WSFM	RICM	YKN1	TSUK
	267	ONSO	WETR	TROM	WSFM	RICM	YKN1	TSUK
	268	ONSO	WETR	TROM	WSFM	RICM	YKN1	TSUK
	269	ONSO	WETR	TROM	WSFM	RICM	YKN1	TSUK

12 from day 266. On day 260, ANKR had several cycle-slips and gaps, forcing us to delete some portions of the one-ways.

Later, we divided the experiment into 5 long-arcs (Table B.20) and performed long-arc, single-session GAMIT solutions with tight and loose constraints on the sites and satellites. Table B.23 shows a typical nrms for the 1991 experiment. On the average, a 0.25 nrms indicated that the rms of LC residuals was less than 15 mm. We ran into some difficulties in obtaining "flat" LC phase residuals on days 258 and 263 and attributed the non-flat residuals to modeling errors and possibly to the atmospheric effects at low elevation. Consequently, the nrms for these days is relatively higher.

Using the quasi-observations in step-two, we investigated the short-term precision of baseline estimates by applying **T**, **M**, **L**, **T_M**, and **T_L** sets of process noise to the

Table B.22: All global tracking sites and long-arc groupings: 1991 experiment.

ARC	DAY	GPS SITES							
1	249	ANKR	ARON	JPLM	KOKB	ONS0	PENT	PIN1	SIO1
		TROM	WETR	YKN1					
	250	ANKR	ARON	JPLM	KOKB	ONS0	PENT	PIN1	SIO1
		TROM	WETR	YKN1					
	251	ANKR	ARON	JPLM	KOKB	ONS0	PENT	PIN1	SIO1
		TROM	WETR	YKN1					
	252	ANKR	ARON	JPLM	KOKB	ONS0	PENT	PIN1	SIO1
		TROM	WETR	YKN1					
	253	ANKR	JPLM	ONS0	PENT	PIN1	SIO1	TROM	WETR
		YKN1							
2	254	ANKR	ARON	JPLM	KOKB	ONS0	PENT	PIN1	SIO1
		TROM	WETR	YKN1					
	255	ANKR	JPLM	KOKB	ONS0	PENT	PIN1	SIO1	TROM
		WETR	YKN1						
	256	ANKR	JPLM	KOKB	ONS0	PENT	PIN1	SIO1	TROM
		USUD	WETR	YAR1	YKN1				
	257	ANKR	JPLM	KOKB	ONS0	PENT	PIN1	SIO1	TROM
		WETR	YKN1						
3	258	ANKR	JPLM	KOKB	ONS0	PENT	PIN1	SIO1	TROM
		USUD	WETR	YKN1					
	259	ANKR	ARON	JPLM	KOKB	ONS0	PENT	PIN1	SIO1
		TROM	USUD	WETR	YAR1	YKN1			
	260	ANKR	ARON	CANB	GOLD	JPLM	KOKB	MADR	ONS0
		PENT	PIN1	SIO1	TROM	USUD	WELL	WETR	YAR1
	261	ANKR	ARON	JPLM	KOKB	ONS0	PENT	PIN1	SIO1
		TROM	USUD	WETR	YAR1	YKN1			
4	262	ANKR	ARON	JPLM	KOKB	ONS0	PENT	PIN1	SIO1
		TRO2	USUD	WETR	YAR1	YKN1			
	263	ANKR	HERS	JPLM	KOKB	KOSG	ONS0	PENT	PIN1
		SIO1	TROM	USUD	WETR	YAR1	YKN1		
	264	ANKR	ARON	HERS	JPLM	KOKB	KOSG	ONS0	PENT
		PIN1	SIO1	TROM	USUD	WETR	YAR1	YKN1	
	265	ANKR	ARON	HERS	JPLM	KOKB	KOSG	ONS0	PIN1
		SIO1	TROM	USUD	WETR	YAR1	YKN1		
5	266	ANKR	ARON	HERS	JPLM	KOKB	KOSG	ONS0	PENT
		PIN1	SIO1	TROM	USUD	WETR	YAR1	YKN1	
	267	ANKR	ARON	JPLM	KOKB	KOSG	ONS0	PENT	PIN1
		SIO1	TROM	USUD	WETR	YAR1	YKN1		
	268	ANKR	HERS	JPLM	KOSG	ONS0	PENT	SIO1	TROM
		USUD	WETR	YAR1	YKN1				
	269	ANKR	ARON	JPLM	KOKB	KOSG	ONS0	PENT	SIO1
		TROM	USUD	WETR	YAR1	YKN1			

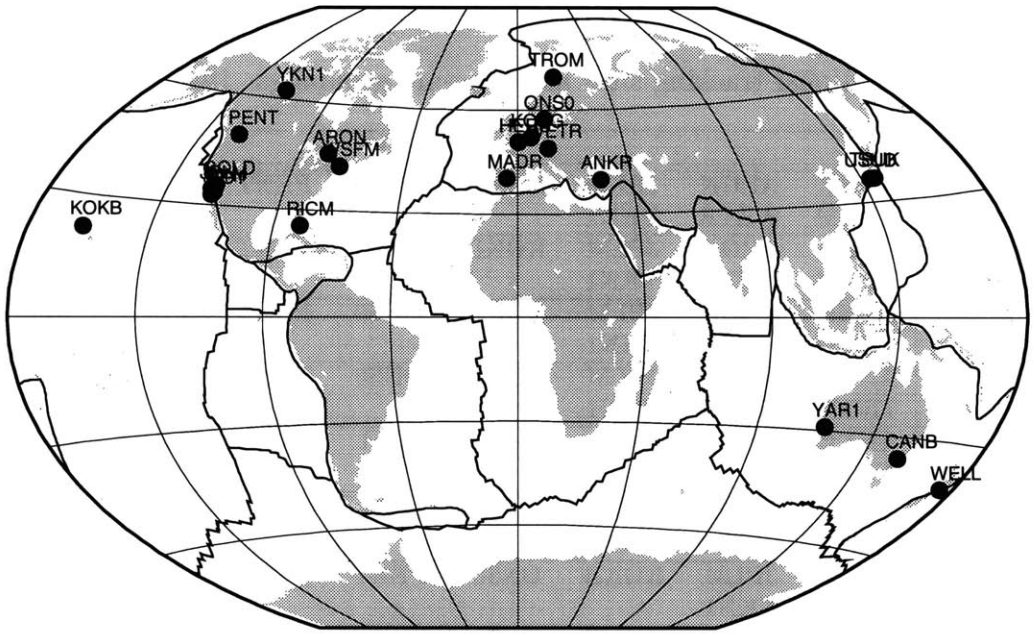

Figure B-20: Distribution of all global tracking sites included in the combination analyses of the 1991 experiment.

satellites. Parameters of the error model for such solutions are shown in Table B.24. We obtained the smallest wrms scatter (Figure B-21) when the eclipsing satellites were ignored and all satellites were treated with tight stochastic constraints (**T**). Proportional errors, especially for the east component, ~16 ppb, implied that we had room for improvement on the orbital parameters even though a core network, stretching from Tsukuba to Yellowknife,was considered. As was the case for all of our solutions with phase ambiguities not resolved to integer-values, the east repeatabilities were slightly worse than those in the north. The mean horizontal wrms was between 8.4 and 13.2 mm. The vertical component wrms scatter ranged to 60 mm. The mean nrms was approximately 2, suggesting that the a priori uncertainties had been underestimated.

To effectively combine the global and regional observations, we obtained another set of long-arc, single-session GAMIT solutions with the 18-site global tracking net-

Table B.23: Normalized RMS of long-arc, single-session GAMIT solutions(core global and regional sites [*reg*]): 1991 experiment.

GPS DAY	tight solution	loose solution
249	0.235	0.225
250	0.270	0.259
251	0.237	0.224
252	0.217	0.214
253	0.213	0.205
254	0.224	0.216
255	0.188	0.181
256	0.231	0.225
257	0.216	0.193
258	0.301	0.279
259	0.227	0.214
260	0.101	0.071
261	0.202	0.186
262	0.272	0.261
263	0.277	0.268
264	0.235	0.225
265	0.213	0.193
266	0.220	0.209
267	0.223	0.210
268	0.239	0.221
269	0.193	0.176

Table B.24: Short-term repeatability (augmented regional data): 1991 experiment.

	N-S component			E-W component			U-D component			Length		
Solution Descriptor	a (mm)	b (ppb)	mean nrms	a (mm)	b (ppb)	mean nrms	a (mm)	b (ppb)	mean nrms	a (mm)	b (ppb)	mean nrms
S_L	6.29	16.04	1.85	6.04	40.33	1.72	24.88	41.59	2.03	5.83	27.87	1.78
S_M	7.13	10.83	1.89	9.59	20.17	1.45	25.48	23.16	1.87	8.33	16.67	1.67
S_T†	7.74	5.73	2.06	9.97	15.79	1.59	25.25	18.08	1.90	9.16	11.53	1.78
S_T_L	7.34	9.79	2.01	9.15	19.96	1.52	26.42	22.25	1.99	8.15	16.91	1.74
S_T_M	7.40	8.00	1.98	10.06	15.80	1.51	26.36	17.82	1.94	8.91	13.91	1.75

† Preferred solution. Obtained by from tight constraints applied to all satellites (*cf.* Table B.2).

work (SIO quasi-observations are derived from short-arc, single session GAMIT solutions). Specific to this experiment, ANKR was considered among this data set. Since the data had been cleaned already by the SIO, we had only to obtain the quasi-

observations by long-arc, single-session GAMIT solutions. On day 261, however, due to inconsistent phase residuals, we had to delete PRN 21. The nrms of this solution was slightly higher at ≈0.4 (Table B.25), indicating that the rms of the LC phase residuals was ∼25 mm.

Table B.25: Normalized RMS of long-arc, single-session GAMIT solutions (global data only): 1991 experiment.

GPS DAY	tight solution	loose solution
249	0.294	0.282
250	0.314	0.305
251	0.283	0.271
252	0.263	0.254
253	0.305	0.284
254	0.262	0.249
255	0.218	0.205
256	0.241	0.230
257	0.258	0.248
258	0.349	0.333
259	0.373	0.358
260	0.313	0.295
261	0.440	0.423
262	0.434	0.411
263	0.301	0.287
264	0.363	0.354
265	0.454	0.439
266	0.437	0.422
267	0.352	0.340
268	0.355	0.338
269	0.324	0.304

We then combined these two sets of quasi-observations (global and the previously obtained augmented regional) using GLOBK, and applied the aforementioned process-noise sets to the satellites. This is an example of the several-site-common type combination solution (Appendix A). With the repeatabilities obtained from the combined solutions, we realized that the GAZI site was an outlier. Though we returned to phase data, we could not identify any particular day's one-way data as problematic. Since this site had no other observations from other experiments, we chose to discard it. Table B.26 shows the error model parameters obtained from a combination type

solution by applying different process noise sets. The highest precision was obtained by applying tight stochastic constraints to the satellites (Figure B-23). The nrms scatter of baselines is shown in Figure B-24. As stated in Appendix A, the baseline length dependent term was reduced considerably. In the east component scatter there is a striking 13 ppb improvement.

Table B.26: Short-term repeatability (augmented regional and global combination): 1991 experiment.

Solution Descriptor	N-S component a (mm)	N-S component b (ppb)	N-S component mean nrms	E-W component a (mm)	E-W component b (ppb)	E-W component mean nrms	U-D component a (mm)	U-D component b (ppb)	U-D component mean nrms	Length a (mm)	Length b (ppb)	Length mean nrms
S_L	6.10	14.03	1.97	6.70	23.55	1.22	23.94	22.43	1.61	6.26	18.12	1.38
S_M	6.76	7.43	2.08	8.57	10.60	1.23	24.35	0.58	1.61	7.93	7.85	1.37
S_T†	6.76	0.57	2.05	8.54	2.74	1.21	22.35	0.58	1.55	8.03	0.77	1.39
S_T_L	6.84	3.18	1.95	8.43	11.86	1.31	24.99	0.58	1.66	7.49	10.20	1.43
S_T_M	6.84	2.18	2.00	8.35	4.77	1.16	23.35	0.58	1.59	7.79	4.25	1.34

† Preferred solution. Obtained from tight constraints applied to all satellites (*cf.* Table B.2).

By performing the **D_T** solution, in which all sites were estimated deterministically, we investigated the level of formal uncertainties for baseline estimates. Below are the propagated formal uncertainties obtained from combining the global and augmented regional data (1–1.5 mm smaller than those obtained from augmented regional data analysis):

$$\sigma_{NS}(\text{mm}) = 1.75(\text{mm}) + 0.30\text{x}10^{-3}\ \text{L(km)} \quad \text{@500km baseline: } 1.90(\text{mm})$$
$$\sigma_{EW}(\text{mm}) = 3.19(\text{mm}) + 1.03\text{x}10^{-3}\ \text{L(km)} \quad \text{@500km baseline: } 3.71(\text{mm})$$
$$\sigma_{UD}(\text{mm}) = 7.62(\text{mm}) + 0.00\text{x}10^{-3}\ \text{L(km)} \quad \text{@500km baseline: } 7.62(\text{mm})$$
$$\sigma_{BL}(\text{mm}) = 2.51(\text{mm}) + 1.30\text{x}10^{-3}\ \text{L(km)} \quad \text{@500km baseline: } 3.16(\text{mm}).$$

Compared to 1990, the formal uncertainties of the 1991 experiment baselines were a factor of 2 better, and they did not exhibit strong length dependency.

During our data analyses, especially in the second half of the experiment, we had difficulties in obtaining "flat" LC phase residuals. Some of the LC residuals in the

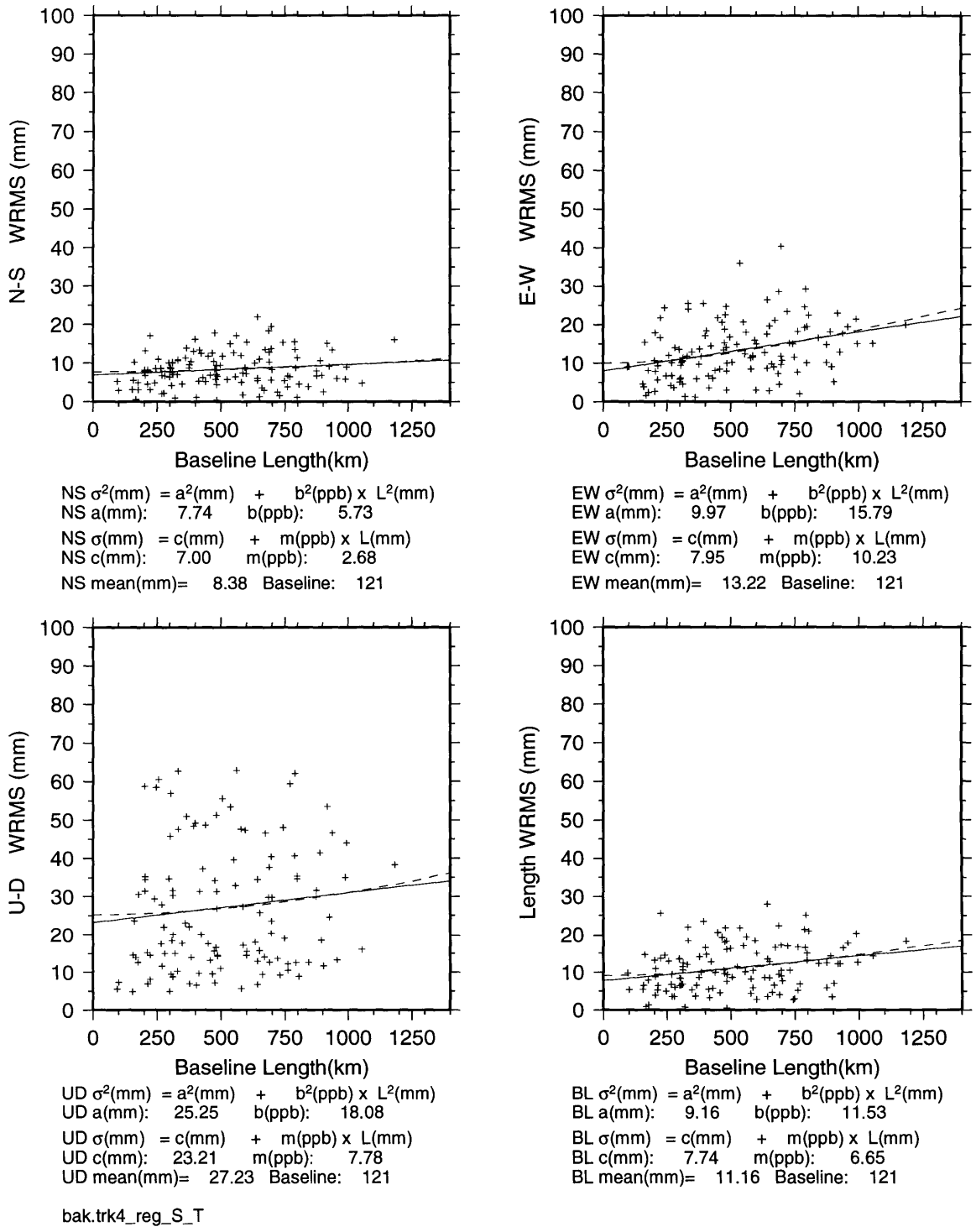

Figure B-21: The wrms scatter and model parameters of NS, EW, UD components and length, as a function of baseline length. They are obtained from the 1991 experiment [augment regional data] with tight (**T**) stochastic constraints applied to the satellites. The wrms of baselines with 2 or more repeat observations are shown. Dashed line is a functional in the form of $\sigma^2 = a^2 + b^2L^2$. Continuous line is a linear fit to the wrms scatter ($\sigma = c + m\ L$).

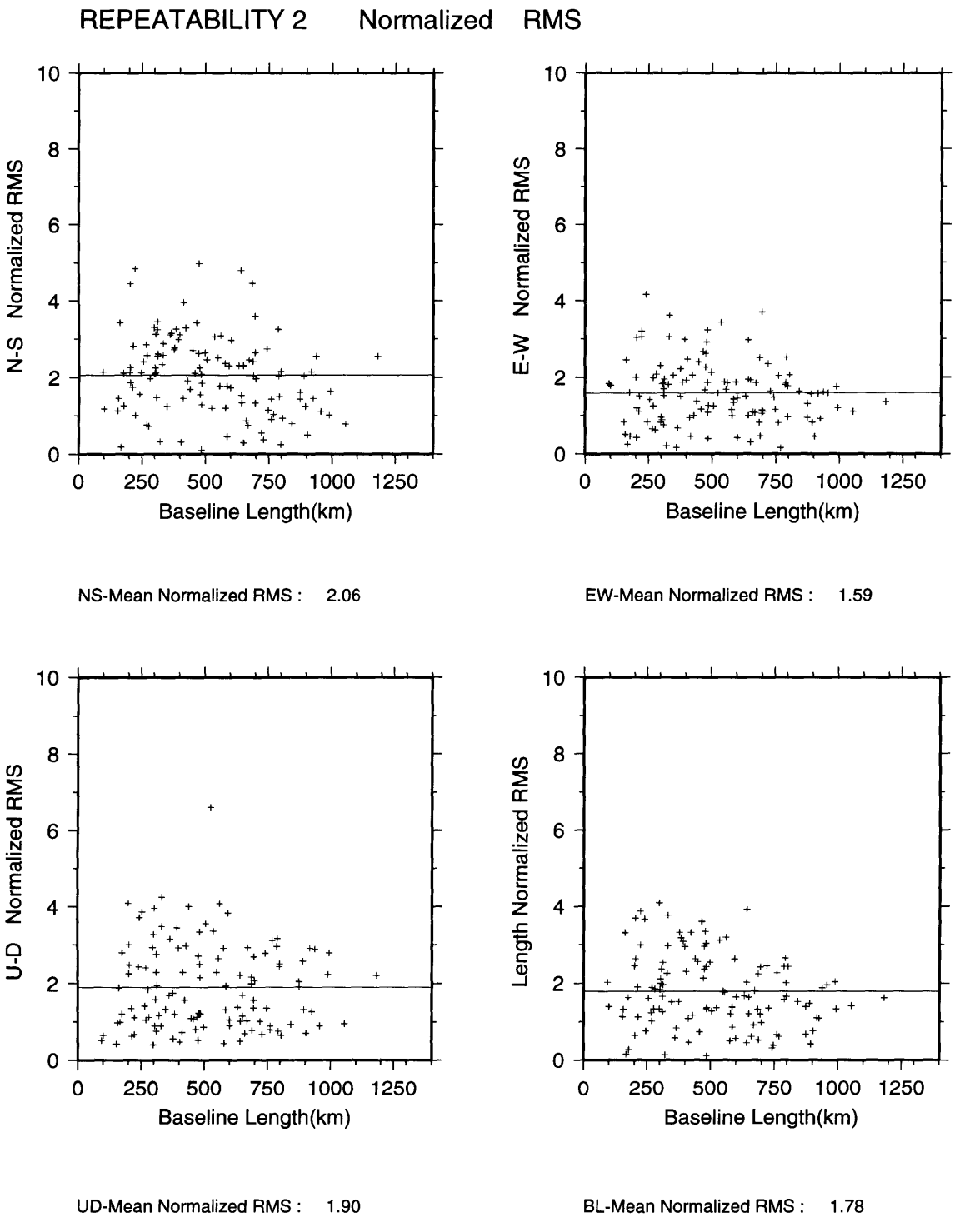

Figure B-22: The nrms scatter of NS, EW, UD components and length [for the solution described in Figure B-22], as a function of baseline length. They are obtained from the 1991 experiment [augment regional data] with tight (**T**) stochastic constraints applied to the satellites. Continuous line represents the mean nrms scatter.

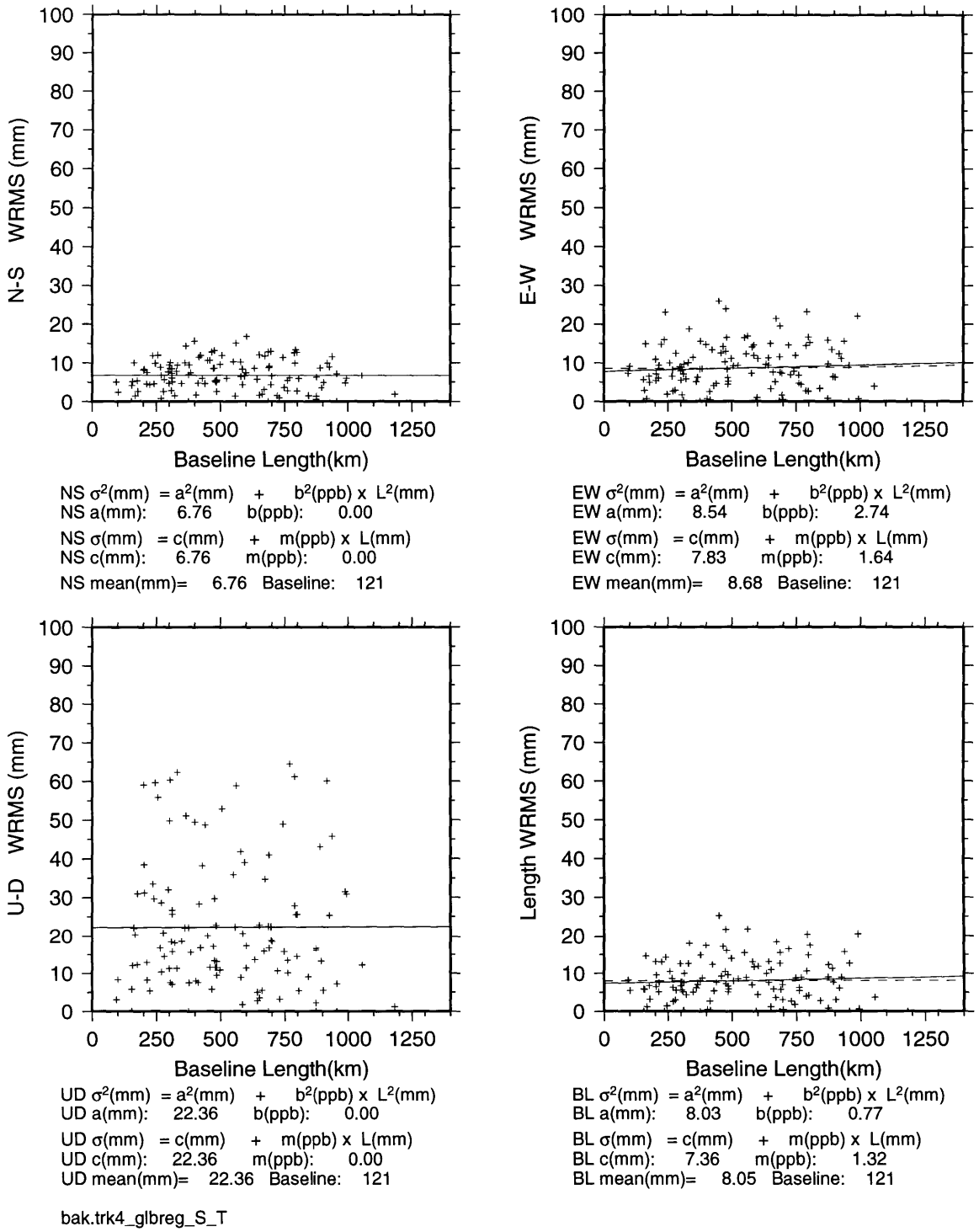

Figure B-23: The wrms scatter and model parameters of NS, EW, UD components and length, as a function of baseline length. They are obtained from the 1991 experiment [augment regional and global data combination] with tight (**T**) stochastic constraints applied to the satellites. The wrms of baselines with 2 or more repeat observations are shown. GAZI is excluded. Dashed line is a functional in the form of $\sigma^2 = a^2 + b^2L^2$. Continuous line is a linear fit to the wrms scatter ($\sigma = c + m\ L$).

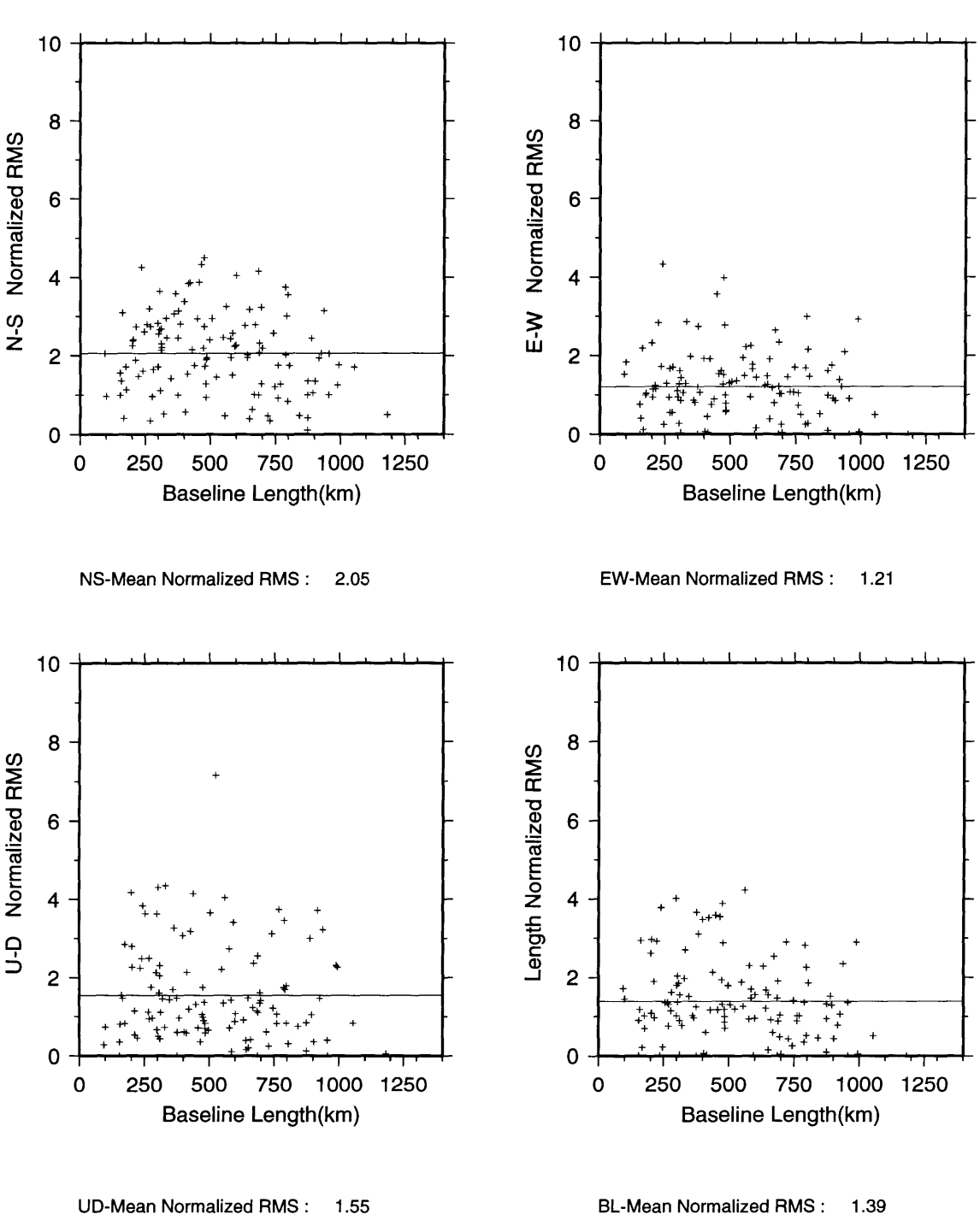

Figure B-24: The nrms scatter of NS, EW, UD components and length [for the solution described in Figure B-23], as a function of baseline length. They are obtained from the 1991 experiment [augment regional and global data combination] with tight (**T**) stochastic constraints applied to the satellites. GAZI is excluded. Continuous line represents the mean nrms scatter.

beginning and end of the double-difference observable were "tilted". As a result, we observed an increase in the nrms of each long-arc, single-session GAMIT solution with respect to those obtained from earlier experiments. We could not pinpoint the problem to a specific site, receiver or satellite. As the global parameters were estimated with GLOBK, we witnessed an increase in the GLOBK χ^2/f to $\sim$4 for tight solutions, from which the best repeatabilities were obtained. The baseline repeatabilities were admissible, and adjustments to orbital parameters for each long-arc were at reasonable values. For instance, the adjustments to the cartesian positions of all satellites were less than 2 meters with 10-20 cm uncertainties. Their day-to-day variation was reasonable and behaved in accordance with the stochastic process noise imposed upon them. That is, adjustments between days varied as much as, or less than, the allowed process noise, which was statistically insignificant. As looser stochastics were applied to the satellites, however, the GLOBK χ^2/f tended to decrease. For instance, the GLOBK χ^2/f was 2 and 1.5 for **M** and **L**, respectively. This meant that defining a single arc (a tightly coupled orbit) for several days might not be possible. We obtained two sets of the compact quasi-observations: one for augmented regional data and the other for the combination of global and augmented regional data. However, we used the compact quasi-observations from the combination analysis to estimate the velocity field to avoid systematic errors which may have been introduced by deficient tracking network.

B.2.5 Spring 1992 Erzincan Earthquake Experiment

As an emergency response to the the 13 March 1992 Erzincan earthquake, we launched a special experiment 12 days after the main shock. We made GPS measurements at 15 sites (Figure B-25) between March 26 and April 7 (days: 86-98) to quantify the co-seismic deformation. Observations were carried out with support from UNAVCO and in collaboration with the GCM.

Eleven new GPS sites (ER01, ER02, ER03, ER04, ER05, ER07, ER08, ER09, ER10, ER11, and ER12) were established around the epicenter of the Erzincan

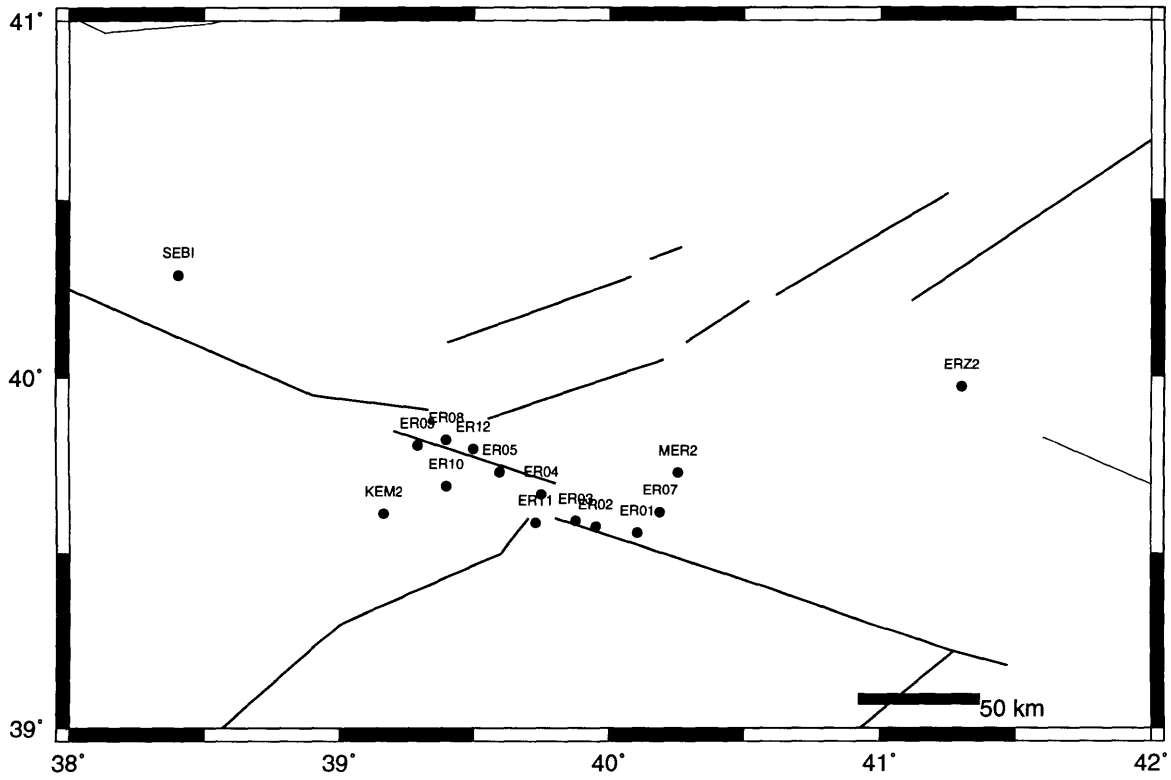

Figure B-25: Distribution of regional sites occupied during the spring 1992 Erzincan earthquake experiment.

earthquake to monitor post-seismic deformation. We also occupied four other sites which had been established in 1988: ERZU, KEMA, MERC, and SEBI. Due to the

potential for co-seismic displacement, we renamed ERZU, KEMA, and MERC as ERZ2, KEM2,and MER2, respectively.

All antennas and receivers were Trimble SST, running version 4.53 data acquisition software. The Ankara permanent station was observed throughout the spring 1992 experiment by GCM, with a Minimac receiver and antenna.

We tracked 10 satellites: PRNs 2, 6, 11, 12, 13, 14, 16, 18, 19, and 24. PRNs 14, 16, 21 and 23 were eclipsing in the first three days of the experiment, while PRNs 2 and 20 continued to be in eclipse for another three days. Due to the malfunctioning of one of our receivers, we had to change our site occupation schedule (Table B.27). We obtained observations on 2 to 3 days each at the newly established earthquake sites.

Table B.27: Regional sites and long-arc groupings: spring 1992 Erzincan earthquake experiment.

ARC	DAY	GPS SITES				
1	086	ANKM	ERZ2	KEM2	MER2	SEBI
	087	ANKM	ERZ2	KEM2	MER2	SEBI
	088	ANKM	ERZ2	KEM2	MER2	SEBI
2	089	ANKM	ER02	ERZ2	KEM2	MER2
	090	ANKM	ER05	ER10	KEM2	MER2
	091	ANKM	ER07	ER11	KEM2	MER2
3	092	ANKM	ER02	ER03	ER08	KEM2
	093	ANKM	ER03	ER08	ER09	
	094	ANKM	ER03	ER04	ER09	
	095	ANKM	ER04	ER09	ER12	
4	096	ANKM	ER01	ER04	ER12	
	097	ANKM	ER01	ER11	ER12	
	098	ANKM	ER05	ER07	ER10	

We obtained the global tracking data from SIO archives in "clean" GAMIT x-file format for 20 sites operating Rogue receivers. We used 5 sites (Figure B-26) as core global tracking sites (KOSG, ONS0, TROM, WETR, and YKN1) to augment

our regional data (Table B.28). We started our reductions with satellite ICs already computed by SIO. Since the core tracking sites were previously cleaned, we had only

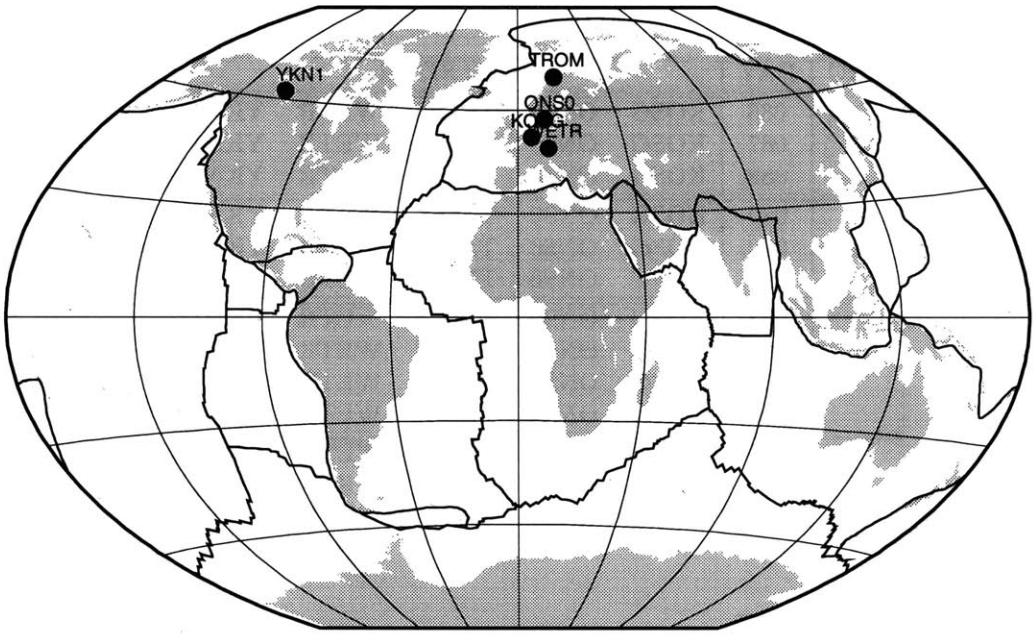

Figure B-26: Distribution of core global tracking sites included in the analyses of the spring 1992 Erzincan earthquake experiment.

to introduce long-arcs and perform single-session GAMIT solutions, using augmented regional data. Four long-arcs were considered, each 3 to 4 days long. At this stage, we cleaned and edited our regional GPS measurements. Table B.29 shows the nrms for each day, obtained from long-arc, single-session GAMIT solutions in which tight and loose constraints were applied to the sites and satellites. A rather small nrms, less than 0.2, indicates that the phase residuals were fairly "flat", and that the LC residual rms was below 15 mm. We also reduced the data from regional sites, excluding global tracking data, with long-arc, single-session GAMIT solutions (see Appendix A). We analyzed the 30-sec and 2-minute samples of regional data (without any fiducials) with GAMIT, and obtained their quasi-observations. The 2-minute-samples of data were obtained by decimating the data, and aligning the Earth Orientation Parameter (EOP) epoch (also, see Appendix A, Table A.1) with that of the global data set, by

Table B.28: Core Global tracking sites and long-arc groupings: spring 1992 Erzincan earthquake experiment.

ARC	DAY	GPS SITES				
1	086	KOSG	ONS0	TROM	WETR	YKN1
	087	KOSG	ONS0	TROM	WETR	YKN1
	088	KOSG	ONS0	TROM	WETR	YKN1
2	089	KOSG	ONS0	TROM	WETR	YKN1
	090	KOSG	ONS0	TROM	WETR	YKN1
	091	KOSG	ONS0	TROM	WETR	YKN1
3	092	KOSG	ONS0	TROM	WETR	YKN1
	093	KOSG	ONS0	TROM	WETR	YKN1
	094	KOSG	ONS0	TROM	WETR	YKN1
	095	KOSG	ONS0	TROM	WETR	YKN1
4	096	KOSG	ONS0	TROM	WETR	YKN1
	097	KOSG	ONS0	TROM	WETR	YKN1
	098	KOSG	ONS0	TROM	WETR	YKN1

Table B.29: Normalized RMS of long-arc, single-session GAMIT solutions(core global and regional sites): spring 1992 Erzincan earthquake experiment.

GPS DAY	tight solution	loose solution
86	0.159	0.156
87	0.172	0.166
88	0.178	0.175
89	0.185	0.181
90	0.184	0.178
91	0.191	0.188
92	0.183	0.176
93	0.177	0.171
94	0.183	0.179
95	0.195	0.193
96	0.162	0.158
97	0.168	0.164
98	0.188	0.184

setting identical start and stop times. (The global tracking data archived by SIO cover 24-hours and span 0:00 – 23:58; their EOP epoch is 11:59.) The nrms of these solutions (Table B.30) were not different from the ones in which core global trackers were considered.

Table B.30: Normalized RMS of long-arc, single-session GAMIT solutions (regional sites only): spring 1992 Erzincan earthquake experiment.

GPS DAY	tight solution	loose solution
86	0.156	0.159
87	0.171	0.172
88	0.171	0.175
89	0.208	0.211
90	0.185	0.189
91	0.203	0.206
92	0.170	0.174
93	0.163	0.167
94	0.188	0.194
95	0.209	0.215
96	0.175	0.178
97	0.173	0.178
98	0.208	0.210

We used 20 global tracking sites (ARON, CAN1, FAIR, GOLD, JPLM, KOKB, KOSG, MADR, MATE, MCMU, NALL, ONS0, PENT, PIN1, SANR, TROM, USUD, WETR, YAR1, and YKN1) in our global analyses (Figure B-27). The availability of these sites was nearly uniform. Compared to earlier experiments, global coverage became much more homogeneous by the spring 1992 Erzincan earthquake experiment, especially with the addition of southern hemisphere sites (e.g., McMurdo and Santiago). We used 2-minute samples of this global data (global data analysis). A decimated ANKM (at 2 minutes) was also included in the reduction of this set with long-arc, single-session GAMIT solutions. Because this data had already been edited by the SIO GPS Orbit Facility, reduction was fairly simple. The nrms of these solutions rose slightly (Table B.31) relative to the augmented analysis. We also simultaneously analyzed the global and regional data (both 2-minute and 30-sec) for a comparison (See Appendix A). The nrms of these solutions did not significantly change from those reported in Table B.31.

Estimates of global parameters and their short-term precision have already been reported in Appendix A, so we need not repeat them here. In the repeatability

Table B.31: Normalized RMS of long-arc, single-session GAMIT solutions (global sites only): spring 1992 Erzincan earthquake experiment.

GPS DAY	tight solution	loose solution
86	0.286	0.265
87	0.323	0.296
88	0.242	0.224
89	0.255	0.235
90	0.272	0.249
91	0.260	0.227
92	0.325	0.303
93	0.258	0.232
94	0.300	0.262
95	0.278	0.245
96	0.312	0.268
97	0.285	0.263
98	0.272	0.250

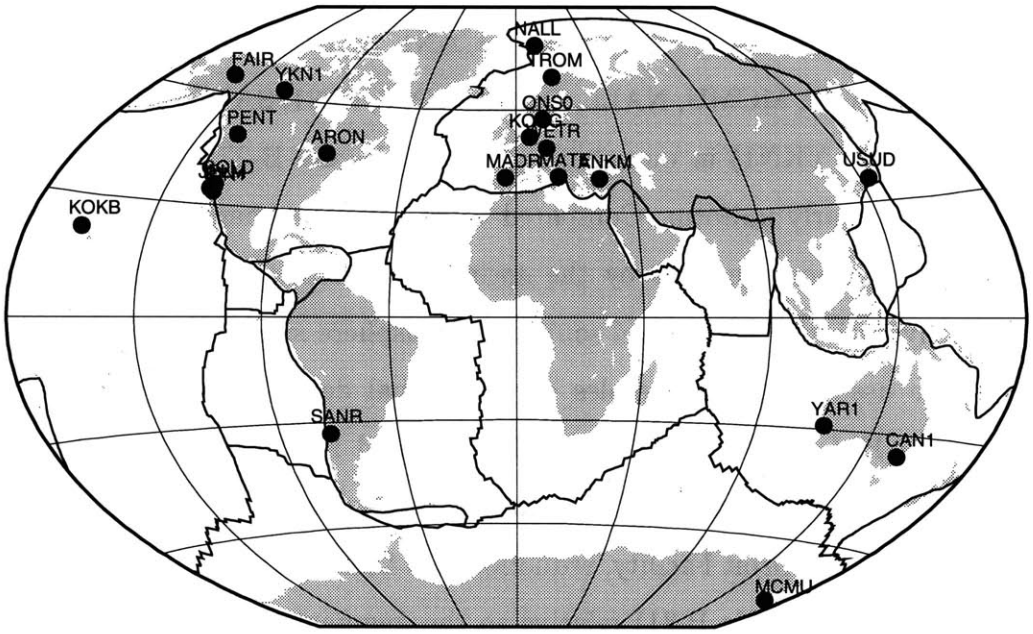

Figure B-27: Distribution of all global tracking sites included in the combination analyses of the spring 1992 Erzincan earthquake experiment.

analyses presented in Appendix A, we had to remove ER12 due to its outlier behavior.

The formal uncertainties of baseline estimates obtained from simultaneous analy-

Table B.32: All global tracking sites and long-arc groupings: spring 1992 Erzincan earthquake experiment.

ARC	DAY	GPS SITES								
1	086	ANKM	ARON	CAN1	FAIR	GOLD	JPLM	KOKB	KOSG	
		MADR	MCMU	NALL	ONS0	PENT	PIN1	SANR	TROM	USUD
		WETR	YAR1	YKN1						
	087	ANKM	ARON	CAN1	FAIR	GOLD	JPLM	KOKB	KOSG	
		MADR	MCMU	NALL	ONS0	PENT	PIN1	SANR	TROM	USUD
		WETR	YAR1	YKN1						
	088	ANKM	ARON	CAN1	FAIR	GOLD	JPLM	KOKB	KOSG	
		MADR	MCMU	ONS0	PENT	PIN1	SANR	TROM	USUD	WETR
		YAR1	YKN1							
2	089	ANKM	ARON	CAN1	FAIR	GOLD	JPLM	KOKB	KOSG	
		MADR	MCMU	NALL	ONS0	PENT	PIN1	SANR	TROM	USUD
		WETR	YAR1	YKN1						
	090	ANKM	ARON	CAN1	FAIR	GOLD	JPLM	KOKB	KOSG	
		MADR	MCMU	NALL	ONS0	PENT	PIN1	TROM	USUD	WETR
		YAR1	YKN1							
	091	ANKM	ARON	CAN1	FAIR	GOLD	JPLM	KOKB	KOSG	
		MADR	MCMU	NALL	ONS0	PENT	PIN1	TROM	USUD	WETR
		YAR1	YKN1							
3	092	ANKM	ARON	CAN1	FAIR	GOLD	JPLM	KOKB	KOSG	
		MADR	MCMU	NALL	ONS0	PENT	PIN1	SANR	TROM	USUD
		YAR1	YKN1							
	093	ANKM	ARON	CAN1	FAIR	GOLD	JPLM	KOKB	KOSG	
		MADR	MCMU	NALL	ONS0	PENT	PIN1	SANR	TROM	USUD
		WETR	YAR1	YKN1						
	094	ANKM	ARON	CAN1	FAIR	GOLD	JPLM	KOKB	KOSG	
		MADR	MCMU	NALL	ONS0	PENT	PIN1	SANR	TROM	USUD
		WETR	YAR1	YKN1						
	095	ANKM	ARON	CAN1	FAIR	GOLD	JPLM	KOKB	KOSG	
		MADR	MCMU	NALL	ONS0	PENT	PIN1	SANR	TROM	USUD
		WETR	YAR1	YKN1						
4	096	ANKM	ARON	CAN1	FAIR	GOLD	JPLM	KOKB	KOSG	MADR
		MCMU	NALL	ONS0	PENT	PIN1	SANR	TROM	USUD	WETR
		YAR1	YKN1							
	097	ANKM	ARON	CAN1	FAIR	GOLD	JPLM	KOKB	KOSG	MADR
		MATE	MCMU	NALL	ONS0	PENT	PIN1	SANR	TROM	USUD
		WETR	YKN1							
	098	ANKM	ARON	FAIR	GOLD	JPLM	KOKB	KOSG	MADR	MCMU
		NALL	ONS0	PENT	PIN1	SANR	TROM	USUD	WETR	YAR1
		YKN1								

ses of all global and regional data are:

σ_{NS}(mm) =	4.87(mm)	+	0.00x10^{-3} L(km)	@500km baseline:	4.87(mm)
σ_{EW}(mm) =	9.32(mm)	+	0.00x10^{-3} L(km)	@500km baseline:	9.32(mm)
σ_{UD}(mm) =	26.68(mm)	+	0.00x10^{-3} L(km)	@500km baseline:	26.68(mm)
σ_{BL}(mm) =	8.80(mm)	+	0.00x10^{-3} L(km)	@500km baseline:	8.80(mm).

We noticed that formal uncertainties were independent of baseline length. Formal errors were 5 mm in the north and 10 mm in the east. Since we had 30 second samples of data for the combination of global and regional observations, these uncertainties were halved:

σ_{NS}(mm) =	2.55(mm)	+	0.00x10^{-3} L(km)	@500km baseline:	2.55(mm)
σ_{EW}(mm) =	4.88(mm)	+	0.00x10^{-3} L(km)	@500km baseline:	4.88(mm)
σ_{UD}(mm) =	13.89(mm)	+	0.00x10^{-3} L(km)	@500km baseline:	13.89(mm)
σ_{BL}(mm) =	4.60(mm)	+	0.00x10^{-3} L(km)	@500km baseline:	4.60(mm).

The uncertainties obtained from the analyses of the augmented regional data had a slight length dependency at comparable magnitudes:

σ_{NS}(mm) =	2.66(mm)	+	3.56x10^{-3} L(km)	@500km baseline:	4.44(mm)
σ_{EW}(mm) =	5.03(mm)	+	7.43x10^{-3} L(km)	@500km baseline:	8.75(mm)
σ_{UD}(mm) =	15.45(mm)	+	0.00x10^{-3} L(km)	@500km baseline:	15.45(mm)
σ_{BL}(mm) =	4.79(mm)	+	4.03x10^{-3} L(km)	@500km baseline:	6.80(mm).

For velocity estimation, we obtained compact quasi-observations from the combination of augmented regional and global data.

B.2.6 Fall 1992 Western Turkey and Erzincan Earthquake Experiments

We conducted our sixth experiment in Turkey between August 27 and September 20, 1992 (days 240-264), benefiting from collaboration with the GCM in the field. This experiment lasted for 24 days and a denser network in Turkey was observed (Figure B-28). We collected GPS measurements at sites in western Turkey (Figure B-

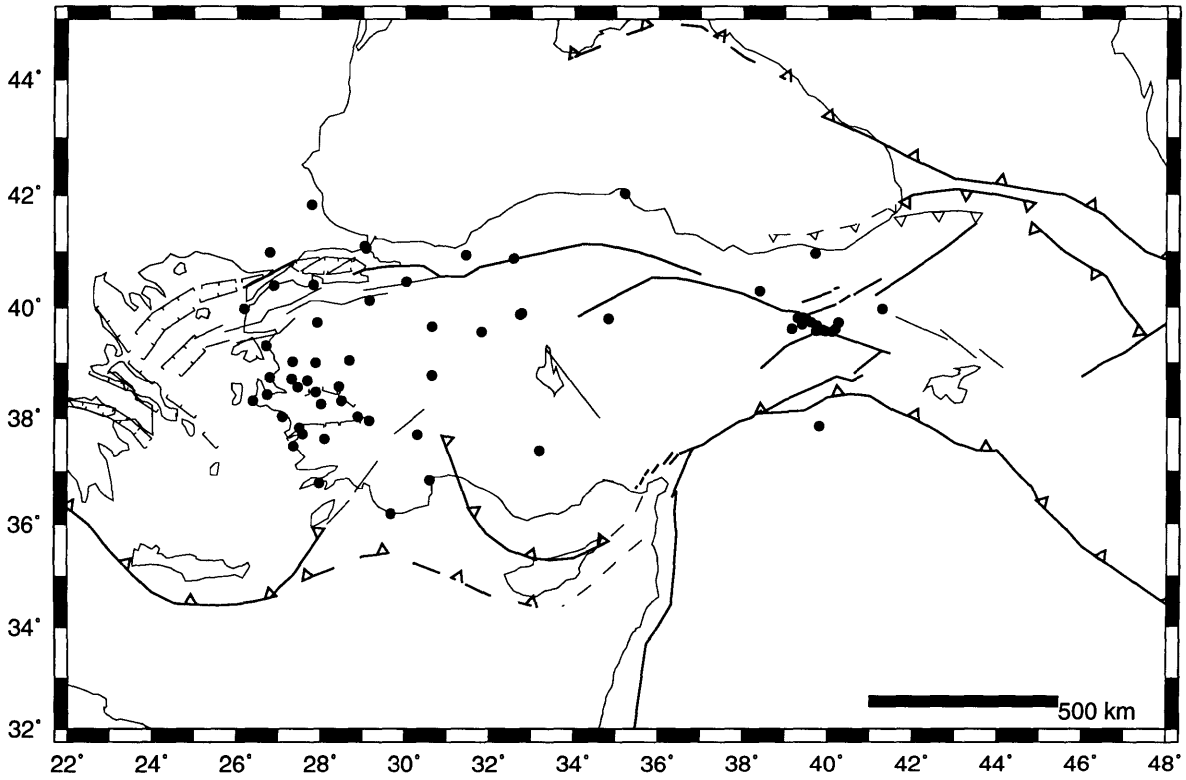

Figure B-28: Distribution of regional sites in western Turkey occupied during the fall 1992 experiment.

29) and the Erzincan earthquake networks, and at a few additional sites in eastern Turkey (Figure B-30). The data obtained from the last 3 days of the experiment were primarily from first epoch measurements and have not yet been included in our analyses. (Data from days 240–259 are incorporated this study.) Originally, we had

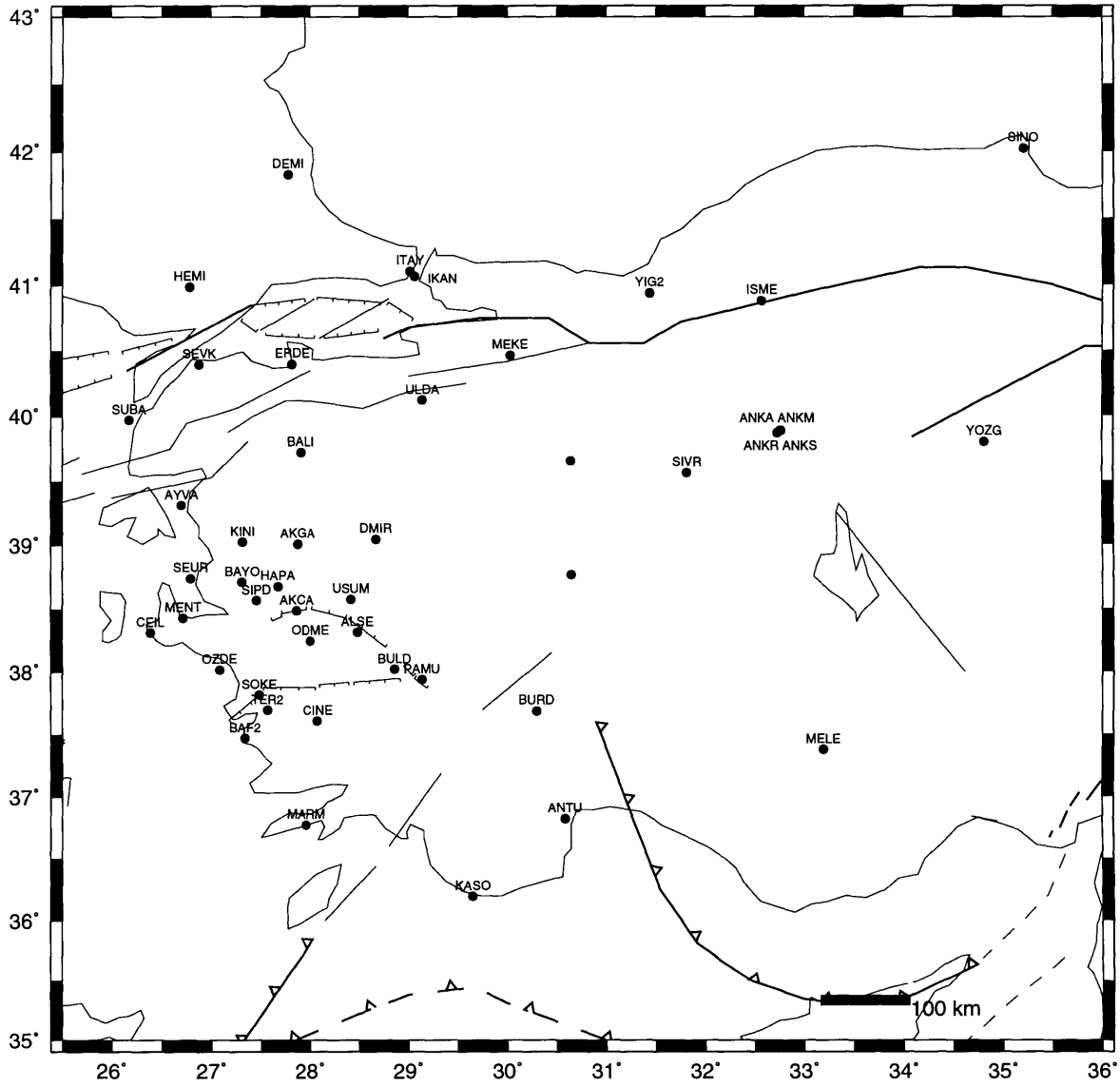

Figure B-29: Distribution of regional sites in western Turkey occupied during the fall 1992 experiment.

planned to occupy the western Turkey network. However, because we observed sites in the Erzincan network in the Spring of 1992 (ER01, ER02, ER03, ER04, ER05, ER07, ER08, ER09, ER10, ER11, ER12, ERZ2, KEM2, MER2, and SEBI), we reoccupied these sites to measure post-seismic deformation. In conjunction with this experiment, we also extended our observations into the eastern network by observing at the AKTO

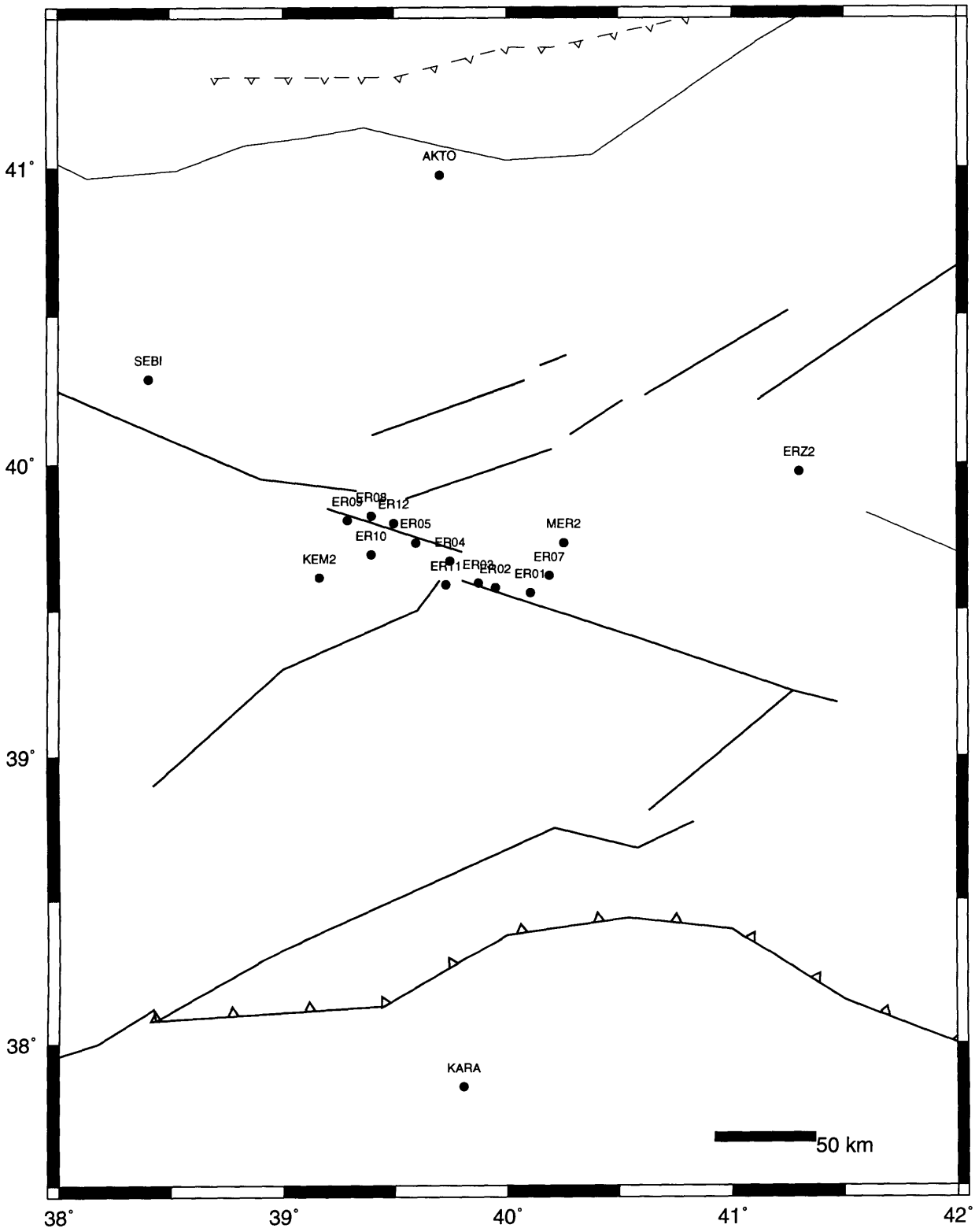

Figure B-30: Distribution of regional sites in eastern Turkey occupied during the fall 1992 experiment.

and KARA sites. In the western Turkey network, we made GPS observations at the 13 sites established in 1988: AKGA, ANTU, AYVA, CEIL, CINE, DEMI, IKAN, ISME, KASO, MEKE, ODME, PAMU, and ULDA. We also established 13 new sites. Four of these (BALI, BURD, MARM and SUBA) were observed between days 240 and 259, and were included in this study. The other 9 sites (AFYO, ALSE, ESKI, USUM, MARM, OZDE, SIVR, SINO, and KINI) were observed on days 262, 263 and 264. We obtained tie observations at all Ankara sites (ANKA, ANKM and ANKR) on two separate days. First epoch measurements were also made at the new Ankara SLR pad, ANKS. We used Trimble SST receivers and antennas with data acquisition software version 4.64 and 4.53.

In coordination with our observations, IfAG also observed at SLR sites MELE and YOZG, and at the Yığılca collocation point, YIG2. With Trimble SSE receivers, they also collected GPS measurements within the Aegean network earlier established by MIT and Durham: AKCA, AKGA, BAF2, BAYO, BULD, CEIL, DMIR, HAPA, MENT, PAMU, SEUR, SIPD, SOKE, and TER2. Independently, ETH-Z carried out GPS observations in the Marmara network, and observed at several sites using WM-102 receivers. Among these were ERDE, HEMI, ITAY, and SEVK, whose RINEX data were provided by the GCM. To provide a unified first degree geodetic network for the GCM, we have included sites from the Marmara and Bozdağ networks in our solutions. We used 30 second samples of data in our analysis, with the exception of the Marmara network sites, which were observed with 1-minute sampling.

In summary, GPS measurements were acquired at a total of 56 sites, for $\sim$8 hours, (Table B.33) during the fall 1992 experiment, with 18 satellites (PRNs 2, 3, 11, 12, 13, 14, 15, 16, 17, 18, 19, 20, 21, 23, 24, 25, 26, and 28) being tracked. PRNs 2, 14, 16, 20, 21, and 23 were in eclipsing season during the fall 1992 experiment.

For this experiment, we considered only the global sites tracked with Rogue re-

Table B.33: Regional sites and long-arc groupings: fall 1992 experiment.

ARC	DAY	GPS SITES							
1	240	ANKA	ANKM	ANKR	ANKS				
	241	ANKA	ANKR	ANKS					
2	244	AKTO	ANKM	AYVA	BAF2	BALI	BULD	ERZU	ISME
		KARA	MELE	ODME	PAMU	SEBI	SOKE	TER2	ULDA
		YIG2	YOZG						
	245	AKTO	ANKM	AYVA	BAF2	BALI	BULD	ERZU	ISME
		KARA	MELE	ODME	PAMU	SEBI	SOKE	TER2	ULDA
		YIG2	YOZG						
	246	AKTO	ANKM	AYVA	BAF2	BALI	BULD	ERZU	ISME
		KARA	MELE	ODME	PAMU	SEBI	SOKE	TER2	ULDA
		YIG2	YOZG						
3	248	AKCA	AKTO	ANKM	ANTU	BAYO	CEIL	ERDE	HAPA
		IKAN	ITAY	KEMA	MEKE	MELE	MENT	MERC	PAMU
		SEBI	SEUR	SEVK	SIPD	SOKE	ULDA	YIG2	YOZG
	249	AKCA	AKTO	ANKM	ANTU	BAYO	CEIL	ERDE	HAPA
		HEMI	IKAN	ITAY	KEMA	MEKE	MELE	MENT	MERC
		PAMU	SEBI	SEUR	SEVK	SIPD	SOKE	ULDA	YIG2
		YOZG							
	250	AKCA	AKTO	ANKM	ANTU	BAYO	CEIL	ERDE	HAPA
		HEMI	IKAN	ITAY	KEMA	MEKE	MELE	MENT	MERC
		PAMU	SEBI	SEUR	SEVK	SIPD	SOKE	ULDA	YIG2
		YOZG							
4	252	AKCA	AKGA	ANKM	BAYO	CEIL	DMIR	ER05	ER10
		HAPA	KASO	KEMA	MEKE	MELE	MERC	SUBA	YIG2
		YOZG							
	253	AKCA	AKGA	ANKM	BAYO	CEIL	DEMI	DMIR	ER07
		ER11	HAPA	KASO	KEMA	MEKE	MELE	MERC	SUBA
		YIG2	YOZG						
	254	AKCA	AKGA	ANKM	BAYO	CEIL	DEMI	DMIR	ER02
		ER03	ER08	HAPA	KASO	KEMA	MEKE	MELE	SUBA
		YIG2	YOZG						
	256	ANKM	ER01	ER04	ER09	ER12			
5	257	AKGA	ANKM	BURD	CINE	ER03	ER07	ER08	ER11
		MARM	MELE	SUBA	YIG2	YOZG			
	258	AKGA	ANKM	BURD	CINE	ER03	ER08	ER09	ER12
		MARM	MELE	SUBA	YIG2	YOZG			
	259	AKGA	ANKM	BURD	CINE	ER01	ER04	ER05	ER10
		MARM	MELE	SUBA	YIG2	YOZG			

ceivers (2-minute samples). We analyzed the fall 1992 experiment data in a fashion similar to that of 1991 and spring 1992 experiments. Unlike the spring 1992 experiment, we did not perform extensive tests, but focused on two types of data: augmented regional and global tracking. The global tracking data for these solutions was provided by SIO in "clean" GAMIT x-file format. Six tracking sites in Europe(KOSG, MADR, MATE, ONS0, TROM, and WETR) constituted our core global tracking network, and were used together with the regional sites (Figure B-31 and Table B.34). For the global analysis, we used data from 26 global tracking sites : ARON, DS42, FAIR, GOLD, HART, JPLM, KOKB, KOSG, MADR, MASP, MATE, MCMU, METS, NALL, ONS0, PAMA, PENT, SANR, SIO2, STJO, TAIW, TROM, USUD, WETR, YAR1, and YKN1 (Table B.35 and Figure B-32).

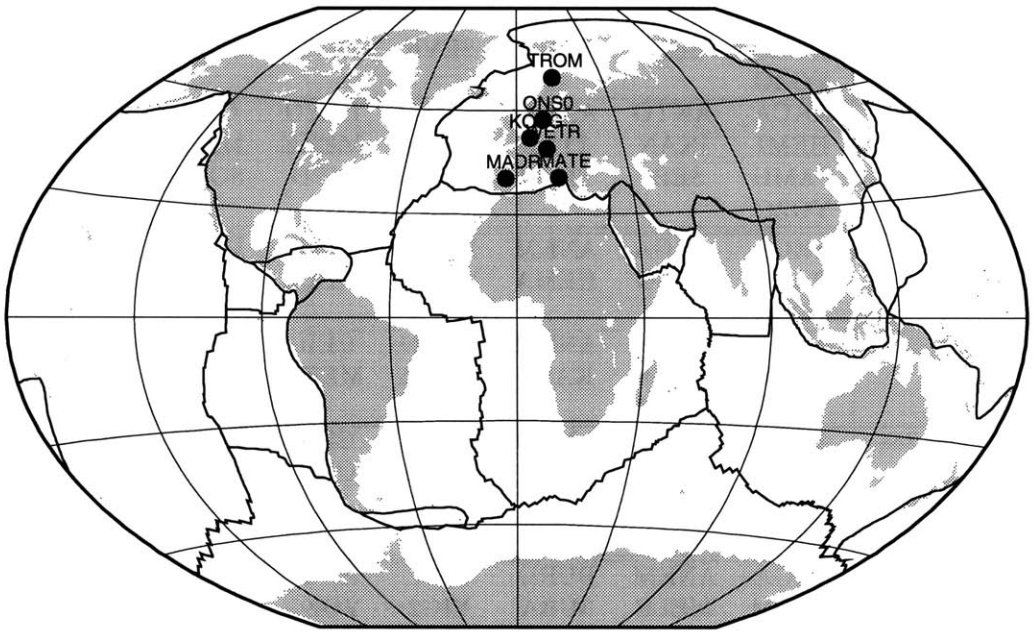

Figure B-31: Distribution of core global tracking sites included in the analyses of the fall 1992 experiment.

We started with the orbits (g-files) generated by the SIO GPS Orbit Facility,

Table B.34: Core global tracking sites and long-arc groupings: fall 1992 experiment.

ARC	DAY	GPS SITES					
	240	KOSG	MADR	MATE	ONS0	TROM	WETR
1	241	KOSG	MADR	MATE	ONS0		WETR
	244	KOSG	MADR	MATE	ONS0	TROM	
2	245	KOSG	MADR	MATE	ONS0	TROM	WETR
	246	KOSG	MADR	MATE	ONS0	TROM	WETR
	248	KOSG	MADR	MATE	ONS0	TROM	WETR
3	249	KOSG	MADR	MATE	ONS0	TROM	WETR
	250	KOSG	MADR	MATE	ONS0	TROM	WETR
	252	KOSG	MADR	MATE	ONS0	TROM	WETR
4	253	KOSG	MADR	MATE	ONS0	TROM	WETR
	254	KOSG	MADR	MATE	ONS0	TROM	WETR
	256	KOSG	MADR	MATE	ONS0	TROM	WETR
	257	KOSG	MADR	MATE	ONS0	TROM	WETR
5	258	KOSG	MADR	MATE	ONS0	TROM	WETR
	259	KOSG	MADR	MATE	ONS0		WETR

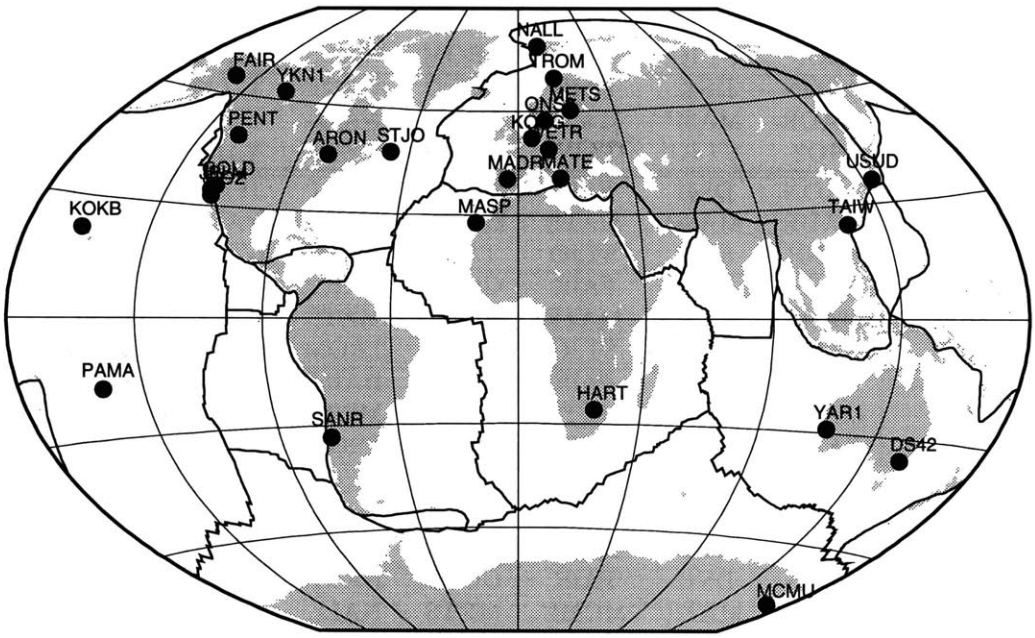

Figure B-32: Global tracking sites used together with regional data: fall 1992 experiment.

Table B.35: All global tracking sites and long-arc groupings: fall 1992 experiment.

ARC	DAY	GPS SITES								
1	240	ARON	DS42	FAIR	GOLD	HART	JPLM	KOKB	KOSG	
		MADR	MASP	MATE	MCMU	METS	NALL	ONS0	PAMA	PENT
		SANR	SIO2	STJO	TAIW	TROM	WETR	YAR1	YKN1	
	241	ARON	DS42	FAIR	GOLD	HART	JPLM	KOKB	KOSG	
		MADR	MASP	MATE	MCMU	METS	NALL	ONS0	PAMA	PENT
		SANR	SIO2	STJO	TAIW	WETR	YAR1	YKN1		
	244	ARON	DS42	FAIR	GOLD	HART	JPLM	KOKB	KOSG	
2		MADR	MASP	MATE	MCMU	METS	NALL	ONS0	PAMA	PENT
		SANR	SIO2	STJO	TAIW	TROM	YAR1	YKN1		
	245	ARON	DS42	FAIR	GOLD	HART	JPLM	KOKB	KOSG	
		MADR	MASP	MATE	MCMU	METS	NALL	ONS0	PAMA	PENT
		SANR	SIO2	STJO	TAIW	TROM	WETR	YAR1	YKN1	
	246	ARON	DS42	FAIR	GOLD	HART	JPLM	KOKB	KOSG	
		MADR	MASP	MATE	MCMU	METS	NALL	ONS0	PAMA	PENT
		SANR	SIO2	STJO	TAIW	TROM	WETR	YAR1	YKN1	
3	248	ARON	DS42	FAIR	GOLD	HART	KOKB	KOSG	MADR	
		MASP	MATE	MCMU	METS	NALL	ONS0	PAMA	PENT	SANR
		STJO	TAIW	TROM	WETR	YAR1	YKN1			
	249	ARON	DS42	FAIR	GOLD	HART	JPLM	KOKB	KOSG	
		MADR	MASP	MATE	METS	NALL	ONS0	PAMA	PENT	SANR
		SIO2	STJO	TAIW	TROM	WETR	YAR1	YKN1		
	250	ARON	DS42	FAIR	GOLD	HART	JPLM	KOKB	KOSG	
		MADR	MASP	MATE	METS	NALL	ONS0	PAMA	PENT	SANR
		SIO2	STJO	TAIW	TROM	WETR	YAR1	YKN1		
3	252	ARON	DS42	FAIR	GOLD	HART	JPLM	KOKB	KOSG	
		MADR	MASP	MATE	MCMU	METS	NALL	ONS0	PAMA	PENT
		SANR	SIO2	STJO	TAIW	TROM	WETR	YAR1	YKN1	
	253	ARON	DS42	FAIR	GOLD	HART	JPLM	KOKB	KOSG	
		MADR	MASP	MATE	MCMU	METS	NALL	ONS0	PAMA	PENT
		SANR	SIO2	STJO	TAIW	TROM	WETR	YAR1	YKN1	
	254	ARON	DS42	FAIR	GOLD	HART	JPLM	KOKB	KOSG	
		MADR	MASP	MATE	MCMU	METS	NALL	ONS0	PAMA	PENT
		SANR	SIO2	STJO	TAIW	TROM	WETR	YAR1	YKN1	
4	256	ARON	DS42	FAIR	GOLD	HART	JPLM	KOSG	MADR	
		MASP	MATE	MCMU	NALL	ONS0	PAMA	PENT	SANR	SIO2
		STJO	TAIW	TROM	USUD	WETR	YAR1	YKN1		
	257	ARON	DS42	FAIR	GOLD	HART	JPLM	KOSG	MADR	
		MASP	MATE	MCMU	METS	NALL	ONS0	PAMA	PENT	SANR
		SIO2	STJO	TAIW	TROM	USUD	WETR	YAR1	YKN1	
	258	ARON	DS42	FAIR	GOLD	HART	JPLM	KOSG	MADR	
		MATE	MCMU	METS	NALL	ONS0	PAMA	PENT	SANR	SIO2
		STJO	TAIW	TROM	USUD	WETR	YAR1	YKN1		
	259	DS42	FAIR	GOLD	HART	JPLM	KOSG	MADR	MASP	
		MATE	MCMU	METS	NALL	ONS0	PAMA	PENT	SANR	SIO2
		STJO	TAIW	USUD	WETR	YAR1	YKN1			

and defined 6 long-arcs for the fall 1992 experiment. We performed two separate long-arc, single-session GAMIT solutions: one with global data only, and the other with both regional and core global tracking sites (augmented regional). At this stage we cleaned the regional data. By applying loose constraints, we obtained two sets of quasi-observations: one for augmented regional data and the other for the global data. In Tables B.36 and B.37, the nrms for both sets of data are shown. The nrms of solutions for the augmented regional data on the days between 248 and 254 were slightly greater. On the average, however, it reflects a 15 to 20 mm rms for the LC residuals. The mean nrms of the global data solution was 0.5, indicating that the LC residual rms was relatively higher at ~30 mm.

We used the quasi-observations in GLOBK, and investigated the short-term precision of baseline estimates by applying **T**, **M**, **L**, **T_M**, and **T_L** sets of process noise to the satellites. To provide a comparison, we considered both augmented regional and the combination of augmented regional and global tracking solutions. Parameters of the error model for such solutions are shown in Table B.38 (augmented regional analyses) and Table B.39 (combination of augmented regional and global data).

We eliminated observations on days 256 and 257 due to the poor determination of orbits. As a result, our data set contains only one day's observations for ER04, ER01, ER12, ER07, and ER11. Two or more repeat observations were available only for ER03, ER05, ER08, and ER10.

A tight process noise set (**T**) on all satellites provided the highest precision. With the several-site-common combination solution (Figure B-35), the baseline length dependency in wrms scatter reduced by 3–4 ppb. Because ambiguity-free quasi-observations were used, the east component wrms is worse than that of the north components. The mean wrms was 7 mm in the north but we observed values as large as 25 mm. Similarly, the mean east component wrms was 13 mm, with a peak value

Table B.36: Normalized RMS of long-arc, single-session GAMIT solutions (augmented regional): fall 1992 experiment.

GPS DAY	tight solution	loose solution
240	0.244	0.251
241	0.204	0.207
244	0.261	0.257
245	0.140	0.134
246	0.223	0.223
248	0.308	0.308
249	0.318	0.316
250	0.311	0.307
252	0.277	0.274
253	0.317	0.315
254	0.311	0.310
256	0.209	0.213
257	0.176	0.169
258	0.207	0.206
259	0.264	0.261

Table B.37: Normalized RMS of long-arc, single-session GAMIT solutions (combination of core global and regional sites): fall 1992 experiment.

GPS DAY	tight solution	loose solution
240	0.482	0.421
241	0.505	0.461
244	0.501	0.442
245	0.487	0.439
246	0.477	0.436
248	0.467	0.408
249	0.383	0.346
250	0.440	0.406
252	0.543	0.496
253	0.443	0.405
254	0.481	0.437
256	0.660	0.594
257	0.325	0.252
258	0.347	0.307
259	0.444	0.375
263	0.327	0.274

Table B.38: Short-term repeatability (augmented regional data): fall 1992 experiment. [Core global tracking and regional sites.]

Solution Descriptor	N-S component a (mm)	b (ppb)	mean nrms	E-W component a (mm)	b (ppb)	mean nrms	U-D component a (mm)	b (ppb)	mean nrms	Length a (mm)	b (ppb)	mean nrms
S_L	6.10	13.64	2.07	11.88	14.45	1.78	15.30	25.29	1.48	8.70	17.33	1.96
S_M	6.44	10.00	2.06	11.76	13.61	1.87	15.17	23.35	1.56	9.21	15.28	2.09
S_T†	6.74	6.39	2.05	11.55	11.48	1.94	15.81	17.23	1.56	9.52	9.89	2.11
S_T_L	6.61	6.67	1.98	10.76	15.73	1.92	15.49	20.66	1.57	8.51	14.90	2.10
S_T_M	6.55	6.94	2.02	10.92	15.67	1.96	15.24	21.04	1.59	8.73	14.66	2.16

† The preferred solution is obtained by applying tight constraints to all satellites (*cf.* Table B.2).

Table B.39: Short-term repeatability (augmented regional and global combination): fall 1992 experiment. [All global tracking and regional sites.]

Solution Descriptor	N-S component a (mm)	b (ppb)	mean nrms	E-W component a (mm)	b (ppb)	mean nrms	U-D component a (mm)	b (ppb)	mean nrms	Length a (mm)	b (ppb)	mean nrms
S_L	6.07	12.18	2.65	11.81	14.18	2.14	15.23	25.87	1.69	9.20	15.35	2.29
S_M	6.23	10.09	2.98	11.96	10.61	2.37	16.11	16.57	1.67	9.70	10.28	2.42
S_T†	7.02	3.47	2.99	12.10	7.69	2.56	15.91	17.44	1.74	10.09	7.33	2.56
S_T_L	6.81	4.57	2.79	11.86	8.31	2.40	15.62	22.01	1.82	9.70	8.97	2.45
S_T_M	6.90	4.61	2.88	12.01	9.23	2.50	15.77	20 47	1.79	9.94	8.88	2.53

† The preferred solution is obtained by applying tight constraints to all satellites (*cf.* Table B.2).

of 30 mm. Some of these rather high wrms values were associated with the WM-102 receivers.

We estimated all sites deterministically for augmented and combination analyses and found GLOBK χ^2/f 3 and 5.7, respectively. The formal uncertainties of baseline estimates were 3 to 5 mm in the horizontal; significantly smaller than for other experiments. Below are uncertainties of baseline estimates obtained from the combination of augmented regional and global tracking sites:

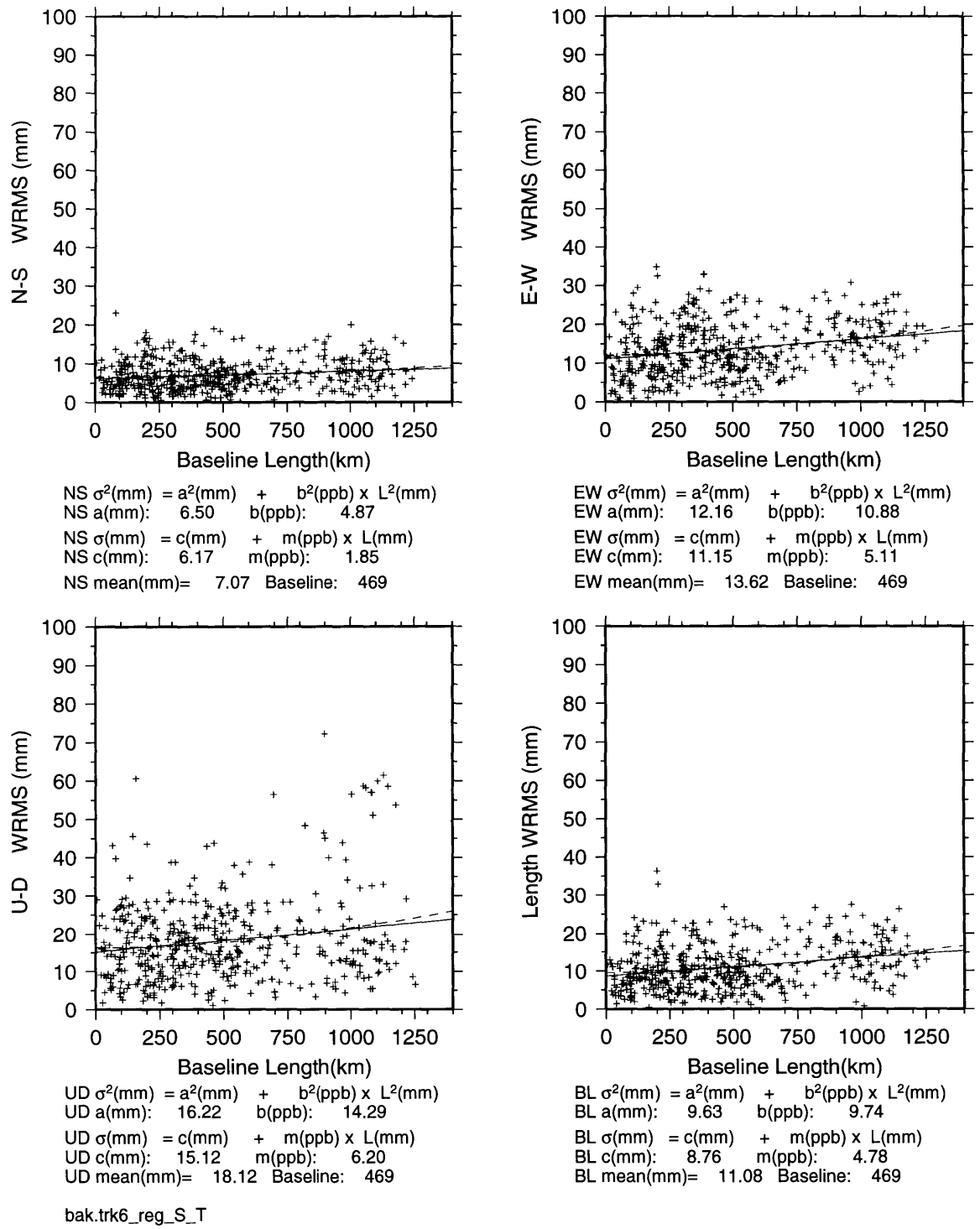

Figure B-33: The wrms scatter and model parameters of NS, EW, UD components and length, as a function of baseline length. They are obtained from the fall 1992 experiment (augmented regional analysis) with tight (**T**) stochastic constraints applied to the satellites. wrms of baselines with 2 or more repeat observations are shown. Dashed line is a functional in the form of $\sigma^2 = \mathrm{a}^2 + \mathrm{b}^2\mathrm{L}^2$. Continuous line is a linear fit to the wrms scatter ($\sigma = \mathrm{c} + \mathrm{m}\ L$).

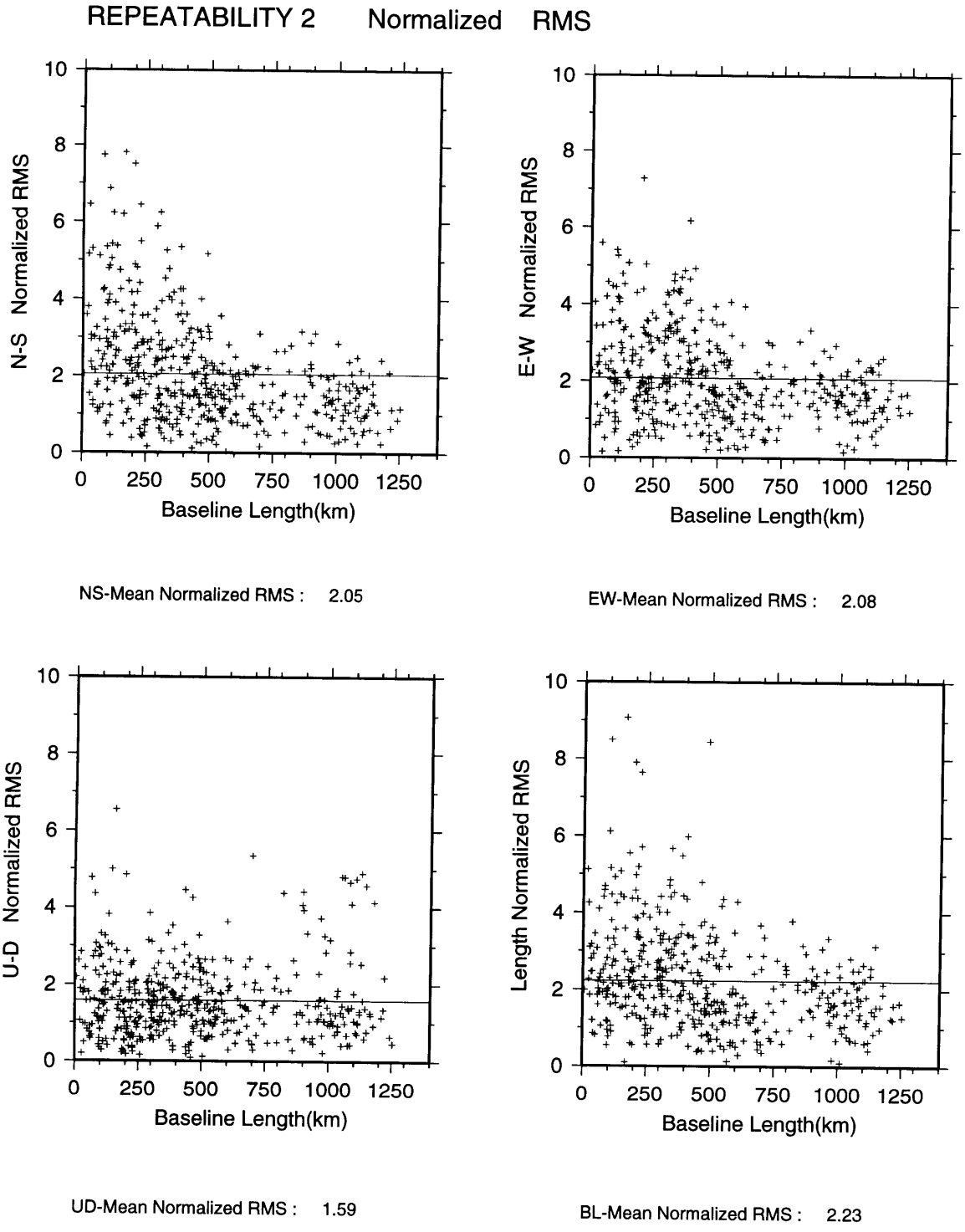

Figure B-34: The nrms scatter of NS, EW, UD components and length [for the solution described in Figure B-33], as a function of baseline length. They are obtained from the fall 1992 experiment (augmented regional analysis) with tight (**T**) stochastic constraints applied to the satellites. Continuous line represents the mean nrms scatter.

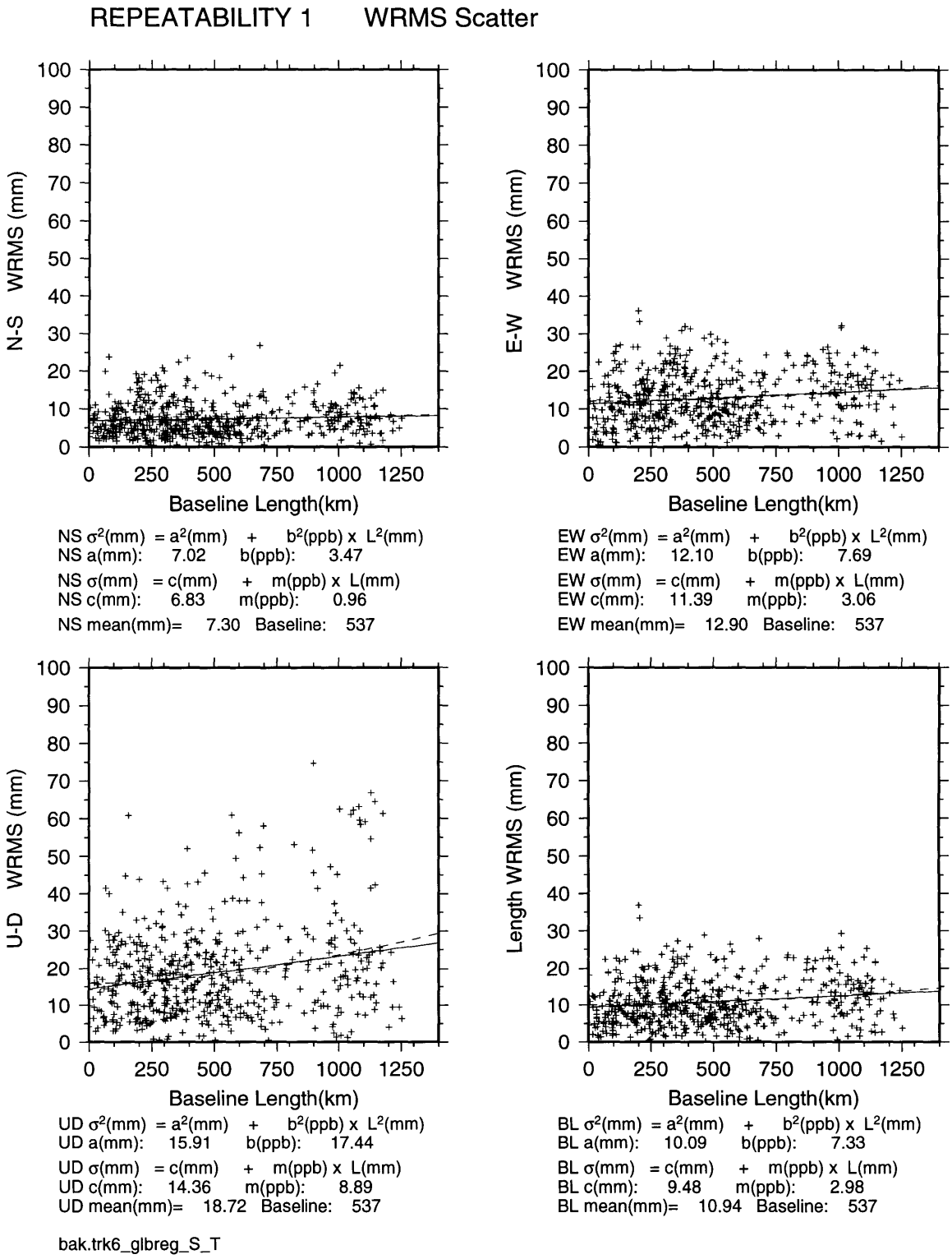

Figure B-35: The wrms scatter and model parameters of NS, EW, UD components and length, as a function of baseline length. They are obtained from the fall 1992 experiment (combination of augmented regional and global tracking sites) with tight (**T**) stochastic constraints applied to the satellites. wrms of baselines with 2 or more repeat observations are shown. Dashed line is a functional in the form of $\sigma^2 = a^2 + b^2L^2$. Continuous line is a linear fit to the wrms scatter ($\sigma = c + m\ L$).

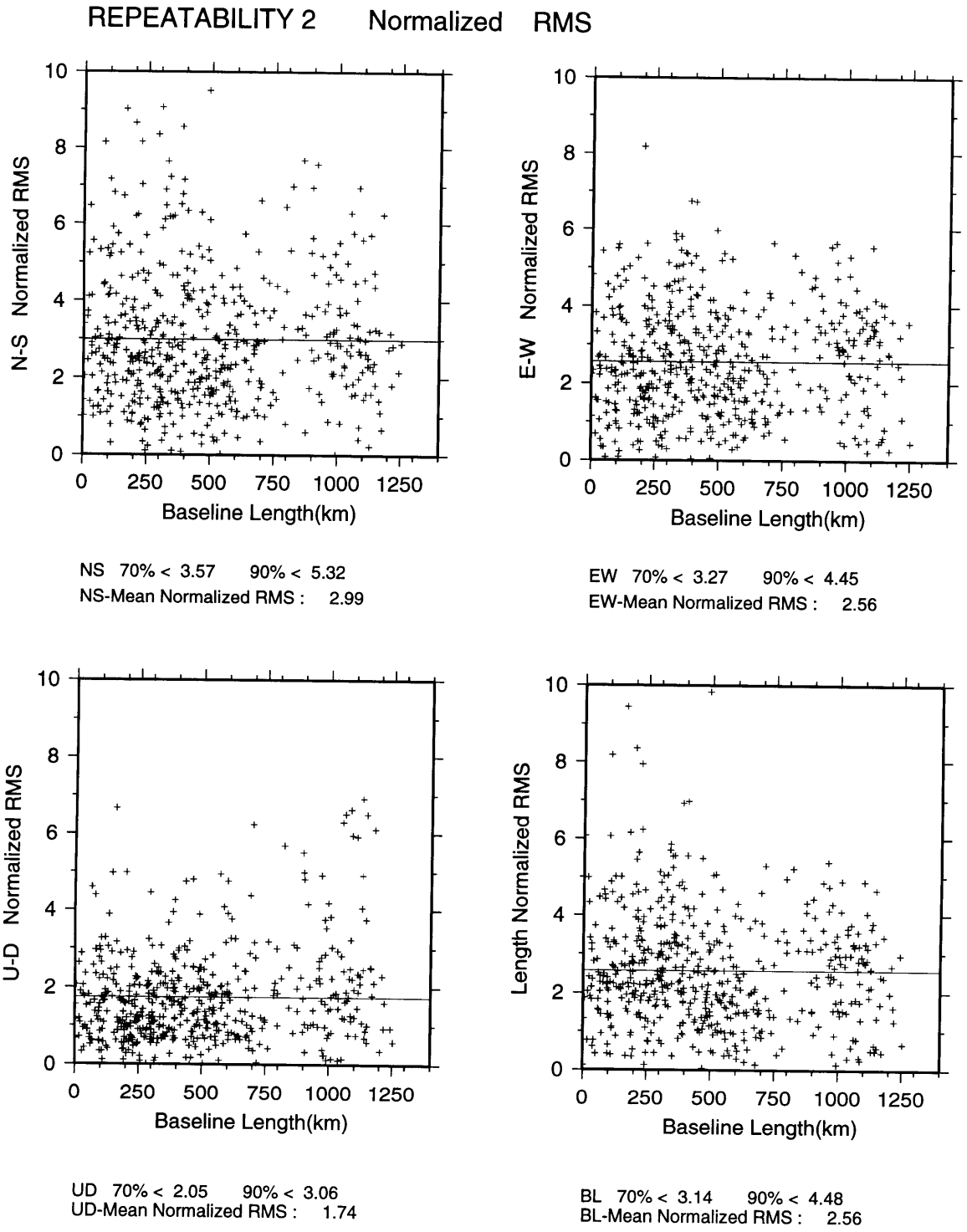

Figure B-36: The nrms scatter of NS, EW, UD components and length [for the solution described in Figure B-35], as a function of baseline length. They are obtained from the fall 1992 experiment (several-site-common combination: combination of augmented regional and global tracking sites) with tight (**T**) stochastic constraints applied to the satellites. Continuous line represents the mean nrms scatter.

σ_{NS}(mm) =	1.38(mm)	+	0.78x10^{-3} L(km)	@500km baseline:	1.77(mm)
σ_{EW}(mm) =	2.76(mm)	+	1.32x10^{-3} L(km)	@500km baseline:	3.42(mm)
σ_{UD}(mm) =	6.54(mm)	+	0.45x10^{-3} L(km)	@500km baseline:	6.76(mm)
σ_{BL}(mm) =	2.00(mm)	+	1.85x10^{-3} L(km)	@500km baseline:	2.92(mm).

We obtained two sets of compact quasi-observations: one for augmented analysis and another for combination analysis. However, in our estimation of velocity field, we used those obtained from the combination analysis.

Appendix C

Analysis of Long-Term Precision and Accuracy

While inspecting the time-series of estimates of baseline components, we encountered several anomalous behaviors at baselines formed between regional and/or global tracking sites. Figure C-1 shows the estimates of some representative, very long baselines ($>$ 2000 km) between regional sites and Onsala. We observed that the earlier experiments (1988, 1989, and 1990) have considerably greater uncertainties (also see Appendix B). The marked reduction in the uncertainties of later experiments (1991 and 1992) is due to the incorporation of a globally evenly distributed tracking network in their analysis. We used the nrms obtained from the short-term precision analysis of each experiment as a calibration factor (Chapter 2 and Appendix B) to equalize formal uncertainties. We did not, however, observe significant change in the position and velocity estimates in the time-series plots, mostly because short-term repeatabilities did not provide a measure for systematic errors. Therefore, we decided to apply a uniform scale to all formal uncertainties. In Figure C-1 we also observe a rather large scatter in the relative position estimates. An incomplete global tracking

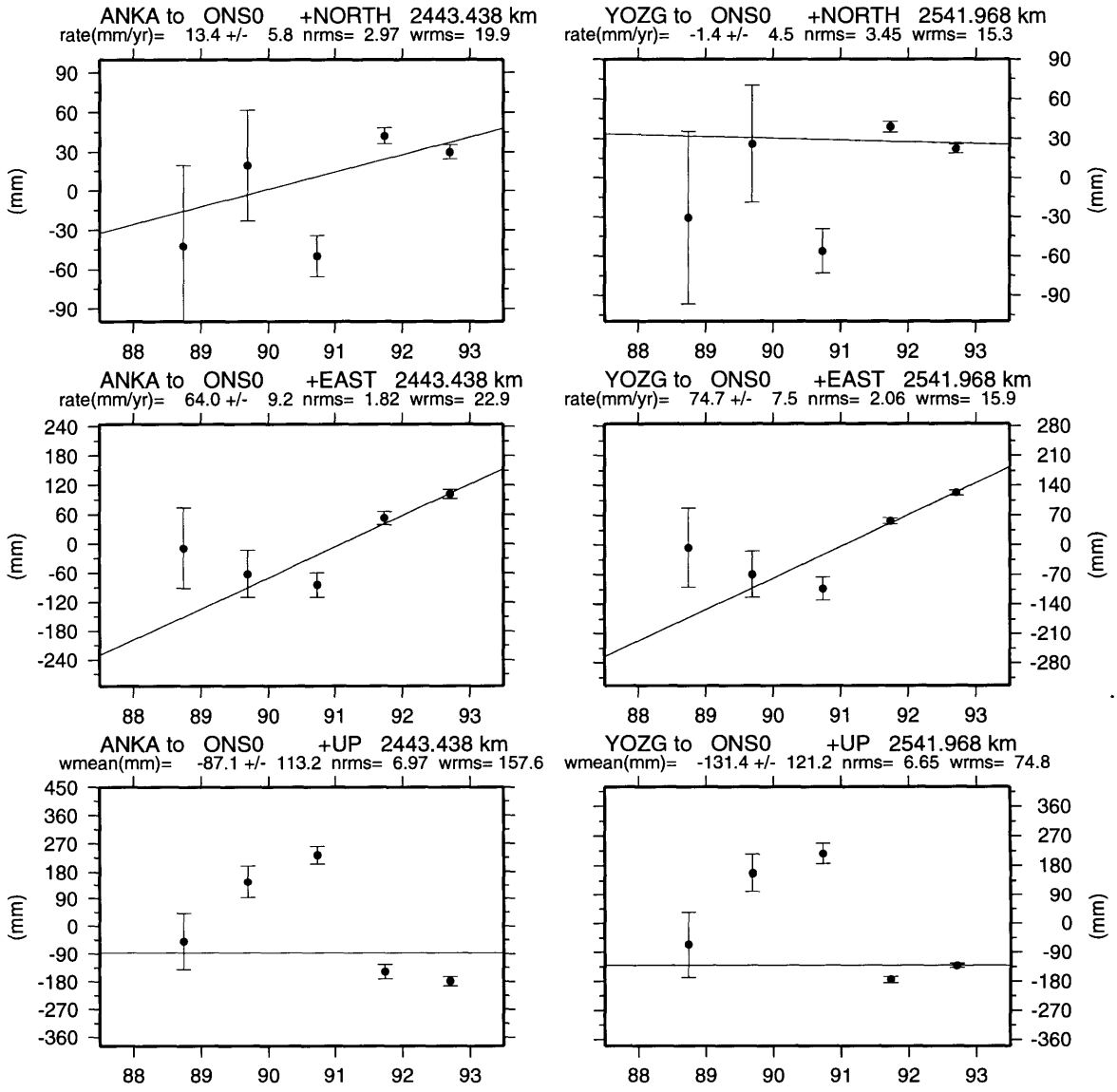

Figure C-1: Time-series plot of very long baselines: Estimates of baseline components. [Scaled all formal uncertainties by 2.]

network used in the earlier experiments could as well have introduced a systematic offset in the estimates from the 1988, 1989, and 1990 experiments (Appendix A: augmented solutions). However, predominant offset is evident only in the 1989 and 1990 estimates of relative positions, as compared to 1988, 1991 and 1992 estimates. The offset of 27–40 cm in their vertical components is rather striking and projects into the estimates of the horizontal components. When Oral et. al [1993][1] used the 1988 and 1990 experiments to obtain relative site motions in Turkey, they were unaware of the vertical systematics and horizontal bias. They also underestimated the 1-σ errors by a factor of two, since there was no long-term repeatability information available at the time. Their relative site velocities were at least 20 mm/yr higher than those we present in this study because the horizontal, and especially the vertical, positions of global sites were overconstrained to their SV5 [Murray, 1991] defined values, which were less accurate than those defined by the VG frame.

Within our regional network, however, such outlier behavior in the vertical was limited to baselines formed to Melengiçlik (MELE), Yığılca (YIGI ad YIGI) or Karacadağ (KARA) in the 1989 and 1990 experiments. For estimates of other regional baselines, we observed a vertical offset less than 5 cm (*cf.* time-series plots below).

We considered several possible causes for such systematic errors. Though the antenna height entries comply with the information supplied by log sheets, we cannot rule out the possibility of incorrect or misinterpreted field log entries. A class of receiver specific errors (e.g., hardware/software related problems, antenna phase center variations, calibration errors) might also have played a role. Modeling errors, such as not accounting for the antenna phase center variations with changing azimuth and elevation, could amount to several centimeters [Simon McClusky, pers. comm., 1993]. This would easily explain a mismatch of 5 cm in the vertical components.

[1]The data analyzed in this study were not available at the time of submission of this paper in 1992.

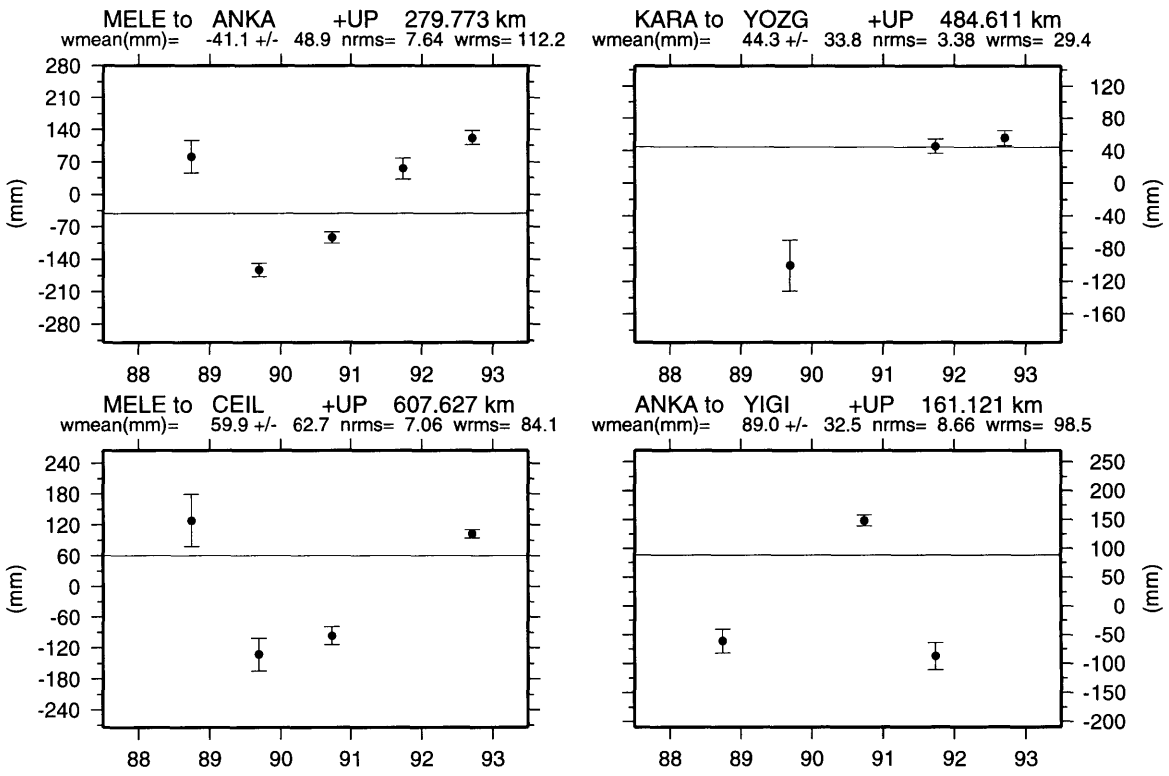

Figure C-2: Time-series plot: Estimates of vertical component of regional baselines (1988-1992). [Scaled formal uncertainties.]

Large systematic errors were observed only at sites occupied by Minimac receivers with the exception of the KARA site in 1989, where a Trimble 4000 SDT receiver was deployed. (The vertical errors at this site were probably due to orbital errors [end-effects] since it was the easternmost site.) The common threads between the 1989 and 1990 experiments are their fiducial sites and the receivers/antennas operated: All fiducial sites were recording with Minimac receivers except Onsala (1989 and 1990), Tromso (1989) and Yellowknife(1989), which had TI4100 receivers. It is possible that the common denominator in these two experiments, viz., the Minimac regional and global trackers (modeling the GPS phase delay data without accounting for the antenna phase center variations with changing azimuth and elevation [Simon McClusky, pers. comm., 1993]) could have been the source of the problem, together with rather poor fiducial tracking coverage [Donellan et al., 1993].

Because we did not have the luxury of replacing either the global or regional sites, no other tests were carried out. Under these circumstances, it was clear that we could not expect a healthy vertical velocity estimate from our data set. Therefore, instead of estimating vertical velocities at regional sites, we stochastically estimated their vertical positions in order to reflect the scatter, and referred their long-term error statistics about their weighted means. Accordingly, we allowed 0.05 m/yr variation for all sites, except 0.5 m/yr at the anomalous sites (MELE, YIGI, YIG2, and KARA).

After baselines involving anomalous sites were excluded, the mean wrms scatter of estimates of vertical components about their weighted means for all baselines, including those for which we have only two epochs, were 23 mm, and 90% of the baselines wrms values were less then 56 mm (Figure C-3). Sites in the eastern Turkey network showed relatively higher scatter compared to those in western Turkey, since a majority of them were observed only in 1989 and 1991. After a scaling of 2 was applied to all formal errors, the mean nrms was 1.2 with a standard deviation of 1.1. Figure C-4 suggests that we should apply an additional scaling of 3 to the formal errors if we were to estimate vertical velocities and obtain no significant rates. Since we obtained a mean nrms of 1 for the long-term repeatability of the horizontal components by scaling the formal errors by 2, this additional factor, of course, presents an upper bound.

Since the 1989 and 1990 experiments have large systematic errors in the vertical, we questioned the possibility of these systematics being aliased into the estimates of the horizontal components. By examining the time-series we concluded that for most of the baselines the estimates from the 1990 experiment are outliers. Time-series for some representative baselines are shown in Figures C-5, C-6, C-7 and C-8. The estimates from the 1990 experiment are offset by about 10 mm. Similar outlier characteristics are clearly evident in the MELE-ANKA, MELE-YOZG and ANKA-YOZG baselines, which were simultaneously observed during all regional experiments.

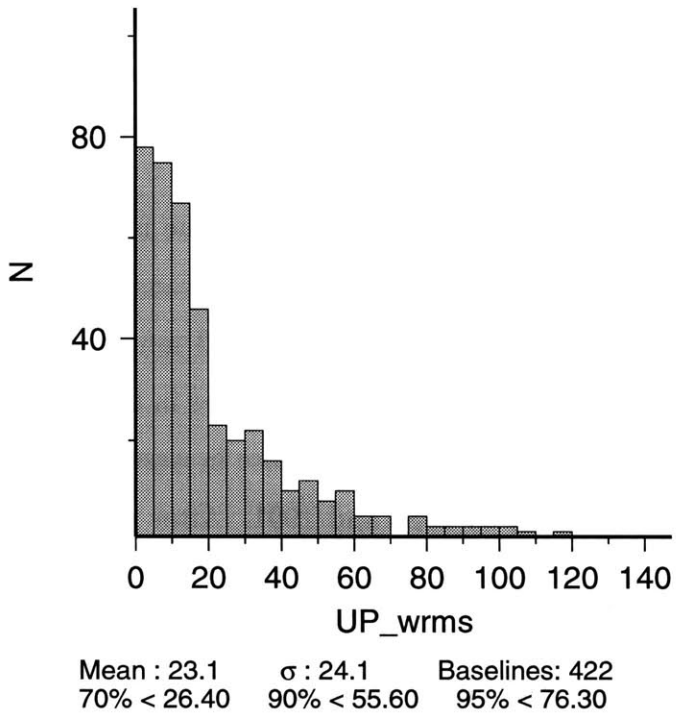

Figure C-3: Histogram of wrms scatter of vertical components about their weighted means after removal of Melengiçlik, Yığılca and Karacadağ. All baselines observed twice or more were included.

Because we have 5 epoch-observations at these baselines, the impact of outliers on the velocity/rate is quite small. However, for sites with only 3 epochs, the errors and small uncertainties in the position estimates for 1990 introduce significant error into the velocity estimates (about 15 mm/yr). Figure C-8 illustrates the effect on the MELE-YIGI baseline.

Outlier characteristics displayed in the estimates of the horizontal components could as well be explained by the possible projection of those errors in the vertical. However, we could not isolate such outliers in the horizontal for the 1989 estimates,

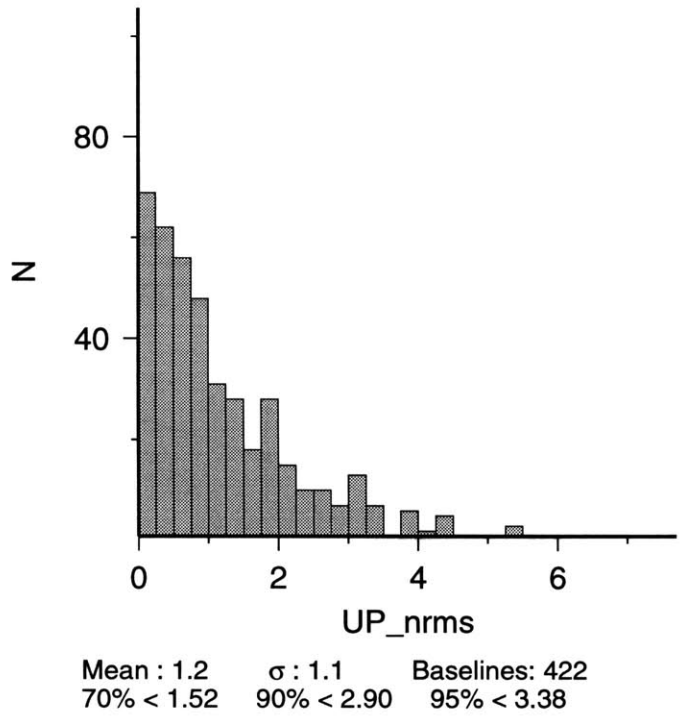

Figure C-4: Histogram of nrms scatter of vertical components about their weighted means. All baselines observed twice or more were included. The formal uncertainties were already scaled by a factor of 2 (see Chapter 2).

as we did for the 1990 estimates, due partly to insufficient repeat observations. We suspect that the fiducial tracking network utilized in the analyses of the 1990 experiment was inadequate. The orbital parameters in this experiment were essentially determined by the global sites located in Europe, and partly by the eastern North American sites. The absence of Yellowknife and Tromso from this network may be key. In the analyses of the 1989 experiment we did not use Wettzell (WETM [Minimac]) because it corrupted our solutions. However, this site was included in our analyses of the 1990 experiment and we suspect that it might have been the cause of this horizontal bias. Even when we carried out analysis of the 1990 experiment

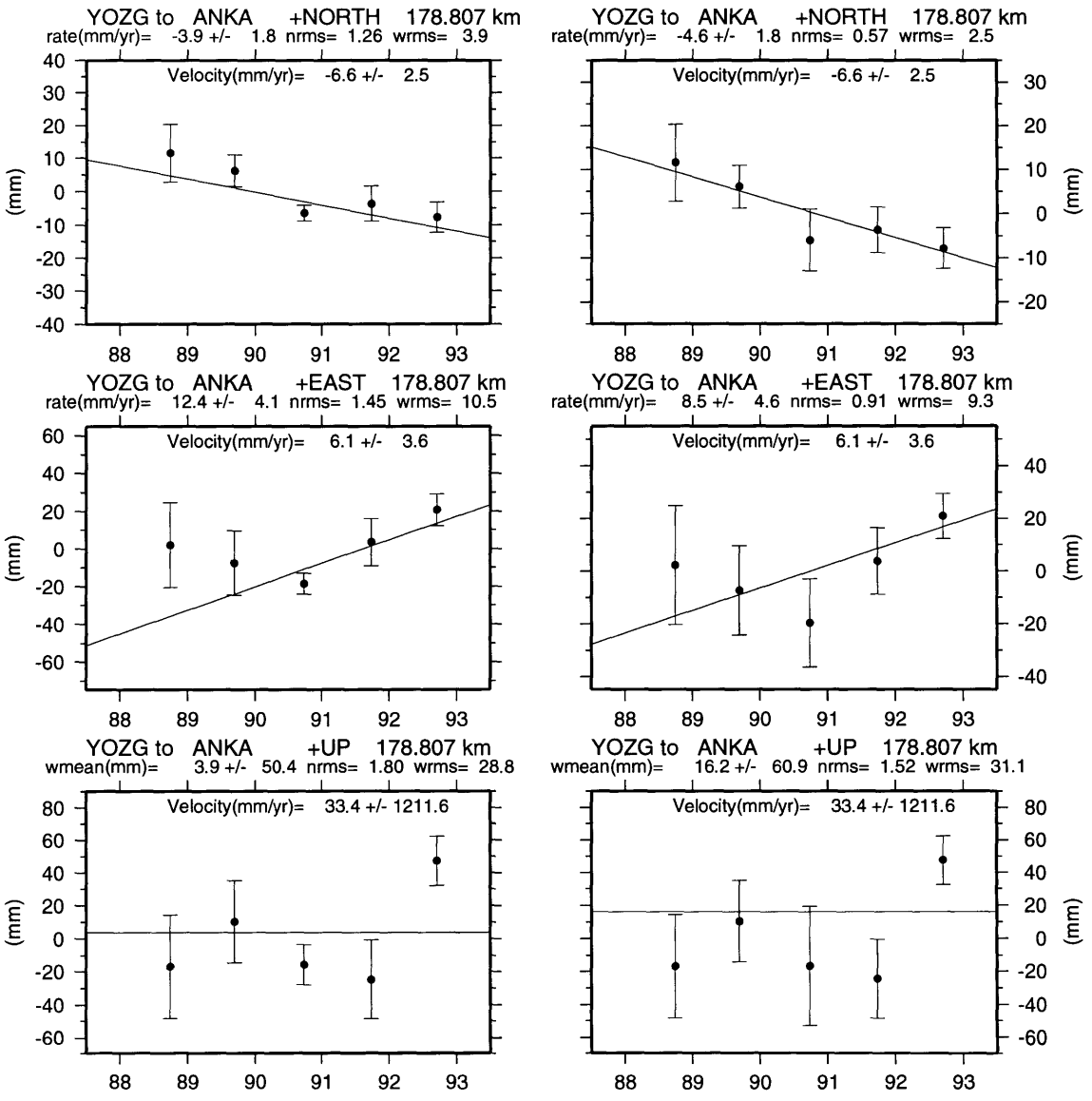

Figure C-5: Time-series plot: Comparing estimates of NS, EW and UD components of regional baselines (1998-1992). In the right panel, the 1990 experiment is downscaled by a factor of 3. The rate is calculated by a naive weighted least squares fit to the estimates of baseline components. The wrms and nrms are about this line. The velocity (inserted in the box) is obtained from GLOBK Kalman filter solutions using the entire data set. We also scaled all formal uncertainties by a factor of 2 to reflect realistic 1-σ errors.

without this site, outliers persisted in the estimates of the horizontal components. The exclusion of Wettzell from the analysis of the 1990 experiment also reduced the strength of the global coverage and worsened short-term precision as the proportional

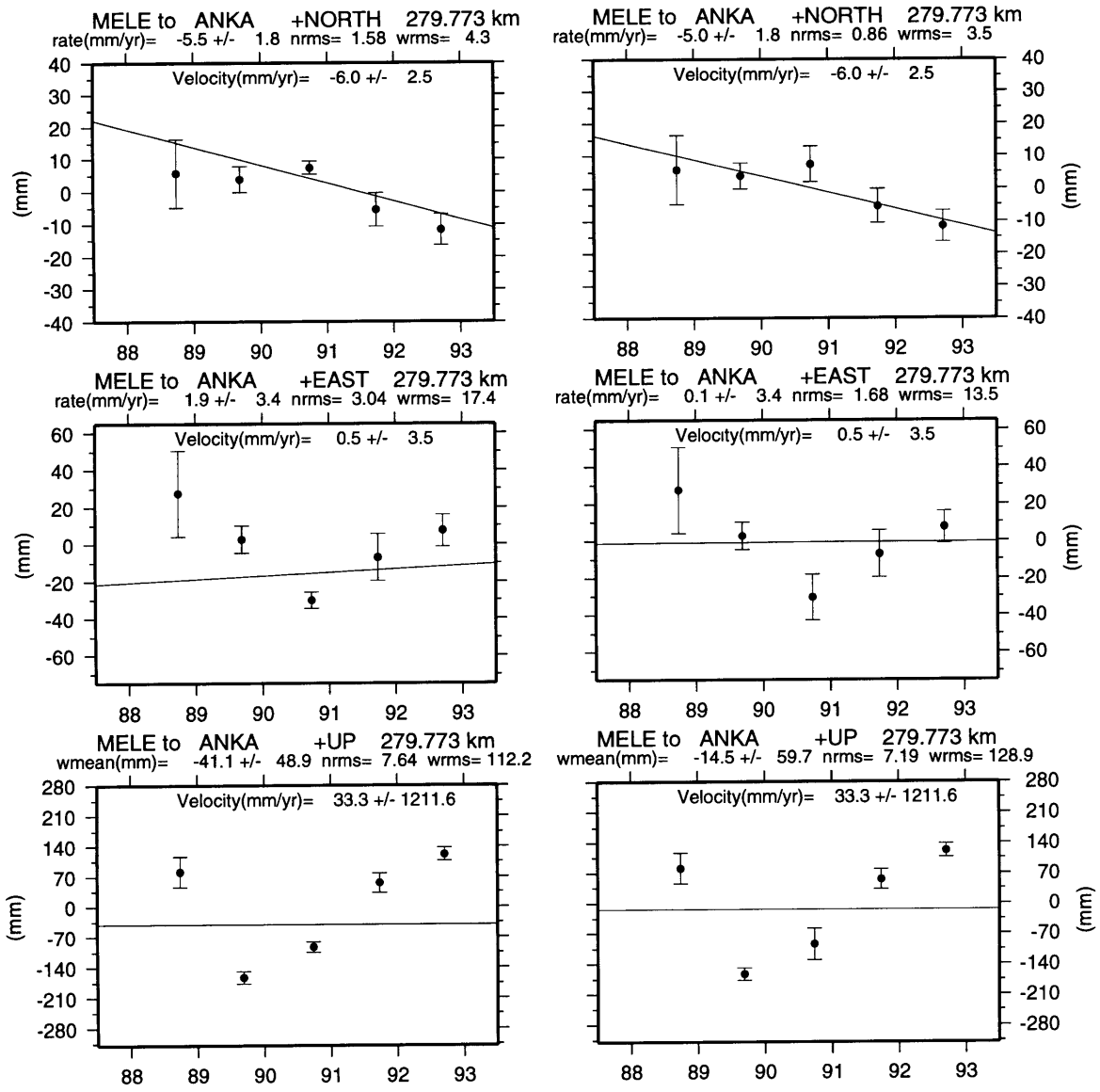

Figure C-6: Time-series plot: Comparing estimates of NS, EW and UD components of regional baselines (1998-1992). In the right panel, the 1990 experiment is downscaled by a factor of 3. The velocity (inserted in the box) is obtained from GLOBK Kalman filter solutions using the entire data set. We also scaled all formal uncertainties by a factor of 2 to reflect realistic 1-σ errors.

errors increased.

In summary, we could not isolate the horizontal outliers to a specific site. In order to minimize the effects of such bias to the velocity estimates, we decided to

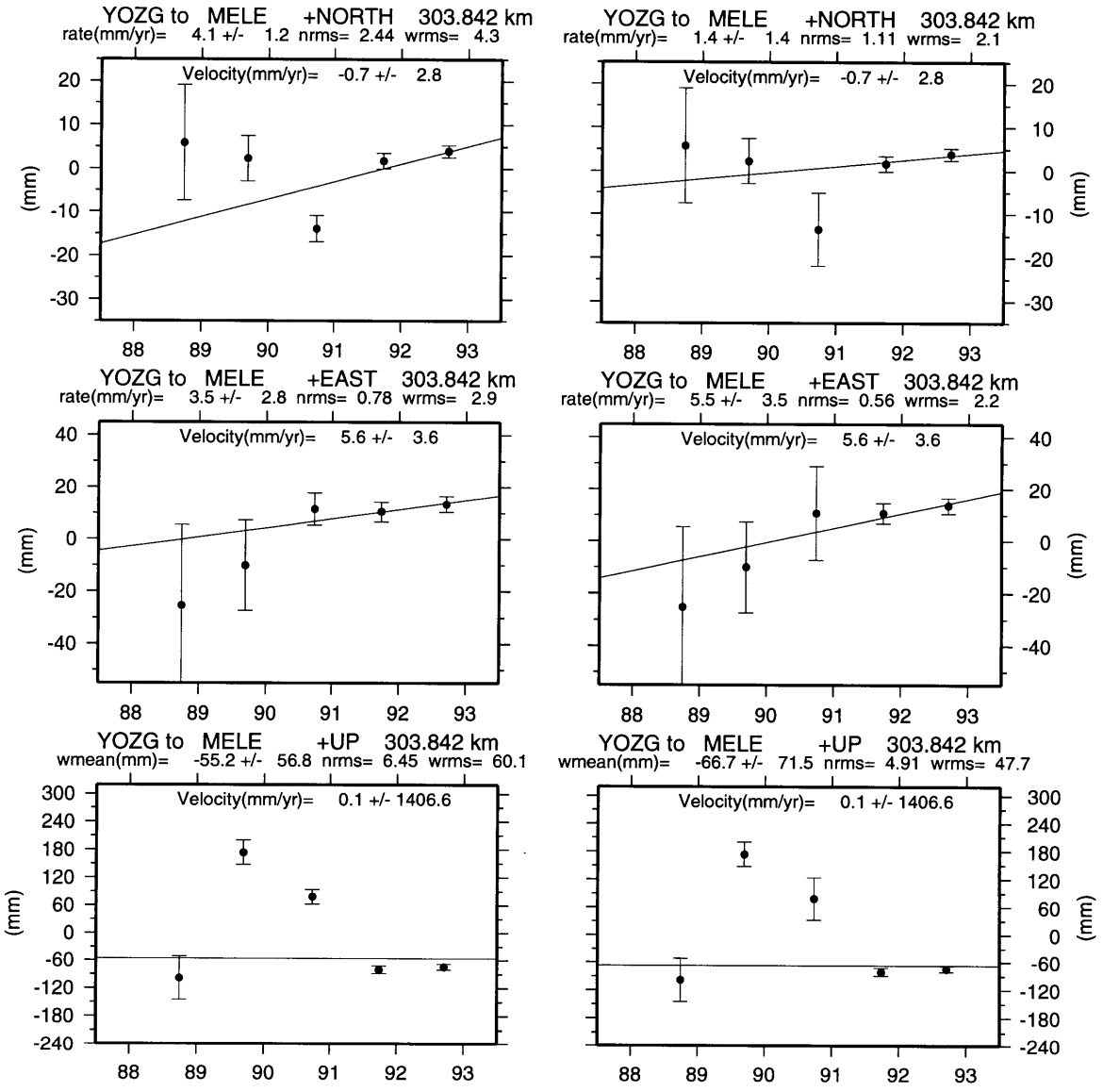

Figure C-7: Time-series plot: Comparing estimates of NS, EW and UD components of regional baselines (1998-1992). In the right panel, the 1990 experiment is downscaled by a factor of 3. The velocity (inserted in the box) is obtained from GLOBK Kalman filter solutions using the entire data set. We also scaled all formal uncertainties by a factor of 2 to reflect realistic 1-σ errors.

rescale the formal errors of the 1990 experiment and sought an appropriate factor by which to multiply the formal uncertainties. We reduced the effects of such a bias by downscaling the 1990 experiment by 3, viz., multiplying the variance-covariance matrix by 9. The right panels in Figures C-5, C-6, C-7 and C-8 depict time evolution

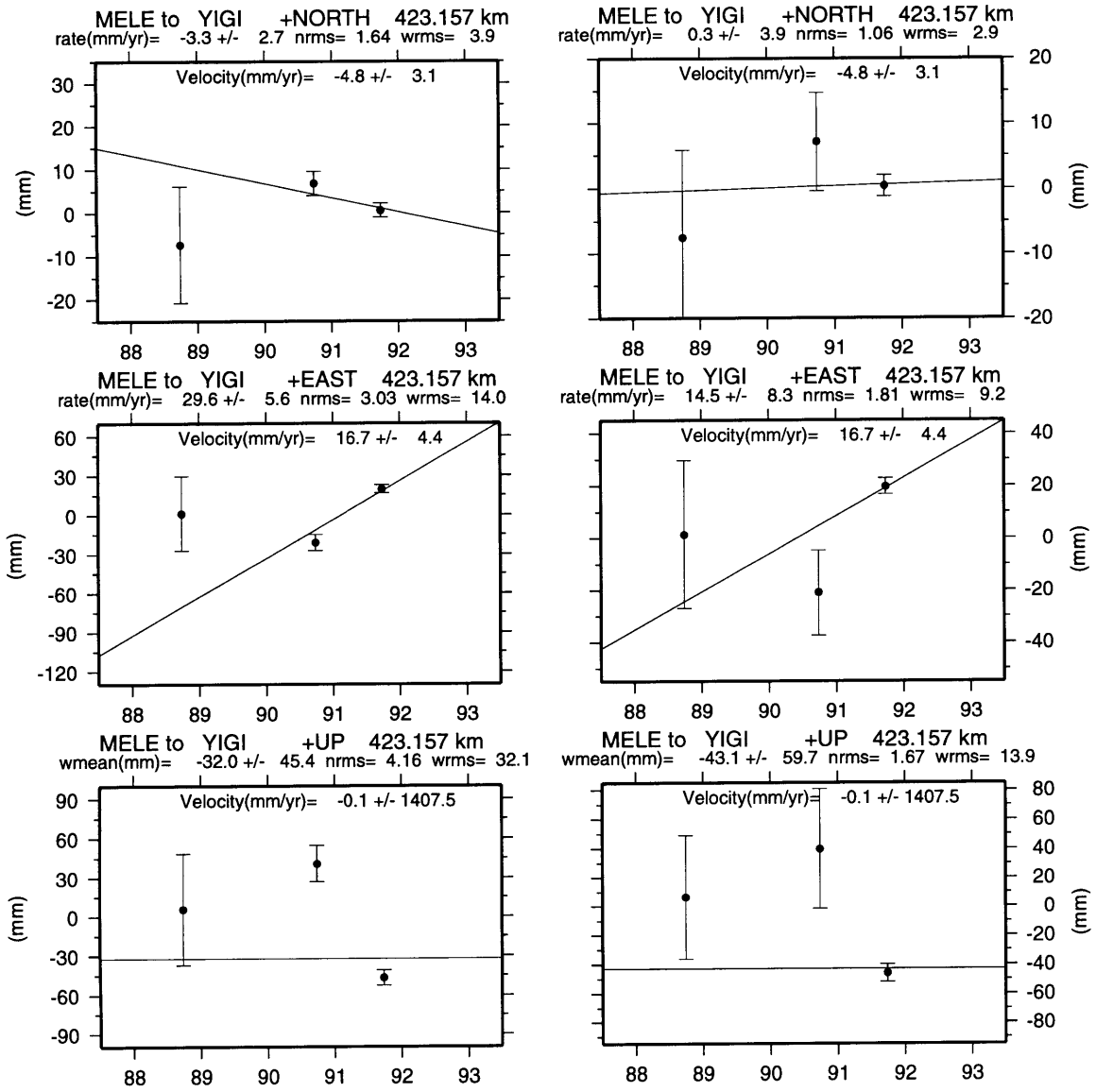

Figure C-8: Time-series plot: Comparing estimates of NS, EW and UD components of regional baselines (1998-1992). In the right panel, the 1990 experiment is downscaled by a factor of 3. The velocity (inserted in the box) is obtained from GLOBK Kalman filter solutions using the entire data set. We also scaled all formal uncertainties by a factor of 2 to reflect realistic 1-σ errors.

of baselines, their statistics (about the best-fitting straight line for the horizontal components and about the weighted mean for the vertical components) and the rates before and after the 1990 experiment was downscaled by 3. We observed a significant change in the easterly velocity of YIGI relative to MELE by 15 mm/yr, as the weight

of the 1990 observations was reduced. Such marked differences are not observed in the other examples, due mostly to a greater number of occupations.

In Figures C-9 and C-10 we present the long-term wrms and nrms scatter of baseline estimates about the best fitting straight-line after scaling all formal errors by a factor of 2. To demonstrate the contribution of the 1990 experiment to the velocity estimates, we compare these plots with those of Figures 2-7 and 2-9, in which we had additionally downscaled formal errors of the 1990 experiment by a factor of 3. Downscaling the 1990 experiment reduced the long-term wrms from 8.1 ppb to 4.2 ppb in the north, and from 28.8 ppb to 18.1 ppb in the east. The nrms was also reduced by 60%.

The impact of the 1990 experiment on the velocity estimates is about 10 mm/yr (Figure C-11). When no downscaling is applied, the 1990 experiment has pronounced effects on the easterly velocities, which are reduced by 6-12 mm/yr. Downscaling the 1990 experiment, in essence, produces velocity estimates similar to those which would exclude this experiment.

We have discussed the systematic errors involved in the estimates of relative site positions and velocities within our regional network. Naturally, we will examine the regional site positions and velocities relative to a distant site on the stable Eurasian plate, i.e., Onsala. However, it is timely to discuss the accuracy/consistency of the velocity fields obtained from our analyses schemes in which different approaches were employed to incorporate the global tracking and the regional networks. Though some of this discussion originally belonged to Appendix A, because it validates the results given in Chapter 2 (Figures 2-12 and C-20, and Tables 2.7 and 2.8) and is relevant to further comparisons we will include it here at the expense of some degree of digression.

The velocity field shown in Figure 2-12 was obtained from GPS measurements between 1988 and 1992. The analyses of the last three experiments (1991 and spring/fall

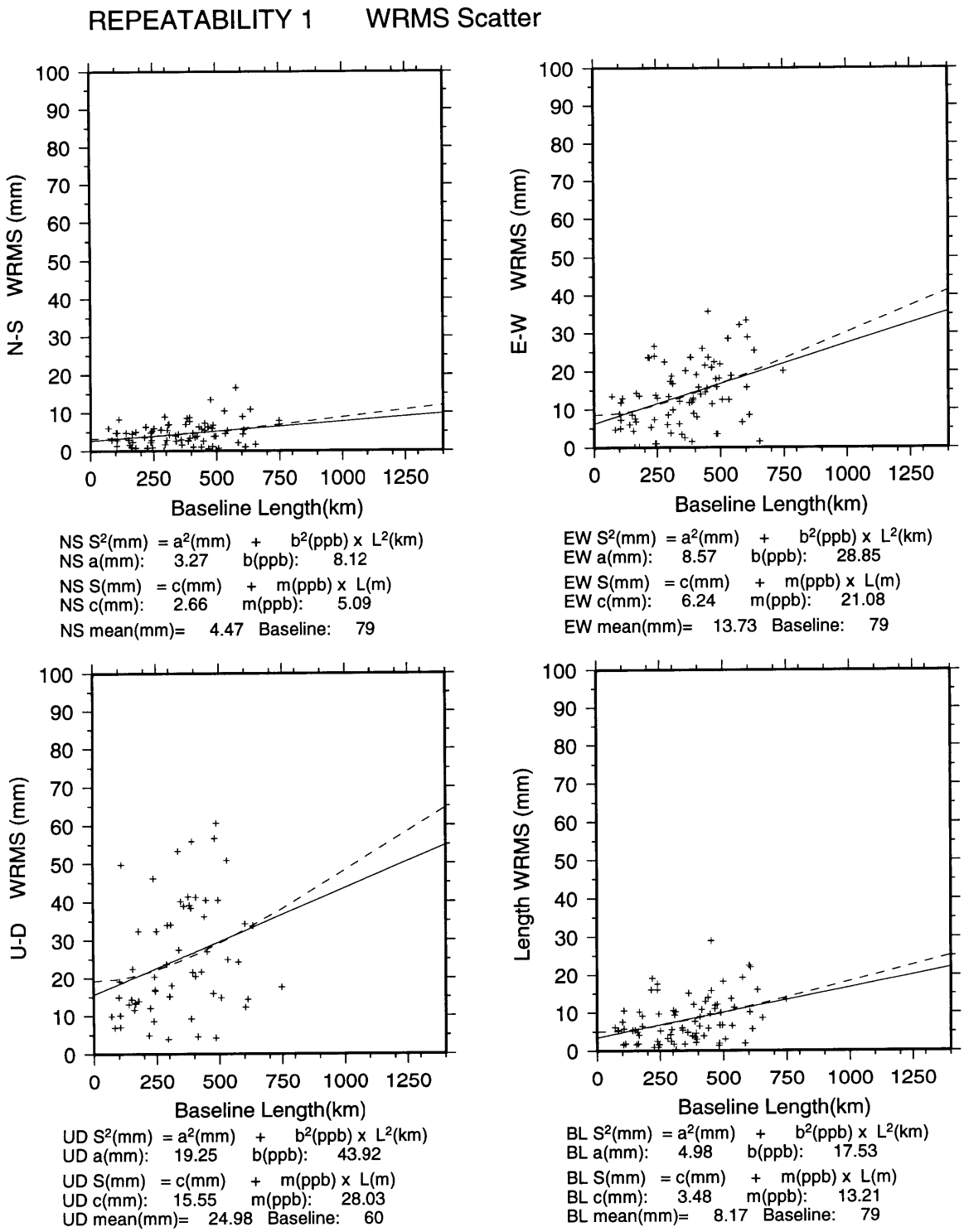

Figure C-9: Long-term wrms scatter and model parameters of NS, EW, UD components and length, as a function of baseline length. Formal uncertainties are scaled by a factor of 2. Dashed line is a functional in the form of $\sigma^2 = a^2 + b^2L^2$. Continuous line is a linear fit to the wrms scatter ($\sigma = c + m\ L$).

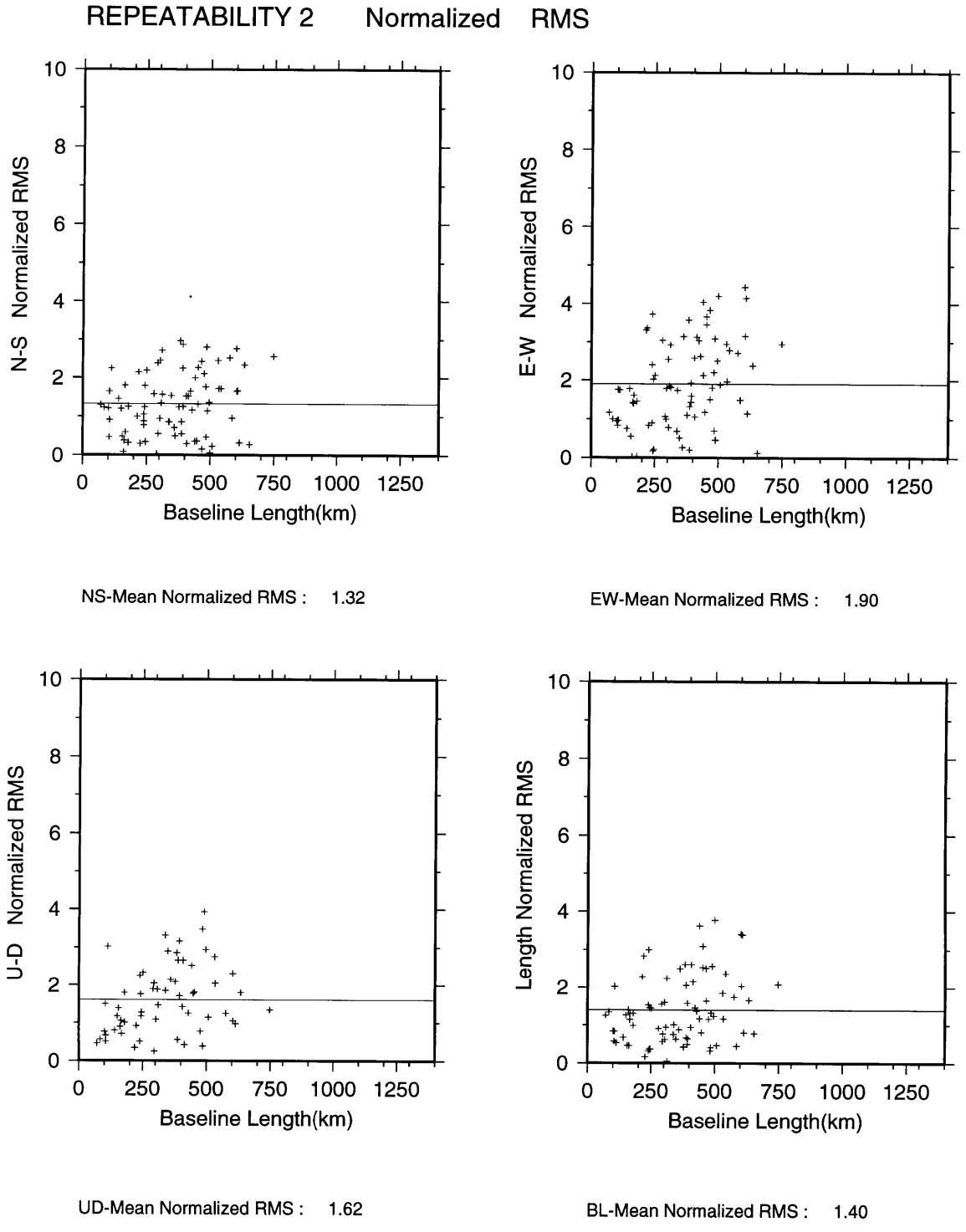

Figure C-10: Long-term nrms scatter of NS, EW, UD components and length [for the solution described in Figure C-9] as a function of baseline length. Formal uncertainties are scaled by a factor of 2. Continuous line represents the mean nrms scatter.

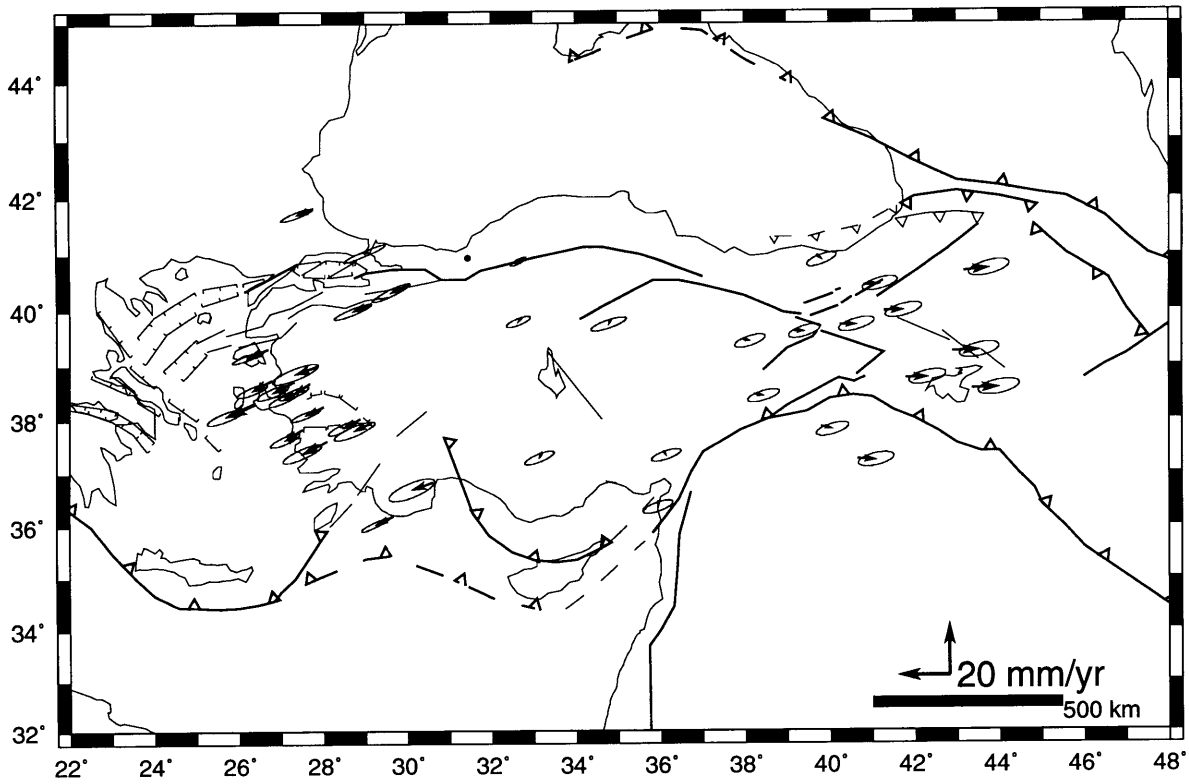

Figure C-11: Difference between two sets of velocity estimates. We subtracted the velocity field (relative to Yığılca) from that in which additional downscaling of 3 applied to the 1990 experiment. The ellipses denote the 95% confidence region obtained from differencing the covariances of two solutions, after scaling as described in the text.

1992) incorporated a large number of global tracking sites using the combination approach (several-site-common). The first three experiments, however, were analyzed using only core global tracking sites. (Even though a simultaneous analysis had been carried out, in terms of global tracking site coverage it was, indeed, an augmented analyses [see Appendix A].) The velocity field shown in Figure C-12, however, was obtained from an analysis in which we used only the core global tracking sites for all experiments: an augmented analysis for each experiment. The differenced velocity field (Figure C-13) shows a significant disagreement of 30 mm/yr at the eastern Turkey sites. This level of discrepancy can also be observed at the western Turkey sites for velocities relative to Karacadağ (Figure C-14). We notice that the relative

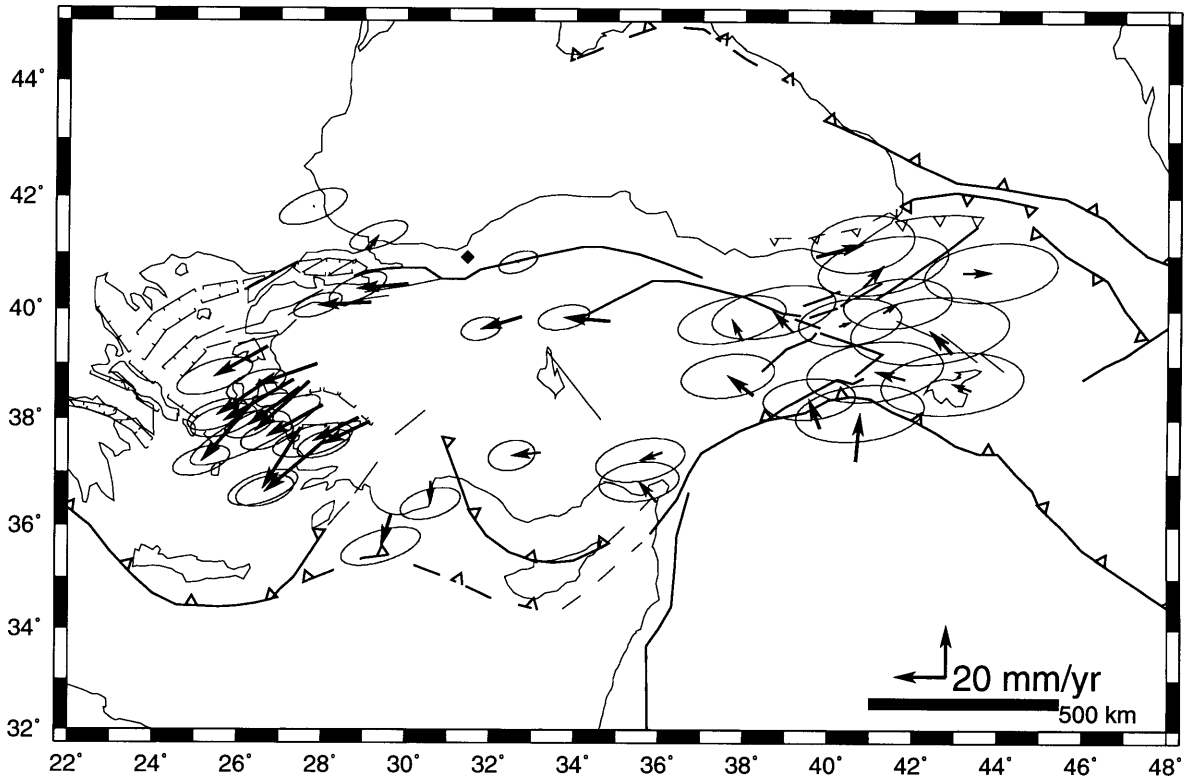

Figure C-12: Observed velocities of all sites relative to Yığılca (shown with a diamond) estimated from GPS observations in Turkey: 1988-1992. The 1991 and spring/fall 1992 experiments were analyzed using the core global tracking network which has been more or less common to all experiments. The ellipses denote the 95% confidence region, after scaling the formal uncertainties, as described in the text.

site motions for short baselines are not severely affected but appear to be magnified for larger station aperture. This suggests that the disagreement between the two solutions is a function of interstation distance. We recall our conclusions in Appendix A with respect to long baselines, and point out that the systematic errors involved in the analysis of regional measurements with an incomplete global tracking network project into velocities as much as they do into the site positions (*cf.* Figure A-9). We argue that using a complete global tracking network provides enhanced precision and accuracy. Further, we argue that the use of implicit velocity ties imposed by common sites would have removed or reduced the deficiency of the 1988, 1989 and 1990 analyses, which were caused by an incomplete global tracking network usage.

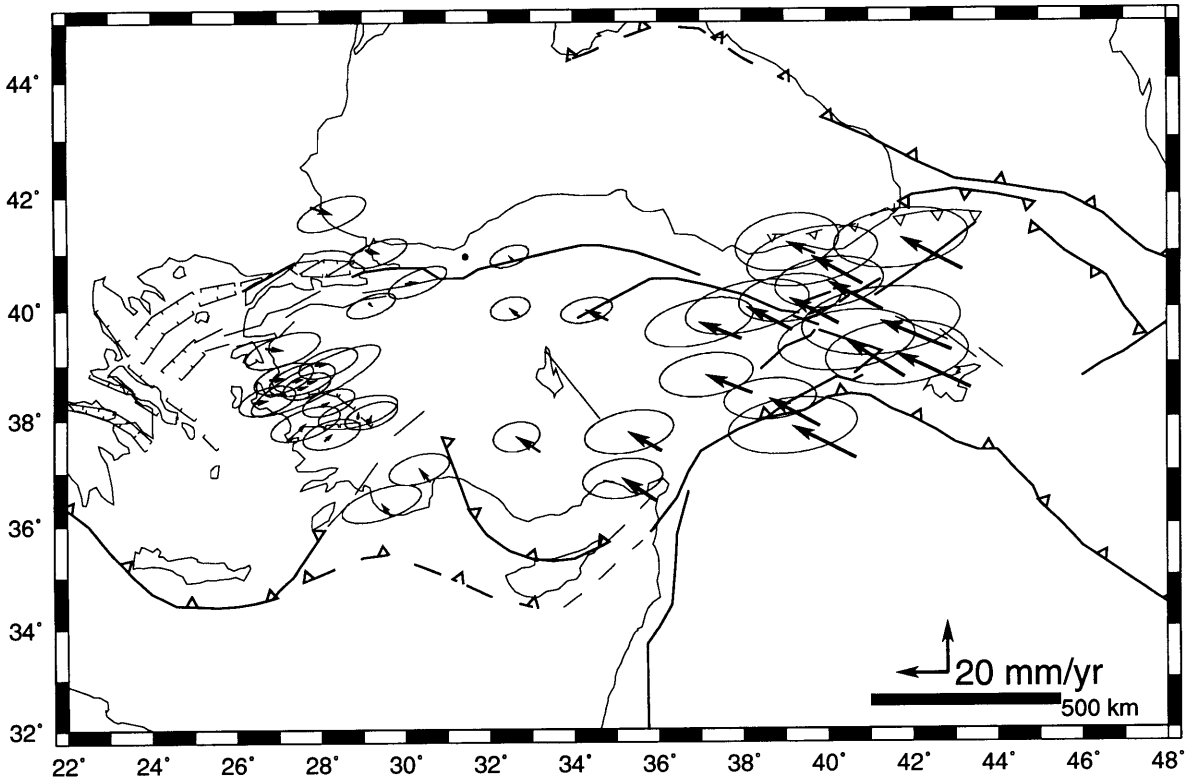

Figure C-13: Differenced velocity field [Figure 2-12 - Figure C-12]. Observed velocities are relative to Yığılca (shown with a dot). The ellipses denote the 95% confidence region, after scaling the formal uncertainties, and are the same as in Figure 2-12.

To demonstrate the strength of these solutions we present the velocity field relative to Onsala (the only benchmark common to all experiments). The velocity field shown in Figure C-15 is obtained from analyses of all experiments with their respective global tracking sites (Appendix B). The uncertainties at the 95% confidence interval are about 30–40 mm/yr and do not allow us to resolve regional site velocities relative to Onsala. Regional site velocities relative to Onsala obtained from including all global tracking sites via combination analyses of the 1991 and spring/fall 1992 experiments, are resolvable and their uncertainties have been reduced to 15–25 mm/yr (Figure C-16). How accurate is this velocity field and do the uncertainties properly account for the contribution of various error sources? Does the Pontus block move westerly at a rate of 41.2 ± 6.4 mm/yr?

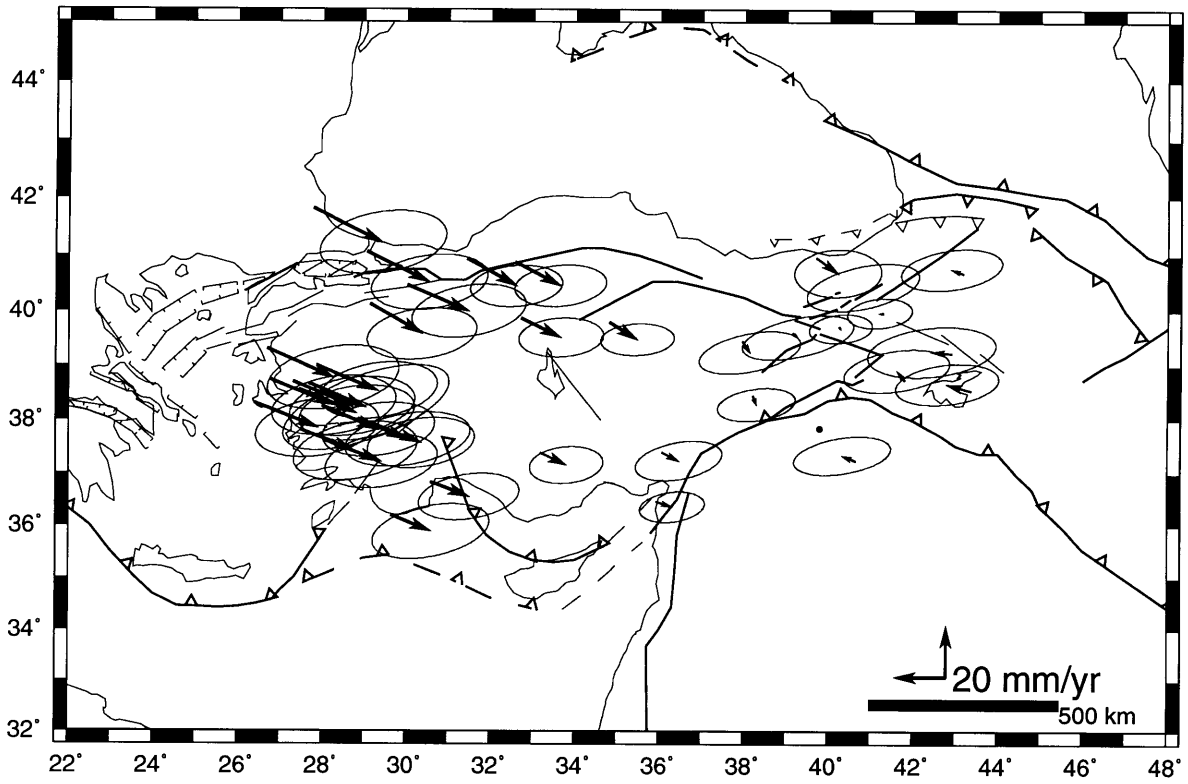

Figure C-14: Differenced velocity field: velocities are relative to Karacadağ (shown with a dot). The ellipses denote the 95% confidence region, after scaling the formal uncertainties, and are the same as in reference solution.

In the beginning of this Appendix we mentioned the large vertical systematics (*cf.* Figure C-1) and their possible projection into the estimates of the horizontal components. A closer inspection of Figure C-1 shows that if we were to omit or further downscale the 1989 and 1990 experiments, the velocity estimates would be drastically reduced. We attribute the adverse effects caused by the 1989 and 1990 estimates to the projection of the vertical errors into the horizontal components. Furthermore, additional downscaling of the 1991 and 1992 estimates might lower the easterly motion, since their rather small uncertainties cause rates to be predominantly estimated from one-year-apart observations obtained in 1991 and 1992. Therefore, the velocity field shown in Figure C-16 has 30–40 mm/yr systematic errors aliased into it. The effects of 1989 systematics have relatively less impact on the velocity field

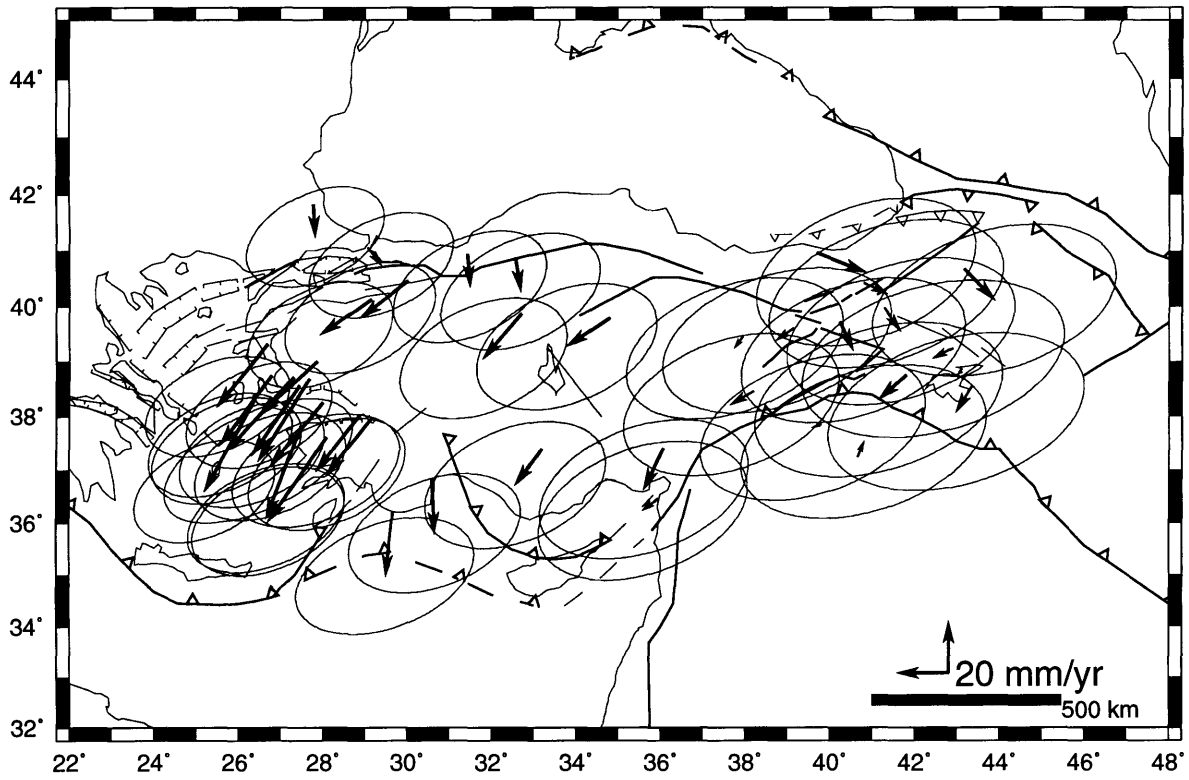

Figure C-15: Observed velocities of all sites relative to Onsala, estimated from GPS observations in Turkey: 1988-1992. All experiments, including the 1991 and spring/fall 1992 experiments, were analyzed using the core global tracking network which has been more or less common to all experiments. The ellipses denote the 95% confidence region, after scaling the formal uncertainties.

(Figures C-5, C-6, C-7, and C-8) compared to those of 1990. However, at interstation distances of ~2500 km, both the 1989 and 1990 estimates behave as outliers, as they do for long-term repeatability.

These systematic errors can be reduced by introducing constraints on the velocities of one or more regional site. Feigl et al [1993] used such an approach for the combined analyses of southern California GPS and VLBI data by constraining (equating) the GPS site velocities to their VLBI values. Given that only SLR observations exist within our GPS network and that currently no combined SLR and GPS analysis is possible, we first chose to explicitly force GPS velocities at two SLR/GPS colloca-

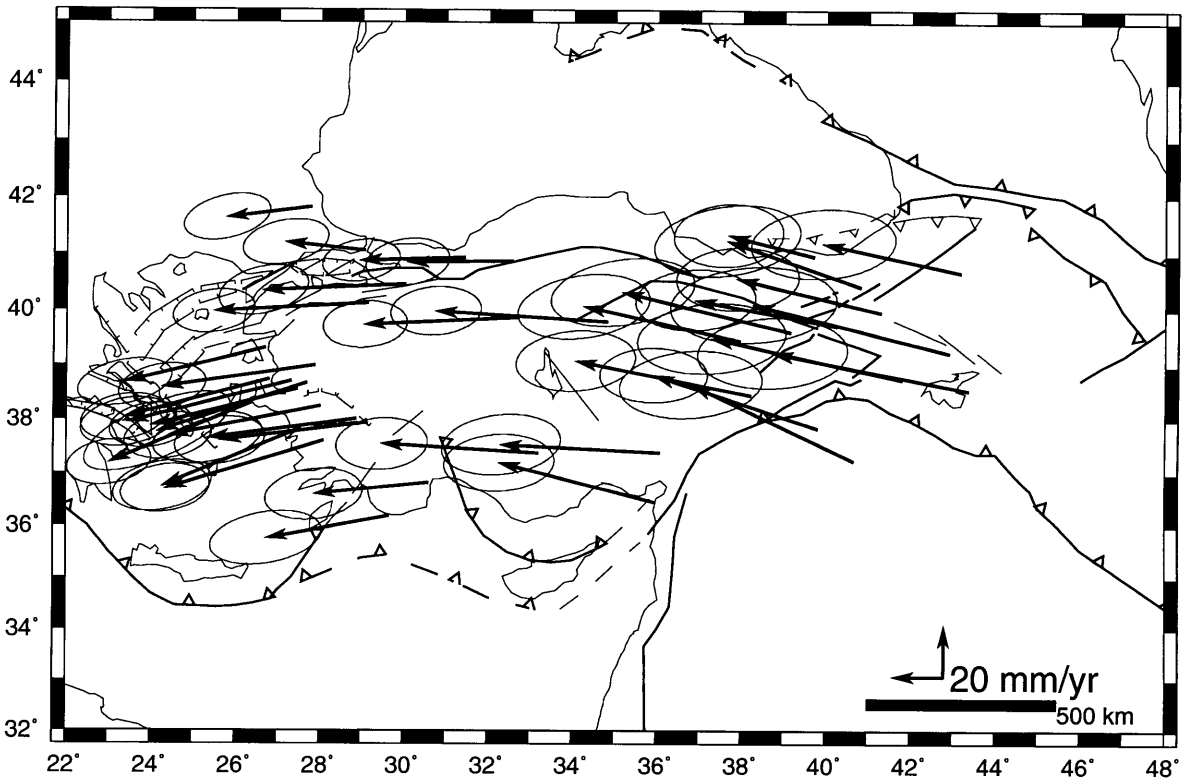

Figure C-16: Observed velocities of all sites relative to Onsala, estimated from GPS observations in Turkey: 1988-1992. The 1991 and spring/fall 1992 experiments were analyzed using the combination approach. The ellipses denote the 95% confidence region, after scaling the formal uncertainties.

tion sites (Yığılca and Melengiçlik) to their SLR estimates [Noomen et al., 1993] in order to obtain regional site velocities relative to Onsala. We found that constraining only one site produced similar results. We performed two constrained solutions: one using the core global tracking network whose velocity field is shown in Figure C-17, and another incorporating a large number of global trackers (1991 and spring/fall 1992 experiments) via the several-site-common approach (Figure C-18). The differences between these two velocity estimates are statistically insignificant at the 95% confidence level (Figure C-19). The implications are several-fold:

In the absence of long-term errors for large baseline apertures, reliable GPS velocity estimates can be derived using a globally evenly distributed tracking network.

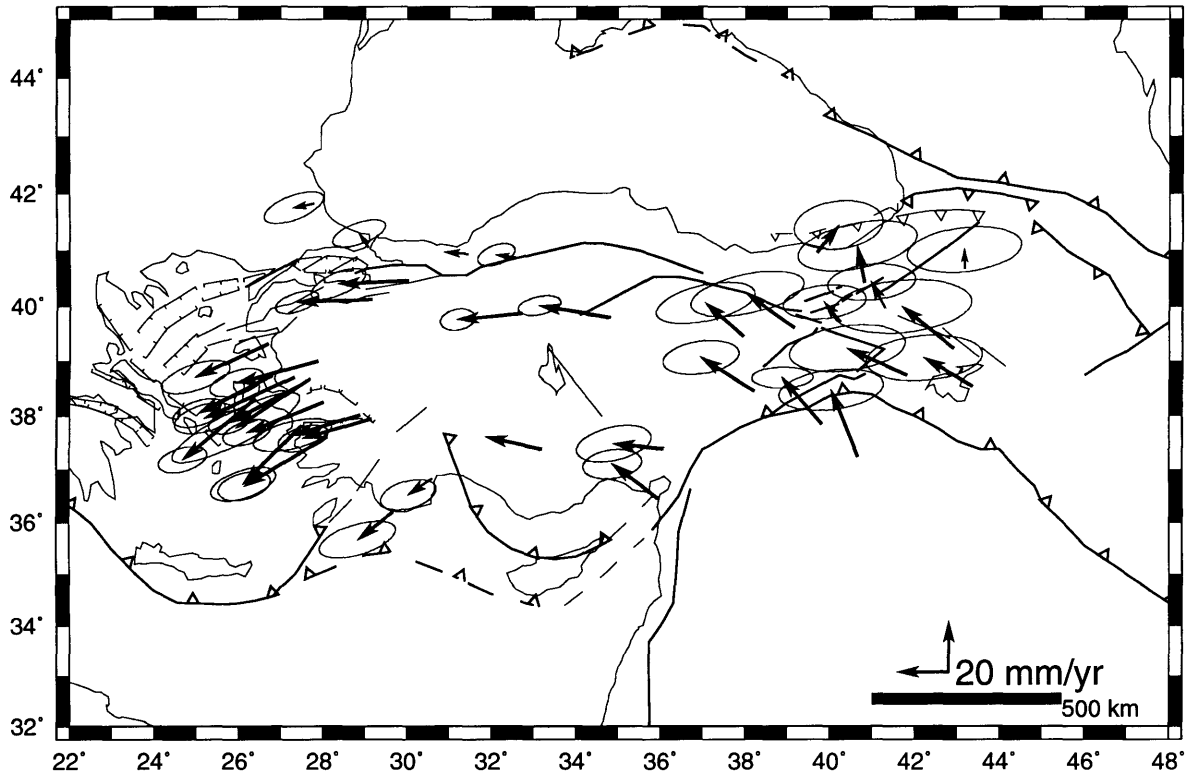

Figure C-17: Observed velocities of all sites relative to Onsala estimated from GPS observations in Turkey: 1988-1992. The velocities at the Yığılca and Melengiçlik sites were forced to those estimated by SLR [Noomen et al., 1993]. All experiments, including the 1991 and spring/fall 1992 experiments, were analyzed using the core global tracking network which has been more or less common to all experiments. The ellipses denote the 95% confidence region, after scaling the formal uncertainties.

Such analysis is stronger than the one obtained by using a smaller tracking network and allows resolution of relative site motions by providing reduced 1-σ errors. When and if long-term systematic errors are encountered, explicit velocity ties are necessary to obtain motions of sites in a regional network relative to distant sites located on stable plate(s). Analysis of regional GPS experiments can be carried out using a subset (core) global tracking network, which may be of intercontinental size, provided that the velocities of some sites within the regional network are explicitly prescribed. Such an analysis approach requires an excellent knowledge of velocities at certain sites. These can be supplied by SLR/VLBI observations. Furthermore, a simultane-

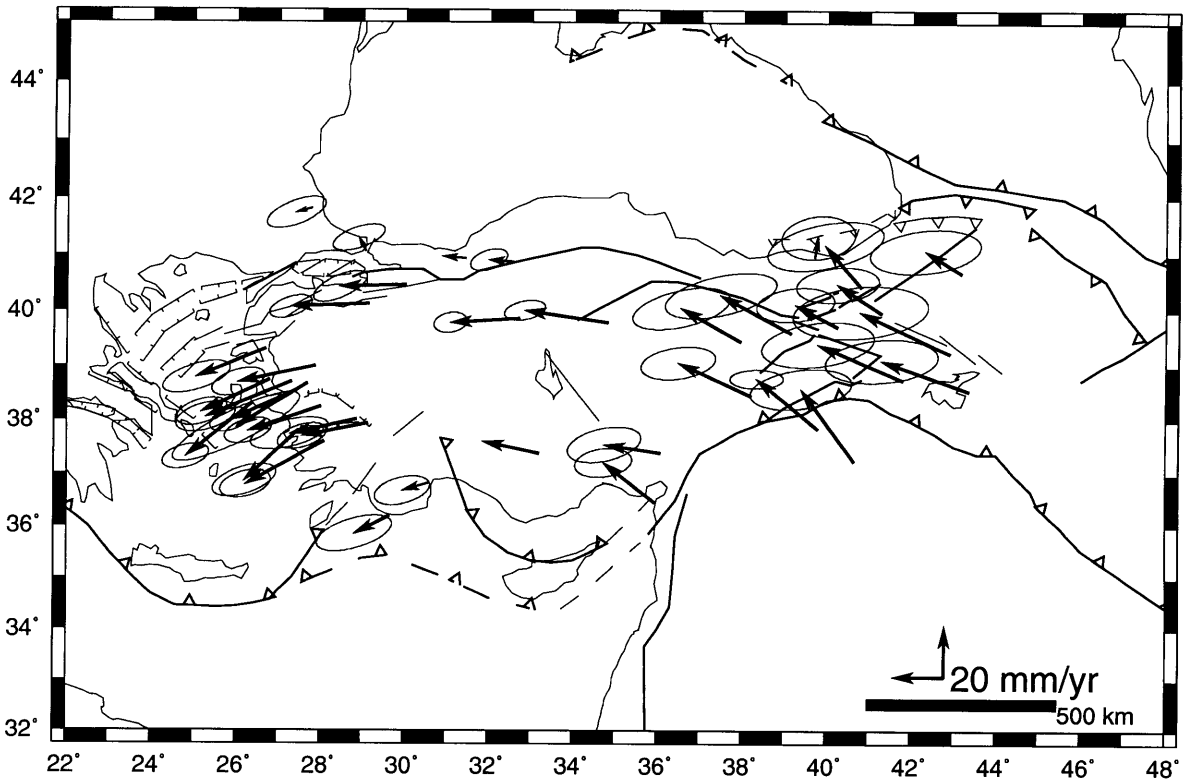

Figure C-18: Observed velocities of all sites relative to Onsala estimated from GPS observations in Turkey: 1988-1992. The velocities at the Yığılca and Melengiçlik sites were forced to those estimated by SLR [Noomen et al., 1993]. The 1991 and spring/fall 1992 experiments were analyzed using all global tracking sites using the several-site-common approach. The ellipses denote the 95% confidence region, after scaling the formal uncertainties.

ous adjustment of GPS and SLR/VLBI (combination analysis) would eliminate the need for explicitly constraining the GPS velocities, since such ties could be implicitly maintained. We also understand that by explicitly imposing SLR velocities at the regional network sites, long-term systematic errors, which may amount to several centimeters, can be reduced or even eliminated.

With these in mind, the differences between Figures 2-12 and C-18 are, therefore, due to a small westerly motion of the Pontus block relative to Eurasia, and the long-term systematic errors are within the 95% confidence area.

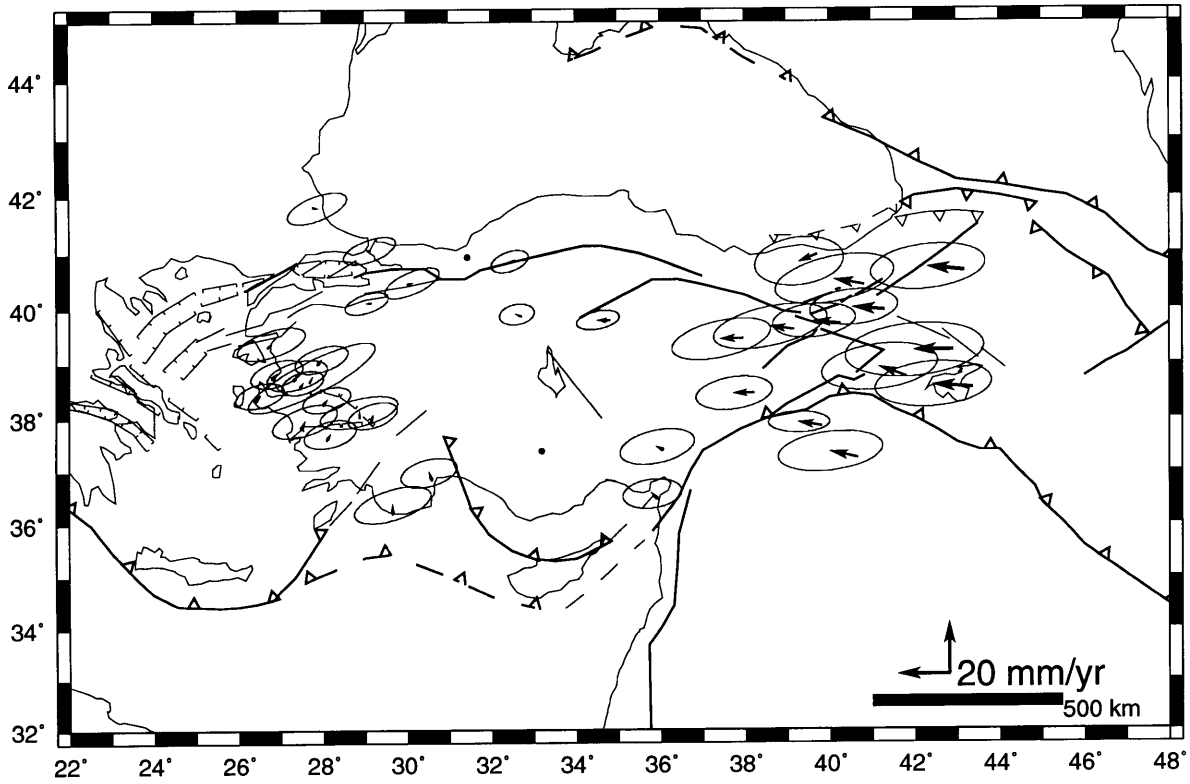

Figure C-19: Differenced velocity field [Figure C-16 - Figure C-15]. Observed velocities are relative to Onsala. The ellipses denote the 95% confidence region, after scaling the formal uncertainties, and are the same as in Figure C-18.

Although we observe no significant differences at the eastern Turkey sites within the 95% confidence area of the reference velocity field, the 10 mm/yr discrepancy is probably due to weakly determined velocities from two epochs. We can further attempt to calibrate the velocity of one site in eastern Turkey forcing it to either SLR or NUVEL-1 determined values. Since we have, as yet, no collocation sites common to both SLR and GPS (outlier Diyarbakır [DIYA] GPS site was discarded earlier; no SLR velocities are presently available at KARA), we choose to force the Karacadağ [KARA] velocity to its NUVEL-1 determined value [Demets et. al, 1990], because explicitly prescribing velocity for one regional site is sufficient. (This also allows for comparisons with SLR.) We also note that the SLR velocity at DIYA [v_H= 33± $15_{95\%}$ mm/yr, θ = -11± $22_{95\%}$ °N] is larger than Nuvel-1 estimates [v_H=25±2 mm/yr, θ =-23±8 °N]

by 8 mm/yr. Figure C-20 shows the velocity field obtained from analyses of regional GPS observations in Turkey with complete global tracking network data, after the velocity at Karacadağ is constrained to its NUVEL-1 determined value. The velocity

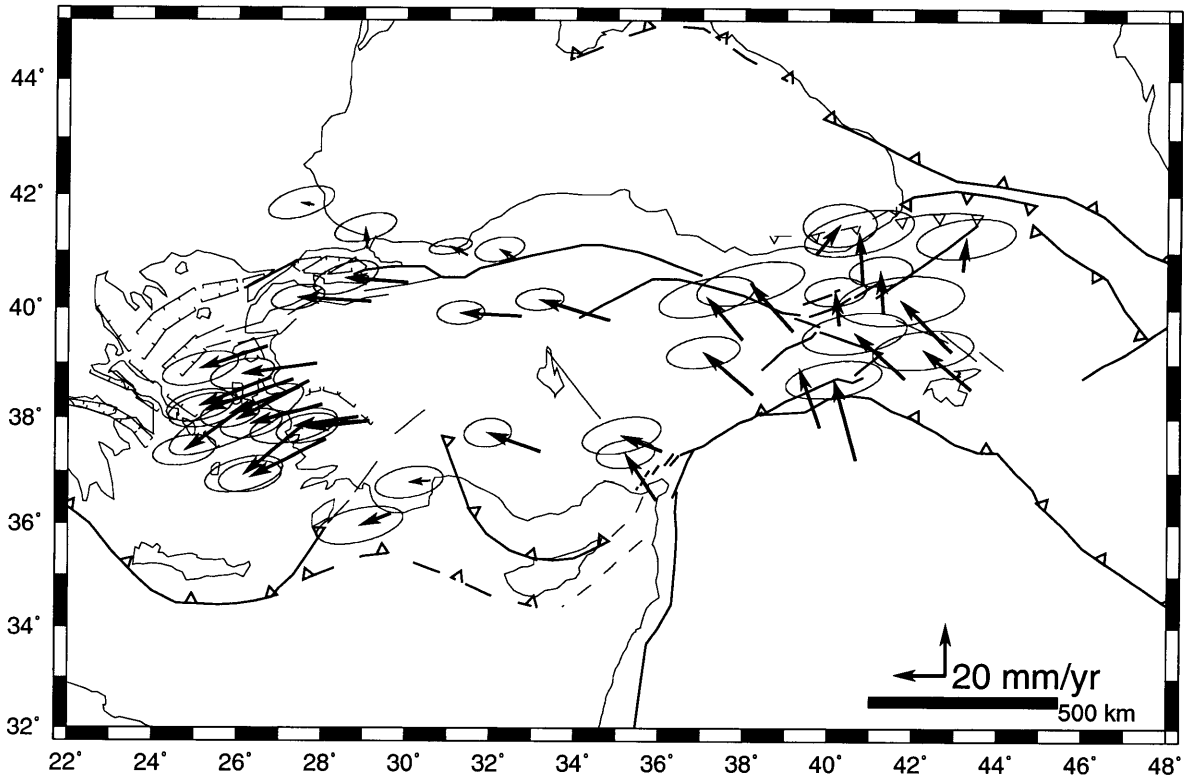

Figure C-20: Observed velocities of all sites relative to Onsala, estimated from GPS observations in Turkey: 1988-1992. The velocity at the Karacadağ site was forced to NUVEL-1 determined value [DeMets et al., 1990]. The 1991 and spring/fall 1992 experiments were analyzed using all global tracking sites with the several-site-common approach. The ellipses denote the 95% confidence region, after scaling the formal uncertainties.

field shown in Figure C-20 is minutely different (a much smaller differences than those in Figure C-19) from that obtained from an analysis in which only the core global tracking network was included. Thus, they are not shown.

We observe that constrained solutions (site velocities forced to SLR or NUVEL-1 determined values) allow us to obtain velocities relative to distant sites, and to

import stability to velocity estimates as long-term systematic errors are reduced. Figures C-21 and C-22 illustrate velocities obtained from constrained (NUVEL-1) and unconstrained solutions relative to Yığılca (western Turkey) and Karacadağ (eastern Turkey), respectively. The differences between the unconstrained and constrained

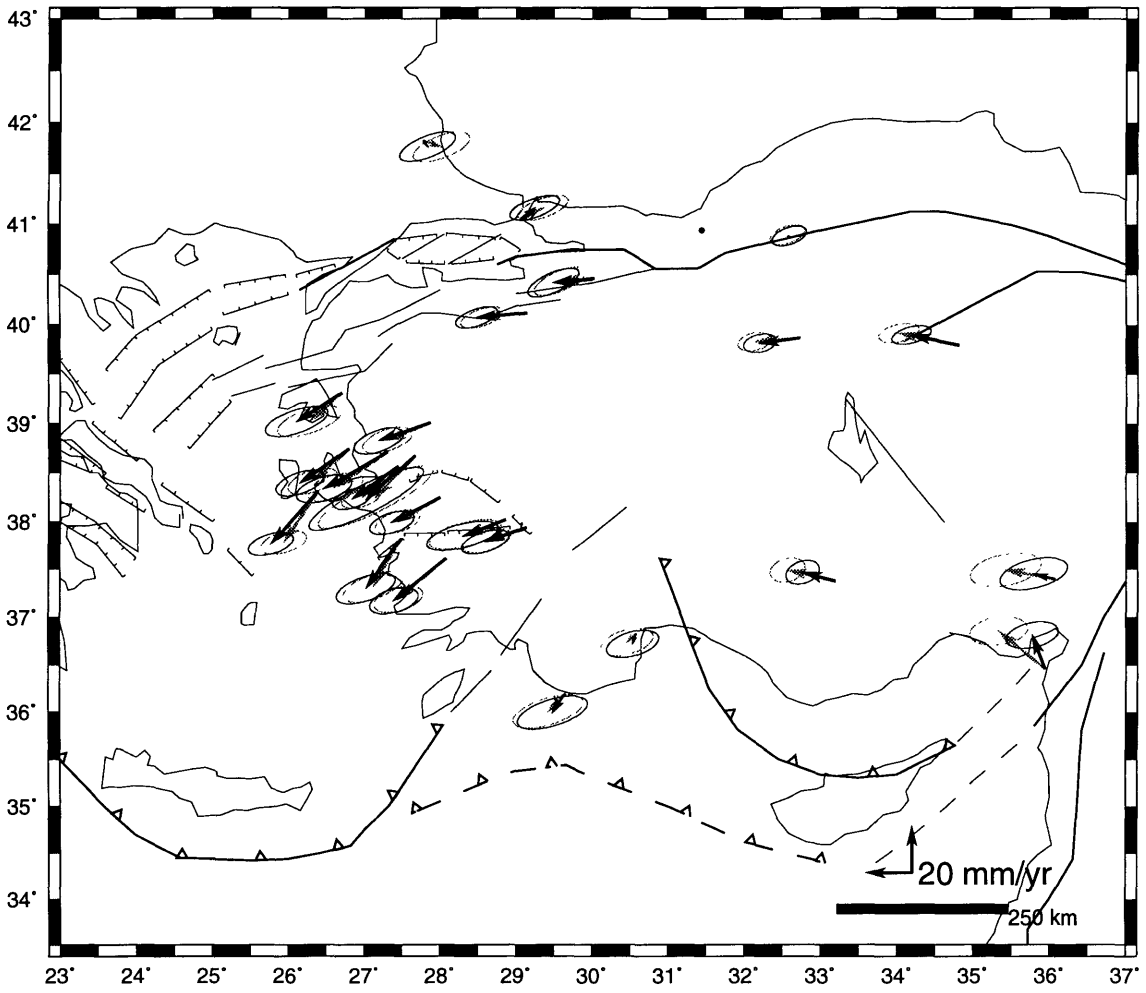

Figure C-21: Observed velocities relative to Yığılca (shown with a dot) estimated from GPS observations in Turkey: 1988-1992. Constrained solution: black arrows; unconstrained solution: grey arrows. Velocity at the Karacadağ site was forced to its NUVEL-1 determined value [DeMets et al., 1990]. The 1991 and spring/fall 1992 experiments were analyzed using all global tracking sites with the several-site-common approach. The ellipses denote the 95% confidence region, after scaling the formal uncertainties.

velocity fields are negligible for short baselines. We also observe that the differences in western Turkey are much smaller than those in eastern Turkey for comparable baseline lengths. This is what we would expect since sites in western Turkey have more that 2 epoch observations.

Time evolution of baseline estimates

Given that minute differences are observed for velocities between closely located baselines, we expected no major changes in the statistical quantities reported in Chapter 2. We performed constrained GLOBK back solutions (Table B.3) in which horizontal velocities at Karacadağ were also prescribed. Our constrained solutions for time evolution of regional baseline estimates did not show any significant difference at the 1-σ level. Hence, statistical quantities reported in Chapter 2 remain unchanged. However, we observed reductions in the easterly velocity for baselines formed between a regional site and a distant site, for instance, Onsala (Figure C-23).

The time evolution of baseline estimates involving primary sites is shown in Figures C-24 – C-63. In these figures, all formal errors were multiplied by 2. Additionally, we multiplied the 1990 formal errors by 3, prior to GLOBK analysis. We analyzed the regional GPS measurements with the core global tracking network for the 1988, 1989 and 1990 experiments, and with a larger global tracking network, using the several-site-common combination approach (Chapter 2, Appendices A and B). Since the baselines involved in these plots are relatively short, we have not constrained the velocity at the Karacadağ site. Hence the time-series plots are obtained from unconstrained GLOBK back solutions in which the global tracking site positions and the velocities were estimated deterministically, whereas we allowed all regional sites to be stochastically estimated (Table B.3).

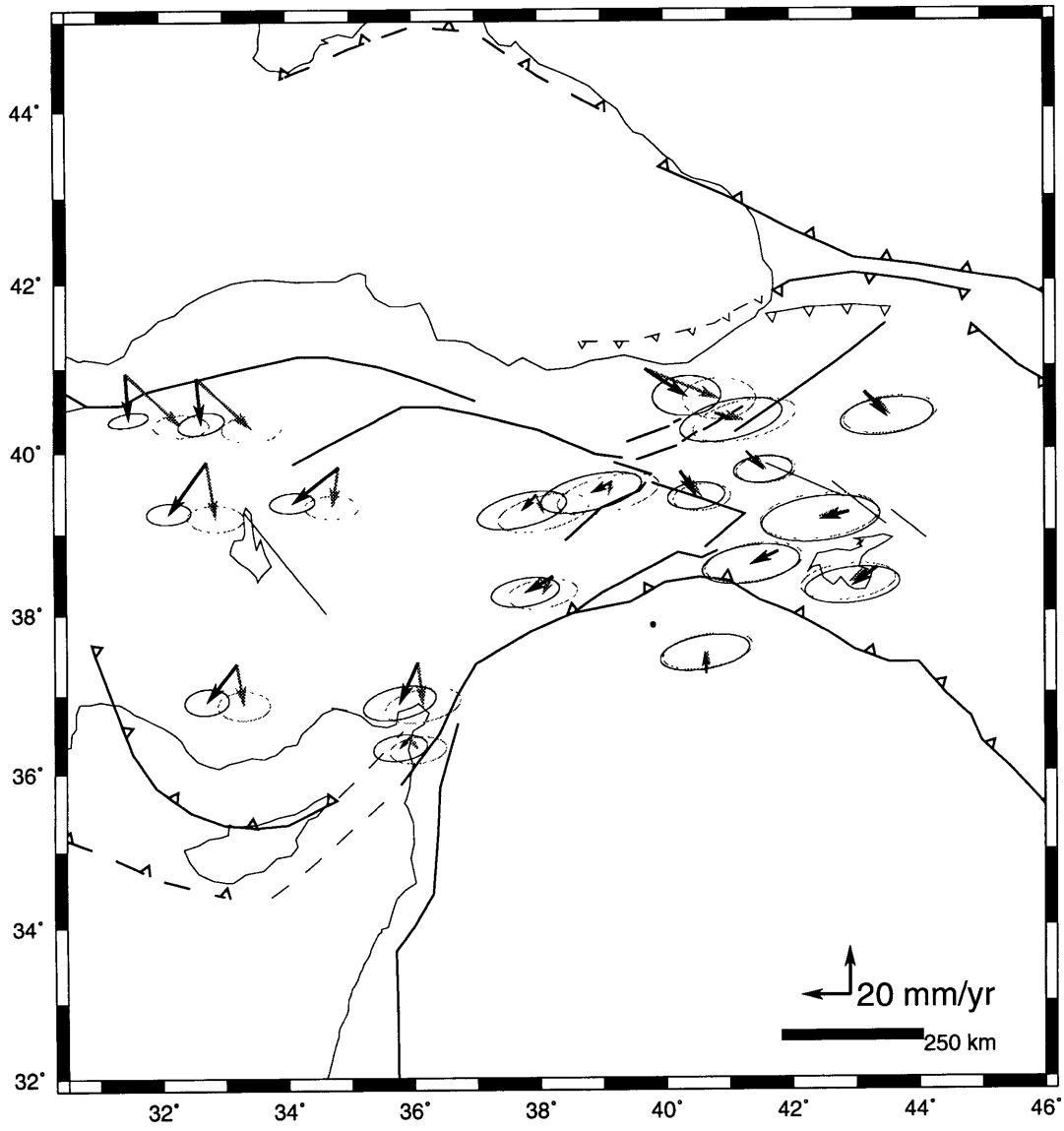

Figure C-22: Observed velocities of eastern Turkey sites relative to Karacadağ (shown with a dot) estimated from GPS observations in Turkey: 1988-1992. Constrained solution: black arrows; unconstrained solution: grey arrows. The velocity at the Karacadağ site was forced to its NUVEL-1 determined value [DeMets et al., 1990]. The 1991 and spring/fall 1992 experiments were analyzed using all global tracking sites with the several-site-common approach. The ellipses denote the 95% confidence region, after scaling the formal uncertainties.

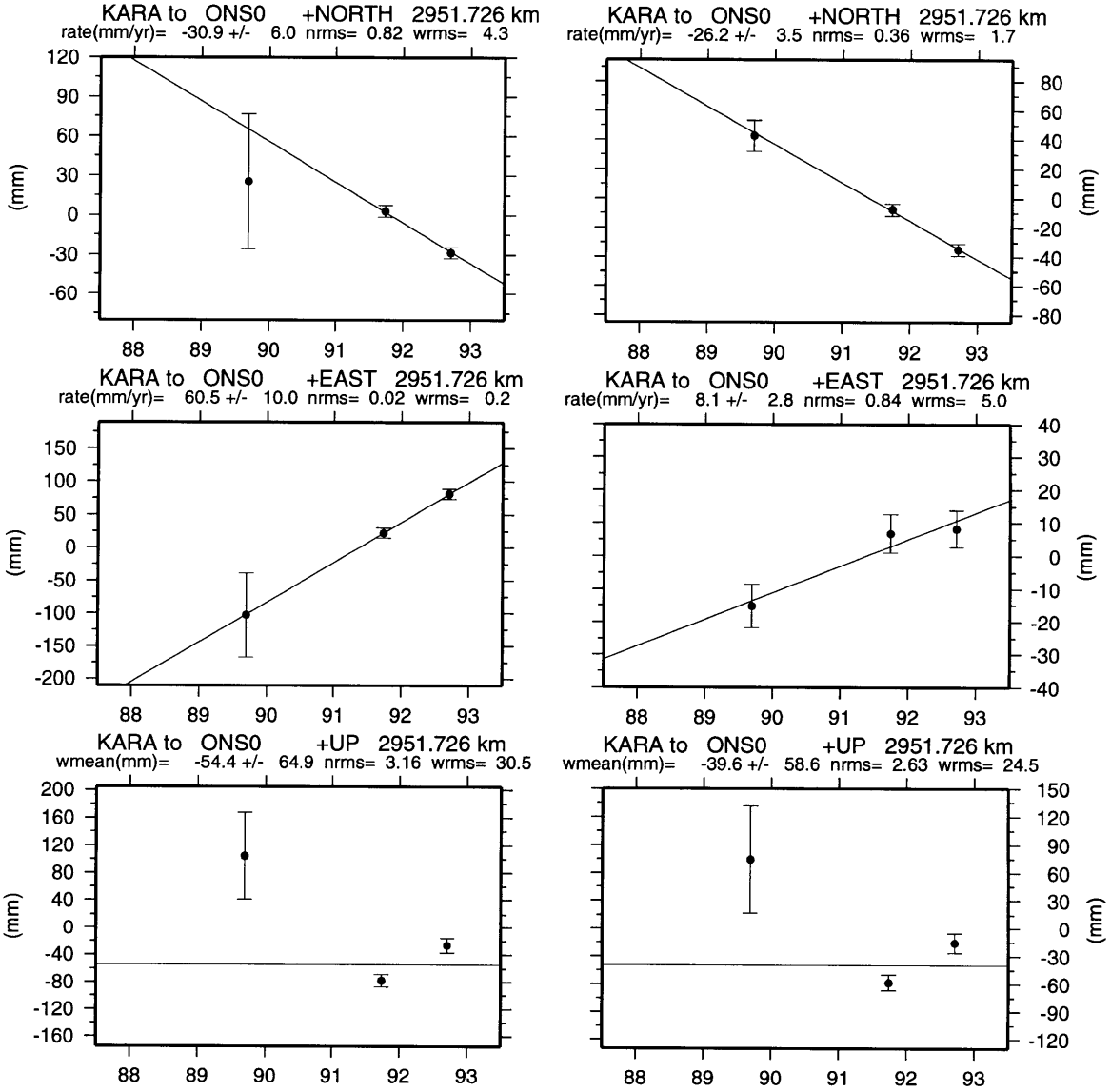

Figure C-23: Time-series plot of very long baseline KARA-ONS0: Estimates of baseline components. Right column: unconstrained solution; left column: constrained solution. In both solutions we multiplied the 1990 formal errors by 3, prior to GLOBK back solution. [Scaled all formal uncertainties by 2.]

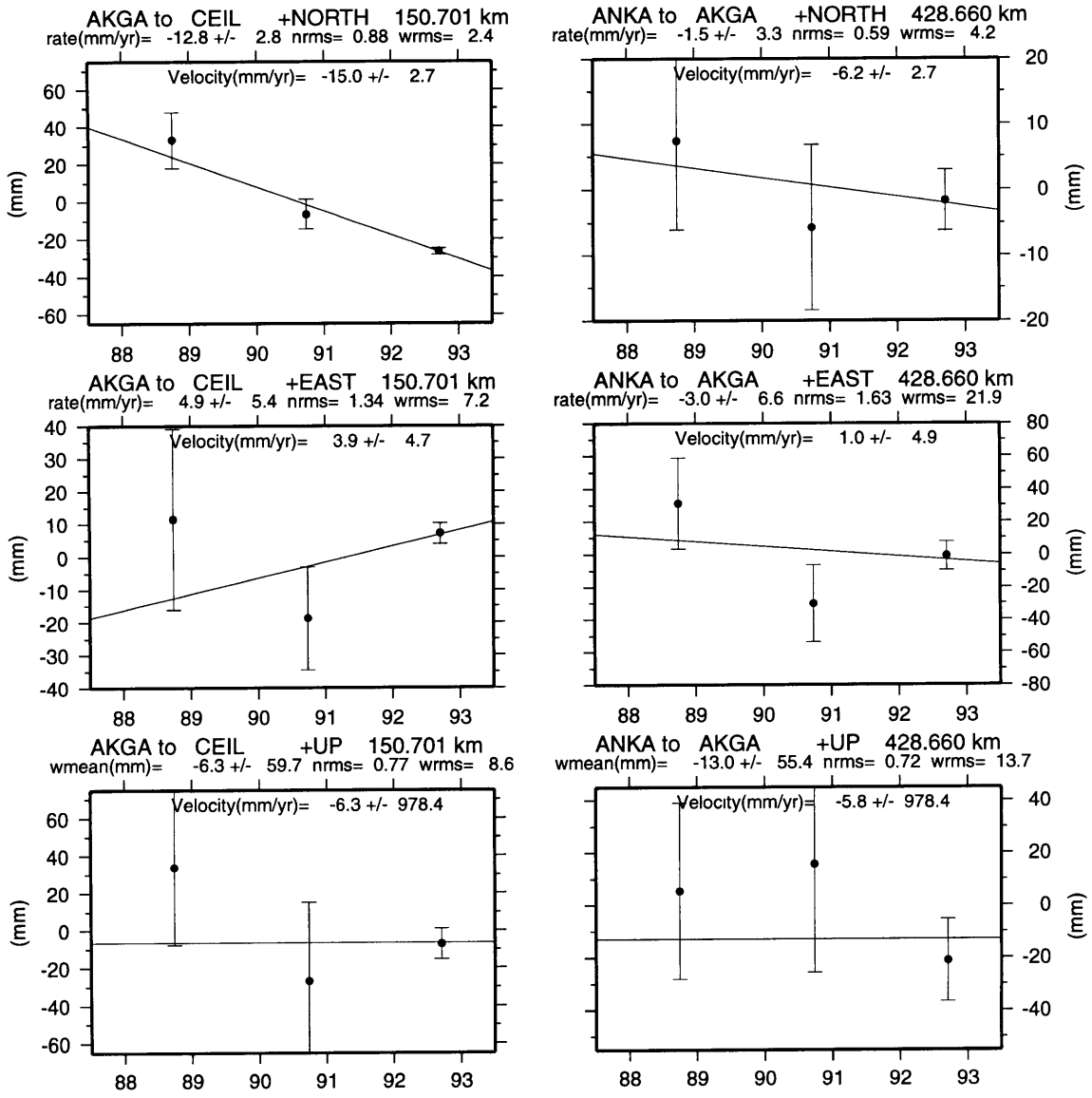

Figure C-24: The time evolution of the north, east and vertical (up) components of the relative position vectors obtained from GLOBK Kalman filter back solutions. Rate/velocity is relative to the first site, where NEU is +. The rate is calculated by a naive weighted least squares fit to the estimates of baseline components. The wrms and nrms are about this best fitting straight-line, except for the vertical, which is about the weighted mean. The velocity (inserted into the box) is obtained from GLOBK Kalman filter forward solutions which use the entire data set. We scaled all formal uncertainties by a factor of 2 (an additional factor of 3 applied to 1990 values) to reflect realistic 1-σ errors.

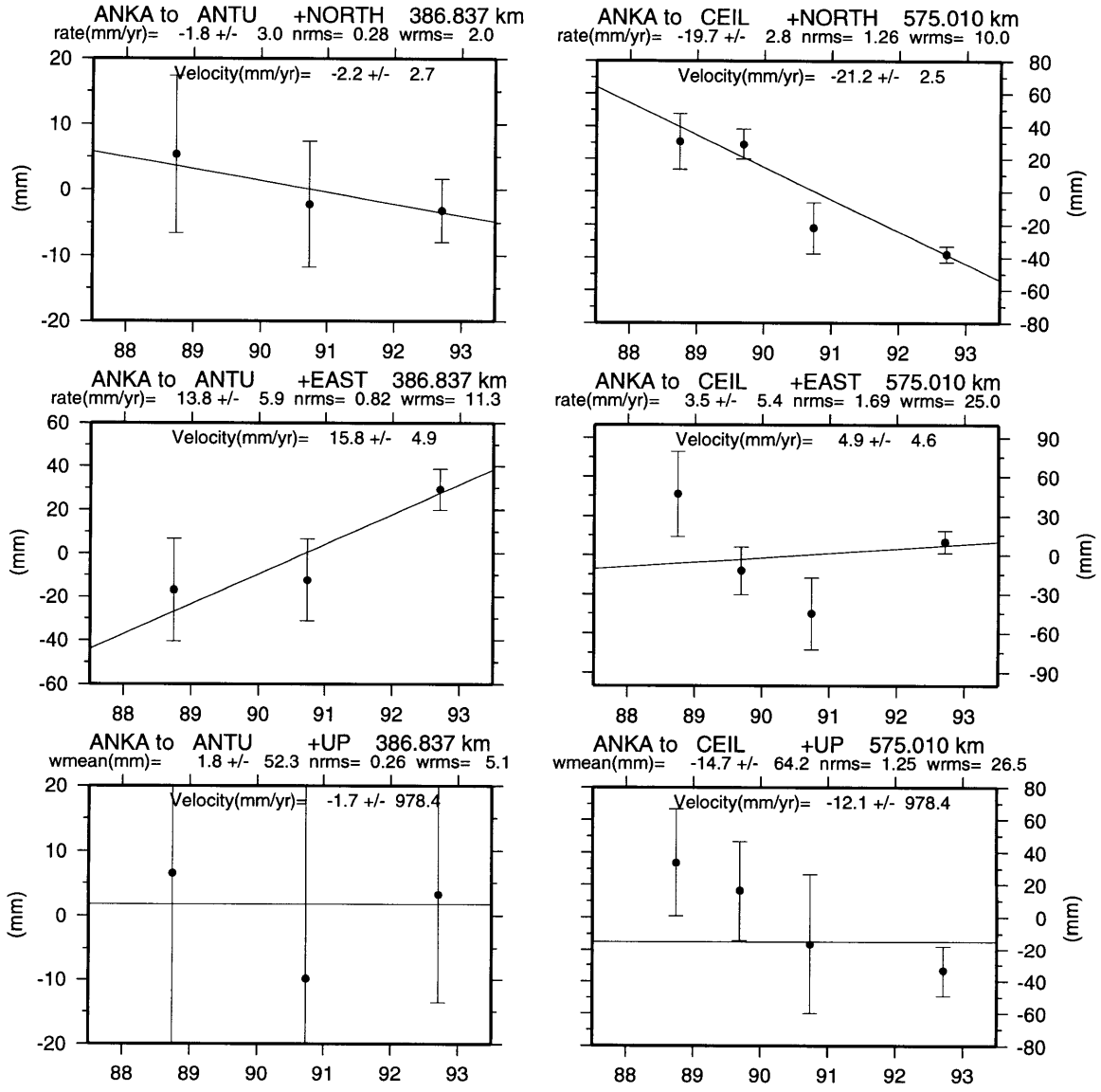

Figure C-25: The time evolution of the north, east and vertical (up) components of the relative position vectors obtained from GLOBK Kalman filter back solutions. Rate/velocity is relative to the first site, where NEU is +. The rate is calculated by a naive weighted least squares fit to the estimates of baseline components. The wrms and nrms are about this best fitting straight-line, except for the vertical, which is about the weighted mean. The velocity (inserted into the box) is obtained from GLOBK Kalman filter forward solutions which use the entire data set. We scaled all formal uncertainties by a factor of 2 (an additional factor of 3 applied to 1990 values) to reflect realistic 1-σ errors.

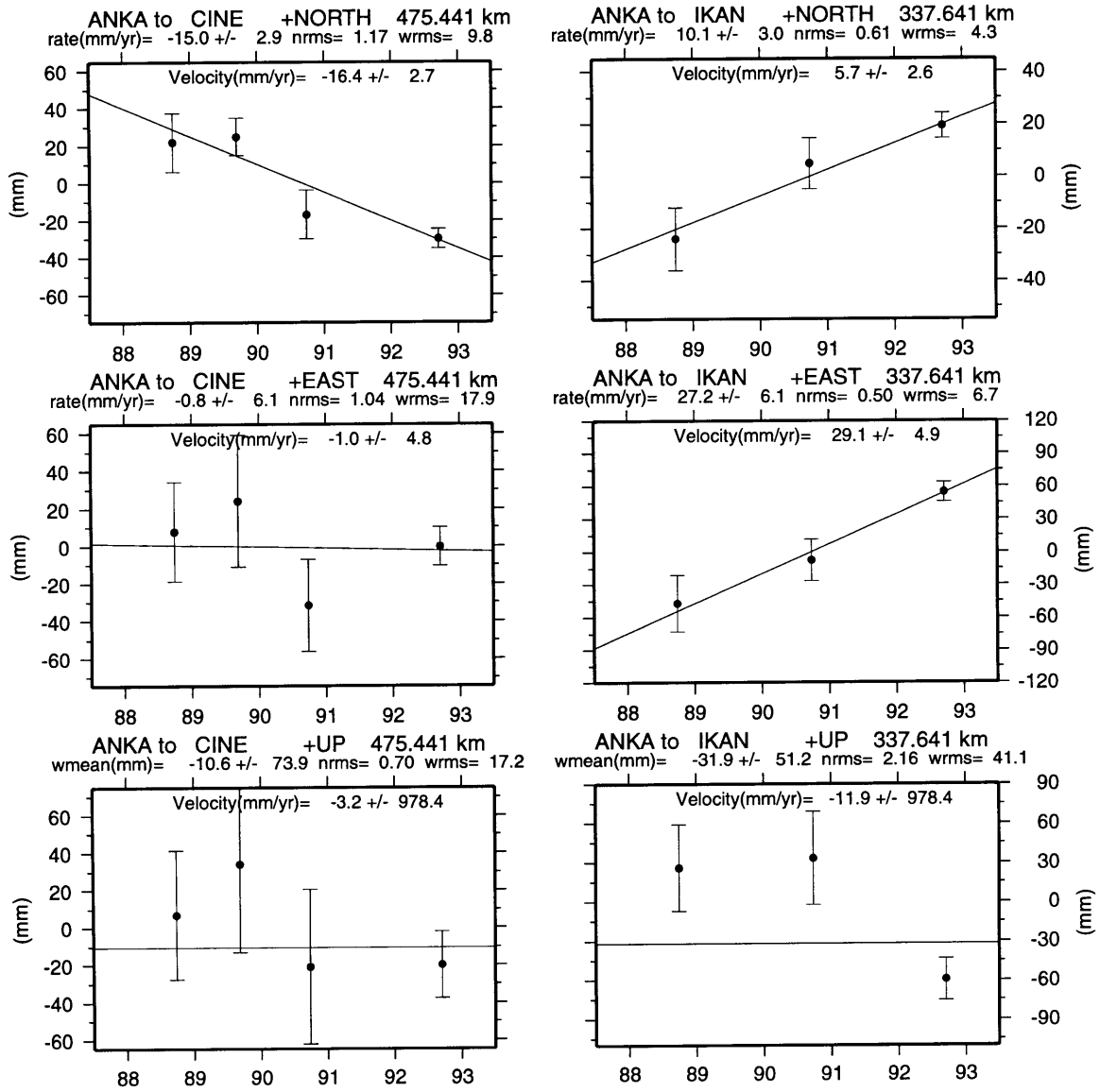

Figure C-26: The time evolution of the north, east and vertical (up) components of the relative position vectors obtained from GLOBK Kalman filter back solutions. Rate/velocity is relative to the first site, where NEU is +. The rate is calculated by a naive weighted least squares fit to the estimates of baseline components. The wrms and nrms are about this best fitting straight-line, except for the vertical, which is about the weighted mean. The velocity (inserted into the box) is obtained from GLOBK Kalman filter forward solutions which use the entire data set. We scaled all formal uncertainties by a factor of 2 (an additional factor of 3 applied to 1990 values) to reflect realistic 1-σ errors.

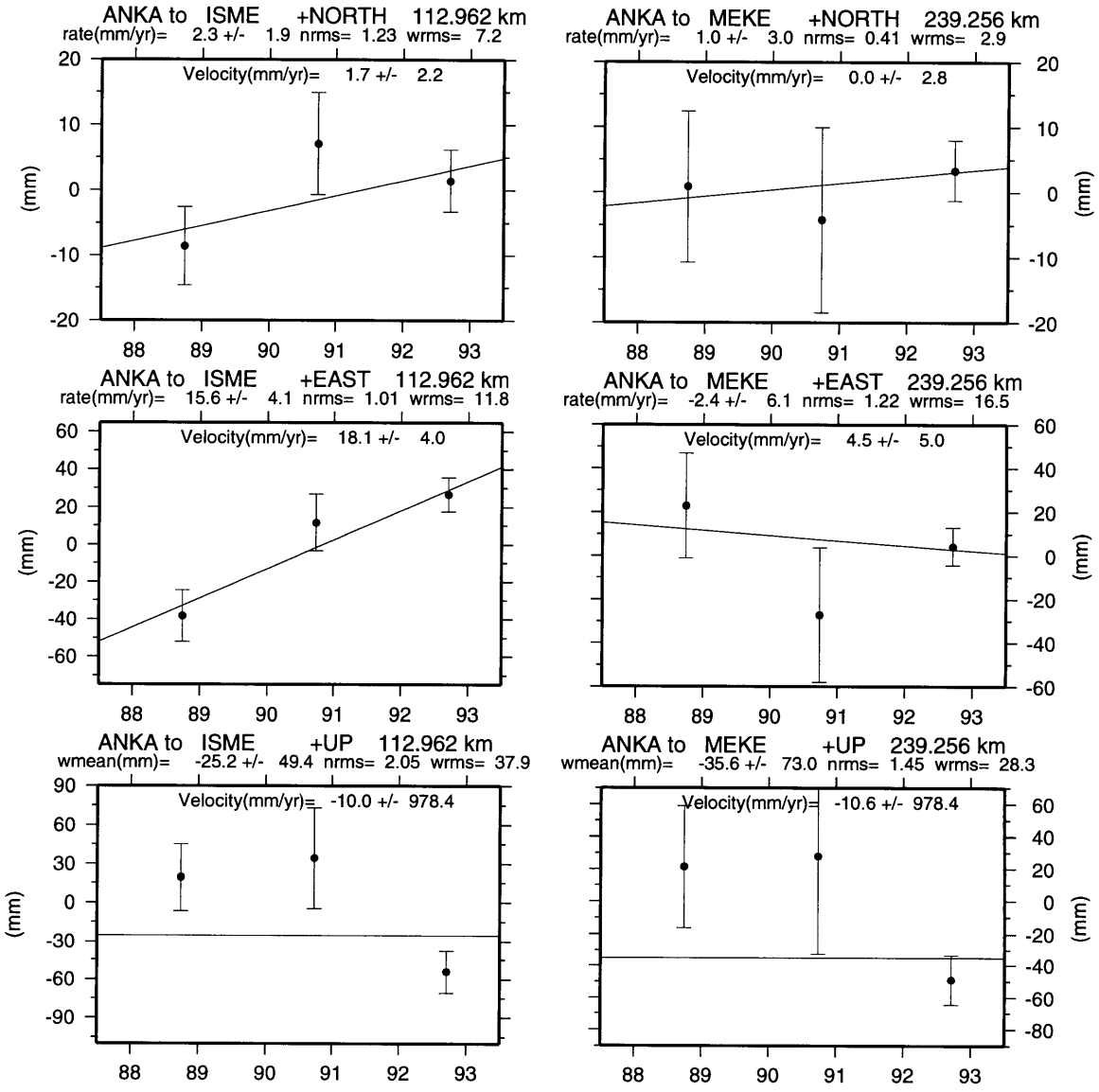

Figure C-27: The time evolution of the north, east and vertical (up) components of the relative position vectors obtained from GLOBK Kalman filter back solutions. Rate/velocity is relative to the first site, where NEU is +. The rate is calculated by a naive weighted least squares fit to the estimates of baseline components. The wrms and nrms are about this best fitting straight-line, except for the vertical, which is about the weighted mean. The velocity (inserted into the box) is obtained from GLOBK Kalman filter forward solutions which use the entire data set. We scaled all formal uncertainties by a factor of 2 (an additional factor of 3 applied to 1990 values) to reflect realistic 1-σ errors.

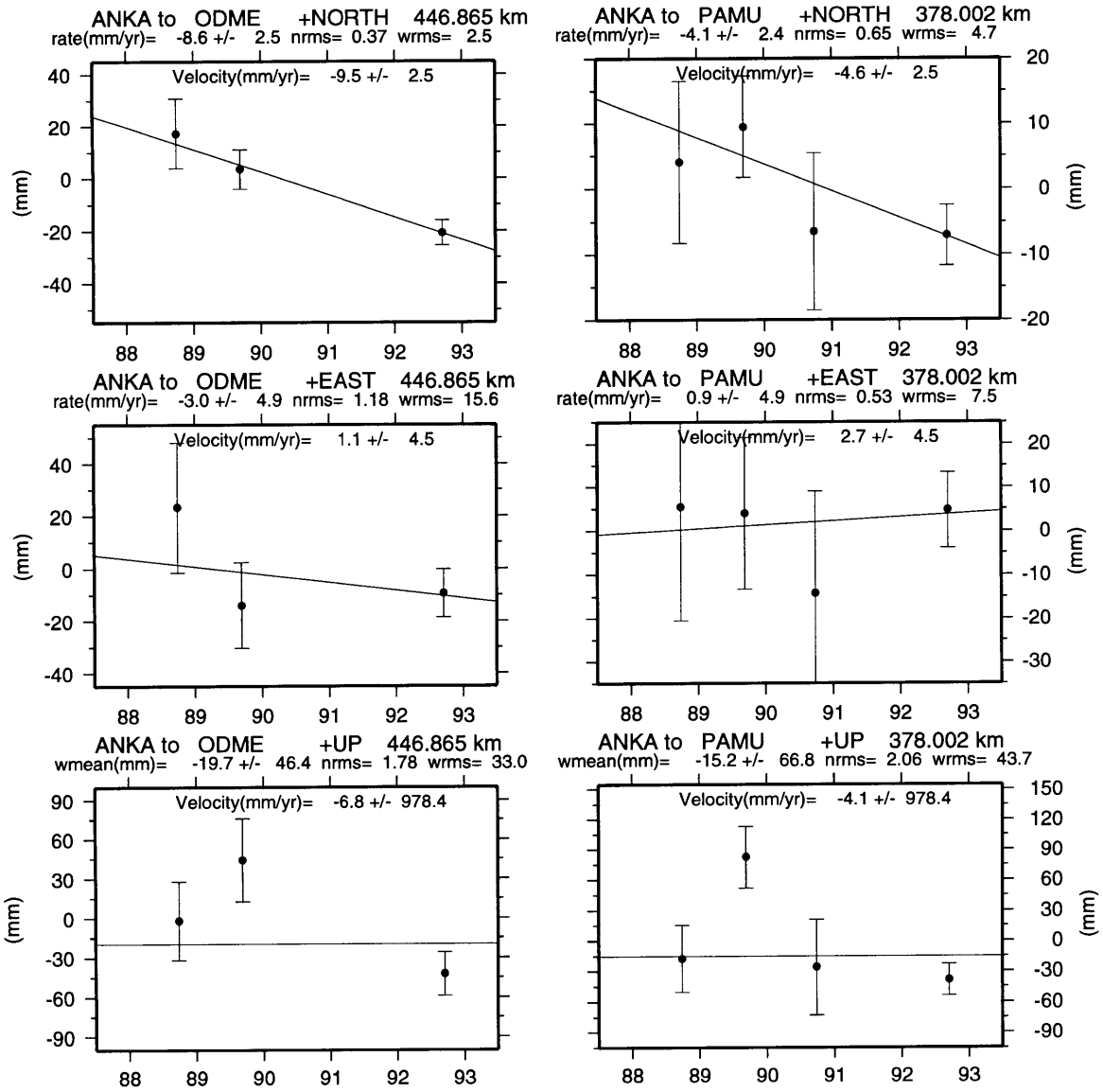

Figure C-28: The time evolution of the north, east and vertical (up) components of the relative position vectors obtained from GLOBK Kalman filter back solutions. Rate/velocity is relative to the first site, where NEU is +. The rate is calculated by a naive weighted least squares fit to the estimates of baseline components. The wrms and nrms are about this best fitting straight-line, except for the vertical, which is about the weighted mean. The velocity (inserted into the box) is obtained from GLOBK Kalman filter forward solutions which use the entire data set. We scaled all formal uncertainties by a factor of 2 (an additional factor of 3 applied to 1990 values) to reflect realistic 1-σ errors.

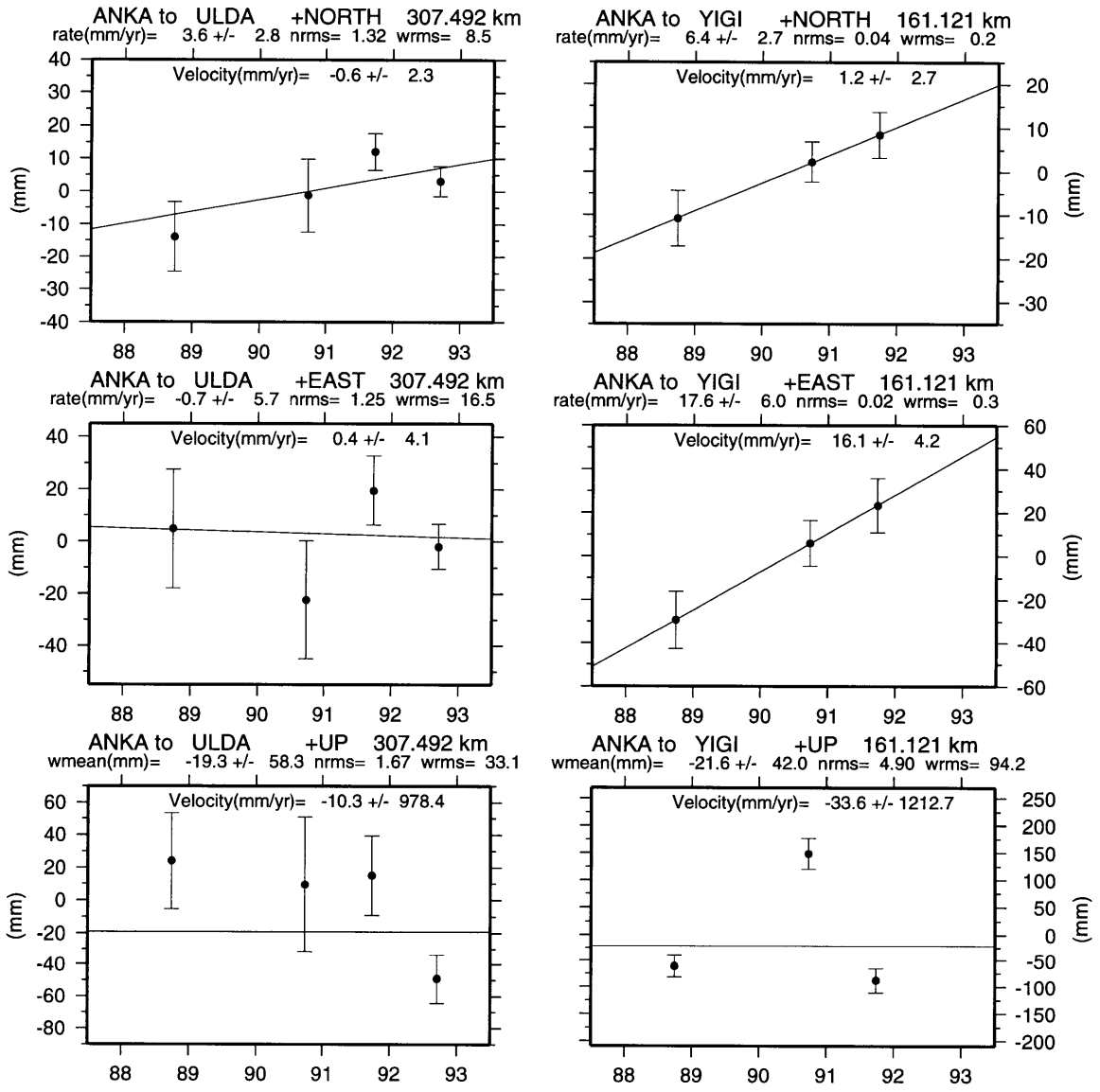

Figure C-29: The time evolution of the north, east and vertical (up) components of the relative position vectors obtained from GLOBK Kalman filter back solutions. Rate/velocity is relative to the first site, where NEU is +. The rate is calculated by a naive weighted least squares fit to the estimates of baseline components. The wrms and nrms are about this best fitting straight-line, except for the vertical, which is about the weighted mean. The velocity (inserted into the box) is obtained from GLOBK Kalman filter forward solutions which use the entire data set. We scaled all formal uncertainties by a factor of 2 (an additional factor of 3 applied to 1990 values) to reflect realistic 1-σ errors.

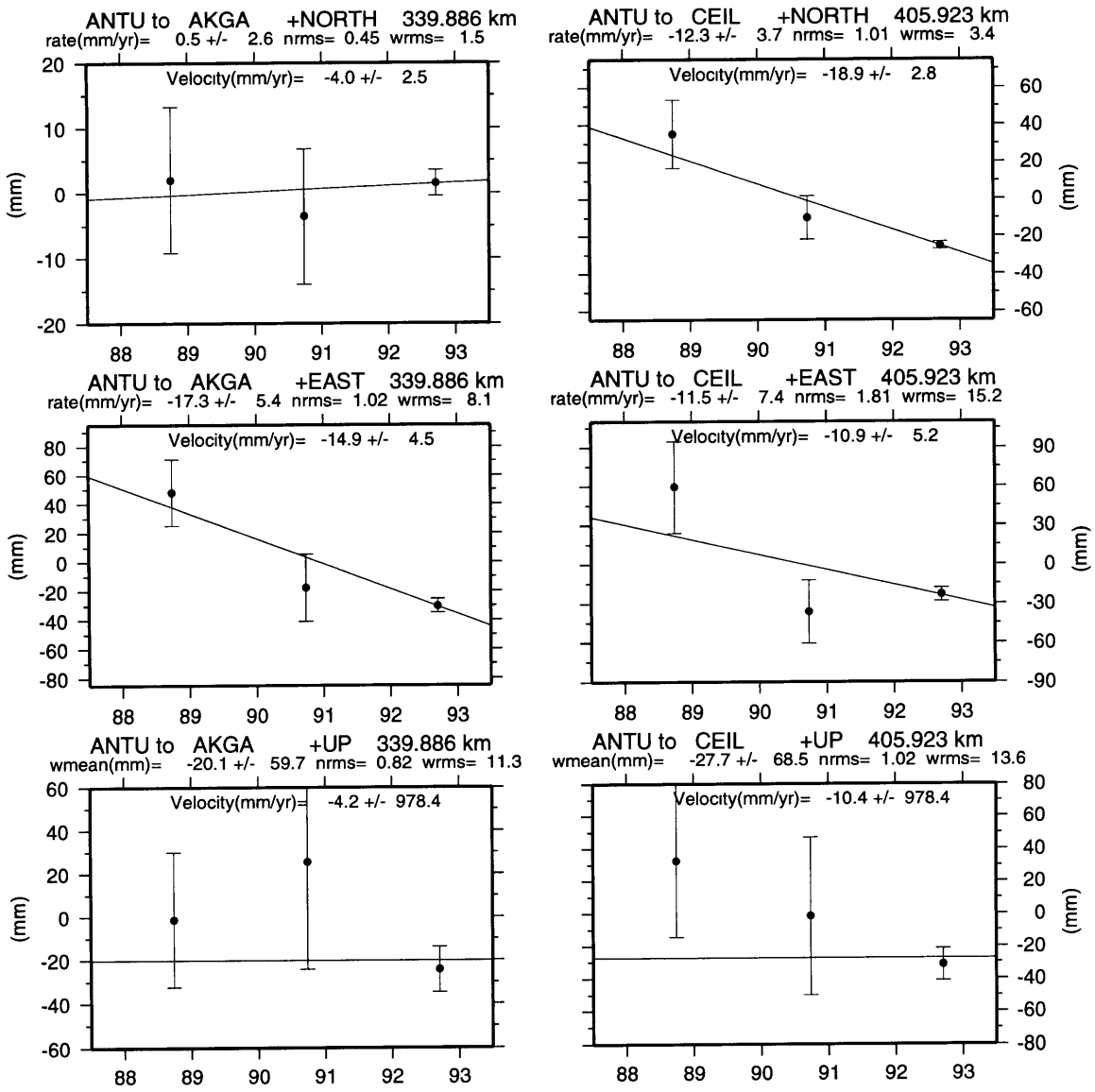

Figure C-30: The time evolution of the north, east and vertical (up) components of the relative position vectors obtained from GLOBK Kalman filter back solutions. Rate/velocity is relative to the first site, where NEU is +. The rate is calculated by a naive weighted least squares fit to the estimates of baseline components. The wrms and nrms are about this best fitting straight-line, except for the vertical, which is about the weighted mean. The velocity (inserted into the box) is obtained from GLOBK Kalman filter forward solutions which use the entire data set. We scaled all formal uncertainties by a factor of 2 (an additional factor of 3 applied to 1990 values) to reflect realistic 1-σ errors.

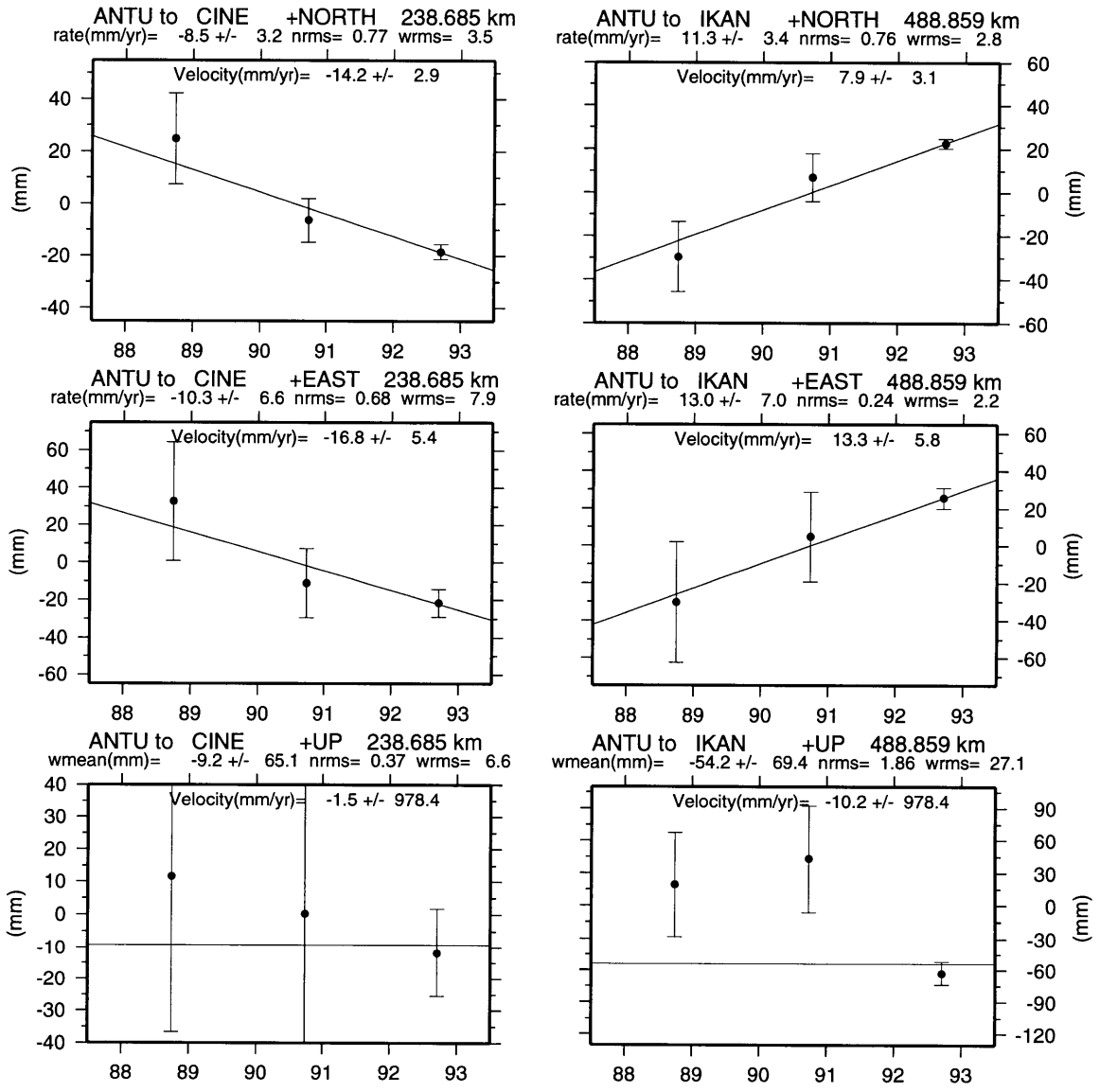

Figure C-31: The time evolution of the north, east and vertical (up) components of the relative position vectors obtained from GLOBK Kalman filter back solutions. Rate/velocity is relative to the first site, where NEU is +. The rate is calculated by a naive weighted least squares fit to the estimates of baseline components. The wrms and nrms are about this best fitting straight-line, except for the vertical, which is about the weighted mean. The velocity (inserted into the box) is obtained from GLOBK Kalman filter forward solutions which use the entire data set. We scaled all formal uncertainties by a factor of 2 (an additional factor of 3 applied to 1990 values) to reflect realistic 1-σ errors.

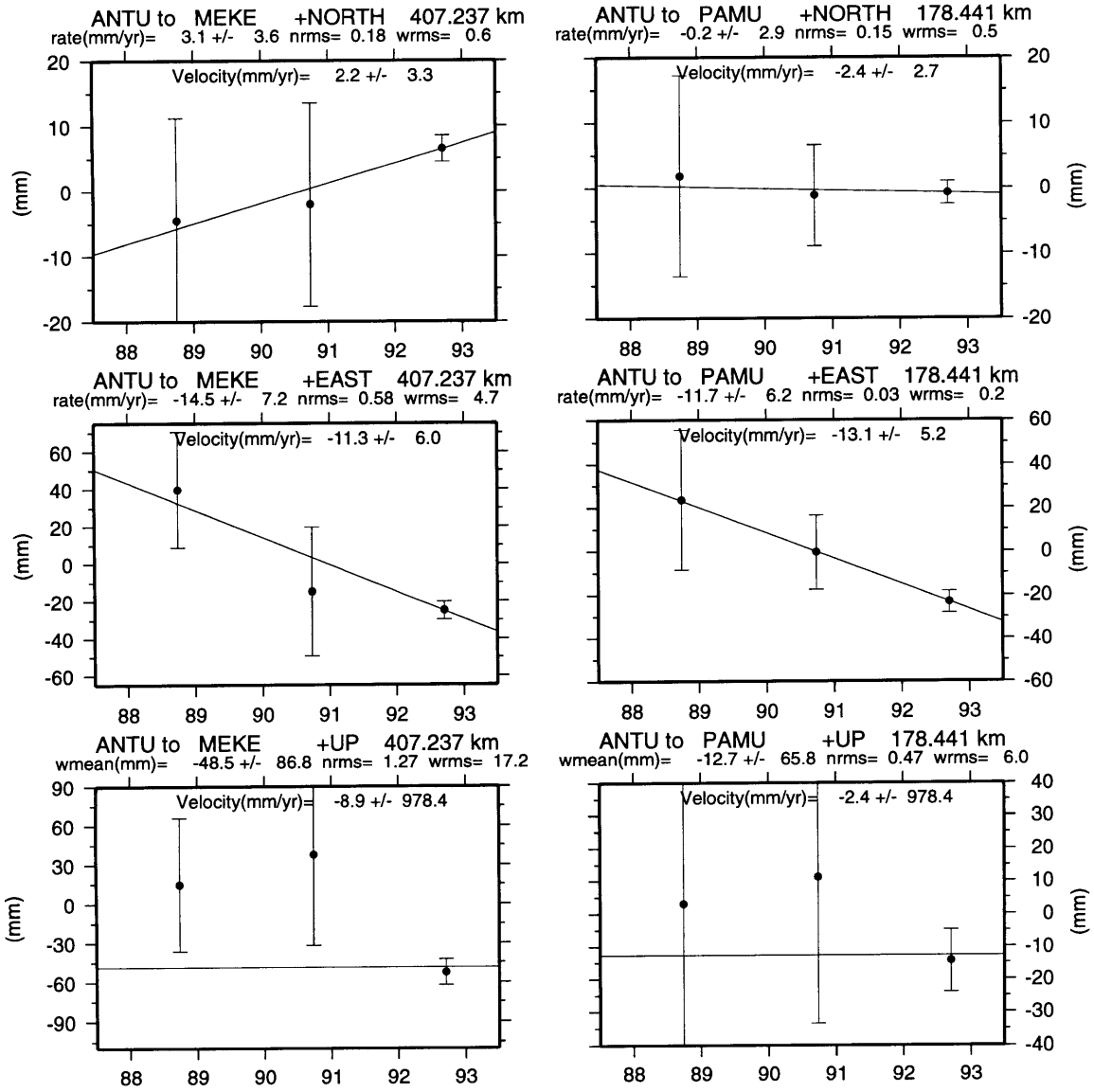

Figure C-32: The time evolution of the north, east and vertical (up) components of the relative position vectors obtained from GLOBK Kalman filter back solutions. Rate/velocity is relative to the first site, where NEU is +. The rate is calculated by a naive weighted least squares fit to the estimates of baseline components. The wrms and nrms are about this best fitting straight-line, except for the vertical, which is about the weighted mean. The velocity (inserted into the box) is obtained from GLOBK Kalman filter forward solutions which use the entire data set. We scaled all formal uncertainties by a factor of 2 (an additional factor of 3 applied to 1990 values) to reflect realistic 1-σ errors.

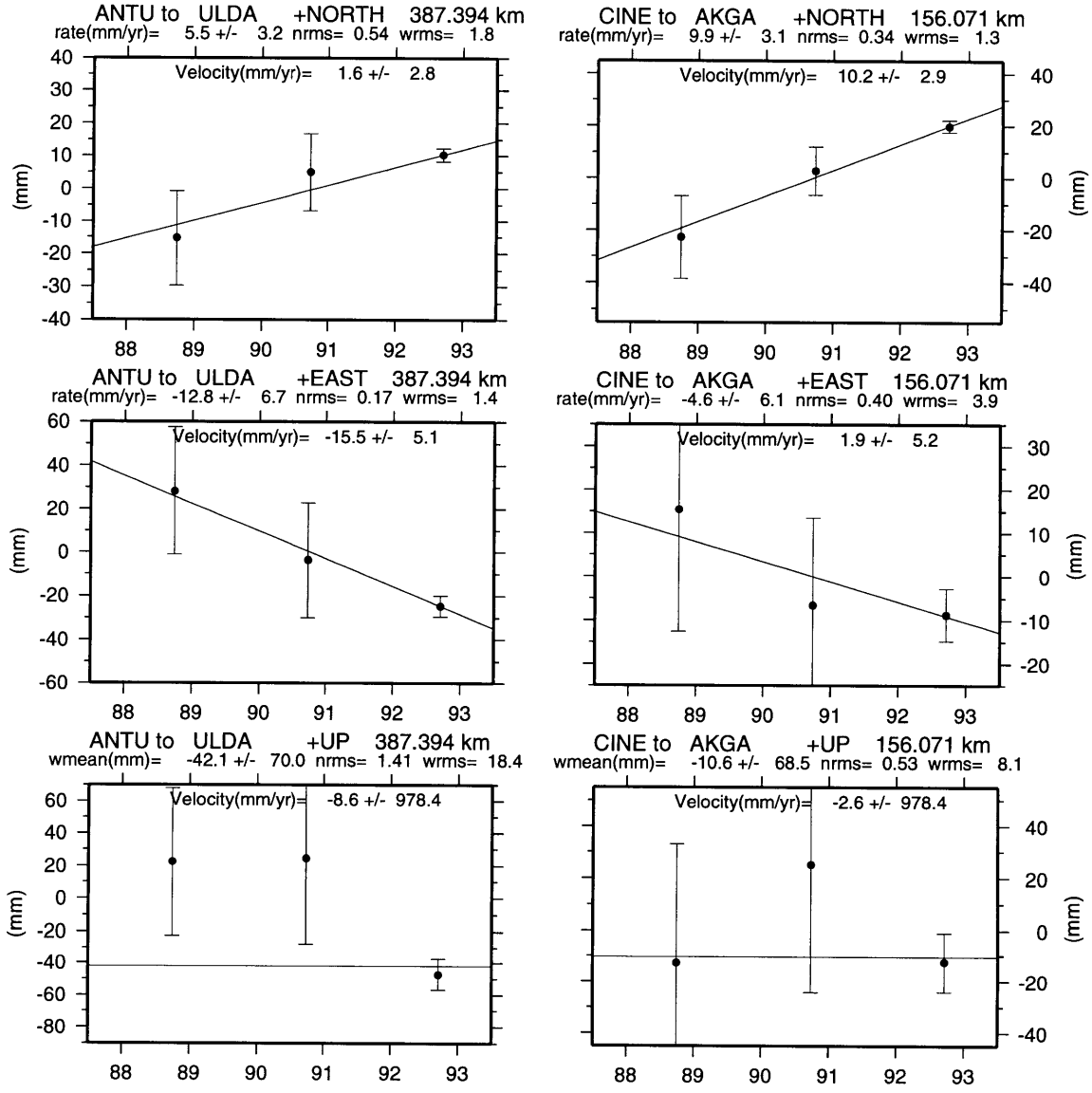

Figure C-33: The time evolution of the north, east and vertical (up) components of the relative position vectors obtained from GLOBK Kalman filter back solutions. Rate/velocity is relative to the first site, where NEU is +. The rate is calculated by a naive weighted least squares fit to the estimates of baseline components. The wrms and nrms are about this best fitting straight-line, except for the vertical, which is about the weighted mean. The velocity (inserted into the box) is obtained from GLOBK Kalman filter forward solutions which use the entire data set. We scaled all formal uncertainties by a factor of 2 (an additional factor of 3 applied to 1990 values) to reflect realistic 1-σ errors.

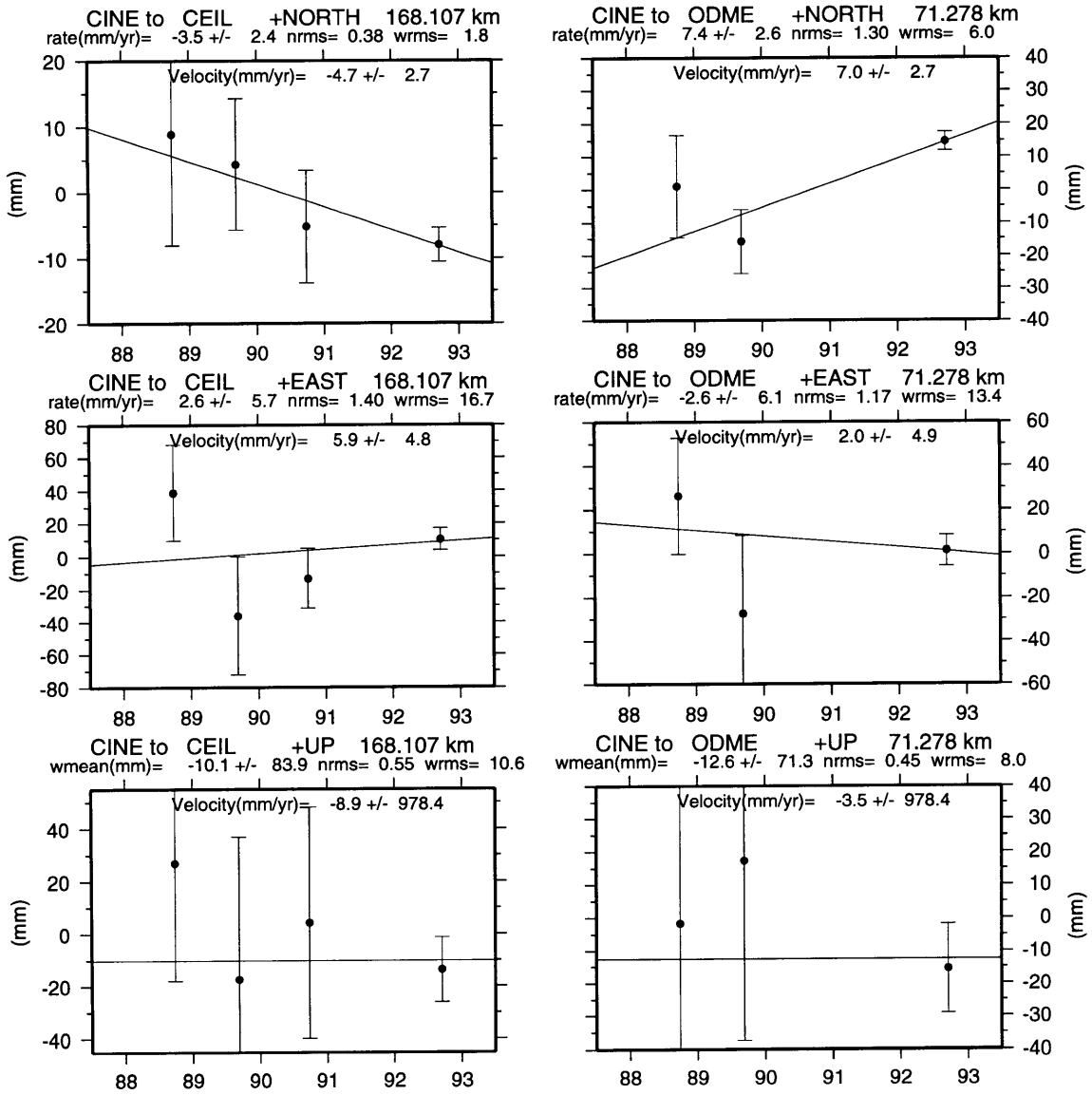

Figure C-34: The time evolution of the north, east and vertical (up) components of the relative position vectors obtained from GLOBK Kalman filter back solutions. Rate/velocity is relative to the first site, where NEU is +. The rate is calculated by a naive weighted least squares fit to the estimates of baseline components. The wrms and nrms are about this best fitting straight-line, except for the vertical, which is about the weighted mean. The velocity (inserted into the box) is obtained from GLOBK Kalman filter forward solutions which use the entire data set. We scaled all formal uncertainties by a factor of 2 (an additional factor of 3 applied to 1990 values) to reflect realistic 1-σ errors.

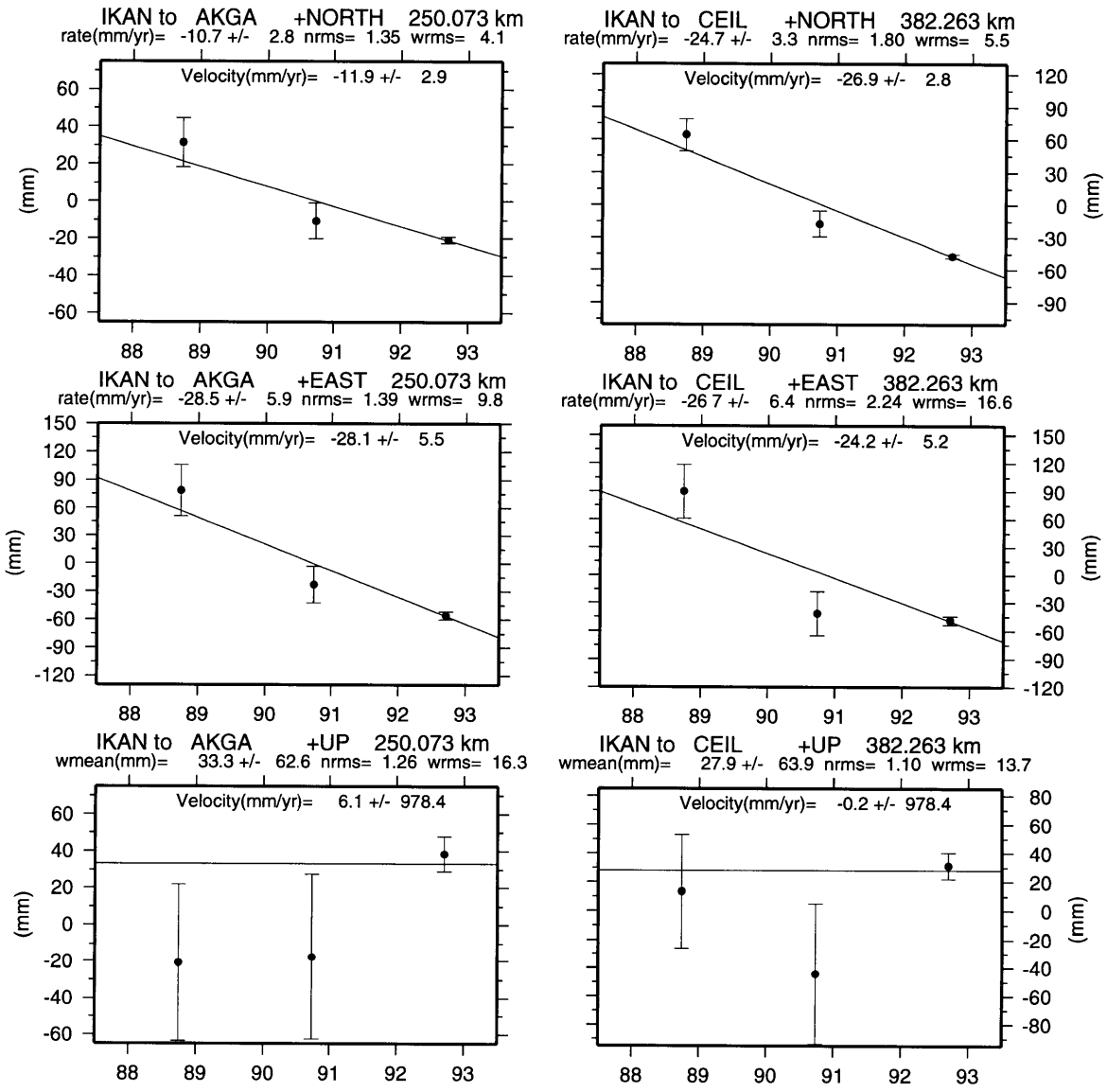

Figure C-35: The time evolution of the north, east and vertical (up) components of the relative position vectors obtained from GLOBK Kalman filter back solutions. Rate/velocity is relative to the first site, where NEU is +. The rate is calculated by a naive weighted least squares fit to the estimates of baseline components. The wrms and nrms are about this best fitting straight-line, except for the vertical, which is about the weighted mean. The velocity (inserted into the box) is obtained from GLOBK Kalman filter forward solutions which use the entire data set. We scaled all formal uncertainties by a factor of 2 (an additional factor of 3 applied to 1990 values) to reflect realistic 1-σ errors.

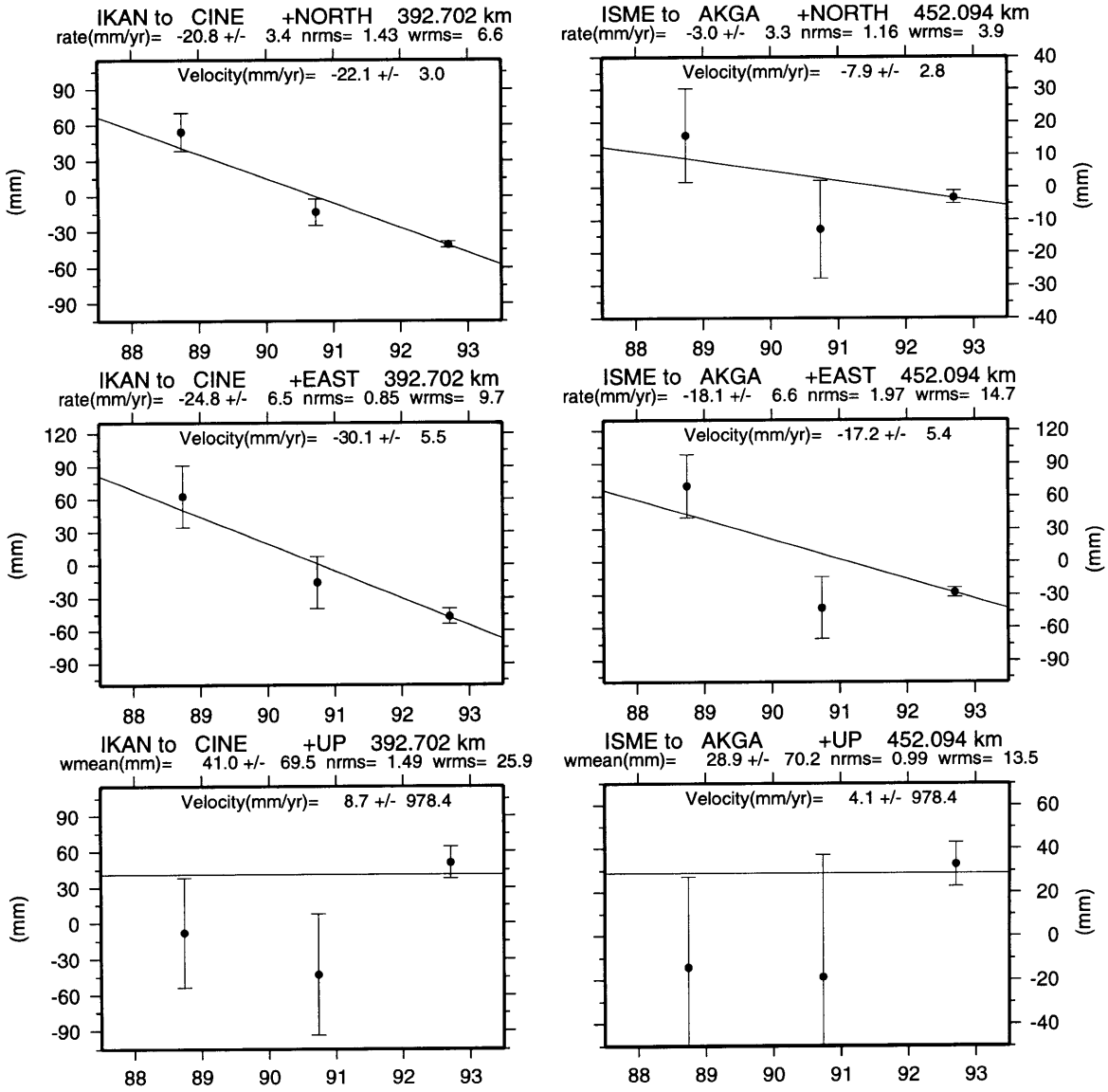

Figure C-36: The time evolution of the north, east and vertical (up) components of the relative position vectors obtained from GLOBK Kalman filter back solutions. Rate/velocity is relative to the first site, where NEU is +. The rate is calculated by a naive weighted least squares fit to the estimates of baseline components. The wrms and nrms are about this best fitting straight-line, except for the vertical, which is about the weighted mean. The velocity (inserted into the box) is obtained from GLOBK Kalman filter forward solutions which use the entire data set. We scaled all formal uncertainties by a factor of 2 (an additional factor of 3 applied to 1990 values) to reflect realistic 1-σ errors.

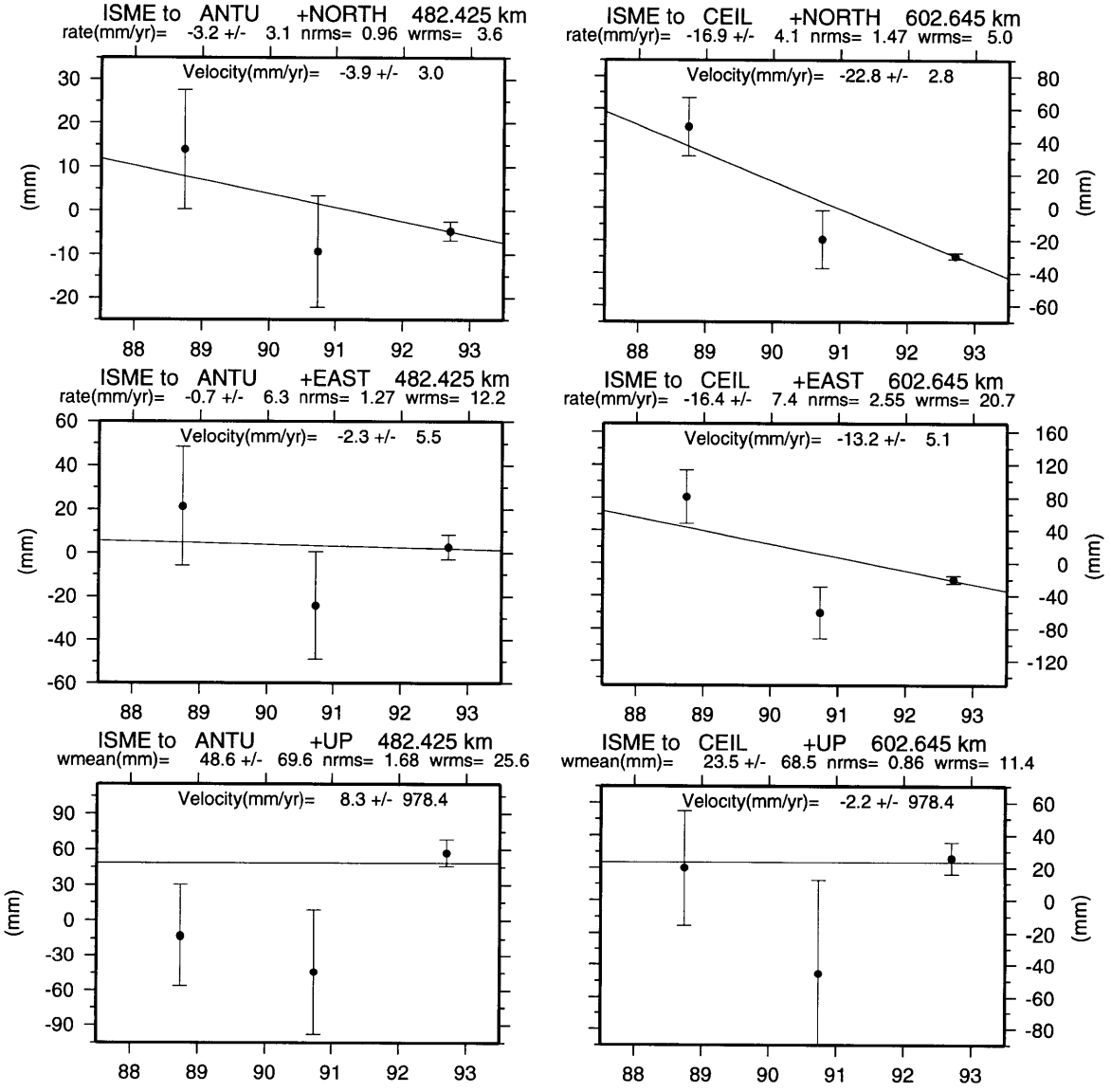

Figure C-37: The time evolution of the north, east and vertical (up) components of the relative position vectors obtained from GLOBK Kalman filter back solutions. Rate/velocity is relative to the first site, where NEU is +. The rate is calculated by a naive weighted least squares fit to the estimates of baseline components. The wrms and nrms are about this best fitting straight-line, except for the vertical, which is about the weighted mean. The velocity (inserted into the box) is obtained from GLOBK Kalman filter forward solutions which use the entire data set. We scaled all formal uncertainties by a factor of 2 (an additional factor of 3 applied to 1990 values) to reflect realistic 1-σ errors.

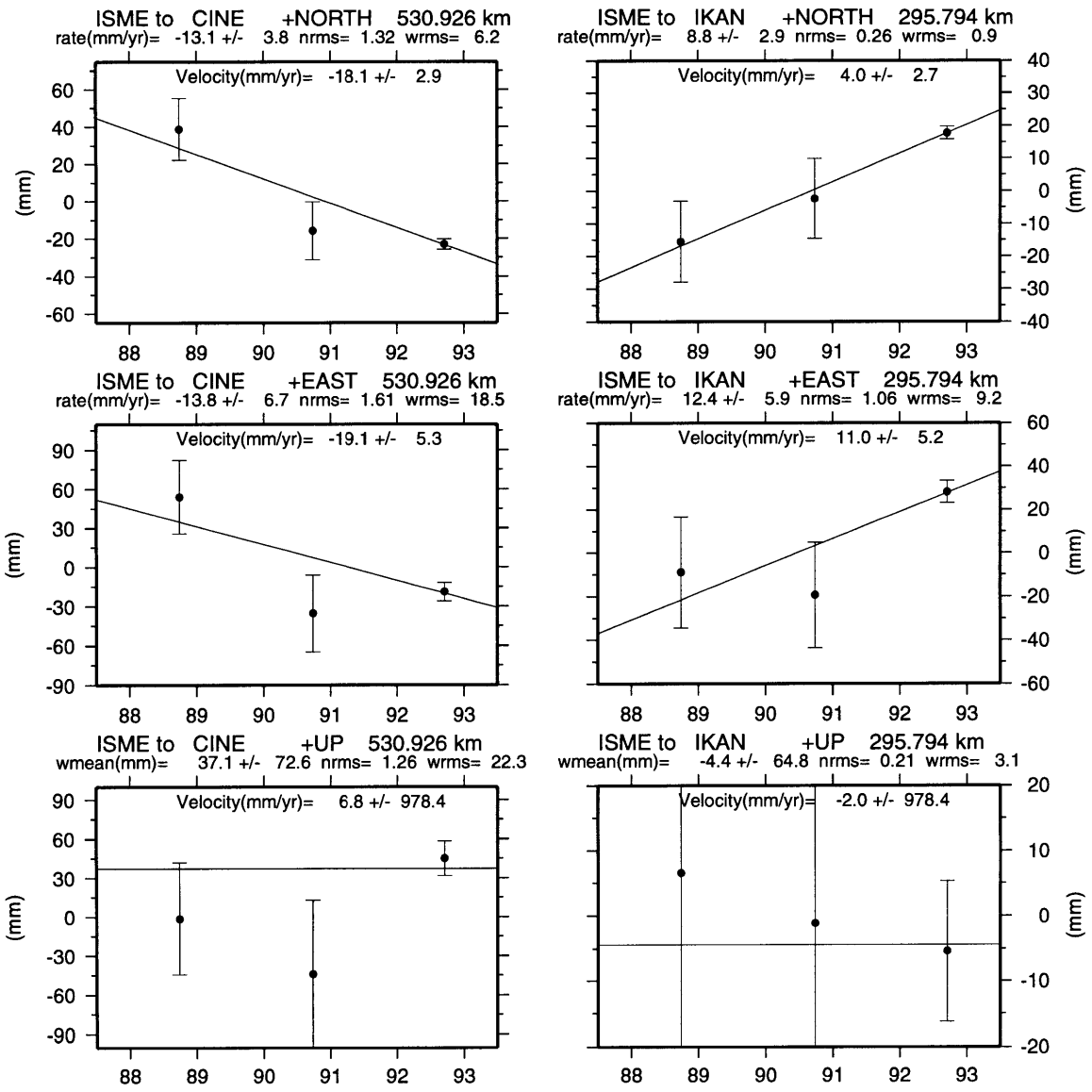

Figure C-38: The time evolution of the north, east and vertical (up) components of the relative position vectors obtained from GLOBK Kalman filter back solutions. Rate/velocity is relative to the first site, where NEU is +. The rate is calculated by a naive weighted least squares fit to the estimates of baseline components. The wrms and nrms are about this best fitting straight-line, except for the vertical, which is about the weighted mean. The velocity (inserted into the box) is obtained from GLOBK Kalman filter forward solutions which use the entire data set. We scaled all formal uncertainties by a factor of 2 (an additional factor of 3 applied to 1990 values) to reflect realistic 1-σ errors.

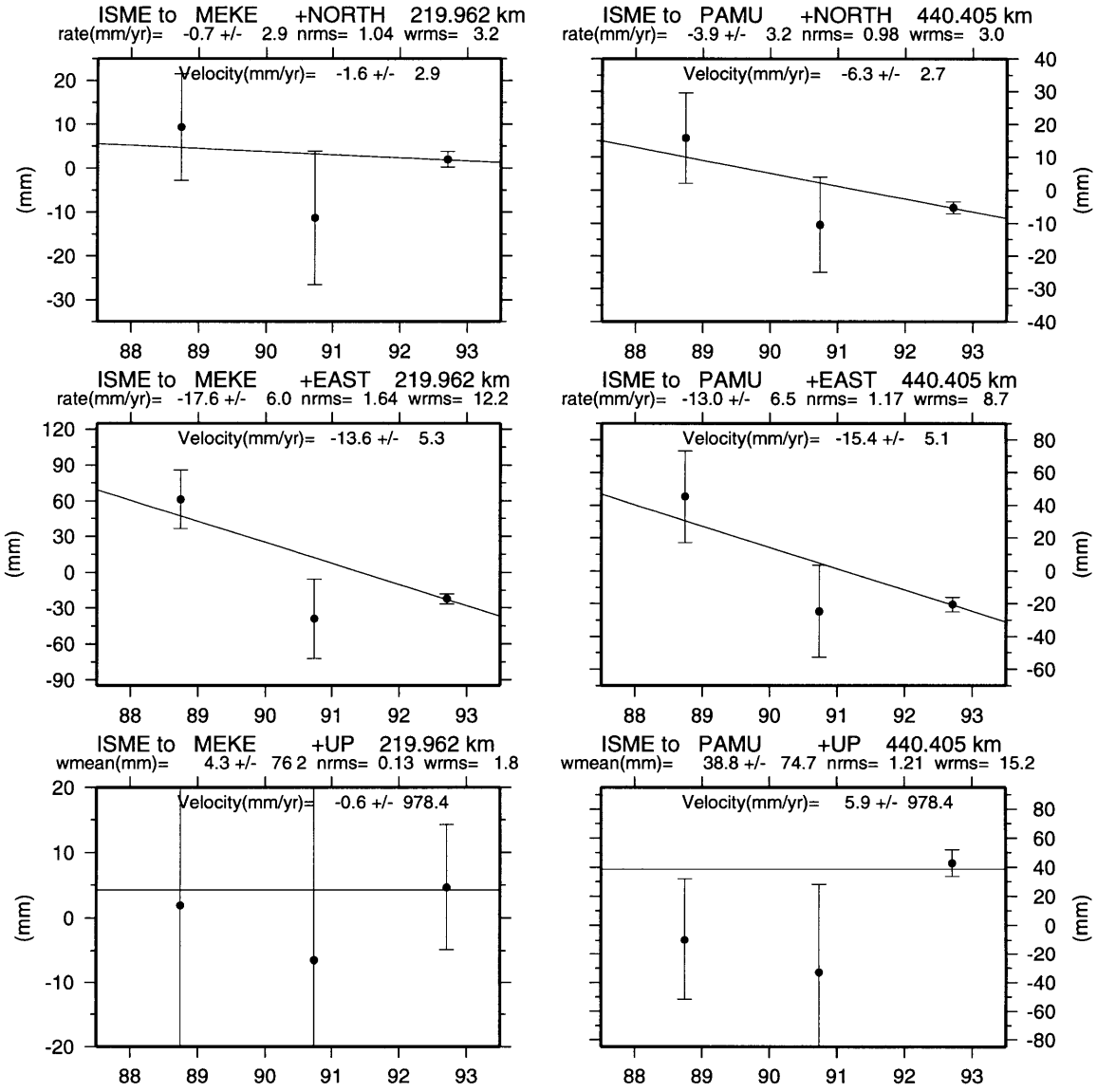

Figure C-39: The time evolution of the north, east and vertical (up) components of the relative position vectors obtained from GLOBK Kalman filter back solutions. Rate/velocity is relative to the first site, where NEU is +. The rate is calculated by a naive weighted least squares fit to the estimates of baseline components. The wrms and nrms are about this best fitting straight-line, except for the vertical, which is about the weighted mean. The velocity (inserted into the box) is obtained from GLOBK Kalman filter forward solutions which use the entire data set. We scaled all formal uncertainties by a factor of 2 (an additional factor of 3 applied to 1990 values) to reflect realistic 1-σ errors.

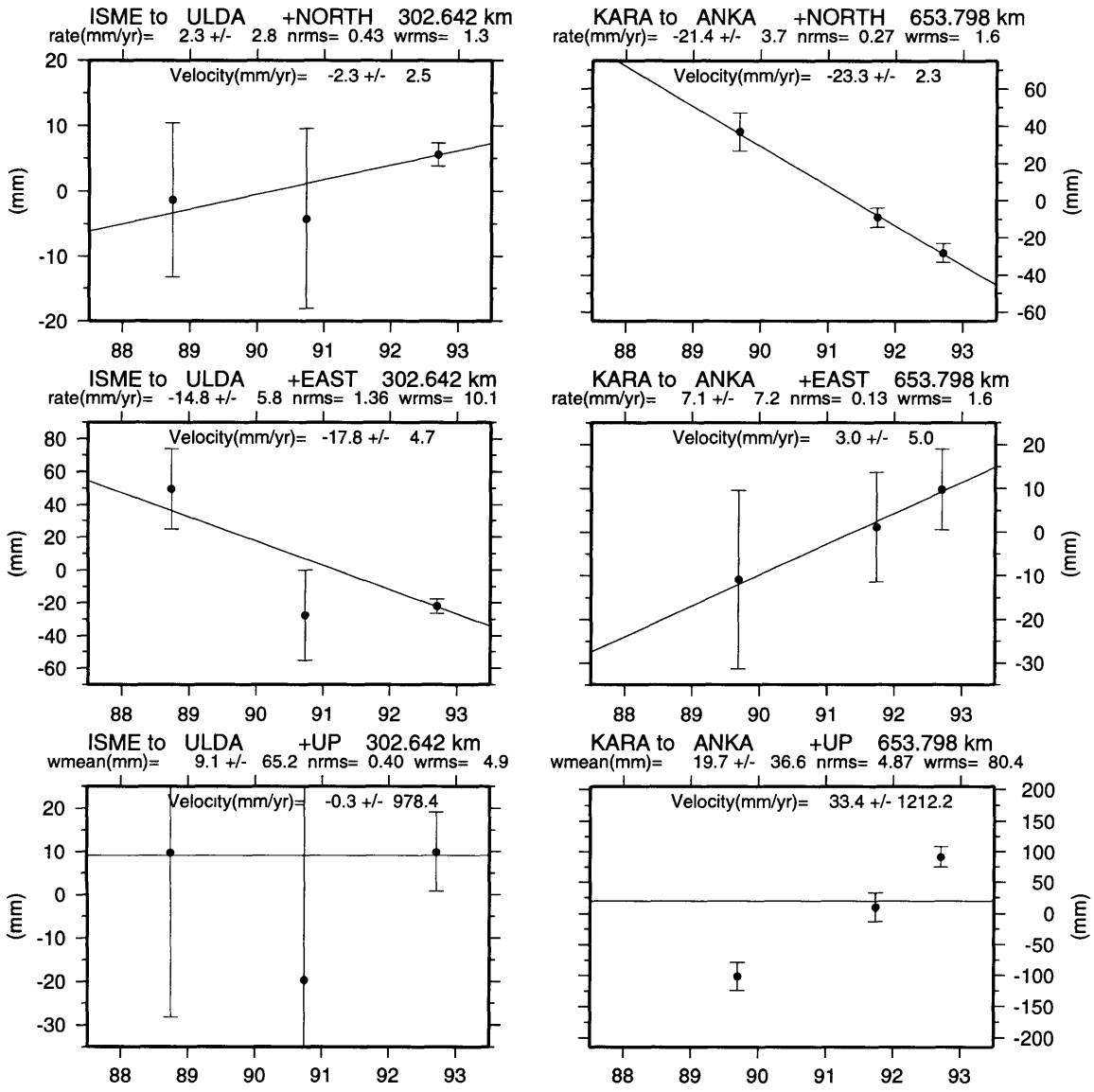

Figure C-40: The time evolution of the north, east and vertical (up) components of the relative position vectors obtained from GLOBK Kalman filter back solutions. Rate/velocity is relative to the first site, where NEU is +. The rate is calculated by a naive weighted least squares fit to the estimates of baseline components. The wrms and nrms are about this best fitting straight-line, except for the vertical, which is about the weighted mean. The velocity (inserted into the box) is obtained from GLOBK Kalman filter forward solutions which use the entire data set. We scaled all formal uncertainties by a factor of 2 (an additional factor of 3 applied to 1990 values) to reflect realistic 1-σ errors.

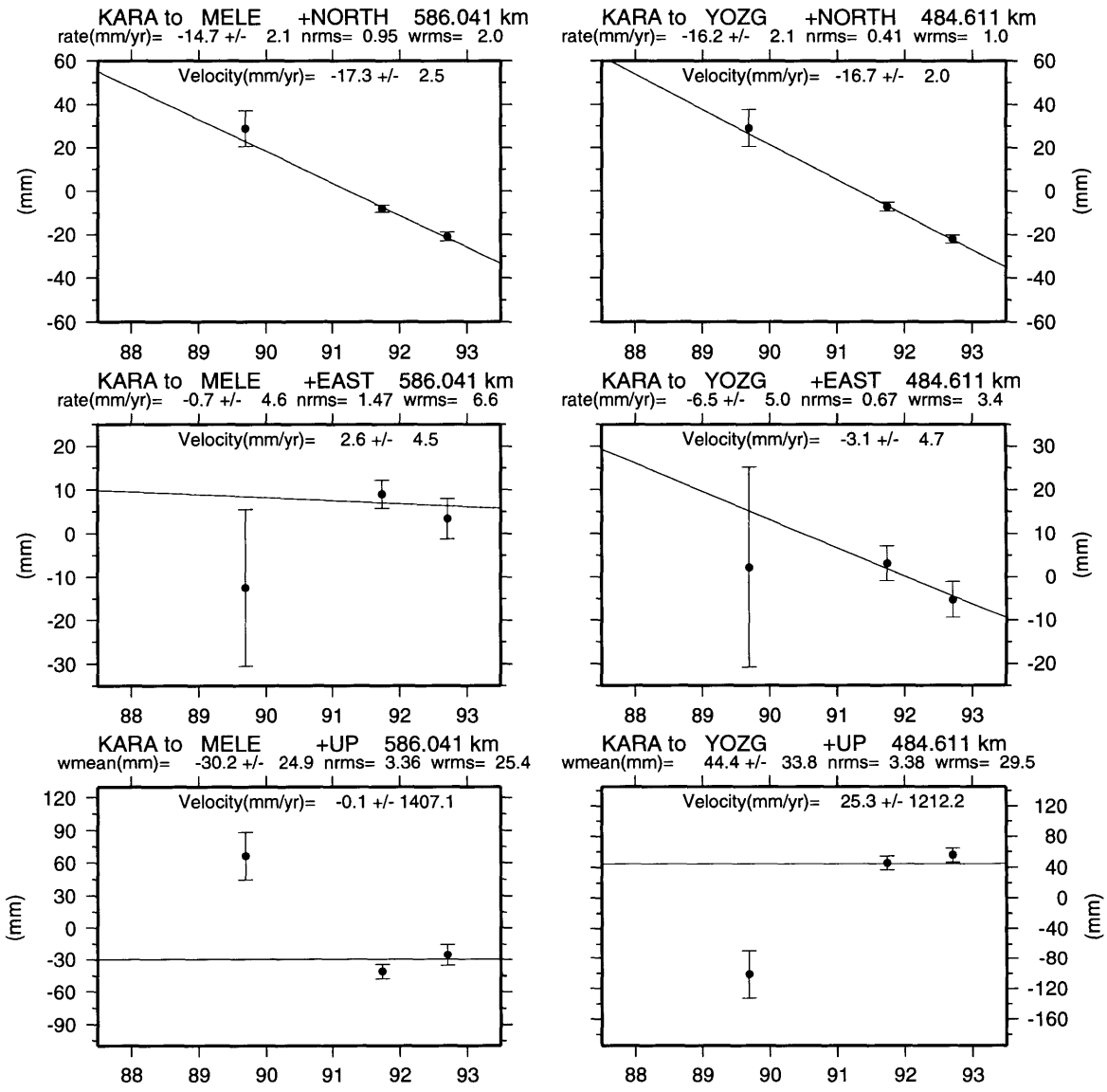

Figure C-41: The time evolution of the north, east and vertical (up) components of the relative position vectors obtained from GLOBK Kalman filter back solutions. Rate/velocity is relative to the first site, where NEU is +. The rate is calculated by a naive weighted least squares fit to the estimates of baseline components. The wrms and nrms are about this best fitting straight-line, except for the vertical, which is about the weighted mean. The velocity (inserted into the box) is obtained from GLOBK Kalman filter forward solutions which use the entire data set. We scaled all formal uncertainties by a factor of 2 (an additional factor of 3 applied to 1990 values) to reflect realistic 1-σ errors.

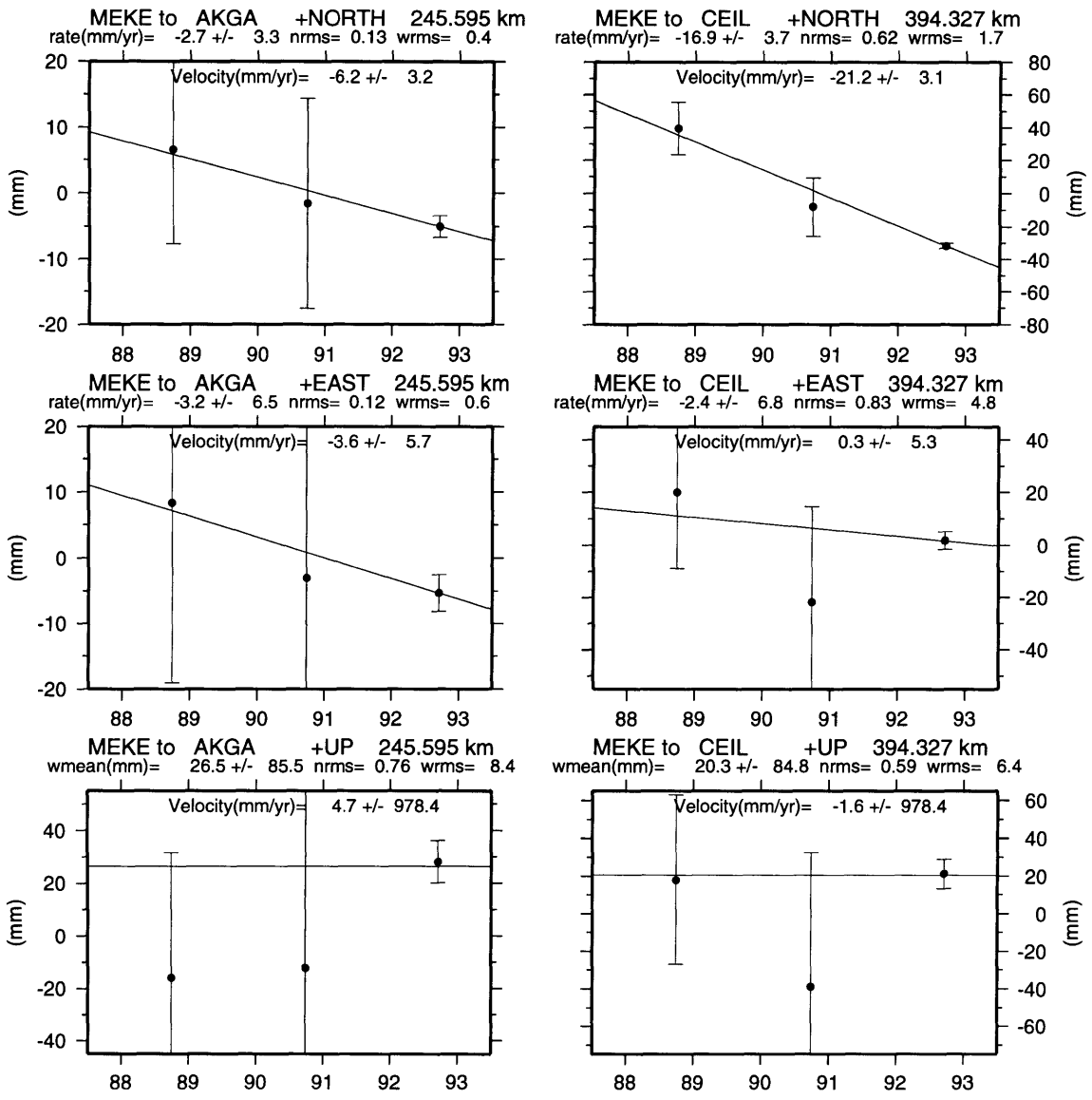

Figure C-42: The time evolution of the north, east and vertical (up) components of the relative position vectors obtained from GLOBK Kalman filter back solutions. Rate/velocity is relative to the first site, where NEU is +. The rate is calculated by a naive weighted least squares fit to the estimates of baseline components. The wrms and nrms are about this best fitting straight-line, except for the vertical, which is about the weighted mean. The velocity (inserted into the box) is obtained from GLOBK Kalman filter forward solutions which use the entire data set. We scaled all formal uncertainties by a factor of 2 (an additional factor of 3 applied to 1990 values) to reflect realistic 1-σ errors.

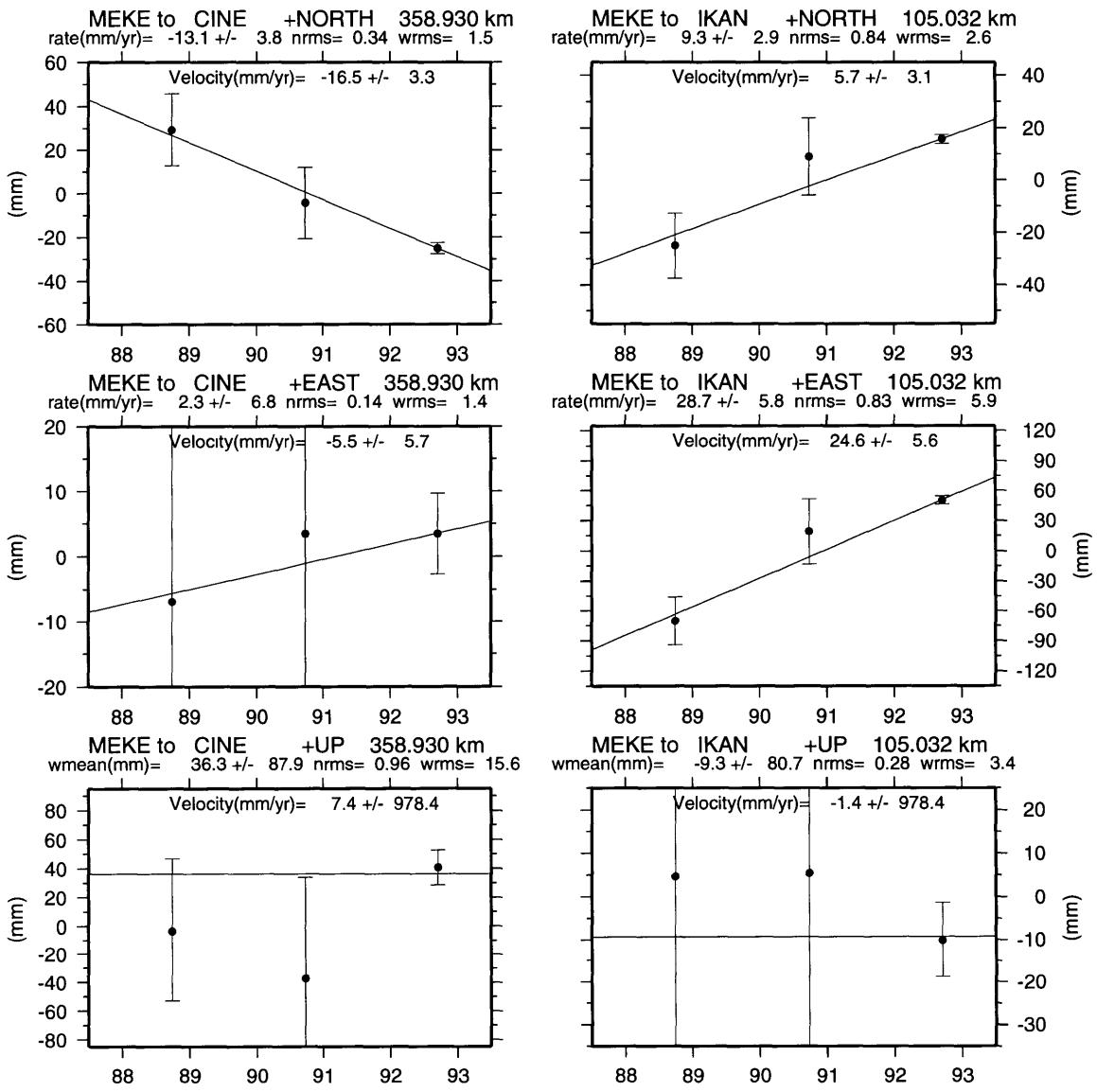

Figure C-43: The time evolution of the north, east and vertical (up) components of the relative position vectors obtained from GLOBK Kalman filter back solutions. Rate/velocity is relative to the first site, where NEU is +. The rate is calculated by a naive weighted least squares fit to the estimates of baseline components. The wrms and nrms are about this best fitting straight-line, except for the vertical, which is about the weighted mean. The velocity (inserted into the box) is obtained from GLOBK Kalman filter forward solutions which use the entire data set. We scaled all formal uncertainties by a factor of 2 (an additional factor of 3 applied to 1990 values) to reflect realistic 1-σ errors.

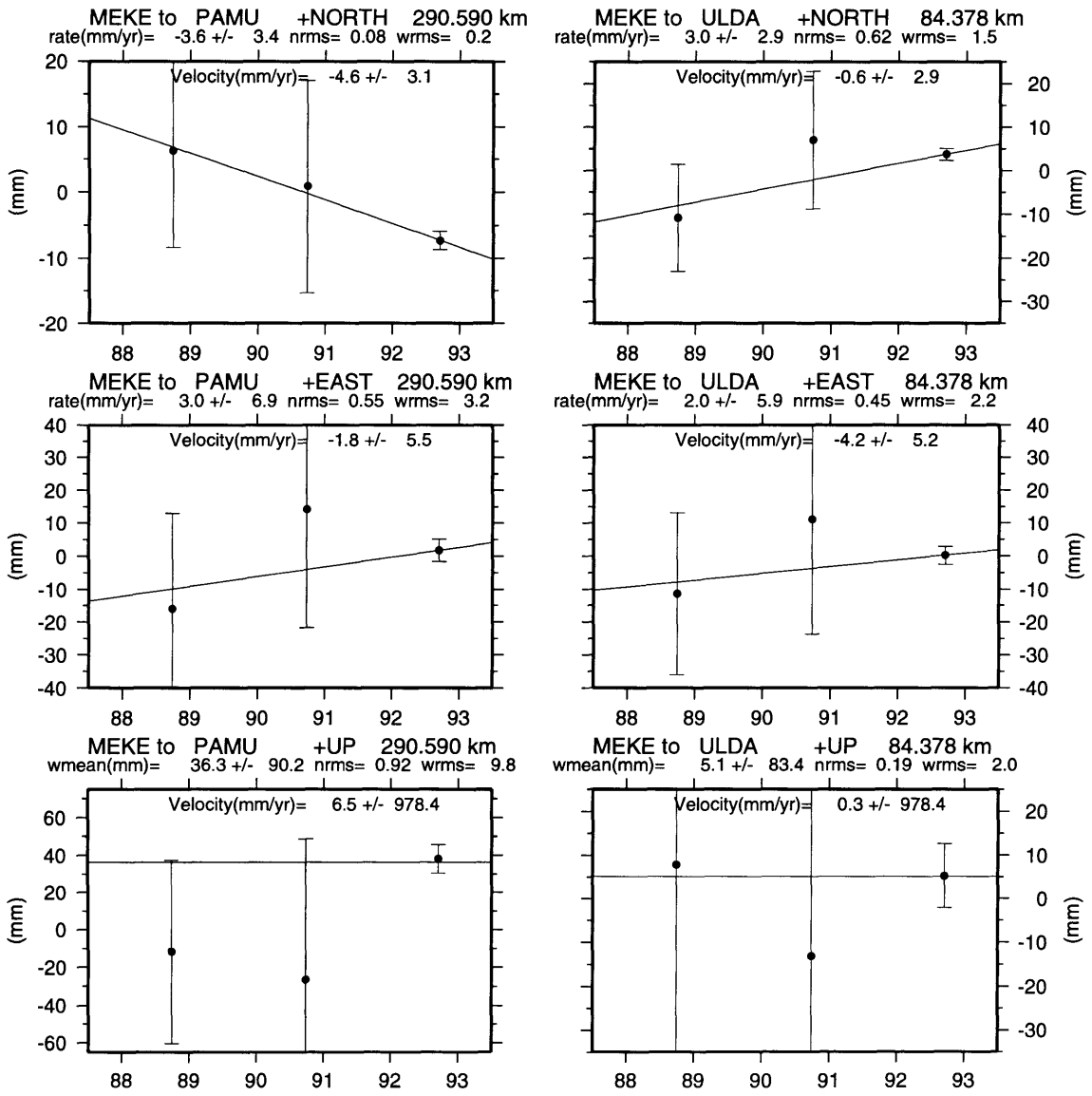

Figure C-44: The time evolution of the north, east and vertical (up) components of the relative position vectors obtained from GLOBK Kalman filter back solutions. Rate/velocity is relative to the first site, where NEU is +. The rate is calculated by a naive weighted least squares fit to the estimates of baseline components. The wrms and nrms are about this best fitting straight-line, except for the vertical, which is about the weighted mean. The velocity (inserted into the box) is obtained from GLOBK Kalman filter forward solutions which use the entire data set. We scaled all formal uncertainties by a factor of 2 (an additional factor of 3 applied to 1990 values) to reflect realistic 1-σ errors.

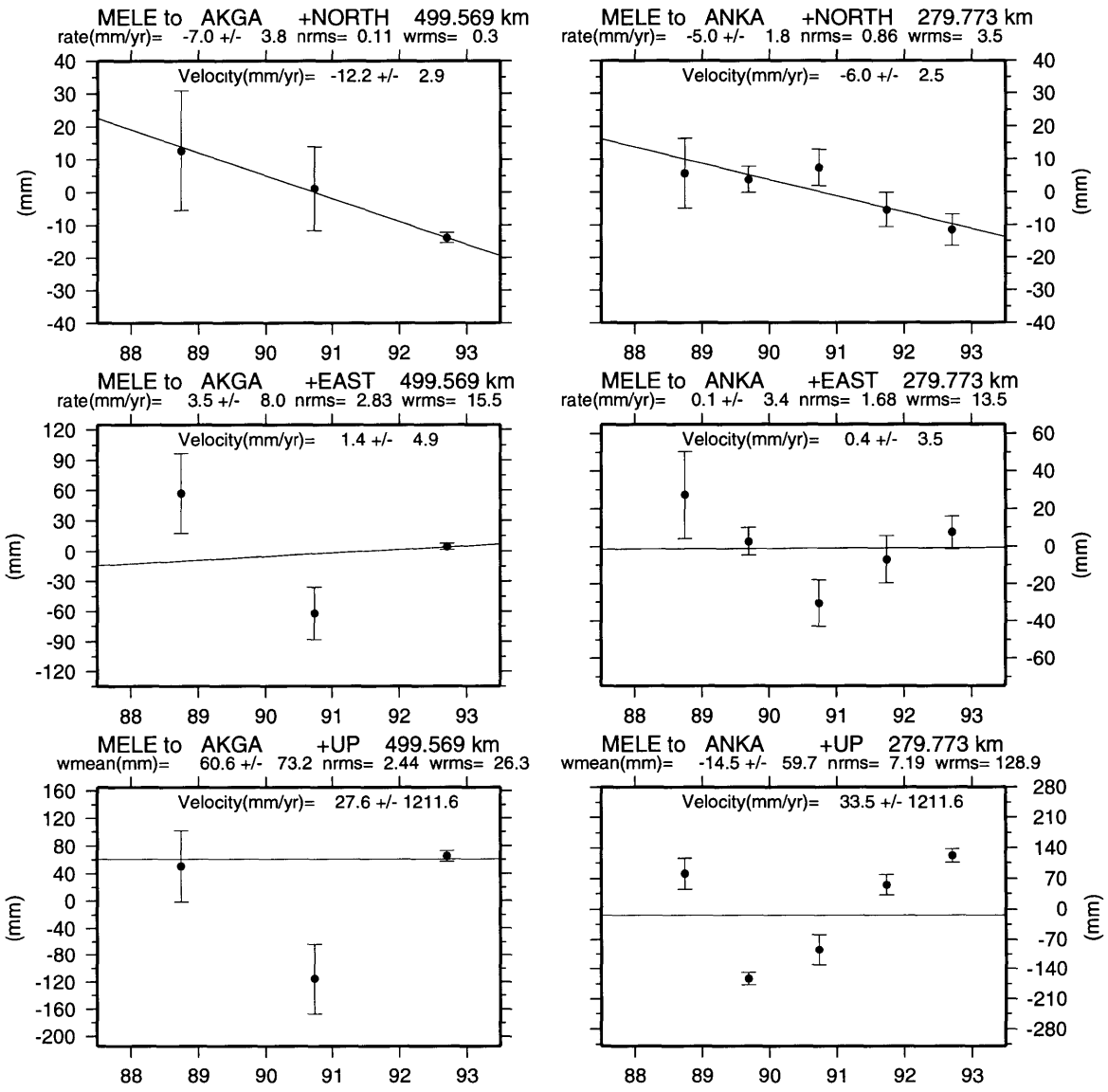

Figure C-45: The time evolution of the north, east and vertical (up) components of the relative position vectors obtained from GLOBK Kalman filter back solutions. Rate/velocity is relative to the first site, where NEU is +. The rate is calculated by a naive weighted least squares fit to the estimates of baseline components. The wrms and nrms are about this best fitting straight-line, except for the vertical, which is about the weighted mean. The velocity (inserted into the box) is obtained from GLOBK Kalman filter forward solutions which use the entire data set. We scaled all formal uncertainties by a factor of 2 (an additional factor of 3 applied to 1990 values) to reflect realistic 1-σ errors.

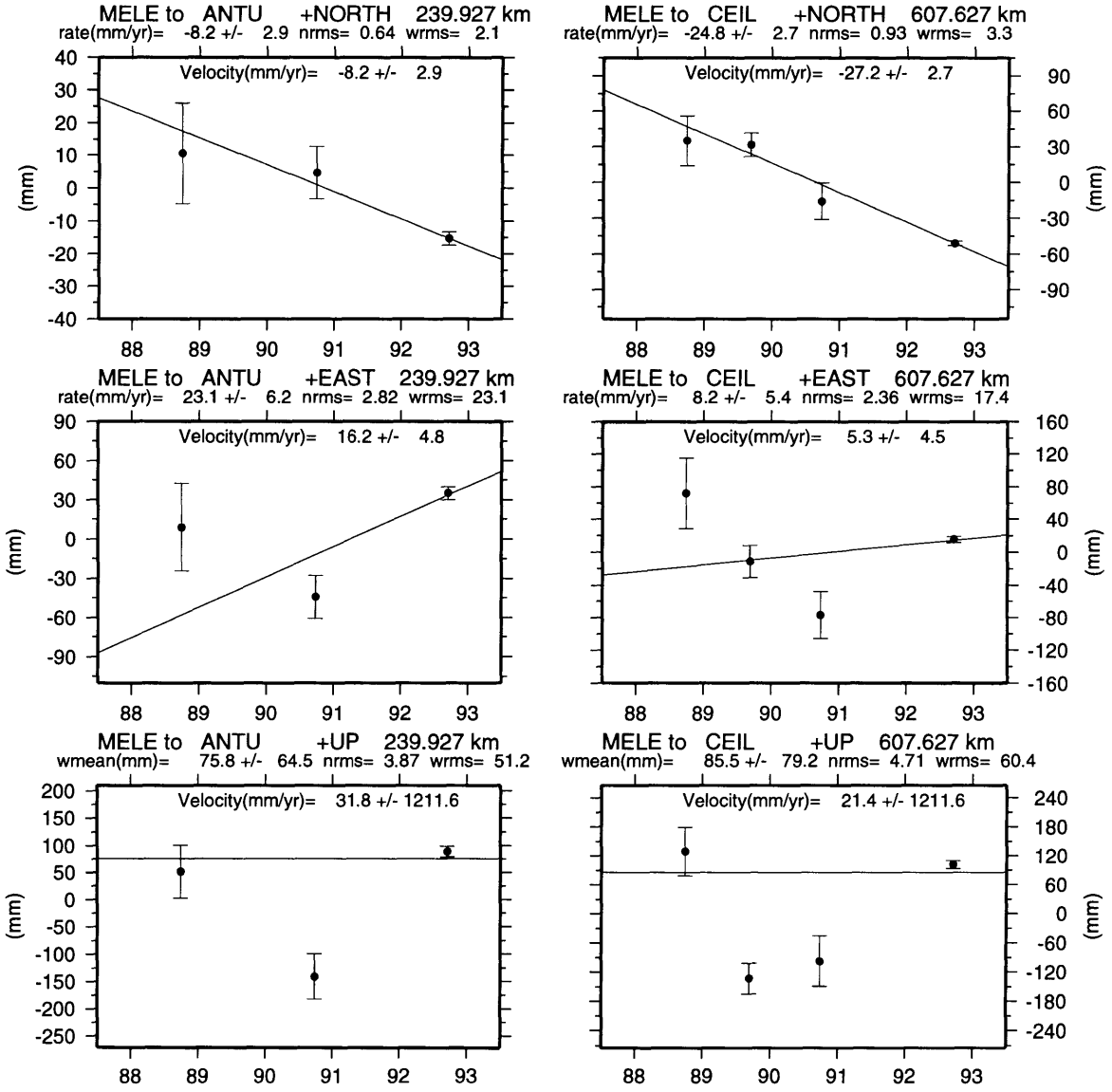

Figure C-46: The time evolution of the north, east and vertical (up) components of the relative position vectors obtained from GLOBK Kalman filter back solutions. Rate/velocity is relative to the first site, where NEU is +. The rate is calculated by a naive weighted least squares fit to the estimates of baseline components. The wrms and nrms are about this best fitting straight-line, except for the vertical, which is about the weighted mean. The velocity (inserted into the box) is obtained from GLOBK Kalman filter forward solutions which use the entire data set. We scaled all formal uncertainties by a factor of 2 (an additional factor of 3 applied to 1990 values) to reflect realistic 1-σ errors.

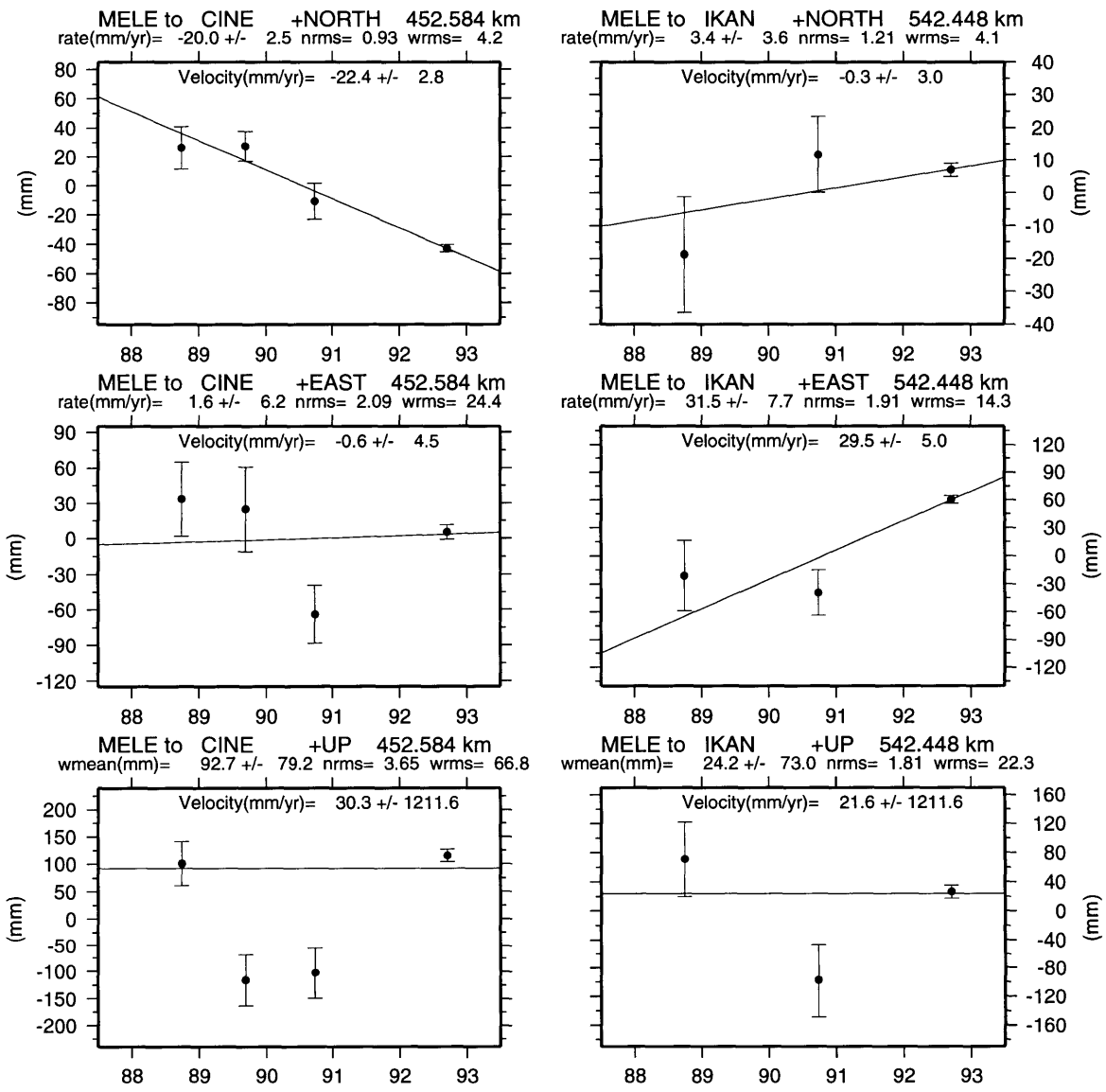

Figure C-47: The time evolution of the north, east and vertical (up) components of the relative position vectors obtained from GLOBK Kalman filter back solutions. Rate/velocity is relative to the first site, where NEU is +. The rate is calculated by a naive weighted least squares fit to the estimates of baseline components. The wrms and nrms are about this best fitting straight-line, except for the vertical, which is about the weighted mean. The velocity (inserted into the box) is obtained from GLOBK Kalman filter forward solutions which use the entire data set. We scaled all formal uncertainties by a factor of 2 (an additional factor of 3 applied to 1990 values) to reflect realistic 1-σ errors.

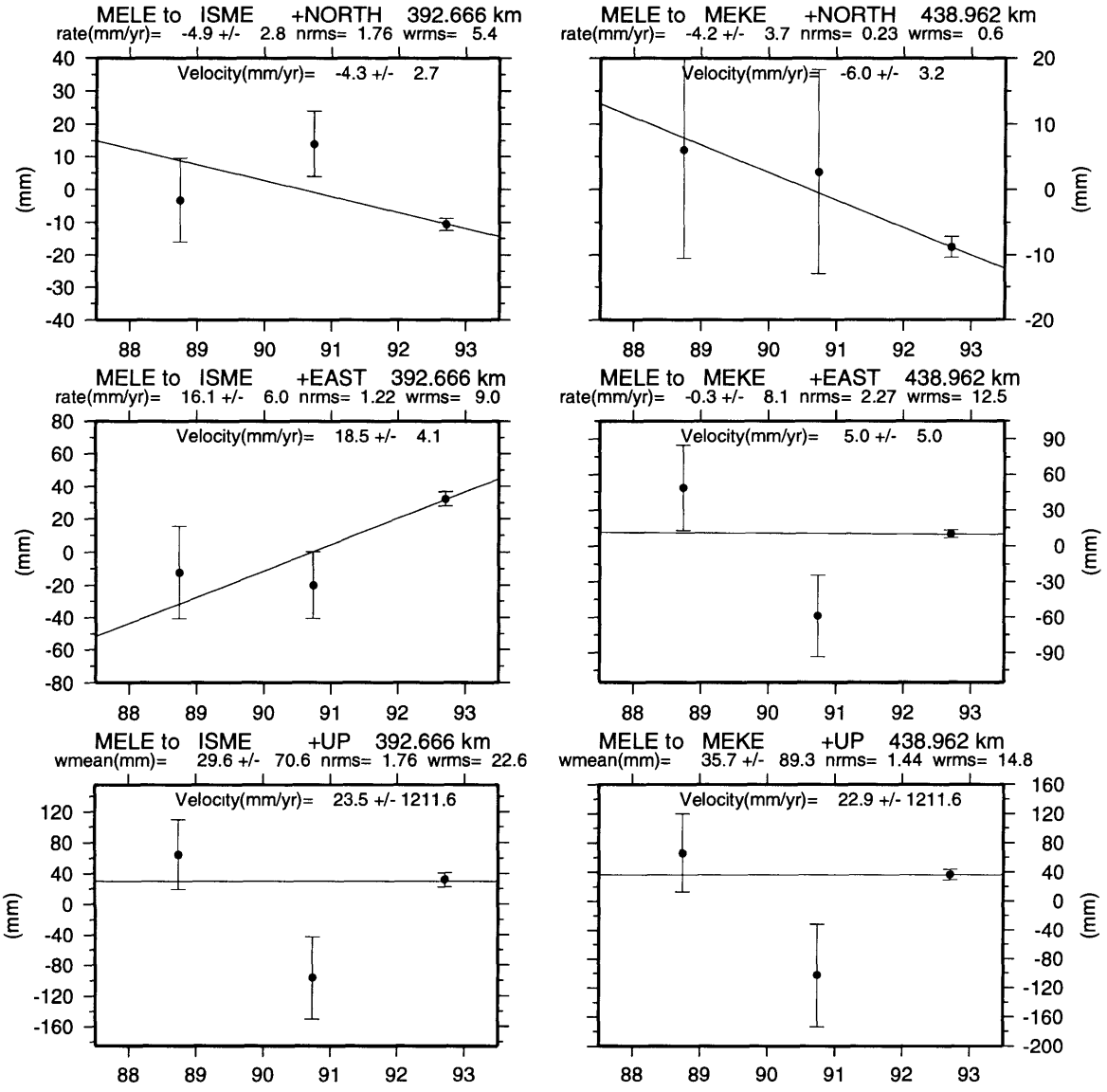

Figure C-48: The time evolution of the north, east and vertical (up) components of the relative position vectors obtained from GLOBK Kalman filter back solutions. Rate/velocity is relative to the first site, where NEU is +. The rate is calculated by a naive weighted least squares fit to the estimates of baseline components. The wrms and nrms are about this best fitting straight-line, except for the vertical, which is about the weighted mean. The velocity (inserted into the box) is obtained from GLOBK Kalman filter forward solutions which use the entire data set. We scaled all formal uncertainties by a factor of 2 (an additional factor of 3 applied to 1990 values) to reflect realistic 1-σ errors.

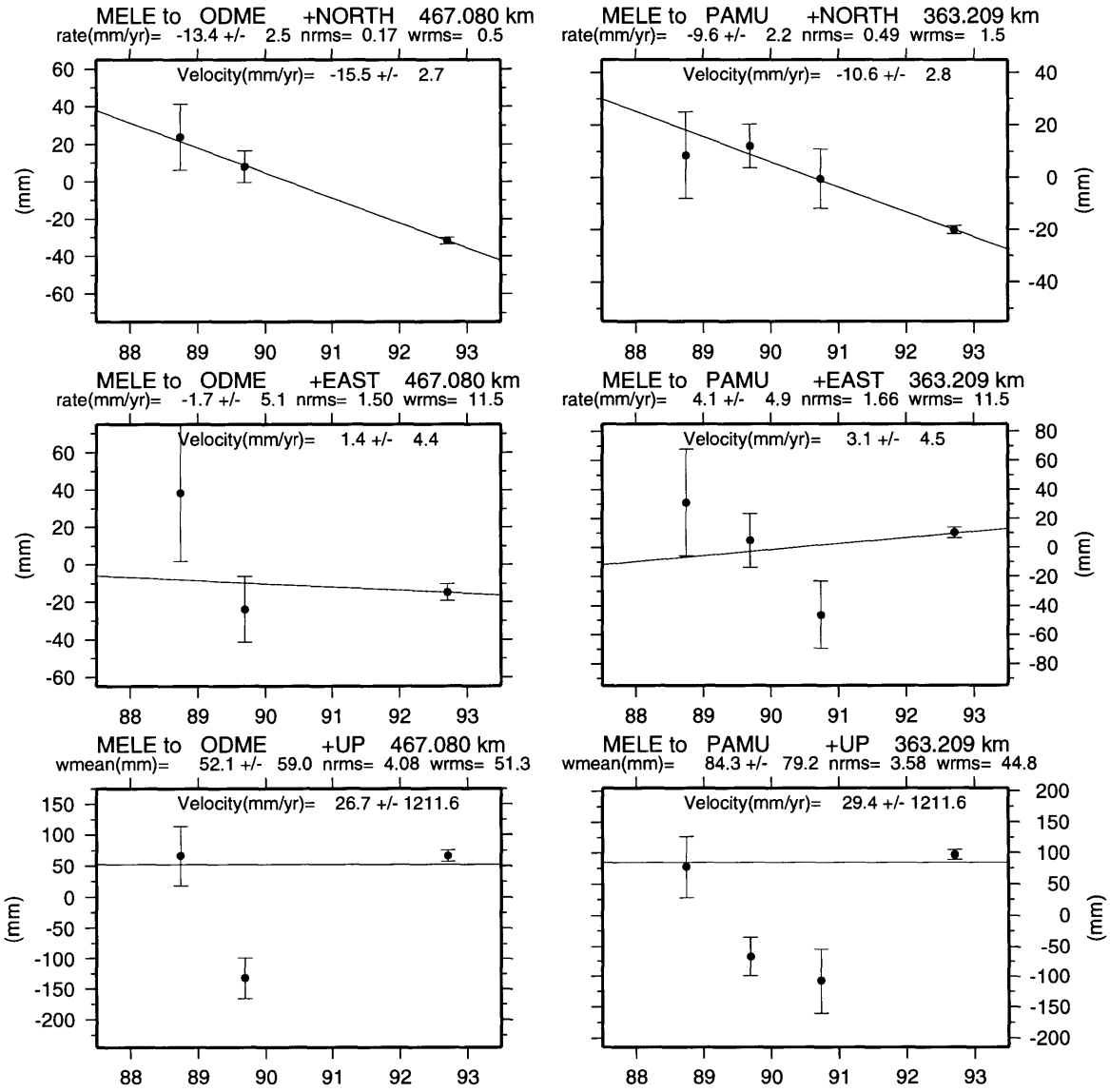

Figure C-49: The time evolution of the north, east and vertical (up) components of the relative position vectors obtained from GLOBK Kalman filter back solutions. Rate/velocity is relative to the first site, where NEU is +. The rate is calculated by a naive weighted least squares fit to the estimates of baseline components. The wrms and nrms are about this best fitting straight-line, except for the vertical, which is about the weighted mean. The velocity (inserted into the box) is obtained from GLOBK Kalman filter forward solutions which use the entire data set. We scaled all formal uncertainties by a factor of 2 (an additional factor of 3 applied to 1990 values) to reflect realistic 1-σ errors.

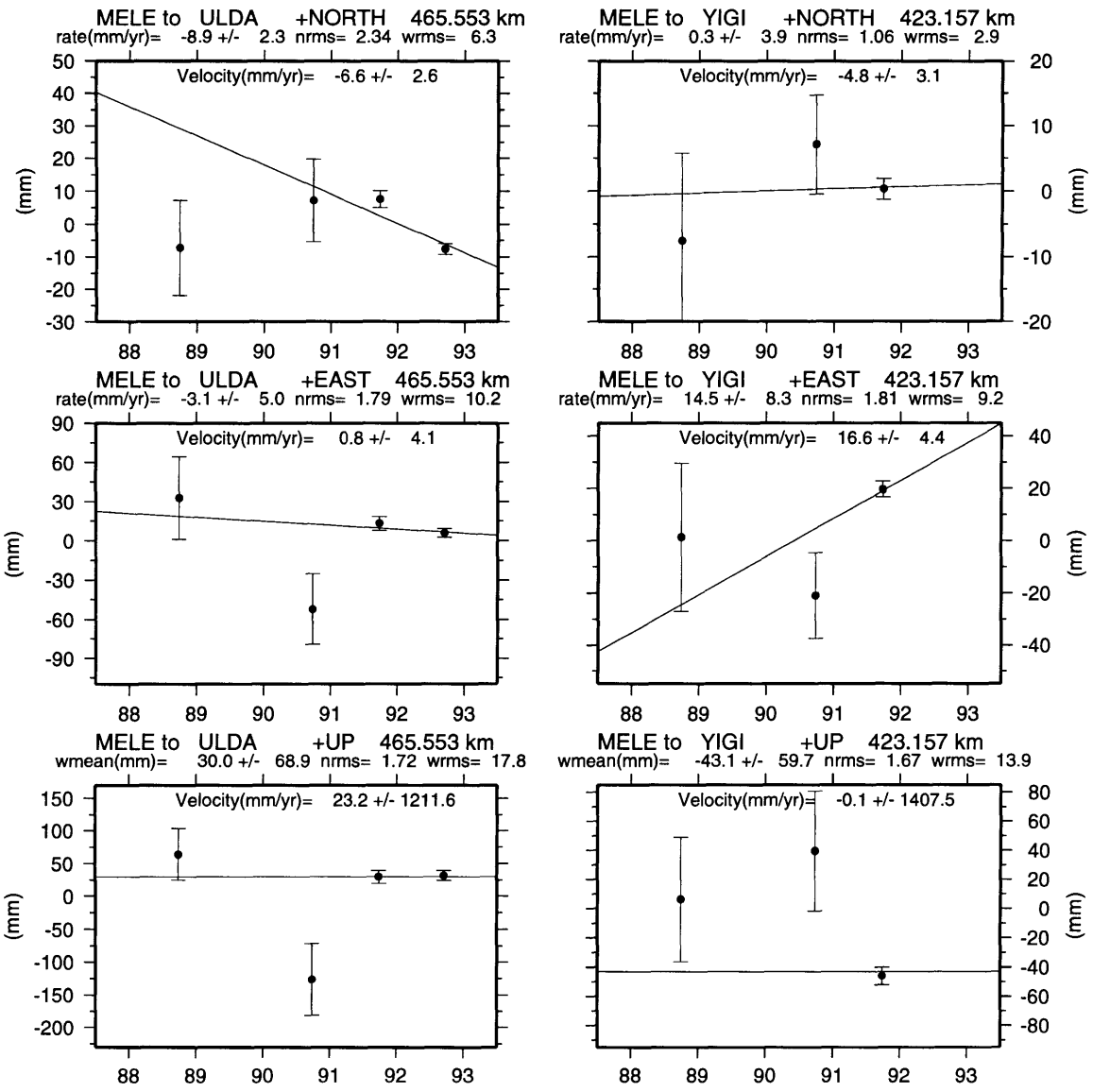

Figure C-50: The time evolution of the north, east and vertical (up) components of the relative position vectors obtained from GLOBK Kalman filter back solutions. Rate/velocity is relative to the first site, where NEU is +. The rate is calculated by a naive weighted least squares fit to the estimates of baseline components. The wrms and nrms are about this best fitting straight-line, except for the vertical, which is about the weighted mean. The velocity (inserted into the box) is obtained from GLOBK Kalman filter forward solutions which use the entire data set. We scaled all formal uncertainties by a factor of 2 (an additional factor of 3 applied to 1990 values) to reflect realistic 1-σ errors.

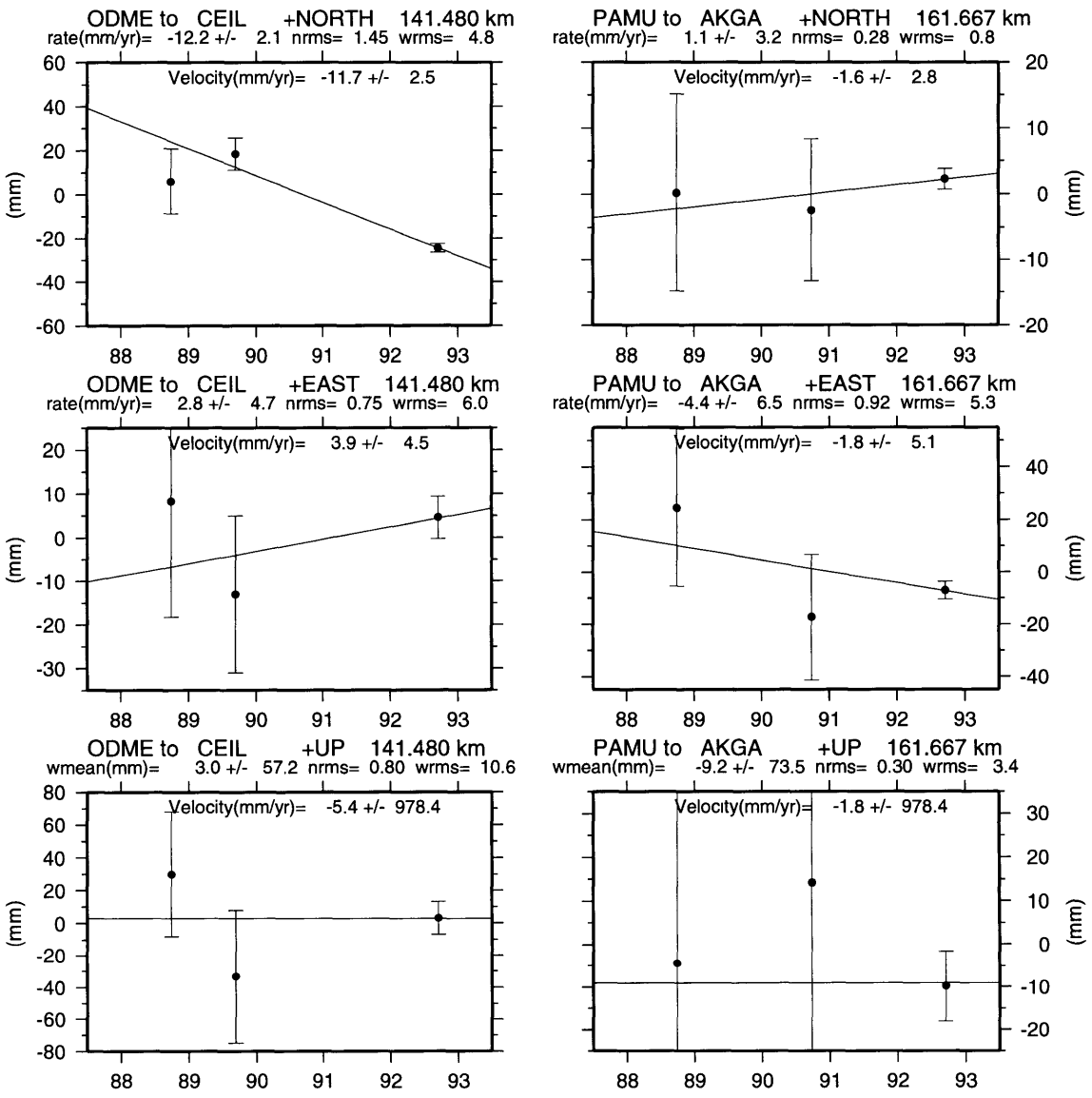

Figure C-51: The time evolution of the north, east and vertical (up) components of the relative position vectors obtained from GLOBK Kalman filter back solutions. Rate/velocity is relative to the first site, where NEU is +. The rate is calculated by a naive weighted least squares fit to the estimates of baseline components. The wrms and nrms are about this best fitting straight-line, except for the vertical, which is about the weighted mean. The velocity (inserted into the box) is obtained from GLOBK Kalman filter forward solutions which use the entire data set. We scaled all formal uncertainties by a factor of 2 (an additional factor of 3 applied to 1990 values) to reflect realistic 1-σ errors.

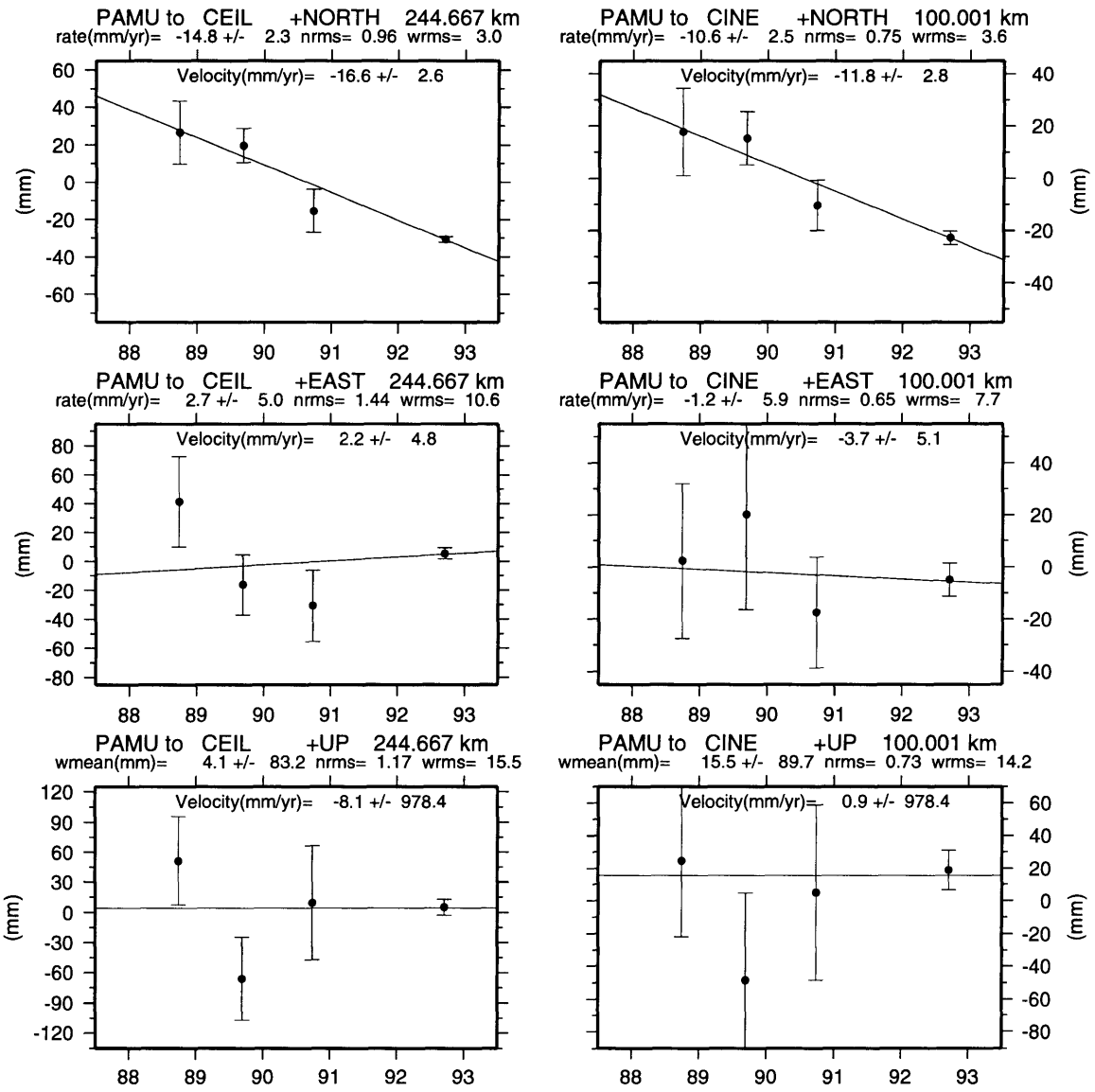

Figure C-52: The time evolution of the north, east and vertical (up) components of the relative position vectors obtained from GLOBK Kalman filter back solutions. Rate/velocity is relative to the first site, where NEU is +. The rate is calculated by a naive weighted least squares fit to the estimates of baseline components. The wrms and nrms are about this best fitting straight-line, except for the vertical, which is about the weighted mean. The velocity (inserted into the box) is obtained from GLOBK Kalman filter forward solutions which use the entire data set. We scaled all formal uncertainties by a factor of 2 (an additional factor of 3 applied to 1990 values) to reflect realistic 1-σ errors.

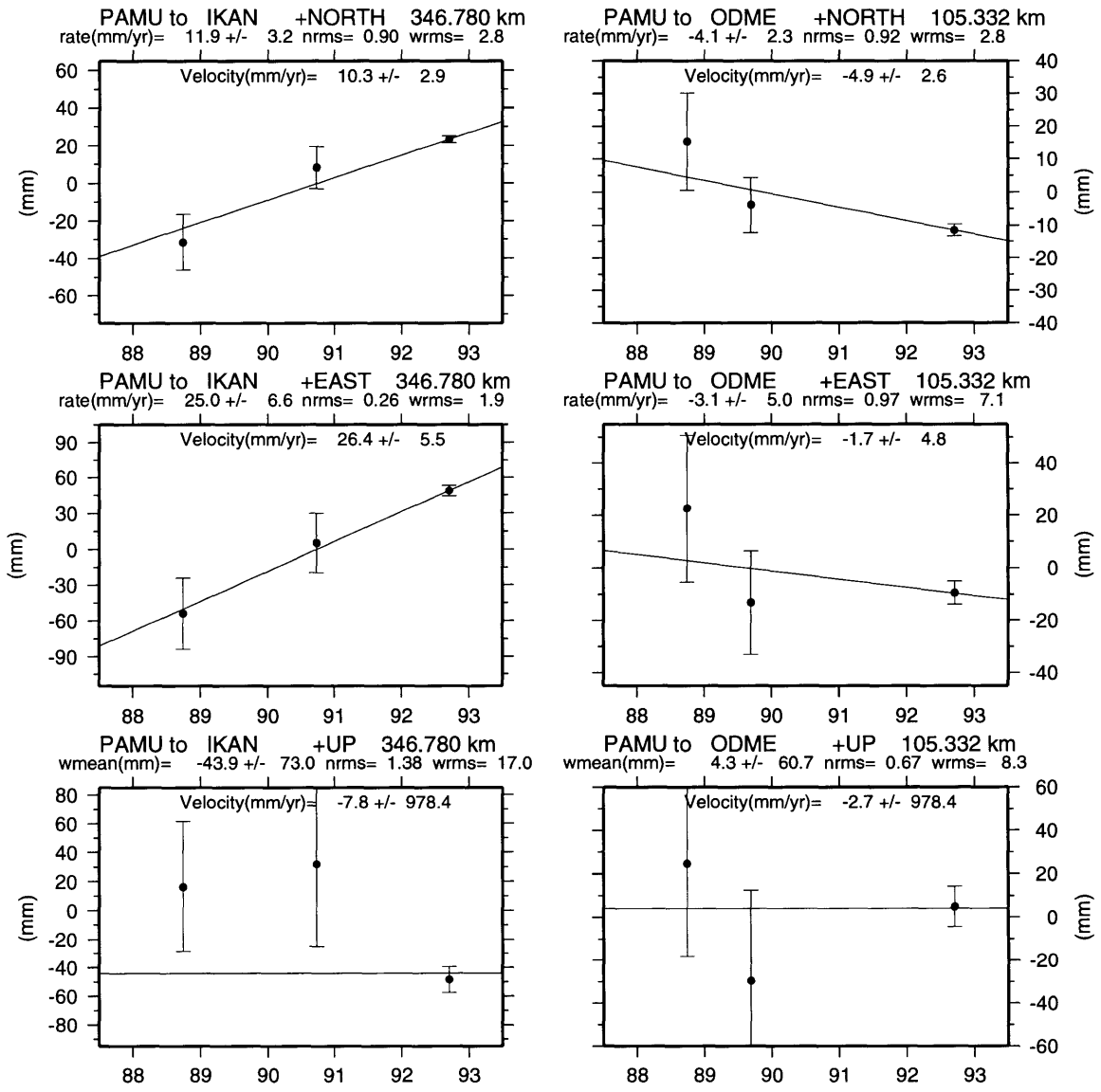

Figure C-53: The time evolution of the north, east and vertical (up) components of the relative position vectors obtained from GLOBK Kalman filter back solutions. Rate/velocity is relative to the first site, where NEU is +. The rate is calculated by a naive weighted least squares fit to the estimates of baseline components. The wrms and nrms are about this best fitting straight-line, except for the vertical, which is about the weighted mean. The velocity (inserted into the box) is obtained from GLOBK Kalman filter forward solutions which use the entire data set. We scaled all formal uncertainties by a factor of 2 (an additional factor of 3 applied to 1990 values) to reflect realistic 1-σ errors.

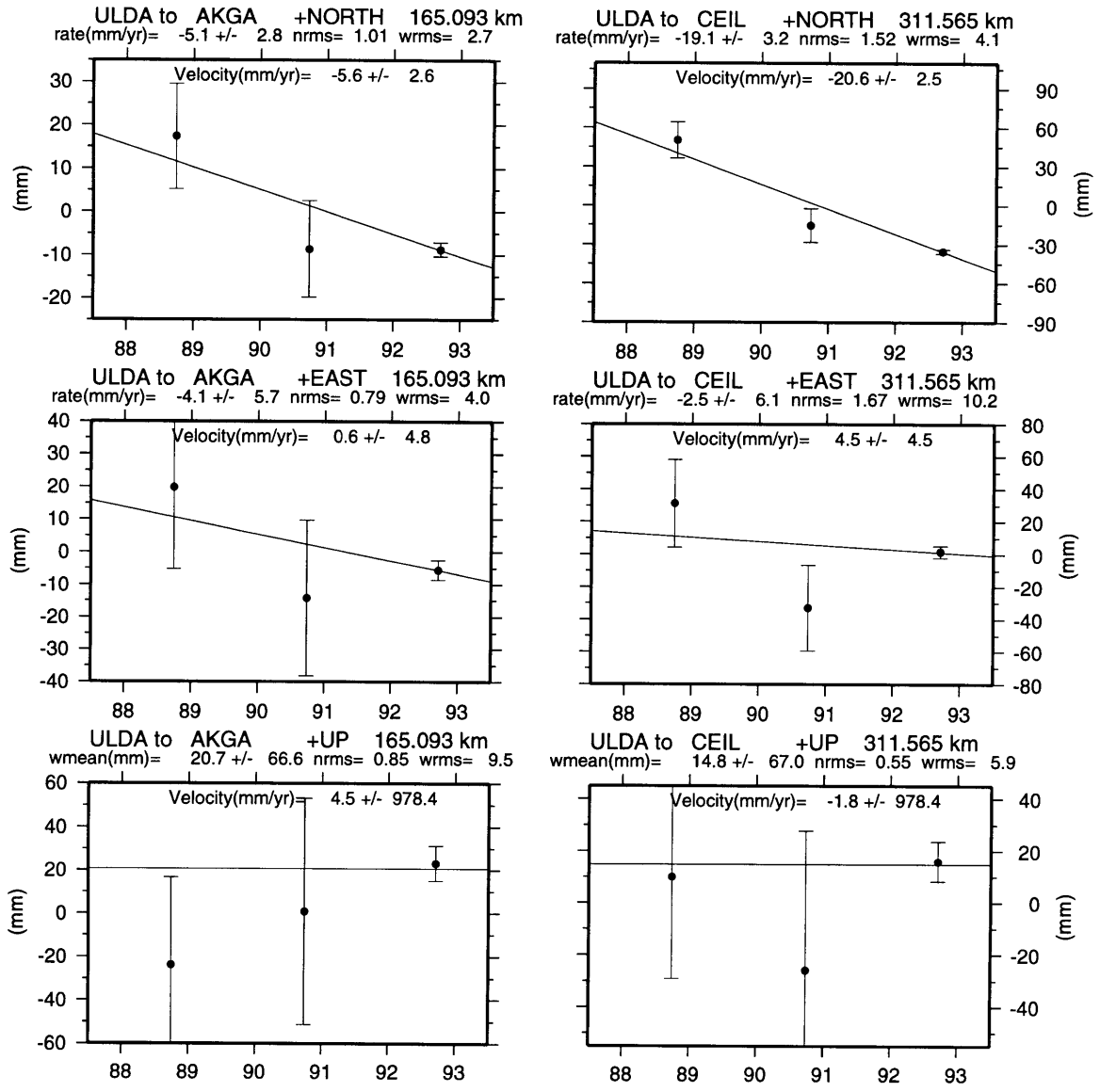

Figure C-54: The time evolution of the north, east and vertical (up) components of the relative position vectors obtained from GLOBK Kalman filter back solutions. Rate/velocity is relative to the first site, where NEU is +. The rate is calculated by a naive weighted least squares fit to the estimates of baseline components. The wrms and nrms are about this best fitting straight-line, except for the vertical, which is about the weighted mean. The velocity (inserted into the box) is obtained from GLOBK Kalman filter forward solutions which use the entire data set. We scaled all formal uncertainties by a factor of 2 (an additional factor of 3 applied to 1990 values) to reflect realistic 1-σ errors.

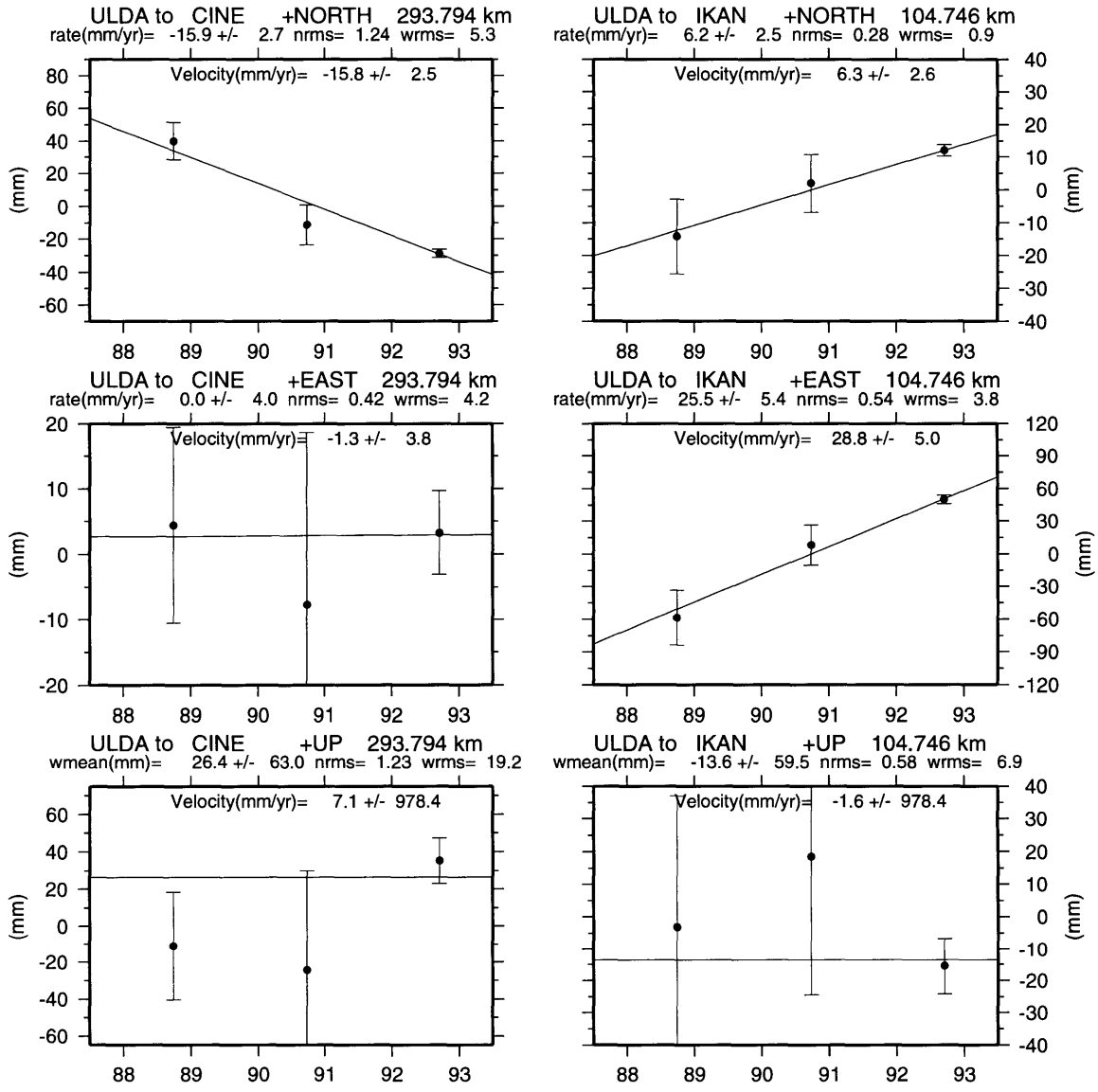

Figure C-55: The time evolution of the north, east and vertical (up) components of the relative position vectors obtained from GLOBK Kalman filter back solutions. Rate/velocity is relative to the first site, where NEU is +. The rate is calculated by a naive weighted least squares fit to the estimates of baseline components. The wrms and nrms are about this best fitting straight-line, except for the vertical, which is about the weighted mean. The velocity (inserted into the box) is obtained from GLOBK Kalman filter forward solutions which use the entire data set. We scaled all formal uncertainties by a factor of 2 (an additional factor of 3 applied to 1990 values) to reflect realistic 1-σ errors.

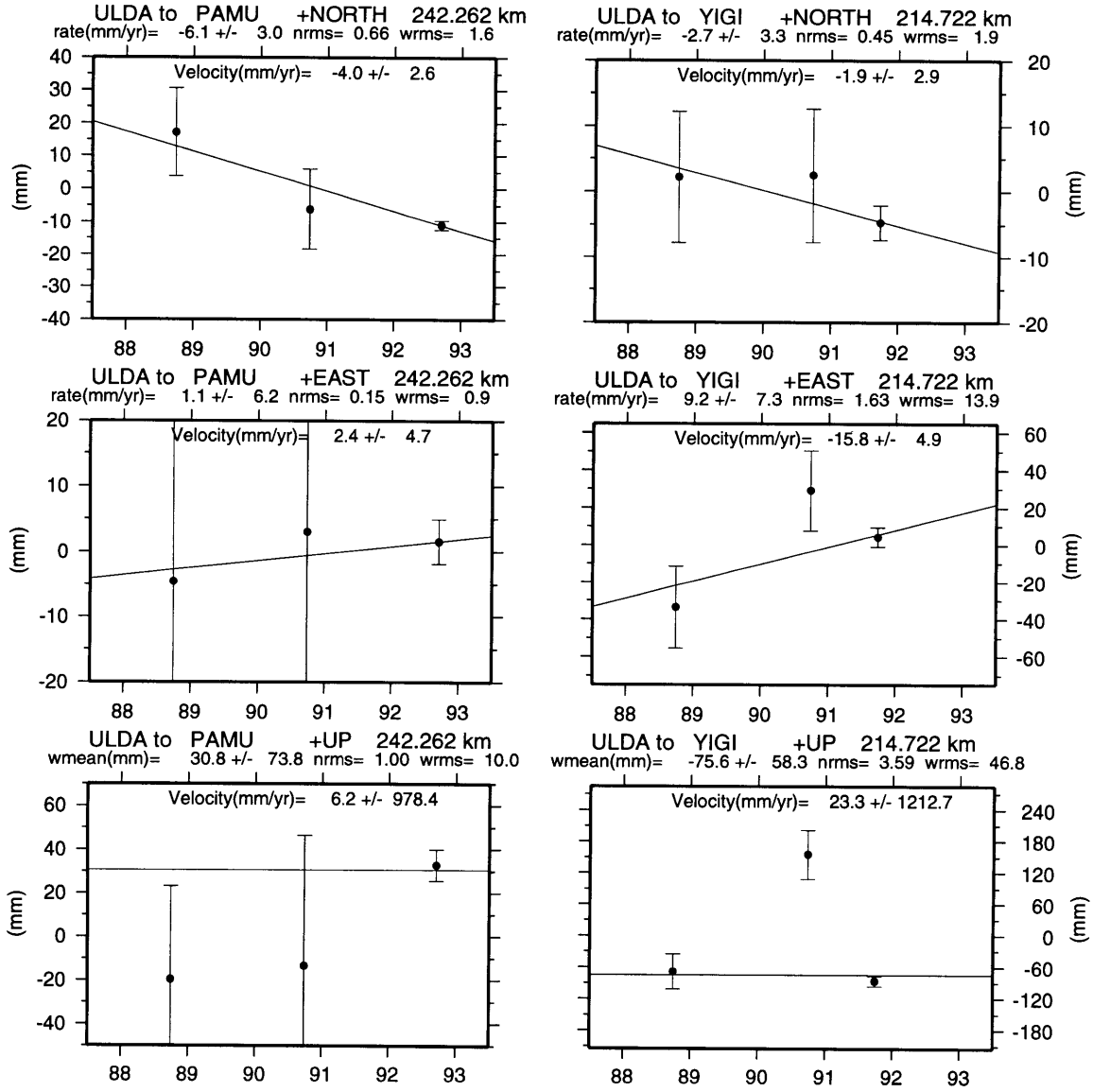

Figure C-56: The time evolution of the north, east and vertical (up) components of the relative position vectors obtained from GLOBK Kalman filter back solutions. Rate/velocity is relative to the first site, where NEU is +. The rate is calculated by a naive weighted least squares fit to the estimates of baseline components. The wrms and nrms are about this best fitting straight-line, except for the vertical, which is about the weighted mean. The velocity (inserted into the box) is obtained from GLOBK Kalman filter forward solutions which use the entire data set. We scaled all formal uncertainties by a factor of 2 (an additional factor of 3 applied to 1990 values) to reflect realistic 1-σ errors.

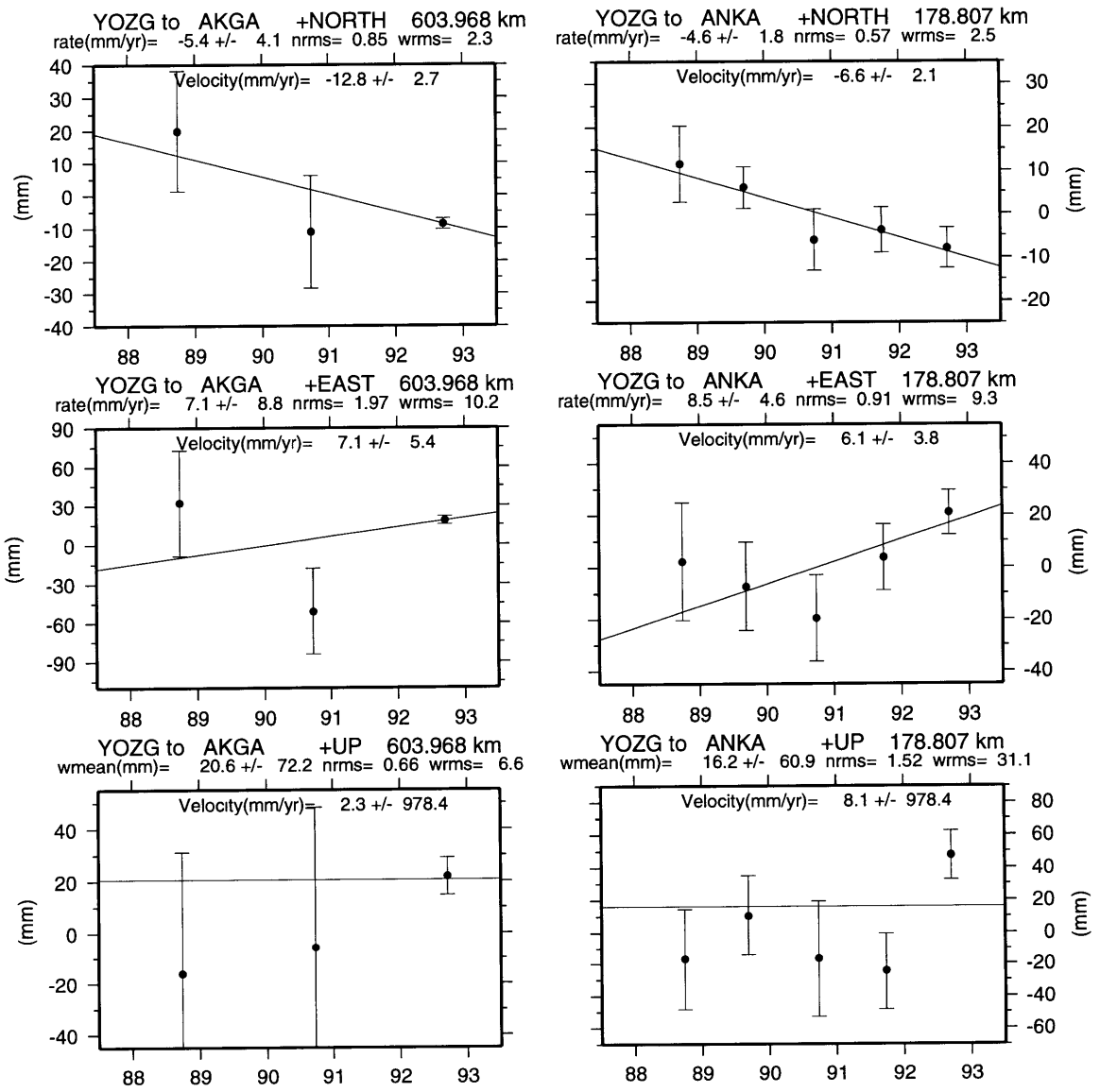

Figure C-57: The time evolution of the north, east and vertical (up) components of the relative position vectors obtained from GLOBK Kalman filter back solutions. Rate/velocity is relative to the first site, where NEU is +. The rate is calculated by a naive weighted least squares fit to the estimates of baseline components. The wrms and nrms are about this best fitting straight-line, except for the vertical, which is about the weighted mean. The velocity (inserted into the box) is obtained from GLOBK Kalman filter forward solutions which use the entire data set. We scaled all formal uncertainties by a factor of 2 (an additional factor of 3 applied to 1990 values) to reflect realistic 1-σ errors.

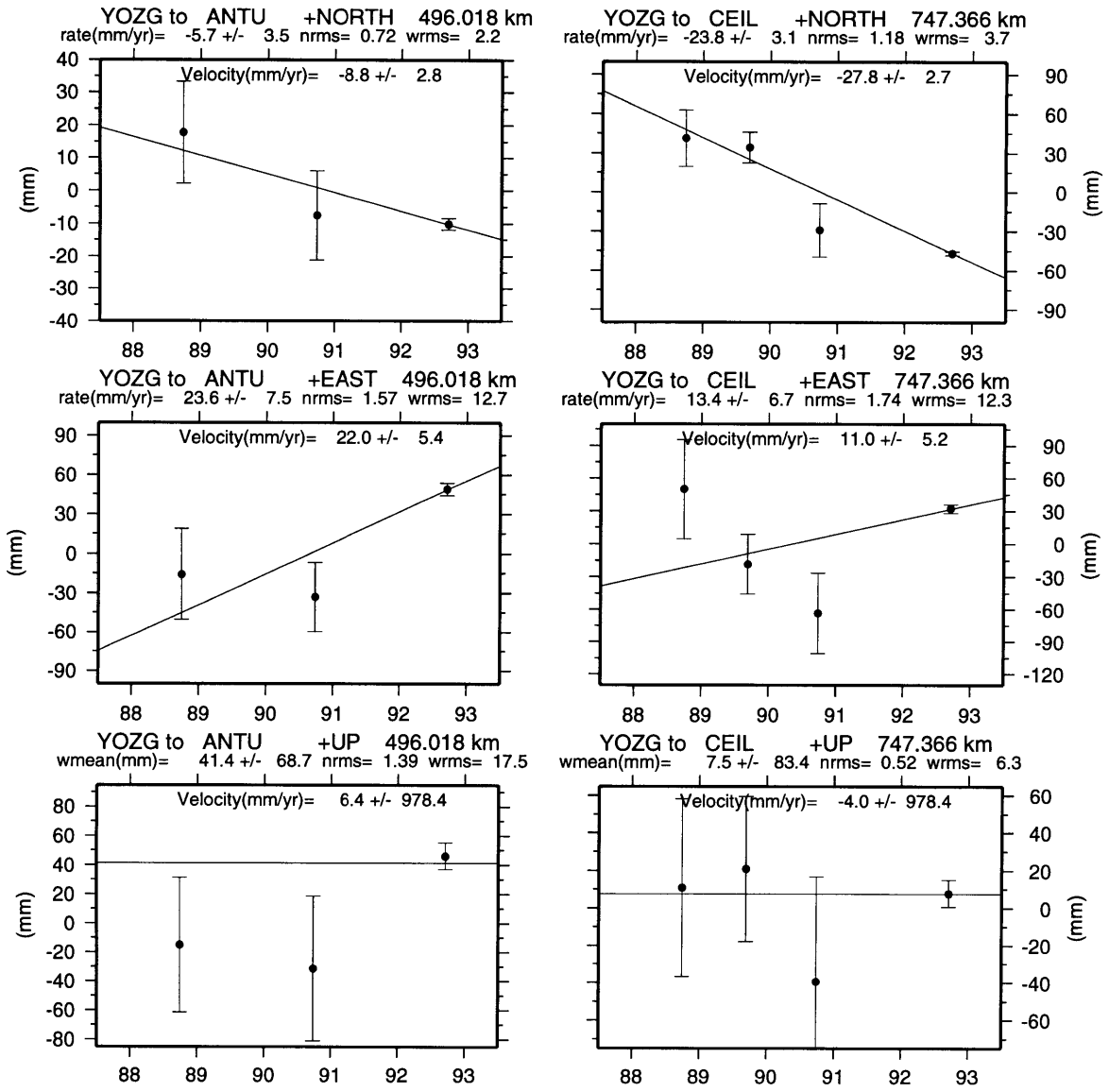

Figure C-58: The time evolution of the north, east and vertical (up) components of the relative position vectors obtained from GLOBK Kalman filter back solutions. Rate/velocity is relative to the first site, where NEU is +. The rate is calculated by a naive weighted least squares fit to the estimates of baseline components. The wrms and nrms are about this best fitting straight-line, except for the vertical, which is about the weighted mean. The velocity (inserted into the box) is obtained from GLOBK Kalman filter forward solutions which use the entire data set. We scaled all formal uncertainties by a factor of 2 (an additional factor of 3 applied to 1990 values) to reflect realistic 1-σ errors.

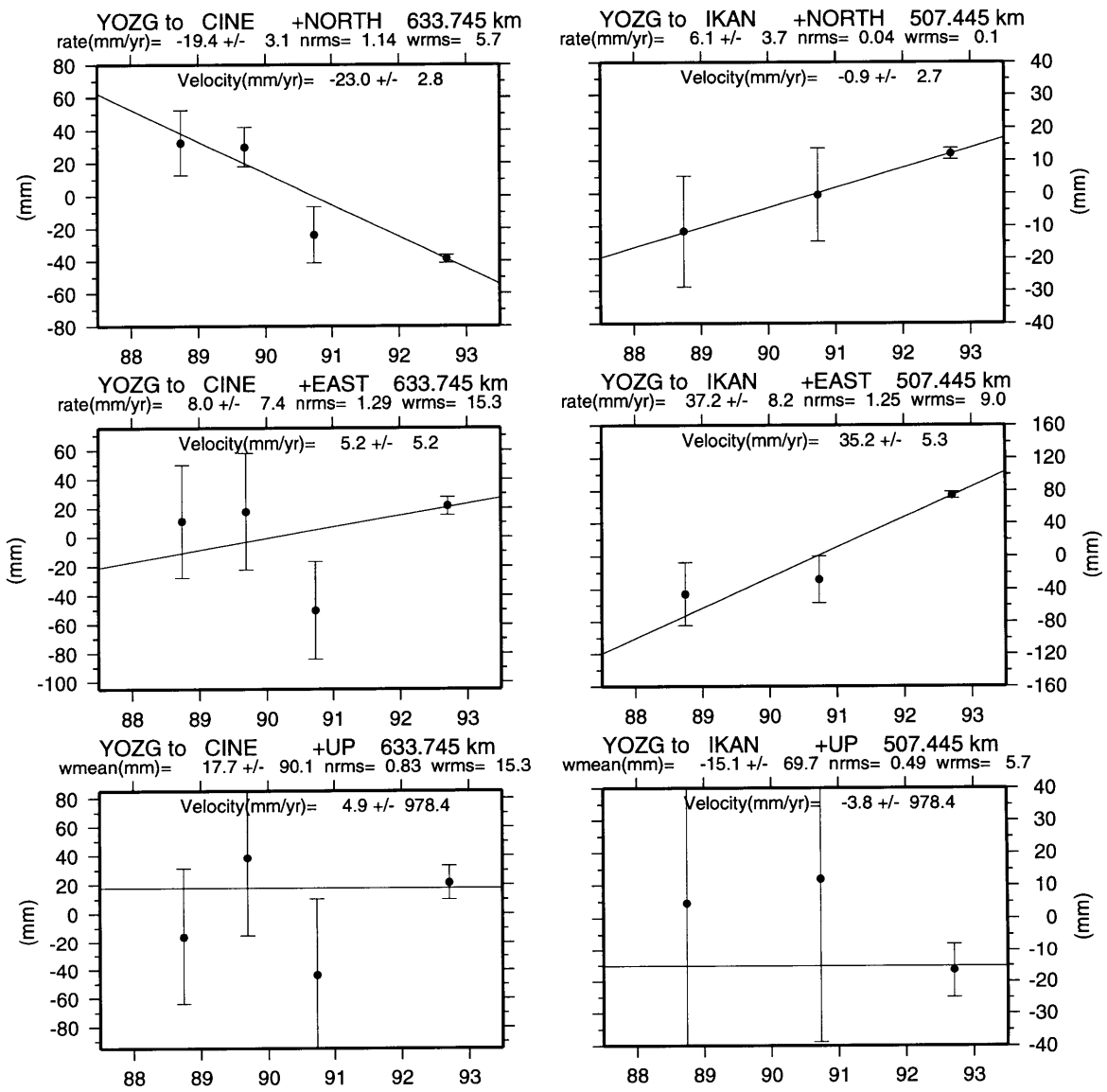

Figure C-59: The time evolution of the north, east and vertical (up) components of the relative position vectors obtained from GLOBK Kalman filter back solutions. Rate/velocity is relative to the first site, where NEU is +. The rate is calculated by a naive weighted least squares fit to the estimates of baseline components. The wrms and nrms are about this best fitting straight-line, except for the vertical, which is about the weighted mean. The velocity (inserted into the box) is obtained from GLOBK Kalman filter forward solutions which use the entire data set. We scaled all formal uncertainties by a factor of 2 (an additional factor of 3 applied to 1990 values) to reflect realistic 1-σ errors.

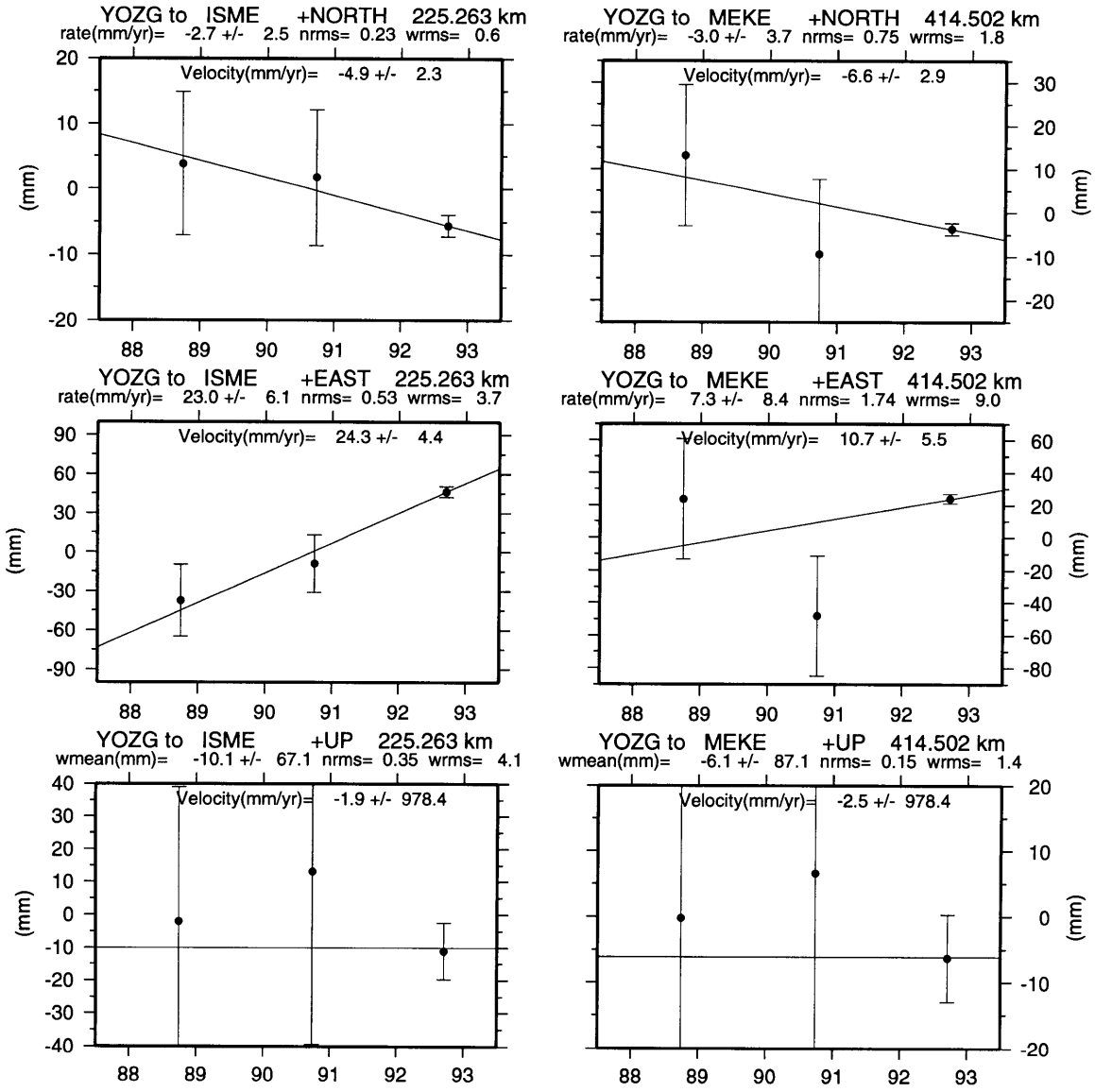

Figure C-60: The time evolution of the north, east and vertical (up) components of the relative position vectors obtained from GLOBK Kalman filter back solutions. Rate/velocity is relative to the first site, where NEU is +. The rate is calculated by a naive weighted least squares fit to the estimates of baseline components. The wrms and nrms are about this best fitting straight-line, except for the vertical, which is about the weighted mean. The velocity (inserted into the box) is obtained from GLOBK Kalman filter forward solutions which use the entire data set. We scaled all formal uncertainties by a factor of 2 (an additional factor of 3 applied to 1990 values) to reflect realistic 1-σ errors.

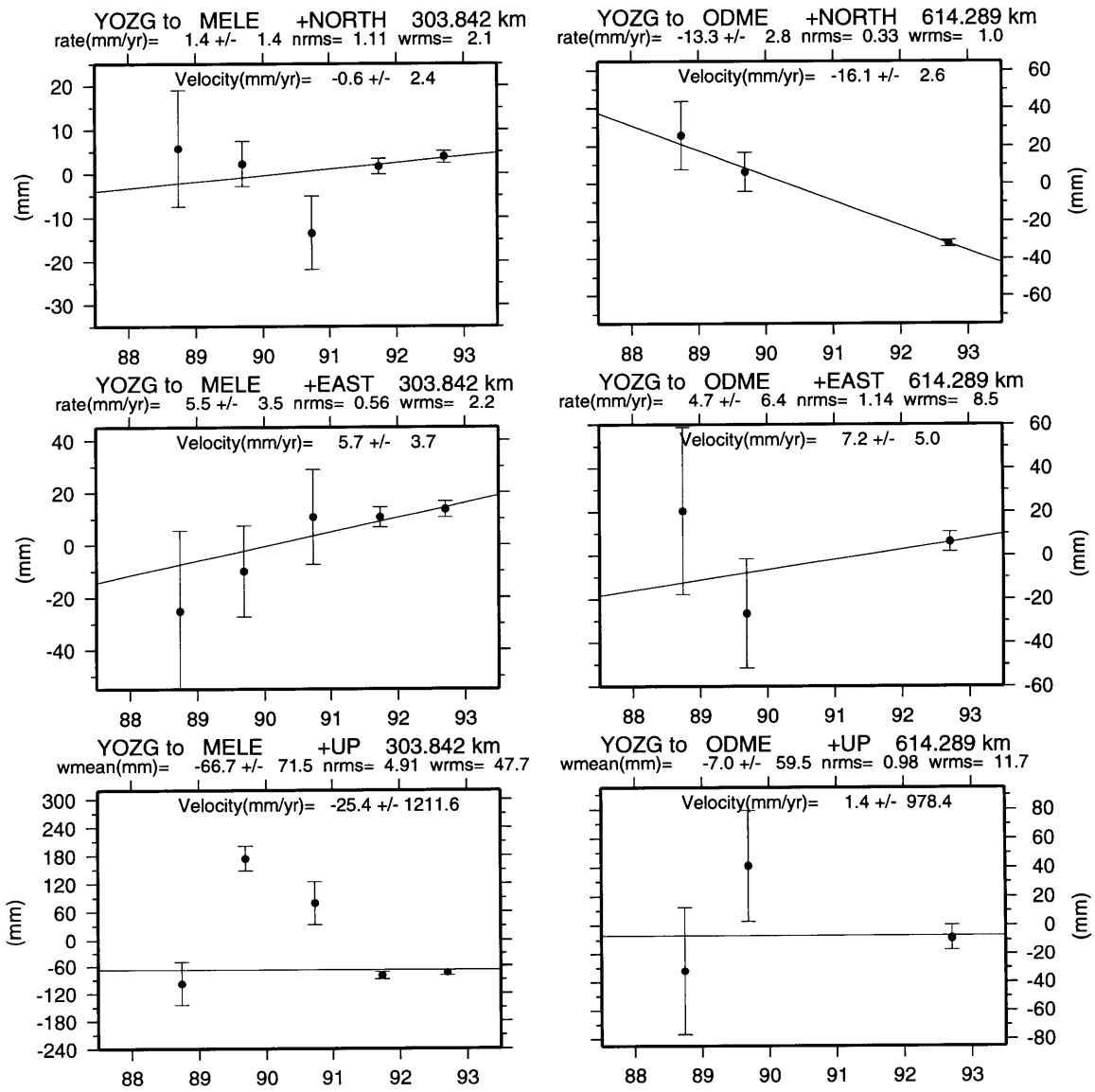

Figure C-61: The time evolution of the north, east and vertical (up) components of the relative position vectors obtained from GLOBK Kalman filter back solutions. Rate/velocity is relative to the first site, where NEU is +. The rate is calculated by a naive weighted least squares fit to the estimates of baseline components. The wrms and nrms are about this best fitting straight-line, except for the vertical, which is about the weighted mean. The velocity (inserted into the box) is obtained from GLOBK Kalman filter forward solutions which use the entire data set. We scaled all formal uncertainties by a factor of 2 (an additional factor of 3 applied to 1990 values) to reflect realistic 1-σ errors.

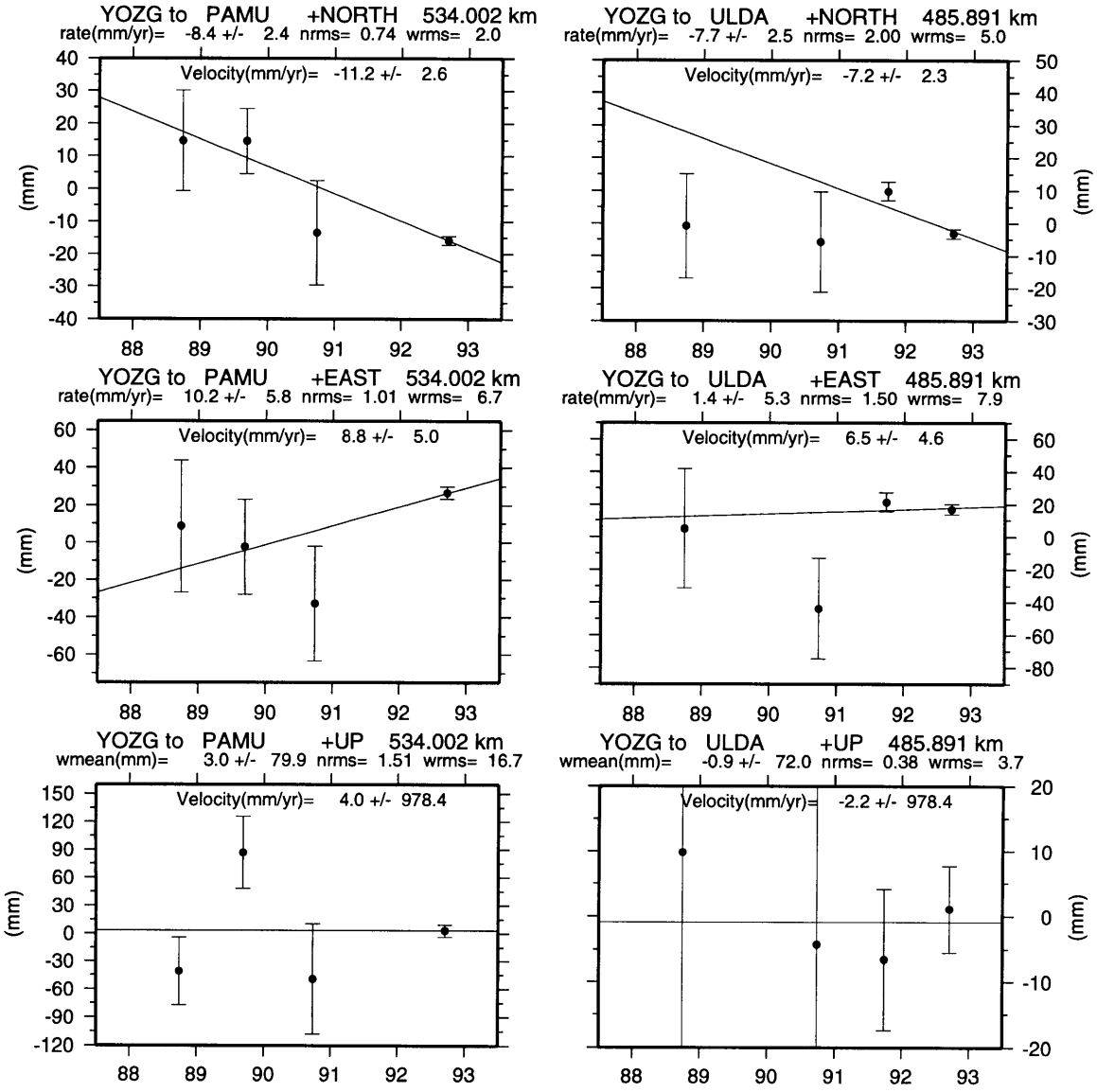

Figure C-62: The time evolution of the north, east and vertical (up) components of the relative position vectors obtained from GLOBK Kalman filter back solutions. Rate/velocity is relative to the first site, where NEU is +. The rate is calculated by a naive weighted least squares fit to the estimates of baseline components. The wrms and nrms are about this best fitting straight-line, except for the vertical, which is about the weighted mean. The velocity (inserted into the box) is obtained from GLOBK Kalman filter forward solutions which use the entire data set. We scaled all formal uncertainties by a factor of 2 (an additional factor of 3 applied to 1990 values) to reflect realistic 1-σ errors.

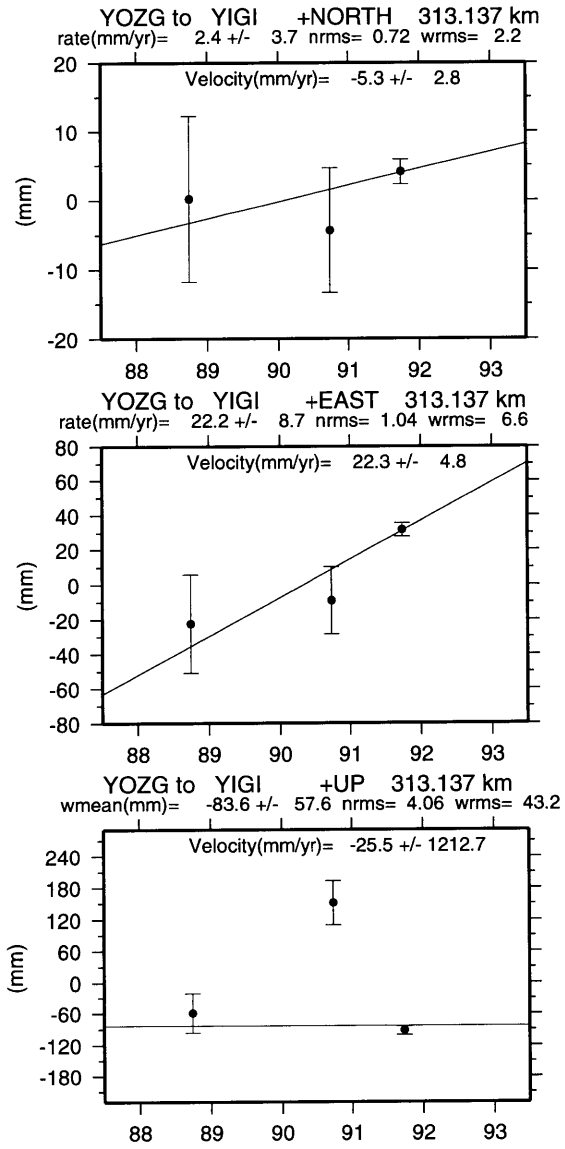

Figure C-63: The time evolution of the north, east and vertical (up) components of the relative position vectors obtained from GLOBK Kalman filter back solutions. Rate/velocity is relative to the first site, where NEU is +. The rate is calculated by a naive weighted least squares fit to the estimates of baseline components. The wrms and nrms are about this best fitting straight-line, except for the vertical, which is about the weighted mean. The velocity (inserted into the box) is obtained from GLOBK Kalman filter forward solutions which use the entire data set. We scaled all formal uncertainties by a factor of 2 (an additional factor of 3 applied to 1990 values) to reflect realistic 1-σ errors.

Appendix D

Seismic Deformation within the GPS Network

Co-seismic deformation

During the period of our observations, one significant seismic event occurred in eastern Turkey, on the Erzincan segment of the North Anatolian fault [Barka and Gülen, 1989]: the Ms=6.8 Erzincan earthquake, 13 March, 1992. The previous major shock at this locality was the Great Erzincan earthquake of 1939 (M_S=8) which had a right-lateral focal mechanism [McKenzie, 1972] and involved a 3.5 m surface displacement [Barka and Gülen, 1988]. Focal mechanism solutions for the 13 March 1992 earthquake indicate a dextral motion (National Earthquake Information Center). Although no surface observations exist, it is believed to have involved 1–1.5 m of predominantly right-lateral, co-seismic slip [Bennett et al., in prep.] which affected at least two of our pre-existing sites (KEMA and MERC). With an additional control survey in the spring of 1992, we measured the co-seismic motion between the Kemah and Mercan sites (a 94 km baseline). (For details, see Appendices A and B). The

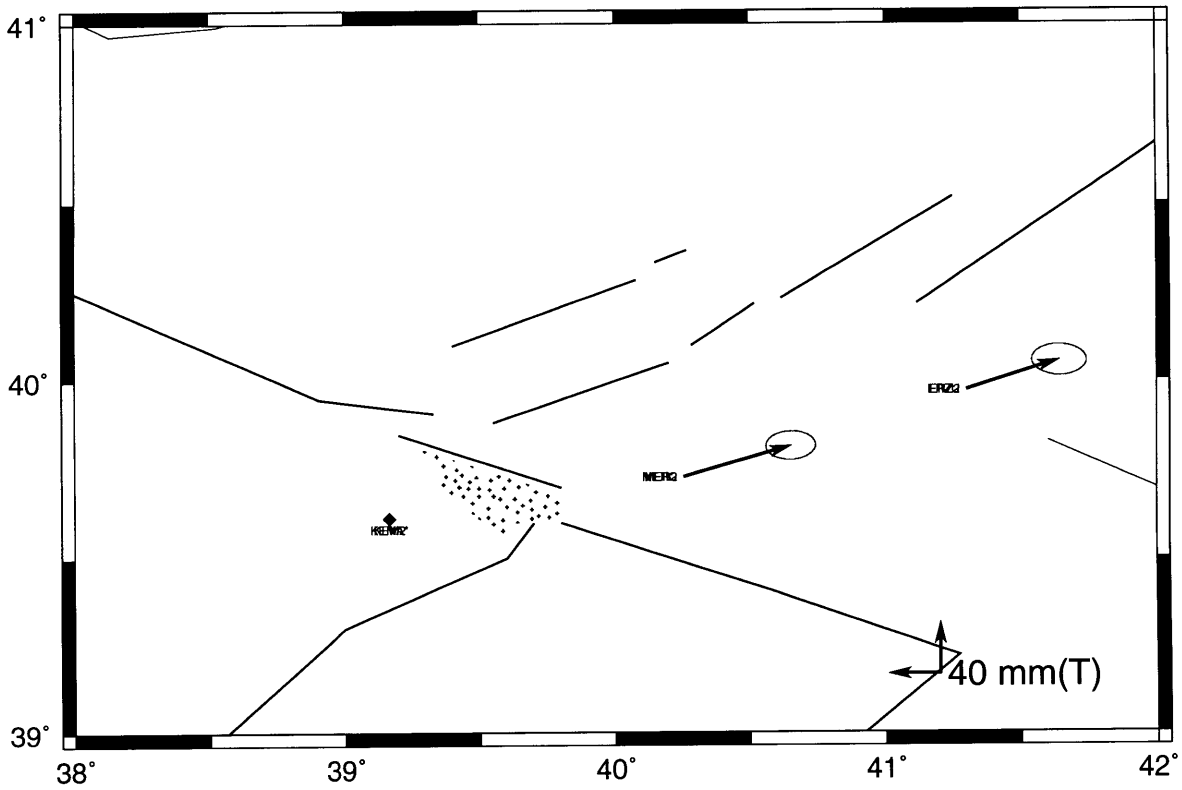

Figure D-1: Total displacement observed at the Erzurum and Mercan sites, relative to Kemah (shown with a diamond), estimated from 1991 and spring 1992 GPS measurements in Turkey. Interval between the two measurements is 0.5318 years. Secular motion has not been removed. The ellipses denote the 95% confidence region, after scaling the formal uncertainties.

total displacements are shown in Table D.1 and Figure D-1. We used the compact quasi-observations of the 1991 and spring 1992 experiments, and applied position ties between KEMA-KEM2, MERC-MER2 and ERZU-ERZ2 in our velocity solutions. Since we renamed the benchmarks, the co-seismic displacement at these sites did not alias into the secular motions reported earlier (see Chapter 2).

The displacement relative to Kemah (Figure D-1) indicates the right lateral motion due to this earthquake (Table D.1). Total motion observed between Kemah and Mercan is $88 \pm 19_{95\%}$ mm/yr. The insignificant displacement between Mercan and Erzurum suggests that the motion has been taken up between Kemah and Mer-

can [KEMA-ERZU: v_H= 12± $20_{95\%}$ mm/yr, θ = -95± $54_{95\%}$ °N], presumably on the North Anatolian Fault.

Table D.1: Total displacement at the Erzincan sites, relative to Kemah, between fall 1991 and spring 1992.

	East (mm/yr)		North (mm/yr)		
SITE	v_E	σ_E	v_N	σ_N	ρ_{EN}
ERZU	72.8	8.8	22.7	5.0	-0.0
MERC	84.6	8.0	23.9	4.5	0.0

Post-seismic deformation

We also estimated post-seismic deformation at an additional 11 sites established around the Erzincan, Tanyeri-Yedisu and Ovacık faults: ER01, ER02, ER03, ER04, ER05, ER07, ER08, ER09, ER10, ER11, and ER12. Since the post-quake observations were referred to the new benchmarks, we used the final quasi-observations (see Chapter 2) to estimate post-seismic deformations. In doing so, however, we assumed no significant post-seismic deformation at the Kemah, Mercan and Erzurum sites, by equating velocities before and after the earthquake. Because we have only two epoch measurements at these sites, we applied the scale factor of 2, obtained for the entire network, to the formal errors of post-seismic displacements. We quote 1-σ in Table D.2, after scaling. In Figure D-2, however, 95% confidence ellipses are shown.

It is rather difficult to observe significant motions at the 95% confidence interval. At all earthquake control sites (except ER08, ER09, ER11, and ER12) we observe insignificant displacements 6 months after the earthquake. The actual errors at the earthquake control sites could be higher since the displacements were estimated from 1–2 measurement sessions in the spring and fall of 1992. For instance, ER12 had to be

Table D.2: Total displacement at the earthquake sites, relative to Kemah, between spring and fall 1992.

	East (mm/yr)		North (mm/yr)		
SITE	v_E	σ_E	v_N	σ_N	ρ_{EN}
ER01	1.6	13.9	-13.9	6.7	-0.2
ER02	18.9	10.2	-1.6	5.5	-0.2
ER03	19.8	9.7	-7.0	5.0	-0.2
ER04	-14.8	10.1	-10.2	5.3	-0.1
ER05	-2.6	9.6	-11.0	5.1	-0.2
ER07	21.8	10.5	-4.5	5.3	-0.1
ER08	12.7	11.2	-16.5	5.4	-0.2
ER09	-3.5	11.4	-20.8	5.2	-0.1
ER10	-8.7	9.8	-6.3	5.0	-0.2
ER11	24.9	10.5	16.5	5.5	-0.1
ER12	21.5	9.4	-35.4	5.2	-0.1
ERZ2	2.5	3.3	-3.1	1.5	0.3
MER2	3.9	3.3	-4.3	1.5	0.3

removed from the analysis of the spring 1992 experiment due to its outlier behavior. (As discussed in Appendix B, there are only one day measurements at the ER01, ER02, ER04, ER07, ER09, ER11, and ER12 sites during the fall 1992 experiment.) We believe, however, that the errors at these sites are currently underestimated. Given that most of the sites involved in our analyses of the 1992 experiment have only one day measurements, we postpone further remarks until the rest of the data are recovered and additional error analysis is performed.

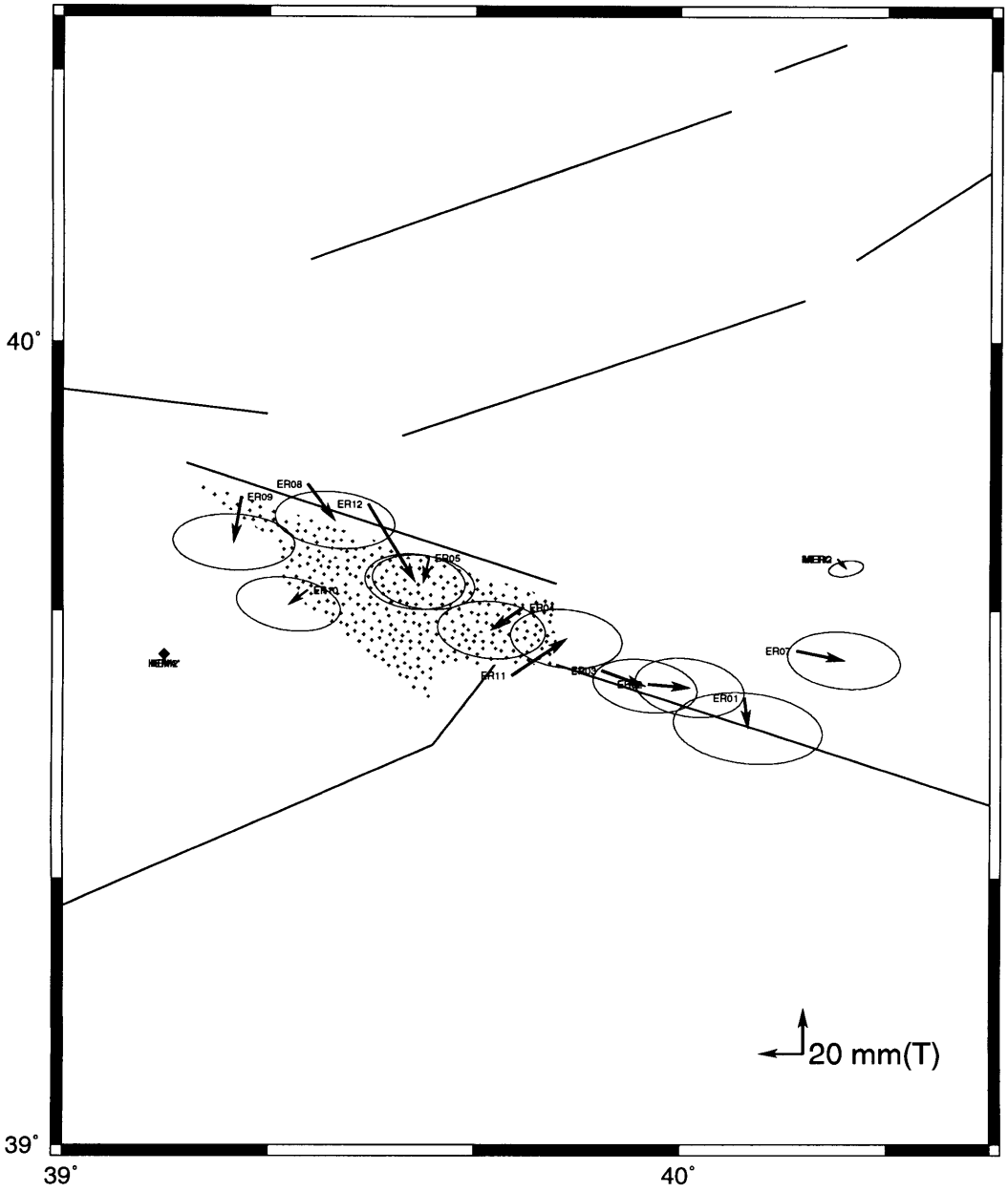

Figure D-2: Total displacement observed at the earthquake sites, relative to Kemah (shown with a diamond), over 0.4410 years. Estimated from spring 1992 and fall 1992 GPS measurements in Turkey. Secular motion has not been removed. The ellipses denote the 95% confidence region, after scaling the formal uncertainties.

References

Alptekin, Ö, J. L. Nabělek, and M. N. Toksöz, Source mechanism of the Bartın earthquake of September 3, 1968 in northwestern Turkey: Evidence for active thrust faulting at the southern Black Sea margin, *Tectonophys., 122,* 73–88, 1986.

Ambraseys, N. N., Some characteristic features of the North Anatolian fault zone, *Tectonophys., 9,* 143–165, 1970.

Arpat, E., and F. Şarağlu, The East Anatolian fault system; thoughts on its development,*Bull. Min. Res. Exp. Inst. Turkey, 78,* 33–39, 1972.

Barka, A. A., and P. L. Hancock, Neotectonic deformation patterns in the convex-northwards arc of the North Anatolian Fault, in *The Geological Evolution of Eastern Mediterranean, Spec. Publ.,* edited by J.G. Dixon and A.H.F. Robertson, 763–773, Geological Society of London, 1984.

Barka, A., and K. Kadinsky-Cade, Strike-slip fault geometry in Turkey and its influence on earthquake activity, *Tectonics, 7,* 663–684, 1988.

Barka, A., and L. Gülen, New constraint of age and total offset of the North Anatolian fault zone: Implications for tectonics of the eastern Mediterranean region, *METU Journal, 21,* 39–63, 1988.

Barka, A., and L. Gülen, Complex evolution of the Erzincan Basin (eastern Turkey, *Jour. Struc. Geol., 11,* 275–283, 1989.

Ben-Menahem, A., Four thousand years of seismicity along the Dead Sea rift, *J. Geophys. Res., 96,* 20195–20216, 1991.

Bennett, R. A., M. N. Toksöz, and M. Bouchon, Source parameters of the 1992 Erzincan, Turkey Earthquake, in preparation, 1994.

Billiris, H. et al., Geodetic determinations of tectonic deformation in central Greece from 1900 to 1988, *Nature, 350,* 124–129, 1991.

Cenci, A., A. Fermi., C. Sciarretta, R. Devoti, and A. Caporali, Tectonic motion in the Mediterranean area from laser ranging to Lageos , in *Contributions of Space Geodesy to Geodynamics: Crustal Dynamics,* edited by D. E. Smith and D. L. Turcotte, 347–358, American Geophysical Union, Washington, DC, 1993.

Bock, Y., S. A. Gourevitch, C. C. Counselman III, R. W. King, and R.I. Abbot,

Interferometric analyses of GPS phase observations, *Manuscr. Geod., 11,* 282–288, 1986.

Bock, Y., D. C. Agnew, P. Fang, J. F. Genrich, and B. H. Hager, Detection of crustal deformation from the Landers earthquake sequence using continuous geodetic measurements. *Nature, 361,* 337, 1993.

Braun J., and C. Beaumont, Three dimensional numerical experiments of strain partitioning at oblique plate boundaries: Implications for contrasting tectonic styles in California and South Island, New Zealand, *J. Geophys. Res., submitted,* 1994.

Canıtez, N., and M.N. Toksöz, Crustal structure in Turkey, *EOS, Trans. Am. Geophys. Union, 61,* 290, 1980.

Chase, C. G., Plate kinematics, The Americas, East Africa, and the rest of the world, *Earth Planet. Sci. Lett., 37,* 355–368, 1978.

Cohen, S. C., and D. E. Smith, LAGEOS Scientific Results: Introduction, *J. Geophys. Res. , 90,* 9217–9220, 1985.

Cox, A., and R. Hart, Plate Tectonics: How it works, Blackwell Scientific Publ., 1986, Boston, 392 pp.

Counselman C. C., and I. I. Shapiro, Miniature interferometry terminals for Earth surveying,*Bull. Geod., 53,* 139–163.

Davis, J. C., Statistical and data analysis in geology, 646 pp., John Wiley and Sons, New York, 1986

Davis, J. L., T.A. Herring, I. I. Shapiro, A. E. E. Rogers, and G. Elgred, Geodesy by radio interferometry: Effects of atmospheric modeling errors on estimates of baseline length, *Radio Science, 20,* 1593–1607, 1985.

DeMets, C., R. G. Gordon, D. F. Argus, and S. Stein, Current Plate Motions, *Geophys. J. Int., 101,* 425–478, 1990.

Dewey, J. F., and A. M. C. Şengör, Aegean and surrounding regions: Complex multiplate and continuum tectonics in a convergent zone, *Geol. Soc. Am. Bull.,* , 90, 89–92, 1979.

Donellan, A., B. Hager, R. W. King, and T. A. Herring, Geodetic measurement of the deformation in the Ventura Basin Region, Southern California, *Jour. Geophys.*

Res., 98, 21727–21-39, 1993.

Dong, D., The horizontal velocity field in souther California from a combination of terrestrial and space-geodetic data, Ph.D. thesis., Massachusetts Institute of Technology, 157 pp., 1993.

Dong, D., and Y. Bock, GPS network analysis with phase ambiguity resolution applied to crustal deformation studies in California, *J. Geophys. Res., 94,* 3949–3966, 1989.

Doutsos, T. and J. W. Piper, Listric faulting, sedimentation, and morphological evolution of the Quaternary eastern Corinth rift, Greece: First stages of continental rifting, *GSA Bull.,* 102, 812–829,1990.

Eren, K., Strain analysis along the North Anatolian fault by using geodetic surveys, *Bull. Geod.,* 137–150, 1984.

Eyidoğan, H., Rates of crustal deformation in western Turkey as deduced from major earthquakes, *Tectonophys., 148,* 83–92, 1988.

Feigl, K. L., Geodetic measurement of tectonic deformation in central California, Ph.D. thesis., Massachusetts Institute of Technology, 222 pp., 1991.

Gealey, W. K., Plate tectonic evolution of the Mediterranean-Middle East region, *Tectonophys., 155,* 285–306, 1988.

Gendt, G., H. Montag, and G. Dick, Plate kinematics in a global and European scale by Lageos Laser Ranging Data from 1983 and 1990, in *Contributions of Space Geodesy to Geodynamics: Crustal Dynamics,* edited by D. E. Smith and D. L. Turcotte, 311–329, American Geophysical Union, Washington, DC, 1993.

Gurtner, W., G. Mader, and D. MacArthur, A common exchange format for GPS data, *5th International Geodetic Symposium on Satellite Positioning,* Las Cruces, New Mexico, 920–932, 1989.

Gülen, L., A. Barka, and M. N. Toksöz, Kıtaların çarpışması ve ilgili kompleks deformasyon: Maraş üçlü eklemi ve çevre yapıları, Yerbilimleri, 14, 319–336, 1987.

Hager, B. H., R. W. King, and M. H. Murray, Measurement of crustal deformation using the Global Positioning System, *Annu. Rev. Earth Planet. Sci., 19,* 351–382, 1991.

Heki, K., G. R. Foulger, B. R. Julian, and C.-H. Jahn, Plate dynamics near divergent plate boundaries: Geophysical implications of postrifting crustal deformation in NE Iceland, *Jour. Geophys. Res., 98,* 14279–14297, 1993.

Herring, T. A., D. Dong, and R. W. King, Submilliarcsecond determination of pole position using Global Positioning data, *Geophys. Res. Let., 18,* 1893–1896, 1991.

Herring, T. A., GLOBK: Global Kalman filter VLBI and GPS analysis program, unpublished documentation, Massachusetts Institute of Technology, 1991.

Herring, T. A., J. L. Davis, and I. I. Shapiro, Geodesy by radio interferometry: The Application of Kalman filtering to the analyses of very long baseline interferometry data, *J. Geophys. Res., 95,* 12561–12581, 1990.

Hempton, M. R., Constraints on the Arabian plate motion and extensional history of the Red Sea, *Tectonics, 6,* 687–705, 1987.

Haines, A. J. and W. E. Holt, A procedure for obtaining the complete horizontal motions within zones of distributed deformation from the inversion of strain rate data, *J. Geophys. Res., 98,* 12057–12082, 1993.

Ison, S., M. Alys, F Müller, D. Kopcha, and M. Scardera, Evaluation of small apparent thrusts in the DMA precise GPS ephemerides, in *Proceedings of Sixth International Geodetic Symposium on Satellite Geodetic Positioning, Volume I,* 98–107, 1992.

Jackson, J., and D. McKenzie, Active tectonics of the Alpine-Himalayan belt between western Turkey and Pakistan, *Geophys. J.R. astr. Soc., 77,* 185–246, 1984.

Jackson, J., and D. McKenzie, The relationship between plate motions and seismic moment tensors, and the rates of active deformation in the Mediterranean and Middle East. *Geophys. J. R. astr. Soc., 93,* 45–73, 1988.

Jackson, J., Partitioning of strike-slip and convergent motion between Eurasia and Arabia in eastern Turkey and the Caucasus, *J. Geophys. Res., 97,* 12471–12479, 1992.

Jackson, J., J. Haines, and W. Holt, The horizontal velocity field in the deforming Aegean Sea region determined from seismic moment tensors of earthquakes, *J. Geophys. Res., 97,* 17657–17684, 1992.

Janickzek, P. M.(ed), Global Positioning System, papers published in Navigation,

reprinted by the institute of Navigation, Washington D.C., Vol I 1980, Vol II 1984, Vol III, 1986.

Jongsma, D., A marine geophysical study of the Hellenic arc, Ph.D. thesis, University of Cambridge, 1975.

Kasapoğlu, K. E., and M. N. Toksöz, Tectonic consequences of the collision of the Arabian and Eurasian plates: finite element models, *Tectonophysics, 100,* 71–95, 1983.

King, R. W., and Y. Bock, Documentation for the M.I.T. GPS analysis Software: GAMIT, Release 8.2, Massachusetts Institute of Technology, 1991.

King, R.W., J. Collins, E.M. Masters, C. Rizos, and A. Stolz, Surveying with GPS, Monograph No. 9, School of Surveying, The University of New South Wales, Kensington, N.S.W., Australia, 132 pp., 1985.

Kiratzi, A. A., Rates of crustal deformation in the North Aegean trough-North Anatolian fault deduced from seismicity, *Pageoph,* 136, 1991.

Kiratzi, A. A., and C. A. Langston, Moment tensor inversion of the 1983 January 17 Keffalinia event of Ionian islands, (Greece), *Geophys. J. Int., 105,* 529–535, 1991.

Kissel C., and C. Laj, The Tertiary geodynamical evolution of the Aegean arc: a paleomagnetic construction, *Tectonophys., 146,* 183–201, 1988.

Kissel C., C. Laj, A. Poisson, and K. Simeakis, A pattern of block rotations in central Aegea, *in Paleomagnetic Rotations and COntinental Deformation*, edited by Kissel C. and C. Laj, 115–129, Kluwer Academic Publishers, Boston, 1989.

Koçyiğit, A., Tectonic setting of the Gölova basin; total offset of the North Anatolian fault zone, E Pontide, Turkey,*Annales Tectonicæ, 4,* 155–170, 1990.

Le Pichon, X., and J.-M. Gaulier, The rotation of Arabia and the Levant fault system, *Tectonophys., 153,* 271–294, 1991.

Le Pichon, X., N. Chamot-Rooke, P. Huchon, and P. Luxey, Implications des nouvelles mesures de géodésie spatiale en Grèce et en Turquie sur l'éxtrusion latérale de l'Anatolie et de l'Egée, (in press), 1993.

Le Pichon, X., and J. Angelier, The Hellenic arc and trench system: a key to the neotectonic evolution of the eastern Mediterranean area, *Tectonophys., 60,* 1–41,

1979.

Le Pichon, X., J. Francheteau, and J. Bonnin, Plate tectonics, Elsevier, New York, 311 pp., 1976.

Lewis G., K. Hurst, K. Kastens, D. Paradissis, G. Veis, H. Billiris, W. Höppe, and W. Schlüter, ,First results from the Aegean GPS network, EOS, 73, 107, 1993.

Lort, J., Geophysics of the Mediterranean Sea Basins, in *The Ocean Basins and Margins,* edited by A.E.M. Nairn, W.H. Kanes, and F.G. Stehli, Plenum Press, New York, 151–213, 1978.

Lyberis, N., Tectonic evolution of the North Aegean trough, in *The Geological Evolution of Eastern Mediterranean, Spec. Publ.,* edited by J. G. Dixon and A. H. F. Robertson, 711–725, Geological Society of London, 1984.

Makris, J., and C. Stöbbe, Physical properties and state of the crust and upper mantle of the Eastern Mediterranean Sea deduced from geophysical data, *Marine Geology, 55,* 347–363, 1984.

Malvern, L. E., Introduction to the mechanics of a Continuous Medium, Prentice Hall, New Jersey, USA, 713 pp., 1969.

McKenzie, D.P., Plate tectonics of the Mediterranean region, *Nature, 226,* 239–243, 1970.

McKenzie, D.P., Active tectonics of the Mediterranean region, *Geophys. J.R. astr. Soc., 30,* 109–185, 1972.

McKenzie, D.P., The East Anatolian fault: a major structure in eastern Turkey,

McKenzie, D.P., Can plate tectonics describe continental deformation, in International symposium on the structural history of the Mediterranean Basins, Split (Yugoslavia), 25–29 October 1976, edited by B. Biju-Duval, and L. Montadert, Editions Technip, Paris, 189–196, 1977.

McKenzie, D.P., Active tectonics of the Alpine-Himalayan belt: the Aegean Sea and surrounding regions, *Geophys. J.R. astr. Soc., 55,* 217–254, 1978.

Menke, W., Geophysical Data Analysis: Discrete Inverse Theory, Academic Press, Inc., New York, 260 pp., 1984.

Meulenkamp, J. E., M. J. R. Wortel, W. A. Van Spakman, W., M. J. R. Wortel, and N. J. Vlaar, The Hellenic subduction zone: A tomographic image and its geodynamic implications, *Geophys. Res. Lett., 15,* 60-63, 1988.

Minster, J. B., and T. H. Jordan, Present-day plate motions, *J. Geophys. Res., 83,* 5331–5354, 1978.

Molnar, P., Brace-Goetze strength profiles, the partitioning of strike-slip and thrust faulting at convergent zones of oblique convergence, and the stress-heat flow paradox of the San Andreas fault, in *Fault Mechanics and Transport of Rocks, A fetsschrift in Honor of W F. Brace*, edited by B. Evans and T.F. Wong, 435–459, 1992.

Morelli, C., Eastern Mediterranean: Geophysical results and implications, *Tectonophys., 46,* 333–346, 1978.

Mueller, S., and H.-G. Kahle, Crust-mantle evolution, structure and Dynamics of the Mediterranean-Alpine Region, in *Contributions of Space Geodesy to Geodynamics: Crustal Dynamics*, edited by D. E. Smith and D. L. Turcotte, 249–298, American Geophysical Union, Washington, DC, 1993.

Murray, M.H., Global Positioning System measurement of crustal deformation in Central California, Ph.D. thesis, Massachusetts Institute of Technology, 310 pp., 1991.

Nishigami, K., Y. Ioi, C. Gürbüz, A. Pınar, N. Aybey, S. B. Üçer, Y. Honkura, and A. M. İsıkara, Microseimic activity and spatial distribution of Coda-Q in the westernmost part of the North Anatolian fault zone, Turkey, in *Multidiciplinary Research on Fault Activity in the western part of the North Anatolian fault Zone(3)*, edited by Y. Honkura and A. M. İsıkara, Tokyo Institute of Technology, 56–78, 1990.

Noomen, R., B. A. C. Ambrosius, and K. F. Wakker, Crustal motions in the Mediterranean region determined from laser ranging to LAGEOS, in *Contributions of Space Geodesy to Geodynamics: Crustal Dynamics,* edited by D. E. Smith and D. L. Turcotte, American Geophysical Union, Washington, DC, 331–346, 1993.

Oral, M. B., et al., Crustal thickness beneath Turkey, in preparation, 1994.

Oral, M. B., R.E. Reilinger, M. N. Toksöz, A. A. Barka and I. Kınık, Preliminary Results of 1988 and 1990 GPS Measurements in Western Turkey and their Tectonic Implications in *Contributions of Space Geodesy to Geodynamics: Crustal Dynamics*, edited by D. E. Smith and D. L. Turcotte, 407–416, American Geophysical Union,

Washington, DC, 1993.

Oral, M. B., M.N. Toksöz, and R.E. Reilinger, GPS measurements and finite element modeling of present-day tectonic deformations in the Eastern Mediterranean (abstract), AGU Chapman Conference, Time Dependent Positioning: Modeling Crustal Deformation (Sept. 23–25, 1991, Annapolis, MD), 1991.

Oral, M. B., Some Remarks on the Gravity Anomalies in Western Turkey and Its Implications of Crustal Structure, M.S. Th., Istanbul Technical University, 200 pp., 1987.

Papazachos, C. B., A. A. Kiratzi, and B.C. Papazachos, Rates of active Crustal deformation in the Aegean and the surrounding area, *J. Geodynamics, 16,* 147–179, 1992.

Papazachos, B.C., and P.E. Comminakis, Deep structure and tectonics of the Eastern Mediterranean, *Tectonophys., 46,* 285–296, 1978.

Pavlides, S., D. Mountrakis, A. Killias, and M. Tranos, The role of strike-slip movements in the extensional area of the northern Aegean (Greece). A case study of transtensional tectonics, *Annales Tectonicæ, 4,* 196–211, 1990.

Perinçek, D., and İ. Çemen, The structural relationship between the East Anatolian and Dead Sea fault zones in southeastern Turkey, *Tectonophys., 172,* 331–340, 1990.

Philip H., A. Cisternas, A. Gviskiani, and A. Gorshkov, The Caucasus: an actual example of the initial stages of continental collision, *Tectonophys., 161,* 1–21, 1989.

Roberts, D., M. B. Oral, R. W. King, R. E. Reilinger, M. Hamburger, and M. Prilepin, Report on the Caucasia Global Posisiting Sysyem experiment short-term solutions, unpubl. report, Dept. of Geomatics, The University of Calgary, Calgary, Alberta, CA, 35 pp., 1993.

Reigber, Ch., P. Schwintzer, F.-H. Massmann, Ch. Foerste, and H. Drewes, Ten years of SLR data analysis at DGFI/I, in *Contributions of Space Geodesy to Geodynamics: Crustal Dynamics*, edited by D. E. Smith and D. L. Turcotte, 359–369, American Geophysical Union, Washington, DC, 1993.

Reinhart, E., P. Wilson, L. Aardom, and E. Vermaat, The WEGENER Mediterranean Laser Tracking Project WEGENER-MEDLAS, CSTG Bulletin No. 8, Munich, F. R. G., 1985.

Rotstein, Y., Counterclockwise rotation of the Anatolian block, *Tectonophys.,* 108, 71–92, 1984.

Robertson A. H. F., and J. G. Dixon, Introduction: aspects of the geological evolution of the Eastern Mediterranean, *Geol. Soc. London, Spec. Publ.,* 1–74, 1984

Royden L., and B. C. Burchfiel, Are systematic variations in thrust belts style related to plate boundary processes? (Western Alps versus the Carpathians), *Tectonics, 8,* 51–61, 1989.

Royden, L., The tectonic expression of slab pull at continental convergent boundaries, *Tectonics, 12,* 303–325, 1993a.

Royden, L., Evolution of retreating subduction boundaries formed during continental collision, *Tectonics, 12,* 629–638, 1993b.

Saastamoinen, J., Atmospheric correction for the troposphere and stratosphere in radio ranging satellites, in *The Use of Artificial Satellites for Geodesy Geophys. Monogr. Ser., 15,* edited by S.W. Henriksen, A. Mancini and B. H. Chowitz, 247–251, AGU, Washington D.C., 1972.

Şaroğlu F., and Y. Yılmaz, Geology of Karlıova region: Intersection of the North Anatolian and East Anatolian transform faults, Bull. Tech. Univ. Ist., 44, 475–493, 1991.

Scholz, C. H., The mechanics of earthquake faulting, Cambridge University Press, Cambridge, U.S.A, 439 pp., 1990.

Seeber, G., Satellite Geodesy: Foundations, Methods, and Applications, Walter de Gruyter, Berlin, New York, 531 pp., 1993.

Snyder, D., and M. Barazangi, Deep crustal structure and flexure of the Arabian plate beneath Zagros collisional mountain, belts as inferred from gravity observations, *Tectonics, 5,* 361–373,1986.

Şengör, A. M. C., and Y. Yılmaz, Tethyan evolution of Turkey: A plate tectonic approach, *Tectonophys., 75,* 181–241, 1981.

Şengör, A. M. C., Tectonics of the Tethysides: Orogenic collage development in a collisional setting, *Ann. Rev. Earth Planet. Sci., 15,* 213–244, 1987a.

Şengör, A. M. C., Cross faults and differential stretching of hanging wall in regions

of low-angle normal faulting: examples from western Turkey, 1987b.

Şengör, A. M. C., The North Anatolian transform Fault: Its age, offset and tectonic significance, *J. Geol. Soc. Lond., 136,* 269–282, 1979.

Şengör, A. M. C., N. Görür, and F. Şaroğlu, Strike-slip faulting and related basin formation in zones of tectonic escape: Turkey as a case study, in *Strike-slip Faulting and Basin Formation,* edited by K.T. Biddle and N. Christie-Blick, *Society of Econ. Paleont. Min. Sec. Pub., 37,* 1985.

Seyitoğlu, G. and B. Scott, Late Cenozoic crustal extension and basin formation in west Turkey, *Geol. Mag.,* 128, 155-166, 1991.

Seyitoğlu , G. and B. Scott, The age of the Büyük Menderes graben (west Turkey) and its tectonic implications, *Geol. Mag.,* 129, 239–242, 1992.

Spakman, W., M. J. R. Wortel, and N. J. Vlaar, The Hellenic subduction zone: A tomographic image and its geodynamic implications, *Geophys. Res. Lett. 15,* 60-63, 1988.

Spakman, W., Tomographic mapping of the upper mantle structure beneath the Alpine collision belt. in *Crust/Mantle Recycling in Convergent Zones,* edited by S. R. Hart and L. Gülen, NATO ASI series, C258, Kluwer Academic Publ., Dordrech, 163–172, 1989.

Taymaz, T., J. Jackson, and D. P. McKenzie, Active tectonics of the north and central Aegean Sea, *Geophys. J. Int., 106,* 433-490, 1991a.

Taymaz, T., H. Eyidoğan, and J. Jackson, Source parameters of large earthquakes in the East Anatolian fault zone (Turkey), *Geophys. J. Int., 106,* 537–550, 1991b.

Tutkun S. Z. and P. L. Hancock,Tectonic landforms expressing strain at the Karlıova continental triple junction (E Turkey), *Annales Tectonicæ, 4,* 182–195, 1990.

Uğur, E., Recent crustal movements in the Gerede-Çerkeş region of the North Anatolian fault zone by geodetic methods, Ph.D. Thesis, Istanbul Technical University, Istanbul, Turkey, 1974.

Wilson, P. and E. Reinhart, The Wegener-Medlas project: Preliminary results on the determination of the geokinematics of the eastern Mediterranean, in *Contributions of Space Geodesy to Geodynamics: Crustal Dynamics,* edited by D. E. Smith and D. L. Turcotte, 299–309, American Geophysical Union, Washington, DC, 1993.

Watson, D. F., ACORD: Automatic counturing of raw data, *Comput. Geosci.,* 8, 97–101, 1982.

Wdowinski, S., R. J. O'Connell, and P. England, A continuum model of continental deformation above subduction zones: Application to the Andes and the Aegean, *J. Geophys. R., 94,* 103311–10346, 1989.

Wernicke, B., Low-angle Normal faults in the Basin and Range province, *Nature,* 291, 645–648, 1981.

Wernicke, B., Uniform-sense normal shear of the continental lithosphere, *Can. Jour. Earth Sci.,* 22, 108–125, 1985.

Wessel, P., and W. H. F. Smith, Free software helps map and display data, *Eos. Trans. AGU, 72,* 441, 1991.

Westaway, R., Block rotations in western Turkey, 1. Observational evidence, *J. Geophys. R., 95,* 19857–19884, 1990.

Van der Berg, J., and H. Zijderveld, Paleomagnetism in the Mediterranean Area, in Alpine-Mediterranean Geodynamics, (eds) H. Berckhemer and K.Hsü, Geodynamics series, 7, 83–112, 1982